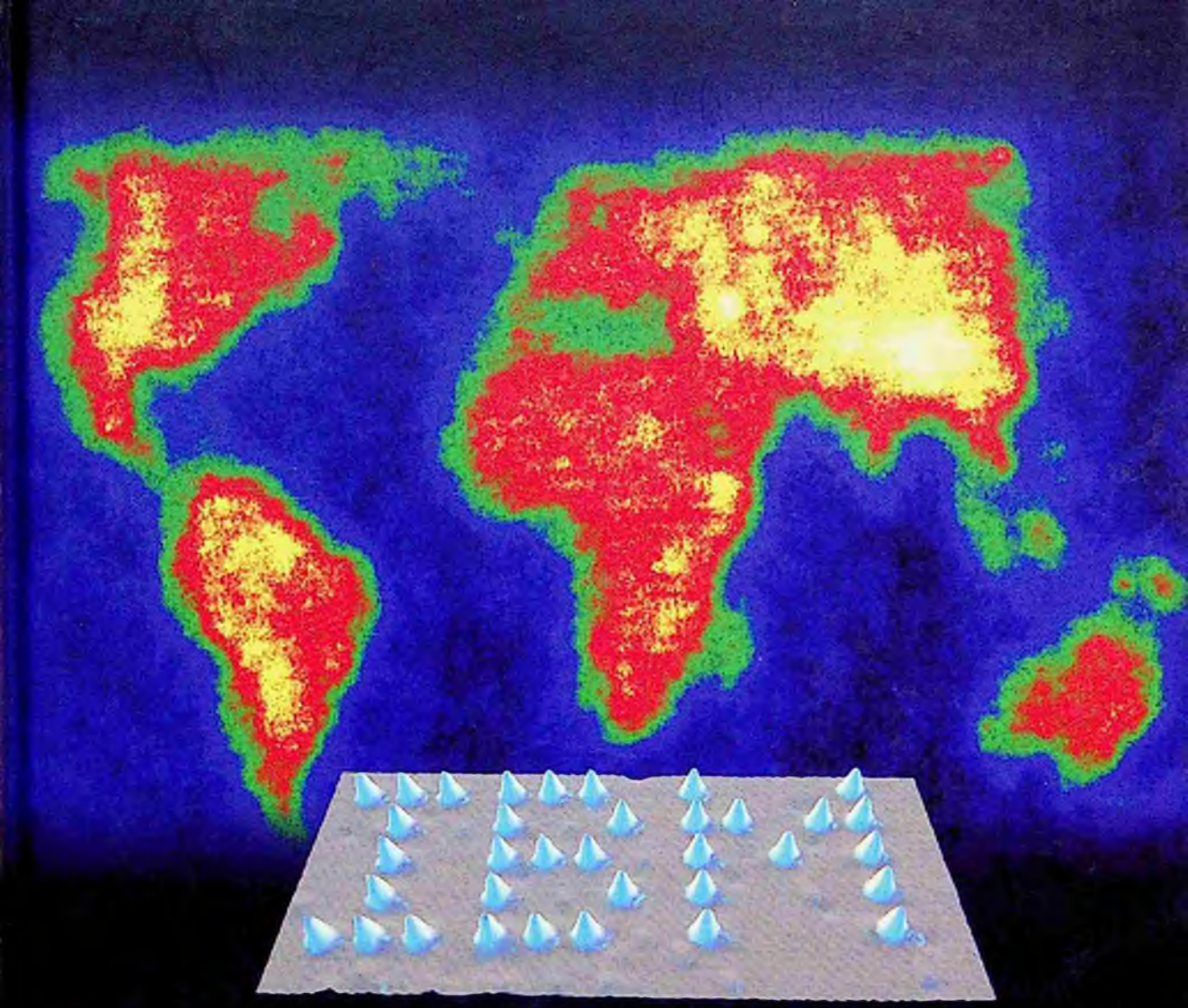

Nanofabrication

Fundamentals and Applications

Ampere A Tseng *Editor*

World Scientific

Nanofabrication
Fundamentals and Applications

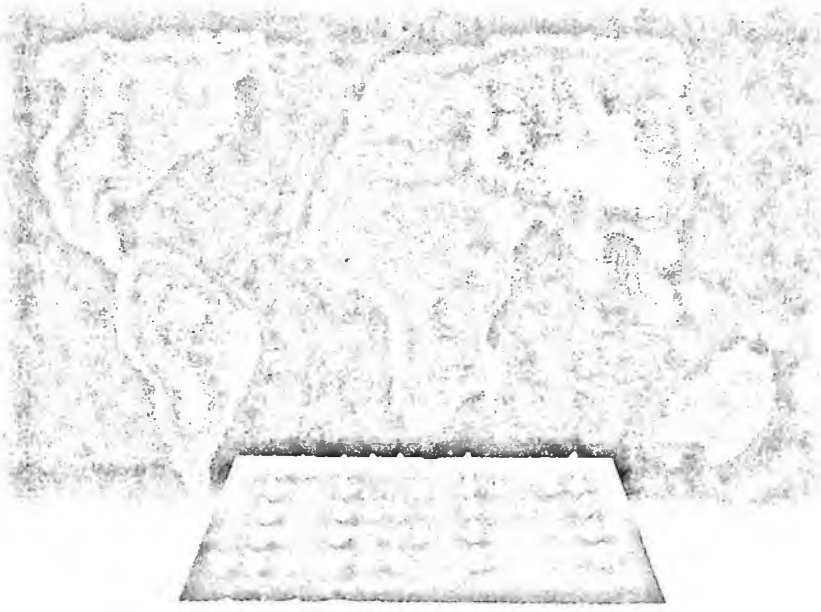

Nanofabrication

Fundamentals and Applications

Editor

Ampere A Tseng

Arizona State University, USA

World Scientific

NEW JERSEY · LONDON · SINGAPORE · BEIJING · SHANGHAI · HONG KONG · TAIPEI · CHENNAI

Published by

World Scientific Publishing Co. Pte. Ltd.

5 Toh Tuck Link, Singapore 596224

USA office: 27 Warren Street, Suite 401-402, Hackensack, NJ 07601

UK office: 57 Shelton Street, Covent Garden, London WC2H 9HE

British Library Cataloguing-in-Publication Data
A catalogue record for this book is available from the British Library.

NANOFABRICATION
Fundamentals and Applications

ISBN-13 978-981-270-076-6
ISBN-10 981-270-076-5
ISBN-13 978-981-270-542-6 (pbk)
ISBN-10 981-270-542-2 (pbk)

Typeset by Stallion Press
Email: enquiries@stallionpress.com

Printed by Fulsland Offset Printing (S) Pte Ltd, Singapore

CONTENTS

Preface		vii
Chapter 1	Atom, Molecule, and Nanocluster Manipulations for Nanostructure Fabrication Using Scanning Probe Microscopy	1
	A. A. Tseng, S. D. Sartale, M. F. Luo, and C. C. Kuo	
Chapter 2	Atomic Force Microscope Lithography	33
	N. Kawasegi, D. W. Lee, N. Morita, and J. W. Park	
Chapter 3	Scanning Probe Arrays for Nanoscale Imaging, Sensing, and Modification	65
	C. Santschi, J. Polesel-Maris, J. Brugger, and H. Heinzelmann	
Chapter 4	Using Biomolecules for Self-Assembly of Engineered Nano-Scale Structures and Devices	127
	R. Mehta, J. Lund, and B. A. Parviz	
Chapter 5	Nanofabrication Based on Self-Assembled Alumina Templates	159
	S. Sen and N. A. Kouklin	
Chapter 6	Nanowire Assembly and Integration	187
	Z. Gu and D. H. Gracias	

Chapter 7 Taper-Drawing Fabrication of Glass Nanowires 213
L. Tong and E. Mazur

Chapter 8 Extreme Ultraviolet Lithography 235
H. Kinoshita

Chapter 9 Electron Projection Lithography 285
T. Miura, K. Suzuki, H. Arimoto, and S. Kawata

Chapter 10 Electron Beam Direct Writing 341
K. Yamazaki

Chapter 11 Electron Beam Induced Deposition 377
K. Mitsuishi

Chapter 12 High-Resolution Electron-Beam-Induced Deposition 399
P. A. Crozier and C. W. Hagen

Chapter 13 Focused Ion Beams and Interaction with Solids 431
T. Ishitani, T. Ohnishi, and T. Yaguchi

Chapter 14 Nano/Microstructuring of Ceramic Surfaces by Unconventional Lithographic Methods 471
R. C. Salvarezza and O. Azzaroni

Chapter 15 Alternative Nanofabrication Approaches for Non-CMOS Applications 499
C. V. Cojocaru, F. Cicoira, and F. Rosei

Chapter 16 Nanofabrication of Nanoelectromechanical Systems (NEMS): Emerging Techniques 543
K. L. Ekinci and J. Brugger

Index 567

PREFACE

Many of the devices and systems used in modern industry are becoming progressively smaller and have reached the nanoscale domain. Nanofabrication aims at building nanoscale structures, which can act as components, devices, or systems, in large quantities at potentially low cost. Nanofabrication is vital to all nanotechnology fields, especially for the realization of nanotechnology involving traditional areas across engineering and science. This is the first book of its kind dedicated solely to examining the manufacturing technology of nanoscale structures, devices, and systems, and is designed to satisfy the growing demands of researchers, professionals, and graduate students. In this monograph, both bottom-up and top-down fabrication technologies are introduced, with an emphasis on multidisciplinary principles, methodologies, and practical applications.

Bottom-up fabrication strategies involve manipulation or synthetic methods of biochemistry in directly assembling subnanoscale building blocks, such as atomic, molecular, and supramolecular elements, into required nanoscale patterns, of which bio-medical, chemical, and physical sensors and actuators are obvious applications. More ambitious is work in large-scale molecular electronics and computers, aimed at constructing circuitry in which individual atomic or molecular parts serve as wires and transistors. However, performing only one atomic or molecular reaction at a time using non-molecular machines, such as scanning probe microscopes, is impractical for making large quantities of a product. It appears that whether the strategy is manipulation, chemical synthesis, or self-assembly, the fabrication must occur in parallel or in arrays to self-form groups of atoms or molecules fast enough to produce useful structures of macroscopic size. Six chapters in this monograph are primarily devoted to examining recent developments in bottom-up approaches.

The top-down strategies have basically evolved from conventional lithographic techniques, in which nanoscale structures or semiconductor chips are fabricated from a bulk material by gradually removing or subtracting bits of the material in series. A key difference from the bottom-up approach is that, in the top-down approach, the parts or chips are both patterned and built in place, so that no assembly step is needed. The top-down approach has been proven to be a critical tool for the sustained evolution of the electronic, computer, photonic, and microsystem industries. However, there continue to be many obstacles and challenges that confront top-down

techniques as these techniques approach their fundamental size limits. Accordingly, I have included ten chapters in this book mainly to address these obstacles and challenges.

Eventually, the most promising strategy for the development of nanofabrication processes in large quantities will a hybrid approach, a combination of the bottom-up and conventional top-down techniques, and an integration of biological and chemical nanoelements in future devices. For example, through the use of the conventional lift-off technique, biological molecules, such as proteins and immunoglobulins with sizes of a few nanometers, have been immobilized in thin-patterned films. In fact, several chapters of this book involve the hybrid strategy.

Each chapter in this volume has been authored by well-known researchers, to whom I am grateful for their contributions. I am also indebted to a large number of reviewers, whose critical reviews have ensured that each chapter is of the highest quality. I would also like to thank Dr. Walt Trybula of Sematech for his advice in editing this book. Finally, I hope that readers will find this book both stimulating and useful.

Ampere A. Tseng
Arizona State University
Tempe, Arizona USA
January 2007

CHAPTER 1

ATOM, MOLECULE, AND NANOCLUSTER MANIPULATIONS FOR NANOSTRUCTURE FABRICATION USING SCANNING PROBE MICROSCOPY

AMPERE A. TSENG

Department of Mechanical and Aerospace Engineering,
Arizona State University,
Tempe, Arizona 85287-6106, USA

S. D. SARTALE and M. F. LUO*

Department of Physics, National Central University,
Chungli, Taiwan, 32001, ROC

C. C. KUO

Department of Physics, National Sun Yat-Sen University,
Kaohsiung, Taiwan, 804, ROC

Over the last decade, scanning probe microscopy (SPM), including scanning tunneling microscopy (STM) and atomic force microscopy (AFM), has become a powerful manipulation technique by virtue of its ability to interact with individual adsorbed nanoparticles with nanoscale precision on the surface. In this article, the principles, procedures and applications of both STM and AFM-based technologies for manipulation of atoms, molecules, and nanoclusters are reviewed with an emphasis on their ability to create a wide variety of nanostructures. In the manipulation of single atoms and molecules, the interaction among the atoms/molecules, surface, and tip are specifically discussed first. The approach for positioning the atom/molecule from and to the desired locations and precisely controlling its movement is also elaborated for each specific manipulation technique. The applications of these techniques for fabricating different nanostructures and nanosystems are then presented. In the manipulation of nanoclusters, different nanocluster-substrate pairs in different environments with their potential applications in electronics, biology, and medicine are specifically evaluated. Finally, concluding remarks are provided, where the scopes for technological improvement and future research are recommended.

*Corresponding author: Department of Physics, National Central University, Chungli, Taiwan 32001, ROC; mfl28@fermi.phy.ncu.edu.tw

Keywords: Atom; atomic force microscopy; manipulation; molecules; scanning probe microscopy; scanning tunneling microscopy; and nanocluster.

CONTENTS

1. Introduction 2
2. Manipulation by Scanning Tunneling Microscope (STM) 3
   2.1. Manipulation of Atoms by STM 6
   2.2. Manipulation of Molecules by STM 9
   2.3. Manipulation of Nanoclusters by STM 12
3. Manipulation by Atomic Force Microscope (AFM) 19
   3.1. Manipulation of Single Atoms by AFM 20
   3.2. Manipulation of Single Molecules by AFM 21
   3.3. Manipulation of Nanoclusters by AFM 22
4. Concluding Remarks 26
Acknowledgments 27
References 27

1. Introduction

Many of the devices and systems used in modern industry are becoming progressively smaller and have reached the scale of nanometers. Nanofabrication is playing an ever increasing role in building these devices and systems as well as understanding the associated characteristics and functionality at the nanoscale. In general, nanofabrication consists of two major approaches: top-down high-resolution and bottom-up directed building processes [1]. The top-down approach has evolved from the conventional lithographic technology, which is the de facto standard used in the semiconductor industry. This approach takes a bulk material, and modifies or breaks it into smaller desired structures and normally involves removing or etching out (sometimes with forming or adding) some materials to make the final ones. As an alternative to the top-down approach, interest has shifted to the bottom-up approach, in which the materials of atom or molecular scales serve as building blocks, for next generation nanoscale devices and systems.

The ultimate bottom-up approach to nanofabrication is the precise control over single atoms and nanoscale particles for the formation of nanostructures, also known as nano-manipulation. In the past decade, scanning probe microscopes (SPM), or more precisely, scanning tunneling microscopy (STM)-based technology has become an increasingly popular tool for manipulating matter at the atomic and molecular level because the tunneling current involved can selectively break chemical bonds and/or induce chemical association among the atoms. Originally, SPM has been used to gain knowledge of surface morphology and molecular organization in the fields

of physics, chemistry, and biology. Currently, SPM has enjoyed widespread acceptance in many areas of nanotechnology, including surface imaging, metrology, spectroscopy and lithography [2, 3]. In this article, an overview of recent developments in the SPM technology for the manipulation of atoms, molecules, and nanoclusters is presented, focusing on its ability in creating a wide variety of nanostructures. Here, a nanocluster is a cluster of atoms or molecules whose characteristic dimensions are a few nanometers. On one side, it overlaps with the structure of nanocrystal, and with (macro)molecule on the other end. Nanoclusters are typically smaller structures than nanocrystals and are important building blocks for functional materials and devices.

SPM-based manipulation involves two major techniques: scanning tunneling microscopy (STM) and atomic force microscopy (AFM). The principles and approaches of each technique are introduced and evaluated separately with emphasis on their abilities, efficiencies, and reliabilities to engineer structures with nanometer resolutions. The nanostructures made by different techniques are specifically presented in order to illustrate the versatility and advancement of these SPM-based techniques. The major variances as well as the associated strengths and weaknesses for the different techniques evaluated are examined. The potential applications for specific techniques and the uniqueness of the fabricated nanostructures are also discussed. Finally, prospective developments and research focuses for SPM-based techniques are presented.

In general, AFM is less restrictive than STM, because AFM can be performed in a normal room environment and can be used to image any kind of material. However, because the underlying principle and configuration of each technique are different, STM can be controlled at higher resolutions with a lower scanning speed while AFM can have higher speeds but lower resolutions. As a result, STM has the ability to manipulate single atoms with sizes at a subnanometer level, while AFM is normally used to manipulate particles, including macromolecules and nanoclusters with sizes ranging between 10 and 100 nm. In addition to manipulation, both STM and AFM have been used for material modification (including resist exposure), material addition (mainly induced deposition), and material removal (including etching) at nanometer scales. Although these applications are important in nanofabrication, they are beyond the scope of this article. The details of these applications can be found in recent review articles by Tseng, Notargiacomo and Chen [2] and Tseng [4].

2. Manipulation by Scanning Tunneling Microscope (STM)

The first SPM was the STM invented in 1981 by Binnig *et al.* [5]. STM uses a sharpened conducting tip with a bias voltage applied between the tip and the target sample. When the tip is within the atomic range ($\sim$1 nm) of the sample, electrons from the sample begin to tunnel through the gap to the tip or vice versa, depending

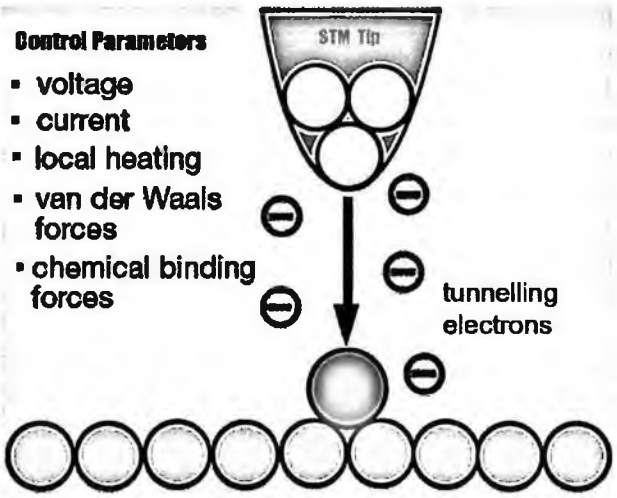

Figure 1. Schematic of controlling parameters between tip and adparticle on the surface in scanning tunneling microscopy (STM).

on the sign of the bias voltage as shown in Fig. 1. The exponential dependence of the distance between the tip and target gives STM its remarkable sensitivity with sub-angstrom precision vertically and sub-nanometer resolution laterally. Two basic modes of operation, known as constant height and constant current modes are usually used for imaging. In the constant height mode, the tip travels in a horizontal plane above the sample. The induced tunneling current, which depends on topography and the electronic properties of the local surface, constitutes the STM image. In a constant current mode, the tip height is adjusted by feedback signals to keep the tunneling current constant during scanning, and the variation of the tip height represents the image.

In operating STM, the tip will approach the sample surface until the set-point current is reached (at a given bias voltage). An adsorbed atom, molecule or nanocluster, which is hereafter referred as an adparticle, is held on the surface by chemical bonds with the surface atoms. In an imaging mode, the distance between the tip apex atom(s) and adparticle is far enough such that any forces between them are negligible as compared to the forces binding the adparticle with the surface, and the adparticle is not disturbed by the passage of the tip over it. However, if the tip-adparticle distance is gradually decreased, the tip-sample interaction changes from the conventional tunneling regime to the electronic-contact regime and then to the mechanical-contact regime [6, 7]. In the manipulation mode, the tip is in close proximity of the surface such that the adparticle bonds to the tip as shown in Figs. 2(a) or 3(a). It implies that by varying the distance between the STM tip and the sample, a force may be exerted on the nanoparticle adsorbed on the surface. A controlled manipulation experiment can thus be performed by lowering the tip towards the target adparticle to enhance the tip-adparticle interaction to overcome

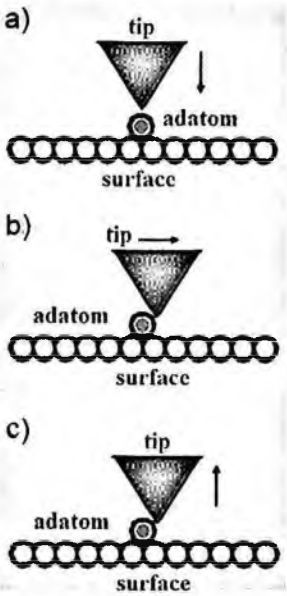

Figure 2. Schematic of lateral manipulation (LM), in which adatom remains bound to surface and pushed or dragged by STM tip: (a) pulling where adatom discontinuously follows tip from one adsorption site to another due to attractive forces, (b) sliding where adatom is trapped under tip and follows its motion instantaneously and continuously, (c) tip is retracted at desired place.

the forces between the adparticle and the surface. By adjusting the tip position and reducing bias voltage, and/or increasing the tunneling current, it is possible to adjust the magnitude and direction of the force, so that the tip can either push or drag an adparticle across a surface while the adparticle remains bound to the surface (Fig. 2(b)). This process is known as lateral manipulation (LM), normally defined in terms of pulling, sliding or pushing, depending on the type of interaction that is used between the tip apex and adparticle (attractive for pulling and sliding and repulsive for pushing) [8]. As shown in Fig. 3, the adparticle can also be picked up by the tip and relocated to another position with the assistance of the electric fields from the STM tip to increase or reduce the tip-adparticle interaction. This process is called vertical manipulation (VM). At any point in the scan after such an operation, the tip can be retracted to the imaging distance by resetting the bias voltage and/or set point current to the imaging values, which thereby terminates the attractive interaction between the adparticle and the tip as shown in Figs. 2(c) and 3(c). These two manipulations require extremely fine control of the local interactions among the tip, adparticle, and surface. In general, it requires less force to move an adparticle along the surface by lateral manipulation than to pull it away from the surface using vertical manipulation. A schematic description of these interactions and the controlling parameters involved are also illustrated in Fig. 1.

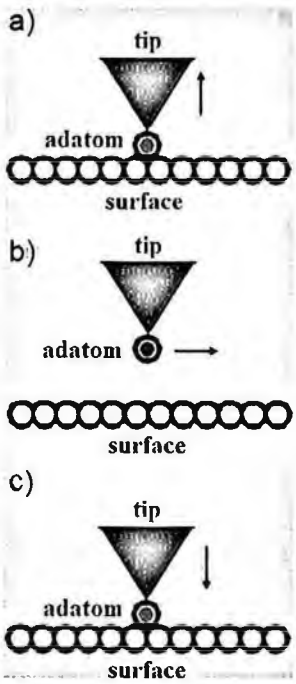

Figure 3. Schematic of steps in vertical manipulation (VM), in which adatom is transferred from surface to STM tip and back to surface: (a) tip picking adatom from adsorption site and adatom dissociation occurring, (b) tip lifting adatom from surface and moving to desired place due to attractive forces, (c) tip with adatom is loaded at desired site.

2.1. *Manipulation of Atoms by STM*

The first pioneering work demonstrating the ability of positioning single atoms on a metallic surface was conducted in 1990 by Eigler and Schweizer [9] with an STM. An STM with a W-tip was used to arrange Xe atoms adsorbed in a company logo of "IBM" on a single Ni (111) surface, as shown in Fig. 4. Experiments are typically conducted using an STM at low temperatures under UHV (ultrahigh vacuum, less than 10^{-9} torr) conditions. After careful cleaning of the sample surface, the construction of quantum structures can be achieved by an atom-by-atom relocation on the surface. The lateral manipulation is adopted and performed by moving the probe in a constant current mode. Given the close distance, the tip is almost in mechanical contact with the atom, and the proximity nature of the tip-atom interaction is the main driving force. The atom is left at the desired final location by retracting the tip to the original imaging height achieved by exploiting atomic resolution STM images of the surface as shown in Fig. 2.

Several different geometrical configurations of atoms have been achieved and the clear interference effect of electron waves has been directly observed. Figure 5 shows the image of two Chinese characters for "atom" made of iron atoms on copper (111)

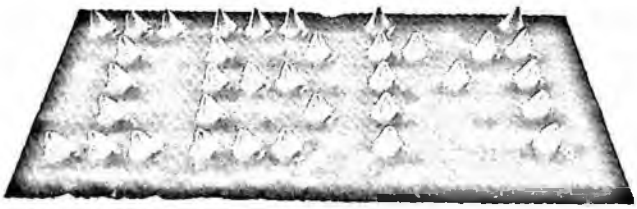

Figure 4. STM image of lateral manipulation of xenon atoms on nickel(110) surface by STM in writing company logo of "IBM" (courtesy of IBM Research, Almaden Research Center).

Figure 5. STM image of atomic manipulation of iron atoms on copper(111) surface in writing Chinese characters for "atom" by C. P. Lutz and D. M. Eigler, to which the literal translation is something like "original child" (courtesy of IBM Research, Almaden Research Center).

surface by D. M. Eigler and C. P. Lutz of IBM. As indicated by Crommie, Lutz, and Eigler [10], the ripples around the characters are the standing-wave patterns in the local density of states of the Cu (111) surface. Recent instrumentation development of STMs for low temperature operations can be found from Libioulle *et al.* [11] and Foley *et al.* [12].

In vertical manipulation, the ability of picking an adatom from and releasing it back to the substrate surface, i.e., the direction of transferring atoms between the tip and the substrate surface is critical. Eigler, Lutz, and Rudge [13] found that the direction of transferring Xe atoms between the tip and the substrate surface is the same as that of the tunneling electrons and the corresponding atom transfer

rate is a power-law function of the tunneling current (I). For the specific experiment conditions considered, i.e., the voltage (V) ranges from 18–180 mV with a tunneling junction such that $V/I = 906\ k\Omega \pm 2\%$, and the transfer rate varies $I^{4.9\pm0.2}$. Lyo and Avouris [14] have also shown that voltage pulses can be used for vertical manipulation by extracting atoms from a Si(111) surface to the tunneling tip and then depositing them elsewhere using an opposite polarity pulse. They noted that the atom motion was in the same direction as the electron motion. Later, Shen *et al.* [15] also observed that the transfer of atomic H to Si surfaces at relatively low voltages is strongly power-law dependent. This reversible field (electron)-induced transfer of a single atom is also known as the Eigler switch [16]. This transfer phenomenon has been studied theoretically by many investigators [16, 17, 18]. Basically, the atom transfer in Eigler switch can be viewed as a potential-barrier crossing problem between the potential wells formed by the interaction of the atom with the tip and the sample, respectively. The main mechanism behind the transfer is that the current excites the atom vibrationally in the double-well potential, sustained by the van der Waals attraction to surface and tip. The bond is broken by overcoming the potential barrier by gaining energy from the tunneling electrons. Also, the Xe atom dissipates energy to the surface phonons, so that the competition between the dissipation to surface phonons and the "heating" by inelastically tunneling electrons should be included in the mechanism. The theoretical predictions generally agree very well with the experimental findings, especially the bond-breaking rate being consistent with the power-law dependence transfer rate.

The electric-field driven vertical-manipulation mechanism has also been used by Salling and Lagally [19] to extract individual atoms from Si(100) surfaces to form nanometer scale rectangular pits. Later, using multiple vertical manipulations, Salling, Kravchenko, and Lagally [20] could write nanoscale trenches in Si (100) surfaces with a 2.4 nm resolution from Si films that are only three atomic-layers thick. Recently, by studying the dynamics of a single cobalt (Co) atom, Stroscio and Celotta [21] have concluded that, at low tunneling voltages (less than 5 meV), the transfer rate between sites is independent of tunneling voltage, current, and temperature. At higher voltages, the transfer rate exhibits a strong dependence on tunneling voltage, indicative of vibrational heating by inelastic electron scattering. Adatoms can not only be laterally manipulated from the surface sites, but also extracted or vertically manipulated from more strongly bound intrinsic sites to create atom-vacancy pair atoms. The differences between the forces involved in lateral and vertical manipulations have been analyzed by Pizzagalli and Baratoff [22].

Normally, stable nanostructures consisting of adsorbed atoms can only be created at low temperatures because the mobility of the adatom can be greatly reduced. Thus, the adatoms become controllable and atomic/molecular manipulation can be performed nearly frozen. The instrumental effects including piezo hysteresis and thermal drifting can also be minimized at low temperatures. For example, the typical 24-hr drift can be less than a few Å for temperatures at a few K, which is

a temperature achieved by cooling with liquid helium. Precision within a few Å is essential in single atom manipulation. However, it is possible to increase the working temperature, even up to room temperature, by using atoms embedded in the surface. Hasegawa and Avouris [23] have used the vertical manipulation of STM to observe the formation of standing wave patterns on Au (111) surfaces at room temperature. The oscillations are imaged from spectroscopic data or maps of $(dI/dV)(I/V)^{-1}$where I and V are the bias current and voltage, respectively, and found near step edges and atomic defects from which the electrons scatter. The 2D standing wave patterns observed are consistent with the oscillations predicted by solving the classic eigenvalue problem in quantum mechanics for a particle in a hard-wall box.

2.2. *Manipulation of Molecules by STM*

Similar to atoms, single molecules, starting with small molecules, such as CO, can be manipulated with an STM tip by managing the tip-adsorbate interaction force, by regulating the induced electric field, or by applying tunneling electrons from the tip. In the early experiments, only one type of manipulation is applied while in recent studies, multiple manipulations have been concurrently performed. The resulting chemical reactions on the molecules can be dissociation, diffusion, adsorption, and/or bond formation for creating molecule-based building blocks for patterning various nanostructures. Numerous experimental and theoretical studies have been reported to quantify these reactions. For example, Dujardin, Walkup, and Avouris [24] studied the dissociation of individual $B_{10}H_{14}$ molecules from an Si(111) surface using low-energy tunneling electrons from the tip in a vacuum chamber of 10^{-8} torr. They found that the probability for the dissociation increases from 0.1 to 0.8 as the applied bias voltage increases from 4 to 8 V with a current of 200 pA. Note that when electron energies higher than the work function of the tip (normally less than 3eV) are applied to the molecule, the tip acts as an electron emission source and the field emission induces the dissociation.

Stroscio and Eigler [25] and Zeppenfeld, Lutz, and Eigler [26] were the first group to study the lateral manipulation of CO molecules adsorbed on Pt(111) surfaces using cryogenic STM. CO molecules have also been laterally manipulated on various surfaces, including Cu(111) and Ag (110) [27]. As shown in Fig. 6, a nanoscale Brandenburg Gate is constructed with 48 CO-molecules regulated on a Cu(211) surface using lateral manipulation at 15 K [28]. At this temperature, the molecules can be sufficiently frozen so that a large number of them can be precisely moved to the desired location. Also the fabricated structure can remain stable for a relatively long time. However, in the lateral manipulation, CO molecules are usually pushed by the STM tip and moved discontinuously in front of the tip due to repulsive forces, while metal adatoms are usually dragged and slid. On close packed surfaces like Cu(111), pushing is not very reliable, as the molecules tend to move to the side

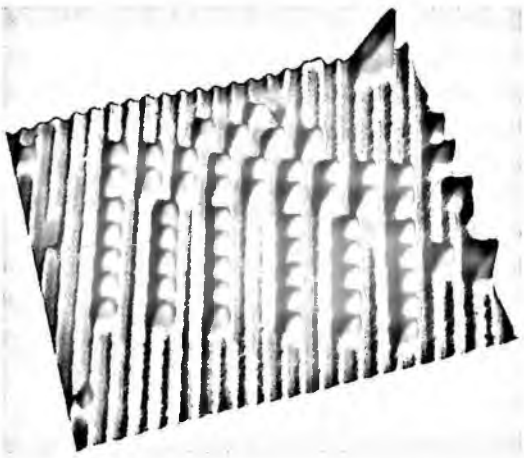

Figure 6. STM image of Brandenburg Gate-like nanostructure constructed on Cu(211) with 48 CO-molecules using lateral manipulation with cryogenic STM at 15 K (courtesy of Professor Karl-Heinz Rieder of Swiss Federal Laboratories for Materials Research, Duebendorf, Switzerland and Dr. Gerhard Meyer of IBM Zurich Research Laboratory, Rüschlikon, Switzerland).

of the tip and get lost. The successful creation of the nanostructure shown in Fig. 6 can be attributed to the proper choice of the orientation of the surface. As shown, the parallel "valleys" (from the top to the bottom in Fig. 6) of the Cu(211) surface can act as "railways", in which the CO adsorbed at the upper part of the intrinsic step edges can be pushed along the railway trails.

Jung *et al.* [29] applied lateral manipulation of bulky hydrocarbon molecules at room temperature. This hydrocarbon group can maintain sufficiently strong interactions with the surface to prevent thermally-activated diffusion at room temperature, but nevertheless allow controllable manipulation. Gimzewski and Joachim [30] have demonstrated that the manipulation of single molecules at room temperature is also feasible; they have exploited the strong interaction with the surface shown by macromolecules such as porphyrins. Furthermore, on the field of increasing the throughput and patterning speed, it is worth mentioning the "automated atom assembly" approach of Stroscio *et al.* [31] in which they performed bottom-up fabrication of nanostructures by providing the STM with computer-controlled capabilities of lateral displacements of atoms. Most manipulations are performed under the constant current mode, but the constant height modes have also been used for manipulation of complicated molecules [32].

In molecular manipulation, an interesting phenomenon called "molecule cascades" has been discovered. It is similar to a row of toppling dominoes. Heinrich *et al.* [33] arranged CO molecules on Cu (111) at low temperature in staggered chains of dimmers, where moving one molecule with the STM tip causes the subsequent motion or hopping of another, and so on. The hopping rate of CO molecules in cascades was found to be independent of temperature below 6 K and to exhibit a pronounced isotope effect, hallmarks of a quantum tunneling process. These molecule

cascades could have many potential applications. For example, logic gates and other devices can be implemented by engineered arrangements of molecules at the intersections of cascades. Heinrich *et al.* [33] have demonstrated that these molecule cascades could be arranged into logic circuits such as one-time logic AND gates and two- and three-input sorters which incorporate logic AND and OR functions.

In vertical manipulation, the molecular flipping during vertical transfer of CO molecules from a Cu surface to the tip has been studied by many investigators. As indicated by Ishi, Ohno and Viswanathan [34], CO stands upright on metal surfaces with the carbon atom binding to the substrate. As the CO molecules have a similar absorption geometry to isolated Cu atoms adsorbed on a Cu surface, the CO molecule turns around when being transferred up to the tip. This additional degree of freedom associated with CO molecules makes the vertical manipulation of CO more complicated and less predicable than that of single atoms. To have a predicable or reliable vertical manipulation procedure, Bartels, Meyer, and Rieder [35] have found that the tunneling voltage must be slowly ramped to zero and the tip-CO distance should be simultaneously reduced to compensate the decrease in the current. In vertical manipulation, Bartels, Meyer, and Rieder [35] reported that the pickup of a single CO molecule can be applied for enhancing the ability of the STM tip. The sharpness of the STM tip can be greatly increased by deliberately transferring a molecule (or atom) to the normally etched tip apex. Thus, the image contrast can be improved. Additionally, the molecule-(or atom-) attached tip can have better chemical contrasts in molecular recognition imaging. For example, a CO-attached tip can distinguish between the adsorbed CO molecules and oxygen atoms relatively easily, which look very similar to the bare etched metal tip. Furthermore, the pickup step in vertical manipulation can be used as a material removal process for making various molecular structures such as nanotrenches, mentioned in the section on manipulation of single atoms. Also, the loading step in vertical manipulation can act like a material addition process. Theoretically, a three-dimensional molecular assembly can be built step by step using either material removal or material addition processes. The vertical manipulation is also capable in transporting the molecules (or atoms) across substrate obstacles, which should be difficult to perform by lateral manipulation.

STM manipulation of atoms and molecules has been used to create various artificial structures at the nanoscale and these structures can be *in situ* characterized and modified by using the tunneling electron current for rotations, diffusional jumps, vibrational excitations, desorption, dissociation. As indicated by Rieder *et al.* [36], by tuning the voltage into the energy levels of specific vibrations or electronic levels, new opportunities for making molecular engines and switches become possible. Iancu, Deshpande, and Hla [37] found that two conformations of isolated single TBrPP-Co molecules on a Cu(111) surface can be manipulated or switched without altering their chemical composition by applying +2.2 V voltage pulses from a STM tip at 4.6 K. As a result, two different Kondo temperatures, which can act

as a molecular switch, are obtained by this single molecular switching mechanism. Grill and Moresco [38] have presented several examples of molecular wire-electrode systems, where single molecules are placed in contact in a controlled way. The associated electronic contact can be characterized using the additional contribution to the tunneling current, but also using the influence on the electronic states of the electrode and the molecule. Changed chemical structures of the molecule resulting in different shapes and dimensions of electrodes can lead to a variety of contact configurations and molecular wire-electrode electronics.

2.3. *Manipulation of Nanoclusters by STM*

In recent years, interest in direct manipulation of deposited nanoclusters using an STM tip has grown significantly, not only because it is easy to operate and control precisely but also because nanoclusters exhibit a wide range of peculiar fundamental properties [39–42]. Realization of precise control and positioning of the supported nanoclusters promises potential applications in optics, electronics, mechanical materials, catalysis as well as biotechnology. For instance, precisely arrayed nanoclusters can be employed in developing high-performance electronic and magnetic devices [43, 44].

Recently, the STM manipulation technique has been used to pattern Co nanoclusters grown on an ordered Al_2O_3/NiAl(100) surface [62]. The tip is placed over a specific cluster and the applied bias is reduced below a threshold value to attract the cluster and subsequently removed it from the patterns. Through this approach, the patterns of the supported Co clusters can be systematically tailored. The removed clusters can also be relocated to other positions by reversing the polarity. The uniform Co clusters formed from vapor deposition are only present on crystalline Al_2O_3 films and are highly aligned by protrusion structures of the crystalline Al_2O_3. Through simple thermal treatments we can control the geometry of the crystalline Al_2O_3 film as well as the protrusion networks on it and thereby manipulate patterns of the Co clusters [45,46]. The patterns of the Co clusters can thus be manipulated [45–46]. This self-organized patterning in combination with the STM manipulation techniques enables one to fabricate desired cluster patterns and subsequently to investigate their physical properties.

Figure 7 displays a sequence of STM images illustrating removal of the Co clusters by reducing the bias during scanning. Figure 7(a) shows the STM image obtained at 2.4 V bias and 0.8 nA tunneling current, where aligned Co nanoclusters are formed on crystalline Al_2O_3. As shown in the square of the zoom-in area in Fig. 7(b), the bias is lowered to different values during scanning (from left to right). As the tunneling current is kept the same, this process brought the tip close to the clusters, as illustrated schematically in the cartoon inset. It is evident that bias voltages below a threshold value of 0.8 V induce the motion of the Co nanoclusters. Figure 7(c) is the same surface region as shown in Fig. 7(a) scanned just after the manipulation process with the same imaging parameters. It can be observed from

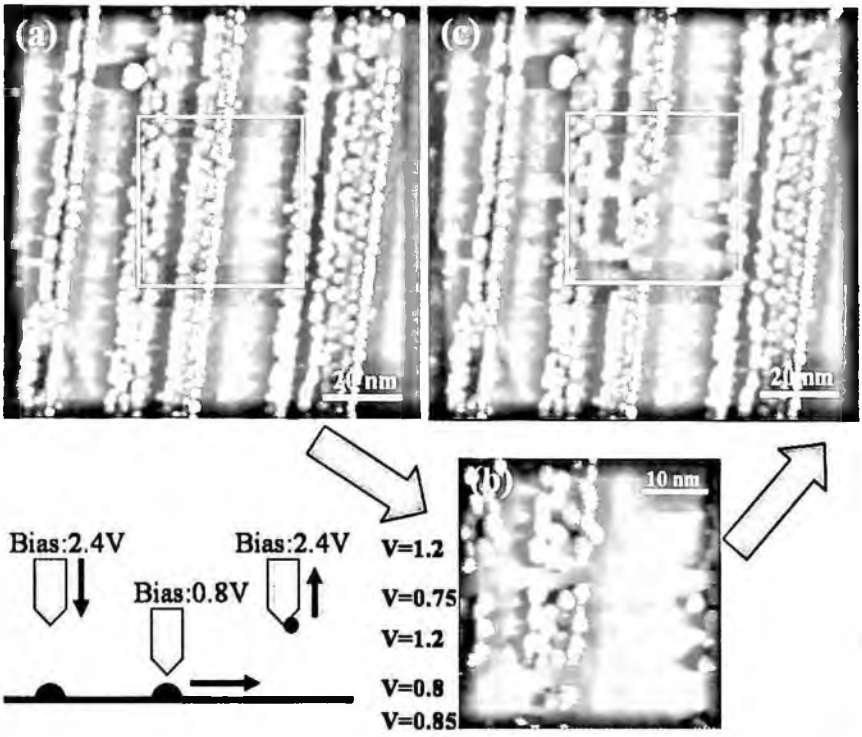

Figure 7. STM images showing removal of Co clusters by reducing bias during scanning: (a) Co clusters grown on ordered Al_2O_3/NiAl(100) surface (bias = 2.4 V and tunneling current = 0.8 nA), (b) zoom-in image of square area shown in Panel (a), where bias was lowered to different values with I = 0.8 nA during scanning, (c) same surface region as in Panel (a) after removal of Co clusters scanned with the same imaging parameters (2.4 V, 0.8 nA). The inset cartoon illustrates the procedure.

the figure images that where the bias is above the threshold value, the Co clusters are in fixed and well-defined locations. On the contrary, the regions where the bias is below the threshold value have no Co clusters. When a higher tunneling current is set, a higher threshold bias can be found. For instance, when 1.6 nA was used as the set point current, the threshold bias was found to be 1.6 V.

Following the approach described above, the desired Co-cluster patterns can be engineered as shown in Fig. 8. Figures 8(a) and 8(b) show that specific clusters are pulled out from the edge of the crystalline regions to create voids or cavities in the pattern. The arrows shown in Fig. 8(a) stand for the process, in which the tip was first moved over the specific clusters (the end sides of the arrows) and brought close to them, by reducing the bias, to induce the motion of the Co clusters, and the tip was translated to the other location to remove them from the pattern. Figure 8(c)–8(e) shows that a long cluster chain can be trimmed and cluster chains with various lengths can thus be fabricated. Figure 8(d) is a zoomed in image of Fig. 8(c) and Fig. 8(e) is the image after the trimming processes denoted by the

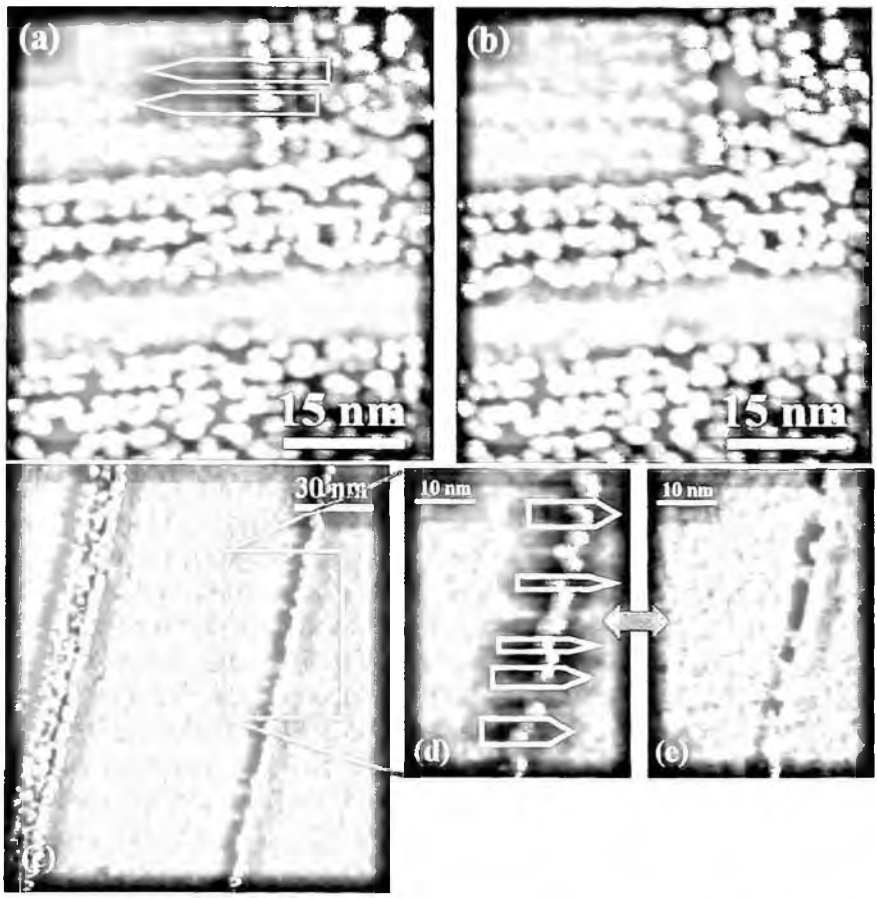

Figure 8. STM images of cluster patterns engineered by STM manipulation: (a) before creation of cavity by removing specific Co clusters, (b) after removing specific Co clusters to create cavity, (c) before trimming long Co clusters chain on crystalline Al_2O_3 strip, (d) zoom-in image of square area shown in Panel (c), (e) after trimming the chain, where condition of 0.8 V and 0.8 nA was used for removing Co clusters and 2.4 V and 0.8 nA were used for imaging.

arrows in Fig. 8(d). Such manipulation processes typically do not damage the oxide support, evident by the remaining oxide protrusion structures after cluster removal, as shown in Fig. 9(a). However, in a few cases, lowering bias below threshold value brings the tip so close that the tip removes not only clusters but also oxide film. Figure 9(b) shows that the oxide film grown at the NiAl step was removed along with the clusters.

At low Co coverage, the Co nanoclusters can be pulled or pushed on the crystalline Al_2O_3 surface by the STM tip. Figure 10 shows the Co clusters in the square area pushed or pulled along the protrusion stripes (the tip moves from bottom upward). After the processes, the clusters were moved to the middle part of the square area. Although we observed that the tip pulls or pushes the Co clusters on

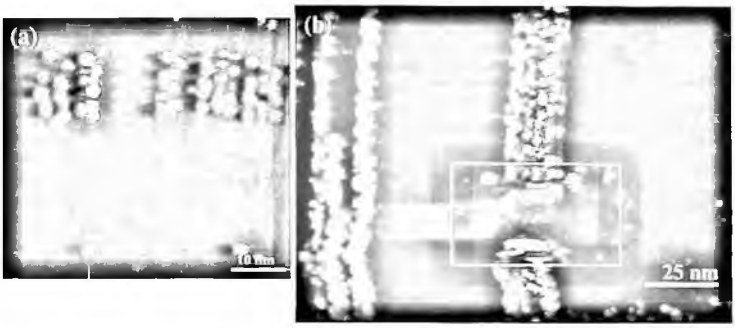

Figure 9. STM images showing clusters and oxide films removed by STM tip with bias below threshold value (bias = 2.4 V and tunneling current = 0.8 nA): (a) Co cluster rows removed from long clusters chains, (b) clusters and oxide films removed, in which oxide film grown at step of NiAl substrate. In the region indicated by square in Panel (b), 0.8 V bias was used.

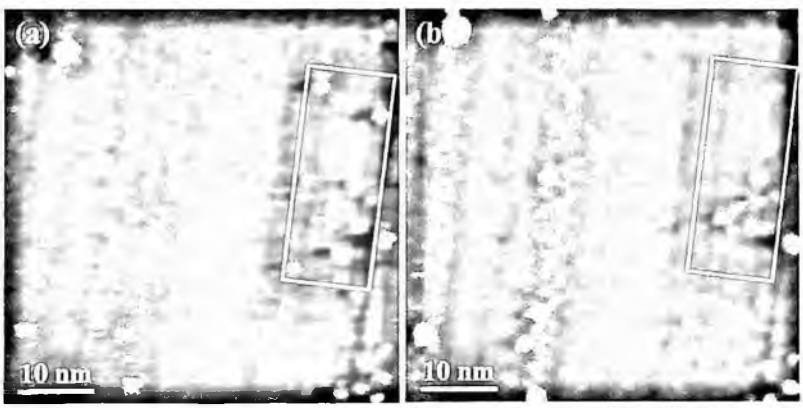

Figure 10. STM images of movement of Co clusters (0.15 ML coverage) on crystalline Al_2O_3 surface by pulling or pushing with STM tip: (a) before moving clusters, (b) after movement, where cluster number after movement is not the same, indicating that some are adsorbed on the tip. Images were obtained at 2.4 V and 0.8 nA.

the oxide surface, in most cases the clusters are attracted and adsorbed on the tip, indicated by the fact that the number of clusters before and after manipulation is not the same. Adsorbing too many clusters sometimes causes multi-tip effect or deteriorates the imaging, as shown in Fig. 11. The image quality can be regained simply by removing the adsorbed clusters from the tip. These adsorbed clusters can be relocated on the surface by simply reversing the bias polarity when the tip is brought closer to the surface. Figure 12 demonstrates that we picked up a Co cluster from the crystalline Al_2O_3 surface and relocated it to the amorphous region. It is worth noting that the size of the Co clusters unloaded from the tip remains similar to those on the surface.

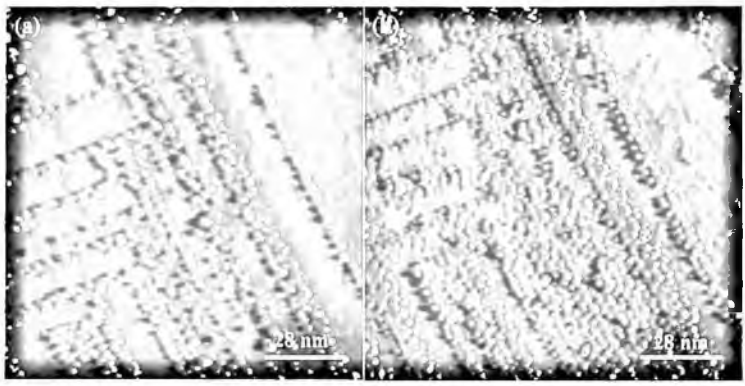

Figure 11. STM images of multi-tip effect due to Co clusters adsorbed on tip: (a) before manipulation, (b) after manipulation, where bias = 2.4 V and tunneling current = 0.8 nA were used in manipulation.

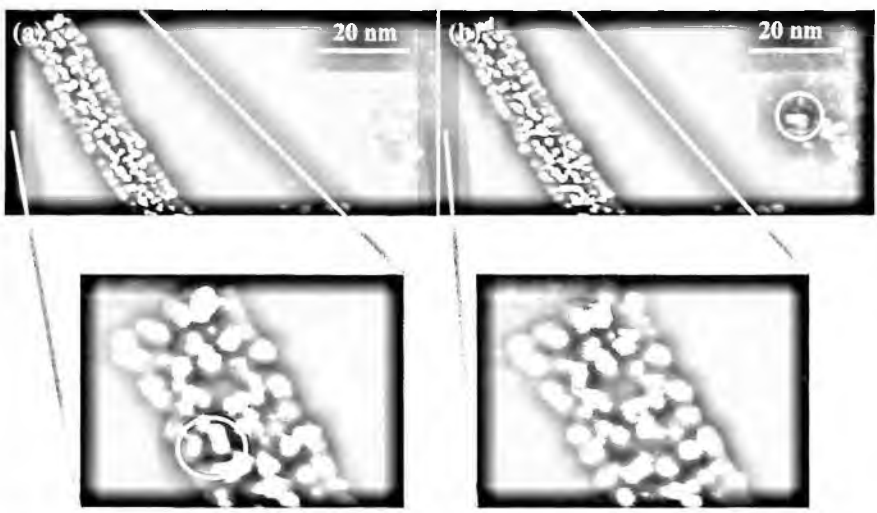

Figure 12. STM images of relocation of specific Co cluster from crystalline Al_2O_3 to amorphous region, where cluster removed is indicated by circles and insets manifest void creation after removing the specific cluster: (a) before picking up the cluster, (b) after relocating it on the amorphous region. Both images were obtained at 2.4 V bias and 0.8 nA tunneling current.

In the context of the STM atom/molecule manipulation, the manipulation process is more like vertical manipulation [47]. At the threshold parameters (bias voltage and tunneling current) the tip-cluster distance is so reduced (<2.5 Å, estimated by a simple tunneling model [48, 49]) that the force between the cluster and the tip, involving a combination of the electric field and chemical boding, is stronger than the adhesion force between the Co cluster and the oxide surface, about 35 eV/Å for a single cluster with the mean size [45, 46], derived from the density-functional-theory calculations. Therefore, the cluster can transfer with the tip upon its withdrawal

[18, 50]. Here, the electron field provides a directional driving force to transfer the cluster in the desired direction. The cluster is unloaded after reversing the bias polarity [51]. In line with the argument, the STM tip may not remove the clusters while competing with much stronger cluster-oxide interactions, such as Pt clusters on ordered Al_2O_3/NiAl(100).

Many groups have been devoting significant efforts to manipulation of metallic nanoclusters on silicon single-crystal surfaces because of silicon's importance in the microelectronics industry and the hope that hybrid organic devices can be integrated with existing silicon technology. Meanwhile, the manipulation of metallic nanostructures on a clean reactive silicon surface has been considered unfeasible for reasons of surface wetting and strong interface bonding. Pretreatment to the clean silicon surface is hence necessary to achieve manipulation. By using the buffer-layer-assisted growth technique, Chey, Huang, and Weaver [52, 53] have demonstrated controlled manipulation of Ag, Cu and mixed Ag-Cu nanoclusters on an Si(111)-(7×7) surface. The buffered (60–300 ML thick layer of Xe) Si surface is used to deposit Ag and Cu atoms, and the Ag and Cu adatoms are sufficiently mobile on Xe to form nanoclusters. Unwanted Ag nanoclusters were removed by laterally pushing the nanoclusters with the STM tip using the following two approaches. In the first approach, fast approach mode, a large area was scanned to derive the image and then a single line scan was performed over the desired feature with a fast scan speed (>10 μm/s), so that the feedback could not respond, to establish contact between the nanocluster and the tip to remove the Ag nanocluster. The second approach is typical, involving a line scan at a slower scan speed (~0.1 μm/s) with the feedback disabled. These manipulation results were dependent on the competition of bonding strengths of nanoclusters with the substrate and the tip. For instance, these Ag nanoclusters with height more than 12 nm (~200000 atoms) could not be moved, as the cluster-substrate contact area, determining the number of Ag-Si bonds and thus the adhesion force, depends on the nanoclusters' sizes [52]. In addition, for Cu nanoclusters on Si(111)-Ag and even Ag nanoclusters on Ag(111) substrates, where the nanocluster-substrate interaction is stronger, the manipulation was not successful. In some cases, such as Mn clusters on C_{60} terminated Si surfaces, the clusters can be removed and transferred to the tip but cannot be released from the tip [54].

Hydrogen-terminated Si surfaces are another kind of popular silicon support for cluster manipulation. Butcher *et al.* have demonstrated that by scanning at either large negative tunneling current or high positive bias voltage, it is possible to remove Ag nanoclusters from hydrogen terminated Si(100) surfaces [55]. By lowering tunneling impedance below a threshold value, individual Ag nanoparticles could be controllably slid across the H-passivated Si(111) surface or picked up by the tip and subsequently re-deposited by applying an appropriate voltage pulse [56]. On the same H-terminated Si(111) surfaces, the manipulation can also be applied on Au nanoclusters prepared by means of field-induced transfer of Au tip material, but was restricted to the Au nanoclusters deposited by using relatively low-amplitude

voltage pulses (<+8 V) [57]. Higher voltage pulses lead to the formation of an Au-Si alloy. Furthermore, it was observed that upon traversing the tip through a wet chemically prepared CdS nanocluster agglomeration, several individuals can be removed to form a desired structure [57].

Chemically passivated nanoclusters are also tried for such manipulation. For instance, it has been demonstrated that chemically passivated Au nanoclusters deposited on a highly oriented pyrolytic graphite (HOPG) surface can be manipulated in a controlled way by using appropriate tunneling parameters [58]. In the cleared area after removal of these $C_{12}H_{25}S$ coated Au clusters, fragments resulting from the cluster dissociation process were observed. These fragments could be laterally displayed by further high current tunneling [58].

All examples discussed above were carried out in an ultrahigh vacuum (UHV) condition. For realistic applications, attempts have been made to perform such manipulation at ambient pressure. Ohgi, Sheng, and Nejoh, [59] have demonstrated that lower-density Au nanoparticles supported on self-assembled monolayers (SAMs) of octanedithiol ($HS(CH_2)$:SH:C_8S_2) molecules formed on an Au(111) surface can be removed easily with lower bias and higher tunneling current than the imaging ones, although the manipulation is difficult at coverages above 1 ML. Rolandi *et al.* [60] have shown that alkanethiol-coated Au nanoparticles on HOPG substrate can also be removed by scanning at low bias voltages. Coulomb blockade was found to be the reason why the tip attracts nanoclusters at low bias voltage. The results for the manipulation in ambient conditions are not abundant; however, they have implied the possibility to succeed. Table 1 summarizes the successful attempts to manipulate nanoclusters on different surfaces.

Table 1. STM-manipulation of nanoclusters on surfaces.

Nanocluster	Surface	Environment	Reference
Co	Al_2O_3/NiAl(100)	UHV	Sartale *et al.* [62]
Ag, Cu and mixed Ag-Cu	Xe (60ML)/Si(111), Ag(111) and others	UHV	Chey *et al.* [52, 53]
Mn	C_{60} terminated Si(111)	UHV	Upward *et al.* [54]
Ag	H-terminated Si(100)	UHV	Butcher *et al.* [55]
Ag	H-passivated Si(111)	UHV	Radojkovic *et al.* [56]
Au and CdS	H-terminated Si(111)		Hartmann *et al.* [57]
Chemically Passivated Au	Highly oriented pyrolytic graphite (HOPG)		Durston *et al.* [58]
Au	Self assembled monolayers (SAMs) of octanedithiol formed on Au(111)	Ambient	Ohgi *et al.* [59]
Alkylthiol coated Au	HOPG	Ambient	Rolandi *et al.* [60]

3. Manipulation by Atomic Force Microscope (AFM)

AFM has evolved from STM and operates by measuring attractive or repulsive forces between the tip and sample, which vary with the spacing between the two. Since the tip is located at the free end of a cantilever, the attractive or repulsive forces cause the cantilever to deflect as shown in Fig. 13. Depending on the situation, forces that are measured in AFM include mechanical contact force, Van der Waals forces, capillary forces, chemical bonding, electrostatic forces, magnetic forces, Casimir forces, solvation forces etc. Typically, the deflection is measured using a laser spot reflected from the top of the cantilever into an array of photodiodes. AFM has a much broader potential and range of applications over its predecessor STM because it can be used for imaging any conducting or non-conducting surface and be performed at room environment [6].

Depending on the application, AFM can be operated in either contact or non-contact modes. In a contact or near contact mode, either the constant height or the constant force mode can be used. In a non-contact (NC) mode, the cantilever tip is made to vibrate near the sample surface with spacing on the order of a few nm or intermittently touches the surface at lowest deflection. Consequently the non-contact is also known as the tapping mode. Furthermore, in NC or tapping mode operations, if the dynamic properties of the cantilever carrying the tip are measured, the specific AFM apparatus can be called frequency modulation (FM) AFM or dynamic force microscopy (DFM). It has been known that frequency modulation is required for resolving reactive surfaces, like Si(111) under UHV, where a chemical bond between a tip and a sample can be formed [61]. However, measuring dynamic response using frequency modulation can restrict the operation speed of AFM.

As compared with STM, the AFM operation principle of manipulation is relatively simple. During scanning, the separation between the AFM tip and the adparticle is such that the lateral attractive van der Waals forces are sufficiently weak to avoid unintentional contact of the adparticle with the tip, as shown in Fig. 13(a).

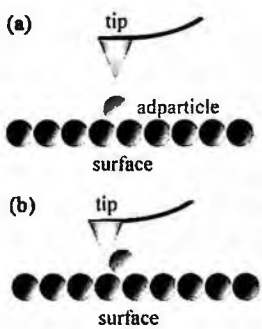

Figure 13. Schematic of AFM tip positions in the imaging and manipulation modes: (a) in imaging mode, lateral attractive van der Waals forces are sufficiently weak to avoid contact between tip and adparticle, (b) in manipulation mode, tip is in contact with adparticle, which is pushed laterally.

Using disabling the feedback loop and advancing the tip into contact with the particle (Fig. 13(b)), the tip can move laterally to push the adparticle to a predefined position on the surface. In this section, the applicability of AFM for manipulation of single atoms, molecules, and nanoclusters is described and assessed.

3.1. *Manipulation of Single Atoms by AFM*

Oyabu *et al.* [63] are believed to be the first group using a cryogenic AFM near a contact mode to study the vertical manipulation of Si atoms on Si(111)–(7×7) surfaces. The experiment was conducted at a temperature of 78 K under UHV (5×10^{-11} Torr). A typical n-doped Si cantilever with a spring constant of 48 N/m and 1st harmonic resonant frequency of 160 Hz was used. The corresponding quality (Q) factor for this cantilever system is 1.7×10^5. In a dynamic system, the Q factor is a measurement of the effect of resistance to oscillation. It compares the frequency at which a system oscillates to the rate at which it dissipates its energy. Roughly speaking, a higher Q has less resistance to oscillation. In manipulation, a soft nanoindentation was first performed by the tip to remove a selected Si atom from its equilibrium position at the surface without additional perturbation of the (7×7) unit cell. The short-range interaction force acting between the atom at the tip apex and closest adatom at surface activated the removing process. Unloading the manipulated atom is achieved by depositing it on a previously created vacancy at the surface. These manipulation processes are purely mechanical, since only short-range chemical interaction forces are involved and neither bias voltage nor voltage pulse is applied between probe and surface.

Later, Oyabu *et al.* [64] extended their study to the lateral manipulation of a Ge adatom on Ge(111)–c(2 × 8) surfaces by frequency-modulation AFM. The study observed that the intrinsic adatoms of Ge(111) surfaces are suitable for lateral manipulation by the short-range interaction force acting between the outermost atoms of a tip and the atoms on the surface. Moreover, an atom inlay was conducted using an FM-AFM with a Si cantilever of 29.5 N/m spring constant under lateral manipulation of Sn adatoms at room temperature on a Ge(111)–c(2 × 8) surface and resulted in an embedded atom letter "Sn" as shown in Fig. 14. The inlay was acquired with an oscillation amplitude of 15.7 nm, setting a frequency shift value of −4.6 Hz with respect to a free oscillation first-mechanical resonant frequency of 160,450 Hz under UHV environment [65]. They observed that small thermal energy of the atom enables stable manipulation for a relatively long period of time.

Kawai and Kawakatsu [66] applied an AFM under the frequency-modulation mode to extend the lateral manipulation of Si adatoms on the Si(111)–(7×7) surface to room temperature under a UHV environment. Pushing and pulling steps were carried out with repulsive and attractive interaction forces between the cantilever tip and the adatom. A small amplitude of 0.4 nm was used to improve the detection sensitivity of the short-range interaction force gradient as well as to enhance the

Figure 14. AFM image ($7.7 \times 7.7\,nm^2$ image size) of atom inlaid letter "Sn" by rearranging Sn atoms on Ge(111)–c(2×8) surface at room temperature with cantilever oscillation amplitude of 15.7 nm, using Si cantilever of 29.5 N/m spring constant, setting frequency shift value of −4.6 Hz with respect to first-mechanical resonant frequency of 160 kHz (courtesy of Dr. Oscar Custance of Osaka University, Japan).

resolution of the manipulation. Enhanced detection sensitivity due to the small amplitude could also avoid accidental modifications of the surface during imaging. Since a stiff cantilever is necessary to realize a small amplitude operation, the 2nd flexural mode was used. In the pushing mode, the 2nd frequency and frequency shift were set to 1,701 kHz and 20 Hz, respectively, with a Q factor of 13,095, while the corresponding values used in the pulling mode are 1,697 kHz and −104 Hz, respectively, with a Q factor of 10,474. They observed that small adatoms can be extracted, attached and laterally manipulated in and over the half unit cell with a repulsive interaction force. In the case of a tip condition that gave a strong image contrast, an adatom beside a vacancy could be pulled to the neighboring stable site with a strong attractive force.

Nishi *et al.* [67] used FM-AFM to investigate the atomic manipulation on an insulator surface, which normally is not suitable for STM manipulation. They adopted the soft nanoindentation approach, similar to that used by Oyabu *et al.* [63], to manipulate atoms on a cleaved ionic crystalline KCl(100) surface in UHV at room temperature with limited success. Very often, more than one surface atom is vertically manipulated or dragged from the surface by nanoindentation, while in rare cases, single-atom manipulation is successfully performed. Lateral manipulation of a vacancy has occasionally succeeded on the KCl(100) surface. They presumed that the lateral manipulation was induced by pulling. The difference between the covalent bonding of Si (Si–Si: 2.32 eV/bond) and the ionic bonding of KCl (K–Cl: 7.2 eV/ion pair) leads to the different results in the atom manipulation. They have introduced thermal drift compensation software for better approaching the target atom.

3.2. *Manipulation of Single Molecules by AFM*

Similar to single atoms, individual molecules are difficult to be manipulated by sliding on or dragging from a surface to chosen sites. The most important reason is

probably the presence of undesired interactions between the AFM tip and surface, including van der Waals, electrostatic and adhesion forces. Also, the non-specificity of the attachments, residuals, and molecules often occurs between the tip and surface [68]. Although many efforts have been made to manipulate single moleculates with AFM, all are with limited success. For example, Chyan *et al.* [69] have used the mechanical forces exerted by AFM to initiate the unfolding transition of individual protein molecules for the characterization of the unfolding and refolding processes. However, actually sliding the molecule to the desired location in a stable and controllable manner is still unachievable. Recently, Hobbs and Kantorovich [70] theoretically studied the response of a C_{60} molecule imaged by an AFM on an insulating surface in an UHV environment and showed that it is possible to identify the intramolecular features of the molecule. Their results may lead to successful manipulation of the molecule using NC-AFM.

3.3. *Manipulation of Nanoclusters by AFM*

Schaefer *et al.* [71] demonstrated first that the gold clusters with diameters ranging from 9 to 20 nm on highly ordered pyrolytic graphite (HOPG) substrate were moved across the surface to a predefined location using the AFM tip. By employing the same approach, these Au clusters were further arranged to form arrays on the WSe_2 substrate [71]. Aerosol nanoparticles can also be manipulated by the AFM. It was found that Ag aerosol particles on an InP substrate were swept by the AFM tip during scans [72]. More delicate manipulation was performed on aerosol Ag particles on SiO_2 substrate, in which the letters "LTL" were written using 45 nm Ag particles [73]. GaAs aerosol particles (30 nm) on GaAs substrates were also positioned with nanometer precision and formed complicated patterns and structures [74]. Modeling based on this sort of aerosol particle manipulation implies again that the tip radius should be minimized in order to reduce the adhesion between tip and particle as reported by Junno *et al.* [74].

Since the AFM manipulation techniques are becoming mature, some have attempted to manufacture nanodevices using such a bottom-up approach. Junno *et al.* [75] had fabricated nanomechnical switches and atomic scale contacts with 50 nm Au nanoparticles in air at room temperature. Electrode patterns were formed previously by e-beam lithography followed by evaporation of 3 nm Ti (for adhesion) and 25 nm Au with a gap of 20–50 nm onto a 300 nm thick SiO_2 layer on a silicon substrate. The manipulation procedure consists of three steps: (i) locating electrodes and gap area and selecting suitable nanoparticle by AFM imaging, (ii) positioning the tip behind the particle according to the desired displacement direction and (iii) moving it while the feedback is disabled. Figure 15 displays the sequence of AFM images recorded during positioning of an Au nanoparticle into the gap between the two Au/Ti electrodes. The ohmic junctions established between the nanoparticle and the electrode were stable for several hours. By pushing the

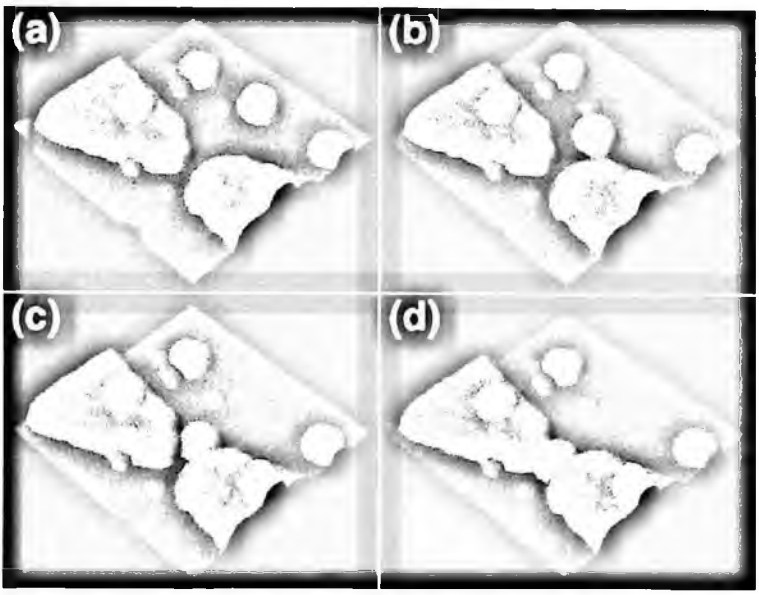

Figure 15. Sequence of AFM images (670 nm by 670 nm) of positioning 50-nm Au particle into gap between Au/Ti electrodes, where heights of particles and electrodes are 30 nm (courtesy of Prof. T. Juno of Lund University, Sweden).

nanoparticle to and fro, the nanoparticle behaves as a bi-stable nanomechanical switch to close and open the circuit.

Similar to atom manipulation, the tapping mode (TM) or frequency modulation (FM) of AFM can be applied for the manipulation of nanoclusters, in which the AFM feedback exploits the change in the amplitude of a cantilever's oscillation driven at a user-defined frequency due to the interaction of a tip mounted at the cantilever's end with a sample. Ramachandran *et al.* [76, 77] observed that variations in the amplitude and the resonance frequency of the cantilevers lead to different contrast in the FM-AFM images for the Au nanoparticles in either UHV or air environments. Further exploration found that tip-nanoparticle contact caused negative contrast, which implied a new protocol for the FM-AFM manipulation. As the tip-nanoparticle contact can be easily identified, one can subsequently use 'feedback off' and 'set-point change' approaches for direct and controlled manipulation. Using these approaches, it was demonstrated that FM-AFM can manipulate 5 nm Au nanoparticles to form a chain-like pattern. Figure 16 shows the lateral manipulation of Au nanoparticles (approximately 24-nm in size) on a cleavaged mica surface by FM-AFM in ambient environment at room temperature to create a chain-like nanostructure. A positive coating of poly-L-lysine on the mica surface allows the negatively charged gold particles to be adsorbed onto the surface. The manipulation was performed on a NanoScope IIIa MultiMode AFM made by Digital Instruments of Santa Barbara, CA. Rectangular Si tips (probe model TESP) with a

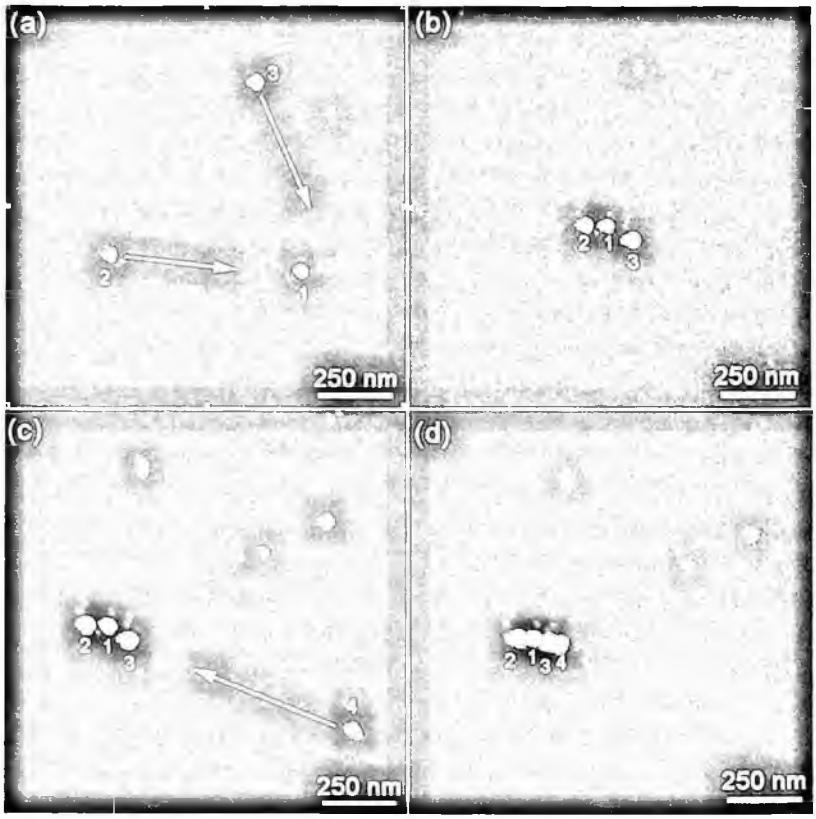

Figure 16. AFM images of lateral manipulation of 24-nm Au nanoparticles to create chain-like nanostructure by FM-AFM: (a) pushing nanoparticles labeled with 2 and 3 along direction shown by arrows, (b) nanoparticles 2 and 3 are pushed close to nanoparticle 1, (c) moving nanoparticle 4 towards nanoparticle 1, (d) final chain-like nanostructure.

spring constant of approximately 50 N/m and a setting frequency of approximately 300 kHz were utilized.

A probe control software (PCS) for the commercially available AFM unit was developed to monitor the underlying phenomena during manipulation processes [78]. It was successfully tested for manipulation of Au nanoparticles on Poly-L-lysine coated mica substrate [78, 79]. FM-AFM in combination with PCS are used to study the manipulation process by analyzing the simultaneously recorded amplitude and cantilever deflection and show that the contact force between tip and nanoparticle is responsible for the onset motion [80]. Moreover, utilizing the PCS [78] for colloidal Au nanoparticle on (Aminopropyl) trimethoxysilane (APTS) coated silicon substrate, more complex manipulation was performed, including building a simple three-dimensional pyramidal structure and also rotating and translating a linked two-particle structure [81].

As reported by Resch *et al.* [82], AFM manipulation in a liquid environment is also possible. It has been shown that the colloidal Au nanoparticles on Polylysine

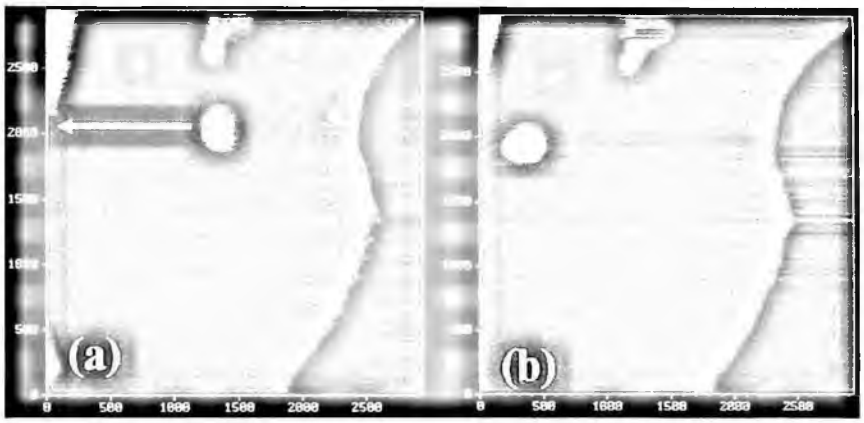

Figure 17. AFM images (2500 nm × 2500 nm) showing removal of a lipid vesicle supported on lipid membrane/mica using AFM manipulation technique: (a) before the vesicle pushed by AFM tip, where an arrow indicates tip's movement, (b) after push.

coated native SiO_2 surface grown from Si substrate can be precisely translated by mechanical pushing in aqueous and non-aqueous (ethanol) environments. Through this procedure, the desired two-dimensional structures were fabricated [82]. Moreover, the AFM tip has been used to move bio-related materials. Figure 17 shows that a lipid vesicle on a lipid membrane supported on mica was pushed by the AFM tip to a desired location. These results are important as they imply potential applications in growing bio-inspired fields, such as biophysics and biomedicine. Table 2 summarizes the major attempts to manipulate nanoclusters on different surfaces by AFM.

Table 2. AFM-manipulation of nanoclusters on surfaces.

Nanocluster	Surface	Environment	Reference
Au	Highly oriented pyrolytic graphite (HOPG) and WSe_2	Ambient	Schaefer *et al.*, 1995 [71]
Ag	InP	Ambient	Junno *et al.* [72, 74]
GaAs	GaAs	Ambient	Martin *et al.* [73]
Ag	SiO_2	Ambient	Junno *et al.* [72, 74]
Au	Ti electrodes on SiO_2	Ambient	Junno *et al.* [75]
Au	Poly-L-lysine coated Mica	Ambient and UHV	Baur *et al.* [78,79]; Resch *et al.* [80, 81]; Ramachandran *et al.* [76, 77]
Au	(Aminopropyl) trimethoxysil ane (APTS) coated silicon	Ambient	Resch *et al.* [80, 81]
Au	Polylysine coated SiO_2/Si	Liquid	Resch *et al.* [82]

4. Concluding Remarks

Scanning probe microscopy (SPM) is an essential tool for creating a variety of nanostructures using the bottom-up approach. This article has selected and reviewed two major manipulation technologies within the family of SPM lithography using scanning tunneling microscopy (STM) and atomic force microscopy (AFM) as well as the AFM based dip-pen technique. The principles, procedures, achievements and potential for each manipulation technique have been presented. In particular, a wide variety of nanostructures manipulated by these techniques have been presented to specifically illustrate their respective feasibilities and limitations.

Both lateral and vertical manipulations can be performed by STM and AFM. In general, STM has achieved manipulation and positioning of a wide range of single atoms and molecules on a surface, while AFM can be performed in room environment and is more popular in manipulation of nanoclusters. This suggests that STM perhaps achieves the ultimate resolution of atom-by-atom control of the surface, i.e., in subnano levels, while AFM is more practical in operating at a nanoscale level only. Many researchers have attempted to implement this level of control into making actual components and devices mentioned in the text, including, nanomechnical switches made by Junno *et al.* [75], molecular logic circuits developed by Heinrich *et al.* [33], molecular engines suggested by Rieder *et al.* [36], and molecular switch presented by Iancu, Deshpande, and Hla [37], and molecular wire-electrode systems reported by Grill and Moresco [38]. The remaining challenge will be transferring such fine manipulation-related components or devices into usable semiconductor or electronic systems. In addition, manipulation possibilities of nanoclusters on synthetic surfaces [62] and in liquid environments [82] for nano-fabrication constitute further experimental challenges very worthwhile to pursue for high-density information storage systems and biomedical applications. As a result nanoscale manipulation has a great potential for providing necessary nanoscale devices and systems for the sustained evolution of electronic, photonic, biomedical, and nanosystem industries.

In STM, three different interactions between the tip and sample, including direct atomic attraction forces, tip-induced electric field, and inelastic scattering by tunneling electrons have been identified and studied as the original sources for the manipulation. In most of the earlier experiments, only one type of these interaction sources was employed. In more recent studies, however, techniques have been developed to integrate one type of the interaction sources with another in manipulation of single atoms/molecules. In this way, a large numbers of nanoparticles can be manipulated and eventually assembled in specific geometries. As a result, nanoscale devices and systems can be constructed from these basic building blocks. In AFM, it offers a room environment manipulation, while the whole manipulation process can be imaged in real time. As a result, AFM manipulation would be relatively easier to be performed and controlled. More detailed comparison between STM and AFM used in nanofabrication can be found in Tseng, Notargiacomo, and Chen [2].

However, from an industrial point of view there are some downsides to the SPM-manipulation technique. It is limited to certain combinations of nanoparticles and surfaces. Frequently, the experiments are performed blindly and the manipulation parameters are optimized by a trial and error method. The interaction between the SPM tip and adparticle is complex but a thorough understanding of such interactions and the mechanism involved in the manipulation process is demanded, in order to perform the manipulation process in an entirely controlled manner. Another major obstacle in the SPM-manipulation is a serial process with low throughput. To increase throughput, multi-tip arrays and massively parallel algorithms have to be developed as those reported by Eleftheriou *et al.* [83]. Finally, the manipulation techniques have developed many new applications in their own right and many new capabilities have been evolved to complement the existing nanofabrication processes. This powerful SPM-manipulation tool should offer significant opportunities for different applications in next generation nanotechnology and is on the verge of having a revolutionary impact in a wide range of industries.

It is worth pointing out that the motivation of this article is not to present an exhaustive review of all significant work in this field. A selection of topics and papers to be cited is necessary and is made without the intention of excluding valuable ones who gave important contribution to the development of SPM manipulation.

Acknowledgments

The authors would like to thank the US National Science Foundation under Grant No. DMI-0423457, the ROC National Science Council under Grant No. NSC 94-2112-M-008-032, the ROC Ministry of Economic Affairs under Grant No. 93-EC-17-A-09-S1-022, and Pacific Technology of Phoenix for their financial supports. The useful information and suggestions in preparing this manuscript from Dr. Zhuang Li of Changchun Institute of Applied Chemistry, Changchun, China, Dr. Oscar Custance of Osaka University, Osaka, Japan, Professor Karl-Heinz Rieder of Swiss Federal Laboratories for Materials Research, and Duebendorf, Switzerland, Dr. Gerhard Meyer of IBM Zurich Research Laboratory, Rüschlikon, Switzerland, should be specifically acknowledged. The authors would also like to express their gratitude to Messrs Christopher T. Wassam of Arizona State University and K. L. Lin of National Sun Yat-Sen University for their assistance in preparing this manuscript.

References

1. A. A. Tseng and A. Notargiacomo, Nanoscale fabrication by nonconventional approaches, *J. Nanosci. Nanotech.* 5, 683–702 (2005).
2. A. A. Tseng, A. Notargiacomo and T. P. Chen, Nanofabrication by scanning probe microscope lithography: a review, *J. Vac. Sci. Technol. B* **23**, 877–894 (2005).
3. R. J. Colton, Nanoscale measurements and manipulation, *J. Vac. Sci. Tech. B* **22**, 1609–1635 (2004).

4. A. A. Tseng, Recent developments in nanofabrication using scanning near-field optical microscope lithography, *Op. Laser Techno.* **39**, 514–526 (2007).
5. G. Binnig, H. Rohrer, C. Gerber and E. Weibel, Surface studies by scanning tunneling microscopy, *Phys. Rev. Lett.* **49**, 57–61 (1982).
6. S. N. Magonov and M.-H. Whangbo, *Surface Analysis with STM and AFM* (Wiley-VCH, New York, 1996).
7. R. Wissendanger, *Scanning Probe Microscopy and Spectroscopy Methods and Applications* (Cambridge Univ. Press, Cambridge, 1998).
8. L. Bartels, G. Meyer and K.-H. Rieder, Basic steps of lateral manipulation of single atoms and diatomic clusters with a scanning tunneling microscope tip, *Phys. Rev. Lett.* **79**, 697–700 (1997).
9. D. M. Eigler and E. K. Schweizer, Positioning single atoms with a scanning tunneling microscope, *Nature* **344**, 524–526 (1990).
10. M. F. Crommie, C. P. Lutz and D. M. Eigler, Confinement of electrons to quantum corrals on a metal surface, *Science* **262**, 218–220 (1993).
11. L. Libioulle, A. Radenovic, E. Bystrenova and G. Dietler, Low noise current-to-voltage converter and vibration damping system for a low-temperature ultrahigh vacuum scanning tunneling microscope, *Rev. Sci. Instrum.* **74**, 1016–1021 (2003).
12. E. T. Foley, N. L. Yoder, N. P. Guisinger and M. C. Hersam, Cryogenic variable temperature ultrahigh vacuum scanning tunneling microscope for single molecule studies on silicon surfaces, *Rev. Sci. Instrum.* **75**, 5280–5287 (2004).
13. D. M. Eigler, C. P. Lutz and W. E. Rudge, An atomic switch realized with the scanning tunnelling microscope, *Nature* **352**, 600–603 (1991).
14. I. W. Lyo and P. Avouris, Field-induced nanometer- to atomic-scale manipulation of silicon surfaces with the STM, *Science* **253**, 173–176 (1991).
15. T. C. Shen, C. Wang, G. C. Abeln, J. R. Tucker, J. W. Lyding, P. Avouris and R. E. Walkup, Atomic-scale desorption through electronic and vibrational-excitation mechanisms, *Science* **268**, 1590–1592 (1995).
16. M. Brandbyge and P. Hedegård, Theory of the eigler switch, *Phys. Rev. Lett.* **72**, 2919–2922 (1994).
17. S. Gao, M. Persson and B. I. Lundqvist, Theory of atom transfer with a scanning tunneling microscope, *Phys. Rev. B* **55**, 4825–4836 (1997).
18. C. J. Chen, A universal relation in NC-AFM, STM and atom manipulation, *Nanotechnology* **16**, S27–S34 (2005).
19. C. T. Salling and M. G. Lagally, Fabrication of atomic-scale structures on Si(001) surfaces, *Science* **265**, 502–506 (1994).
20. C. T. Salling, I. I. Kravchenko and M. G. Lagally, Atomic manipulation for patterning ultrathin films, *J. Vac. Sci. Tech. B* **13**, 2828–2831 (1995).
21. J. A. Stroscio and R. J. Celotta, Controlling the dynamics of a single atom in lateral atom manipulation, *Science* **306**, 242–247 (2004).
22. L. Pizzagalli and A. Baratoff, Theory of single atom manipulation with a scanning probe tip: force signatures, constant-height and constant-force scans, *Phys. Rev. B* **68** 115427:1–12 (2003).
23. Y. Hasegawa and P. Avouris, Direct observation of standing wave formation at surface steps using scanning tunneling spectroscopy, *Phys. Rev. Lett.* **71**, 1071–1074 (1993).
24. G. Dujardin, R. E. Walkup and P. Avouris, Dissociation of individual molecules with electrons from the tip of a scanning tunneling microscop, *Science, New Series* **255**, 1232–1235 (1992).

25. J. A. Stroscio and D. M. Eigler, Atomic and molecular manipulation with the scanning tunneling microscope, *Science* **254**, 1319–1326 (1991).
26. P. Zeppenfeld, C. P. Lutz and D. M. Eigler, Manipulating atoms and molecules with a scanning tunneling microscope, *Ultramicroscopy* Vols. 42–44, pp. 128–133 (1992).
27. N. Lorente and H. Ueba, CO dynamics induced by tunneling electrons: differences on Cu(110) and Ag(110), *Eur. Phys. J. D* **35**, 341–348 (2005).
28. G. Meyer, F. Moresco, S. W. Hla, J. Repp, K.-F. Braun, S. Folsch and K. H. Rieder, Manipulation of atoms and molecules with the low-temperature scanning tunneling microscope, *Jpn. J. Appl. Phys.* **40**, 4409–4413 (2001).
29. T. A. Jung, R. R. Schlittler, J. K. Gimzewski, H. Tang and C. Joachim, Controlled room-temperature positioning of individual molecules: molecular flexure and motion, *Science* **271**, 181–184 (1996).
30. J. K. Gimzewski and C. Joachim, Nanoscale science of single molecules using local probes, *Science* **283**, 1683–1688 (1999).
31. J. A. Stroscio, E. W. Hudson, S. R. Blankenship, R. J. Celotta and A. P. Fein, A facility for nanoscience research: an overview, in *Nanostructure Science Metrology and Technology, Proceedings of SPIE*, Vol. 4608, pp. 112–115, 2002.
32. F. Moresco, G. Meyer, K. H. Rieder, H. Tang, A. Gourdon and C. Joachim, Low temperature manipulation of big molecules in constant height mode, *App. Phys. Lett.* **78**, 306–308 (2001).
33. J. Heinrich, C. P. Lutz, J. A. Gupta and D. M. Eigler, Molecule cascades, *Science* **298**, 1381–1387 (2002).
34. S.-I. Ishi, Y. Ohno and B. Viswanathan, An overview on the electronic and vibrational properties of adsorbed CO, *Surf. Sci.* **161**, 349–372 (1985).
35. L. Bartels, G. Meyer and K.-H. Rieder, Controlled vertical manipulation of single CO molecules with the scanning tunneling microscope: a route to chemical contrast, *Appl. Phys. Lett.* **71**, 213–215 (1997).
36. K.-H. Rieder, G. Meyer, F. Moresco, K. Morgenstern, S.-W. Hla, J. Repp, M. Alemani, L. Grill, L. Gross, M. Mehlhorn, H. Gawronski, V. Simic-Milosevich, J. Henzl, K. F. Braun, S. Foelsch and L. Bartels, Force induced and electron stimulated STM manipulations: routes to artificial nanostructures as well as to molecular contacts, engines and switches, *J. Physics: Conf. Series* **19**, 175–181 (2005).
37. V. Iancu, A. Deshpande and S. W. Hla, Manipulating Kondo temperature via single molecule switching, *Nano Lett.* **6**, 820–823 (2006).
38. L. Grill and F. Moresco, Contacting single molecules to metallic electrodes by scanning tunnelling microscope manipulation: model systems for molecular electronics, *J. Physics: Condens. Matter* **18**, S1887–S1908 (2006)
39. W. A. deHerr, The physics of simple clusters: experimental aspects and simple modelling, *Rev. Mod. Phys.* **65**, 611–676 (1993).
40. C. Binnis, Nanoclusters deposited on surfaces, *Surf. Sci. Rep.* **44**, 1–49 (2001).
41. U. Heiz and E. L. Bullock, Fundamental aspects of catalysis on supported metal clusters, *J. Mater. Chem.* **14**, 564–577 (2004).
42. A. P. Alivisatos, The use of nanocrystals in biological detection, *Nat. Biotech.* **22**, 47–52 (2004).
43. G. Schmid, Nanoclusters-building blocks for future nanoelectronic devices? *Adv. Eng. Mater.* **3**, 737–743 (2001).
44. T.-H. Lee and R. M. Dickson, Nanocomputing with nanoclusters, *Optics Photonic News* **15**, 22–27 (2004).
45. M. F. Luo, C. I. Chiang, H. W. Shiu, S. D. Sartale and C. C. Kuo, Patterning Co nanoclusters on thin-film Al_2O_3/NiAl(100), *Nanotechnology* **17**, 360–366 (2006)

46. M. F. Luo, C. I. Chiang, H. W. Shiu, S. D. Sartale, P. L. Wang and C. C. Kuo, Growth of Co clusters on thin films Al_2O_3/NiAl(100), *J. Chem. Phys.* **124**, 164709:1–6 (2006).
47. S.-W. Hla, Scanning tunneling microscopy single atom/molecule manipulation and its application to nanoscience and technology, *J. Vac. Sci. Technol. B* **23**, 1351–1360 (2005).
48. U. Dürig, O. Zürig and D. W. Pohl, Observation of metallic adhesion using scanning tunneling microscope, *Phys. Rev. Lett.* **65**, 349–352 (1990).
49. L. Olesen, M. Brandbyge, M. R. Sørensen, K. W. Jacobsen, E. Laegsgaard, I. Stensgaard and F. Besenbacher, Apparent barrier height in scanning tunneling microscopy revisited, *Phys. Rev. Lett.* **76**, 1485–1488 (1996).
50. D. Drakova, Theoretical modelling of scanning tunnelling microscopy, scanning tunnelling spectroscopy and atomic force microscopy, *Rep. Prog. Phys.* **64**, 205–290 (2001).
51. K. Hirose and M. Tsukada, First principle calculation of the electronic structure for a bielectrode junction system under strong field and current, *Phys. Rev. B* **51**, 5278–5290 (1995).
52. S. J. Chey, L. Huang and J. H. Weaver, Manipulation and writing with Ag nanocrystals on Si(111)–7 × 7, *Appl. Phys. Lett.* **72**, 2698–2700 (1998).
53. S. J. Chey, L. Huang and J. H. Weaver, Interface bonding and manipulation of Ag and Cu nanocrystals on Si(111)–(7×7)-based surfaces, *Phys. Rev. B* **59**, 16033–16041 (1999).
54. M. D. Upward, P. Moriarty, P. H. Beton, S. H. Baker, C. Binns and K. Edmonds, Measurement and manipulation of Mn clusters on clean and fullerene terminated Si(111)–7 × 7, *Appl. Phys. Lett.* **70**, 2114–2116 (1997).
55. M. J. Butcher, F. H. Jones and P. H. Beton, Growth and modification of Ag islands on hydrogen terminated Si(100) surfaces, *J. Vac. Sci. Technol. B* **18**, 13–15 (2000).
56. P. Radojkovic, M. Schwartzkopff, T. Garbrei and E. Hartmann, STM-assisted manipulation of Ag nanoparticles, *Appl. Phys. A* **66**, S701–S705 (1998).
57. E. Hartmann, M. Enachescu, P. Radojkovic, M. Schwartzkopff and F. Koch, Imaging and manipulation properties of nanoparticles in scanning tunneling microscopy, *Nanotechnology* **7**, 376–380 (1996).
58. P. J. Durston, R. E. Palmer and J. P. Wilcoxon, Manipulation of passivated gold clusters on graphite with the scanning tunneling microscope, *Appl. Phys. Lett.* **72**, 176–178 (1998).
59. T. Ohgi, H.-Y. Sheng and H. Nejoh, Au particle deposition onto self-assembled monolayers of thiol and dithiol molecules, *Appl. Surf. Sci.* **130–132**, 919–924 (1998).
60. M. Rolandi, K. Scott, E. G. Wilson and F. C. Meldrum, Manipulation and immobilization of alkane-coated gold nanocrystals using scanning tunneling microscopy, *J. Appl. Phys.* **89**, 1588–1594 (2001).
61. F. J. Giessible, Atomic resolution of the silicon(111)–(7 × 7) surface by atomic force microscopy, *Science* **267**, 68–71 (1995).
62. S. D. Sartale, K. L. Lin, C. I. Chiang, C. C. Kuo and M. F. Luo, Engineering patterns of Co nanoclusters on thin film Al_2O_3/NiAl(100) using STM manipulation techniques, *Appl. Phys. Lett.* **89**, 063118:1–3 (2006).
63. N. Oyabu, O. Custance, I. Yi, Y. Sugawara and S. Morita, Mechanical vertical manipulation of selected single atoms by soft nanoindentation using near contact atomic force microscopy, *Phys. Rev. Lett.* **90**, 176102:1–4 (2003).

64. N. Oyabu, Y. Sugimoto, M. Abe, O. Custance and S. Morita, Lateral manipulation of single atoms at semiconductor surfaces using atomic force microscopy, *Nanotechnology* **16**, S112–S117 (2005).
65. M. Sugimoto, S. Abe, N. Hirayama, N. Oyabu, O. Custance and S. Morita, Atom inlays performed at room temperature using atomic force microscopy, *Nat. Mater.* **4**, 156–159 (2005).
66. S. Kawai and H. Kawakatsu, Mechanical atom manipulation with small amplitude dynamic force microscopy, *App. Phys. Lett.* **89**, 23113:1–3 (2006).
67. R. Nishi, D. Miyagawa, Y. Seino, Y. Insook and S. Morita, Non-contact atomic force microscopy study of atomic manipulation on an insulator surface by nanoindentation, *Nanotechnology* **17**, S142–S147 (2006).
68. F. Ritort, Single-molecule experiments in biological physics: methods and applications, *J. Phys.: Condens. Matter* **18** R531–R583 (2006).
69. C.-L. Chyan, F.-C. Lin, H. Peng, J.-M. Yuan, C.-H. Chang, S.-H. Lin and G. Yang, Reversible mechanical unfolding of single ubiquitin molecules, *Biophys. J.* **87**, 3995–4006 (2004).
70. C. Hobbs and L. Kantorovich, Non-contact AFM images of a C_{60} molecule adsorbed on the Si(001) surface: an *ab initio* method, *Sur. Sci.* **600**, 551–558 (2006).
71. D. M. Schaefer, R. Reifenberger, A. Patil and R. P. Andres, Fabrication of two-dimensional arrays of nanometer-size clusters with the atomic force microscope, *Appl. Phys. Lett.* **66**, 1012–1014 (1995).
72. T. Junno, S. Anand, K. Deppert, L. Montelius and L. Samuelson, Contact mode atomic force microscopy imaging of nanometer-sized particles, *App. Phys. Lett.* **66**, 3295–3297 (1995).
73. M. Martin, L. Roschier, P. Hakonen, Ü. Parts, M. Paalanen, B. Schleicher and E. I. Kauppinen, Manipulation of Ag nanoparticles utilizing noncontact atomic force microscopy, *App. Phys. Lett.* **73**, 1505–1507 (1998).
74. T. Junno, K. Deppert, L. Montelius and L. Samuelson, Controlled manipulation of nanoparticles with an atomic force microscope, *App. Phys. Lett.* **66**, 3627–3629 (1995).
75. T. Junno, S.-B. Carlsson, H. Xu, L. Montelius and L. Samuelson, Fabrication of quantum devices by Ångstörm-level manipulation of nanoparticles with an atomic force microscope, *App. Phys. Lett.* **72**, 548–550 (1998).
76. T. R. Ramachandran, C. Baur, A. Bugacov, A. Madhukar, B. E. Koel, A. Requicha and C. Gazen, Direct and controlled manipulation of nanometer-sized particles using the non-contact atomic force microscope, *Nanotechnology* **9**, 237–245 (1998).
77. T. R. Ramachandran, A. Madhukar, P. Chen and B. E. Koel, Imaging and direct manipulation of nanoscale three-dimensional features using the noncontact atomic force microscope, *J. Vac. Sci. Technol. B* **16**, 1425–1429 (1998).
78. C. Baur, B. C. Gazen, B. Koel, T. R. Ramachandran, A. A. G. Requicha and L. Zini, "Robotic nanomanipulation with a scanning probe microscope in a networked computing environment, *J. Vac. Sci. Technol. B* **15**, 1577–1580 (1997).
79. C. Baur, A. Bugacov, B. E. Koel, A. Madhukar, N. Montoya, T. R. Ramachandran, A. A. G. . Requicha, R. Resch and P. Will, Nanoparticle manipulation by mechanical pushing: underlying phenomena and real-time monitoring, *Nanotechnology* **9**, 360–364 (1998).
80. R. Resch, A. Bugacov, C. Baur, B. E. Koel, A. Madhukar, A. A. G. Requicha and P. Will, Manipulation of nanoparticles using dynamic force microscopy: simulation and experiments, *App. Phys. A* **67**, 265–271 (1998).

81. R. Resch, C. Baur, A. Bugacov, B. E. Koel, A. Madhukar, A. A. G. Requicha and P. Will, Building and manipulating three-dimensional and linked two-dimensional structures of nanoparticles using scanning force microscopy, *Langmuir* **14**, 6613–6616 (1998).
82. R. Resch, D. Lewis, S. Meltzer, N. Montoya, B. E. Koel, A. Madhukar, A. A. G. Requicha and P. Will, Manipulation of gold nanoparticles in liquid environments using scanning force microscopy, *Ultramicroscopy* **82**, 135–139 (1999).
83. E. Eleftheriou, T. Antonakopoulos, G. K. Binnig, G. Cherubini, M. Despont, A. Dholakia, U. Durig, M. A. Lantz, H. Pozidis, H. E. Rothuizen and P. Vettiger, Millipede — a MEMS-based scanning-probe data-storage system, *IEEE Trans. Magnetics* **39**, 938–945 (2003).

CHAPTER 2

ATOMIC FORCE MICROSCOPE LITHOGRAPHY

NORITAKA KAWASEGI

Central Research Institute, Toyama Industrial Technology Center,
150 Futagami, Takaoka, Toyama 933-0981, Japan
kawasegi@itc.pref.toyama.jp

DEUG WOO LEE

Department of Nanosystem and Process Engineering, Pusan National University,
50 Cheonghak-ri, Samnangjin-eup, Miryang,
Gyeongsangnam-do, 627-706, Korea
dwoolee@pusan.ac.kr

NOBORU MORITA

Graduate School of Science and Engineering for Research, University of Toyama,
3190 Gofuku, Toyama 930-8555, Japan
nmorita@eng.u-toyama.ac.jp

JEONG WOO PARK*

Department of Nanofusion Technology, Pusan National University,
50 Cheonghak-ri, Samnangjin-eup, Miryang,
Gyeongsangnam-do, 627-706, Korea
calcci@pusan.ac.kr

Atomic force microscopy (AFM) was originally developed for atomic resolution surface topography observations. Nowadays, it is also widely used for nanolithography. AFM-based lithography is an effective method compared to conventional photolithographic processes due to its simplicity, high resolution, and low cost. It can provide nanoscale stage control and the probing tip can be used as a lithographic tool. Therefore, various AFM-based nanoscale fabrication methods have been proposed using electrochemical oxidation, material transfer, mechanical lithography, and thermally

*Corresponding author: Department of Nanofusion Technology, Pusan National University, 50 Cheonghak-ri, Samnangjin-eup, Miryang, Gyeongsangnam-do, 627-706, Korea; calcci@pusan.ac.kr

induced modifications. This chapter will introduce the detailed processes and applications of AFM-based lithographic techniques.

Keywords: Atomic Force Microscope (AFM); Scanning Tunneling Microscope (STM); Scanning Probe Microscope (SPM); Scanning Near-Field Optical Microscope (SNOM); Focused Ion Beam (FIB); Electron Beam (EB); Cantilever; Nanolithography; Oxidation; Material Transfer; Carbon Nanotube (CNT); Ultra High Vacuum (UHV); Aspect Ratio; Self Assembled Monolayer (SAM); Tetra-Methyl Ammonium Hydroxide (TMAH); Isopropyl Alcohol (IPA); Octadecyltrichrolosilane (OTS); Alkyl Monolayer; Electric Field; Full Width at Half Maximum (FWHM); Scanning Electron Microscopy (SEM); Tip-Wear; Dip-Pen Nanolithography (DPN); Relative Humidity; Photolithography; Feedback; Nano Stage; Mechanical Lithography; Poly-methylmethacrylate (PMMA); Reactive Ion Etching (RIE); Diamond; Tribo-Nanolithography (TNL); Millipede; Data Strange Device; Cantilever Array; Etching

CONTENTS

1. Introduction 34
2. Electrochemical Oxidation 35
   2.1. Simple Oxidation Processes 35
   2.2. Modified Oxidation Processes 39
3. Material Transfer Process 46
4. Mechanical Lithography 48
   4.1. Material Removal 50
   4.2. Resist Removal and Etching 52
   4.3. Direct Patterning and Wet Etching 55
5. Thermally Induced Modifications 56
6. Conclusions 58
References 58

1. Introduction

Nanofabrication technology is an important field of research. Numerous attempts have been made to improve this technology in recent years. Photolithography and subsequent etching is the most widely used technique, and has contributed to the advancement of large-scale integration (LSI) and micro-electro-mechanical systems (MEMS). Photolithography is suitable for mass producing microstructures and nanostructures because it is a high-throughput fabrication process. Lithographie galvanoformung, abformung (LIGA) [1] can also be used to fabricate high aspect ratio structures; however, it requires the use of complex instruments and is time-consuming. Several successful attempts have been made at using scanning probe microscopy (SPM), electron beam (EB) [2], and focused ion beam (FIB) [3] lithography to fabricate nanoscale to microscale structures. SPM lithography is a particularly effective method due to its simplicity, precision, and low cost.

SPM, which includes scanning tunneling microscopy (STM) [4], atomic force microscopy (AFM) [5], and scanning near-field optical microscopy (SNOM) [6], was developed to observe surface characteristics by detecting interactions between the probe and solid material. STM and AFM are the most widely used technologies in the SPM family. STM was developed by Binning *et al.* [4] in 1982, and is used to measure the surface topography to an atomic resolution by detecting the tunneling current. After the development of STM, several microstructuring and nanostructuring technology approaches [7] using STM were developed to enable researchers to manipulate even single atoms. Thus, SPM can be used as not only a measuring tool but also as a nanostructuring tool. However, as STM is controlled by detecting a tunneling current between the probe and sample, the measured sample is limited to conductive material. To overcome this problem, AFM was developed by Binning *et al.* [5] in 1986. AFM detects minute forces between the probe and sample instead of the tunneling current. The advantage of AFM is that any type of material can be measured and machined and the operation can be conducted under normal atmospheric conditions. AFM permits nanoscale movements, and uses a probing tip that can also be used as a microtool. Therefore, AFM is appropriate for nanoscale lithography.

Nanolithographic techniques that make use of AFM are discussed in this chapter. Four categories of technique are considered: electrochemical oxidation, material transfer, mechanical lithography, and thermally induced modifications. The fundamental characteristics and applications of these methods are described in the following sections.

2. Electrochemical Oxidation

Among known scanning probe techniques, AFM-based direct oxidation is particularly significant because of the remarkable level of cross-fertilization and incremental progress that has been achieved over the past decades by several laboratories worldwide. The technique is particularly suited for practical applications because it can be performed in air. During the oxidation process, an electrically biased AFM tip operated at ambient humidity acts as a nanoscopic electrochemical cell to the localized oxidation on the sample surface. The lateral size of the oxidized features is typically in the range of 10 to 100 nm for various materials, including semiconductors and metals. This process was recently used to achieve sub 10-nm lateral resolution using carbon nanotube (CNT) AFM tips as the anodizing electrode. In this section, lithography processes based on AFM oxidation will be introduced. These include simple oxidation and modified oxidation processes.

2.1. *Simple Oxidation Processes*

The basic idea of AFM-based oxidation is straightforward [8]: using a conducting AFM tip held either in contact with or within a nanometer of an electrically biased,

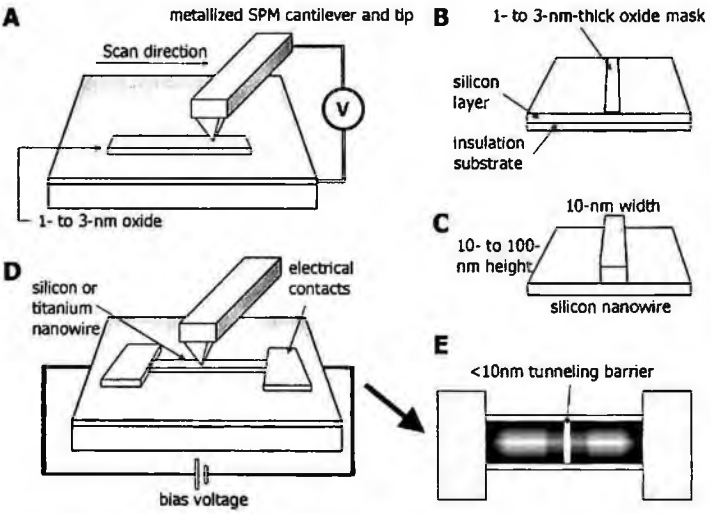

Figure 1. Thin oxide line. Scanning an electrically biased metallized AFM tip over the surface (A) can form a 1- to 3-nm-thick oxide line on many substrates. The pattern then can be used as an etch mask to create freestanding silicon nanowires (B,C). Further processing of the nanowire can also be carried out with the AFM tip (D) to create other confined structures. Reprinted with permission from [8] by Science.

stable, homogeneous substrate, one can induce highly localized enhanced oxidation of the substrate, as shown in Fig. 1. An oxide layer a few monolayers to a few nanometers in thickness rapidly forms on the substrate at the tip-sample junction. Typical line widths are ten to several tens of nanometers, and writing speeds of up to 1 mm/s are possible, depending on the material, voltage bias between the tip and substrate, and available oxygen. Voltages used range from three to several tens of volts, and both molecular oxygen and oxygen from adsorbed water layers that exist under ambient conditions at the tip-sample junction provide the reactant source. The presence of these impurities normally causes significant complications in other lithographic processes. Technical improvements began with Snow and Campbell's use of metallized AFM tips in place of STM [9]. They presented a method of fabricating Si nanostructures with an air-operated AFM. An electrically conducting AFM tip was used to oxidize regions ranging from 10 to 30 nm of an H-passivated Si (100) surface at writing speeds of up to 1 mm/s. This oxide served as an effective mask to transfer a pattern into the substrate by selective etching. The initial oxide growth rate depended exponentially on the applied voltage and produced an effective "tip sharpening" effect that allowed small features to be produced by a relatively large-diameter tip.

STM-based non-contact lithography has been previously studied in field-emission mode and is generally operated in ultra-high vacuums (UHVs) to maintain a stable emission current [10–13]. The local oxidation of silicon has also been performed using AFM in non-contact mode based on the force gradient [14]. Operation in UHVs can be cumbersome and time-consuming, and STM patterning also

suffers from poor alignment capabilities since imaging may expose the resist. Wilder *et al.* [15], who are part of Quate's group, introduced an alternative non-contact lithography technique based on AFM operated in air. They found that by using an active current feedback circuit with an appropriate high gain, they could maintain a stable field emission of electrons from the AFM tip, which were then used as the feedback signal to control the tip-to-sample spacing. This permitted reliable lithography in air. AFM apparatuses with fine vertical positioning and precise control of a constant current from the tip have been used to obtain feature sizes below 30 nm in 65-nm-thick resist. These features have been transferred through reactive ion etching into Si (100) substrates, yielding a 10:1 aspect ratio, as shown in Fig. 2. The ability to reliably pattern with AFM in a non-contact mode facilitates extension

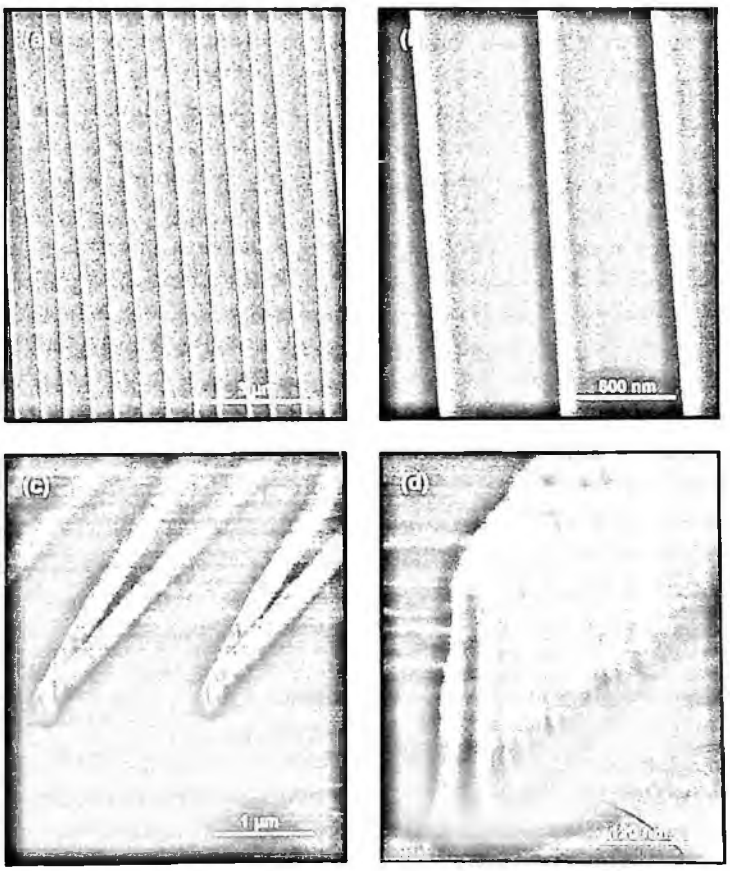

Figure 2. SEM micrographs of lines written using the noncontact AFM mode and etched into the underlying silicon. (a) Top-down image of 28-nm-wide lines written with an exposure dose of 20 nC/cm and a sample bias of 84 V. (b) Higher magnification image showing pattern continuity and uniformity. (c) The sample was tilted to show the ends of the zig-zag patterns. (d) A higher magnification of the turn-around point. The feature is 32 nm wide and etched 320 nm deep into the silicon, yielding a 10:1 aspect ratio. Reprinted with permission from [15] by American Institute of Physics (AIP).

to parallel lithography to increase the throughput of SPM-based lithography. However, a challenge for parallel lithography is maintaining independent control of the exposure properties of each tip. Minne *et al.* [16] developed an expandable system to operate multiple AFM probes in parallel at high speeds. The combined improvements from the parallelism and enhanced tip speeds in this system represented an increase in throughput by over two orders of magnitude. They also developed an array of 50 cantilevers with a 200 μm pitch that contained a dedicated integrated sensor and integrated actuator, permitting the probes to be scanned at 4 mm/s.

H-passivated Si surfaces have been successfully used in many nanoscale Si-oxide fabrication AFM processes because these surfaces are relatively stable in air [17–19]. In contrast, H-terminated Si surfaces are easily oxidized in humid ambient air, restricting their applications [32]. Ueno *et al.* [20] found that a bilayer-GaSe terminated Si (111) surface was very stable against heating and oxidation under UHV conditions. This surface was not oxidized even after exposure to ambient air for one month, although it could be oxidized through electrochemical reactions based on AFM oxidation processes. Ueno *et al.* reported that higher sample voltages, slower scan velocities, and/or higher ambient humidity levels produced wider and/or thicker oxide patterns, similar to conventional AFM oxidation processes based on Si substrates.

AFM-based nanoscale fabrication processes using various crystal planes or materials have also been reported. Chien *et al.* [21], in Gwo's group, introduced Si (110) nanomachining using an AFM oxidation lithography process. Silicon nanostructures with high aspect ratios (~400 nm structural height and ~55 nm lateral dimension) can be fabricated using this process and aqueous KOH orientation-dependent etching on H-passivated Si (110) wafers. Chien *et al.* also demonstrated that an AFM-induced local oxidation technique is a very effective way to convert the nanoscale thin Si_3N_4 film (<5 nm) on an Si (001) surface to SiO_X [22]. From experiments, they found that the threshold voltage for 4.2-nm-thick film was as low as 5 V and the initial growth rate was on the order of 10^3 nm/s at 10 V. They believed that the reaction of oxidants and silicon nitride resulted in the replacement of nitrogen by oxygen. Hence, the local intensive field induced by an AFM probe could turn silicon nitride into silicon oxides or silicon oxynitrides. Later, Klauser *et al.* [23] reported the exact oxide states in the AFM-induced localized area on a silicon nitride layer using scanning photoemission microscopy. A spatially resolved photoemission analysis with submicron resolution was used to study the oxidation states of converted silicon oxide patterns compared to the surrounding Si_3N_4 layer. The core level shift of the Si 2p photoelectron peak and the spectral features in the valence band revealed a complete conversion of silicon nitride to silicon oxide at a bias voltage of 10 V with no remaining nitrogen left. The main oxide was SiO_2.

Boisen *et al.* [24] studied AFM oxidation-based writing on a 7-nm-thick aluminum film. They obtained a line width of approximately 100 nm. Nonpatterned aluminum could be dissolved selectively in a wet chemical etch, leaving the patterned

areas as an etch mask. Alternatively, the aluminum oxide could be etched to form a positive etch mask. Aluminum and aluminum oxide are both excellent etch masks for reactive ion etching (RIE) of silicon and silicon oxide. Hence, by combining RIE processes, a variety of structures can be fabricated from aluminum-based masks. By demonstrating the fabrication of submicron cantilevers and bridges defined in silicon and silicon oxide, Boisen *et al.* showed the potential of fabricating advanced nanomechanical structures with integrated microelectronics. After this publication, many researchers fabricated nanostructures using Al surfaces on Si or SiO_2 [25–27]. Shirakashi *et al.* [28] investigated the AFM oxidation lithography process on a niobium-deposited SiO_2/Si substrate. The modified structures were fabricated by applying negative bias voltages to the metal-coated conductive cantilever in air, similar to conventional Si-based AFM oxidation lithography. They showed the results of varying the line width and height according to the scan speeds and bias voltages, and suggested that the modified structure was Nb oxide using an auger electron spectroscopy (AES) analysis. Their findings were similar to previously reported results for Ti, Cr, and GaAs depositions.

2.2. *Modified Oxidation Processes*

AFM oxidation lithography processes have been studied by a number of investigators and used for a variety of applications, including writing oxide patterns for use as etch masks to pattern metal silicides and for fabricating Si and metal-oxide nanoelectronic devices, because AFM provides fine controllable lateral and vertical movements. These processes coupled with additional mechanical or chemical treatments will be described in the following paragraphs.

The advancement of AFM oxidation lithography processes allowed the technique to be integrated into the processing of complementary metal-oxide semiconductor (CMOS) devices, as demonstrated by Snow and Campbell [29]. During the fabrication of metal wires and metal-oxide-metal (Ti-TiO_X-Ti) junctions using AFM oxidation with a conducting tip, the width of the wires and resistance of the junctions were controlled by real-time, *in situ* measurements of the device resistance. Because the properties of nanoscale devices are very sensitive to size variations, such measurements provide a more accurate method of controlling the device properties than using geometry alone. In this way, Snow and Campbell fabricated structures with critical dimensions of less than 10 nm with precisely tailored electrical properties. Similar to this work, Davis *et al.* [27] reported that the AFM oxidation of Al could be used to fabricate nanomechanical CMOS systems. It was necessary to precisely control the distance between the conductive tip and sample substrate to obtain accurate line widths of less than 10 nm, as shown in Fig. 3. By optimizing AFM parameters, line widths down to 10 nm have been routinely obtained on CMOS processed chips. Shirakashi *et al.* [30] applied an AFM oxidation lithography process based on a niobium-deposited SiO_2/Si substrate, as described in Ref. 28, to

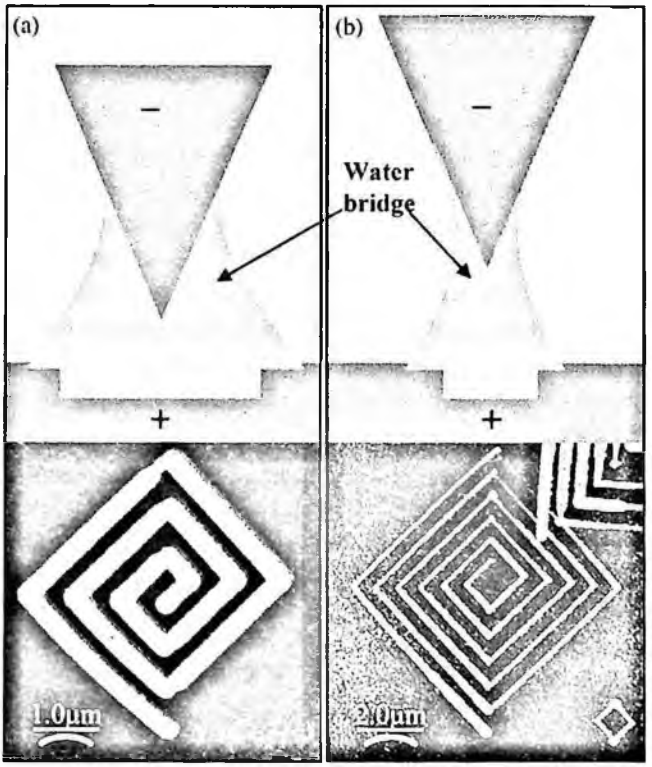

Figure 3. Schematic diagram and non-contact AFM image of an oxidized pattern with (a) a small tip/sample distance and high voltage and (b) large tip/sample distance and low voltage. Reprinted with permission from [27] by Elsevier.

thin Nb films on SiO_2/Si substrates to fabricate metal- and insulator-based electron devices with a Nb/Nb oxide system. The fabricated planar metal/insulator/metal (MIM) diodes showed non-linear I-V characteristics, implying that the Nb oxide wires formed by the AFM oxidation acted as insulating barrier material for the electrons. Thus, there is potential for using AFM oxidation processes to fabricate metal- and insulator-based devices.

Many research reports have been issued on lateral tunneling devices, such as tunneling transistors and single-electron transistors, based on lateral metal/oxide structures made from Ti/TiO_X and Nb/NbO_X using a STM or photolithography process [31–34]. These results indicate that this fabrication process is well-suited for constructing lateral tunneling devices. However, Snow *et al.* [35] demonstrated that the magnitude of the tunneling current in such metal/oxide devices is irreproducible because of the variability of the oxide stoichiometry, and that the devices were unstable under bias because of electromigration effects [29,31]. A PtSi/Si system can be an attractive alternative for such lateral quantum tunneling devices because the tunneling occurs through a crystalline Si layer of a back-to-back PtSi/Si/PtSi

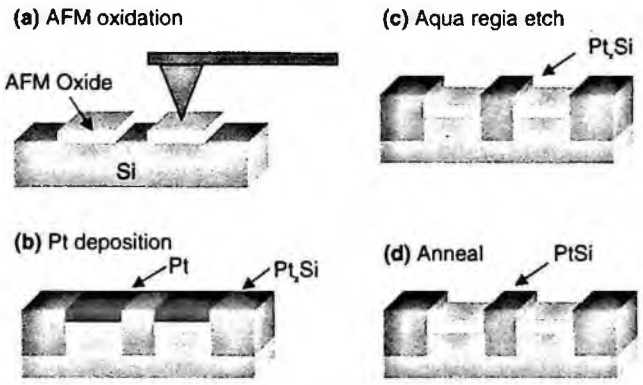

Figure 4. Diagram depicting the process for patterning PtSi by using scanned probe anodic oxidation as a diffusion mask. Annealing after the selective etch greatly restricts the lateral diffusion of the PtSi under the oxide mask. Reprinted with permission from [35] by American Institute of Physics (AIP).

Schottky barrier. Snow *et al.* reported a process for patterning ultra-thin layers of PtSi with high spatial resolution using AFM oxidation on an H-passivated Si surface, as shown in Fig. 4. This oxide pattern prevented the reaction of the deposited Pt film with the underlying Si to form PtSi. The unreacted Pt on the oxide was removed by selective etching before any annealing. This process greatly reduced lateral diffusion and produced a 2-nm-thick PtSi layer with good electrical properties. Consequently, the ability to fabricate nanoscale PtSi/Si features was an important step toward the realization and exploration of lateral Si-based quantum devices.

In practice, AFM oxidation is not suitable for patterning large features since the writing speed is limited by the inherent low throughput of single-probe lithography and the high scan speed stability of typical probe-based instrumentation. Since photonic device structures require both coarse and fine patterning, an alternative approach for prototyping such devices combines optical lithography and AFM oxidation, in which the optical lithography defines microsized coarse structures and the AFM oxidation defines only sub-100-nm fine structures. AFM-induced oxide can also be used as a mask for selective plasma nitridation of silicon to reverse the pattern, and negative-contrast structures can be produced by subsequent KOH etching [36]. Due to mobile ion (K^+) contamination, however, KOH is not favorable to the integrated circuit (IC) production process. In addition, the aggressive etching properties of KOH lead to a noticeable degree of roughness on the surface and sidewalls. Cohn *et al.* [37] proposed an alternative to KOH etching using a combination of SPM oxidation and TMAH etching. Tabata *et al.* [38] demonstrated anisotropic etching of silicon with a tetra-methyl ammonium hydroxide (TMAH) solution, which yielded a smooth surface, was a selective and nontoxic process, and was compatible with ICs. Hence, Chien *et al.* [39] used a combined process of optical lithography and AFM oxidation followed by additional wet chemical etching

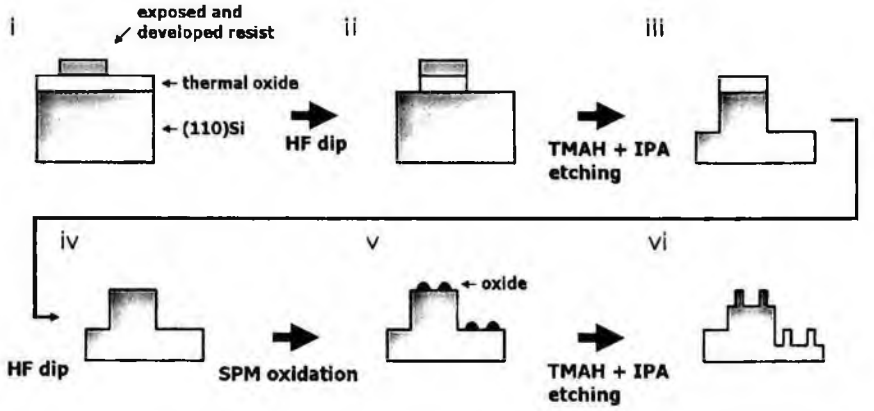

Figure 5. Schematic flowchart of the combination of optical lithography and SPM oxidation. Reprinted with permission from [39] by American Institute of Physics (AIP).

in a TMAH plus isopropyl alcohol (IPA) solution, as shown in Fig. 5. Functional photonic devices can be produced using such a combined process. For example, to fabricate a waveguide grating, optical lithography can be employed to define the waveguide structure and AFM oxidation can be used to define the grating structure.

There have also been many research reports related to the AFM oxidation processes of chemically modified surfaces. The surface of H-Si is, however, not as stable against oxidation when the entire surface area is oxidized gradually in air [40]. In addition, friction occurs while scanning the silicon strips on metal coatings away from the cantilever surfaces. A bilayer-GaSe terminated Si (111) substrate was employed in Ref. 20 to protect both surfaces from these problems. Another approach is to use organic self-assembled monolayers (SAMs) as resist materials for chemical modifications. It has been demonstrated that SAMs are available for ultra-thin uniform resists in lithography with UV [41] and SPM oxidation [42,43]. Ara *et al.* [44] proposed nanoscale modifications of alkyl monolayers covalently bound to Si (111) surfaces using an AFM oxidation process with platinum-coated AFM cantilevers. Alkylation of silicon is of growing interest since it provides an organic/inorganic system based on Si–C covalent bonds [40,45–47]. After the AFM oxidation, chemical modifications were performed, including 1-octadecene ($CH_2{=}CH{-}(CH_2)_{15}{-}CH_3$) treatment on etched surfaces in NH_4F solution and selective coverings with octadecyltrichrolosilane (OTS; $CH_3(CH_2)_{17}SiCl_3$), as illustrated in Fig. 6. Ara *et al.* reported that surfaces covered with alkyl monolayers did not change after more than one week in air, and that OTS was adsorbed on oxide layers through siloxane coupling. These siloxane monolayers are used as resist films in lithography [42,43]. There have also been attempts to cover the selectively etched surface on the local AFM oxidized area with fluorocarbons [48]. This process implies that nanoscale patterning of alkyl monolayers will prove useful in preparing nanoscale organic/inorganic interfaces. Yasuda *et al.* [49] reported selective epitaxial growths of Si based on the

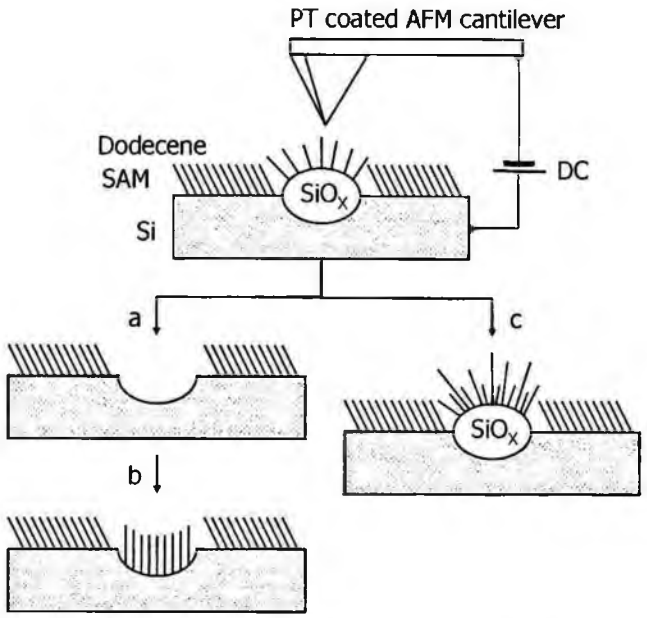

Figure 6. Schematic view of the chemical modification process: (a) removing the silicon oxide and terminating the surface of grooves with hydrogen using NH_4F; (b) covering the etched surface with 1-octadecene molecules; and (c) covering the silicon oxide with octadecyltrichlorosilane molecules. Reprinted with permission from [44] by American Institute of Physics (AIP).

subsequent etching of the local AFM oxidized area, similar to the previous process, using an ultra-thin bilayer mask. The key feature of this process was the direct writing of nanoscale patterns from the local AFM oxidation of the Si_3N_4 layer in air, as shown in Fig. 7. Windows for selective growth were defined by wet etching the locally oxidized regions. High growth selectivity after the chemical vapor deposition of Si was accomplished by employing a bilayer mask structure, which was formed by oxidizing the Si_3N_4 surface and then selectively desorbing SiO_2 in the windows. High-quality homoepitaxial growth of the Si was verified by transmission electron microscopy (TEM), which suggested the possibility of applying this technique to the heteroepitaxial growth of various materials on Si with a minimal junction area [50].

The AFM oxidation process can be used to fabricate nanoscale polymer structures. Lyuksyutov *et al.* [51] used amplitude-modulated electrostatic lithography on 20- to 50-nm-thick polymer films. The current flow through the thin polymer film, arising from a bias between the conductive substrate and AFM tip, resulted in localized Joule heating of the polymer attoliters above their glass transition temperature. Polarization and electrostatic attraction of the molten polymer toward the AFM tip in the strong (108–109 V/m) nonuniform electric field was believed to produce raised structures as small as 10–50 nm wide and 1–10 nm high. Several investigators have studied the detailed kinetics of this process in an attempt to understand the mechanism controlling the oxidation rate [52–58]. These studies have established two

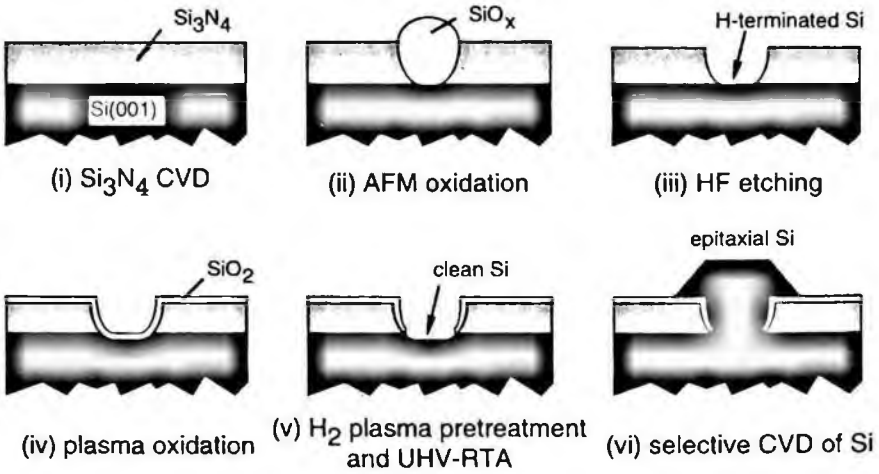

Figure 7. Procedures for preparation of a SiO_2/Si_3N_4 bilayer mask and selective epitaxial growth of Si. Reprinted with permission from [49] by American Institute of Physics (AIP).

empirical relationships that describe the growth kinetics: the oxide height increases as the logarithm of the growth time [54,55,57,58] and, for a fixed exposure time, the oxide height increases linearly with the applied voltage [53,57,58]. However, the oxide height can be controlled and modified by additional etching processes. In addition, there are many ways to reduce the line width of AFM-induced oxide lines. For example, scan speeds, bias voltages, tip-sample distances, humidity levels, and bias exposure times can be varied. The oxide width (full width at half maximum, FWHM) generated by AFM oxidation is largely dependent on the formation of water bridges between the tip end and sample surface. Hence, minimization of the water bridge in the lateral direction is a direct approach that can be used to reduce the oxide width. The width can be as small as a few nanometers if a single-wall CNT is used as the probe [59]. Dai *et al.* [60] first showed that CNTs might constitute well-defined tips for SPM imaging. They attached individual nanotubes, several micrometers in length, to the silicon cantilevers used in conventional AFM. There are several ways to attach CNTs to the AFM tip. Dai *et al.* [60] and Wong [61], in Lieber's group, presented a method of mechanically attaching nanotube bundles to fabricate the tips; however, it was time consuming and could not be used with the smallest nanotubes, limiting the quality of the tips. A new technique was developed, shown in Fig. 8, in which individual CNT probe tips were grown directly by chemical vapor deposition (CVD), providing control over the orientation [62,63]. The ends of the silicon tips were flattened at their apex by contact AFM imaging and were then anodized in hydrogen fluoride to create nanopores 50–100 nm in diameter along their axis. Nishijima *et al.* [64,65] attached CNTs to an AFM tip by preparing a CNT cartridge using electrophoresis. They demonstrated that individual CNTs could be transferred to an AFM tip by the driving force generated from electrostatic attraction under the precise stage movement control provided by

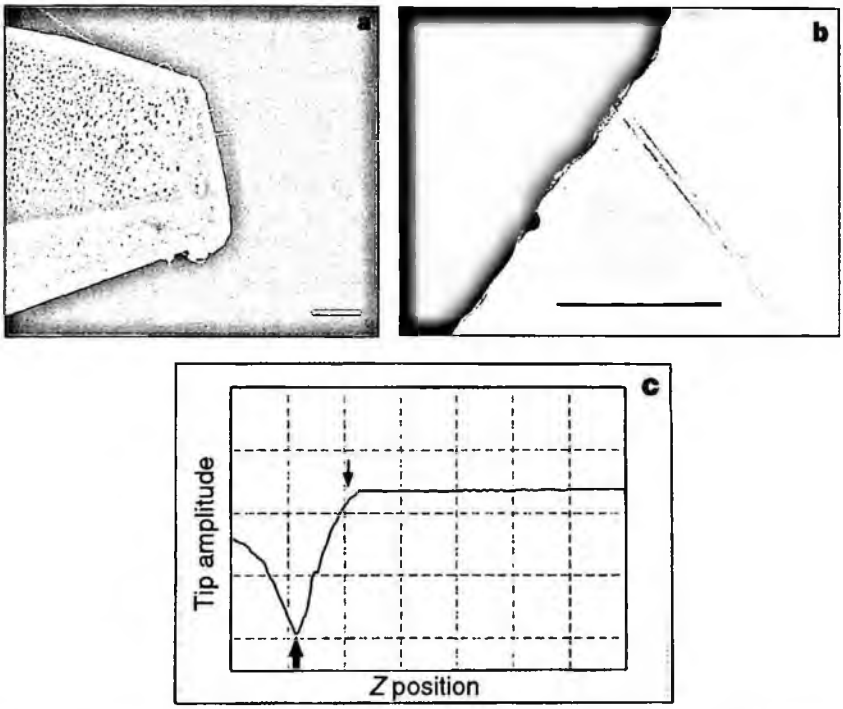

Figure 8. Characterization of CVD nanotube tips. (a) FE-SEM image of a CVD nanotube tip that has been shortened for imaging. Nanotubes were grown from a uniform pore structure consisting of pores about 60 nm in diameter, with 150 pores per μm^2. Scale bar, 1 μm. (b) Transmission electron microscope (TEM) image of a CVD nanotube tip. The entire AFM cantilever/tip assembly with nanotube tip was mounted on a custom TEM holder for imaging. Scale bar, 100 nm. (c) Tip oscillation amplitude (grid marks 5 nm apart) as a function of height above the sample (Z position; grid marks 2 nm apart) recorded in force calibration mode with a Nanoscope III (Digital Instruments). The right of the plot corresponds to free oscillation of the tip above the surface. As the tip approaches and begins to tap the surface (thin arrow), the amplitude decreases to zero. The oscillation amplitude increases again after the nanotube buckles (thick arrow). CVD nanotubes were grown in a tube furnace. Tips (with catalyst) were heated by 15°C per min to 750°C in a flow of 950 STP $cm^3\,min^{-1}$ argon and 40 STP $cm^3\ min^{-1}$ hydrogen. At 750°C, 10 STP $cm^3\ min^{-1}$ ethylene was added for 10 min, and the furnace was cooled at 15°C per min in 500 STP $cm^3\ min^{-1}$ argon. Reprinted with permission from [62] by Nature Publishing Group.

a scanning electron microscope. After the development of the CNT AFM tip, Dai *et al.* [66] applied it to the AFM oxidation lithography processes on H-terminated Si substrates. They verified that nanotubes could write nanostructures with a 10-nm line width at speeds up to 0.5 mm/s over large surface areas, and presented a solution to the long-standing tip-wear problem. Cooper [67] and Nishijima [68] also reported similar lithography processes using a CNT AFM tip on titanium and organic polysilane films, respectively.

AFM oxidation lithography allows us to produce nanoscale patterns and has become a powerful technique for prototyping novel device structures under the

system to monitor the tip position and write the pattern because the line width and patterning speed in DPN are independent of the contact force. The modified DPN process, which was used to construct protein arrays with 100- to 350-nanometer features, provided an opportunity to study a variety of surface-mediated biological recognition processes [75]. The fabrication of magnetic nanoparticle arrays [76], direct DNA patterning on metals and insulators [77], and optically active colored ink patterning [78] were also reported. Recently, Nelson *et al.* [79] introduced a modified thermal DPN (tDPN) process based on metal transfer from a metal-coated AFM tip onto the sample substrate. The AFM cantilever tip was coated with indium metal, like a miniature soldering iron, which could be deposited onto a surface forming lines with a width of less than 80 nm under heating conditions, as shown in Fig. 10. When the cantilever was unheated, no metal was deposited from the tip, allowing the writing to be registered to existing features on the surface. The ability to deposit a solid metal locally could enable the direct prototyping of nanoelectronics or masks. Moreover, deposition could be coupled with AFM surface metrology to perform *in situ* inspections and repairs of nanoelectronics.

4. Mechanical Lithography

Mechanical lithography is a method in which a solid material is mechanically removed and/or deformed by a tool to fabricate a groove pattern on a substrate. In conventional machining methods, such as turning, milling, and drilling, it is difficult to machine materials with machining depths of less than a hundred nanometer because of the motion error and thermal deformation of the machine tool and the elastic-plastic deformation that occurs on the tool and machined material [80]. It is also difficult to fabricate a micro/nano-machining tool that has a precise small shape with microscale/nanoscale resolution. AFM with friction force microscopy (FFM) was originally developed to observe solid materials at a nanoscale resolution [5,81], and therefore is capable of nanoscale movement and has a small probing tip for observations. By applying AFM and a probing tip as a machining and a nanomachining tool, respectively, it is possible to nanomachine various materials. In conventional machining, the cutting depth is controlled using the undeformed chip thickness. However, in AFM-based mechanical machining, the cutting depth is controlled by the normal force between the tool and the machined material, which is kept constant using feedback control from a piezo scanner. This method of control overcomes the problem of elastic-plastic deformation that disturbs the tool cutting the material. The primary advantage of AFM-based mechanical machining is the simplicity and low-cost of the fabrication process, because additional systems, such as those required for atmospheric control and electrochemical reactions, are not necessary. In addition, various materials can be machined using this method, whereas other methods are limited. Therefore, AFM-based mechanical machining is an effective tool for nanoscale lithography.

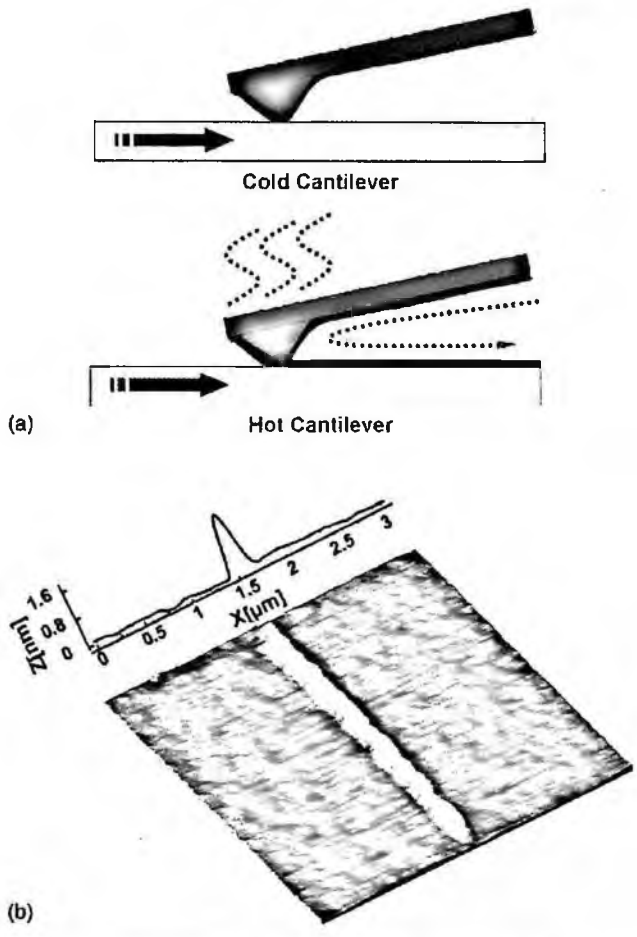

Figure 10. (a) Schematic of the operation of tDPN, which uses a heated AFM cantilever with a tip coated with a solid "ink." When the tip is hot enough to melt the ink, it flows onto the substrate. No deposition occurs when the tip is cold, allowing imaging without unintended deposition. (b) A topographic AFM image of a continuous nanostructure deposited from an In-coated tip onto a borosilicate glass substrate. Reprinted with permission from [79] by American Institute of Physics (AIP).

There are two AFM-based mechanical lithography techniques. The first is a material removal process in which the nanostructure is directly fabricated by mechanical machining, similar to mechanical scratching. The other is a combination of mechanical patterning and etching in which the material is patterned with a mechanical method and the structure is fabricated with subsequent etching. There are two methods of performing the latter process: one in which an etching mask made from another material is patterned by mechanical machining, and one in which an etching mask is formed directly by the mechanical patterning. These AFM-based mechanical lithographic techniques are described in the following paragraphs.

4.1. *Material Removal*

AFM makes use of a cantilever to detect forces between the tip and solid surface in the observation process. Machining at a nanometer resolution is made possible by applying the cantilever as a machining tool. Several attempts at direct mechanical patterning on materials have been reported. Göbel *et al.* [82] fabricated periodic structures and nonlinear complex structures on a gold surface. A 5-nm-deep periodic structure and a 25-nm-deep and 350-nm-wide scratched pattern were fabricated using an applied normal force of 25 μN. They applied these results to modify the gold structure fabricated by LIGA. Only the resist that adhered to the gold structure was successfully removed and smooth structures could be obtained by applying the highest normal force. Their results indicate that AFM machining is an effective tool not only for nanoscale patterning but also for modifying microscale/nanoscale structures. Sumomogi *et al.* [83] machined Ni, Cu, and Au films with a diamond tip. They applied normal forces ranging from 0.98 to 19.6 μN and machined these surfaces to a depth of over 100 nm by repeated machining. When machining Cu and Au, ridges caused by the adhesion of removed material were observed on the machined surface, whereas a smooth surface was formed after machining Ni, indicating that the nanomachining behavior is determined by several factors, such as the plasticity, adhesive, and properties of the materials.

Miyake [84] machined muscovite mica using a silicon nitride tip. Fractures occurred on the cleavage plane of the SiO_4-K and K-SiO_4 interfaces when the applied normal force was greater than 130 nN, and a 1-nm-deep groove was formed on the machined area. Kato *et al.* [85] demonstrated that machining aluminum covered with anodic oxide in various solutions, such as NaOH, $CuSO_4$, pure water, and Cu-electroless solution, enhanced the machining depth. As a result, a groove depth of 400–500 nm was fabricated by repeatedly scratching the surface 1600 times using a Si cantilever and NaOH or $CuSO_4$ solutions. They suggested that the ability to obtain deep grooves in NaOH and $CuSO_4$ solutions resulted from the dissolution of thin aluminum oxide layers in the solutions. Since stable oxides form in water, the resulting groove depth was shallower. Extensive tool wear of the silicon tip was observed after machining in the NaOH solution since the solution dissolved the silicon. The wear was improved by using a diamond tip; in this case, there was no noticeable wear after 16000 repetitions.

As described above, nanoscale patterning is possible using AFM-based mechanical machining. However, only soft materials can be effectively machined using this method while hard materials are limited to a maximum groove depth of a few nanometers. In addition, several thousand machining repetitions are required to machine a deep groove, which is time-consuming. Major limitations in the direct mechanical method include the shallow machining depth and tool wear. A conventional AFM cantilever has a low stiffness because it is necessary to detect minute forces between the tip and the sample in the observation process. To overcome these problems, several attempts to fabricate a scanning probe for mechanical patterning

have been reported. The most widely used material for a direct machining cantilever is diamond because of its extreme mechanical hardness and wear resistance. Unno *et al.* [86] developed a diamond cantilever by combining anodic bonding microfabrication techniques employing a CVD diamond film. The anodic bonding yielded a high-throughput fabrication process that produced pyramidal diamond tips. Oesterschulze *et al.* [87] fabricated a polycrystalline diamond probe using photolithography and CVD processes to create in-plane gate transistors made from GaAs/AlGaAs heterostructures. Grooves that were 0.5 and 5.0 nm deep were formed on a GaAs surface at normal forces of 1 μN and 10 μN, respectively, using the fabricated diamond cantilever. The in-plane gate transistors were fabricated using less machining repetitions than those machined with a silicon lever, and the wear problems were also reduced.

The diamond probes described above can eliminate probe tool wear, but the resulting groove depth is shallow due to the reduced lever stiffness. Therefore, it is necessary to develop a cantilever with high stiffness to fabricate deeper structures. Ashida *et al.* [88] developed a nanomachining and measuring system based on FFM that can machine a material with a removal depth of several tens of nanometers. The lateral force in the machining process can be measured using the FFM mechanism, resulting in effective realizations of nanoscale phenomena. This system uses a diamond tip cantilever with high stiffness. The cutting edge consists of a single diamond grain attached to the silicon lever. The stiffness of the cantilever is 820 N/m, over one thousand times greater than conventional cantilevers. The cantilever allows machining of single-crystal silicon surfaces, a material that is difficult to machine, to a maximum depth of 70 nm. Chip observations by SEM revealed that continuous and curled cutting chips were formed around the machined area, as shown in Fig. 11. This indicates that the silicon substrate was machined in a ductile mode. However, since the cantilever used a single diamond grain, which had an irregular shape, as the cutting edge, it was necessary to improve the irregularities to obtain higher precision nanomachining and patterning. Therefore, Kawasegi *et al.* [89] developed a diamond tip using a combination of photolithography and

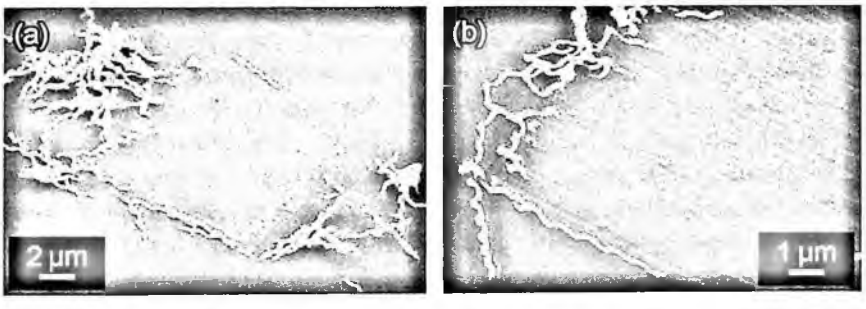

Figure 11. SEM image of cutting chips generated after machining a silicon substrate. The silicon was machined using diamond tip cantilever at a normal load of 2403 μN, and a scanning pitch of 157 nm (a), and 470 nm (b).

anisotropic wet etching of silicon. Their diamond tip has a sharp cutting edge with a tip radius less than 100 nm, and is attached to the silicon lever. It can machine a silicon substrate to a depth of 400 nm when the applied normal force is greater than 500 μN. This machining depth is significantly larger than that obtained using other cantilevers. In addition, the cantilever performs well for a machining distance greater than 1700 nm.

The mechanical removal process is an effective patterning method because of its simplicity and low-cost. Soft materials can easily be patterned using a conventional cantilever. The shallow machining depths and significant tool wear that are sometimes encountered for harder materials can be eliminated using a diamond cantilever. The machining resolution and groove depth are controlled by the accuracy of the machining tool. Therefore, the development of accurate machining tools is the most important factor when machining and patterning materials.

4.2. *Resist Removal and Etching*

In direct machining, structures are fabricated by removing materials, so it is easy to produce concave structures. However, it is necessary to remove large amounts of material to fabricate convex structures, which is a time-consuming process. The machining process described in the following paragraphs requires modifications to the etching mask only, and structures are fabricated by subsequent dry or wet etching. Etching can remove large amounts of material at a time, and therefore it is suitable for fabricating convex structures. In addition, various structural materials can be used simultaneously by applying different conventional lithographic techniques.

Magno and Bennett [90] fabricated nanometer-scale structures on GaSb/InAs film by machining and then wet etching, yielding a 20-nm-thick InAs layer covered with a 5-nm-thick GaSb layer, using a cantilever with normal forces between 70 and 350 nN and a scan rate of 0.07 μm/s. Consequently, 2-μm-long, 10-nm-deep, and 100-nm-wide grooves were formed. Then the InAs underlying the groove was etched in citric acid/hydrogen peroxide for 15 s while the GaSb layer acted as an etching mask. Therefore, the InAs under the machined area was selectively etched but the area covered with the GaSb layer was not. This produced a deeper and wider structure with a 72 ± 5 nm deep and 298 ± 16 nm wide groove after selective etching the GaSb layer in ammonium hydroxide/water. Magno and Bennett proposed using this technique for quantum wire and in-plane gated structures requiring trench isolation. Avramescu *et al.* [91] patterned a SiO_2 surface using a similar method. A 5-nm-thick poly-methylmethacrylate (PMMA) layer on 35-mm-thick SiO_2 was machined using a Si_3N_4 tip at a normal force of 1400 nN and scanning speed of 0.05 μm/s. The resulting product was then etched in buffered hydrofluoric acid (BHF) for 30 s. The machined pattern on the PMMA was transferred to the underlying SiO_2, and an array of lines with a period of 200 nm and a line width of 50 nm

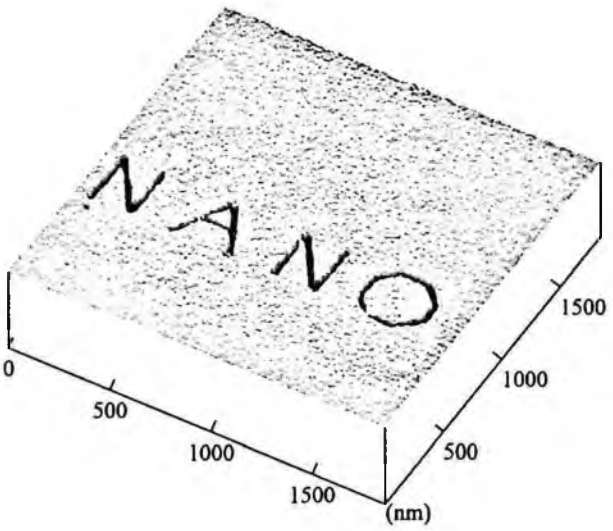

Figure 12. AFM topography image of letters on a SiO_2 surface with a line width of 40 nm. The structure was fabricated by patterning of resist layer applying tapping mode patterning and subsequent wet etching in BHF solution. Reprinted with permission from [92] by Elsevier.

was fabricated. To fabricate a precise structure, Klehn and Kunze [92] used a tapping mode to pattern a resist layer on a thermally grown SiO_2 and silicon surface. The frequency of the tapping mode was 300 kHz and the resist was patterned using a Si tip. After etching in BHF, an array of line structures was fabricated on the patterned area of the SiO_2, and the silicon line pattern was fabricated by subsequent KOH etching. Klehn and Kunze fabricated letters with a line width of 40 nm on a SiO_2 surface using this method, as shown in Fig. 12. Sung and Kim [93] demonstrated high-speed patterning of a resist layer on a workpiece substrate. To produce sub-100-nm-wide grooves using high-speed patterning, an ultra-thin self-assembled monolayer was applied as a resist layer. They used a diamond-coated tip (spring constant of 47 N/m, tip diameter of 200 nm) and fabricated a sub-100-nm-wide pattern over an area of $10000\,\mu m^2$ at a patterning speed of 1 mm/s and a normal force of $1.5\,\mu N$. The machining speed was significantly faster than other methods, enabling a high-throughput fabrication process.

The combination of resist removal and wet etching can be used to fabricate deeper and wider structures than a simple mechanical removal process. The etching mask material is soft (e.g. resist and PMMA) and therefore the tool wear is small. Several attempts have been made to fabricate structures from metal by applying conventional photolithographic techniques with AFM-based lithography. Sohn and Willett [94] demonstrated a combination of AFM lithography and a lift off process, and fabricated 42 nm-wide and 50 nm-thick Cr wires on a GaAs surface, as shown in Fig. 13. A PMMA layer on a blanket exposed poly methylmethacrylate/methacrylic acid (PMMA/MAA) layer was machined using AFM with a conventional Si_3N_4

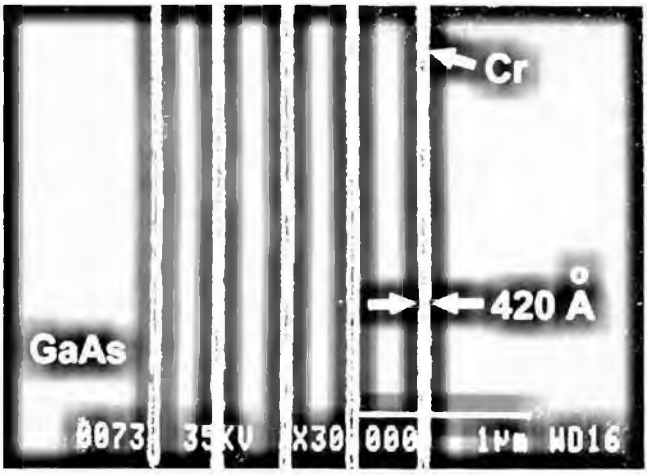

Figure 13. SEM image of Cr wires of 42 nm wide and 50 nm thick fabricated on a GaAs surface. The structure was fabricated using machining, development, and lift off processes. Reprinted with permission from [94] by American Institute of Physics (AIP).

cantilever at a normal force range of 1100–1180 nN. The sample was then baked and Cr was deposited. After the resist layers had been lifted off, the Cr wires were fabricated on the machined area. Sohn and Willett reported that the linewidth was affected by the fabrication conditions, such as the normal force, development time, and resist thickness. Bouchiat and Esteve [95] fabricated a single-electron transistor using RIE and a lift off process with AFM lithography. A 15- to 20-nm-thick PMMA layer on a 5- to 15-nm-thick germanium layer and a 200- to 300-nm-thick PMMA/MAA layer were machined using a silicon cantilever ($k = 5\,\mathrm{N/m}$), and then etched using RIE. After the RIE, a freestanding structure was formed under the germanium layer due to the under-etching of the PMMA/MAA layer. This method allows fabrication of a suspended germanium mask and provides a freestanding area under the mask. Using this mask, a tunnel junction can be fabricated by deposition at two angles through the suspended mask, thereby producing a 40-nm-wide metal line and single electron transistors. Hu *et al.* [96] used AFM mechanical lithography to fabricate a reactive ion etching (RIE) mask. A 3-nm-thick Ti layer and a 65-nm-thick PMMA layer on silicon were machined using a silicon cantilever with a tapping mode. The sample was etched by O_2 RIE; then a Cr structure was fabricated using deposition and a lift off process. Line structures that were 30 nm wide and 20 nm thick, and nanodots that were 20–40 nm wide were fabricated using the Cr structure as an etching mask for $SF_6 + O_2$ RIE.

AFM-based resist removal and subsequent etching provide more precise and low-cost patterning than using a conventional photolithographic method. A deeper or thicker structure with a height (depth) of several tens to hundreds of nanometers can be fabricated using this method. Since narrow metal structures can also be fabricated, the method is suitable for electronic devices that require such structures.

4.3. *Direct Patterning and Wet Etching*

In the following paragraphs, we will consider a simpler method of structure fabrication using direct patterning by AFM machining and subsequent wet etching.

Lee *et al.* [97] used H-passivated Si (100) to fabricate a structure by direct patterning and wet etching. The silicon surface was machined at a normal force of 25 nN and a scanning speed of 20 μm/s using a conventional Si_3N_4 tip with a 20-nm radius, and then etched in KOH for 10 s. As a result, a structure 8 nm high and 80 nm wide was fabricated on the machined area. Silicon atoms were bonded with hydrogen atoms on the surface of the sample. After the AFM machining, the Si-H bonds were broken, and dangling bonds of the silicon atoms then bonded with oxygen atoms in air, resulting in the formation of a native oxide layer on the machined area. The oxide layer acted as an etching mask in the KOH, so structures could be fabricated on the machined area. However, structures could not be fabricated when the tip force was less than 20 nN since this was too weak to break the Si–H bond.

The height of a structure fabricated by this method is very small because the native oxide layer is thin and the etch resistance against KOH is low. But by applying higher normal forces that are several hundreds of micronewtons, AFM machining can induce affected layers on silicon substrate, and these layers can be used as an etching mask. Park *et al.* [98] and Kawasegi *et al.* [99] proposed a direct mechanical patterning method known as tribo-nanolithography (TNL). They used TEM and secondary ion mass spectrometry (SIMS) analyses to show that an amorphous layer 100 nm wide and 20 nm deep was formed on a single-crystal silicon surface after machining with a diamond tip at a normal force of 350 μN due to pressure-induced phase transition. The amorphous layer formed had etch resistance against KOH and therefore could be used as an etching mask. A high-stiffness cantilever with a diamond tip [88] was used, and the applied normal force was several micronewtons. After machining, the machined area was not removed due to the large tip radius and it therefore protruded at a height of 1–2 nm due to the phase transition from a crystal to an amorphous silicon structure. During etching in KOH, the amorphous layer that formed on the machined area withstood the etching while the non-machined area was etched, creating a protruding structure with a height of several tens to hundreds of nanometers. However, the amorphous layer that formed on the machined area was selectively etched in HF, forming a concave structure with a depth of 10 to 20 nm [100]. These results indicate that two types of structure, convex and concave, can be fabricated by changing the etchant. Structures of various shapes have been fabricated using these phenomena. The depth and width of the amorphous layer formed depends on the machining conditions, such as the normal force and number of repetitions. Thus, etch resistance against KOH is controlled by these parameters. A step and a slanted structures fabricated by TNL and wet chemical etching are shown in Fig. 14. The silicon surface was machined by a diamond tip at five normal forces in the range of 124–372 μN and subsequently etched in 10 wt% KOH. As a result, a structure with five different heights was fabricated on the machined area,

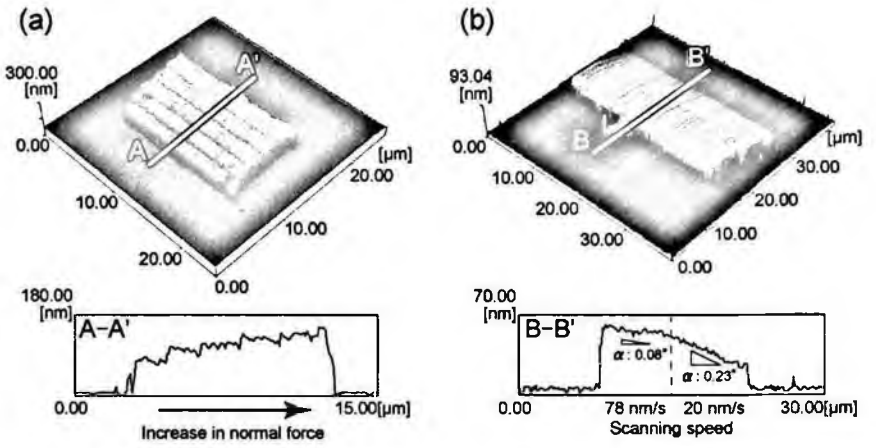

Figure 14. TNL-modified structures. (a) Step structure prepared by TNL and additional wet chemical etching. The silicon surface was machined at five normal forces in the range of 124-372 μN and subsequently etched in 10 wt.% KOH for 10 min. (b) Slanted structure prepared by TNL in 5 wt.% KOH solution. The speed in the y-direction was changed from 78 to 20 nm/s after modifying half of the area. Reprinted with permission from [98] by American Institute of Physics (AIP).

utilizing the change in thickness of the amorphous layer due to the normal force. A slanted structure can also be fabricated by machining in KOH, in which the formation of an amorphous layer and the etching of silicon occur simultaneously. A slanted, protruding structure is fabricated by taking advantage of the time lag in the machining process. Therefore, the inclination of the structure can be controlled by the scanning speed of the feed direction.

The techniques presented here can be used to fabricate a structure with a height of several tens to hundreds of nanometers using a simple process because the formation and development of a resist layer is not required. In addition, the etch resistance of the amorphous layer is controlled by the machining conditions, permitting the effective fabrication of three-dimensional structures.

This section examined nanopatterning using AFM-based mechanical machining. The advantage of these methods is the simplicity and low cost of the patterning process. However, there are several problems associated with these methods, such as tool wear and low machining depth for hard materials. The accuracy and efficiency of the fabricated structure depend on the machining tool. These problems can be eliminated by selecting an appropriate method and using a diamond tool. Therefore, the development of an appropriate cantilever for these applications is an important issue.

5. Thermally Induced Modifications

Thermally induced lithography forms a pattern on the material surface using heat-induced deformation. A heated cantilever is used to pattern the surface. AFM enables us to pattern the surface to a nanoscale resolution.

This method was mainly developed by IBM to build a high-density data storage device known as a Millipede. The method aims to write, read, and erase data on a thin polymer surface using a two-dimensional AFM array. In earlier work, Mamin *et al.* [101] fabricated pits on a PMMA surface using thermally induced modifications. An AFM tip irradiated by an infrared laser is in contact with a PMMA substrate. The heat from the tip softens the PMMA and forms pits on the contact area. The size of the pits varies from a few tens of nanometers to one micrometer, depending on the force and size of the laser pulse. Later, Vettiger *et al.* [102] developed a 32×32-AFM cantilever array located in a 3×3-mm^2 area that permitted high-speed thermomechanical writing/reading processes. Lutwyche *et al.* [103] demonstrated the writing and reading of 1024 data using a 32×32-cantilever array, as shown in Fig. 15. The 1024 data were written on a PMMA surface, and then read back. More than 80 percent of the levers were able to write and read back data. Indentations that were 40 nm wide with a pitch of 120 and 40 nm were fabricated. The pattern of 64×64 bits was written and read back by 128×128 pixels. The resulting data corresponded to 13–30 GB/in^2. Data density up to 1 TB/in^2 has been achieved [104]. This technology is expected to be used in ultra-high-density data storage devices that cannot be produced using conventional fabrication methods.

In another approach, Bae *et al.* [105] developed a diamond probe for thermomechanical nanolithography to eliminate tool wear. The diamond probe was fabricated using a silicon-lost mold and CVD techniques, and milled with a focused ion beam to sharpen the tip. Thermomechanical lithography was demonstrated on a PMMA surface and line patterns with a pitch of 40 nm were fabricated.

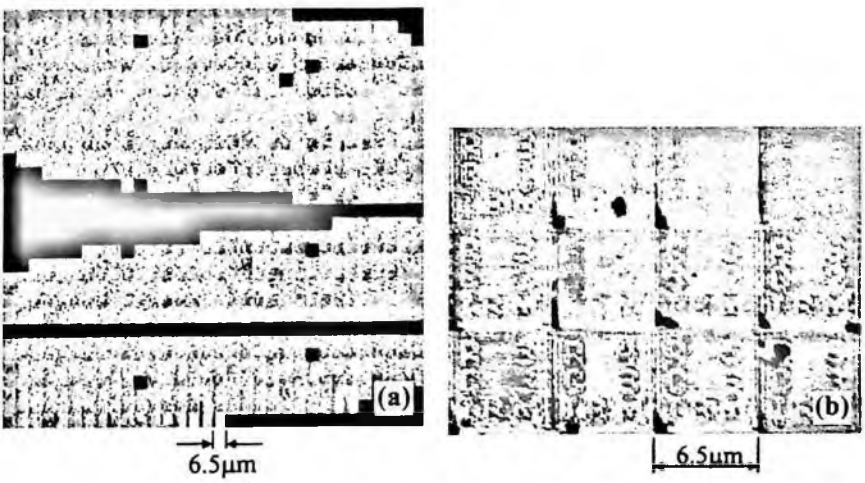

Figure 15. (a) 1024 AFM image read and written by 32×32 cantilever array. (b) Enlarged image of (a). Numbers in image indicate the row and column of each lever. Reprinted with permission from [103] by American Institute of Physics (AIP).

6. Conclusions

AFM-based lithography can be used to obtain nanoscale patterning and has become a powerful technique for prototyping novel device structures under the base of fine movements in the lateral or vertical directions of AFM. It is particularly suited to practical applications because it can be performed in air. This chapter has clearly shown that AFM-based lithography can ensure spatial resolution of under 10 nm, which is much better than most common lithographic process, including common photolithography and emerging next-generation lithography processes, for example, SNOM [6.106], FIB [3.107], EB [2.108] based modifications. However, AFM-based lithography has some unresolved problems for applications that require high throughput and wider patterning to centimeter scales. Most of these problems are related to system design and the lithography technique itself. In terms of system design, the parallel cantilever system reviewed in this chapter and high-speed stages with sub-nanometer feedback systems can provide a high throughput and wider patterning that can be applied to massive industrial applications. While the vertical resolution is controllable to sub-nanoscales by the feedback system in AFM, the lateral resolution is mainly dependent on the calibrated data of the PZT-actuated nanostages, which do not have feedback systems due to their high cost. Hence, the next generation of AFM, covering wider travel ranges under controllable sub-nanometer movements, must be developed in the near future. In addition, high-speed oxidation, material transfer, mechanical scratching, and other processing techniques that maintain patterning uniformity on a substrate must also be developed; these include cantilever design, advanced materials for transfer, and stable environmental control. Many worthy research studies reported worldwide have attempted to downscale the pattern size and apply AFM lithography, because researchers believe that this technique has the potential to become an essential tool for emerging nanotechnology and nanoscience related to electronic, photonic, biomedical, and nanosystem engineering.

References

1. E. W. Becker, W. Ehrfeld, P. Hagmann, A. Maner and D. Munchmeyer, Fabrication of microstructures with high aspect ratios and great structural heights by synchrotron radiation lithography, aalvanoforming, and plastic moulding (LIGA process), *Microelectoron. Eng.* **4**, 35–56 (1986).
2. K. Yamazaki, T. Yamaguchi and H. Namatsu, Three-dimensional nanofabrication with 10-nm resolution, *Jpn. J. Appl. Phys.*, **43**, L1111–L1113 (2004).
3. B. Schmidt, L. Bischoff and J. Teichert, Writing FIB implantation and subsequent anisotropic wet chemical etching for fabrication of 3D structures in silicon, *Sensors Actuators A*, **61**, 369–373 (1997).
4. G. Binnig, H. Rohrer, Ch. Gerber and E. Weibel, Surface studies by scanning tunneling microscopy, *Phys. Rev. Lett.*, **49**, 57–61 (1982).
5. G. Binnig, C. F. Quate and Ch. Gerber, Atomic Force Microscope, *Phys. Rev. Lett.*, **56**, 930–933 (1986).

6. D. W. Pohl, W. Denk and M. Lanz, Optical stethoscopy: Image recording with resolution $\lambda/20$, *Appl. Phys. Lett.*, **44**, 651–653 (1984).
7. A. A. Tseng, A. Notargiacomo and T. P. Chen, Nanofabrication by scanning probe microscope lithography: a review, *J. Vac. Sci. Technol. B*, **23**, 877–894 (2005).
8. J. A. Dagata, Device fabrication by scanned probe oxidation, *Science*, **270**, 1625–1626 (1995).
9. E. S. Snow and P. M. Campbell, Fabrication of Si nanostructures with an atomic force microscope, *Appl. Phys. Lett.*, **64**, 1932–1934 (1994).
10. M. A. McCord and R. F. W. Pease, Lift-off metallization using poly (methyl methacrylate) exposed with a scanning tunneling microscope, *J. Vac. Sci. Technol. B*, **6**, 293–296 (1988).
11. C. R. K. Marrian, E. A. Dobisz and R. J. Colton, Lithographic studies of an e-beam resist in a vacuum scanning tunneling microscope, *J. Vac. Sci. Technol. A*, **8**, 3563–3569 (1990).
12. C. R. K. Marrian, E. A. Dobisz and J. A. Dagata, Electron-beam lithography with the scanning tunneling microscope, *J. Vac. Sci. Technol. B*, **10**, 2877–2881 (1992).
13. J. Moreland and P. Rice, High-resolution, tunneling-stabilized magnetic imaging and recording, *Appl. Phys. Lett.*, **57**, 310–312 (1990).
14. D. Wang, L. Tsau and K. L. Wang, Nanometer-structure writing on Si(100) surfaces using a non-contact-mode atomic force microscope, *Appl. Phys. Lett.*, **65**, 1415–1417 (1994).
15. K. Wilder, C. F. Quate, D. Adderton, R. Bernstein and V. Elings, Noncontact nano-lithography using the atomic force microscope, *Appl. Phys. Lett.*, **73**, 2527–2529 (1998).
16. S. C. Minne, G. Yaralioglu, S. R. Manalis, J. D. Adams, J. Zesch, A. Atalar and C. F. Quate, Automated parallel high-speed atomic force microscopy, *Appl. Phys. Lett.*, **72**, 2340–2342 (1998).
17. Ph. Avouris, T. Hertel and R. Martel, Atomic force microscope tip-induced local oxidation of silicon: kinetics, mechanism, and nanofabrication, *Appl. Phys. Lett.*, **71**, 285–287 (1997).
18. T. Teuschler, K. Mahr, S. Miyazaki, M. Hundhausen and L. Ley, Nanometer-scale field-induced oxidation of Si(111):H by a conducting-probe scanning force microscope: Doping dependence and kinetics, *Appl. Phys. Lett.*, **67**, 3144–3146 (1995).
19. R. García, M. Calleja, and F. Pérez-Murano, Local oxidation of silicon surfaces by dynamic force microscopy: Nanofabrication and water bridge formation, *Appl. Phys. Lett.*, **72**, 2295-2297 (1998).
20. K. Ueno, R. Okada, K. Saiki and A. Koma, Nano-scale anodic oxidation on a Si (111) surface terminated by bilayer-GaSe, *Surf. Sci.*, **514**, 27–32 (2002).
21. F. S.-S. Chien, C.-L. Wu, Y.-C. Chou, T. T. Chen, S. Gwo and W.-F. Hsieh, Nanomachining of (110)-oriented silicon by scanning probe lithography and anisotropic wet etching, *Appl. Phys. Lett.*, **75**, 2429–2431 (1999).
22. F. S.-S. Chien, J.-W. Chang, S.-W. Lin, Y.-C. Chou, T. T. Chen, S. Gwo, T.-S. Chao and W.-F. Hsieh, Nanometer-scale conversion of Si_3N_4 to SiO_X, *Appl. Phys. Lett.*, **76**, 360–362 (2000).
23. R. Klauser, I.-H. Hong, H.-J. Su, T. T. Chen, S. Gwo, S.-C. Wang, T. J. Chuang and V. A. Gritsenko, Oxidation states in scanning-probe-induced Si_3N_4 to SiO_X conversion studied by scanning photoemission microscopy, *Appl. Phys. Lett.*, **79**, 3143–3145 (2001).

24. A. Boisen, K. Birkelund, O. Hansen and F. Grey, Fabrication of submicron suspended structures by laser and atomic force microscopy lithography on aluminum combined with reactive ion etching, *J. Vac. Sci. Technol. B*, **16**, 2977–2981 (1998).
25. G. Abadal, A. Boisen, Z. J. Davis, O. Hansen and F. Grey, Combined laser and atomic force microscope lithography on aluminum: Mask fabrication for nanoelectromechanical systems, *Appl. Phys. Lett.*, **74**, 3206–3208 (1999).
26. G. Abadal, Z. J. Davis, A. Boisen, F. Pérez-Murano, N. Barniol and X. Borrisé, Combining laser and jumping mode AFM lithography on aluminum for the fabrication of nanoelectromechanical devices, *Probe Microsc.*, **2**, 121–128, (2001).
27. Z. J. Davis, G. Abadal, O. Hansen, X. Borisé, N. Barniol, F. Pérez-Murano and A. Boisen, AFM lithography of aluminum for fabrication of nanomechanical systems, *Ultramicroscopy*, **97**, 467–472 (2003).
28. J. Shirakashi, M. Ishii, K. Matsumoto, N. Miura and M. Konagai, Surface modification of niobium (Nb) by atomic force microscope nano-oxidation process, *Jpn. J. Appl. Phys.*, **35**, L1524–L1527 (1996).
29. E. S. Snow and P. M. Campbell, AFM Fabrication of Sub-10-Nanometer Metal-Oxide Devices with *in situ* Control of Electrical Properties, *Science*, **270**, 1639–1641 (1995).
30. J. Shirakashi, K. Matsumoto, N. Miura and M. Konagai, Nb/Nb oxide-based planar-type metal/insulator/metal (MIM) diodes fabricated by atomic force microscope (AFM) nano-oxidation process, *Jpn. J. Appl. Phys.*, **36**, L1120–L1122 (1997).
31. E. S. Snow, P. M. Campbell, R. W. Rendell, F. A. Buot, D. Park, C. R. K. Marrian and R. Magno A, Metal/oxide tunneling transistor, *Appl. Phys. Lett.*, **72**, 3071–3073 (1998).
32. K. Matsumoto, M. Ishii and K. Segawa, Application of scanning tunneling microscopy nanofabrication process to single electron transistor, *J. Vac. Sci. Technol. B*, **14**, 1331–1335 (1996).
33. K. Matsumoto, M. Ishii, K. Segawa, Y. Oka, B. J. Vartanian and J. S. Harris, Room temperature operation of a single electron transistor made by the scanning tunneling microscope nanooxidation process for the TiOx/Ti system, *Appl. Phys. Lett.*, **68**, 34–36 (1996).
34. K. Fukushima, R. Sasajima, K. Fujimaru and H. Matsumura, A novel nanoscale metal transistor fabricated by conventional photolithography, *Jpn. J. Appl. Phys.*, **38**, 7233–7236 (1999).
35. E. S. Snow, P. M. Campbell, M. Twigg and F. K. Perkins, Ultrathin PtSi layers patterned by scanned probe lithography, *Appl. Phys. Lett.*, **79**, 1109–1111 (2001).
36. S. Sharma, M. K. Sunkara, M. M. Crain, S. F. Lyuksyutov, S. A. Harfenist, K. M. Walsh and R. W. Cohn, Selective plasma nitridation and contrast reversed etching of silicon, *J. Vac. Sci. Technol. B*, **19**, 1743–1746 (2001).
37. R. W. Cohn, S. F. Lyuksyutov, K. M. Walsh and M. M. Crain, Nanolithography considerations for multi-passband grating filters, *Opt. Rev.*, **6**, 345–354 (1999).
38. O. Tabata, R. Asahi, H. Funabashi, K. Shimaoka and S. Sugiyama, Anisotropic etching of silicon in TMAH solutions, *Sens. Actuators A*, **34**, 51–57 (1992).
39. F. S.-S. Chien, W.-F. Hsieh, S. Gwo, A. E. Vladar and J. A. Dagata, Silicon nanostructures fabricated by scanning probe oxidation and tetra-methyl ammonium hydroxide etching, *J. Appl. Phys.*, **91**, 10044–10050 (2002).
40. A. Bansal, X. Li, I. Lauermann, N. S. Lewis, S. I. Yi and W. H. Weinberg, Alkylation of Si Surfaces using a two-step halogenation/grignard route, *J. Am. Chem. Soc.*, **118**, 7225–7226 (1996).

41. H. Sugimura, K. Ushiyama, A. Hozumi and O. Takai, Micropatterning of alkyl- and fluoroalkylsilane self-assembled monolayers using vacuum ultraviolet light, *Langmuir*, **16**, 885–888 (2000).
42. L. Brandow, J. M. Calvert, E. S. Snow and P. M. Campbell, Metal pattern fabrication using the local electric field of a conducting atomic force microscope probe, *J. Vac. Sci. Technol. A*, **15**, 1455–1459 (1997).
43. H. Sugimura, O. Takai and N. Nakagiri, Scanning probe lithography for electrode surface modification, *J. Electroanal. Chem.*, **473**, 230–234 (1999).
44. M. Ara, H. Graaf and H. Tada, Nanopatterning of alkyl monolayers covalently bound to Si(111) with an atomic force microscope, *Appl. Phys. Lett.*, **80**, 2565–2567 (2002).
45. M. R. Linford, P. Fenter, P. M. Eisenberger and C. E. D. Chidsey, Alkyl monolayers on silicon prepared from 1-alkenes and hydrogen-terminated silicon, *J. Am. Chem. Soc.*, **117**, 3145–3155 (1995).
46. M. M. Sung, G. J. Kluth, O. W. Yauw and R. Maboudian, Thermal behavior of alkyl monolayers on silicon surfaces, *Langmuir*, **13**, 6164–6168 (1997).
47. A. B. Sieval, V. Vleeming, H. Zuilhof and E. J. R. Sudhölter, An improved method for the preparation of organic monolayers of 1-alkenes on hydrogen-terminated silicon surfaces, *Langmuir*, **15**, 8288–8291 (1999).
48. M. Ara and H. Tada, Friction force microscopy using silicon cantilevers covered with organic monolayers via silicon–carbon covalent bonds, *Appl. Phys. Lett.*, **83**, 578–580 (2003).
49. T. Yasuda, S. Yamasaki and S. Gwo, Nanoscale selective-area epitaxial growth of Si using an ultrathin SiO_2/Si_3Ni_4 mask patterned by an atomic force microscope, *Appl. Phys. Lett.*, **77**, 3917–3919 (2000).
50. D. Zubia, S. H. Zaidi, S. R. Brueck and S. D. Hersee, Nanoheteroepitaxial growth of GaN on Si by organometallic vapor phase epitaxy, *Appl. Phys. Lett.*, **76**, 858–860 (2000).
51. S. F. Lyuksyutov, P. B. Paramonov, S. Juhl and R. A. Vaia, Amplitude-modulated electrostatic nanolithography in polymers based on atomic force microscopy, *Appl. Phys. Lett.*, **83**, 4405–4407 (2000).
52. J. A. Dagata, T. Inoue, J. Itoh, K. Matsumoto and H. Yokoyama, Role of space charge in scanned probe oxidation, *J. Appl. Phys.*, **84**, 6891–6900 (1998).
53. D. Stiévenard, P. A. Fontaine and E. Dubois, Nanooxidation using a scanning probe microscope: An analytical model based on field induced oxidation, *Appl. Phys. Lett.*, **70**, 3272–3274 (1997).
54. Ph. Avouris, T. Hertel and R. Martel, Atomic force microscope tip-induced local oxidation of silicon: kinetics, mechanism, and nanofabrication, *Appl. Phys. Lett.*, **71**, 285–287 (1997).
55. R. Garcıa, M. Calleja and F. Pérez-Murano, Local oxidation of silicon surfaces by dynamic force microscopy: Nanofabrication and water bridge formation, *Appl. Phys. Lett.*, **72**, 2295–2297 (1998).
56. J. A. Dagata, T. Inoue, J. Itoh and H. Yokoyama, Understanding scanned probe oxidation of silicon, *Appl. Phys. Lett.*, **73**, 271–273 (1998).
57. P. A. Fontaine, E. Dubois and D. Stiévenard, Characterization of scanning tunneling microscopy and atomic force microscopy-based techniques for nanolithography on hydrogen-passivated silicon, *J. Appl. Phys.*, **84**, 1776–1781 (1998).
58. E. S. Snow, G. G. Jernigan and P. M. Campbell, The kinetics and mechanism of scanned probe oxidation of Si, *Appl. Phys. Lett.*, **76**, 1782–1784 (2000).
59. S. Iijima, Helical microtubules of graphitic carbon, *Nature*, **354**, 56–58 (1991).

60. H. Dai, J. H. Hafner, A. G. Rinzler, D. T. Colbert and R. E. Smalley, Nanotubes as nanoprobes in scanning probe microscopy, *Nature*, **384**, 147–150 (1996).
61. S. S. Wong, E. Joselevich, A. T. Wooley, C. L. Cheung and C. M. Lieber, Covalently functionalized nanotubes as nanometre-sized probes in chemistry and biology, *Nature*, **394**, 52–55 (1998).
62. J. H. Hafner, C. L. Cheung and C. M. Lieber, Growth of nanotubes for probe microscopy tips, *Nature*, **398**, 761–762 (1999).
63. C. L. Cheung, J. H. Hafner and C. M. Lieber, Carbon nanotube atomic force microscopy tips: Direct growth by chemical vapour deposition and application to high-resolution imaging, *PNAS*, **97**, 3809–3813 (2000).
64. H. Nishijima, S. Kamo, S. Akita, Y. Nakayama, K. I. Hohmura, S. H. Yoshimura and K. Takeyasu, Carbon-nanotube tips for scanning probe microscopy: Preparation by a controlled process and observation of deoxyribonucleic acid, *Appl. Phys. Lett.*, **74**, 4061–4063 (1999).
65. Y. Nakayama, H. Nishijima, S. Akita, K. I. Hohmura, S. H. Yoshimura and K. Takeyasu, Microprocess for fabricating carbon-nanotube probes of a scanning probe microscope, *J. Vac. Sci. Technol. B*, **18**, 661–664 (2000).
66. H. Dai, N. Franklin, and J. Han, Exploiting the properties of carbon nanotubes for nanolithography, *Appl. Phys. Lett.*, **73**, 1508–1510 (1998).
67. E. B. Cooper, S. R. Manalis, H. Fang, H. Dai, K. Matsumoto, S. C. Minne, T. Hunt and C. F. Quate, Terabit-per-square-inch data storage with the atomic force microscope, *Appl. Phys. Lett.*, **75**, 3566–3568 (1999).
68. A. Okazaki, S. Akita, H. Nishijima and Y. Nakayama, Nanolithography of organic polysilane films using carbon nanotube tips, *Jpn. J. Appl. Phys.*, **39**, 3744–3746 (2000).
69. S. C. Minne, J. D. Adams, G. Yaralioglu, S. R. Manalis, A. Atalar and C. F. Quate, Centimeter scale atomic force microscope imaging and lithography, *Appl. Phys. Lett.*, **73**, 1742–1744 (1998).
70. S. C. Minne, S. R. Manalis and C. F. Quate, Parallel atomic force microscopy using cantilevers with integrated piezoresistive sensors and integrated piezoelectric actuators, *Appl. Phys. Lett.*, **67**, 3918–3920 (1995).
71. D. M. Kolb, R. Ullmann and T. Will, Nanofabrication of small copper clusters on gold(111) electrodes by a scanning tunneling microscope, *Science*, **275**, 1097–1099 (1997).
72. R. D. Piner, J. Zhu, F. Xu, S. Hong and C. A. Mirkin, "Dip-Pen" nanolithography, *Science*, **283**, 661–663 (1999).
73. R. D. Piner and C. A. Mirkin, Effect of water on lateral force microscopy in air, *Langmuir*, **13**, 6864–6868 (1997).
74. S. Hong and C. A. Mirkin, A nanoplotter with both parallel and serial writing capabilities, *Science*, **288**, 1808–1811 (2000).
75. K. B. Lee, S. J. Park, C. A. Mirkin, J. C. Smith and M. Mrksich, Protein nanoarrays generated by dip-pen nanolithography, *Science*, **295**, 1702–1705 (2002).
76. X. Liu, L. Fu, S. Hong, V. P. Dravid and C. A. Mirkin, Arrays of magnetic nanoparticles patterned via "dip-pen" nanolithography, *Adv. Mater.*, **14**, 231–234 (2002).
77. L. M. Demers, D. S. Ginger, S.-J. Park, Z. Li, S.-W. Chung and C. A. Mirkin, Direct patterning of modified oligonucleotides on metals and insulators by dip-pen nanolithography, *Science*, **296**, 1836–1838 (2002).
78. M. Su and V. P. Dravid, Colored ink dip-pen nanolithography, *Appl. Phys. Lett.*, **80**, 4434–4436 (2002).

79. B. A. Nelson, W. P. King, A. R. Laracuente, P. E. Sheehan and L. J. Whitman, Direct deposition of continuous metal nanostructures by thermal dip-pen nanolithography, *Appl. Phys. Lett.*, **88**, 033104 (2006).
80. N. Taniguchi, Current status in, and future trends of, ultraprecision machining and ultrafine materials processing, *Annals of the CIRP*, **32**, 573–582 (1983).
81. G. Meyer and N. M. Amer, Simultaneous measurement of lateral and normal forces with an optical-beam-deflection atomic force microscope, *Appl. Phys. Lett.*, **57**, 2089–2091 (1990).
82. H. Gobel and P. Blanckenhagen, Atomic force microscope as a tool for metal surface modifications, *J. Vac. Sci. Technol. B*, **13**, 1247–1251 (1995).
83. T. Sumomogi, T. Endo, K. Kuwahara, R. Kaneko and T. Miyamoto, Micromachining of metal surfaces by scanning probe microscope, *J. Vac. Sci. Technol. B*, **12**, 1876–1880 (1994).
84. S. Miyake, 1 nm deep mechanical processing of muscovite mica by atomic force microscopy, *Appl. Phys. Lett.*, **67**, 2925–2927 (1995).
85. Z. Kato, M. Sakairi and H. Takahashi, Nanopatterning on aluminum surfaces with AFM probe, *Surf. Coat. Technol.*, **169–170**, 195–198 (2003).
86. K. Unno, T. Shibata and E. Makino, Micromachining of diamond probes for atomic force microscopy applications, *Sensors Actuators A*, **88**, 247–255 (2001).
87. E. Oesterschulze, A. Malave, U. F. Keyser and R. J. Haug, Diamond cantilevers with integrated tip for nanomachining, *Diam. Relat. Mater.*, **11**, 667–671 (2002).
88. K. Ashida, N. Morita and Y. Yoshida, Study on nano-machining process using mechanism of a friction force microscope, *JSME Int. J. Ser. C*, **44**, 244–253 (2001).
89. N. Kawasegi, N. Takano, D. Oka, N. Morita, S. Yamada, K. Kanda, S. Takano, T. Obata and K. Ashida, Nanomachining of silicon surface using atomic force microscope with diamond tip, *ASME J. of Manuf. Sci. and Eng.*, **128**, 723–729 (2006).
90. R. Magno and B. R. Bennett, Nanostructure patterns written in III-V semiconductors by an atomic force microscope, *Appl. Phys. Lett.*, **70**, 1855–1857 (1997).
91. A. Avramescu, K. Uesugi and I. Suemune, Atomic force microscope nanolithography on SiO_2/semiconductor surfaces, *Jpn. J. Appl. Phys.*, **36**, 4057–4060 (1997).
92. B. Klehn and U. Kunze, SiO_2 and Si nanoscale patterning with an atomic force microscope, *Superlatt. Microstruc.*, **23**, 441–444 (1998).
93. I. H. Sung and D. E. Kim, Nano-scale patterning by mechano-chemical scanning probe lithography, *Appl. Surf. Sci.*, **239**, 209–221 (2005).
94. L. L. Sohn and R. L. Willett, Fabrication of nanostructures using atomic-force-microscope-based lithography, *Appl. Phys. Lett.*, **67**, 1552–1554 (1995).
95. V. Bouchiat and D. Esteve, Lift-off lithography using an atomic force microscope, *Appl. Phys. Lett.*, **69**, 3098–3100 (1996).
96. S. Hu, A. Hamidi, S. Altmeyer, T. Koster, B. Spangenberg and H. Kurz, Fabrication of silicon and metal nanowires and dots using mechanical atomic force lithography, *J. Vac. Sci. Technol. B*, **16**, 2822–2824 (1998).
97. H. T. Lee, J. S. Oh, S. J. Park, K. H. Park, J. S. Ha, H. J. Yoo and J. Y. Koo, Nanometer-scale lithography on H-passivated Si(100) by atomic force microscope in air, *J. Vac. Sci. Technol. A*, **15**, 1451–1454 (1997).
98. J. W. Park, N. Kawasegi, N. Morita and D. W. Lee, Tribonanolithography of silicon in aqueous solution based on atomic force microscopy, *Appl. Phys. Lett.*, **85**, 1766–1768 (2004).
99. N. Kawasegi, N. Morita, S. Yamada, N. Takano, T. Oyama and K. Ashida, Etch stop of silicon surface induced by tribo-nanolithography, *Nanotechnology*, **16**, 1411–1414 (2005).

100. J. W. Park, N. Kawasegi, N. Morita and D. W. Lee, Mechanical approach to nanomachining of silicon using oxide characteristics based on tribo nanolithography (TNL) in KOH solution, *ASME J. Manuf. Sci. Eng.*, **126**, 801–806 (2004).
101. H. J. Mamin and D. Rugar, Thermomechanical writing with an atomic force microscope tip, *Appl. Phys. Lett.*, **61**, 1003–1005 (1992).
102. P. Vettiger, M. Despont, U. Drechsler, U. Durig, W. Haberle, M.I. Lutwyche, H.E. Rothuizen, R. Stutz, R. Widmer and G. K. Binnig, The "millipede"-more than one thousand tips for future AFM data storage, *IBM J. Res. Develop.*, **44**, 323–340 (2000).
103. M. I. Lutwyche, M. Despont, U. Drechsler, U. Durig, W. Haberle, H. Rothuizen, R. Stutz, R. Widmer, G. K. Binnig and P. Vettiger, Highly parallel data storage system based on scanning probe arrays, *Appl. Phys. Lett.*, **77**, 3299–3301 (2000).
104. P. Vettiger, G. Cross, M. Despont, U. Drechsler, U. Durig, B. Gotsmann, W. Haberle, M. A. Lantz, H. E. Rothuizen, R. Stutz and G. K. Binnig, The "millipede" – nanotechnology entering data storage, *IEEE Trans. Nanotechnol.*, **1**, 39–55 (2002).
105. J. H. Bae, T. Ono and E. Esashi, Scanning probe with an integrated diamond heater element for nanolithography, *Appl. Phys. Lett.*, **82**, 814–816 (2003).
106. A. A. Tseng, Recent developments in nanofabrication using scanning near-field optical microscope lithography, *Opt. Laser Technol.*, **39**, 514–526 (2007).
107. A. A. Tseng, Recent developments in nanofabrication using focused ion beams, *Small*, **1**, 924–939 (2005).
108. A. A. Tseng, K. Chen, C. D. Chen and K. J. Ma, Electron beam lithography in nanoscale fabrication: recent development, *IEEE Trans. Electron. Packag. Manuf.*, **26**, 141–149 (2003).

CHAPTER 3

SCANNING PROBE ARRAYS FOR NANOSCALE IMAGING, SENSING, AND MODIFICATION

CHRISTIAN SANTSCHI, JERÔME POLESEL-MARIS, JÜRGEN BRUGGER* and HARRY HEINZELMANN†

Centre Suisse d'Electronique et de Microtechnique SA (CSEM), Rue Jaquet-Droz 1, P.O. Box, CH-2002 Neuchâtel, Switzerland

**Microsystems Laboratory, Ecole Polytechnique Fédérale de Lausanne (EPFL), Station 17, CH-1015 Lausanne, Switzerland*

Nowadays tools based on Scanning Probe Methods (SPM) have become indispensable in a wide range of applications such as cell imaging and spectroscopy, profilometry, or surface patterning on a nanometric scale. Common to all SPM techniques is a typically slow working speed which is one of their main drawbacks. The SPM speed barrier can be improved by operating a number of probes in parallel mode. A key element when developing probe array devices is a convenient read-out system for measurements of the probe deflection. Such a read-out should be sufficiently sensitive, resistant to the working environment, and compatible with the operation of large number of probes working in parallel. In terms of fabrication, the geometrical uniformity i.e. the realisation of large numbers of identical probes, is a major concern but also the material choice compatible with high sensitivity, the detection scheme and the working environment is a challenging issue. Examples of promising applications using parallel SPM are dip-pen-nanolithography, data storage, and parallel imaging.

Keywords: Actuation; Atomic Force Microscopy (AFM); Atomic resolution; Antibody; Block-copolymer; Bragg grating; Carbon Nano Tubes (CNT); Contact mode; Dielectric; Diamond; Doping; Dry etch; Electrochemical sensing; Electronic noise; External sensing; Ferroelectric; Flicker noise; Focused electron beam (FEB); Focused Ion Beam (FIB); Force distance curves (FDC); Glycerol; Heterodyne; Homodyne; Interferometry; Magnetostrictive; Microfluidic channel; Millipede; MOSFET; Mould; Multi-Wall Carbon Nano Tubes (MWCNT); μWalker; Noise; Optical path difference; Oxidation sharpening; Piezoelectric effect; Piezoresistive coefficient; Piezoresistive effect; Polymer; Potassium hydroxide

†to whom correspondence should be addressed, harry.heinzelmann@csem.ch

KOH; Tip-surface interaction; Replication; Resonance frequency; Sacrificial layer; Scanning Electrochemical Microscopy (SECM); Scanning Probe Methods (SPM); Scanning Thermal Microscopy (SThM); Scanning Tunnelling Microscopy (STM); Self-Assembled Monolayer (SAM); Self sensing; Sensitivity; Silicon nitrate Si_xN_y; Silicon oxide (SiO_2); Single-Wall Carbon Nano Tubes (SWCNT); Spectral density; Stress; Tapping mode; Thermal noise; Thermal sensing; Tomographic imaging; Topographical imaging; Voltammetry; Wave-guide; Wet etch.

Nomenclature

A	:	Area
C	:	Capacitance
D	:	Distance between cantilever end and the photodiode
D_O	:	Diffusion coefficient
E	:	Electric Field
F	:	Force
F_{th}	:	Thermal forces
I	:	Intensity
$I_{T,\infty}$	:	Steady state current
OPD	:	Optical path difference
P	:	Power
Q	:	Electrical charge
Q_c	:	Quality factor
R	:	Resistance
$S_{A_{th}}$	:	Spectral density of thermal noise
$S_{F_{th}}$	:	Spectral force density
T	:	Temperature
V	:	Voltage
a	:	Electrode Diameter
c	:	Specific heat
c_O	:	Concentration of oxidised species
d	:	Thickness of air gap
d_Q	:	Charge coefficient
k	:	Thermal conductivity
k_B	:	Boltzman constant
k_c	:	Spring constant
l	:	Cantilever length
n	:	number of electrons
w	:	Cantilever width
t	:	Cantilever thickness
$\Delta_{Photodiode}$	:	Spot displacement
ΔR	:	Change in resistance
Φ	:	Faraday constant
δ	:	Deflection

ε : Strain
ε_0 : Permittivity in vacuum
ε_r : Relative permittivity
φ : Phase
λ : Wavelength
μ : Thermal diffusion length
π : Piezoresistive coefficient
ρ : Density
σ : Stress
ω : Modulation frequency of temperature
ω_0 : Resonance frequency
ω_l : Laser frequency
ω_s : Shifted frequency

CONTENTS

1. Introduction 68
2. Materials and Fabrication Processes 69
   2.1. Probe materials 70
   2.2. Tip fabrication processes 71
   2.3. Cantilever fabrication processes 74
3. Parallel Detection in Scanning Probe Arrays 75
   3.1. General considerations 76
      3.1.1. Sensitivity 76
      3.1.2. Noise limit 77
   3.2. External sensing 78
      3.2.1. Optical beam deflection 78
      3.2.2. Optical diffraction sensing 80
      3.2.3. Interferometric sensing 81
   3.3. Self sensing 83
      3.3.1. Piezoresistive sensing 84
      3.3.2. Piezoelectric sensing 86
      3.3.3. Capacitive sensing 87
      3.3.4. Alternative methods of self sensing 88
   3.4. Tip-surface interaction sensing 93
      3.4.1. Electrochemical sensing 93
      3.4.2. Thermal sensing 94
4. Examples and Applications of Scanning Probe Arrays 95
   4.1. Imaging applications of probe arrays 96
      4.1.1. Imaging by parallel force microscopy 96
      4.1.2. Imaging of ultra-large scan areas 99

4.1.3. Electrochemical imaging with probe arrays 100
4.1.4. Thermal imaging with probe arrays 102
4.2. Force spectroscopy 103
4.3. Surface modification 103
4.3.1. Data storage 106
4.3.2. Nano-dispensing of liquids 109
4.3.3. Dip-Pen-Nanolithography (DPN) 111
4.4. Hybrid arrays of probes 112
5. Conclusion 113
References 114

1. Introduction

The development of the Scanning Tunneling Microscope (STM) [23] and shortly thereafter the Atomic Force Microscope (AFM) [22] in the 1980s for many people represents the most significant breakthrough of nanotechnology, if not its real starting point. For the first time, it was possible to image solid surfaces with atomic resolution[a], to measure interaction forces on a molecular level [73], and to manipulate matter at the atomic scale [46].

Today, Scanning Probe Methods (SPM) include a wide range of microscopy techniques which have found countless applications. STM is mostly used for high resolution work on electrically conductive surfaces under controlled conditions (high vacuum or ultra-high vacuum (UHV), and local electron spectroscopy. On the other hand, force microscopy has become the commonly used technique to get microscopic (topography) information on virtually any type of surface. Its operation is more robust and less prone to disturbances from ambient conditions, and it is more flexible with regards to environmental conditions and sample properties. In controlled environments such as UHV, force microscopy has demonstrated lateral resolution comparable to the best STM data ("true atomic resolution" [59]). Further SPM representatives include the Scanning Near-Field Optical Microscope (SNOM) [114, 152], the Scanning ElectroChemical Microscope (SECM) [14], the Scanning Thermal Microscope (SThM) [154], and many more.

Characteristic to all SPM techniques is that a nanoscale probe is raster scanned in close proximity across the sample surface, and that its interaction with that sample surface is recorded to generate a surface map (the surface "image"). In most operation modes, a feedback loop constantly compares the measured interaction to a previously chosen set value, and controls the vertical location of the probe to keep it at a constant distant to the surface. As a consequence, common to all SPM

[a] It is true that field ion microscopy (FIM), introduced in the first half of the last century, is capable of atomic scale imaging, but it is limited to selected conducting surfaces at high electric field conditions.

techniques is a typically long acquisition time of an individual image frame. A higher resolution data set of 512 × 512 data points at a scan speed of 1 sec/line requires several minutes of acquisition time. This limitation is due to amplifier or detection bandwidths which limits signal detection below a certain frequency, mechanical resonances of the scanner and the instrument which would destabilize the instrument beyond acceptable levels, and/or signal to noise issues which require a certain minimum acquisition time to improve measurement statistics.

Some of these issues can be addressed by video rate operation of SPM [77, 124, 162]. Here, the setup is optimized so that images can be taken at rates of 25 frames sec^{-1}. To the operator such a microscope with its "real-time" panning and zooming capabilities feels more like a Scanning Electron Microscope (SEM) than a conventional SPM.

The article presented here deals with an alternative approach to break the SPM speed barrier. By operating a number of N probes in parallel, N images can be acquired simultaneously. Such a setup allows the rapid investigation of larger scan areas, or the execution of high resolution or high sensitivity experiments N-times in parallel, adding to the statistical significance of the SPM data. The N-fold gain in acquisition time or data quality for some applications justifies a largely increased complexity of the setup, and its associated increased cost.

In the following section, we describe the most relevant microfabrication techniques and materials used to fabricate the nanometric probes used in SPM. Particular weight will be put on those processes that can lead to an integration of probes into arrays. The next section is devoted to the detection of the cantilever deflection. Numerous detection schemes have been demonstrated in the past, but only few have proven that they are valid technologies for the read-out of many probes in parallel. Finally, the most relevant applications will be presented, along with a discussion of the additional advantages gained from the probe arrays.

2. Materials and Fabrication Processes

In scanning probe methods such as force microscopy, the probe is composed of the nanometric tip responsible for sensing with high lateral resolution, and a transduction element composed of a flexible cantilever. Materials for probes include semiconductors, dielectrics, metals and polymers. It is important, however, to distinguish between materials used for the cantilever and materials used for the tip. Depending on the application, a probe needs to have well-defined cantilever and tip specifications. The cantilever is characterized by its compliance, i.e. spring constant k_c, and its resonance frequency ω_0. The tip is characterized by its shape i.e. aspect ratio, height, and apex radius. Microfabricated tips can be realized in distinct ways: direct and indirect fabrication by etching and moulding, respectively. Both methods have good reproducibility and are suitable for high-volume tip and/or tip array manufacturing. Additional techniques include sharpening or deposition of tips using

focused beam methods. Some applications require that the tip and cantilever are made of different materials. This can be done by post-growing or post-assembling processes. For integrated manufacturing processes, however, such hybrid probes represent considerable difficulties. With a few exceptions [3], tip and cantilever are typically fabricated from the same material when integrated fabrication processes are used.

Several fundamentally different methods for producing nanometer sharp tips and tip arrays have been presented. Additional complications arise when nanotips have to be integrated onto cantilevers. Therefore, not all of the presented techniques are compatible with micromachining technology, and suitable for mass manufacturing of MEMS based nanoprobe systems.

For parallel probe implementation the issue of geometrical uniformity becomes central, which in turn affects the process control for a given manufacturing process. It is therefore important to address the question: can a process that works reliably for the fabrication of individual sharp tips be used for probe array fabrication? An example of a parallel probe array is shown in Fig. 1.

2.1. *Probe materials*

The first AFM system was built with a hand-cut aluminium foil as cantilever tip which was bent to allow one edge to act as a tip. Later, diamond fragments were glued to the cantilever in order to form a tip-like protrusion. The use of dielectric thin films led to a breakthrough in cantilever and tip fabrication. They can be reproducibly and precisely made with well-controlled thickness, structured with conventional lithography, and made free-standing by micromachining methods using sacrificial layers or removing the dispensable part of the Si-substrate. Furthermore,

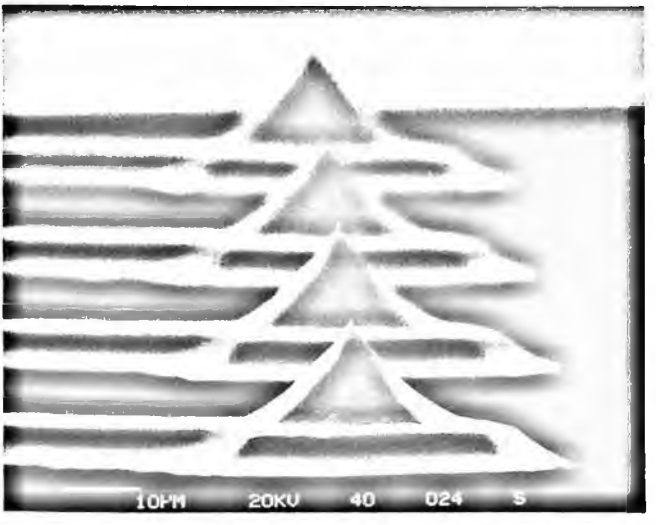

Figure 1. SEM micrograph of an array of 4 microfabricated silicon cantilevers with tips. The probes have been fabricated using a combination of dry and wet silicon etching [32].

they are mechanically and chemically robust. Silicon oxide SiO_2 and silicon nitrate Si_xN_y (Si_3N_4) probes can be formed on silicon by standard microfabrication processes such as thermal oxidation or chemical vapour deposition (CVD). The ability to fill a sharp potassium hydroxide (KOH) -etched pyramidal mould that is defined by the <111> etch stop planes of silicon was exploited for the first mass-fabricated SPM tips [9]. The moulding method allows fabrication of SPM probes with virtually any material that can be deposited as thin film. For instance, diamond and diamond-like carbon tips [70,144,145], metallic probes made of nickel [160,210] and tungsten [181] for conductive probes have been realized.

Polymer probes of ultraviolet (UV) sensitive spin-coated photoplastic layers have been fabricated in a similar way and presented by Genolet *et al.* for SPM applications [56]. Akiyama *et al.* developed a wafer-scale process for batch fabrication and mounting polymer tips on a quartz tuning fork [6]. A microscopic four-point probe for resistivity measurements on thin films was fabricated using high-aspect ratio, negative photoresist as probe and cantilever material [94]. The use of UV light-structurable material allows a very simple fabrication technique in order to create sharp polymer probes with an apex radius in the range of 20 to 50 nm, depending on the mould, which does not require high-end thin film processing equipment. The major drawback of polymer probes however, is their poor resistance to mechanical wear. Silicon tips have been fabricated by dry and wet etching techniques [32,201]. These have very good mechanical properties and are used in standard probes for commercial AFM instruments. Akamine *et al.* developed microfabricated SiN cantilevers with an integral single-crystal silicon tip [3]. The silicon tip is self-aligned to the end of the cantilever and created by a process which simultaneously fabricates and sharpens the silicon tip with an apex radius in the range from 20 to 40 nm. Examples for such probes have been presented by Akamine *et al.*, Folch *et al.* and Grow *et al.* [3,52,66].

An interesting material for AFM tips are carbon nanotubes, either in single- or multi-wall form (SWCNT, MWCNT), since they can be made with a precise diameter in the sub-5 nm range, have a shape with a well-defined aspect ratio, and are mechanically very robust. Carbon nanotube tips have been assembled [68] or catalytically grown onto cantilevers [36]. Although, significant progress has been made recently, a major difficulty remains in the uniform fabrication and integration of CNT onto cantilevers, particularly in view of parallel probe systems, where a large number of tips must be fabricated.

An overview of the various materials along with the possibilities to realize nanoprobes is listed in Table 1, where material, shape and technology are compared.

2.2. *Tip fabrication processes*

Sharp tips can be fabricated either by direct or indirect methods in which a sharp mould is created prior to a replication step. Both methods are used for reliable mass-manufacturing of cantilevers with sharp tips. Other methods include beam-induced deposition. Focused beams of charged particles can be used to locally deposit

Table 1. Overview of tips for scanning probe applications.

Fabrication technique	Tip material	Tip shape	Aspect ratio	Tip apex [nm]	Batch process	Type of application	References
Direct tip fabrication (etching)							
Dry etching/dry + wet etching	Si	Conical	10:1	40	Yes	SPM	[29, 32, 201]
Wet etching (isotropic)	Si	Conical	2:1	50	Yes	Field emission	[11]
Wet etching (anisotropic)	Si	Pyramidal		15	Yes	Field emission	[11]
Indirect tip fabrication: (moulding)							
Si mould	Si_3N_4	Pyramid	1:1	30	Yes	SPM	[9]
		Pencil	4:1	30	Yes		
Sharpened Si mould	Si_3N_4			<10	Yes		[4]
	Metal (W, Pt)	Pyramid	1:1	50	Yes	Conducting SPM	[5, 181]
Tunable mould radius	Any thin film	Pyramid	1:1	20–200	Yes	SPM, NSOM	[97]
Sharpened Si mould	SU-8	Pyramid	1:1	~30	Yes	SPM	[56, 57]
Deposition							
Shadow mask	Metal	Conical	2:1	50	Yes		[10]
FEB	Organic composites	Shaft	90:1	10	No	SPM for high aspect ratio imaging (trenches)	[76, 112, 165, 190]
FIB	Pt plus organic composites	Shaft	10:1	30	No	SPM	[89]
Milling							
Focused ion beam	SiO_2 or any dielectric	Arbitrary		10	No	SPM NADIS	[79, 106, 132, 136, 150]
	Diamond	Pyramid	1:1	~30	Yes	Wear resistance SPM	[70]
Tip assembly							
	CNT	Shaft	Up to 100:1	<5	No	High resolution SPM	[68]
Tip growth							
	CNT	Shaft	Up to 100:1	<5	Eventually	High resolution SPM	[36]

tip-like structures with high aspect ratios. Focused Electron Beam (FEB) [76,190] and Focused Ion Beam (FIB) [89,136] induced deposition have been developed for the fabrication of appropriate probe tips. FEB and FIB methods are very useful for rapid prototyping but due to the serial approach they are less suited for batch fabrication.

Tips made of thin film materials (dielectrics, metals) are typically made via moulding and replication methods [9]. First, a sharp mould is created in a sacrificial substrate (typically silicon) or a substrate covered by a sacrificial layer. The mould shape can vary from pyramidal, semi-spherical to conical, depending on the material and mould fabrication method. If necessary, the mould can be further sharpened by oxidation processes [4]. In a second step, the dielectric or metal layer is deposited on the substrate and inside the mould and structured by photolithography. Finally, the probe material is released by etching the substrate or the sacrificial layer [56]. In some cases, a thin organic monolayer is added in order to allow the easy removal of the probe from the mould [96]. For example, a layer of dodecyltrichlorosilane forming self-assembled monolayers (SAM) on a SiO_2 substrate reduces the adhesion between the SiO_2 and a 100 nm thick evaporated aluminium (Al) film. Subsequently, a 100 μm thick layer of photoplastic polymer material has been spun onto the SiO_2-SAM-Al sandwich layer and structured by photolithography. In a final step, the polymeric micro-part together with the Al-layer could be mechanically lifted off from the substrate due to the low adhesion between SAM and Al layer. The organic SAM provides enough resistance for the microfabrication process including photoresist spinning and thermal steps. This process has been used for the fabrication of photoplastic probes for scanning near-field optical microscopy [96]. In contrast to the deposition of a sacrificial layer which needs to be relatively thick, this method has the advantage of preserving the mould sharpness.

Tips in silicon are etched by wet, dry, or combined methods [32,201]. The most important parameter to control is the etch duration in order to prevent the tips from being over-etched and becoming blunt. Reproducibility in lithography, as well as variations of the global and local etch rates play a crucial role (Fig. 2) in order to obtain the uniformity that must be achieved for parallel probes in terms of height,

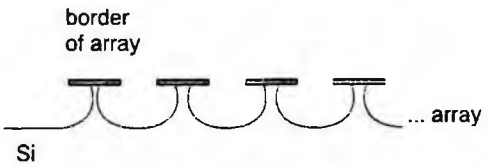

Figure 2. Tip formation by underetching showing inhomogeneities over an array. Due to loading effects in plasma etch process, the silicon probe at the edge of the array has a different etch rate than those in the centre of the array. This leads to a different shape of the etched probes. The underetch rate at the border of the array is higher than in the centre due to more available reactive ions, whereas etching in the centre is ion depletion limited. Such effects can be minimized by appropriate mask design, e.g. larger etch masks, or fabrication of blank structures at the borders [29].

shape and sharpness. The different etch ratios of high index planes in Si can be exploited for high fabrication yield. Oxidation sharpening of silicon can also be used to improve the sharpness of the probes. It can be used for etched probes [127] as well as for silicon moulds and has in particular increased the manufacturing yield of nanoprobes.

2.3. *Cantilever fabrication processes*

In the case of dielectric thin film cantilevers (e.g. Si_xN_y) the lever thickness is precisely determined by the deposited film thickness, typically in the order of 100–500 nm, depending on the targeted mechanical properties. In the case of single-crystal silicon as cantilever material, a double-side micromachining process with wafer-through etching yields free-standing silicon cantilevers. Silicon-On-Insulator (SOI) substrates, where the buried silicon dioxide serves as an etch stop layer, can be used in cases where well-defined thickness control of the cantilever is required.

Silicon and SOI wafers are also used for the fabrication of cantilevers with integrated piezoresistive sensors [188]. Typically, a locally and shallow doped region of boron creates a conductive path through parts of the cantilever whose resistivity changes as a function of cantilever bending. The piezoresistive effect is described in more details below. The force sensibility of piezoresistor devices can in general be maximized keeping the thickness of the piezoresisitve layer as thin as possible. Implanted ions have an enhanced diffusivity prior to annealing [71], the diffusion coefficient of implanted boron (B) ions being 10^3 times the intrinsic value. Harley *et al.* fabricated 890 Å thick cantilevers using epitaxially grown piezoresistors [71]. The boron is incorporated into the lattice during the epitaxy process and therefore, diffusion could be minimised for the post processed annealing. Saya *et al.* have proposed another approach to realise ultrathin piezoresistors in which germanium (Ge) has been implanted prior to boron implantation [171]. The Ge bombardment results in a preamorphised Ge layer, which avoids channelling effects during boron implantation. A subsequent short annealing step at 950°C further minimises boron diffusion.

Constant force measurements performed with probe arrays require activation of each cantilever which allows force control for the individual cantilevers. Therefore, other types of cantilevers needed to be developed that include structures with integrated piezoelectric films allowing *in-situ* actuation. Minne *et al.* showed piezoelectric cantilever arrays that enable z-actuation allowing parallel constant force imaging at high speed [139]. The actuator has been realised by integrating a thin zink oxide (ZnO) layer at the base of the cantilever. Kim *et al.* reported a CMOS process combining 34×34 and 100×100 thermo-piezoelectric Si_3N_4 cantilevers into an array. The array is composed of lead zirconate titanate (PZT) cantilevers with integrated heaters and piezoelectric sensors forming a high-speed and low-power SPM-based data-storage system [100, 142]. Although piezoelectric films show interesting characteristics, their dimensions are necessarily larger to those of the thin-film

cantilevers, and the associated processing methods today are still too complex to allow reliable manufacturing. Electrothermal excitation is another frequently used method for cantilever actuation. Akiyama *et al.* integrated Al-Si thermal bimorph structures at the base of the cantilever. Applying a heating power of 45 mW a static deflection of 8 μm has been achieved on a 580 μm long cantilever.

Occasionally, the fabrication techniques for tip, cantilever and peripheral interface systems are not compatible. In such cases parallel wafer-to-wafer transfer methods using bonding techniques have also been developed [42].

The fabrication steps to realize single probes must be critically reviewed for their compatibility if parallel probe systems need to be made. Not only is the height of the tip important, but the initial shape, thickness and bending of the cantilever also plays a crucial role. This has consequences in particular for the variation of the probe properties such as initial bending, compliance, and resonance frequency ω_0. During a SPM single probe experiment, the approach angle for a cantilevered single probe to a planar substrate is not a critical issue. However, in the case of a linear parallel probe arrangement, the approach angle becomes critical in the plane parallel to the surface. The alignment of the cantilevers and the approach of the array determine which tip comes in contact with the surface first. Often, the two outermost probes are intentionally made longer to serve as adjustment probes (Fig. 3). It is obvious that a similar approach must also be considered for a 2D probe array where at least three adjustment probes should be used for the alignment of the array.

3. Parallel Detection in Scanning Probe Arrays

The first realization of atomic force microscopy relied on a tunnelling contact to the backside of the cantilever in order to detect its deflection δ with high sensivity [22]. However, this method turned out to be too unreliable under ambient conditions, and it was soon replaced by other methods. In recent years, various cantilever deflection schemes have been developed, such as optical beam deflection or interferometry, piezoelectric and piezoresistive sensing of stress in the deflected cantilever, change in the capacitance formed by the cantilever and a counter electrode, and magnetic methods.

In this section, the state-of-the art in probe sensing systems is presented. Advantages and limitations for cantilever arrays are highlighted.

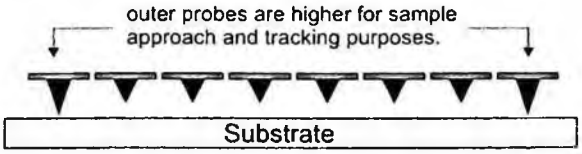

Figure 3. Schematic illustration of probe-to-sample approach. Outermost tips are larger to allow approach monitoring and array alignment [29].

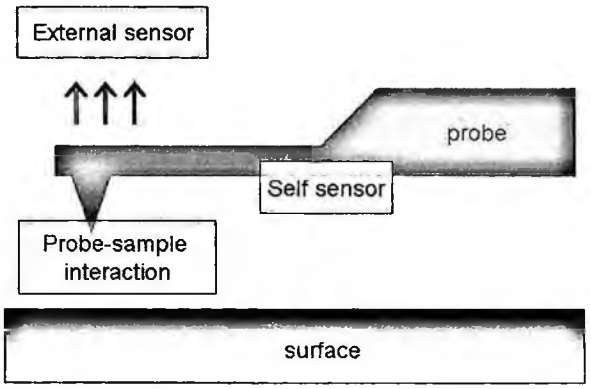

Figure 4. Schematic illustration showing the three main classes of sensors used for deflection detection in scanning probe microscopy. (i) external sensor: sensor is not integrated in the cantilever (ii) self sensing: sensor is integrated in the cantilever (iii) Tip-surface interaction sensor: other tip-surface than force interactions are detected, e. g. thermal or electrochemical interactions. (Courtesy of J. Polesel-Maris).

Probe sensing systems can be separated into three main classes (Fig. 4): (i) external sensing achieved by schemes not directly linked to the cantilever, which have to be aligned prior to the experiments. With external sensors the deflection can directly be detected; (ii) self sensing, where the sensor is incorporated in the probe, often in the form of stress sensors usually located at the base of the cantilever where the maximal stress occurs; and (iii) sensing of additional probe-surface interactions that serve as indicator for tip to sample distance; examples are thermal [62] and electrochemical sensors [15], spin-valve probes [183] in scanning magnetoresistance microscopy, or scanning Hall probes [24,27,28].

3.1. *General considerations*

3.1.1. *Sensitivity*

The quality of the data depends essentially on the quality of the probes and the instrument. In this section, the mechanical and geometrical aspects of cantilevers influencing the sensitivity of the setup are described.

For a rectangular beam with thickness t, length l, width w (Fig. 5) and a Young's modulus E, the deflection δ at the free end, and the stress σ at the base of the beam can be expressed according to eqs. (1) and (2), respectively:

$$\delta = \frac{4l^3}{Ewt^3}F \tag{1}$$

$$\sigma = \frac{3}{2}\frac{Et}{l^2}\delta, \tag{2}$$

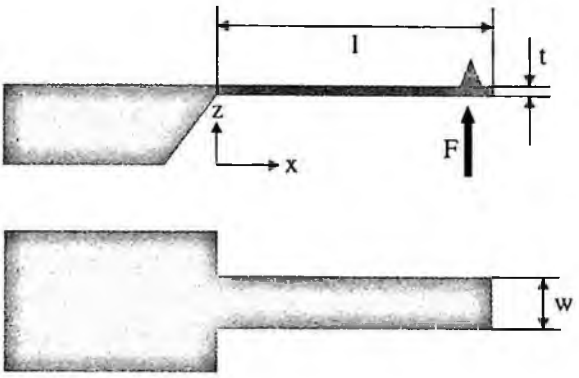

Figure 5. Geometry of a rectangular cantilever. (Courtesy of Ch. Santschi).

where F is the force applied at the free end of the cantilever. The spring constant k_c is given by eq. (3):

$$k_c = \frac{Ewt^3}{4l^3}. \tag{3}$$

Eqs. (1)–(3) give the rules for optimisation of the probe sensitivity in terms of geometry and material of the beam.

3.1.2. *Noise limit*

The detection limit of a sensing system is determined by various intrinsic or extrinsic disturbances of the device [167] including noise of various origins. Some of them are unavoidable since their origins are intimately related to the presence of the probe and the detection unit. Examples are thermal Brownian or thermomechanical noise [83,161], flicker or 1/f noise in piezoresistive sensors [191], electronic noise related to the signal treatment, and finally, noise due to mechanical and acoustical excitations from the macroscopic environment. The origins of noise related to cantilever beams have been the subject of several intensive studies [47,204].

A cantilever is a mechanical system, which can be described using a damped oscillator model. Damping is described by the quality factor Q_c and directly related to the energy dissipation of the system. Systems which dissipate energy are necessarily sources of noise as described by the equilibrium fluctuation-dissipation theorem, known as the Nyquist-Johnson theorem [148]. It should be noted that the reverse case is also often true [33]. The fluctuation-dissipation theorem applied to mechanical resonators with thermal energy k_BT as the only source of energy describes the generation of thermal noise having its origin in the coupling between the oscillators and its medium. Thermal forces, F_{th}, are non-correlated for time scales larger than the average time of intermolecular collisions. The equipartition theorem, thus, leads

to the spectral force density of white noise (eq. [4]):

$$S_{F_{th}} = \frac{4k_BTk_c}{Q_c\omega_0}, \tag{4}$$

where ω_0 is the resonance frequency of the cantilever in vacuum, k_B the Boltzman constant and T the temperature. The spectral density of thermal noise-driven amplitude $S_{A_{th}}$ of the free mechanical oscillator is given by eq. (5) [39]:

$$S_{A_{th}}(\omega) = \frac{1}{k_c^2} \frac{S_{F_{th}}}{\left(1 - \frac{\omega^2}{\omega_0^2}\right)^2 + \left(\frac{\omega}{Q_c \cdot \omega_0}\right)^2} \tag{5}$$

The detection limit of the sensor is given by the deflection δ equivalent to the amplitude $S_{A_{th}}$ induced by thermal noise. Other sources of noise stem from the conversion of the deflection δ into an exploitable signal, for instance, the shot-noise of the photodetector [64]. Using the SPM in contact mode, the low frequency mechanical noise of the platform [204] also contributes to the total noise to a not negligible extent. In dynamic mode, working close to the resonance frequency ω_0, the most relevant source of noise is thermomechanical noise of the beam. On the other hand shot noise of the photodetector and the 1/f noise due to low frequency phenomena become dominant in contact mode AFM. Expressions for the signal-to-noise ratio in the different operating modes can be found in Sarid [167].

3.2. *External sensing*

External sensors are the most commonly used detectors for deflection measurements of AFM cantilevers [167]. Various other methods for the detection of the cantilever deflection δ have been developed in the last few years.

3.2.1. *Optical beam deflection*

In 1988, Meyer *et al.* [137] proposed an optical system based on the measurement of the deflection δ of a collimated laser beam focused on the rear side of the cantilever (Fig. 6). The reflected beam is collected using a photodiode which is divided into two or four quadrants. The quadrants are closely positioned to each other in order to detect the spot displacement induced by the deflection of the cantilever [64]. The normal deflection δ and torsional bending correspond to the normal and lateral (friction) forces, respectively.

The key advantage of such a system is its large geometrical amplification of the deflection δ leading to a high sensitivity. With the distance D between the free end of the cantilever and the photodiode the displacement of the spot $\Delta_{photodiode}$ on

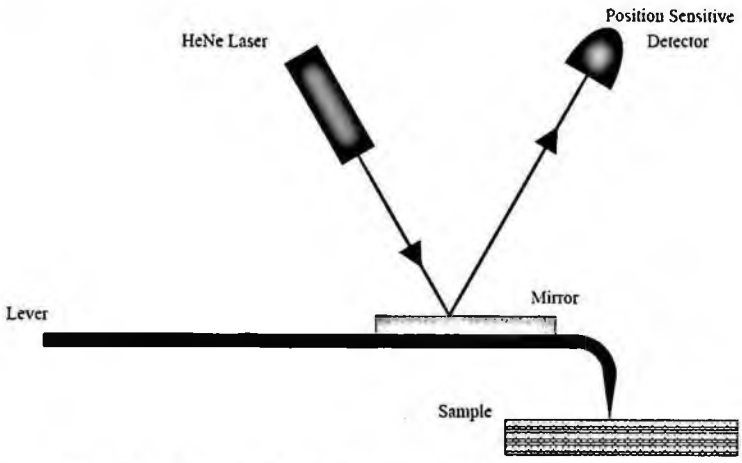

Figure 6. Principle of detection by optical beam deflection [137].

the photodiode can be written as:

$$\Delta_{photodiode} = \frac{D}{l}\delta. \tag{6}$$

A deflection δ of 1 Å for a cantilever with $l = 100\,\mu m$ and a distance $D = 4\,cm$ leads to a spot shift of 40 nm, corresponding to a geometrical amplification of 400. This method is mainly used by AFM manufacturers because its implementation is simple and results in a very sensitive optical read-out. Using this method, atomic resolution has been achieved with a detection limit of 0.1 Å [59]. Moreover, its pN force sensitivities allow molecular force spectroscopy which is described in more details in Section 4.2. According to theoretical sensitivity calculations the minimum detectable deflection δ, presented in various publications [156, 157, 169], atomic resolution in a 10 kHz bandwidth is achievable. But it should be noted that, in practice, the sensitivity is limited by the amplitude of the thermal vibration of the cantilever and not by the minimum detectable deflection δ [137]. Finally, with a fast photodiode [69] and a pre-amp bandwidth of tens of MHz this set-up is appropriated for both, contact and dynamic mode.

A few studies have been done with multiple photodiodes in order to decrease the shot noise effect [172]. Fukuma *et al.* optimized this detection method using an optimally adapted photodetector [53,54], a pulsed laser source to remove interferences artefacts [91], and a very low-noise electronics. Noise density as low as $17\,fm\,Hz^{-\frac{1}{2}}$ was achieved.

The implementation of the optical beam deflection method has recently been demonstrated for probe array read-out. Alvarez *et al.* [12] used a sequential read-out of a 1D array consisting of five cantilevers. Using voice-coil actuators, the laser beam is moved from one cantilever to the other in order to determine their deflections. Subnanometer resolution has been obtained with a scan speed of about ten

cantilevers per second. This sequential method is suitable for experiments where updating of the deflection in time intervals larger than hundreds of milliseconds is sufficient. But this technique is not adapted for imaging or fast force spectroscopy. Indeed, the computing time for the tracking of each spot and the frame rate of the CCD sensor are the bottlenecks of this parallel read-out method.

3.2.2. *Optical diffraction sensing*

Yaralioglu *et al.* [204] proposed an alternative method to the conventional optical beam detection described above. The method is based on the idea of a cantilever containing interdigital arms forming a Bragg grating (Fig. 7). Such a configuration simplifies the alignment procedure in arrays and more importantly, improves the signal-to-noise ratio by cancelling the laser pointing noise, the thermally excited mechanical vibrations and reduces the sensitivity to vibrations of the photodetector. The presented Bragg grating method has a vertical resolution of 1 Å in a 1 kHz bandwidth. Since an optical intensity is measured, photodetector alignment is less important compared to the optical beam deflection method where the position of an optical spot is detected.

The diffraction pattern has multiple maxima, and is thus, split into several orders depending on the relative displacement between the two finger sets as illustrated in Fig. 8. At deflections δ larger than $\lambda/4$, the diffraction pattern changes from the zero to the first order which limits the maximum deflection range that can be detected using a single photodetector. Taking advantage of the different orders in the diffraction pattern and using a set of multiple photodiodes allow the extension of the maximum range of deflection δ that can be measured. For practical reasons,

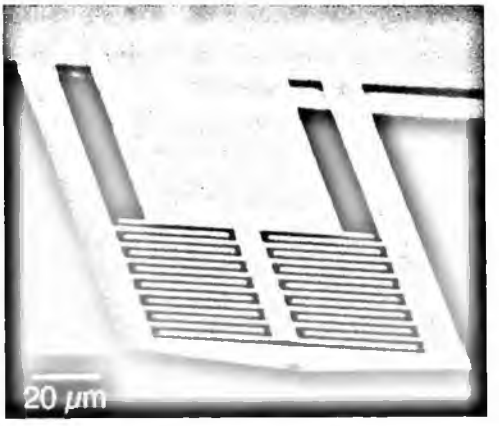

Figure 7. SEM image of an interdigital cantilever. The length of the cantilever is 215 μm. Length and width of the fingers are 30 and 3 μm, respectively and the thickness of the structure is 2.5 μm. The center part serves as reference and the outer moving part as measuring beam [204].

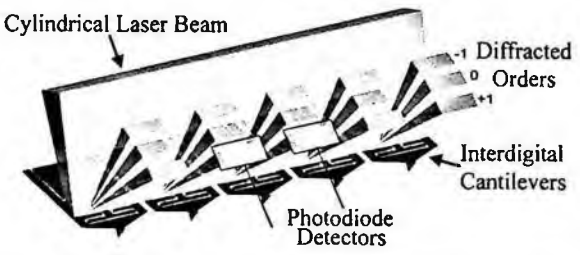

Figure 8. Schematic illustration of the interdigital cantilever array and the diffracted orders. The signal of the orders are detected by photodiodes [182].

this method is limited to a maximum cantilever deflection δ of about 300 nm using two photodiodes.

The authors demonstrated the usability of this method on vector probe arrays of five interdigitated cantilevers [182] using a single laser diode ($P = 10\,\text{mW}$, $\lambda = 635\,\text{nm}$) as illumination source. Using such a configuration, true parallel imaging of a grating with 220 nm high features has been carried out.

The same team also designed a 2-dimensional array of 6×4 spiral cantilevers and used the diffraction method for deflection measurements. The reflected laser beams were projected onto a CCD sensor for parallel measurements [126].

Recent work has been done on various diffractive methods of deflection detection. Karabacak *et al.* used an optical knife-edge method to compare the position of a double clamped beam to a fixed reference cantilever [90]. A noise density of $1\,\text{pm/Hz}^{\frac{1}{2}}$ operating in the MHz regime using short cantilevers ($t = 125\,\text{nm}$, $w = 200\,\text{nm}$, $l = 14\,\mu\text{m}$) was achieved. Onaran *et al.* proposed a membrane probe with a tip situated in the centre of the membrane with a stiffness of $1\,\text{Nm}^{-1}$ [149]. A Bragg grating and a liquid-sealed electrostatic actuator working up to 20 MHz were integrated at the rear side of the membrane. A photodetector placed at the 1st order diffracted beam allowed to detect the detection δ with a noise density of $10\,\text{fm Hz}^{-\frac{1}{2}}$ and force resolution of pN in a 10 kHz bandwidth.

3.2.3. *Interferometric sensing*

Interferometric detection of cantilever motion has been presented soon after the invention of AFM in 1986 [49, 128, 164]. While an optical beam deflection scheme measures essentially the bending angle at a given point on the cantilever, an interferometric setup measures the displacement of a certain point on the cantilever with comparable intrinsic sensitivity [157]. The basic idea of interferometric sensing is the comparison of a light beam, reflected by the rear side of the cantilever, with a reference beam from the same light source, in general monochromatic source of wavelength λ. In most setups the optical length of the reference arm is kept constant, whereas the length of the signal or measuring arm changes. The interfering light intensity detected by a photodiode is a function of the interferometric Optical

Path Difference (OPD), which is the length difference between the reference and the signal arms. The periodic intensity is given by a cosine function:

$$\mathrm{I(OPD)} = \frac{\mathrm{I_0}}{2}\left(1 + \cos\left(2\frac{2\pi}{\lambda}OPD\right)\right). \tag{7}$$

The OPD can be written as:

$$OPD = \lambda\left(n + \frac{\varphi}{2\pi}\right), \tag{8}$$

where φ represents the phase of the signal with respect to the reference wave, n is an integer number corresponding to the number of complete periods the signal arm is mismatched with respect to an equal armed system where the interferometer is perfectly balanced. The phase ambiguity due to monochromatic coherent light limits an unequivocal measurement to the range of $\lambda/2$. In order to overcome this limitations, Dändliker *et al.* proposed methods using two light sources [40].

Homodyne detection is a simple type of interferometry (Fig. 9(a)) where a light source of a specific and constant wavelength λ is used. Anselmetti *et al.* used a compact Nomarski setup in order to detect the deflection δ of a cantilever with the relatively high stiffness of 150 Nm-1 [13]. A remarkably low noise level of 0.035 Å in a bandwidth from 0.01 Hz to 2 kHz has been obtained. Rugar *et al.* proposed a compact and mechanically robust fibre optic interferometer based on the optical interference occurring in a micron-sized cavity formed between the cleaved end of a single mode optical fibre and the cantilever [164]. They achieved a peak-to-peak noise value of 0.1 Å in a bandwidth of 1 kHz. More details on fibre optic interferometry for AFM cantilever detection can be found in Shie [175].

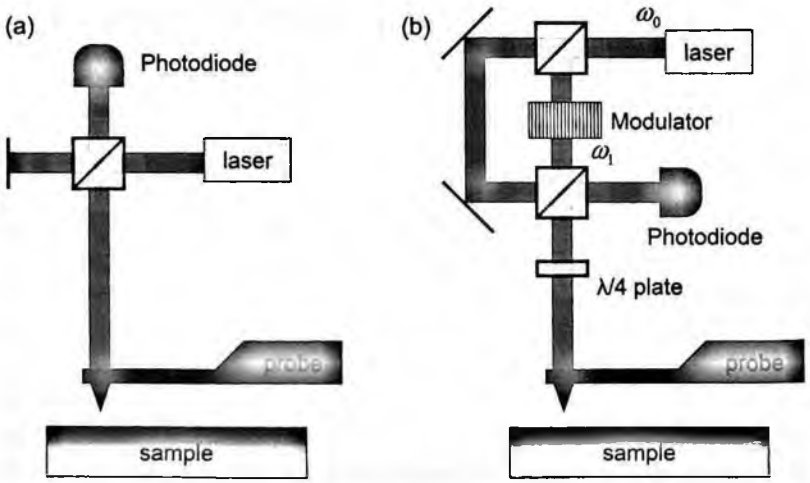

Figure 9. Schematics of homodyne (a) and heterodyne (b) interferometers used for detection of cantilever deflection. (Courtesy of J. Polesel-Maris).

Using a configuration as shown in Fig. 9(a), the measurement of the phase φ is very sensitive to fluctuations of the laser intensity, to variations of the fringe visibility due to beam divergence, and to small misalignments of the interferometer. In order to reduce this disturbing effects, optical heterodyne detection [49, 95, 128] has been introduced. Fig. 9(b) shows a scheme of such a setup.

The first beam splitter divides the incoming beam with frequency ω_l into two beams, each of them having half of the total intensity. The frequency of one of the resulting beams is transferred to ω_s using an acousto-optic modulator ω_s. Mixing of the two frequencies leads to the generation of two new frequencies, one at the sum of the two frequencies, and the other at their difference. The low frequency $\omega_l - \omega_s$ produced in this manner is referred too as beat frequency (eq. (9)).

$$I(t) = I_{dc} + I_{ac} \cos\left(2\pi(\omega_l - \omega_s)t + 2\pi\frac{OPD}{\lambda}\right). \tag{9}$$

The DC component I_{dc} does not carry any information about the OPD. In fact, only the second term of the cosine argument carries information about the cantilever displacement. For a heterodyne system Kikuta *et al.* [95] report an rms noise of 0.35 Å in a bandwidth of 200 Hz. The noise level of interferometric methods is comparable to that of optical beam deflection measurements.

Using large collimated signal beams, interferometric techniques are particularly well adapted for parallel detection of cantilever arrays. The fringes pattern on each beam allows a true highly parallel measurement of the cantilever bending avoiding the problem of beam-crossing as it occurs in optical beam deflection for large cantilever deflections δ. The interferogram can be used in a different manner to extract the deflection δ. Helm *et al.* use white light interferometry in order to determine the bending of micromechanical cantilever sensors with an typical error less than 1 ppm [19, 72]. Deflections δ smaller than 2 nm have been measured in parallel with a lateral resolution of 2 µm via the interference fringes pattern on the rear side of eight cantilevers.

3.3. *Self sensing*

In self sensors, the sensing elements are integrated in the cantilever structure. Advantages of such configurations are lack of inconvenient alignment, and the possibility to work in non-transparent media. Frequently used detection schemes are based on piezoresistive [187] and piezoelectric [82, 110, 184] effects which allow detection of stress σ occurring at the base of the cantilever upon bending. Unfortunately, these schemes necessitate more sophisticated microfabrication processes for the implementation of self-sensing elements as cantilevers for external sensing. Recently, research on self sensing methods has opened the door to new optical, carbon nanotubes and magnetostrictive self sensing cantilevers. These promising results lead to new detection methods which are shortly described below.

3.3.1. *Piezoresistive sensing*

A method for measuring the deflection of AFM cantilevers based on the piezoresistive effect was first presented 1991 by Tortonese *et al.* [188]. Their method benefits from the stress dependent resistance of piezoresistive elements in order to transform mechanical deflection δ, thus, mechanical stress σ, into analysable electrical signals. The deflection δ of a cantilever is linearly dependent on the maximal σ as shown in eq. (2) for a rectangular cantilever. The piezoresistive effect of doped germanium and silicon has been characterized by Smith [177]. Applying a stress σ to these materials changes the volume V which in turn causes a change in the energy gap between valence and conduction band. This alters the number and mobility of the charge carriers and, thus, varies the resistance ΔR.

For a rectangular cantilever with an embedded Wheatstone bridge at its base, the change in resistance ΔR can be expressed as follow:

$$\frac{\Delta R}{R} = \frac{6\pi Fl}{wt^2} \tag{10}$$

where F, l , w, and t are the applied force, the length, width and thickness of the beam (Fig. 5), respectively [159]. π represents the piezoresistive coefficient.

The piezoelectric effect in boron doped p-type Silicon is anisotropic and is most pronounced in the <110> direction and amounts to $\pi_L = 71.8\ 10^{-11}\ m^2N^{-1}$ [71]. A formalism for the linear piezoresistive effect is summarized by Gerlach [58]. The highest values for the piezoresistive coefficients have been measured for π_{44}. Table 2 shows a summary of the experimentally determined piezoresistive coefficients π.

The number of charge carriers in semiconducting materials is, for the most part, determined by the dopant concentration. Doping of crystalline Si is accompanied with unavoidable diffusion process, which is an important issue in reducing the thickness of the cantilever. The highest sensibility can be achieved if the piezoresistive zone is placed as far as possible from the stress neutral axis and remains as thin as possible. If the dopant concentration is uniformly spread out above and below

Table 2. Piezoresistive coefficients of silicon and germanium [71].

	$\pi_{11}[10^{-11}m^2N^{-1}]$	$\pi_{12}[10^{-11}m^2N^{-1}]$	$\pi_{44}[10^{-11}m^2N^{-1}]$
n-type silicon (11.7 Ω cm)	−102.2	53.4	−13.6
p-type silicon (7.8 Ω cm)	6.6	−1.1	138.1
n-type germanium (9.9 Ω cm)	−4.7	−5.0	−137.9
p-type germanium (15 Ω cm)	−10.6	5.5	46.5

the neutral axis, the stress would be neutralized leading to an average signal of zero. Harley *et al.* fabricated 890 Å thick cantilevers [71], as described in Section 2.3, with a force sensitivity of 500 fN in the bandwidth from 10 Hz to 1k.

AFM cantilevers with atomic resolution have been fabricated [87, 176, 187]. The change in resistance ΔR has been analyzed integrating a Wheatstone bridge without reference resistance for thermal drift cancelling. But this apparent disadvantage allows the integration of three low noise resistors (thin metal film resistors) in order to reduce the level of flicker noise. The relative variation of resistance $\frac{\Delta R}{R}$ depends on the geometry of the cantilever and the material properties according to eq. (10). With $\frac{\Delta R}{R} = 3 \times 10^{-6}$, corresponding to a $75 \times 7 \times 4.2\,\mu m^{-3}$ rectangular cantilever, an rms noise value for the amplitude of 0.1 Å in a bandwidth from 10 Hz to 1 kHz has been found. The spring constants k_c of the cantilevers leading to these rather low noise values are in the order of $k_c = 106\,Nm^{-1}$ and are unfortunately too high for imaging of soft materials in contact mode.

Stress dependent resistivities have also been observed in polymers. For example Daoud *et al.* [41] coated conductive polyamide fibres in an aqueous dispersion of poly(3,4 ethylenedioxythiophene-poly(4-styrenesulfonite)) (PEDOT-PSS). The conductivity of the fibres related to humidity, temperature, and mechanical strain has been investigated. The resistance as a function of the applied strain over 10 strain-relaxation cycles is shown in Fig. 10.

The piezoresitive effect can be enhanced using integrated MOSFET-structures as sensing element. Due to the confinement of charge carriers perpendicular to the cantilever surface, quantum aspects have to be taken into account [84, 196]. The calculated coefficient π_L in a confined Si resistor along the <110> direction is $174\,m^2N^{-1}$ which is an increase of more than a factor of two compared to the

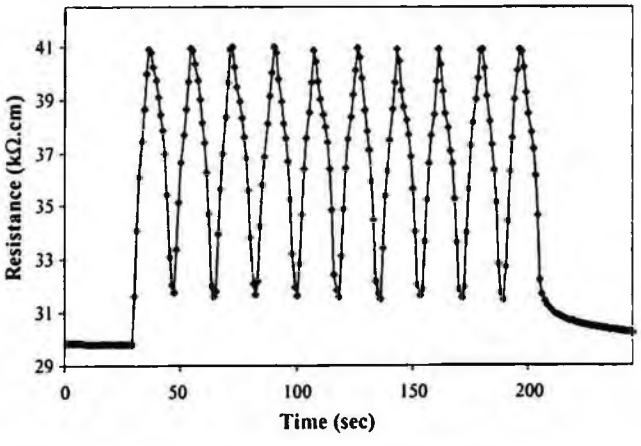

Figure 10. Variation in resistance of 2.54 cm long PEDOT-PSS coated fibres over 10 strain-relaxation cycles. The fibres were subjected to a strain level of 35% [41].

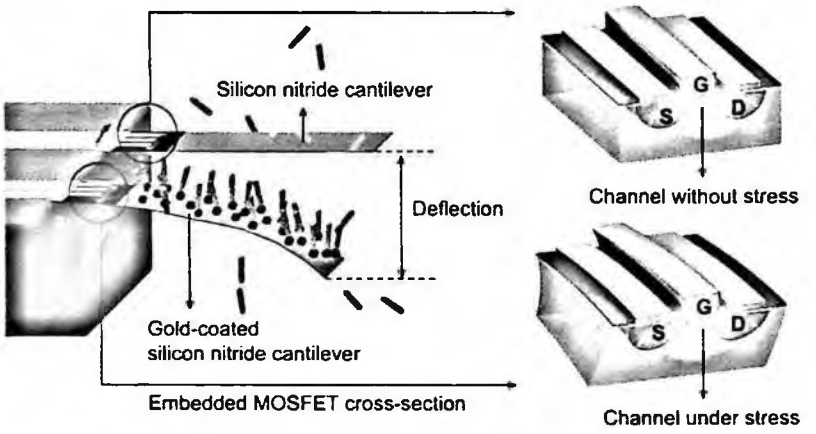

Figure 11. Illustration of cantilever deflection measurements using an embedded MOSFET as sensing element. The SiN cantilever is a reference and the gold-coated cantilever is used as sensing cantilever. Magnified view of embedded MOSFET in cross section shows stressed gate region when the cantilever bends, resulting in a change of drain current due to conductivity modulation of the channel underneath [174].

non-confined piezoresistive coefficient π_L. Figure 11 shows the working principle of a MOSFET structure used as a piezoresistive sensor. Shekhawat *et al.* [174] used MOSFETs embedded in a micro-cantilever in order to detect its deflection δ. The change in drain current due to the induced stress in the drain channel has been measured. The sensitivity of the device is on the order or 0.1 to 0.2 mA nm^{-1}. At low frequencies, a current noise of 40 to 60 nA in a bandwith of 1 kHz has been measured leading to a detection limit on the order of 0.01 Å.

Piezoresistive sensing is promising for applications in probe arrays. A drawback is that the piezoresistive effect is restricted to certain materials, such as Si with a rather high elastic modulus E. Biological applications on the other hand often require very low spring constants k_c. Non-piezoresistive materials such as Si_xN_y have a lower Young's Modulus E than Si leading to softer cantilevers. Examples of probe arrays with embedded piezoresistive elements are presented in Section 4.

As the probes often are considered as wear and tear elements, cost-efficient production is an important issue, which may be a further disadvantage as the fabrication of piezoresistive sensors is rather costly.

3.3.2. *Piezoelectric sensing*

The piezoelectric effect in quartz was discovered by Jacques and Pierre Curie in 1880. A mechanical force applied on a piezoelectric crystal generates an electrical field E due to an asymmetric charge displacement. An applied mechanical force F on a piezoelectric cube with faces of area A and thickness t induces a voltage across the material according to eq. (11):

The piezoelectric block behaves similar to a charged capacitor with a capacitance C, therefore, the induced voltage V can be written as:

$$V = \frac{Q}{C} = \frac{d_Q t}{\varepsilon_0 \varepsilon_r A} F, \tag{11}$$

where d_Q is denoted charge coefficient and is commonly given in pCN^{-1}. ε_0 and ε_r are the permittivity of vacuum and relative permittivity of the material, respectively. Ferroelectric materials may also exhibit piezoelectric behaviour, however, they must be polarized before. Crystals such as quartz, Rochelle salt, and ZnO are naturally piezoelectric, while other materials like the ceramics barium titanate and PZT, or the polymer polyvinylidene fluoride (PVDF) are ferroelectric. PZT has the highest piezoelectric constant among all available piezoelectric materials but also quartz, ZnO, and PVDF are suitable materials for piezoelectric sensing. The potential of these materials for deflection sensing in AFMs has been demonstrated and is presented in the following. Guthner *et al.* demonstrated the capability of creating topographic images using a vibrating tip part of a high-Q quartz oscillator [65,67]. The frequency was modulated by tip-surface forces which depend on the probe-sample distance. Later, Giessibl used the same type of high-Q quartz sensor [61] in UHV and achieved atomic resolution on Si(111)-(7 × 7) surfaces [60].

Tansock and Williams demonstrated the capability of piezoelectric PVDF polymers sensors [184]. The incorporation of a ZnO film into a microfabrication process is not difficult due to low process temperatures. Itoh and Suga fabricated ZnO displacement sensors on a micro-fabricated cantilever [81,82]. Wanatabe and Fuji demonstrated successfully the use of PZT piezoelectric films as cantilever sensors [197] allowing to resolve mono atomic steps with a height of 4 Å.

Imaging soft biological samples in contact mode is not possible with piezoelectrical cantilevers due to its high stiffness up to $1800\,Nm^{-1}$.

Furthermore, imaging in buffer solutions requires a good sealing of the electrical wiring. Lee *et al.* demonstrated PZT microcantilever operation in dynamic mode in 2-propanol with an amplitude resolution of 0.27 nm in a bandwidth of 125 Hz at a resonance frequency of 60 kHz [110]. Kageshima *et al.* developed a force sensor for dynamic atomic force microscopy in liquid environment with oscillation amplitude of 1 nm combining MWCNT tips with a quartz tuning fork [88].

3.3.3. *Capacitive sensing*

Capacitive deflection sensing has been developed by several research teams [31,63, 143]. A schematic illustration of a capacitive cantilever setup is shown in Fig. 12.

The sensitivity at zero deflection $\delta = 0$ is described as follows:

$$\left.\frac{\Delta C}{\Delta z}\right|_{z=0} = \varepsilon_0 \frac{3wl}{8d^2} \tag{12}$$

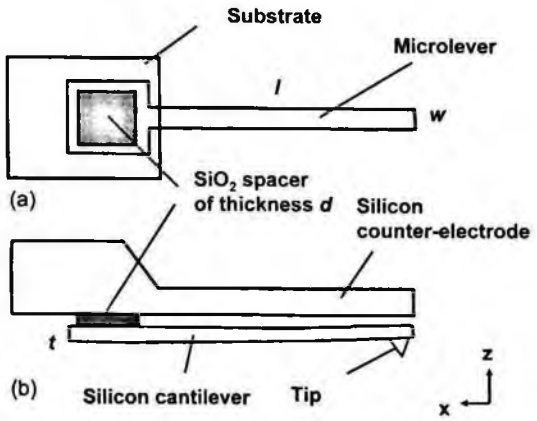

Figure 12. Schematic illustration of a capacitive cantilever (a) top view, (b) side view showing air gap and SiO_2 spacer. The capacitance is formed between the Si cantilever and the counter-electrode [31].

Figure 13 shows SEM micrographs of an array of micromachined capacitive cantilever sensors. The holes in the cantilevers serve to promote etching of the thin SiO_2 layer used for the fabrication of the gap between cantilever and counter-electrode [30].

Göddenhenrich *et al.* developed an instrument which works in constant-capacitance mode realized by feedback-controlled adjustment of the capacitance. The sensing capacity is adjusted to a reference value using a piezoelectric device [63]. A detection limit corresponding to a change in the distance between the two plates of 0.01 Å has been achieved. The obtained force resolution is comparable to that of optical beam deflection measurements.

3.3.4. *Alternative methods of self sensing*

In addition to standard detection techniques such as optical or piezoresistive methods, other self-sensing methods for stress σ and deflection δ sensing of cantilevers have been explored recently.

Photonic wave guide

The implementation of a $SiO_2/SiON/SiO_2$ waveguide as deflection self sensor in a cantilever [74] has been proposed by Hoffmann *et al.* The authors used cantilevers with resonance frequencies of $\omega_0 = 50 \ldots 200\,\text{kHz}$ and quality factors of $Q = 100$. Optical coupling between the optical waveguides in the cantilever and a fixed waveguide on the chip across a $2\,\mu\text{m}$ gap allows measuring the cantilever deflection δ. Two different arrays made of 8 cantilevers with 8 different resonance frequencies ω_0 ranging from 96 to 103 and 30 to 100 kHz have been fabricated and tested. The frequencies ω_0 are separated by 1 and 10 kHz steps, respectively. The embedded

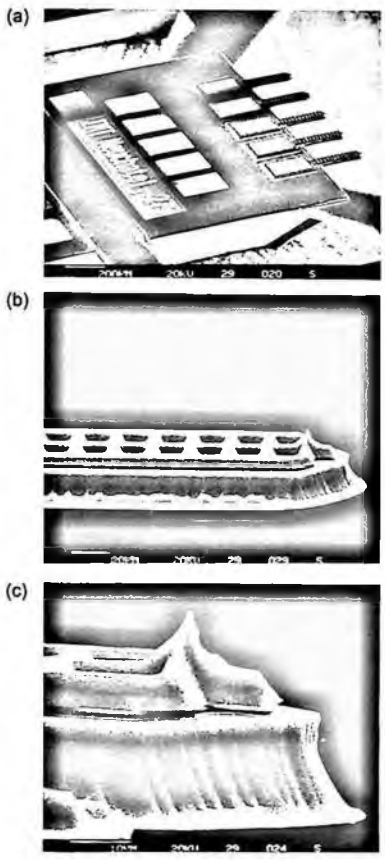

Figure 13. (a) SEM micrograph of an array of mircofabricated capacitive cantilever sensors. (b), (c) Enlarged view of the cantilever ends, showing the gap between the cantilever and the counter-electrode as well the tip in more details. The perforation of the cantilever promotes the removal of SiO_2 between the cantilever and the counter-electrode [29].

waveguides were optically interconnected via 1×8 waveguide branching structure containing cascaded Y-junctions.

A recent and more detailed work based on this optical method has been published by Nordin *et al.* [146] and Zinoviev *et al.* [207, 208] where minimal detection of 0.4 Å has been reported A schematic set-up is presented in Fig. 14.

The potential of using micro ring resonators [102] and Bragg gratings [104], shown in Figs. 15 and 16, as stress sensors has been theoretically described by Kiyat *et al.* [102] and Kocabas *et al.* [104]. The calculated sensitivities on the order of $2\ 10^{-4}$ Å^{-1}, for typical AFM cantilevers with lengths, width, and thicknesses of 100–400, 20–50, and 0.4–10 μm, respectively, are promising as the achievable sensitivities are as high as for interferometric detection. The crucial point for a good sensitivity is the design of the resonator and the waveguide.

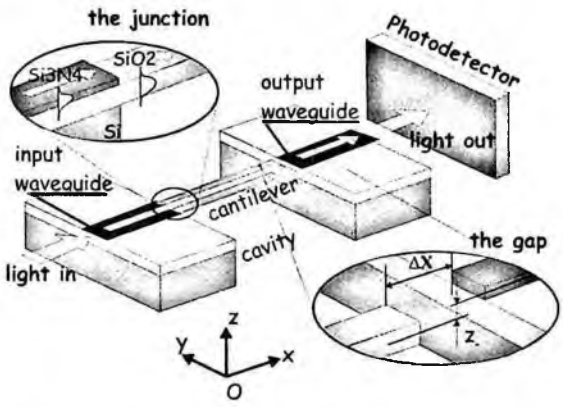

Figure 14. Scheme of a waveguide cantilever deflection sensor. The dependence of coupling efficiency between two waveguides (cantilever and output waveguide) is monitored with respect to their misalignment [207].

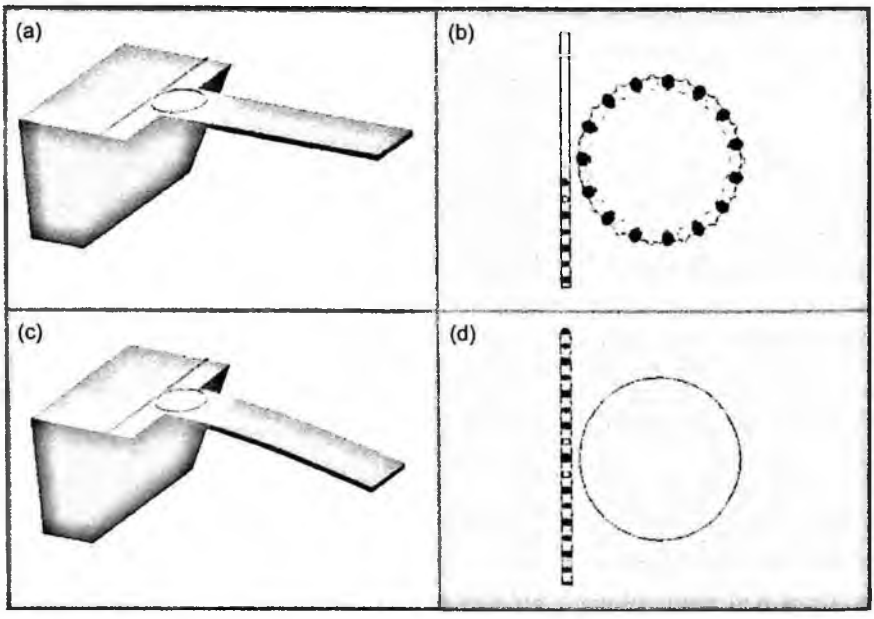

Figure 15. Schematic illustration of an integrated micro ring resonator displacement sensor. The ring resonator is integrated at the base of the cantilever where the maximal stress occurs. (a), (c) the cantilever for unbent and bent conditions; (b), (d) the field distribution on the ring resonator on the cantilever [102].

Carbon Nanotubes (CNT) sensors

Recent progress in growth and placement control of CNTs [205] allow the development of new types of stress sensors. Li *et al.* have presented an overview of recent studies on SWCNT based sensors for mass, strain, pressure and temperature

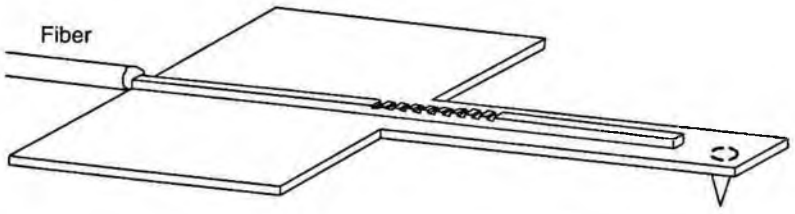

Figure 16. Drawing of a cantilever containing a waveguide which modified by a Bragg grating. The Bragg grating is located at the base of the cantilever [104].

measurements at the nanoscale [115]. CNTs change their electronic properties when subjected to strain. Dharap *et al.* demonstrated experimentally the strain sensitive effect of CNT films [43]. Closer to applications for cantilever sensors, Dohn *et al.* proposed a self-sensing cantilever using MWCNTs [44,45]. A MWCNT is placed at the base of the cantilever where maximal stress occurs, and is subsequently connected to metallic on-chip electrodes (Fig. 17). To characterize the sensitivity of this stress sensor, a force F is applied and the change of the CNT's conductance as a function of strain has been analyzed. The obtained data show large variations between different cantilever/CNT samples and low gauge factors on the order of 24. The piezoresistive gauge factor of Si, for instance, lies in the range from 40 to 150 [71].

SWCNTs for cantilever self sensing were used by Stampfer *et al.* [179,180]. Electrodes and cantilever have been post-processed after positioning of the SWCNTs. A bridge configuration is connecting the electrodes to the cantilever (Fig. 18). A gauge factor of 2900 has been measured, a value 15 times higher than in piezoresistive sensors, which demonstrates a very good sensitivity of these CNT sensors.

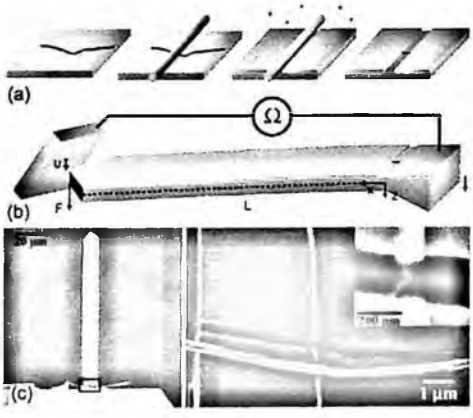

Figure 17. (a) Procedure for fabrication of the CNT strain sensor (b) Sketch of the setup for electromechanical measurements (c) Scanning electron microscope (SEM) images of an 8 µm wide cantilever with a silicon nanowire used as a shadow mask, positioned across. The right image shows the nanowire released with the electrode gap across a 60 nm MWCNT [45].

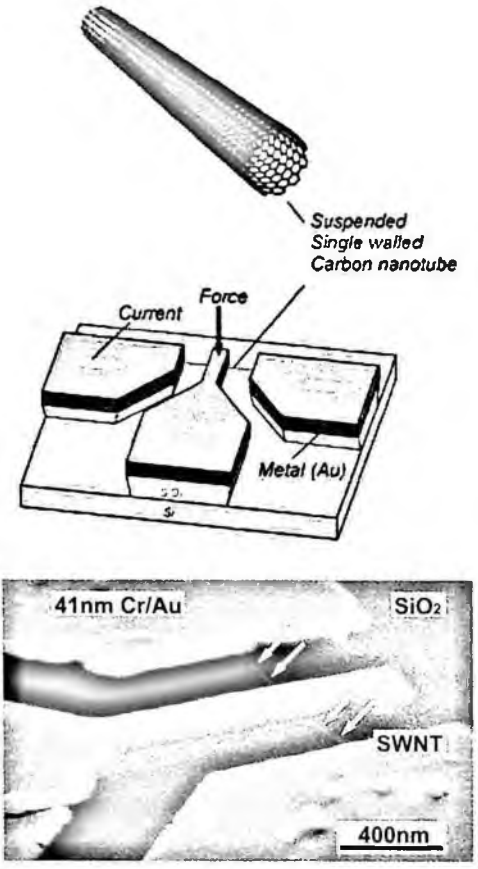

Figure 18. Schematic drawing and scanning electron microscope images of a cantilever-SWNT-based sensing device. The white arrows indicate the location of the suspended SWCNT. Deflections of the cantilever induce strains in the CNT leading to a change in its resistivity [180].

Low adhesion between CNT and substrate, leading to a displacement of the CNT, might be an explanation for the low gauge factor obtained in the described MWCNT setup [45].

The main source of noise in CNTs is 1/f noise [20,26,78]. In order to know if the signal-to-noise ratio is large enough for force spectroscopy in the pN range, noise characterization have to be performed at low frequency.

Magnetostrictive sensors

Stress dependence of magnetic properties of materials are known as Joule and Villari effects [86]. The magnetic stress sensor detection dates from 1976 [103]. Magnetic stress sensors have been used to measure the deflection of macroscopic cantilevers in order to measure the magnetostriction coefficient of ferromagnetic films [38]. Tunnelling magnetoresistance shows an enhancement of the magnetic stress effects. Lohndorf *et al.* [117] have measured up to 48% of relative change in the electrical

resistance of quadratic $20 \times 20\,\mu m^2$ large and 2.5 nm thick magnetic tunnelling junctions which are made of magnetostrictive $Co_{50}Fe_{50}$. Gauge factors $(\Delta R/R)\varepsilon^{-1}$ on the order of 600 have been calculated.

Mamin *et al.* used the properties of spin-valve sensors in order to detect the deflection δ of commercially available Si_xN_y cantilevers [125]. A gauge factor of 150, which is similar to doped crystalline Si used in piezoresistive sensors, has been achieved. The measured noise is on the order of the thermal–mechanical noise of a cantilever, which suggests a high sensitivity of the device. A 1/f noise component has been observed in the range of 1 to 10 kHz. This noise was attributed to the poor quality of the electrical contacts, stemming from the oxidation of the Ta capping layer. The easy fabrication of these self-sensors is the main advantage compared to other self-sensing methods with equivalent sensitivity such as, for instance, piezoresistive sensing.

3.4. *Tip-surface interaction sensing*

With tip-surface interaction sensing methods, another interaction different from the force is taken as imaging signal. Very often these methods are subject to image artefacts stemming from the ambiguity of the signals.

3.4.1. *Electrochemical sensing*

Electrochemical sensing is similar to the method of tunnel current sensing used in scanning tunnel microscopy (STM). One important difference is that in STM, the current between tip and substrate does not induce chemical changes of the environment [15]. In order to perform electrochemical sensing, an insulated tip with a conductive apex is immerged in an electrolytic solution. When the potential at the conductive apex is sufficiently negative, a redox reaction occurs at a diffusion controlled rate [14] leading to a steady-state current if the tip-substrate distance is large enough that the diffusion is not hindered by the surface. This steady-state current represents the diffusive flux of oxidants O from the bulk solution to the electrode.

The electrochemical response is based on the current change due to the influence of the present substrate. For a planar, tip the steady-state current $I_{T,\infty}$ can be written according to eq. (13):

$$I_{T,\infty} = 4n\Phi D_O c_O a, \tag{13}$$

where D_O and c_O are the diffusion coefficient and the concentration of the oxidised species, respectively. a represents the diameter of the electrode and Φ the Faraday constant. n is the number of electrons transferred in the tip reaction ($O + ne \rightarrow R$). In scanning electrochemical microscopy (SECM), the current response, recorded as a function of the tip position, depends on the tip-sample distance, thus, the topography, but also on the chemical composition, thus, the reactivity of the surface.

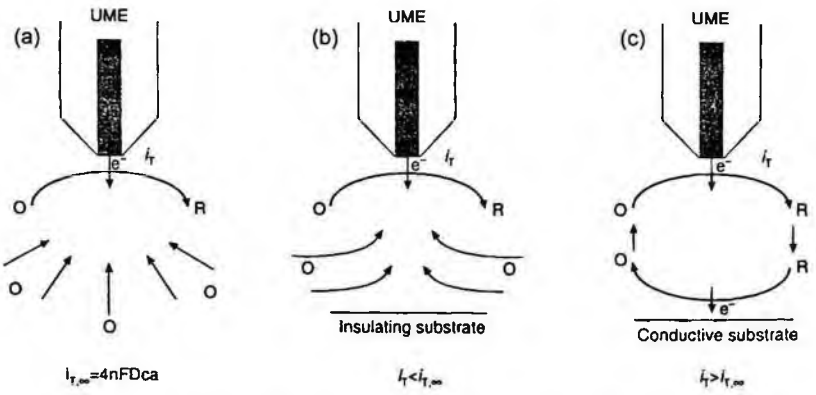

Figure 19. Basic principle of SECM. (a) tip far from the substrate leading to a steady state current, (b) tip near insulating substrate, hindered diffusion of O leads to decrease of current, negative feedback, and (c) tip near conductive substrate leading to an increase of current, positive feedback [14].

Chemically not uniform surfaces are subject to a crosstalk of chemical and topographical information. Lowering the tip towards a conductive sample leads to a current increase, a positive feedback, whereas the approach towards an insulator causes a decrease, a negative feedback. Figs. 19 and 20 show the basic principles of SECM and current profiles of both, positive and negative feedback.

Topographical imaging may also be performed using SECM techniques but the separation of chemical and topographic information turns out to be very difficult. Therefore, reliable imaging of samples showing both variations in topography and reactivity is not possible [123].

These limitations can be overcome using combined AFM-SECM probes or probe arrays containing both, AFM and SECM probes, as described in Section 4.1.3.

3.4.2. *Thermal sensing*

Properties such as specific heat or thermal conductivity may be locally detected using thermal microprobes [154]. These near-field thermal information of a substrate is obtained by scanning the surface with a very small temperature sensor situated at the end of a probe tip [62,199]. When the tip is in close proximity to the surface of the substrate, the tip temperature is changed by thermal coupling between the tip and the substrate. By modulation the probe temperature sub-surface information becomes accessible, allowing tomographic thermal imaging [154].

Various types of thermal probes have been developed. Examples include thermocouple junctions, thin film temperature sensors, as well as resistive sensors [120,199]. The advantage of resistive sensors is that they can both, locally supply heat and measure the temperature in one system. Resistive sensors allow operation in constant temperature mode, requiring a feedback with self-heating.

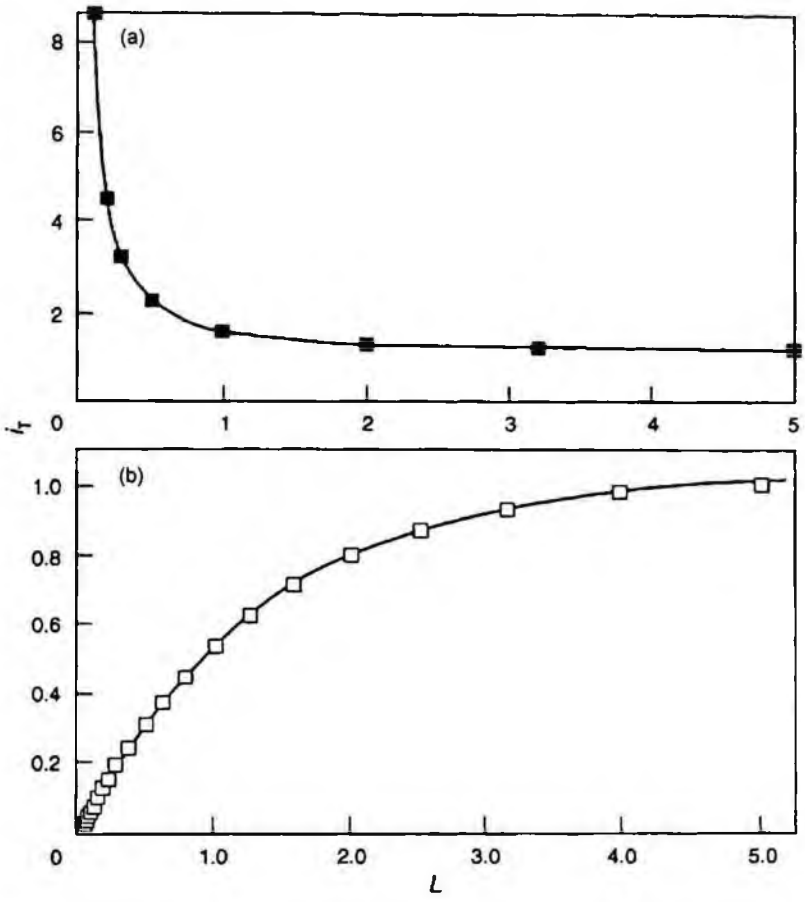

Figure 20. Current as a function of the tip-substrate distance (a) conductive substrate, and (b) insulating substrate [14].

Thermal sensing and AFM can be combined (Fig. 21). However, given by the non-ideal geometry of the thermal probe topographical imaging has not been achieved in the same quality as with using standard AFM probes. Hybrid probe arrays, with dedicated probes for thermal mapping and for topographic imaging might improve this situation. SThM has been successfully applied in data storage, which is presented in more detail in Section 4.3.1.

4. Examples and Applications of Scanning Probe Arrays

This section provides an overview of applications based on probe arrays. A wide spectrum of applications using scanning probe arrays for fabrication or data storage purposes is documented in the literature. On the other hand, imaging applications using probe arrays still lag behind due to a lack of simple, sensitive, and efficient

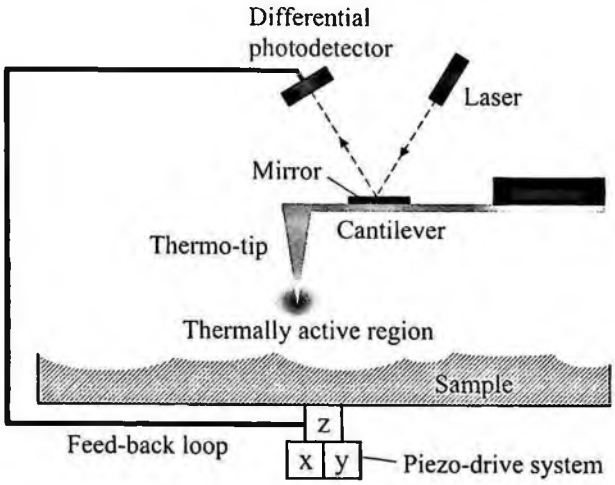

Figure 21. Schematic illustration of a SThM-AFM setup. A standard AFM setup modified with a probe equipped with thermal sensor embedded at the apex of the tip [62].

read-out methods for the deflection of the cantilever. In many cases, data storage applications do not need a versatile and sensitive detection method since the sample properties and environment parameters are controlled and the contrast is optimised.

Most fabrication or measurement techniques based on probe arrays techniques have been developed as single probes techniques as described in more detail.

4.1. *Imaging applications of probe arrays*

The feasibility of high resolution imaging with probe arrays has been demonstrated for various imaging modes. Large images can be composed from multiple small images, and high resolution information, e.g. on surface roughness, can be obtained by zooming in to smaller dimensions. Some examples are presented in the following sections.

4.1.1. *Imaging by parallel force microscopy*

One of the common applications of scanning force microscopy is atomic force imaging or microscopy, allowing topographical imaging with vertical resolution of atomic dimensions [23]. Nowadays, the AFM is a commercially available tool used for many applications in domains such as biology, microelectronics, or material science.

AFMs can be used in three different imaging modes, namely, contact mode, non-contact mode, and intermittent contact or tapping mode. The most appropriate mode is determined by the type of experiment, characteristics of the sample, the environment, and other experimental conditions. For example, soft samples often necessitate tapping mode imaging and measurements of rigid samples performed in air environment may preferably be done in contact mode.

Minne *et al.* presented a one dimensional cantilever array, which allows parallel constant force imaging at high speed [142]. The array contains 50 cantilevers spaced by 200 μm, leading to a total range of 1 cm. 200 μm has been the minimal achievable tip-to-tip spacing due to design limitations. In order to sustain a constant force on the cantilever, the architecture of the individual cantilevers has been separated into activator and sensor regions as shown in Fig. 22. For the actuation a piezoelectric approach was chosen, and the force detection was realized incorporating a piezoresistive sensor. Special attention had been paid to minimize electrical coupling between actuator and sensor signals. Parallel scanning at a speed of 4 mm s^{-1} was demonstrated with a vertical detection limit better than 5 nm. Unfortunately, the scan range of an individual probe is limited to $100 \times 100\,\mu m^2$, which is not sufficient to achieve overlapping frames and thus a complete coverage of the surface.

A 2 × 1 cantilever array for parallel scanning force microscopy was developed by Akiyama *et al.* [7,8]. A single chip accommodates two cantilevers and an offset compensation and signal conditioning circuit. Moreover, a thermal actuator and stress-sensitive MOS transistors are integrated. Similar to the probes described by Minnes, the cantilever is divided into an actuator part, where three thermal actuators for feedback and self-excitation are positioned, and a sensor zone, as shown in Fig. 23. The Si tips were fabricated in a separate process and later transferred onto the cantilevers [144,145]. Figure 24 shows the Si tips glued onto the cantilever. Using this setup a vertical sensitivity of 40 Å in a bandwidth of 10 kHz has been achieved.

A two-dimensional 4 × 4 piezoresistive probe array adapted for parallel atomic force imaging in air and liquid environments was developed by Polesel-Maris *et al.* [153]. A vertical and lateral resolution of 2.6 and 20 nm, respectively, has been demonstrated. Force spectroscopy on fibroblast cells in a liquid environment has

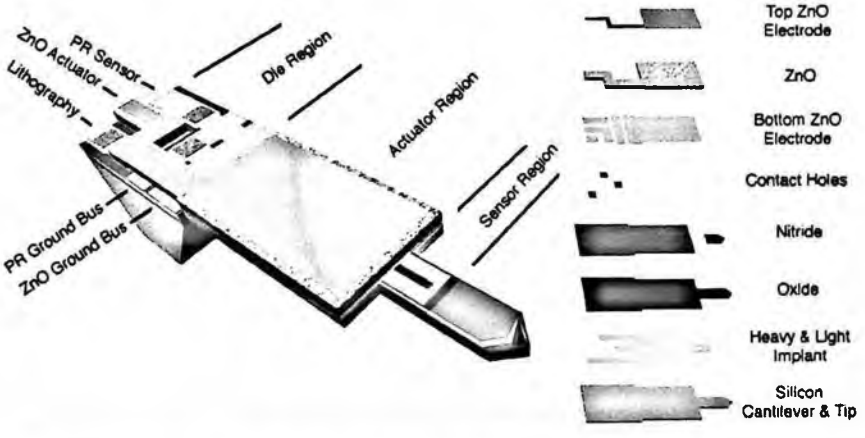

Figure 22. Schematic illustration of a scanning probe with integrated piezoresistive sensor and piezoelectric ZnO actuator. The cantilever is divided into a actuator and sensor region [142].

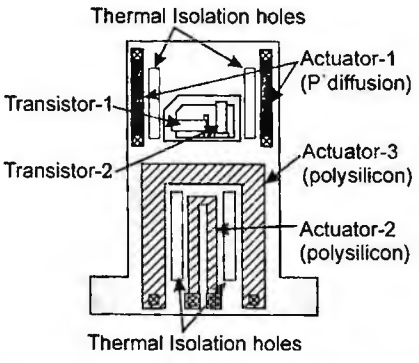

Figure 23. Close-up view of a cantilever containing thermal actuators and two PMOS transistors delineated for sensing the deflection of the front part. The three thermal bimorph actuators are integrated in the rear stiff part and the side of the sensor, respectively [7].

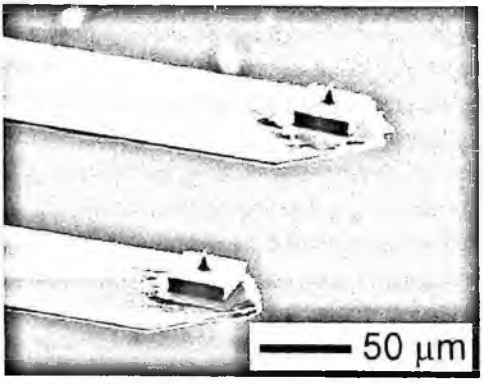

Figure 24. SEM images of hand-glued and wafer-scale transferred Si tips. The tips are glued either by epoxy or hard baked photoresist [7].

been performed with sensitivities down to 160 pN. An SEM image of a 4×4 probe array is shown in Fig. 25.

A process enabling the fabrication of an array of millions of cantilevers corresponding to a density of more than 1000 cantilevers per square centimetre was presented by Kawakatsu *et al.* [92, 93]. Si-cantilevers with lengths in the range of 500 nm to 100 μm, thicknesses of 30 to 100 nm and tetrahedral tips can be fabricated using the same process. Figure 26 shows SEM micrographs of single crystal silicon cantilevers.

The read-out was realized using an optical heterodyne system. For cantilevers of 2 μm length and 120 nm in thickness the natural frequency ω_0 and Q factor have been measured to be 36 MHz and 8000, respectively. The effective noise amplitude has been below 10 pm at frequencies above 10 MHz.

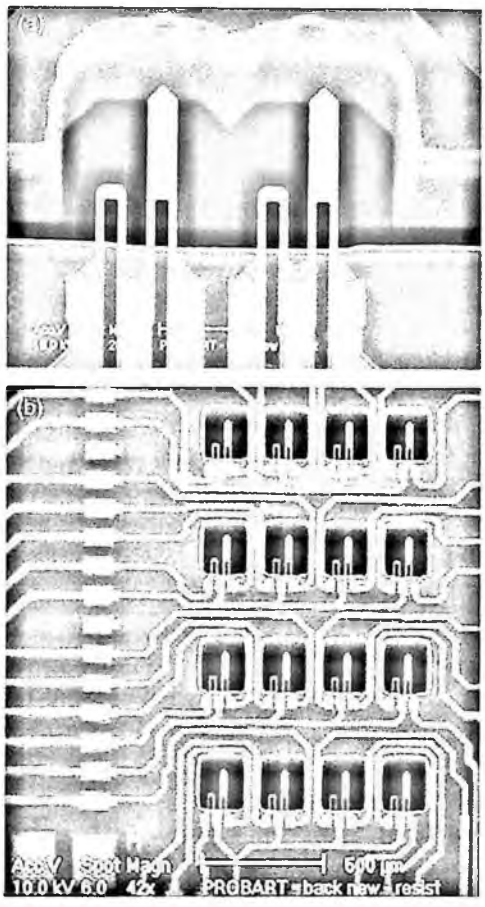

Figure 25. Scanning electron microscope images of (a) 2×1 and (b) 4×4 cantilever arrays. Each piezoresistive cantilever is accompanied by a reference piezoresistor. Three electrical connections are necessary, one of them is the common ground [153].

A probe array containing piezoelectric cantilevers with ZnO sensors was fabricated by Itoh *et al.* [80]. Each cantilever is composed of five layers, namely 1.8 µm SiO_2, 0.3 µm Au/Cr, 1.0 µm ZnO, 0.2 µm Au/Cr, and 0.2 µm SiO_2. The metal layers are used to electrically contact the ZnO and the SiO_2 layers served as surface passivation. The dimensions of the cantilevers are $125 \times 50 \times 3.5\,\mu m^3$ with a resonance frequency in the range 145 to 147 kHz. In static mode an actuation sensitivity of $20\,nmV^{-1}$ has been achieved resulting in a displacement of 100 nm applying a voltage of 5 V.

4.1.2. *Imaging of ultra-large scan areas*

High-resolution imaging over large areas recorded in a reasonable time is desirable in many applications, for instance, in semiconductor device analysis. The maximal

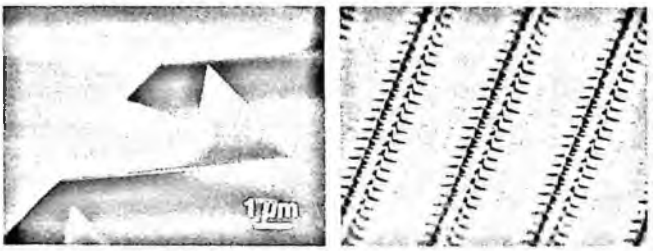

Figure 26. SEM micrograph of single-crystal silicon cantilevers of 3 µm length, 60 nm thickness, and 10 µm spacing. A tip of 2 µm height is positioned at the end of each cantilever. No self sensing or actuation is provided in this probe array [93].

lateral scan range of a piezoelectric tube is limited to less than 200 µm for voltages up to 200 V, which limits the maximal range for a precise lateral probe positioning. Using probe arrays with subsequent image stitching extends the maximal continuous image area. Parallel recording enables image acquisition of large areas at high speed and allows a zoomed view of an area of interest due to the high resolution of the individual pictures. This may be of interest for micro electronic applications where features of nanometric size are dispersed over large areas.

Minne *et al.* [138] presented arrays with 10, 32 and 50 cantilevers arranged in a single line. The piezoresistive sensors provide a vertical resolution of 3.5 nm in a bandwidth of 20 kHz. A typical image size recorded using a conventional AFM configuration is on the order of $100 \times 100\,\mu m^2$. Figure 27 shows a $2 \times 2\,mm^2$ AFM image of an integrated circuit chip. The image has been recorded with a 10×1 cantilever array each of them scanning a vertical swath of $0.2 \times 2\,mm^2$. The pixel size is roughly $400 \times 400\,nm^2$.

With 10 cantilevers working in parallel an area corresponding to 512×5120 pixels can be covered with a single scan. The whole $2 \times 2\ mm^2$ image corresponds to a data file larger than 100 Mbytes which is not very convenient for data processing.

McNamara *et al.* [129] fabricated a 1×8 probe array in order to combined individual thermal images of a commercial IC into an image covering a total surface of $750 \times 200\ \mu m^2$. The scan speed of an individual probe was $25\,\mu m\ s^{-1}$ resulting in an apparent total scan speed of $1600\,\mu m\ s^{-1}$ with a lateral resolution 2 µm.

4.1.3. *Electrochemical imaging with probe arrays*

SECM has been shown to be a promising method for localized studies of surface reactions and their kinetics [158,173,200]. In particular for biological applications is SECM an interesting tool. For instance, Zhu *et al.* investigated plant stress induced by cadmium [206] and Bard *et al.* recorded chemical images of living cells [16]. Again, the distinction between topographical and chemical contributions to the SECM image contrast is very difficult. In order to overcome those problems, multi-purpose

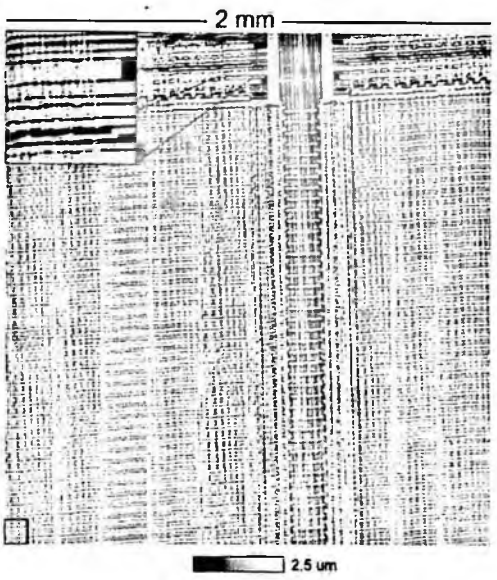

Figure 27. $2 \times 2\,mm^2$ AFM image of an integrated circuit chip. The image was recorded with 10 cantilevers in parallel. The entire image was acquired in 30 min with a scan speed of $1\,mm\ s^{-1}$. The box at the top left hand side is a zoomed view of the chip and the box at the bottom left hand side of the image represents the maximum scan size of $100 \times 100\,\mu m^2$ from a typical AFM [138].

scanning probes have been developed. Lugstein *et al.* used FIB technique to integrate electrodes into an AFM tip for simultaneous force microscopy and SECM measurements, thus, allowing simultaneously record of electrochemical and topographical information [118, 119]. Macpherson *et al.* used similar probes to achieve sub-micrometer resolution [55, 123]. The main drawback of combined SECM/AFM probes consists in simultaneously providing good insulation for SECM and good tip properties for AFM.

As in force microscopy, efforts have been made in SECM for parallel imaging using probe arrays. Fasching *et al.* presented a process enabling the fabrication of a probe array for simultaneous SECM and AFM analysis in order to perform synchronous observation of electrochemical and topographical sample properties [50, 185]. The presented process allows getting away from single tip production scheme which were previously used. Figure 28 shows different arrangements of combined probe arrays.

Barker *et al.* [17] presented an SECM array with 16 individually addressable linearly arranged probes, consisting of sixteen $10\,\mu m$ diameter microdots, with a pitch of $120\,\mu m$ sufficient large to ensure no overlap of the steady-state diffusion fields between neighbouring electrodes. Linear sweep voltammetry has been performed for all 16 probes for the one-electron reduction ($n = 1$) of $Ru(NH_3)_6^{3+}$ in a solution containing 10 mM $Ru(NH_3)_6Cl_3$ and 0.2 M KCl.

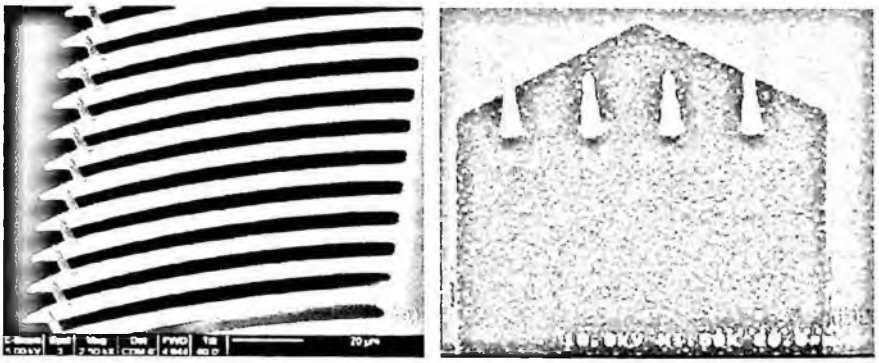

Figure 28. SEM images of two types of electrochemical probe arrays (a) Cantilever array with single tips. The thickness, width and length of the cantilevers are 0.4, 20, and 100 μm, respectively. (b) Tip array on single silicon nitride cantilever. The thickness, width and length of the cantilever are 0.4, 60, and 100 μm, respectively [50].

4.1.4. *Thermal imaging with probe arrays*

Mapping of surface temperature, thermal conductivity, thermal capacitance, and performing micro-calorimetry with sub-50 nm resolution is possible with Scanning Thermal Microscopy (SThM). Applications range from studying the temperature distribution in a cell during mitosis to thermal mapping of the chemical changes of photoresist due to immoderate baking times [116]. Simultaneously recorded topographic and thermal images of photoresist are displayed in Fig. 29.

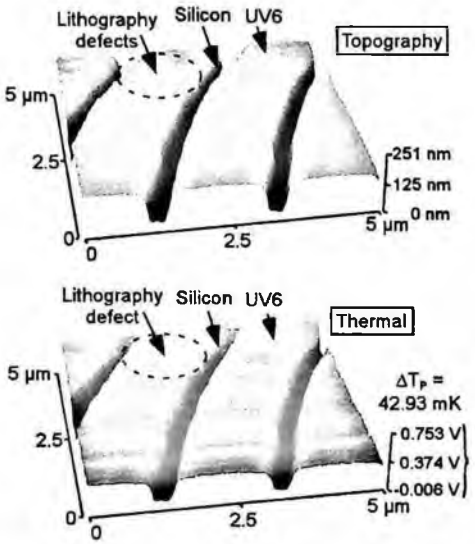

Figure 29. Topographic and thermal images of developed UV6^{TM} photoresist sample with thickness of 350 nm obtained with z-direction feedback. In the cavities, the output voltage of the thermal sensor drops as the probe scans across the higher thermal conductive material [116].

McNamara *et al.* developed 1×8 thermal probe arrays based on polyimide [129]. The use of polyimide as cantilever material offers not only a high thermal isolation necessary to minimise thermal cross-talk, but also a high mechanical flexibility resulting in 10–100 times smaller contact forces when compared to conventional scanning probes.

A particularity of this cantilever array is that no feedback is needed for force control or to keep the probe tip at a controlled distance from the surface. Due to the extremely low Young's modulus E of polyimide, the contact force exerted by each cantilever remains low over a wide deflection range, preventing tip damage upon contact with the sample. In order to perform reliable measurements simultaneously, the structure has to be designed in a manner such that the cantilevers are thermally and mechanically decoupled. Figure 30 shows two dimensional thermal images simultaneously obtained from two probes.

4.2. *Force spectroscopy*

Force spectroscopy can be used to investigate specific molecular interaction forces, or to analyze local variations in the elastic properties of the surface. A force microscope combines high lateral resolution with the ability to measure midget forces of tip sample-interactions of elastic and rigid samples. Figure 31 shows Force-Distance Curves (FDC) of different types of samples.

Chemical functionalization of the tip and the sample surface is possible to guarantee a molecule specificity of the interaction force [109]. Common functionalization techniques are, for instance, thiol chemistry on gold and silane chemistry on activated silicon surfaces. Performing force measurements with functionalized AFM tips single bond ruptures have been observed [51, 111]. Extensive reviews of single-molecule force spectroscopy have been published [35, 85, 198, 209].

Saya *et al.* fabricated piezoresistive cantilever arrays adapted for force detection applications in parallel mode [171]. Piezoresistive detection was chosen because of its adaptability to miscellaneous environmental conditions, such as high or low temperature, or operation in liquids. For the detection of the cantilever deflection δ, a modified Wheatstone bridge was chosen, where two resistors were replaced by adjustable current sources. The possibility for current adjustment allows measurements under optimal conditions.

4.3. *Surface modification*

With appropriate modifications, scanning probe techniques give access to new methods of nanofabrication. Different nanofabrication methods using scanning probe techniques have recently been reviewed by Tseng [189]. Equal to single SPM the operation speed can be improved using probe arrays.

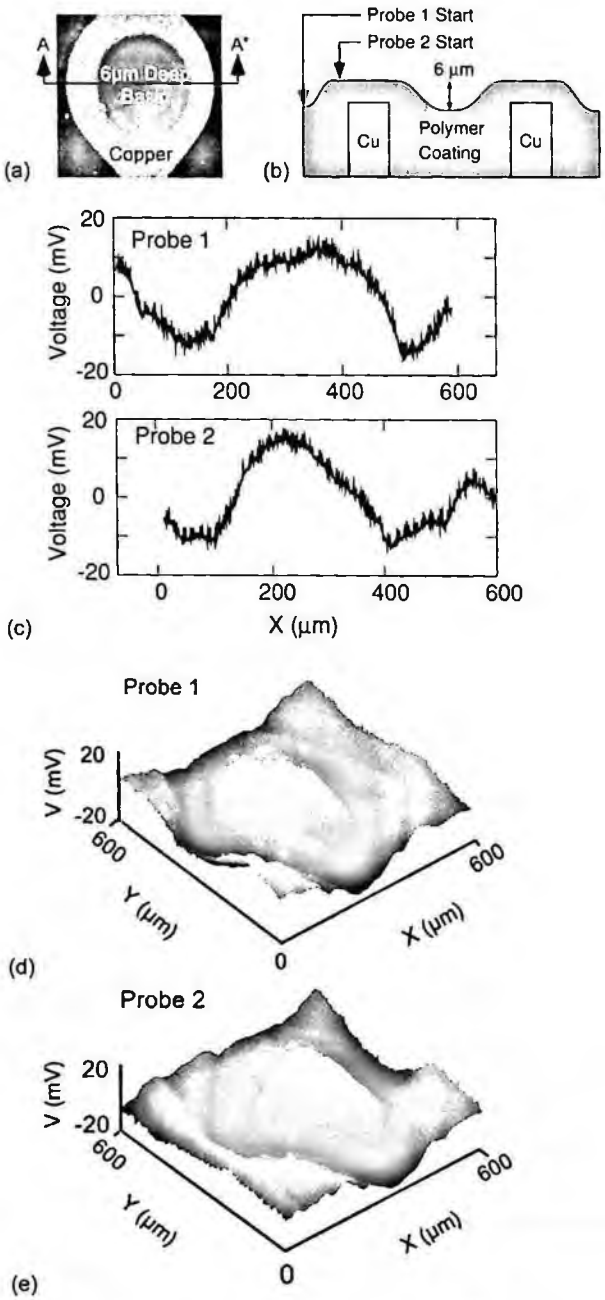

Figure 30. (a) Optical image of a via of a printed circuit board, (b) A-A' cross section of a via with 6 μm topography, (c) Simultaneous line scans taken from two probes, (d), (e) Two-dimensional thermal images simultaneously obtained from two probes [129].

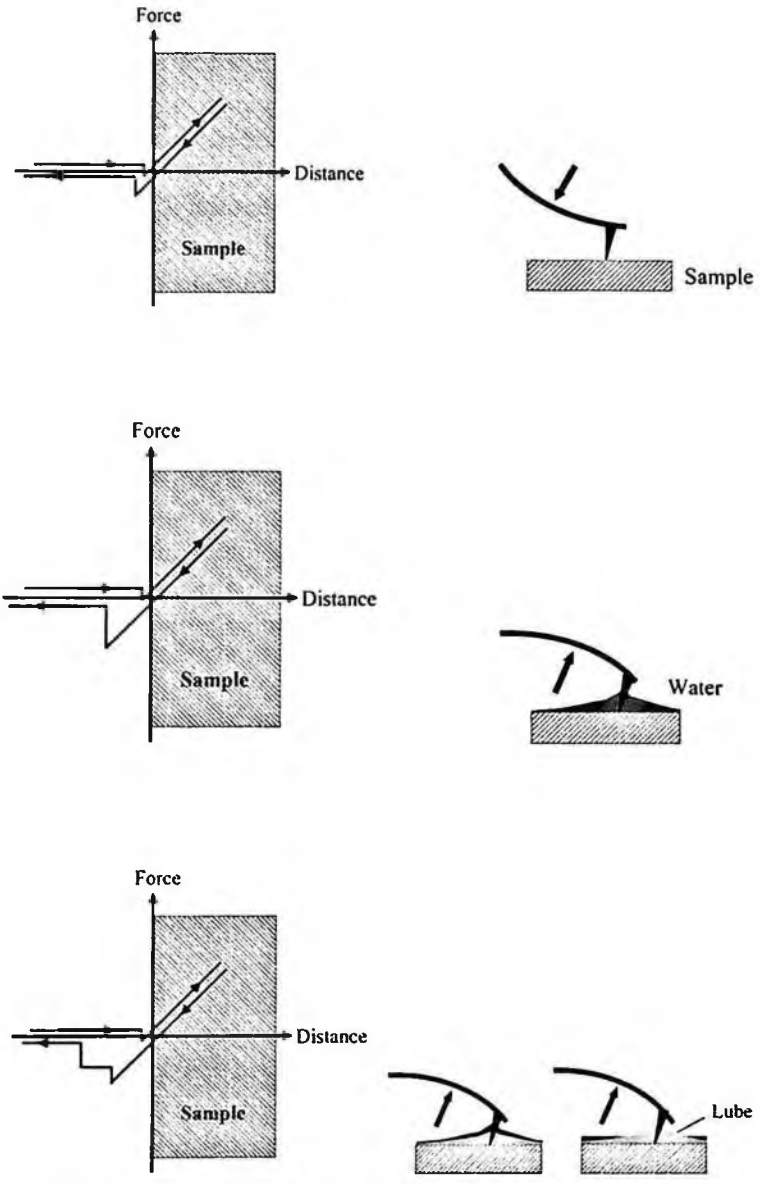

Figure 31. Illustration of force vs. distance curves (FDC). In vacuum (top): the snap-in mainly is governed by van der Waals forces. In air (middle): capillary forces due a thin film of adsorbed water retard the cantilever to snap-out. Air with a contamination layer (bottom): multiple snap-back can occur [1].

4.3.1. *Data storage*

As magnetic data storage is likely to reach its ultimate limits in storage density given by the instability of the magnetic domains (super-paramagnetic limit), researchers are investigating new technologies for high density data storage. The invention of STM led to the development of scanning probe based data storage devices [141]. An AFM-based storage system, presented by Sauerbach *et al.* [170] is based on the properties of ferroelectric materials such as PZT. Furthermore, SNOM [21] and Magnetic Force Microscopy (MFM) [105] techniques have been used for data storage. By modifying magnetic domains in magneto-optic thin films using SNOM, data densities of $45\,\mathrm{Gb\,in^{-2}}$ have been achieved. Using the MFM approach, data densities up to $10\,\mathrm{Gb\,in^{-2}}$ have been obtained. The magnetic Ni domains were fabricated using nanoimprint and lift-off processes. Carley *et al.* [34] suggested a method based on magneto-optic storage materials such as Pt/Co multilayered films or rare-earth /transition element alloys. A scanning probe based method patented by Gibson *et al.* and HP converts materials from a polycrystalline to an amorphous state or *vice versa* using electron field emitters [141]. Furthermore, electrothermal probes were fabricated by Yang *et al.* Using these probes data density on the order of $30\,\mathrm{Gb\,in^{-2}}$, with a writing rate of nearly 100 kHz can be obtained [203]. Data reading is performed by measuring the resistivity of the heater [193]. Changes in current can be analyzed as the heater is powered by a constant dc-voltage. A detected dint leads to enhanced heat dissipation at the tip of the cantilever due to a better thermal contact with the sample, and thus, to a change of the heater is resistivity. An entire reading cycle is illustrated in Fig. 32.

Again, in order to speed up reading and writing rate, probe arrays are of great interest since speed is a critical issue for data storage technique. Figure 33 displays a schematic drawing of a 2D cantilever array used for data storage technique called "Millipede" [194]. The IBM group [48,101,121,122,193,194] presented several designs of probe arrays for storage purposes. They fabricated a 32×32 probe array and demonstrated dot sizes with diameters of 50 nm allowing storage densities of $100\text{–}200\,\mathrm{Gb\,in^{-2}}$. For data reading and writing, rates which are on the order of $\mathrm{Mb\,s^{-1}}$ and $100\,\mathrm{kb\,s^{-1}}$, respectively, have been demonstrated. This rates are rather slow compared with transfer rates of hard disk drives (HDD) on the order of $30\,\mathrm{Mb\,s^{-1}}$ [141].

Kim *et al.* [99] introduced a wafer-level transfer method of Si_3N_4 cantilever arrays onto a conventional CMOS circuit. They developed a 34×34 probe array containing thermo-piezoresistive read/write configuration with integrated heater in the AFM tip and piezoelectric PZT sensors for writing and reading cycles, respectively.

Bolks *et al.* presented a different design than that of current hard disk technology [25], which is based on scanning probe MEMS technologies. The key advantage of this design is that thousands of heads can be used in parallel. For data reading, a MFM approach has been chosen [155]. Their device is made of two individual silicon wavers as illustrated in Fig. 34. One of them contains the magnetic media where

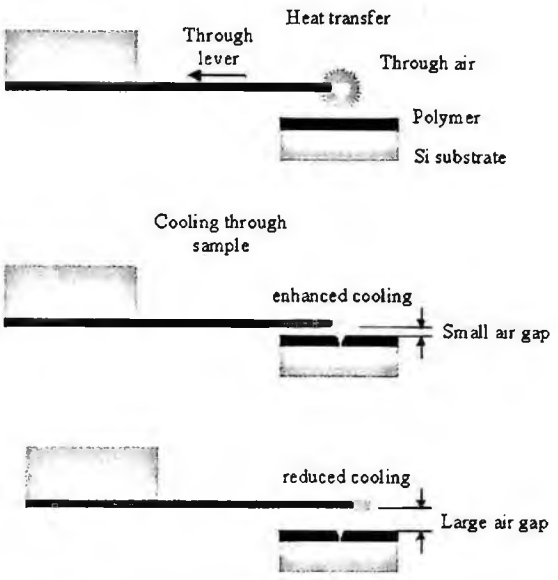

Figure 32. Principle of SP thermal sensing. The cantilever is continuously heated by a dc power supply while it is being scanned and the heater resistivity measured. If the tip enters in a cavity the sensing part approaches to the surface leading to an enhanced heat exchange [194].

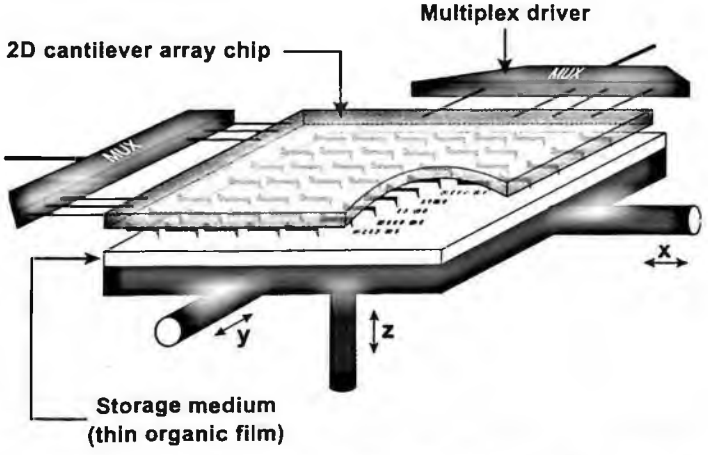

Figure 33. Millipede is based on a mechanical parallel scanning of the storage device or the entire cantilever array chip. Millipede is not based on individual z-feedback for each cantilever requiring stringent control and uniformity of tip height and cantilever bending [194].

the data are stored whereas the probes are integrated on the other. The magnetic media is scanned in the $x - y$ plane using a so called μWalker. Its working principle is illustrated in Fig. 35 and a more detailed description can be found elsewhere [186]. Using this technique, a capacity of 65 Gb in^{-2} and a maximum reading speed of 50 Mb s^{-1} have been obtained. The storage device exhibits a very low power

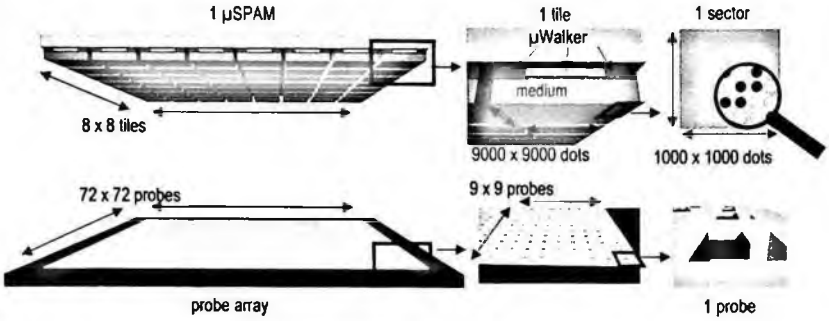

Figure 34. Schematic illustration of the working principle and assembly of the scanning probe array memory. The lower and upper plates accommodate the probe array and the magnetic storage medium, respectively. Moving the medium across the probe array data can be written or read. The movement of the medium is carried out using a μWalker [25].

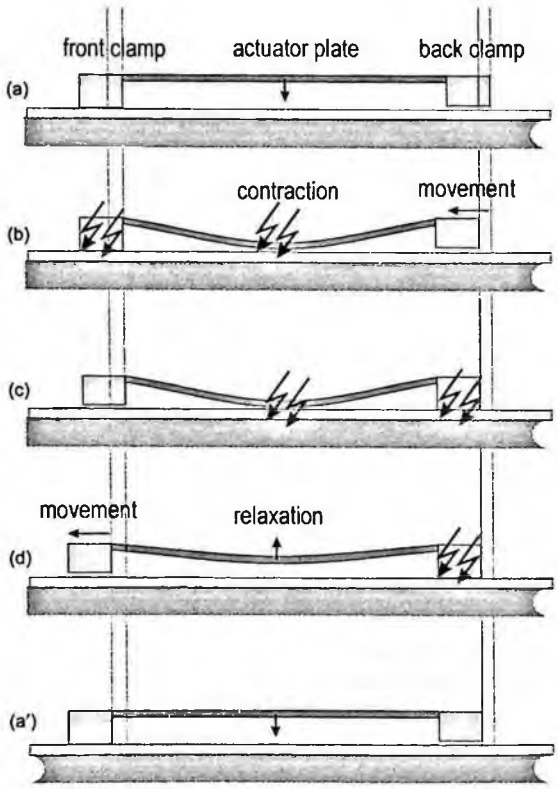

Figure 35. The principle of μWalker is based on the sequences (a)–(d). The step size is in the range of 10–100 nm [25].

consumption which, moreover, scales linearly with the number of implemented tiles which facilitate an extension of the device towards more storage capacity.

Rosenwaks *et al.* [163] reported a method based on parallel SPM for writing in ferroelectric domains of $LiNbO_3$ and $RbTiOPO_4$. The writing speed of ferroelectric

domain based devices is limited by both, the physical processes in a single domain, and the velocity of the scanning tip. In order to obtain reasonable throughput for areas in the mm^2 range arrayed, scanning probes fabricated by NanoInk Inc were used. The standard Si_3N_4 tip arrays were coated with Cr in order to ensure a good conductivity. Using this setup, periodic structures have been written in $RbTiOPO_4$ with a velocity of $120\,\mu m\,s^{-1}$.

4.3.2. *Nano-dispensing of liquids*

Belaubre *et al.* [18] presented a technique, based on microcantilever arrays that allows deposition of microspots using a direct contact technique. Electrostatic fields have been applied in order to load an integrated reservoir with, for instance, biological samples. Deposition of spots in the volume range from femto- to picoliters has been achieved with this method. Quill-type cantilever arrays have been developed by Xu *et al.* [192,202]. From a reservoir, the liquid is delivered through a microchannel to the tip of a cantilever. Using this tool, routine spot sizes of 2–3 μm have been achieved using this cantilever array.

A scanning probe based nano-dispenser (NADIS) was developed by Meister *et al.* [130, 132]. Using NADIS, small droplets of liquids can be lodged at specific places on the substrate of interest. NADIS technique is based on a cantilever with a tip at its end, akin to AFM-probes. A nanometric hole through which the liquid of choice can be deposited is located at the apex of the tip. The liquid is provided through a micro fluidic channel connecting the apex with a reservoir. By controlling the wetting properties of probe and substrate, the transport of the liquid through the probe (Fig. 36) small drop sizes can be achieved. Furthermore, the contact time is an important parameter for the volume control of the deposited liquid. The deposition of volumes on the order of attoliters was demonstrated [134].

Chips containing individual NADIS probes can easily be mounted on standard AFM tools using its deflection feed-back for distance control between tip and sample. Moving the tip towards the surface leads to a surface-tip contact, and consequently well-defined amounts of liquids can be placed on the substrates.

Sub-100 nm apertures centred at the apex of the tip were realised using FIB technique [135]. Another approach to produce nanoholes at the apex of the tip was presented by Song *et al.* They demonstrated the realization of sub-100 nm tip apertures for optical near-field applications [178]. This approach represents a potential method for the realisation of nanofluidic channels used for NADIS devices.

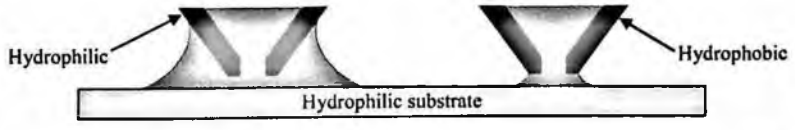

Figure 36. Schematic illustration showing the influence of probe hydrophilicity and hydrophobicity on the droplet size. A hydrophilic outer wall of the tip leads to a broadening of the meniscus between tip and substrate [130].

Consistently with other scanning probe techniques, NADIS, is an equally, slow method when single probes are used. The deposition speed is limited for the most part by the viscosity of the liquid to deposit and is, for instance, 0.5 s per deposition cycle using glycerol. Hence, parallel operation is strongly desirable for commercial applications, and therefore, the realization of arrays of NADIS probes is in preparation [131].

Dot arrays were deposited using NADIS technique. The smallest height and diameter of the droplets are on the order of 20 and 70 nm, respectively, corresponding to a volume of approximately 40 attoliter. In a further experiment, the glycerol was fed with 20 nm polystyrene nanoparticles prior to its selective dispersion on the Si wafers demonstrating the feasibility of local deposition of nano-particles using NADIS technique. Figure 37 shows an array of nanoparticles deposited on a Si wafer. Finally, self-organised micellar monolayer made of polystyrene-poly-2-vinylpyridine block co-polymers were locally inverted by glycerol deposition. Figure 38 shows AFM-picture of the glycerol induced transformation [107, 108, 133].

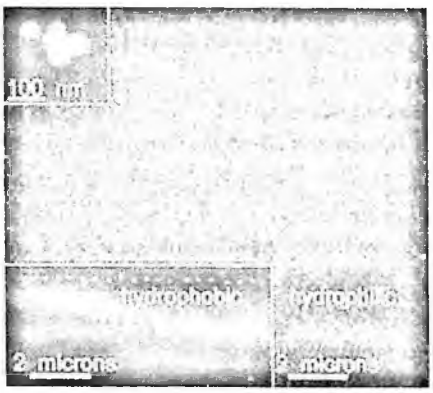

Figure 37. Array of 20 nm polystyrene nanoparticle clusters selectively dispensed using NADIS technique. The dots consists of a few beads (upper inset) [134].

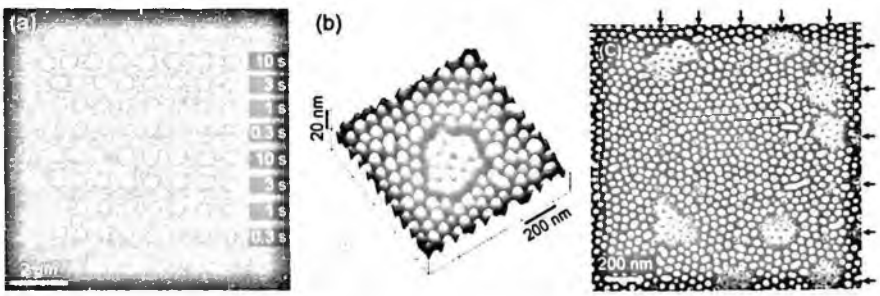

Figure 38. (a) Array of spots made of reconfigured micelles after exposure to glycerol droplets. The contact-time of the NADIS probe with the substrate is mentioned for each line on the left-hand side of the image. (b) Detailed view of a smaller dot. (c) Some individual reconfigured micelles are visible [133].

4.3.3. *Dip-Pen-Nanolithography (DPN)*

DPN allows fabrication and imaging of nanostructures on the sub-100 nm length scale. The nanostructures are created in a similar fashion to an old-style quill pen [151] and line-widths as small as 10–15 nm can be achieved using a conventional AFM setup. Application examples for nanostructuring using DPN are deposition of alkylamines on gold substrates covered with SAMs terminating in interchain carboxylic anhydride groups [37], and fabrication of templates for Fe_3O_4 nanoparticles [147].

The line-width in DPN is independent of contact force over a large contact force range (0–10 μN) [75, 166] and therefore, a DPN array requires minimal single-tip feedback control and is rather straightforward. Using parallel DPN leads to very precise patterns as the individual probes are rigidly coupled and move simultaneously over the substrate. Lee *et al.* [113] presented an approach for the fabrication of centimetre-scale features with biologically active antibodies. A SAM of $NHSC_{11}SH$ was deposited on gold surfaces using parallel DPN technique (Fig. 39) prior to immersing in an aqueous protein solution. The resulting nanoscale dot arrays were incubated in a solution of Alexa Flour 594-labeled human IgG. By adjusting the tip-surface contact time, the diameter of the nanodots could be modified in a range from 100 to 650 nm. In a further example of parallel DPN, Salaita *et al.* [166] demonstrated using a custom-made linear array of 250-pen that one can generate nanopatterns distributed over distances of 1.25 cm, which is 100 times larger than the scan range of a typical AFM instrument. They achieved scanning speeds of almost 1 cm min^{-1} and demonstrated that massively parallel DPN can be performed without loosing its basic attributes such as feature sizes well below 100 nm. For the control of the 250-pen array only a single-tip feedback system is required and a standard AFM configured for lithography can be used for the process.

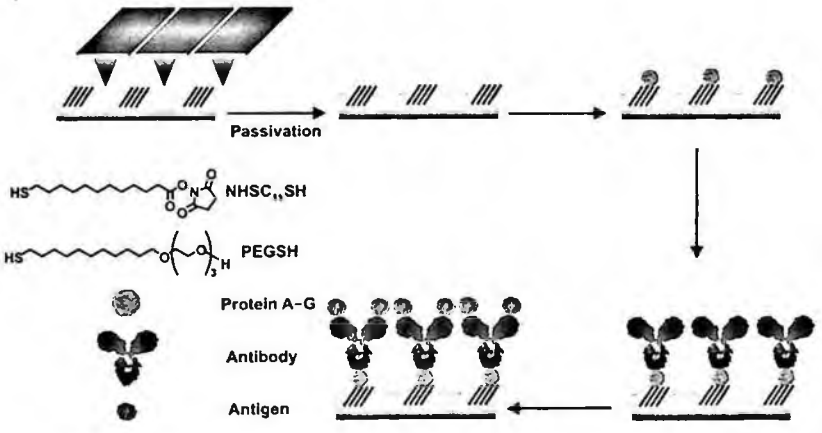

Figure 39. Schematic illustration of the process used to bind proteins on biologically active antibodies, which are covalently bound to nanoscale features patterned using DPN [113].

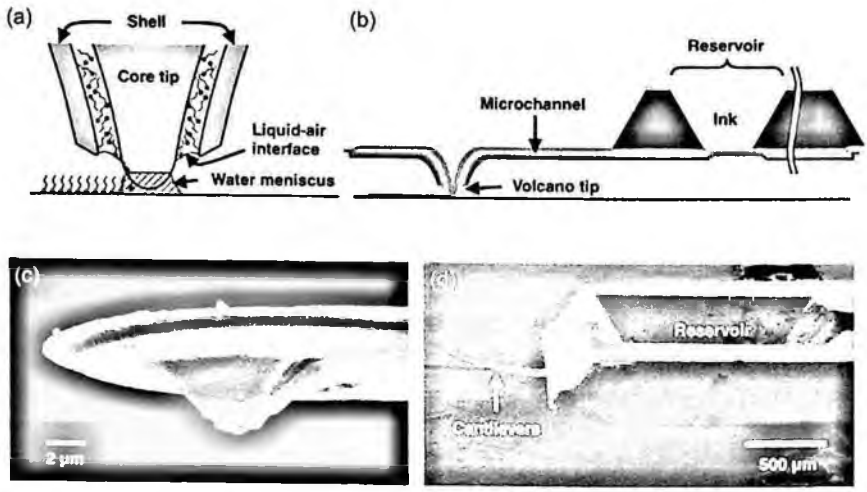

Figure 40. (a) Writing mechanism of DPN device. A molecular ink fed from the reservoir forms a liquid-air interface at the annular aperture of the volcano tip. (b) Ink from the reservoir is delivered to the tip via capillary forces. (c,d) SEM images of a volcano dispensing tip [98].

A further variation of DPN probe arrays has been developed by Moldovan *et al.* [98,140]. In this model, a microfluidic channel continuously delivers the liquid from a reservoir to the apex of the tip, as depicted in Fig. 40. This approach minimises the re-ink and re-position cycles which increase the efficiency of the operation. Using this approach, a scanning speed of 0.05 cm s^{-1} has been successfully tested, and line widths as small as 40 nm have been achieved. These demonstrations were carried out with a saturated solution of 16-mercaptohexadecanoic acid (MHA) in ethanol.

4.4. *Hybrid arrays of probes*

Multifunctional probes, e.g. SECM/AFM, have already been presented above. Probe arrays offer the possibility of implementation of diverse independent functions within one probe array, which allows simultaneous execution of different processes, such as writing and imaging. This can be of large interest in many applications. Using a non-multifunctional probe often holds the risk of cross contamination while altering between writing and imaging process execution. Working with multifunctional arrays of monofunctional probes allows simultaneous imaging and writing processes without cross contamination or incommodious and time consuming exchange of the probe. Wang *et al.* [195] developed a multifunctional array of probes including DPN, scanning probe contact printing (SPCP) and additional AFM probe, which allows sequential or simultaneous patterning and imaging. Experiments of DPN and SPCP patterning combined with imaging using the same probe array have not revealed any evidence of cross contamination. Furthermore, spatial coordination of multiple tips becomes feasible as the tip-to-tip distance between the probes is predetermined in design and ensured in micromachining processes.

The fabrication of Si multiprobes with independent lateral actuators was demonstrated by Ahn *et al.* [2]. They developed a four-probe-array with integrated electrostatic actuators as shown in Fig. 41. Multi-folded hinge structures have been used for individual comb drive actuation. Topographic imaging of carbon nano tubes (CNT) was successfully carried out in tapping mode using the multi-probe array. Moreover, I-V characterisation of CNT by two-probe measurements was possible using two individual probes of the array.

5. Conclusion

Scanning Probe Methods have changed the way we look at surfaces, and the way we think about manipulating matter down to the molecular level. For many practical applications, however, it is essential to arrive at meaningful results and statistics, or achieving adequate throughput, in a meaningful timeframe. Using standard SPM instrumentation is often too time-consuming. One possible solution to the problem is to operate SPMs at high speeds, all the way to video rates. Some limitations in image quality, in the control of interaction forces, and associated sample damage can often be accepted. Another strategy to achieve faster SPM throughput is to work with many probes in parallel, while keeping the optimum imaging parameters such as interaction force and imaging speed, for each individual probe.

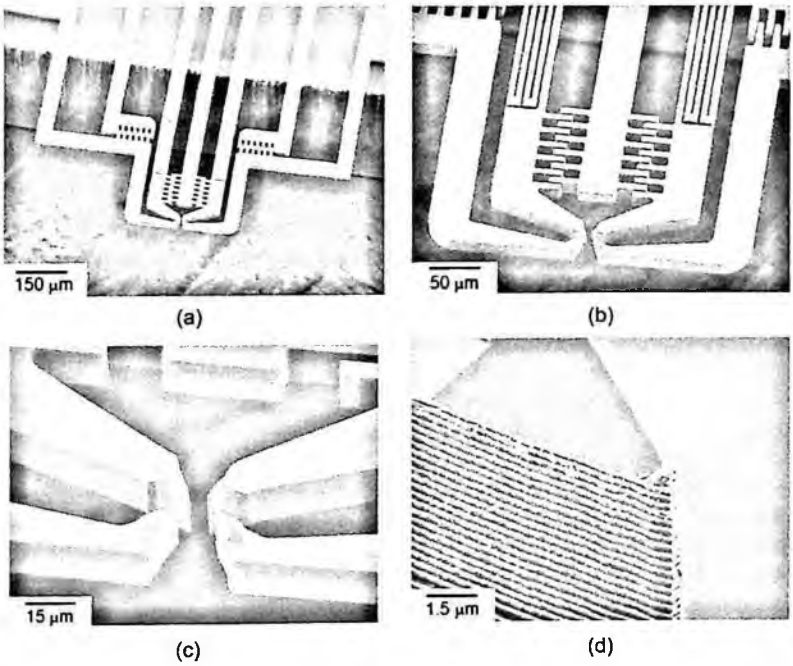

Figure 41. SEM images of four probe configuration (a) cantilever with actuator, (b) comb drive, (c) 1 × 4 probe array, (d) magnified view of the tip [2].

The key challenge when developing probe array devices is to design read-out systems that are sufficiently sensitive for the application at hand, resistant to the working environment, and compatible with the operation of a large number of probes in parallel. To avoid major difficulties stemming from the necessary alignment of read-out system and probe array, self-sensing schemes have been developed, which in turn have their limitations in detection sensitivity. Often, passivation layers are necessary to enable operation of the probe arrays e.g. in buffer solutions, and add to the design challenges.

Microfabrication methods have been developed that allow production of arrays made from thousands, and more, of probes uniform enough to allow their simultaneous operation. In many cases, a method to allow self-sensing of the cantilever deflection is built-in, often in the form of piezoresistive layers and the corresponding electrical contacts. In other cases, external sensing schemes are being adapted from single probe to probe array operation, such as (interferometric) optical methods. When it comes to applications, disposable probe arrays may become a must and their price important.

In some specialized applications, the substrate properties and other environmental conditions can be controlled to the extent that some particular interaction between probe and surface can be used to sense their proximity with sufficient precision. The Millipede developed for data storage application is such an example, and the change in heat transfer between probe-tip and substrate-surface allows to detect small variations in surface topography, such as individual bits written into a polymer film. However, as a general strategy this concept suffers from too much ambiguity when the sample properties are not precisely controlled.

Other applications include the imaging of surfaces for large scale characterization, the deposition of small amounts of liquids for prototyping and microarray preparation, and the measurement of molecular interaction forces where increased statistics is necessary. For such different domains and objectives, different technological solutions appear appropriate. The ongoing developments are encouraging, and first probe array devices have been brought to the market recently. It is likely that with their wider availability, probe arrays will strongly contribute to the information gained from Scanning Probe Methods.

References

1. Force vs. Distance Curves, http://mechmat.caltech.edu/~kaushik/park/1-6-2.htm
2. Y. Ahn, T. Ono and M. Esashi, Si multiprobes integrated with lateral actuators for independent scanning probe applications, *J. Micromech. Microeng.* **15**(6), 1224–1229 (2005).
3. S. Akamine, R. C. Barrett and C. F. Quate, Improved Atomic Force Microscope Images Using Microcantilevers with Sharp Tips, *Appl. Phys. Lett.* **57**(3), 316–318 (1990).
4. S. Akamine and C. F. Quate, Low-Temperature Thermal-Oxidation Sharpening of Microcast Tips, *J. Vac. Sci. Technol. B* **10**(5), 2307–2310 (1992).

5. T. Akiyama, M. R. Gullo, N. F. De Rooij, A. Tonin, H. R. Hidber, P. Frederix, A. Engel and U. Staufer, Development of insulated conductive probes with platinum silicide tips for atomic force microscopy in cell biology, *Japanese J. Appl. Phys. Part 1-Regular Papers Short Notes & Review Papers* **43**(6B), 3865–3867 (2004).
6. T. Akiyama, U. Staufer, N. F. De Rooij, L. Howald and L. Scandella, Lithographically defined polymer tips for quartz tuning fork based scanning force microscopes, *Microelectron. Eng.* **57–8**, 769–773 (2001).
7. T. Akiyama, U. Staufer, N. F. De Rooij, D. Lange, C. Hagleitner, O. Brand, H. Baltes, A. Tonin and H. R. Hidber, Integrated atomic force microscopy array probe with metal-oxide-semiconductor field effect transistor stress sensor, thermal bimorph actuator, and on-chip complementary metal-oxide-semiconductor electronics, *J. Vac. Sci. Technol. B* **18**(6), 2669–2675 (2000).
8. T. Akiyama, A. Tonin, H. R. Hidber, J. Brugger, P. Vettiger, U. Staufer and N. F. De Rooij, Characterization of an integrated force sensor based on a MOS transistor for applications in scanning force microscopy, *Sensor. Actuator A-Physical* **64**(1), 1–6 (1998).
9. T. R. Albrecht, S. Akamine, T. E. Carver and C. F. Quate, Microfabrication of cantilever styli for the atomic force microscope, *J. Vac. Sci. Technol. A (Vacuum, Surfaces, and Films)* **8**(4), 3386–3396 (1990).
10. T. R. Albrecht and C. F. Quate, Atomic resolution with the atomic force microscope on conductors and nonconductors, *J. Vac. Sci. Technol. A: Vacuum, Surfaces, and Films* **6**(2), 271–274 (1988).
11. P. C. Allen, Silicon field emitter arrays: fabrication and operation, Vacuum Microelectronics 1989. *Proceedings of the Second International Conference*, 17–20 (1989).
12. M. Alvarez and J. Tamayo, Optical sequential readout of microcantilever arrays for biological detection, *Sensor Actuat. B-Chem.* **106**(2), 687–690 (2005).
13. D. Anselmetti, C. Gerber, B. Michel, H. J. Guntherodt and H. Rohrer, Compact, Combined Scanning Tunneling Force Microscope, *Rev. Sci. Instrum.* **63**(5), 3003–3006 (1992).
14. M. Arca, A. J. Bard, B. R. Horrocks, T. C. Richards and D. A. Treichel, Advances in Scanning Electrochemical Microscopy - Plenary Lecture, Analyst **119**(5), 719–726 (1994).
15. A. J. Bard, F. R. F. Fan, J. Kwak and O. Lev, Scanning Electrochemical Microscopy - Introduction and Principles, *Anal. Chem.* **61**(2), 132–138 (1989).
16. A. J. Bard, X. Li and W. Zhan, Chemically imaging living cells by scanning electrochemical microscopy, *Electrochem. Commun.* **article in press** (2006).
17. A. L. Barker, P. R. Unwin, J. W. Gardner and H. Rieley, A multi-electrode probe for parallel imaging in scanning electrochemical microscopy, *Electrochem. Commun.* **6**(1), 91–97 (2004).
18. P. Belaubre, M. Guirardel, G. Garcia, J. B. Pourciel, V. Leberre, A. Dagkessamanskaia, E. Trevisiol, J. M. Francois and C. Bergaud, Fabrication of biological microarrays using microcantilevers, *Appl. Phys. Lett.* **82**(18), 3122–3124 (2003).
19. R. Berger, M. Helm and F. Saurenbach, Read-out of inhomogeneously coated micromechanical cantilever sensors, **119** (2006). Copenhagen, Denmark, DTU, Technical University of Denmark, DK-2800 Kongens Lyngby, Denmark. Proceedings of the International Workshop on Nanomechanical Sensors.
20. M. Berliocchi, S. Orlanducci, A. Reale, P. Regoliosi, A. Di Carlo, P. Lugli, M. L. Terranova, F. Brunetti, G. Bruni and M. Cirillo, Single wall carbon nanotube based aggregates and their electrical characterization, *Synthetic Met.* **145**(2–3), 171–176 (2004).

21. E. Betzig, J. K. Trautman, R. Wolfe, E. M. Gyorgy, P. L. Finn, M. H. Kryder and C. H. Chang, Near-Field Magnetooptics and High-Density Data-Storage, *Appl. Phys. Lett.* **61**(2), 142–144 (1992).
22. G. Binnig, C. F. Quate and C. Gerber, Atomic Force Microscope, *Phys. Rev. Lett.* **56**(9), 930–933 (1986).
23. G. Binnig and H. Rohrer, Scanning Tunneling Microscopy, *Helv. Phys. Acta* **55**(6), 726–735 (1982).
24. G. Boero, I. Utke, T. Bret, N. Quack, M. Todorova, S. Mouaziz, P. Kejik, J. Brugger, R. S. Popovic and P. Hoffmann, Submicrometer Hall devices fabricated by focused electron-beam-induced deposition, *Appl. Phys. Lett.* **86**(4) (2005).
25. M. Bolks, F. Hanssen, L. Abelmann, P. Havinga, P. Hartel, P. Jansen, C. Lodder and G. Smit, Micro Scanning Probe Array Memory, University of Twente, P.O. Box 217, 7500 AE Enschede, The Netherlandswww.ub.utwente.nl/webdocs/ctit/1/0000006d.pdf
26. M. Briman, K. Bradley and G. Gruner, Source of 1/f noise in carbon nanotube devices, *J. Appl. Phys.* **100**(1) (2006).
27. A. J. Brook, S. J. Bending, J. Pinto, A. Oral, D. Ritchie, H. Beere, M. Henini and A. Springthorpe, Integrated piezoresistive sensors for atomic force-guided scanning Hall probe microscopy, *Appl. Phys. Lett.* **82**(20), 3538–3540 (2003).
28. A. J. Brook, S. J. Bending, J. Pinto, A. Oral, D. Ritchie, H. Beere, A. Springthorpe and M. Henini, Micromachined III-V cantilevers for AFM-tracking scanning hall probe microscopy, *J. Micromech. Microeng.* **13**(1), 124–128 (2003).
29. J. Brugger, Microfabricated Tools for the Scanning Force Microscope, (1995). University of Neuchatel, Institute of Microtechnology.
30. J. Brugger, G. Beljakovic, M. Despont, N. F. deRooij and P. Vettiger, Silicon micro/nanomechanical device fabrication based on focused ion beam surface modification and KOH etching, *Microelectron. Eng.* **35**(1–4), 401–404 (1997).
31. J. Brugger, N. Blanc, P. Renaud and N. F. deRooij, Microlever with Combined Integrated Sensor Actuator Functions for Scanning Force Microscopy, *Sensor Actuat. A-Phys.* **43**(1–3), 339–345 (1994).
32. J. Brugger, R. A. Buser and N. F. De Rooij, Silicon cantilevers and tips for scanning force microscopy, *Sensor Actuat. A: Phys.* **34**(3), 193–200 (1992).
33. H. B. Callen and T. A. Welton, Irreversibility and Generalized Noise, *Phys. Rev.* **83**(1), 34–40 (1951).
34. L. R. Carley, J. A. Bain, G. K. Fedder, D. W. Greve, D. F. Guillou, M. S. C. Lu, T. Mukherjee, S. Santhanam, L. Abelmann and S. Min, Single-chip computers with microelectromechanical systems-based magnetic memory (invited), *J. Appl. Phys.* **87**(9), 6680–6685 (2000).
35. M. Carrion-Vazquez, A. F. Oberhauser, T. E. Fisher, P. E. Marszalek, H. B. Li and J. M. Fernandez, Mechanical design of proteins-studied by single-molecule force spectroscopy and protein engineering, *Prog. Biophys. Mol. Bio.* **74**(1–2), 63–91 (2000).
36. C. L. Cheung, J. H. Hafner, T. W. Odom, K. Kim and C. M. Lieber, Growth and fabrication with single-walled carbon nanotube probe microscopy tips, *Appl. Phys. Lett.* **76**(21), 3136–3138 (2000).
37. Y. S. Chi and I. S. Choi, Dip-pen nanolithography using the amide-coupling reaction with interchain carboxylic anhydride-terminated self-assembled monolayers, *Adv. Funct. Mater.* **16**(8), 1031–1036 (2006).
38. H. Chiriac, M. Pletea and E. Hristoforou, Magnetoelastic characterization of thin films dedicated to magnetomechanical microsensor applications, *Sensor Actuat. A-Phys.* **68**(1–3), 414–418 (1998).

39. A. N. Cleland and M. L. Roukes, Noise processes in nanomechanical resonators, *J. Appl. Phys.* **92**(5), 2758–2769 (2002).
40. R. Dandliker, Y. Salvade and E. Zimmermann, Distance measurement by multiple-wavelength interferometry, *J. Opt.* **29**(3), 105–114 (1998).
41. W. A. Daoud, J. H. Xin and Y. S. Szeto, Polyethylenedioxythiophene coatings for humidity, temperature and strain sensing polyamide fibers, *Sensor Actuat. B-Chem.* **109**(2), 329–333 (2005).
42. M. Despont, U. Drechsler, R. Yu, H. B. Pogge and P. Vettiger, Wafer-scale microdevice transfer/interconnect: Its application in an AFM-based data-storage system, *J. Microelectromech. S.* **13**(6), 895–901 (2004).
43. P. Dharap, Z. L. Li, S. Nagarajaiah and E. V. Barrera, Nanotube film based on single-wall carbon nanotubes for strain sensing, *Nanotechnology* **15**(3), 379–382 (2004).
44. S. Dohn, O. Hansen, and A. Boisen, Cantilever based mass sensor with hard contact readout, *Appl. Phys. Lett.* **88**(26) (2006).
45. S. Dohn, J. Kjelstrup-Hansen, D. N. Madsen, K. Molhave and P. Boggild, Multi-walled carbon nanotubes integrated in microcantilevers for application of tensile strain, *Ultramicroscopy* **105**(1–4), 209–214 (2005).
46. D. M. Eigler and E. K. Schweizer, Positioning Single Atoms with a Scanning Tunneling Microscope, *Nature* **344**(6266), 524–526 (1990).
47. K. L. Ekinci and M. L. Roukes, Nanoelectromechanical systems, *Rev. Sci. Instrum.* **76**(6) (2005).
48. Eleftheriou. E, T. Antonakopoulos, G. K. Binnig, G. Cherubini, M. Despont, A. Dholakia, U. Dürig, M. A. Lantz, H. Pozidis, H. E. Rothuizen and P. Vettiger, Millipede- a MEMS-based Scanning-Probe Data-Storage System, *IEEE Transactions on Magnetics* **Preprint**(Special Issue), 1–8 (2002).
49. R. Erlandsson, G. M. McClelland, C. M. Mate and S. Chiang, Atomic Force Microscopy Using Optical Interferometry, *J. Vac. Sci. Technol. A* **6**(2), 266–270 (1988).
50. R. J. Fasching, Y. Tao and F. B. Prinz, Cantilever tip probe arrays for simultaneous SECM and AFM analysis, *Sensor Actuat. B-Chem.* **108**(1–2), 964–972 (2005).
51. E. L. Florin, V. T. Moy and H. E. Gaub, Adhesion Forces Between Individual Ligand-Receptor Pairs, *Science* **264**(5157), 415–417 (1994).
52. A. Folch, M. S. Wrighton and M. A. Schmidt, Microfabrication of oxidation-sharpened silicon tips on silicon nitride cantilevers for atomic force microscopy, *J. Microelectromech. S.* **6**(4), 303–306 (1997).
53. T. Fukuma, K. Kimura, K. Kobayashi, K. Matsushige and H. Yamada, Frequency-modulation atomic force microscopy at high cantilever resonance frequencies using the heterodyne optical beam deflection method, *Rev. Sci. Instrum.* **76**(12) (2005).
54. T. Fukuma, M. Kimura, K. Kobayashi, K. Matsushige and H. Yamada, Development of low noise cantilever deflection sensor for multienvironment frequency-modulation atomic force microscopy, *Rev. Sci. Instrum.* **76**(5) (2005).
55. C. E. Gardner, P. R. Unwin and J. V. Macpherson, Correlation of membrane structure and transport activity using combined scanning electrochemical-atomic force microscopy, *Electrochem. Commun.* **7**(6), 612–618 (2005).
56. G. Genolet, J. Brugger, M. Despont, U. Drechsler, P. Vettiger, N. F. De Rooij and D. Anselmetti, Soft, entirely photoplastic probes for scanning force microscopy, *Rev. Sci. Instrum.* **70**(5), 2398–2401 (1999).
57. G. Genolet, M. Despont, P. Vettiger, D. Anselmetti and N. F. De Rooij, All-photoplastic, soft cantilever cassette probe for scanning force microscopy, *J. Vac. Sci. Technol. B* **18**(2), 617–620 (2000).

58. G. Gerlach and R. Werthschütsky, 50 Jahre Entdeckung des piezoresistiven Effekts – Geschicht und Entwicklungsstand piezoresistiver Sensoren, *Technisches Messen* **72**(2), 53–76 (2005).
59. F. J. Giessibl, Advances in atomic force microscopy, *Rev. Mod. Phys.* **75**(3), 949–983 (2003).
60. F. J. Giessibl, S. Hembacher, H. Bielefeldt and J. Mannhart, Subatomic features on the silicon (111)-(7 × 7) surface observed by atomic force microscopy, *Science* **289**(5478), 422–425 (2000).
61. F. J. Giessibl, S. Hembacher, M. Herz, C. Schiller and J. Mannhart, Stability considerations and implementation of cantilevers allowing dynamic force microscopy with optimal resolution: the qPlus sensor, *Nanotechnology* **15**(2), S79–S86 (2004).
62. E. Gmelin, R. Fischer and R. Stitzinger, Sub-micrometer thermal physics– An overview on SThM techniques, *Thermochimi. Acta* **310**(1–2), 1–17 (1998).
63. T. Goddenhenrich, H. Lemke, U. Hartmann and C. Heiden, Force Microscope with Capacitive Displacement Detection, *J. Vac. Sci. Tech. A* **8**(1), 383–387 (1990).
64. J. G. Graeme, Photodiode Amplifiers, Op Amp Solutions, 252 (1996). Boston, McGraw-Hill.
65. R. D. Grober, J. Acimovic, J. Schuck, D. Hessman, P. J. Kindlemann, J. Hespanha, A. S. Morse, K. Karrai, I. Tiemann and S. Manus, Fundamental limits to force detection using quartz tuning forks, *Rev. Sci. Instrum.* **71**(7), 2776–2780 (2000).
66. R. J. Grow, S. C. Minne, S. R. Manalis and C. F. Quate, Silicon nitride cantilevers with oxidation-sharpened silicon tips for atomic force microscopy, *J. Microelectromech. S.* **11**(4), 317–321 (2002).
67. P. Guthner, J. Glatzreichenbach and K. Dransfeld, Investigation of Local Piezoelectric Properties of Thin Copolymer Films, *J. Appl. Phys.* **69**(11), 7895–7897 (1991).
68. J. H. Hafner, C. L. Cheung, T. H. Oosterkamp and C. M. Lieber, High-yield assembly of individual single-walled carbon nanotube tips for scanning probe microscopies, *J. Phys. Chem. B* **105**(4), 743–746 (2001).
69. Hamamatsu, http://jp.hamamatsu.com/
70. T. Hantschel, S. Slesazeck, P. Niedermann, P. Eyben and W. Vandervorst, Integrating diamond pyramids into metal cantilevers and using them as electrical AFM probes, *Microelectron. Eng.* **57–8**, 749–754 (2001).
71. J. A. Harley and T. W. Kenny, High-sensitivity piezoresistive cantilevers under 1000 angstrom thick, *Appl. Phys. Lett.* **75**(2), 289–291 (1999).
72. M. Helm, J. J. Servant, F. Saurenbach and R. Berger, Read-out of micromechanical cantilever sensors by phase shifting interferometry, *Appl. Phys. Lett.* **87**(6) (2005).
73. C. S. Hodges, Measuring forces with the AFM: polymeric surfaces in liquids, *Adv. Colloid Interfac.* **99**(1), 13–75 (2002).
74. M. Hoffmann, H. Bezzaoui and E. Voges, Micromechanical Cantilever Resonators with Integrated Optical Interrogation, *Sensor Actuat. A-Phys.* **44**(1), 71–75 (1994).
75. S. H. Hong and C. A. Mirkin, A nanoplotter with both parallel and serial writing capabilities, *Science* **288**(5472), 1808–1811 (2000).
76. B. Hubner, H. W. P. Koops, H. Pagnia, N. Sotnik, J. Urban and M. Weber, Tips for scanning tunneling microscopy produced by electron-beam-induced deposition, *Ultramicroscopy* **42–44**(Part 2), 1519–1525 (1992).
77. A. D. L. Humphris, M. J. Miles and J. K. Hobbs, A mechanical microscope: High-speed atomic force microscopy, *Appl. Phys. Lett.* **86**(3) (2005).
78. M. Ishigami, J. H. Chen, E. D. Williams, D. Tobias, Y. F. Chen and M. S. Fuhrer, Hooge's constant for carbon nanotube field effect transistors, *Appl. Phys. Lett.* **88**(20) (2006).

79. T. Ishitani, T. Ohnishi and Y. Kawanami, Micromachining and Device Transplantation Using Focused Ion-Beam, *Jpn. J. Appl. Phys. 1* **29**(10), 2283–2287 (1990).
80. T. Itoh, T. Ohashi and T. Suga, Piezoelectric cantilever array for multiprobe scanning force microscopy, 451–455 (1996). Proceedings: IEEE Micro Electro Mechanical Systems Workshop.
81. T. Itoh and T. Suga, Piezoelectric Force Sensor for Scanning Force Microscopy, *Sensor Actuat. A-Phys.* **43**(1–3), 305–310 (1994).
82. T. Itoh and T. Suga, Scanning Force Microscope Using a Piezoelectric Microcantilever, *J. Vac. Sci. Techol. B* **12**(3), 1581–1585 (1994).
83. T. Itoh and T. Suga, Minimum Detectable Force Gradients of Piezoelectric Microcantilever, *J. Micromech. Microeng.* **5**(3), 231–236 (1995).
84. T. Ivanov, T. Gotszalk, T. Sulzbach and Rangelow.I.W., Quantum size aspects of piezoresistive effect in ultra thin piezoresitors, *Ultramicroscopy* **97**, 377–384 (2003).
85. A. Janshoff, M. Neitzert, Y. Oberdorfer and H. Fuchs, Force spectroscopy of molecular systems—Single molecule spectroscopy of polymers and biomolecules, *Angewandte Chemie-International Edition* **39**(18), 3213–3237 (2000).
86. D. C. Jiles, Theory of the Magnetomechanical Effect, *J. Phys. D-Appl. Phys.* **28**(8), 1537–1546 (1995).
87. R. Jumpertz, A. der Hart, O. Ohlsson, F. Saurenbach and J. Schelten, Piezoresistive sensors on AFM cantilevers with atomic resolution, *Microelectron. Eng.* **42**, 441–444 (1998).
88. M. Kageshima, H. Jensenius, M. Dienwiebel, Y. Nakayama, H. Tokumoto, S. P. Jarvis and T. H. Oosterkamp, Noncontact atomic force microscopy in liquid environment with quartz tuning fork and carbon nanotube probe, *Appl. Surf. Sci.* **188**(3–4), 440–444 (2002).
89. M. Kageshima, H. Ogiso, S. Nakano, M. A. Lantz and H. Tokumoto, Atomic force microscopy cantilevers for sensitive lateral force detection, *Jpn. J. Appl. Phys. 1* **38**(6B), 3958–3961 (1999).
90. D. Karabacak, T. Kouh, C. C. Huang and K. L. Ekinci, Optical knife-edge technique for nanomechanical displacement detection, *Appl. Phys. Lett.* **88**(19) (2006).
91. R. Kassies, K. O. van der Werf, M. L. Bennink and C. Otto, Removing interference and optical feedback artifacts in atomic force microscopy measurements by application of high frequency laser current modulation, *Rev. Sci. Instrum.* **75**(3), 689–693 (2004).
92. H. Kawakatsu, S. Kawai, D. Saya, M. Nagashio, D. Kobayashi, H. Toshiyoshi and H. Fujita, Towards atomic force microscopy up to 100 MHz, *Rev. Sci. Instrum.* **73**(6), 2317–2320 (2002).
93. H. Kawakatsu, D. Saya, A. Kato, K. Fukushima, H. Toshiyoshi and H. Fujita, Millions of cantilevers for atomic force microscopy, *Rev. Sci. Instrum.* **73**(3), 1188–1192 (2002).
94. S. Keller, S. Mouaziz, G. Boero and J. Brugger, Microscopic four-point probe based on SU-8 cantilevers, *Rev. Sci. Instrum.* **76**(12) (2005).
95. H. Kikuta, K. Nasu, N. Kato and K. Iwata, Atomic-Force Microscope Using Optical Heterodyne-Detection Incorporated in an Optical Microscope, *Rev. Sci. Instrum.* **66**(1), 87–90 (1995).
96. G. M. Kim, B. J. Kim, E. S. Ten Have, F. Segerink, N. F. Van Hulst and J. Brugger, Photoplastic near-field optical probe with sub-100 nm aperture made by replication from a nanomould, *J. Microsc.-Oxford* **209**, 267–271 (2003).

97. G. M. Kim, A. Kovalgin, J. Holleman and J. Brugger, Replication molds having nanometer-scale shape control fabricated by means of oxidation and etching, *J. Nanosci. Nanotechno.* **2**(1), 55–59 (2002).
98. K. H. Kim, N. Moldovan and H. D. Espinosa, A nanofountain probe with sub-100 nm molecular writing resolution, *Small* **1**(6), 632–635 (2005).
99. S. Y. Kim, H. J. Nam, S. S. Jang, C. S. Lee, W. H. Jin, I. J. Cho, J. U. Bu, S. I. Chang and E. Yoon, Wafer-Level Transfer of Thermo-Piezoelectric Si3N4 Cantilever Array on a CMOS Circuit for High Density Probe-Based Data Storage, 922–925 (2006). 22-1-2006.
100. Y. S. Kim, C. S. Lee, W. H. Jin, S. Jang, H. J. Nam and J. U. Bu, 100×100 thermo-piezoelectric cantilever array for SPM nano-data-storage application, *Sensor Mater.* **17**(2), 57–63 (2005).
101. W. P. King, T. W. Kenny, K. E. Goodson, G. L. W. Cross, M. Despont, U. T. Durig, H. Rothuizen, G. Binnig and P. Vettiger, Design of atomic force microscope cantilevers for combined thermomechanical writing and thermal reading in array operation, *J. Microelectromech. S.* **11**(6), 765–774 (2002).
102. I. Kiyat, C. Kocabas and A. Aydinli, Integrated micro ring resonator displacement sensor for scanning probe microscopies, *J. Micromech. Microeng.* **14**(3), 374–381 (2004).
103. E. Klokholm, Measurement of Magnetostriction in Ferromagnetic Thin-Films, *IEEE Transactions on Magnetics* **12**(6), 819–821 (1976).
104. C. Kocabas and A. Aydinli, Design and analysis of an integrated optical sensor for scanning force microscopies, *IEEE Sensors Journal* **5**(3), 411–418 (2005).
105. L. S. Kong, L. Zhuang and S. Y. Chou, Writing and reading 7.5 Gbits/in(2) longitudinal quantized magnetic disk using magnetic force microscope tips, *IEEE Transactions on Magnetics* **33**(5), 3019–3021 (1997).
106. C. Kranz, G. Friedbacher and B. Mizaikoff, Integrating an ultramicroelectrode in an AFM cantilever: Combined technology for enhanced information, *Anal. Chem.* **73**(11), 2491 (2001).
107. S. Krishnamoorthy, R. Pugin, J. Brugger, H. Heinzelmann and C. Hinderling, Tuning the dimensions and periodicities of nanostructures starting from the same polystyrene-block-poly(2–vinylpyridine) diblock copolymer, *Adv. Funct. Mater.* **16**(11), 1469–1475 (2006).
108. S. Krishnamoorthy, R. Pugin, J. Brugger, H. Heinzelmann, A. C. Hoogerwerf and C. Hinderling, Block copolymer micelles as switchable templates for nanofabrication, *Langmuir* **22**(8), 3450–3452 (2006).
109. A. Kueng, C. Kranz and B. Mizaikoff, Scanning probe microscopy with integrated biosensors, *Sens. Lett.* **1**(1), 2–15 (2003).
110. C. K. Lee, T. Itoh, T. Ohashi, R. Maeda and T. Suga, Development of a piezoelectric self-excitation and self-detection mechanism in PZT microcantilevers for dynamic scanning force microscopy in liquid, *J. Vac. Sci. Techol. B* **15**(4), 1559–1563 (1997).
111. G. U. Lee, D. A. Kidwell and R. J. Colton, Sensing Discrete Streptavidin Biotin Interactions with Atomic-Force Microscopy, *Langmuir* **10**(2), 354–357 (1994).
112. K. L. Lee, D. W. Abraham, F. Secord and L. Landstein, Submicron Si Trench Profiling with an Electron-Beam Fabricated Atomic Force Microscope Tip, *J. Vac. Sci. Technol. B* **9**(6), 3562–3568 (1991).
113. S. W. Lee, B. K. Oh, R. G. Sanedrin, K. Salaita, T. Fujigaya and C. A. Mirkin, Biologically active protein nanoarrays generated using parallel dip-pen nanolithography, *Adv. Mater.* **18**(9), 1133–+ (2006).

114. A. Lewis, M. Isaacson, A. Muray and A. Harootunian, Scanning Optical Spectral Microscopy with 500A Spatial-Resolution, *Biophys. J.* **41**(2), A405 (1983).
115. C. Y. Li and T. W. Chou, Atomistic modeling of carbon nanotube-based mechanical sensors, *J. Intel. Mat. Syst. Str.* **17**(3), 247–254 (2006).
116. M. H. Li and Y. B. Gianchandani, Applications of a low contact force polyimide shank bolometer probe for chemical and biological diagnostics, *Sensor Actuat. A-Phys.* **104**(3), 236–245 (2003).
117. M. Lohndorf, T. Duenas, M. Tewes, E. Quandt, M. Ruhrig and J. Wecker, Highly sensitive strain sensors based on magnetic tunneling junctions, *Appl. Phys. Lett.* **81**(2), 313–315 (2002).
118. A. Lugstein, E. Bertagnolli, C. Kranz, A. Kueng and B. Mizaikoff, Integrating micro- and nanoelectrodes into atomic force microscopy cantilevers using focused ion beam techniques, *Appl. Phys. Lett.* **81**(2), 349–351 (2002).
119. A. Lugstein, E. Bertagnolli, C. Kranz and B. Mizaikoff, Fabrication of a ring nanoelectrode in an AFM tip: novel approach towards simultaneous electrochemical and topographical imaging, *Sur. Interface Anal.* **33**(2), 146–150 (2002).
120. K. Luo, Z. Shi, J. Lai and A. Majumdar, Nanofabrication of sensors on cantilever probe tips for scanning multiprobe microscopy, *Appl. Phys. Lett.* **68**(3), 325–327 (1996).
121. M. Lutwyche, C. Andreoli, G. Binnig, J. Brugger, U. Drechsler, W. Haberle, H. Rohrer, H. Rothuizen, P. Vettiger, G. Yaralioglu and C. Quate, 5X5 2D AFM cantilever arrays a first step towards a Terabit storage device, *Sensor Actuat. A-Phys.* **73**(1–2), 89–94 (1999).
122. M. I. Lutwyche, M. Despont, U. Drechsler, U. Durig, W. Haberle, H. Rothuizen, R. Stutz, R. Widmer, G. K. Binnig and P. Vettiger, Highly parallel data storage system based on scanning probe arrays, *Appl. Phys. Lett.* **77**(20), 3299–3301 (2000).
123. J. V. Macpherson and P. R. Unwin, Combined scanning electrochemical-atomic force microscopy, *Anal. Chem.* **72**(2), 276–285 (2000).
124. H. J. Mamin, H. Birk, P. Wimmer and D. Rugar, High-Speed Scanning-Tunneling-Microscopy – Principles and Applications, *J. Appl. Phys.* **75**(1), 161–168 (1994).
125. H. J. Mamin, B. A. Gurney, D. R. Wilhoit and V. S. Speriosu, High sensitivity spin-valve strain sensor, *Appl. Phys. Lett.* **72**(24), 3220–3222 (1998).
126. S. R. Manalis, S. C. Minne, C. F. Quate, G. G. Yaralioglu and A. Atalar, Two-dimensional micromechanical bimorph arrays for detection of thermal radiation, *Appl. Phys. Lett.* **70**(24), 3311–3313 (1997).
127. R. B. Marcus, T. S. Ravi, T. Gmitter, K. Chin, D. Liu, W. J. Orvis, D. R. Ciarlo, C. E. Hunt and J. Trujillo, Formation of silicon tips with <1 nm radius, *Appl. Phys. Lett.* **56**(3), 236–238 (1990).
128. Y. Martin, C. C. Williams and H. K. Wickramasinghe, Atomic Force Microscope Force Mapping and Profiling on a Sub 100-a Scale, *J. Appl. Phys.* **61**(10), 4723–4729 (1987).
129. S. McNamara, A. S. Basu, J. Lee and Y. B. Gianchandani, Ultracompliant thermal probe array fol scanning non-planar surfaces without force feedback, *J. Micromech. Microeng.* **15**(1), 237–243 (2005).
130. A. Meister, Nanoscale Dispensing of Single Ultrasmall Droplets, Philosophisch-Natur-wissenschaftliche Fakultät der Universität Bassel, Thesis pp156 (2004).
131. A. Meister, personal communication, (2006).
132. A. Meister, S. Jeney, M. Liley, T. Akiyama, U. Staufer, N. F. De Rooij and H. Heinzelmann, Nanoscale dispensing of liquids through cantilevered probes, *Microelectron. Eng.* **67–8**, 644–650 (2003).

133. A. Meister, S. Krishnamoorthy, C. Hinderling, R. Pugin and H. Heinzelmann, Local modification of micellar layers using nanoscale dispensing, *Microelectron. Eng.* **83**(4–9), 1509–1512 (2006).
134. A. Meister, M. Liley, J. Brugger, R. Pugin and H. Heinzelmann, Nanodispenser for attoliter volume deposition using atomic force microscopy probes modified by focused-ion-beam milling, *Appl. Phys. Lett.* **85**(25), 6260–6262 (2004).
135. A. Meister, P. Niedermann, E. Dujardin, R. Pugin and H. Heinzelmann, Hollow Atomic Force Microscopy Cantilevered Probes for Nanoscale Dispensing of Liquids, International Workshop on Nanomechanical Sensors, Copenhagen, Demark, 1–2 (7-10-2006).
136. C. Menozzi, G. C. Gazzadi, A. Alessandrini and P. Facci, Focused ion beam-nanomachined probes for improved electric force microscopy, *Ultramicroscopy* **104**(3–4), 220–225 (2005).
137. G. Meyer and N. M. Amer, Novel Optical Approach to Atomic Force Microscopy, *Appl. Phys. Lett.* **53**(12), 1045–1047 (1988).
138. S. C. Minne, J. D. Adams, G. Yaralioglu, S. R. Manalis, A. Atalar and C. F. Quate, Centimeter scale atomic force microscope imaging and lithography, *Appl. Phys. Lett.* **73**(12), 1742–1744 (1998).
139. S. C. Minne, G. Yaralioglu, S. R. Manalis, J. D. Adams, J. Zesch, A. Atalar and C. F. Quate, Automated parallel high-speed atomic force microscopy, *Appl. Phys. Lett.* **72**(18), 2340–2342 (1998).
140. N. Moldovan, K. H. Kim and H. D. Espinosa, Design and fabrication of a novel microfluidic nanoprobe, *J. Microelectromech. S.* **15**(1), 204–213 (2006).
141. S. Naberhuis, Probe-based recording technology, *J. Magn. Magn. Mater.* **249**(3), 447–451 (2002).
142. H. J. Nam, Y. S. Kim, C. S. Lee, W. H. Jin, S. S. Jang, L. J. Cho and J. U. Bu, Integrated nitride cantilever array with Si heaters and piezoelectric detectors for nano-data-storage application, 247–250 (2005). Proceedings: IEEE Micro Electro Mechanical Systems Workshop.
143. G. Neubauer, S. R. Cohen, G. M. McClelland, D. Horne and C. M. Mate, Force Microscopy with A Bidirectional Capacitance Sensor, *Rev. Sci. Instrum.* **61**(9), 2296–2308 (1990).
144. P. Niedermann, W. Hanni, D. Morel, A. Perret, N. Skinner, P. F. Indermuhle, N. F. De Rooij and P. A. Buffat, CVD diamond probes for nanotechnology, *Appl. Phys. A-Mater.* **66**, S31–S34 (1998).
145. P. Niedermann, W. Hanni, S. Thurre, M. Gjoni, A. Perret, N. Skinner, P. F. Indermuhle, U. Staufer and N. F. De Rooij, Mounting of micromachined diamond tips and cantilevers, *Sur. Inter. Anal.* **27**(5–6), 296–298 (1999).
146. G. P. Nordin, S. Kim, J. Noh and Q. Y., In-plane photonic transduction for micro-cantilever arrays, 119 (2006). Copenhagen, Denmark, DTU, Technical University of Denmark, DK-2800 Kongens Lyngby, Denmark. Proceedings of the International Workshop on Nanomechanical Sensors.
147. D. Nyamjav and A. Ivanisevic, Templates for DNA-templated Fe3O4 nanoparticles, *Biomaterials* **26**(15), 2749–2757 (2005).
148. H. Nyquist, Thermal agitation of electric charge in conductors, *Phys. Rev.* **32**(1), 110–113 (1928).
149. A. G. Onaran, M. Balantekin, W. Lee, W. L. Hughes, B. A. Buchine, R. O. Guldiken, Z. Parlak, C. F. Quate and F. L. Degertekin, A new atomic force microscope probe with force sensing integrated readout and active tip, *Rev. Sci. Instrum.* **77**(2) (2006).

150. G. N. Phillips, M. Siekman, L. Abelmann and J. C. Lodder, High resolution magnetic force microscopy using focused ion beam modified tips, *Appl. Phys. Lett.* **81**(5), 865–867 (2002).
151. R. D. Piner, J. Zhu, F. Xu, S. H. Hong, and C. A. Mirkin, "Dip-pen" nanolithography, Science **283**(5402), 661–663 (1999).
152. D. W. Pohl, W. Denk and M. Lanz, Optical Stethoscopy—Image Recording with Resolution Lambda/20, *Appl. Phys. Lett.* **44**(7), 651–653 (1984).
153. J. Polesel-Maris, L. Aeschimann, A. Meister, R. Ischer, E. Bernard, T. Akiyama, M. Giazzon, P. Niedermann, U. Staufer, R. Pugin, N. F. De Rooij, P. Vettiger and H. Heinzelmann, Piezoresistive Cantilever Arrays for Life Science Applications, *J. Phys.: Conf. Series* **61**, 955–959 (2007).
154. H. M. Pollock and A. Hammiche, Micro-thermal analysis: techniques and applications, *J. Phys. D-Appl. Phys.* **34**(9), R23–R53 (2001).
155. S. Porthun, L. Abelmann and C. Lodder, Magnetic force microscopy of thin film media for high density magnetic recording, *J. Magn. Magn. Mater.* **182**(1–2), 238–273 (1998).
156. C. A. J. Putman, B. G. Degrooth, N. F. Vanhulst and J. Greve, A Detailed Analysis of the Optical Beam Deflection Technique for Use in Atomic Force Microscopy, *J. Appl. Phys.* **72**(1), 6–12 (1992).
157. C. A. J. Putman, B. G. Degrooth, N. F. Vanhulst and J. Greve, A Theoretical Comparison between Interferometric and Optical Beam Deflection Technique for the Measurement of Cantilever Displacement in AFM, *Ultramicroscopy* **42**, 1509–1513 (1992).
158. B. M. Quinn, I. Prieto, S. K. Haram and A. J. Bard, Electrochemical observation of a metal/insulator transition by scanning electrochemical microscopy, *J. Phys. Chem. B* **105**(31), 7474–7476 (2001).
159. I. W. Ranglow, Piezoresistive Scanning Proximity Probes for Nanoscience, *Technisches Messen* **72**(2), 103–110 (2005).
160. J. P. Rasmussen and P. T. Tank, Fabrication of All-Metal Atomic Force Microscope Probe, (1997). International Conference on Solid-State Sensors and Actuators (TRANSDUCERS 97), Chicago.
161. S. Rast, C. Wattinger, U. Gysin and E. Meyer, The noise of cantilevers, *Nanotechnology* **11**(3), 169–172 (2000).
162. B. Rogers, T. Sulchek, K. Murray, D. York, M. Jones, L. Manning, S. Malekos, B. Beneschott, J. D. Adams, H. Cavazos and S. C. Minne, High speed tapping mode atomic force microscopy in liquid using an insulated piezoelectric cantilever, *Rev. Sci. Instrum.* **74**(11), 4683–4686 (2003).
163. Y. Rosenwaks, D. Dahan, M. Molotskii and G. Rosenman, Ferroelectric domain engineering using atomic force microscopy tip arrays in the domain breakdown regime, *Appl. Phys. Lett.* **86**(1) (2005).
164. D. Rugar, H. J. Mamin and P. Guethner, Improved Fiber-Optic Interferometer for Atomic Force Microscopy, *Appl. Phys. Lett.* **55**(25), 2588–2590 (1989).
165. M. Ruhrig, S. Porthun, J. C. Lodder, S. McVitie, L. J. Heyderman, A. B. Johnston and J. N. Chapman, Electron beam fabrication and characterization of high-resolution magnetic force microscopy tips, *J. Appl. Phys.* **79**(6), 2913–2919 (1996).
166. K. Salaita, S. W. Lee, X. F. Wang, L. Huang, T. M. Dellinger, C. Liu and C. A. Mirkin, Sub-100 nm, centimeter-scale, parallel dip-pen nanolithography, *Small* **1**(10), 940–945 (2005).

167. D. Sarid, Scanning Force Microscopy, 263 (1994). New York, Oxford University Press, Inc. Oxford series in optical and imaging sciences.
168. D. Sarid, D. A. Iams, J. T. Ingle, V. Weissenberger and J. Ploetz, Performance of a Scanning Force Microscope Using a Laser Diode, *J. Vac. Sci. Technol. A* **8**(1), 378–382 (1990).
169. D. Sarid, V. Weissenberger, D. A. Iams and J. T. Ingle, Theory of the Laser Diode Interaction in Scanning Force Microscopy, *IEEE Journal of Quantum Electronics* **25**(8), 1968–1972 (1989).
170. F. Saurenbach and B. D. Terris, Imaging of Ferroelectric Domain-Walls by Force Microscopy, *Appl. Phys. Lett.* **56**(17), 1703–1705 (1990).
171. D. Saya, P. Belaubre, F. Mathieu, D. Lagrange, J. B. Pourciel and C. Bergaud, Si-piezoresistive microcantilevers for highly integrated parallel force detection applications, *Sensor Actuat. A-Phys.* **123–24**, 23–29 (2005).
172. T. E. Schaffer, M. Richter and M. B. Viani, Array detector for the atomic force microscope, *Appl. Phys. Lett.* **76**(24), 3644–3646 (2000).
173. I. Serebrennikova, S. Lee and H. S. White, Visualization and characterization of electroactive defects in the native oxide film on aluminium, *Faraday Discussions* **121**, 199–210 (2002).
174. G. Shekhawat, S. H. Tark and V. P. Dravid, MOSFET-embedded microcantilevers for measuring deflection in biomolecular sensors, *Science* **311**(5767), 1592–1595 (2006).
175. N. C. Shie, T. L. Chen and K. Y. Cheng, Use of fibre interferometer for AFM cantilever probe displacement control, (295–296), 77–82 (2005). Key Engineering Materials.
176. I. Shiraki, Y. Miyatake, T. Nagamura and K. Miki, Demonstration of low-temperature atomic force microscope with atomic resolution using piezoresistive cantilevers, *Rev. Sci. Instrum.* **77**(2) (2006).
177. C. S. Smith, Piezoresistance Effect in Germanium and Silicon, *Phys. Rev.* **94**(1), 42–49 (1954).
178. K. B. Song, E. K. Kim, S. Q. Lee and K. H. Park, Fabrication of a high-throughput cantilever-style aperture tip by the use of the bird's-beak effect, *Jpn. J. Appl. Phys. 1* **42**(7A), 4353–4356 (2003).
179. C. Stampfer, A. Jungen and C. Hierold, Fabrication of discrete nanoscaled force sensors based on single-walled carbon nanotubes, *IEEE Sensors Journal* **6**(3), 613–617 (2006).
180. C. Stampfer, A. Jungen, R. Linderman, D. Obergfell, S. Roth and C. Hierold, Nano-electromechanical displacement sensing based on single-walled carbon nanotubes, *Nano Lett.* **6**(7), 1449–1453 (2006).
181. J. A. J. Steen, J. Hayakawa, T. Harada, K. Lee, F. Calame, G. Boero, A. J. Kulik and J. Brugger, Electrically conducting probes with full tungsten cantilever and tip for scanning probe applications, *Nanotechnology* **17**(5), 1464–1469 (2006).
182. T. Sulchek, R. J. Grow, G. G. Yaralioglu, S. C. Minne, C. F. Quate, S. R. Manalis, A. Kiraz, A. Aydine and A. Atalar, Parallel atomic force microscopy with optical interferometric detection, *Appl. Phys. Lett.* **78**(12), 1787–1789 (2001).
183. T. Takezaki, D. Yagisawa and K. Sueoka, Magnetic field measurement using scanning magneto resistance microscope with spin-valve sensor, *Jpn. J. Appl. Phys. 1* **45**(3B), 2251–2254 (2006).
184. J. Tansock and C. C. Williams, Force Measurement with a Piezoelectric Cantilever in a Scanning Force Microscope, *Ultramicroscopy* **42**, 1464–1469 (1992).
185. Y. Tao, R. J. Fasching, and F. B. Prinz, Ultra-sharp High-aspect-ratio Probe Array for SECM and AFM Analysis, Proceedings of SPIE **5389**, 431–442 (2004).

186. N. Tas, J. Wissink, L. Sander, T. Lammerink and M. Elwenspoek, Modeling, design and testing of the electrostatic shuffle motor, *Sensor Actuat. A-Phys.* **70**(1–2), 171–178 (1998).
187. M. Tortonese, R. C. Barrett and C. F. Quate, Atomic Resolution with An Atomic Force Microscope Using Piezoresistive Detection, *Appl. Phys. Lett.* **62**(8), 834–836 (1993).
188. M. Tortonese, H. Yamada, R. C. Barrett and C. Quate, Atomic Force Microscopy Using a Piezoresistive Cantilever, *IEEE*, 448–451 (1991).
189. A. A. Tseng, A. Notargiacomo and T. P. Chen, Nanofabrication by scanning probe microscope lithography: A review, *J. Vac. Sci. Technol. B* **23**(3), 877–894 (2005).
190. I. Utke, P. Hoffmann, R. Berger and L. Scandella, High-resolution magnetic Co supertips grown by a focused electron beam, *Appl. Phys. Lett.* **80**(25), 4792–4794 (2002).
191. A. Vanderziel, Flicker Noise in Highly Doped Semiconductors, *Appl. Phys. Lett.* **34**(6), 400–401 (1979).
192. S. G. Vengasandra, M. Lynch, J. T. Xu and E. Henderson, Microfluidic ultramicroscale deposition and patterning of quantum dots, *Nanotechnology* **16**(10), 2052–2055 (2005).
193. P. Vettiger, J. Brugger, M. Despont, U. Drechsler, U. Durig, W. Haberle, M. Lutwyche, H. Rothuizen, R. Stutz, R. Widmer and G. Binnig, Ultrahigh density, high-data-rate NEMS-based AFM data storage system, *Microelectron. Eng.* **46**(1–4), 11–17 (1999).
194. P. Vettiger, M. Despont, U. Drechsler, U. Durig, W. Haberle, M. I. Lutwyche, H. E. Rothuizen, R. Stutz, R. Widmer and G. K. Binnig, The "Millipede" – More than one thousand tips for future AFM data storage, *Ibm Journal of Research and Development* **44**(3), 323–340 (2000).
195. X. F. Wang and C. Liu, Multifunctional probe array for nano patterning and imaging, *Nano Lett.* **5**(10), 1867–1872 (2005).
196. Z. Z. Wang, J. Suski and D. Collard, Piezoresistive Simulation in Mosfets, *Sensor Actuat. A-Phys.* **37–8**, 357–364 (1993).
197. S. Watanabe and T. Fujii, Micro-fabricated piezoelectric cantilever for atomic force microscopy, *Rev. Sci. Instrum.* **67**(11), 3898–3903 (1996).
198. O. H. Willemsen, M. M. E. Snel, A. Cambi, J. Greve, B. G. De Grooth and C. G. Figdor, Biomolecular interactions measured by atomic force microscopy, *Biophys. J.* **79**(6), 3267–3281 (2000).
199. C. C. Williams and H. K. Wickramasinghe, Scanning Thermal Profiler, *Appl. Phys. Lett.* **49**(23), 1587–1589 (1986).
200. G. Wittstock and W. Schuhmann, Formation and imaging of microscopic enzymatically active spots on an alkanethiolate-covered gold electrode by scanning electrochemical microscopy, *Anal. Chem.* **69**(24), 5059–5066 (1997).
201. O. Wolter, T. Bayer and J. Greschner, Micromachined silicon sensors for scanning force microscopy, *J. Vac. Sci. Tech. B* **9**(2, Part 2), 1353–1357 (1991).
202. J. T. Xu, M. Lynch, J. L. Huff, C. Mosher, S. Vengasandra, G. F. Ding and E. Henderson, Microfabricated quill-type surface patterning tools for the creation of biological micro/nano arrays, *Biomed. Microdevice.* **6**(2), 117–123 (2004).
203. Z. X. Yang, Y. Yu, X. X. Li and H. F. Bao, Nano-mechanical electro-thermal probe array used for high-density storage based on NEMS technology, *Microelectron. Reliab.* **46**(5–6), 805–810 (2006).
204. G. G. Yaralioglu, A. Atalar, S. R. Manalis and C. F. Quate, Analysis and design of an interdigital cantilever as a displacement sensor, *J. Appl. Phys.* **83**(12), 7405–7415 (1998).

205. T. D. Yuzvinsky, A. M. Fennimore, A. Kis and A. Zettl, Controlled placement of highly aligned carbon nanotubes for the manufacture of arrays of nanoscale torsional actuators, (17), 434 (2006).
206. R. K. Zhu, S. M. Macfie and Z. F. Ding, Cadmium-induced plant stress investigated by scanning electrochemical microscopy, *J. Exp. Bot.* **56**(421), 2831–2838 (2005).
207. K. Zinoviev, C. Dominguez, J. A. Plaza, V. J. C. Busto and L. M. Lechuga, A novel optical waveguide microcantilever sensor for the detection of nanomechanical forces, *J. Lightwave Technol.* **24**(5), 2132–2138 (2006).
208. K. Zinoviev, C. Dominguez, J. A. Plaza, V. Cadarso and L. M. Lechuga, Light coupling into an optical microcantilever by an embedded diffraction grating, *Appl. Optics* **45**(2), 229–234 (2006).
209. J. Zlatanova, S. M. Lindsay and S. H. Leuba, Single molecule force spectroscopy in biology using the atomic force microscope, *Prog. Biophys. Mol. Bio.* **74**(1–2), 37–61 (2000).
210. J. Zou, X. F. Wang, D. Bullen, K. Ryu, C. Liu and C. A. Mirkin, A mould-and-transfer technology for fabricating scanning probe microscopy probes, *J. Micromech. Microeng.* **14**(2), 204–211 (2004).

CHAPTER 4

USING BIOMOLECULES FOR SELF-ASSEMBLY OF ENGINEERED NANO-SCALE STRUCTURES AND DEVICES

RANJANA MEHTA, JOHN LUND, and BABAK A. PARVIZ*

Department of Electrical Engineering,
University of Washington, Paul Allen Center – Room AE100R
Campus Box 352500 Seattle, WA 98195-2500, USA

Nature offers an astonishing array of complex structures and functional devices. The most sophisticated examples of functional systems with multiple interconnected nano-scale components can be found in biology. Biology uses a limited number of building blocks to create complexity and to extend the size and the functional range of basic nano-scale structures to new domains. Three main groups of molecular tools used by biology include oligonucleotides (linear chains of nucleotides), proteins (folded chains of amino acids), and polysaccharides (chains of sugar molecules). Nature uses these tools to store information, to create structures, and to build nano-scale machines.

Recent advances in understanding the structure and function of these building blocks has enabled a number of novel uses for them outside the biological domain. Of particular interest to us is the use of these building blocks to self-assemble nano-scale electronic, photonics, or nanomechanical systems. In this chapter we will look at two groups of building blocks (oligonucleotides and proteins) and review how they have been used to self-assemble engineered structures and build functional devices in the nano-scale.

We will begin by a review of the basic structure and properties (both physical and chemical) of oligonucleotides and proteins. This section is meant to be used as a self-contained reference for the readers from the engineering community that may be less familiar with the symbols and jargon of biochemistry. The most salient properties of the biomolecules are emphasized and listed here to facilitate future research in the area. We continue by a review of recent advances in designing artificial nano-scale DNA structures that can be constructed entirely via engineered self-assembly. Rapid advances in the design and construction of self-assembled DNA structures has resulted in an impressive level of understanding and control over this type of nano-scale manufacturing. Polypeptides and proteins are decidedly less understood and their use in engineered self-assembly has been relatively limited. Nevertheless,

*Corresponding author: University of Washington, Department of Electrical Engineering, Paul Allen Center – Room AE100R Campus Box 352500 Seattle, WA 98195-2500 USA; babak@ee.washington.edu

as we discuss in the concluding sections of the chapter, both genetically engineered polypeptides and proteins can be used to guide self-assembly processes in nano-scale and help in interfacing nano-scale objects with micron-scale components and templates.

Keywords: DNA; genetic code; hydrogen bond; replication; proteins; primary structure; secondary structure; super secondary structure; tertiary structure; quaternary structure; hydrophobic; electrostatic; van der Waals; oligonucleotide synthesis; polymerase chain reaction; solid-phase peptide synthesis; artificial synthesis; self-assembly; nanofabrication; quantum dots; gold binding polypeptides; holliday junction; origami; transcription; translation; phosphodiester bond; peptide bond; adenine; guanine; cytosine; thymine; double helix; codons; amino acids.

CONTENTS

1. An Introduction to Deoxyribonucleic Acid (DNA) 129
   1.1. Structure of DNA 129
   1.2. The importance of the hydrogen bond in DNA 130
   1.3. The genetic code 132
   1.4. DNA replication 134
   1.5. RNA-transcription 134
   1.6. Translation 135
2. Protiens 135
   2.1. Primary Structure 136
   2.2. Secondary Structure 138
   2.3. Super-Secondary Structure 139
   2.4. Tertiary Structure 140
   2.5. Quaternary Structure 140
   2.6. Complex protein structures 140
   2.7. Forces controlling the protein structure 140
      2.7.1. Hydrogen bonding 140
      2.7.2. Hydrophobic forces 141
      2.7.3. Electrostatic forces 141
      2.7.4. van der Waals forces 142
   2.8. Protein folding 142
3. Artifical Synthesis of DNA and Polypeptides 143
   3.1. DNA/RNA oligonucleotide synthesis 143
   3.2. Polymerase chain reaction (PCR) 144
   3.3. Solid-phase peptide synthesis (SPPS) 144
4. DNA and Proteins in Nanofabrication 145
   4.1. DNA Self-Assembly 145
   4.2. Proteins for nanofabrication 149
      4.2.1. Polypeptide directed assembly of quantum dots on microfabricated templates 150

4.2.2. Biomolecular self-assembly of nano-transistors 153
5. Conclusions 154
References 155

1. An Introduction to Deoxyribonucleic Acid (DNA)

Instructions providing all of the information necessary for a living organism to grow and live reside in the nucleus of every cell. The instructions come in the form of a large molecule called DNA, which encodes a detailed set of plans, similar to a blueprint, for building different parts of the cell. DNA is organized to compartments called chromosomes. Each chromosome contains a number of genes. Each gene provides the recipe for building a specific protein. The proteins are used in most vital tasks of life from building structures to conversion of energy and molecular signaling.

The structure of DNA was elucidated over 50 years ago by James Watson and Francis Crick in 1953 [1]. Every cell in an organism contains the genetic information and the DNA is therefore duplicated before a cell divides (replication). When proteins are needed, the corresponding genes are transcribed into Ribonucleic Acid (RNA) (transcription). The RNA is first processed so that non-coding parts are removed (processing) and is then transported out of the nucleus (transport). Outside the nucleus, the proteins are built based upon the code in the RNA (translation). This view of information flow from DNA to protein is often referred to as the central dogma of biology [2]. It is important to note that DNA and its close associate RNA not only store and transport information but constitute parts of the machinery that is responsible for the execution of a number of functions mentioned above.

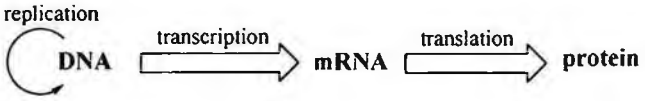

A genome is the total content of DNA in a virus or in a cell. The genome of viruses and bacteria contains one molecule of DNA. In eukaryotes (cells with nuclei), the genome is one cell's collection of chromosomes, each chromosome presumably consisting of one molecule of DNA. The overall genome size for various organisms varies widely (Table 1). For example, the total DNA from a single human cell is more than one meter long. Packaging, manipulation, and replication of this DNA constitute one of the most impressive demonstrations of what is possible to achieve in the nano-scale.

1.1. *Structure of DNA*

A molecule of DNA consists of *two chains*, strands composed of a large number of chemical compounds, called nucleotides, linked together to form a chain. These chains are arranged like a ladder that has been twisted into the shape of a winding staircase, called a double helix. Each nucleotide consists of three units: a sugar

Table 1. Comparative genome sizes of various species.

Organism	Estimated size	Chromosome number
Fritillary assyrica (Plant)	130000 million bases	—
Homo sapiens (human) [3]	2900 million bases	46
Mus musculus (mouse) [4]	2500 million bases	40
Drosophila melanogaster (fruit fly) [5]	180 million bases	8
Arabidopsis thaliana (plant) [6]	125 million bases	10
Saccharomyces cerevisiae (yeast) [7]	12 million bases	32
Escherichia coli (bacteria) [8]	4.7 million bases	1

Genome size does not correlate with evolutionary status, nor is the number of genes proportionate with genome size.

molecule (Fig. 1[a]) called deoxyribose, a phosphate group, and one of four different nitrogen-containing compounds called bases. The four bases are adenine (A), guanine (G), thymine (T), and cytosine (C), shown in Fig. 1[b].

The deoxyribose molecule occupies the center position in the nucleotide, flanked by a phosphate group on one side and a base on the other. The DNA backbone is a polymer with an alternating sugar-phosphate sequence (Fig. 1[c]). The deoxyribose sugars are joined at both the 3′-hydroxyl and 5′-hydroxyl groups to phosphate groups in ester links, also known as "phosphodiester" bonds. These linked deoxyribose-phosphate subunits form the parallel side rails of the ladder. The bases face inward toward each other, forming the rungs of the ladder (Fig. 1[d]).

Each strand of DNA has polarity, such that the 5′-hydroxyl (or 5′-phospho) group of the first nucleotide begins the strand and the 3′-hydroxyl group of the final nucleotide ends the strand; thus, this strand runs 5′ to 3′ ("*Five prime to three prime*"). Also, the two strands of DNA forming the ladder run *antiparallel* such that one strand runs 5′ → 3′ while the other one runs 3′ → 5′. At each nucleotide residue along the double-stranded DNA molecule, the nucleotides are complementary. That is, **A** forms two hydrogen-bonds with **T** represented as (T = A); **C** forms three hydrogen bonds with **G** represented as (C ≡ G) (Fig. 2[a]). The bases can selectively recognize and bind to each other. The two-stranded, antiparallel, complementary DNA molecule folds to form a helical structure which resembles a spiral staircase. This is the reason why DNA has been referred to as the "Double Helix" (Fig. 2[b]). The diameter of the helix is 20 Å.

1.2. *The importance of the hydrogen bond in DNA*

Hydrogen bonding is essential for forming the three-dimensional structure of DNA. Hydrogen bonds are relatively weak and the orientation of the bases must be just right for the interactions to take place. The A-T and C-G hydrogen bonds with bond lengths of 1.80 Å and 1.86 Å [9], respectively, and bond energy of about

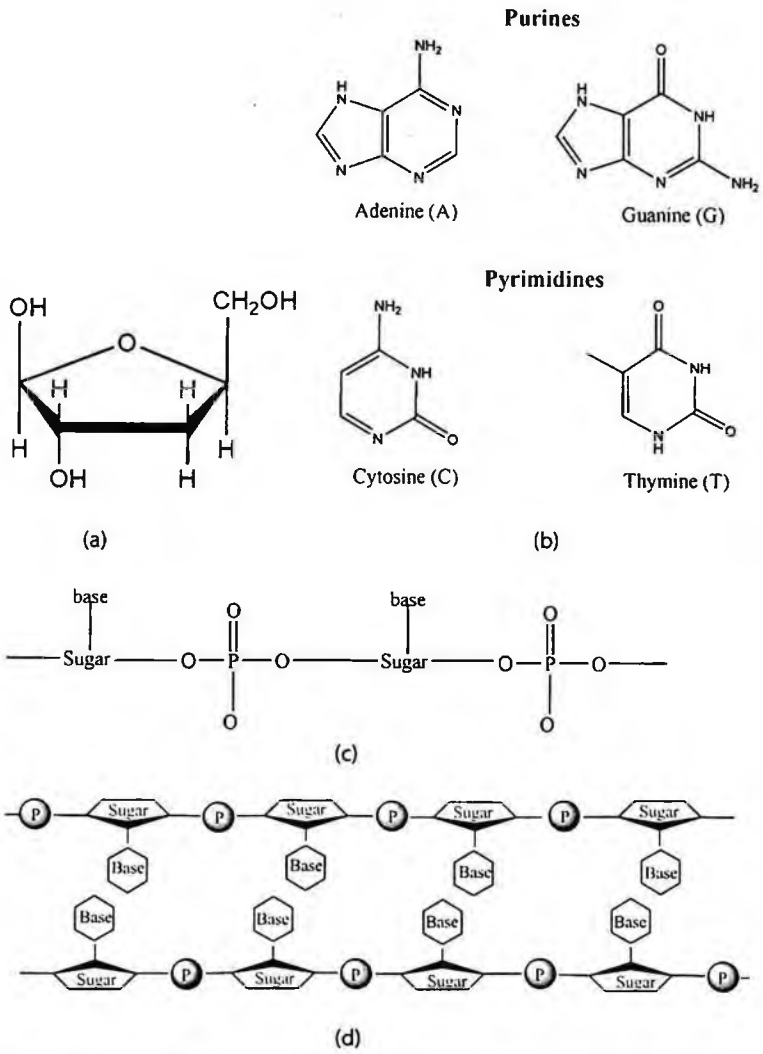

Figure 1. (a) The sugar molecule. (b) The four bases adenine (A), guanine (G), thymine (T), and cytosine (C). (c) The polynucleotide chain. (d) Schematic of the bonding of one DNA strand to another.

71 kJ/mole [10] are very weak when compared to the H-O covalent bond (0.96 Å bond length and 366 kJ/mole bond energy) [11] and the N-H covalent bond (1.0 Å bond length and 391 kJ/mole bond energy) [11]. The large number of hydrogen bonds present in a double helix of DNA leads to a cumulative effect of stability. Hydrogen bonding is most important for the specificity of the chains. Since the hydrogen bonds rely on strict patterns of hydrogen bond donors and acceptors, and because these structures must be in just the right spots, hydrogen bonding allows

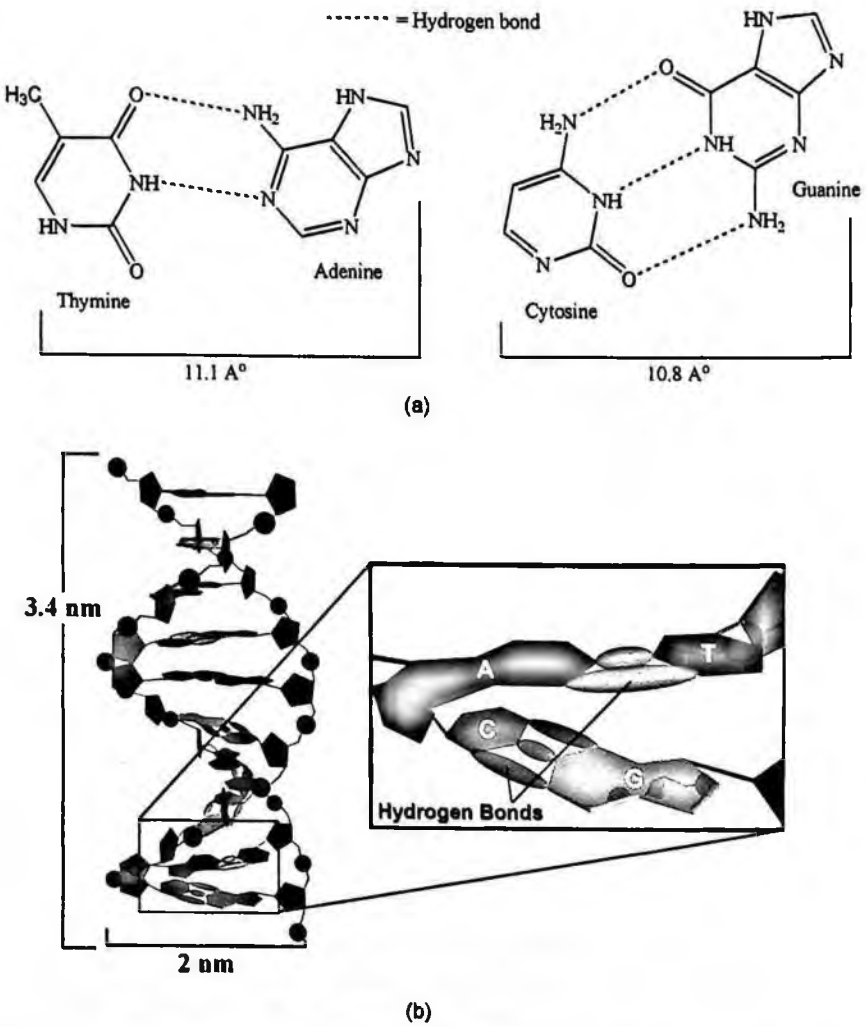

Figure 2. (a) Recognition and pairing of the complementary bases. (b) Structure of two hybridized complementary DNA strands.

for only complementary strands to come together programmed by the A-T and C-G sequences.

1.3. *The genetic code*

The information stored by DNA and the encoding scheme has been deciphered to a large extent. The genetic code consists of 64 triplets of nucleotides. These triplets are called **codons**. Each codon encodes for one of the 20 amino acids used in the synthesis of proteins. The scheme produces some redundancy in the code: most of the amino acids being encoded by more than one codon. One codon, **AUG**

Table 2. The Genetic Code.

		Second position of codon					
		T	**C**	**A**	**G**		
	A	ATT Ile [I]	ACT Thr [T]	AAT Asn [N]	AGT Ser [S]	**T**	
		ATC Ile [I]	ACC Thr [T]	AAC Asn [N]	AGC Ser [S]	**C**	
		ATA Ile [I]	ACA Thr [T]	AAA Lys [K]	AGA Arg [R]	**A**	
		ATG Met [M]	ACG Thr [T]	AAG Lys [K]	AGG Arg [R]	**G**	
First	**C**	CTT Leu [L]	CCT Pro [P]	CAT His [H]	CGT Arg [R]	**T**	**Third**
Position		CTC Leu [L]	CCC Pro [P]	CAC His [H]	CGC Arg [R]	**C**	**Position**
		CTA Leu [L]	CCA Pro [P]	CAA Gln [Q]	CGA Arg [R]	**A**	
		CTG Leu [L]	CCG Pro [P]	CAG Gln [Q]	CGG Arg [R]	**G**	
	G	GTT Val [V]	GCT Ala [A]	GAT Asp [D]	GGT Gly [G]	**T**	
		GTC Val [V]	GCC Ala [A]	GAC Asp [D]	GGC Gly [G]	**C**	
		GTA Val [V]	GCA Ala [A]	GAA Glu [E]	GGA Gly [G]	**A**	
		GTG Val [V]	GCG Ala [A]	GAG Glu [E]	GGG Gly [G]	**G**	
	T	TTT Phe [F]	TCT Ser [S]	TAT Tyr [Y]	TGT Cys [C]	**T**	
		TTC Phe [F]	TCC Ser [S]	TAC Tyr [Y]	TGC Cys [C]	**C**	
		TTA Leu [L]	TCA Ser [S]	TAA *Ter* [end]	TGA *Ter* [end]	**A**	
		TTG Leu [L]	TCG Ser [S]	TAG *Ter* [end]	TGGTrp [W]	**G**	

serves two related functions: it signals the start of translation and also codes for the incorporation of the amino acid methionine (Met) into the growing protein chain (Table 2) [12].

One strand of DNA holds the information that codes for various genes; this strand is often called the template strand or antisense strand (containing anti-codons). The other complementary strand is called the coding strand or sense strand (containing codons). Since RNA is made from the template strand, it has the same information as the coding strand. The table mentioned above refers to triplet nucleotide codons along the sequence of the coding or sense strand of DNA as it runs $5' \rightarrow 3'$; the code for the RNA would be identical but for the fact that RNA contains **U** (uridine) rather than **T**.

Here is an example of two complementary strands of DNA would be:

($5' \rightarrow 3'$) **ATGGAATTCTCGCTC** (Coding, sense strand)
($3' \leftarrow 5'$) **TACCTTAAGAGCGAG** (Template, antisense strand)

This is the associated RNA structure:

($5' \rightarrow 3'$) **AUGGAAUUCUCGCUC** (RNA made from Template strand)

Since amino acid residues of proteins are specified as triplet codons, the protein sequence made from the above example would be Met-Glu-Phe-Ser-Leu... (MEFSL...). The Genetic Code in the table [13] mentioned above has also been called "The Universal Genetic Code", owing to the fact that it is used by all known

organisms as a code for DNA and RNA. The universality of the genetic code encompasses animals (including humans), plants, fungi, archaea, bacteria and viruses.

1.4. *DNA replication*

In most cellular organisms, replication of a DNA molecule takes place in the cell nucleus and occurs just before the cell divides. Replication begins with the separation of the two polynucleotide chains, each of which then acts as a template for the assembly of a new complementary chain. As the old chains separate, each nucleotide in the two chains attracts a complementary nucleotide that has been formed earlier by the cell. The nucleotides are joined to one another by hydrogen bonds to form the rungs of a new DNA molecule. As the complementary nucleotides are fitted into place, an enzyme called DNA polymerase links them together by bonding the phosphate group of one nucleotide to the sugar molecule of the adjacent nucleotide, forming the side rail of the new DNA molecule. This process continues until a new polynucleotide chain has been formed alongside the old one, forming a new double-helix molecule. Thus, each of the daughter DNA double helices is composed of one original (conserved) strand and one newly synthesized strand. This is called semiconservative replication and results in the original strands remaining intact throughout many cell generations. The replication of DNA is relatively fast (3000 nucleotides/min in human and 30,000 nucleotides/min in *E. coli*) and precise (the sequence of bases in a DNA molecule is copied with less than one mistake per 10^9 nucleotides added [13]) process. However, mutation or change in a DNA molecule can take place due to errors in the replication process or the environmental effects.

1.5. *RNA-transcription*

In almost all eukaryotic cells, DNA never leaves the nucleus; instead the genetic code (the genes) is copied into RNA which then in turn is decoded (translated) into proteins in the cytoplasm. The cytoplasm is a dangerous environment for the DNA and the daily transcription of genes to proteins would be very harmful to the DNA, which has to stay intact in order to maintain the original life code. Therefore, RNA works as an intermediate, transferring the information coded in the DNA to a new area for use in protein production. Unlike DNA, the RNA molecule is single stranded, folded in various shapes, has uracil instead of thymine, and ribose sugar instead of deoxyribose.

The biosynthesis of RNA, called **transcription**, proceeds in much the same fashion as the replication of DNA and also follows the base pairing principle. Again, a section of DNA double helix is uncoiled and only one of the DNA strands serves as a template for RNA polymerase enzyme to guide the synthesis of RNA. RNA polymerase synthesizes the RNA at a speed near 20–80 nucleotides/second for a

bacterial RNA polymerase [14]. After the synthesis is complete, the RNA separates from the DNA and the DNA recoils into its helix.

1.6. *Translation*

Translation, the final step on the path from DNA to protein, is the synthesis of proteins directed by an RNA template. The protein-making machinery, called the ribosome, reads the RNA sequence (as codons) and translates it into the amino acid sequence of the protein. The ribosome starts at the sequence AUG, then reads three nucleotides at a time. Each three-nucleotide codon specifies a particular amino acid. The "stop" codons (UAA, UAG, and UGA) tell the ribosome that the protein synthesis is complete. The complete synthesis of an average-size protein of 400 amino acids in a bacterium is accomplished in about 20 seconds [13]. After translation the protein usually undergoes some further modifications before it becomes fully active.

DNA is a truly nano-scale object with three exceedingly interesting properties: (i) it can recognize and bind to a strand with a complementary sequence of bases allowing for creation of programmable bonds, (ii) it can store information with an extremely high density (the spacing between two neighboring bases on a chain is about 0.3 nm), and (iii) it can be replicated allowing for mass production. These properties and the established expertise to artificially construct a strand with an arbitrary sequence of bases via chemical synthesis make DNA an attractive candidate as a building block and a programming mechanism for construction of nano-scale structures by design.

2. Protiens

We now turn our attention to the second class of biomolecules widely used in cellular machinery. Many proteins act as enzymes, and catalyze very specific chemical reactions. Other proteins have roles in the transport of substances, self-defense and structure. All these proteins are made from the same 20 amino acids, and all are made in the same way. The amino acids have a general formula as shown in Fig. 3(a). The twenty amino acids found in biological systems are shown in Fig. 3(b). To form protein, the amino acids are linked by dehydration synthesis to form peptide bonds (Fig. 3(c)). The chain of amino acids is also known as a polypeptide.

Some proteins contain only one polypeptide chain while others, such as hemoglobin, contain several polypeptide chains all twisted together. The sequence of amino acids in each polypeptide or protein is unique to that protein, so each protein has its own, unique three-dimensional (3-D) shape or native conformation. If even one amino acid in the sequence is changed, that can potentially change the protein's ability to function. The structural features of proteins are usually described at four levels of complexity.

2.1. *Primary Structure*

Primary structure is the linear arrangement of amino acids in a protein and the location of covalent linkages such as disulfide bonds between amino acids (Fig. 4(a)). The convention for the designation of the order of amino acids is that the N-terminal end (i.e. the end bearing the residue with the free α-amino group) is to the left (and the number 1 amino acid) and the C-terminal end (i.e. the end with the residue containing a free α-carboxyl group) is to the right.

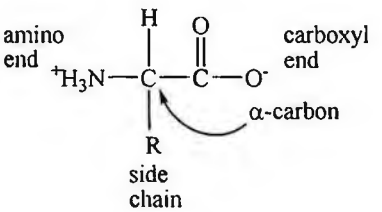

(a)

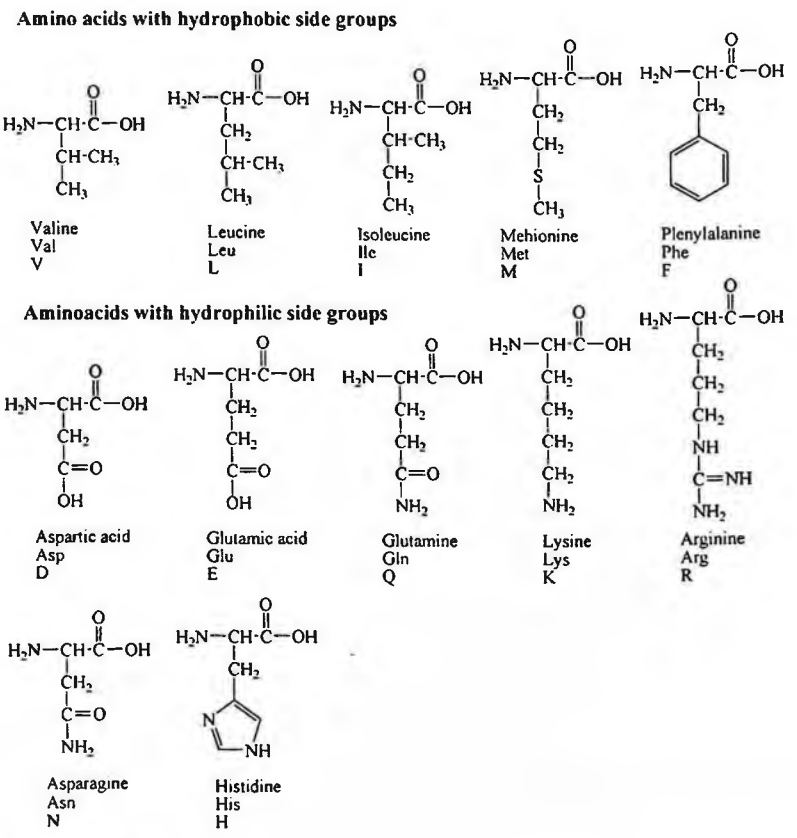

Figure 3. (*Continued*)

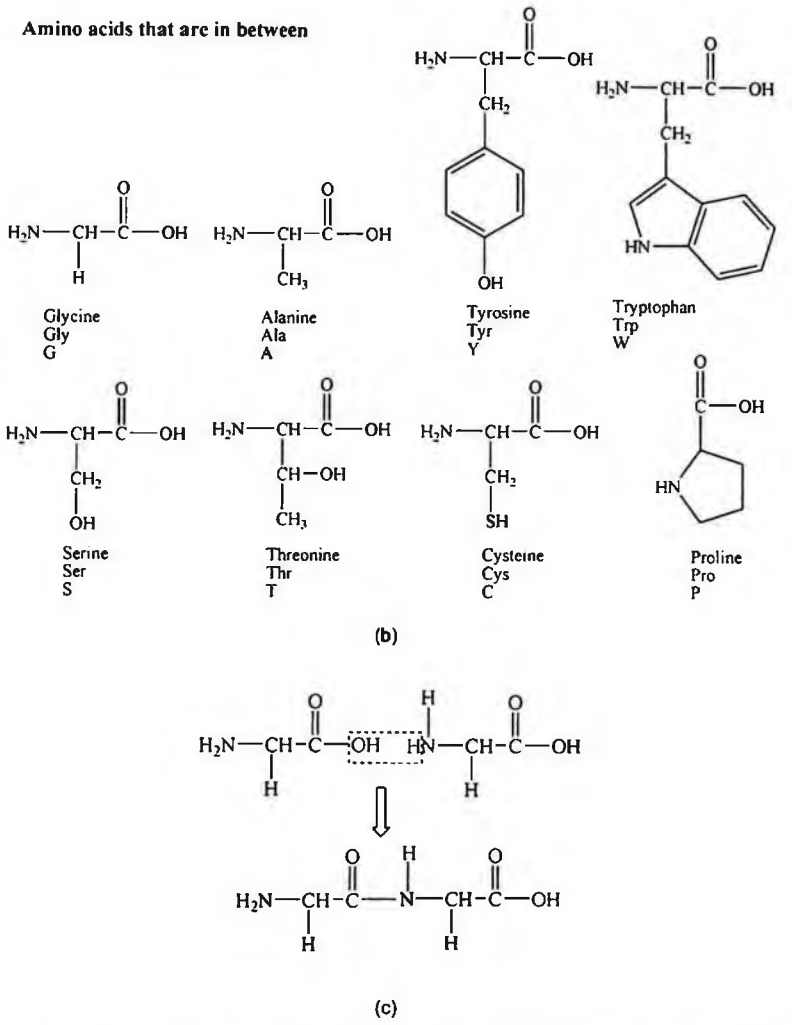

Figure 3. (a) The general formula for all amino acids. (b) The twenty amino acids found in biological systems. (c) Schematic showing how a peptide bond connects two amino acids. Here, a molecule of water is removed from two glycine amino acids to form a peptide bond.

Proteins are remarkably versatile with respect to the type of structures they can form. One example is the family of collagen molecules found in the extracellular space. Collagen is a triple helix of about 1.5 nm, formed by three extended protein chains that wrap around one another. Many rod-like collagen molecules are cross-linked together to form unextendable collagen fibrils that have a tensile strength rivaling that of steel ($\sim 1 \times 108\,\mathrm{N/m^2}$). Another example is the extracellular protein elastin, in which the polypeptide chains are covalently cross-linked to form rubber-like elastic fibers. Each elastin molecule uncoils into a more extended conformation when the fiber is stretched and will recoil spontaneously as soon as the stretching force is relaxed (Modulus of elasticity $\approx 0.6 \times 10^6\,\mathrm{N/m^2}$).

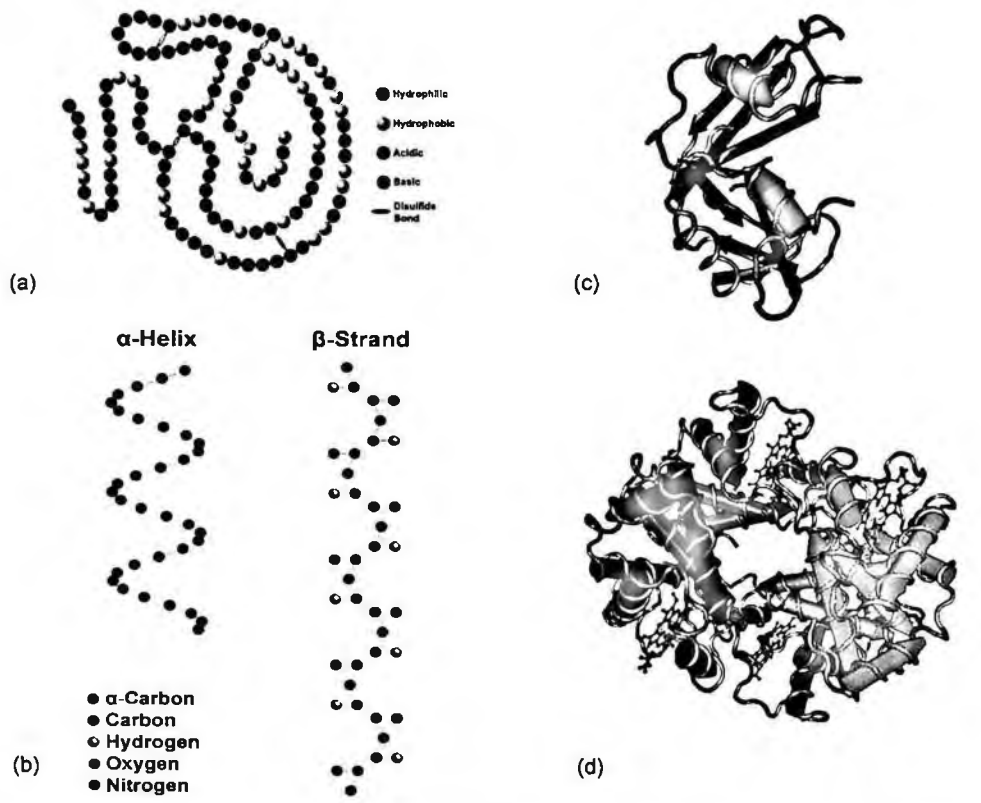

Figure 4. (a) An example of the primary structure of a protein (Ribonuclease A). (b) Secondary structure of proteins. (c) An example of the tertiary structure of a protein (Bovine pancreatic ribonuclease A). The helices are shown as red arrows and β-sheets are shown as blue arrows. The disulphide bonds are shown in green. (d) An example of the quaternary structure of a protein (human hemoglobin). Different polyproteins are colored differently and the heme groups are colored in red.

2.2. *Secondary Structure*

Secondary structure is the ordered array of amino acids in a protein that confers regular conformational forms upon that protein. In general, proteins fold into two broad classes of structure termed globular proteins and fibrous proteins. Globular proteins are compactly folded and coiled, whereas, fibrous proteins are more filamentous or elongated. It is the partial double-bond character of the peptide bond that defines the conformations a polypeptide chain may assume. Within a single protein, different regions of the polypeptide chain may assume different conformations determined by the primary sequence of the amino acids; examples include α-helices and β-pleated sheets, which are stabilized by hydrogen bonding. Some of the β-sheets are parallel and some are anti-parallel. Other parts of the protein structure are not highly stable.

The α-helix is a common secondary structure encountered in proteins of the globular class. The formation of the α-helix is spontaneous and is stabilized by hydrogen bonding between amide nitrogens and carbonyl carbons of peptide bonds spaced four residues apart. This orientation of H-bonding produces a helical coiling of the peptide backbone such that the R-groups lie on the exterior of the helix and perpendicular to its axis (Fig. 4(b)). The α-helices are generally between 5 and 20 residues in length, but some proteins and coiled-coil structures can be considerably longer. They generally have a pitch of about 3.5 residues per turn, but there are forms of helices with tighter (3 residues per turn) and longer (4 residues per turn) [15].

Not all amino acids favor the formation of the α-helix due to steric constraints of the R-groups. Amino acids such as A, D, E, I, L and M favor the formation of α-helices, whereas, G and P favor disruption of the helix. This is particularly true for **P** since it is a pyrrolidine-based imino acid (HN =) whose structure significantly restricts movement about the peptide bond in which it is present, thereby, interfering with extension of the helix. The disruption of the helix is important as it introduces additional folding of the polypeptide backbone to allow the formation of globular proteins.

Whereas an α-helix is composed of a single linear array of helically disposed amino acids, β-sheets are composed of 2 or more different regions of stretches of at least 5–10 amino acids. The folding and alignment of stretches of the polypeptide backbone aside one another to form β-sheets is stabilized by H-bonding between amide nitrogens and carbonyl carbons. However, the H-bonding residues are present in adjacently opposed stretches of the polypetide backbone as opposed to a linearly contiguous region of the backbone in the α-helix (Fig. 4(b)). β-Sheets are said to be pleated. This is due to positioning of the α-carbons of the peptide bond which alternates above and below the plane of the sheet. β-Sheets are either parallel or antiparallel [16]. In parallel sheets, adjacent peptide chains proceed in the same direction (i.e. the direction of N-terminal to C-terminal ends is the same), whereas, in antiparallel sheets, adjacent chains are aligned in opposite directions. Anti-parallel beta stands are often linked by short loops containing 3–5 residues in highly characteristic conformations. Longer loops are occasionally found where the loop plays an important role in substrate binding or an active site. The antigen-combining site of the immunoglobulins is an important example of this.

2.3. *Super-Secondary Structure*

Some proteins contain an ordered organization of secondary structures that form distinct functional domains or structural motifs. Examples include the helix-turn-helix domain of bacterial proteins that regulate transcription and the leucine zipper, helix-loop-helix and zinc finger domains of eukaryotic transcriptional regulators. These domains are termed super-secondary structures.

2.4. *Tertiary Structure*

Tertiary structure is the final three-dimensional structure of a protein, which results from a large number of non-covalent interactions between amino acids. It is the way random coils, α-helixes and β-pleated sheets fold with respect to each other (Fig. 4(c)) [17]. Tertiary structure refers to the complete three-dimensional structure of the polypeptide units of a given protein. Included in this description is the spatial relationship of different secondary structures to one another within a polypeptide chain and how these secondary structures themselves fold into the three-dimensional form of the protein. Secondary structures of proteins often constitute distinct domains. Therefore, tertiary structure also describes the relationship of different domains to one another within a protein. The interactions of different domains are governed by several non-covalent forces: hydrogen bonding, hydrophobic interactions, electrostatic interactions and van der Waals forces.

2.5. *Quaternary Structure*

Quaternary structure is the arrangement of polypeptide subunits within complex proteins made up of two or more subunits, sometimes associated with non proteic groups. Various non-covalent interactions, similar to those that stabilize the tertiary structure of proteins, bind multiple polypeptides into a single, larger protein. For example Hemoglobin has quaternary structure due to association of two α globin and two β globin polyproteins and contains four heme groups (Fig. 4(d)) [18].

2.6. *Complex protein structures*

Some proteins also are found to be covalently conjugated with carbohydrates. These modifications occur following the synthesis (translation) of proteins and are, therefore, termed post-translational modifications. These forms of modification impart specialized functions upon the resultant proteins. Proteins covalently associated with carbohydrates are termed glycoproteins. There are extremely important glycoproteins found on the surface of erythrocytes. It is the variability in the composition of the carbohydrate portions of many glycoproteins and glycolipids of erythrocytes that determines blood group specificities. Structural complexes involving protein associated with lipid via non-covalent interactions are termed lipoproteins. Their major function in the body is to aid in the storage and transport of lipid and cholesterol.

2.7. *Forces controlling the protein structure*

2.7.1. *Hydrogen bonding*

Polypeptides contain numerous proton donors and acceptors both in their backbone and in the R-groups of the amino acids. The environment in which proteins are

found also contains the ample H-bond donors and acceptors of the water molecules. H-bonding, therefore, occurs not only within and between polypeptide chains but with the surrounding aqueous medium. Hydrogen bonds can vary in strength from very weak (1–2 kJ mol^{-1}) to so strong (40 kJ mol^{-1}) so as to be indistinguishable from a covalent bond. Typical H-bond values are [10]:

O—H$^{\cdots}$: N (7 kcal/mol)
O—H$^{\cdots}$: O (5 kcal/mol)
N—H$^{\cdots}$: N (3 kcal/mol)
N—H$^{\cdots}$: O (2 kcal/mol)

The length of hydrogen bonds depends on bond strength, temperature and pressure. The typical length of a hydrogen bond in water is 1.97 Å.

2.7.2. *Hydrophobic forces*

Proteins are composed of amino acids that contain either hydrophilic or hydrophobic R-groups. It is the nature of the interaction of the different R-groups with the aqueous environment that plays the major role in shaping protein structure. The spontaneous folded state of globular proteins is a reflection of a balance between the opposing energetics of H-bonding between hydrophilic R-groups and the aqueous environment and the repulsion from the aqueous environment by the hydrophobic R-groups. The hydrophobicity of certain amino acid R-groups tends to drive them away from the exterior of proteins and into the interior. This driving force restricts the available conformations into which a protein may fold. The hydrophobic force is one of the largest determinants of protein structure.

2.7.3. *Electrostatic forces*

Electrostatic forces observed in the protein folding context are from: charge-charge, charge-dipole and dipole-dipole interactions. Typical charge-charge interactions that favor protein folding are those between oppositely charged R-groups such as K or R and D or E. A substantial component of the energy involved in protein folding is charge-dipole interactions. This refers to the interaction of ionized R-groups of amino acids with the dipole of the water molecule. The slight dipole moment that exists in the polar R-groups of amino acid also influences their interaction with water. It is, therefore, understandable that the majority of the amino acids found on the exterior surfaces of globular proteins contain charged or polar R-groups. It is strongest in a vacuum and 80 fold weaker in water and weaker still at elevated salt solutions. Water and ions can shield electrostatic interactions reducing both their strength and distance over which they operate [19].

2.7.4. *van der Waals forces*

There are both attractive and repulsive van der Waals forces that control protein folding. Attractive van der Waals forces involve the interactions among induced dipoles that arise from fluctuations in the charge densities that occur between adjacent uncharged non-bonded atoms. Repulsive van der Waals forces involve the interactions that occur when uncharged non-bonded atoms come very close together but do not induce dipoles. The repulsion is the result of the electron-electron repulsion that occurs as two clouds of electrons begin to overlap. Van der Waals interactions occur at distances between 3 and 4 Å [19]. They are very weak beyond 5 Å and electron repulsion prevents atoms from getting much closer than 3 Å. Van der Waals interactions are non-directional and very weak. However, significant energy of stabilization can be obtained in the central hydrophobic core of proteins by the additive effect of many such interactions.

2.8. *Protein folding*

A typical protein would contain a few salt-bridges, several hundred hydrogen bonds and several thousand van der Waals interactions. In spite of all these interactions, proteins are only marginally stable. Typical ΔG values for folding of proteins are in the range of -5 to -15 kcal/mol i.e. not much greater than the energy of 2 or 3 hydrogen bonds. This is because of several effects which cancel each other out (The Gibbs free energy change is $\Delta G = \Delta H - T.\Delta S$). The enthalpy change of protein folding (ΔH) is dominated by hydrogen bonds. In the unfolded state, the polar groups of the protein will H-bond to solvent molecules and in the folded state these polar groups will H-bond with each other. Hence, the overall enthalpy change on folding is small [15]. The hydrophobic effect is thought to make the largest contribution to ΔG. The hydrophobic effect attributes the poor solubility of non-polar groups in water to the ordering of the surrounding water molecules causing them to form an ice-like cluster (as seen in following Fig. 5).

The decrease in entropy (i.e. negative ΔS) of the solvent means that dissolving the non-polar molecule in water is thermodynamically unfavorable (i.e. positive ΔG). Hence the driving force of protein folding is thought to be the hydrophobic effect i.e. the hydrophobic side chains aggregate excluding water molecules as the protein folds. The resulting increase in entropy of these water molecules gives rise to a large positive ΔS causing the ΔG of folding to be negative i.e. thermodynamically favorable. Note that the entropy of the polypeptide itself decreases on folding which will counteract the increase in ΔS due to the waters.

As we discuss below, similar to DNA, it is possible to artificially synthesize short chains of amino acids. Although in general, proteins are less understood/characterized than DNA and are more sensitive to the environment of the experiment (the protein machine functions only when in the proper conformation), they provide a vital bridge between the organic world of biology and the inorganic world of materials that are useful for device construction. As noted in the application

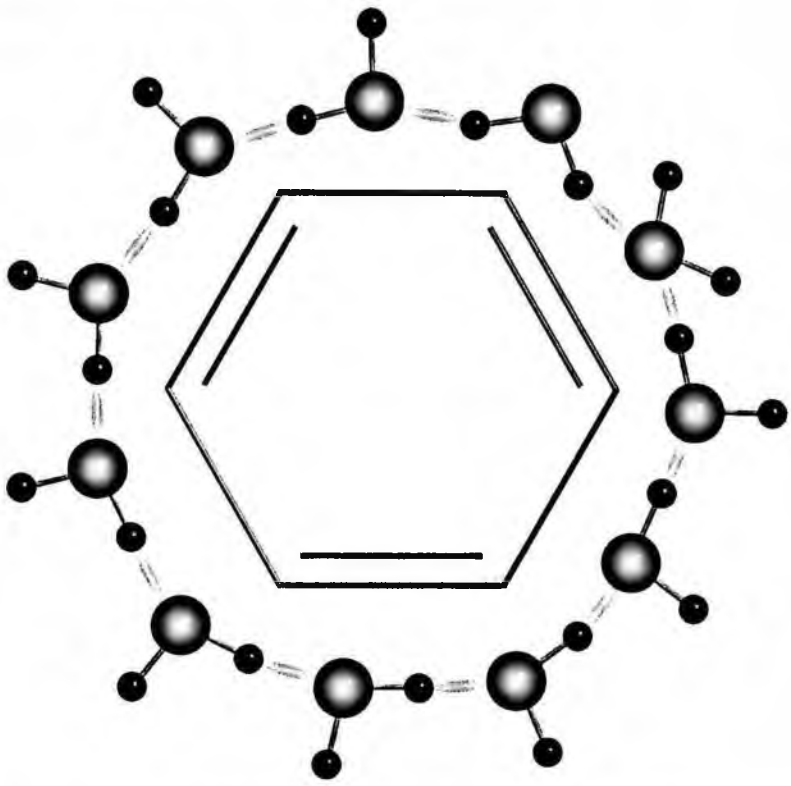

Figure 5. The ordering of water molecules surrounding a hydrophobic molecule. Pink ellipsoides indicate hydrogen bonds.

sections below, polypeptides can be used to direct the self-assembly and material deposition of nano-scale components and inorganic materials.

3. Artifical Synthesis of DNA and Polypeptides

The ability to mass produce DNA and polypeptides with an arbitrary sequence of units is crucial for the developent of nanofabrication processes that rely on these building blocks for construction of structures and devices. Thanks to recent advances in chemical synthesis, both these tasks are feasible today albeit with a number of limitations. A number of commercial sources are available offering custom polypeptide and oligonucleotide production.

3.1. *DNA/RNA oligonucleotide synthesis*

DNA/RNA oligonucleotide synthesis is a remarkably simple, fully automated process. Custom oligonucleotides are generally synthesized using Commerical Nucleic Acid Synthesizers and are typically 15–25 bases in length.

The solid support, onto which the oligonucleotide is synthesized, is loaded into the reaction column. In each step, all the solutions required for carrying out the oligonucleotide synthesis are pumped through the column. The reaction column is attached to the reagent delivery lines and the nucleic acid synthesizer. Each DNA/RNA base is added via computer control of the reagent delivery. After all bases have been added, the oligonucletide is cleaved from the solid support and deprotected before it can be effectively used. This step is done by incubating the chain in concentrated ammonia at a high temperature for an extended amount of time. After the DNA segment is produced, it can be used as a template for further replication.

3.2. *Polymerase chain reaction (PCR)*

Polymerase chain reaction (PCR) is a molecular biology technique for enzymatically replicating DNA without using a living organism, such as *E. coli* or yeast. Like amplification using living organisms, the technique allows a small amount of the DNA molecule to be replicated exponentially. However, because it is an *in vitro* technique, it can be performed without restrictions on the form of DNA and it can be extensively modified to perform a wide array of genetic manipulations. Unlike living organisms, the PCR process can copy only short DNA fragments, usually up to 10 kb. Certain methods can copy fragments up to 47 kb in size, which is still much shorter than the chromosomal DNA of a eukaryotic cell.

The PCR process is also fully automated and is carried out in a thermal cycler. This is a machine that heats and cools the reaction tubes to the precise temperature required for each step of the reaction. To prevent evaporation of the reaction mixture (typically volumes between 15–100 µl per tube), a heated lid is placed on top of the reaction tubes or a layer of oil is put on the surface of the reaction mixture. The DNA fragment to be amplified is determined by selecting primers. Primers are short, artificial DNA strands — usually only 18 to 25 base pairs long — that are complementary to the beginning or the end of the DNA fragment to be amplified. They anneal by adhering to the DNA template at these starting and ending points, where the DNA polymerase binds and begins the synthesis of the new DNA strand.

3.3. *Solid-phase peptide synthesis (SPPS)*

Solid-phase peptide synthesis (SPPS) is the widely used method for creating peptides and proteins in the lab in a synthetic manner. This allows the synthesis of natural peptides which are difficult to express in bacteria, incorporation of unnatural amino acids, peptide/protein backbone modification, and the synthesis of D-proteins, which consist of D-amino acids.

SPPS was pioneered by Bruce Merrifield [20] allows for one-by-one addition of amino acids into a peptide chain. In this method, the most important consideration is to generate an extremely high yield in each step. For example, if each step were

to have 99% yield, a 26-amino acid peptide would be synthesized in 77% final yield, if each step were 95%, it would be synthesized in 25% yield. Thus, each amino acid is added in major excess (2 $\sim$ 10x) and coupling, amino acids together is highly optimized by a series of well-characterized agents.

There are two widely used forms of SPPS — **FMOC** [(F)luorenyl-(M)eth(O)xy-(C)arbonyl] and **t-BOC** [(tert)-(B)utyl (O)xy (C)arbonyl]. Unlike ribosome protein synthesis, solid-phase peptide synthesis proceeds in a C-terminal to N-terminal fashion. The N-termini of amino acid monomers is protected by these two groups and added onto a deprotected amino acid chain.

Automated synthesizers are available for both techniques, though many research groups continue to perform SPPS manually. SPPS is limited by yields, and typically peptides and proteins in the range of 70 $\sim$ 100 amino acids are pushing the limits of synthetic accessibility. Synthetic difficulty also is sequence dependent; typically amyloid peptides and proteins are difficult to make. Longer lengths can be accessed by using native chemical ligation to couple two peptides together with quantitative yields.

4. DNA and Proteins in Nanofabrication

4.1. *DNA Self-Assembly*

Unique properties of DNA such as specific base-pair recognition have made DNA an attractive candidate as a programmable building block for nanofabrication [21,22]. As DNA synthesis techniques and tools become more readily available, access to the building blocks has become more cost-effective and expedient. One can now readily engineer DNA molecules with specific base pair sequences such that they hybridize in a pre-defined orientation and immediately mass produce them. Relying on hybridization of complementary strands of DNA to create one-dimensional double-stranded DNA (dsDNA) structures has limited applicability in the construction of shapes that can be used as platforms for fabrication of nano-scale devices and eventually systems. It is important to be able to combine linear strands of DNA to create two and three-dimensional structures. The capability of DNA to form two-dimensional junctions was discovered by Robin Holliday in 1964 [23]. The Holliday junction is a crossover point between two dsDNA molecules where a single strand from one of the molecules hybridizes with a single strand of the other, forming a junction with four arms. This branched DNA structure occurs naturally during homologous recombination; however, because the sequences of DNA involved in homologous recombination are similar, the junction position is not fixed and is capable of sliding along the DNA strands in a process known as branch migration. As shown in Fig. 6, properly engineered oligonucleotides can form a stable Holliday junction wherein any deviation of the branch point from its specified location results in base pair mismatching. These stable branched DNA structures are the foundation of almost all DNA-based self-assembly techniques.

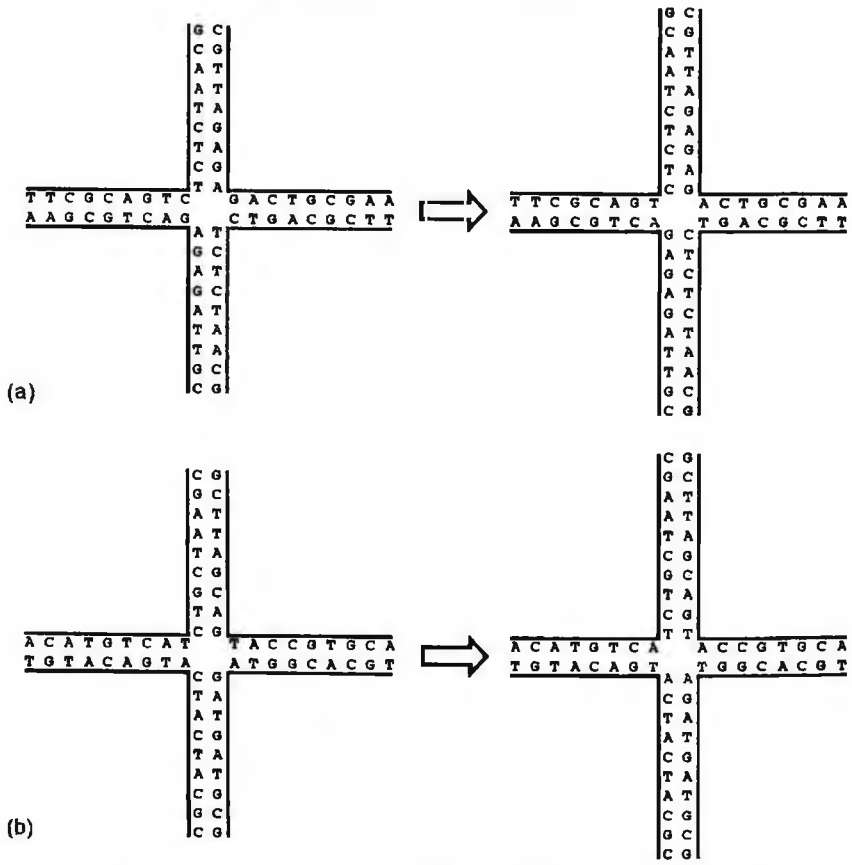

Figure 6. Holliday junctions occur naturally during homologous recombination where the branch point can shift freely (a) or they can be engineered using oligonucleotides to create a stable branch point (b). Notice the energetically unfavorable pairing that occurs when the branch point shifts in (b).

It is important to consider the physical characteristics of branched DNA structures in order to understand the capabilities of DNA nanofabrication. Nucleic acid junctions are flexible with rigid arms. Experiments performed using three-arm nucleic acid junctions with arm lengths of 10 bases show that junction angles easily deviate by 60° from their naturally-occurring orientation [24]. Other reseach using scanning-probe tips and laser-trapped beads to manipulate individual DNA molecules has shown the persistence length of DNA, the length at which worm-like chain molecules can be considered stiff (half the Kuhn length in a freely jointed chain model), is 450–1000 Å [25]. This is an important consideration when designing DNA-based structures, as designs exceeding 500 Å tend to lack structural stability. However, the flexibility of DNA junctions means that they are not limited to lying in a two-dimensional plane and can fold to form the corner of a three-dimensional shape.

DNA junctions bridge the gap separating linear strands of DNA and non-linear shapes, but multiple junctions must be connected together to create a useful structure. Assembly of branched DNA junctions is possible using sticky-ended ligation [26]. Sticky-ended ligation is a process in which two dsDNA molecules with short complimentary single-stranded DNA molecules at their endpoints hybridize via the natural hydrogen bonding of complementary DNA bases to form a single dsDNA molecule. Hybridization does not repair the phosphate backbone of the DNA molecule, so DNA ligase, an enzyme which repairs the broken phosphate bonds, is added following hybridization. It is also possible to assemble relatively stable structures without the final ligation step [27]; however, ligation helps prevent disassembly and makes DNA structures more stable at increased temperatures.

DNA junctions, and the ability to combine them arbitrarily with sticky-ended ligation, make possible a wide variety of structures using DNA self-assembly. One of the most important designs is the DNA tile, which is a combination of four junctions that form the corners of a square of DNA with a hollow cavity [28]. The size of these tiles is tunable based on the length of DNA junction arms used. Because these tiles are composed of four four-arm junctions, the eight unused arms of the tile can be designed with sticky-ends such that they assemble into two-dimensional arrays (Fig. 7). DNA arrays have the potential to act as nano-scale molecular templates which assemble and interconnect functional electronic, photonic, and magnetic structures. This potential has driven many researchers to attempt to create DNA arrays with long-range order and low defect rates. One of the primary setbacks to research in this area, is the flexibility of DNA junctions. Large arrays are flexible and tend to curl due to parasitic interactions between DNA base pairing and nearby phosphate backbones.

One solution to the problem of flexible DNA structures is the use of double crossover (DX) molecules. Unlike the standard Holliday junction which has a single flexible crossover point, the DX molecule combines two dsDNA molecules with two crossovers, resulting in a much more rigid junction [30]. There have been multiple variations of the DX molecule including triple crossover (TX) molecules and crossover molecules with an additional DNA domain which extends perpendicular

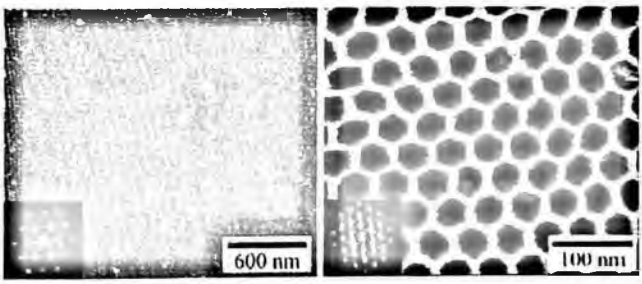

Figure 7. Two-dimensional array of three-arm DNA stars forming hexagonal patterns. Insets show the Fourier transform of each image. Courtesy of Dr C. Mao of Purdue University.

to the crossover point [31]. This perpendicular DNA can be engineered with a specifically-encoded sticky end, offering addressable locations within a DNA array.

DNA-based arrays are relatively simple periodic structures, requiring a limited number of constituent DNA sequences. DNA tiles can be assembled separately, purified, and then combined to form an array. When working with complex 2D and 3D structures, however, assembly becomes a much more complicated task. DNA systems requiring multiple strands of DNA which all must assemble in a precise orientation cannot be efficiently constructed stochastically by simply combining the sequences in solution. Instead, difficulties maintaining proper stoichiometry lead to extremely low yields. To combat this problem, many assembled 3D structures use a number of restriction, ligation, and purification steps to precisely control each stage of assembly. Moreover, these assemblies often involve the use of a support on which the structure is grown. Even with such strict control of assemblies, the overall yield of these experiments is typically 1% [32].

Recently, a new approach to DNA self-assembled structures has been developed, which permits the construction of complex shapes while avoiding the stoichiometry problems associated with traditional assemblies. This technique uses one long strand of ssDNA and folds this strand on itself in a raster pattern using short sequences of DNA which hybridize with two specific locations on the long DNA. By stitching together a complete double helix, the resulting structure takes the shape of the predefined folding pattern. This technique has produced dramatic results with significantly improved yields and low error rates (Fig. 8) [33].

Another important tool for DNA nanofabrication is a form of DNA replication called rolling-circle amplification (RCA) [34]. RCA uses plasmids, short circular strands of DNA, to produce a long strand of DNA with repeated occurrences of the sequence of DNA contained in the plasmid. When DNA polymerase makes a copy of a normal strand of DNA, it begins transcription at a primer sequence and ends at a terminator or the end of the strand of DNA. In the case of RCA, a circular loop of DNA with no terminator is used so replication continues without end. This technique can be used to create an arbitrarily long strand of DNA with known periodicity. This periodicity is of particular importance to DNA-based nanofabrication where periodic structures are a necessity.

The ability to create precise nano-scale structures with DNA is only one step towards practical DNA nanofabrication. For DNA self-assembly to be a viable fabrication technique, methods to assemble functional components on DNA templates must be devised. For a semiconductor nano-electronic researcher, the materials of interest for further assembly are: conductors, semiconductors, and insulators. With this goal in mind, a number of groups have begun to assemble different materials, primarily metals, on DNA templates. Metals such as silver [35] and palladium [36] can be electrolessly deposited on DNA by adding a reducing agent to a solution of dissolved metal ions. Arbitrarily thick metal layers can be formed using multiple deposition steps (Fig. 9) [37]. When metals which tend to form small

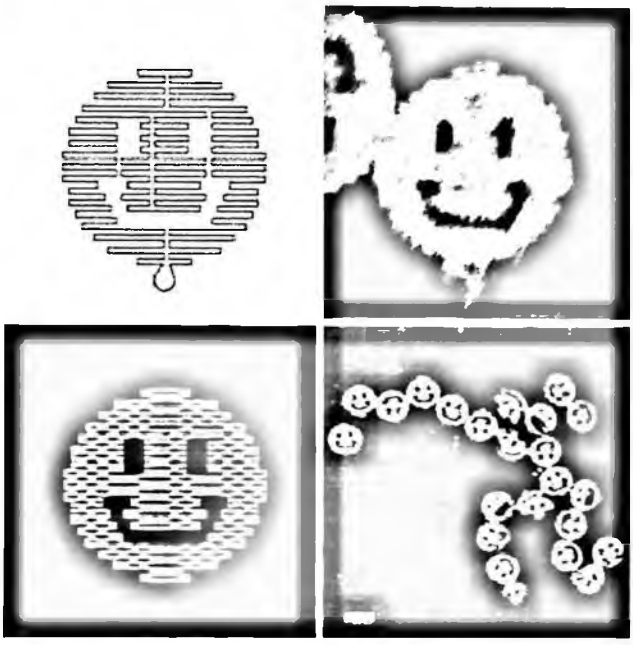

Figure 8. "DNA origami." These structures are formed by folding a long strand of DNA with 32-mer oligonucleotides that compliment the long strand in specific folded regions. The scale bar in the AFM image is 100 nm. Courtesy of Dr P. W. K. Rothemund of California Institute of Technology.

grains are used, metallization on single strands of dsDNA can result in nanoscale discontinuities which can significantly impact conductivity. Another approach to metallizing DNA is to use a tightly-packed array as the metallization template. Using this approach, electroless deposition proceeds uniformly on the array, resulting in high conductivities [38]. Researchers have also used DNA templates made of DX tiles with a protruding linker strand of ssDNA for the selective attachment of gold nanoparticles [39]. Different sizes of gold nanoparticles functionalized with different oligonucleotides hybridize to specific regions of the array. This approach has produced arrays with bands of alternating 5 and 10 nm gold particles.

4.2. *Proteins for nanofabrication*

Many folded proteins in their proper conformation act as complete nano-scale machines in biology. Currently, artificial nanofabrication cannot produce structures, let alone devices or machines, with complexities that can approach that of biological ones. Nevertheless, understanding proteins and their functions offer a number of lessons and tools to a designer of a nano-scale manufacturing technology. Perhaps most importantly, the proteins offer examples of functional machine design in the nano-scale. The concept of building the core of a machine from a single chain

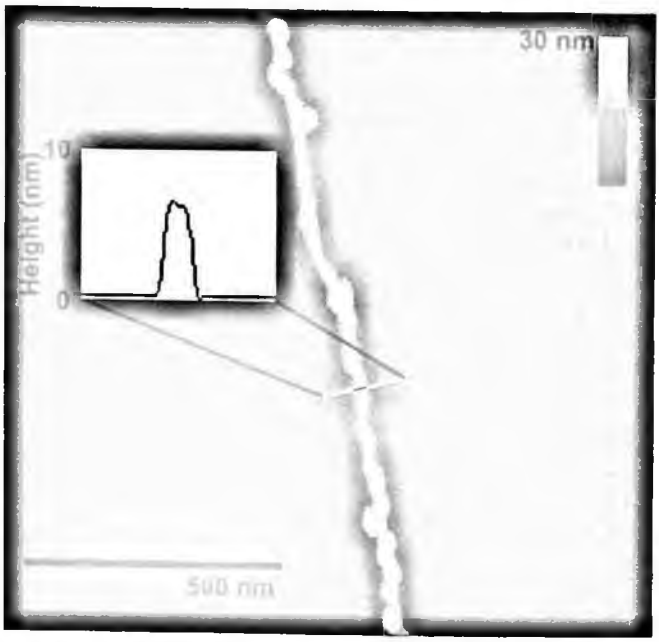

Figure 9. Atomic Force Microscope image of a DNA molecule stretched on a surface and metallized with a layer of palladium.

of a limited number of building blocks (amino acids) and then allowing the chain to fold into the proper 3D shape (self-packaging) and perform a function points toward an intriguing approach for designing the nano-scale machines of future. Of more immediate interest is taking advantage of molecular binding specificity and control afforded by proteins and polypeptides for guiding self-assembly processes in the nano-scale.

4.2.1. *Polypeptide directed assembly of quantum dots on microfabricated templates*

Most naturally occurring proteins and peptides do not have a special affinity to inorganic surfaces and materials. Inorganic materials such as metals and semiconductors are crucial for construction of nano-scale electronic and photonics devices. Efforts are underway to genetically engineer polypeptides that can selectively bind to materials of interest in electronics such as metals and silicon dioxide. These polypeptides can be used as molecular erectors to guide/program the self-assembly of other nano-scale objects (such as quantum dots) onto microfabricated templates for construction of heterogeneous structures [40]. This approach can potentially enable room-temperature self-assembly of Nanoelectromechanical Systems (NEMS) and Microelectromechanical Systems (MEMS) from aqueous solutions using proteins as

the basic building blocks or the mediators. Development of such polypeptide-based nanofabrication method involves two important steps:

(i) Genetic engineering and identification of polypeptides that bind specifically to selected inorganic materials.
(ii) Development of self-assembly procedures for placing nanoscale (or microscale) objects on micro-scale templates mediated by polypeptides.

Here, we use a gold binding polypeptide (GBP) as an example to explain the method. Following a similar procedure, polypeptides binding to other inorganic materials such as Pt and SiO_2 could also be identified and used to direct self-assembly [40].

(i) Polypeptide Identification

The selection of a polypeptide that specifically binds to an inorganic material can be performed *in vivo* by combinatorial biology protocols via different display methods, either phage display (PD) [41,42] or cell surface display (CSD) [43,44]]. In our example, the selection of GBP was performed by cell surface display. Fig. 10 shows the schematics of the selection of the polypeptide binding to specific materials by the CSD system of the bacteria, the *E. coli.* The displayed protein was fused with the major flagella protein FliC of the *E. coli.* To identify the polypeptide with the desired binding capability, first a specific segment of a DNA sequence was randomized and encoded in the bacterial plasmid. As the result, different polypeptide sequences were displayed within a flagella protein of the cell. By comparing the binding strengths of the polypeptides to the target inorganic surface, a better

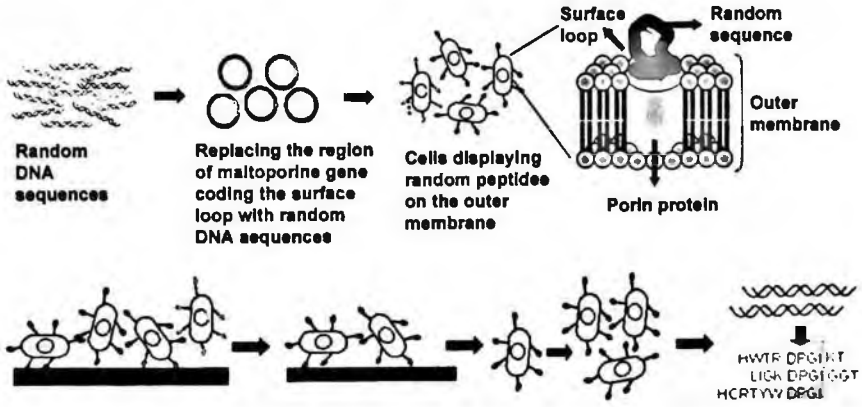

Figure 10. Combinatorial selection of gold binding polypeptide by Cell Surface Display. After cells that adhere well to the gold substrate are identified, their genome is sequenced to determine the order of amino acids in the peptide displayed on their surface. Courtesy of Dr M. Sarikaya of University of Washington, Seattle.

binding cell was selected. The DNA sequence of cells with a strong binding affinity was extracted, and the polypeptide sequence was determined. The PD method resembles this technique in many aspects. Instead of using the bacteria, the phage M13 can be used, and the displayed protein can be fused to the P8 minor coating protein at the tip. Using CSD, the amino acid sequence MHGKTQATSGTIQS has been identified as a polypeptide that selectively and specifically binds to gold [45,46].

(ii) Polypeptide Immobilization and Self-Assembly

The polypeptide identified with the above method can be used to direct the self-assembly of nano-scale objects onto microfabricated templates containing gold regions. Figure 11 shows the schematic flow of the polypeptide immobilization and self-assembly processes. First, a silicon dioxide coated substrate was prepared with microfabricated gold and platinum patterns. To immobilize the GBP, the substrate was incubated in the GBP solution. To demonstrate the method, synthesized biotinylated three-repeated GBP (42 amino acids) was used for the self-assembly experiment. After the GBP immobilization, streptavidin conjugated quantum dots (QDs) were added to the solution. As the result, the QDs could be self-assembled on the GBP immobilized on the Au patterns on the substrate. As the red QDs bind to the bio-GBP, red patterns in the florescent image indicate the existence of the bio-GBP and the directed self-assembly of the QDs. It has also been demonstrated that the binding of the polypeptide to the gold patterns can be modulated by applying a voltage to the metallic structures during the incubation period. This level of control presents the ability to electronically program an array of microelectrodes with different polypeptides by sequentially exposing the pads to the peptide solutions and applying the proper bias. The combination of the identification of polypeptides that selectively bind to a noble metal such as gold and the electronic control over the binding process presents a powerful new tool for fabrication of nano-scale array structures and hybrid organic/solid-state devices.

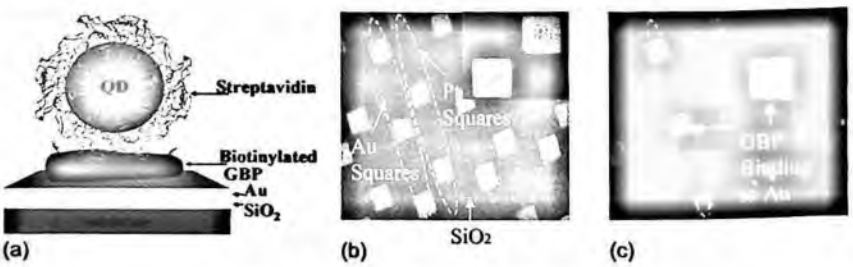

Figure 11. (a) Details of the hierarchical self-assembly scheme, (b) optical microscope image of microfabricated gold and platinum squares on a silicon dioxide covered substrate, and (c) fluorescent image of self-assembled QDs selectively attaching only to the gold pads. The squares are $100 \times 100\,\mu m^2$. The inserted images at the upper right corner are zoomed images of a pair of Au and Pt pads.

4.2.2. *Biomolecular self-assembly of nano-transistors*

Carbon nanotubes, which have remarkable electronic properties and are only about one nanometre in diameter, have been regarded as a highly promising material to help drive further miniaturization of nanoelectronics. Forming interconnects to nanotubes and building functional circuitry from an interconnected collection of them however, has proven to be a very challenging task. A recent work shows how self-assembly on a DNA strand mediated by proteins can be used to position a nanotube and form the electrical contacts to it without photolithography or other top-down patterning techniques [47]. The process began by coating a central part of a long DNA molecule with proteins from an *E. coli* bacterium (Fig. 12). Next, nanotubes coated with antibodies were added, which bound onto the protein. After this, a solution of silver ions was added. The ions coordinated to the phosphate backbone

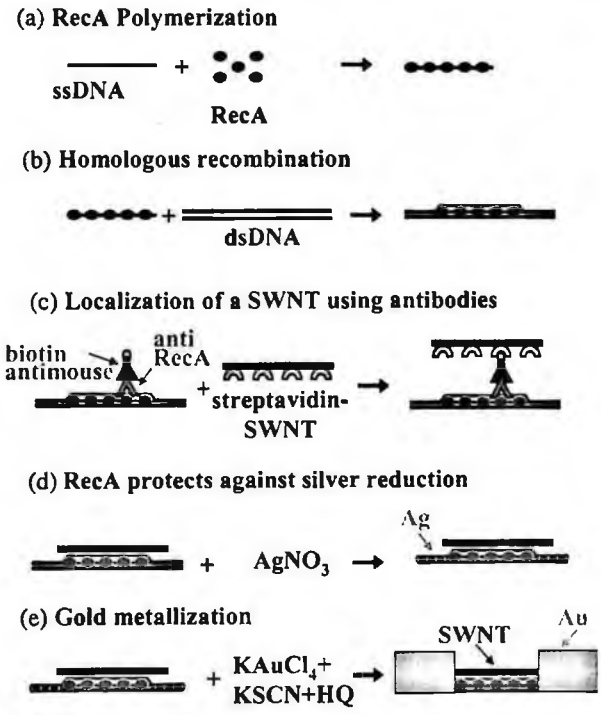

Figure 12. Assembly of a DNA-templated field effect transistor and contact wires. Steps are as follows: (a) RecA monomers polymerize on a ssDNA molecule to form a nucleoprotein filament. (b) Homologous recombination reaction leads to binding of the nucleoprotein filament at the desired address on an aldehyde-derivatized scaffold dsDNA molecule. (c) The DNA-bound RecA is used to localize a streptavidin-functionalized SWNT, utilizing a primary antibody to RecA and a biotin-conjugated secondary antibody. (d) Incubation in an $AgNO_3$ solution leads to the formation of silver clusters on the segments that are unprotected by RecA. (e) Electroless gold deposition, using the silver clusters as nucleation centers, results in the formation of two DNA-templated gold wires contacting the SWNT bound at the gap. Courtesy of Dr E. Braun of Technion-Israel Institute of Technology.

of the DNA, but only where no protein had attached. Aldehyde was then used to reduce the ions to silver metal, forming the foundation of a conducting wire. To complete the device, gold was electrolessly deposited using the silver atoms as the seed layer. The end result is a carbon nanotube device connected at each end by a gold wire (Fig. 13). The device operates as a field effect transistor with the two gold terminals as source and drain and the substrate on which the device is positioned as gate.

5. Conclusions

In the previous sections, we have cataloged and reviewed some of the important properties of two classes of biomolecules: oligonucleotides and proteins. The crucial roles played by these molecules in biological systems has guided an extremely large effort by a number of groups to understand the molecules, to develop the relevant science to describe their interactions, and even to develop artificial synthetic methods to construct the molecules by design. The sizable knowledge and collection of techniques available in the area can be employed in the nanofabrication of electronic, photonic, and nanomechanical devices. In most demonstrations to this date, the specific/programmable binding properties of these molecules have been used to guide self-assembly processes in the nano-scale and to make structures. A brief look at the complexity of functional systems in biology and what in principle is possible, reinforces the opinion that we are at the beginning of a rapid development path in

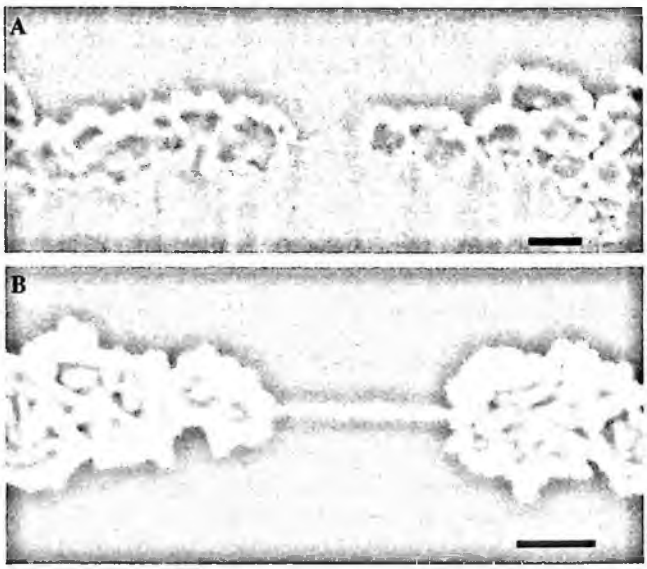

Figure 13. A DNA-templated carbon nanotube FET and metallic wires contacting it. SEM images of SWNTs contacted by self-assembled DNA-templated gold wires. (a) An individual SWNT. (b) A rope of SWNTs. The scale bars are 100 nm. Courtesy of Dr E. Braun of Technion-Israel Institute of Technology.

taking advantage of biomolecules to build sophisticated nano-scale structures and devices. Two areas are especially worthy of attention in the coming period. First, is the use of biomolecules to help in programming and guiding the synthesis and formation of inorganic structures. Unlike biomolecules, most engineered devices are made of inorganic materials such as metals and crystalline semiconductors. Pioneering efforts in genetically engineering polypeptides that can specifically recognize and bind to inorganics point towards a very promising development path for nanofabrication using self-assembly and bottom-up synthesis. The second promising area is machine design inspired by protein function. Proteins are functional nano-scale machines that self-package to reach their final conformation. A number of design, fabrication, and packaging ideas may be borrowed from the protein domains and adopted for nanofabrication of engineered devices and machines. The synergy between molecular biology and nanofabrication offers a number or exciting and intriguing opportunities for development of hybrid nanofabrication/nanomanufacturing of future.

References

1. J. D. Watson and F. H. C. Crick, A structure for Deoxyribose Nucleic Acid, *Nature*, **171**, 737–738 (1953).
2. F. Crick, Central Dogma of Molecular Biology, *Nature*, **227**, 561–563 (1970).
3. International Human Genome Sequencing Consortium, Initial sequencing and analysis of the human genome, *Nature*, **409**, 860–921 (2001).
4. Mouse Genome Sequencing Consortium, Initial sequencing and comparative analysis of the mouse genome, *Nature*, **420**, 520–562 (2002).
5. M. D. Adams, S. E. Celniker, R. A. Holt, C. A. Evans, J. D. Gocayne, P. G. Amanatides, S. E. Scherer, P. W. Li, R. A. Hoskins, R. F. Galle, R. A. George, S. E. Lewis, S. Richards, M. Ashburner, S. N. Henderson, G. G. Sutton, J. R. Wortman, M. D. Yandell, Q. Zhang, L. X. Chen, R. C. Brandon, Y. H. Rogers, R. G. Blazej, M. Champe, B. D. Pfeiffer, K. H. Wan, C. Doyle, E. G. Baxter, G. Helt, C. R. Nelson, G. L. Gabor, J. F. Abril, A. Agbayani, H. J. An, C. Andrews-Pfannkoch, D. Baldwin, R. M. Ballew, A. Basu, J. Baxendale, L. Bayraktaroglu, E. M. Beasley, K. Y. Beeson, P. V. Benos, B. P. Berman, D. Bhandari, S. Bolshakov, D. Borkova, M. R. Botchan, J. Bouck, P. Brokstein, P. Brottier, K. C. Burtis, D. A. Busam, H. Butler, E. Cadieu, A. Center, I. Chandra, J. M. Cherry, S. Cawley, C. Dahlke, L. B. Davenport, P. Davies, B. de Pablos, A. Delcher, Z. Deng, A. D. Mays, I. Dew, S. M. Dietz, K. Dodson, L. E. Doup, M. Downes, S. Dugan-Rocha, B. C. Dunkov, P. Dunn, K. J. Durbin, C. C. Evangelista, C. Ferraz, S. Ferriera, W. Fleischmann, C. Fosler, A. E. Gabrielian, N. S. Garg, W. M. Gelbart, K. Glasser, A. Glodek, F. Gong, J. H. Gorrell, Z. Gu, P. Guan, M. Harris, N. L. Harris, D. Harvey, T. J. Heiman, J. R. Hernandez, J. Houck, D. Hostin, K. A. Houston, T. J. Howland, M. H. Wei, C. Ibegwam, M. Jalali, F. Kalush, G. H. Karpen, Z. Ke, J. A. Kennison, K. A. Ketchum, B. E. Kimmel, C. D. Kodira, C. Kraft, S. Kravitz, D. Kulp, Z. Lai, P. Lasko, Y. Lei, A. A. Levitsky, J. Li, Z. Li, Y. Liang, X. Lin, X. Liu, B. Mattei, T. C. McIntosh, M. P. McLeod, D. McPherson, G. Merkulov, N.V. Milshina, C. Mobarry, J. Morris, A. Moshrefi, S. M. Mount, M. Moy, B. Murphy, L. Murphy, D. M. Muzny, D. L. Nelson,

D. R. Nelson, K. A. Nelson, K. Nixon, D. R. Nusskern, J. M. Pacleb, M. Palazzolo, G. S. Pittman, S. Pan, J. Pollard, V. Puri, M. G. Reese, K. Reinert, K. Remington, R. D. Saunders, F. Scheeler, H. Shen, B. C. Shue, I. Siden-Kiamos, M. Simpson, M. P. Skupski, T. Smith, E. Spier, A. C. Spradling, M. Stapleton, R. Strong, E. Sun, R. Svirskas, C. Tector, R. Turner, E. Venter, A. H. Wang, X. Wang, Z. Y. Wang, D. A. Wassarman, G. M. Weinstock, J. Weissenbach, S. M. Williams, T. Woodage, K. C. Worley, D. Wu, S. Yang, Q. A. Yao, J. Ye, R. F. Yeh, J. S. Zaveri, M. Zhan, G. Zhang, Q. Zhao, L. Zheng, X. H. Zheng, F. N. Zhong, W. Zhong, X. Zhou, S. Zhu, X. Zhu, H. O. Smith, R. A. Gibbs, E. W. Myers, G. M. Rubin and J. C. Venter, The genome sequence of *Drosophila melanogaster*. Science, 287, 2185–2195 (2000).

6. The Arabidopsis Genome Initiative. Analysis of the genome sequence of the flowering plant Arabidopsis thaliana, *Nature*, **408**, 796–815 (2000).
7. A. Goffeau, B. G. Barrell, H. Bussey, R. W. Davis, B. Dujon, H. Feldmann, F. Galibert, J. D. Hoheisel, C. Jacq, M. Johnston, E. J. Louis, H. W. Mewes, Y. Murakami, P. Philippsen, H. Tettelin and S. G. Oliver, Life with 6000 genes, *Science*, **274**, **546**, 563–567 (1996).
8. F. R. Blattner, G. 3^{rd} Plunkett, C. A. Bloch, N. T. Perna, V. Burland, M. Riley, J. Collado-Vides, J. D. Glasner, C. K. Rode, G. F. Mayhew, J. Gregor, N. W. Davis, H. A. Kirkpatrick, M. A. Goeden, D. J. Rose, B. Mau and Y. Shao, The complete genome sequence of Escherichia coli K-12, *Science*, **277**, 1453–1474 (1997).
9. Z. Wu, A. Ono, M. Kainosho and A. Bax, H...N hydrogen bond lengths in double stranded DNA from internucleotide dipolar couplings, *J. Biomol. NMR*, **19**, 361–365 (2001).
10. P. Faletra, DNA Decomposition, http://www.newton.dep.anl.gov/askasci/mole00/mole00390.htm, (April 14, 2003).
11. C. Chieh, Bond lengths and energies, http://www.science.uwaterloo.ca/~cchieh/cact/c120/bondel.html.
12. S. D. Black, The Genetic Code, http://psyche.uthct.edu/shaun/SBlack/genet-icd.html, (August 25, 1998).
13. B. Alberts, K. Roberts, J. Lewis, J. D. Watson, M. Raff and D. Bray, Molecular Biology of the Cell (Garland Publishing, New York, 1994)
14. T. Pan and T. Sosnick, RNA folding during transcription, *Annual Review of Biophysics and Biomolecular Structure*, **35**, 161–175 (2006).
15. T. E. Creighton, Protein Folding (W. H. Freeman & Co., New York, 1992)
16. L. Stryer Biochemistry (W. H. Freeman & Co., New York, 1995)
17. E. Chatani, R. Hayashi, H. Moriyama and T. Ueki, Conformational strictness required for maximum activity and stability of bovine pancreatic ribonuclease A as revealed by crystallographic study of three Phe120 mutants at 1.4 Å resolution, *Protein Sci.* **11**, 72–81 (2000).
18. S.-Y. Park, T. Yokoyama, N. Shibayama, Y. Shiro and J. R. H. Tame, 1.25 Å resolution crystal structures of human hemoglobin in the oxy, deoxy and carbon monoxy forms (To be Published).
19. D. Brutlag, Protein Structure, http://biochem118.stanford.edu/Papers/Protein%20Papers/Protein%20Structure.pdf, (January 11, 2000).
20. G. R. Marshall and R. B. Merrifield, Synthesis of angiotensins by the solid-phase method, *Biochemistry-US*, **4**, 2394–2401 (1965).
21. N. C. Seeman, Nucleic acid junctions and lattices, *J. Theor. Biol.*, **99**, 237–247 (1982).
22. N. C. Seeman, The Use of Branched DNA for Nanoscale Fabrication, *Nanotechnology*, **2**, 149–159 (1991).

23. R. Holliday, A Mechanism for Gene Conversion in Fungi, *Genet. Res.*, **5**, 282–304 (1964).
24. N. R. Ma, R. I. Kallenbach, R. D. Sheardy, M. L. Petrillo and N. C. Seeman, Three-arm nucleic acid junctions are flexible, *Nucleic Acids Res.* **14**, 9745–9753 (1986).
25. P. J. Hagerman, Flexibility of DNA, *Ann. Rev. Biophys. and Biophys. Chem.*, **17**, 265–286 (1988).
26. S. N. Cohen, A. C. Y. Chang, H. W. Boyer and R. B. Helling, Construction of biologically functional bacterial plasmids in vitro, *Proc. Natl. Acad. Sci. USA*, **70**, 3240–3244 (1973).
27. E. Winfree, F. Liu, L. A. Wenzler and N. C. Seeman, Design and self-assembly of two-dimensional DNA crystals, *Nature*, **394**, 539–544 (1998).
28. C. Mao, W. Sun and N. C. Seeman, Designed Two-Dimensional DNA Holliday Junction Arrays Visualized by Atomic Force Microscopy, *J. Am. Chem. Soc.*, **121**, 5437–5443 (1999).
29. Y. He, Y. Chen, H. Liu, A. E. Ribbe and C. Mao, Self-Assembly of Hexagonal DNA Two-Dimensional (2D) Arrays, *J. Am. Chem. Soc.*, **127**, 12202–12203 (2005).
30. P. Sa-Ardyen, A. V. Vologodskii and N. C. Seeman, The flexibility of DNA double crossover molecules, *Biophys. J.*, **84**, 3829–3837 (2003).
31. T. LaBean, T. H. Yan, H. J. Kopatsch, F. Liu, E. Winfree, J. H. Reif and N. C. Seeman, The construction, analysis, ligation and self-assembly of DNA triple crossover complexes, *J. Am. Chem. Soc.*, **122**, 1848–1860 (2000).
32. Y. Zhang and N. C. Seeman, Construction of a DNA-Truncated Octahedron, *J. Am. Chem. Soc.*, **116**, 1661–1669 (1994).
33. P. W. K. Rothemund, Folding DNA to create nanoscale shapes and patterns, *Nature*, **440**, 297–302 (2006).
34. A. Fire and S. Q. Xu, Rolling replication of short DNA circles, *Proc. Natl. Acad. Sci. USA*, **92**, 4641–4645 (1995).
35. E. Braun, Y. Eichen, U. Sivan and G. Ben-Yoseph, DNA-templated assembly and electrode attachment of a conducting silver wire, *Nature*, **391**, 775–778 (1998).
36. Z. Deng and C. Mao, DNA-templated Fabrication of 1D-Parallel and 2D-Crossed Metallic Nanowire Arrays, *Nano Letters*, **11**, 1545–1548 (2003).
37. J. Lund, J. Dong, Z. Deng, C. Mao and B. Parviz, Electrical conduction in 7 nm wires constructed on λ-DNA, *Nanotechnology*, **17**, 2752–2757 (2006).
38. H. Yan, S. H. Park, G. Finkelstein, J. H. Reif and T. H. LaBean, DNA-Templated Self-Assembly of Protein Arrays and Highly Conductive Nanowires, *Science*, **301**, 1882–1884 (2003).
39. Y. Pinto, J. Le, N. C. Seeman, K. Musier-Forsyth, T. A. Taton and R. A. Kiehl, Sequence-Encoded Self-Assembly of Multiple-Nanocomponent Arrays by 2D DNA Scaffolding, *Nano Lett.*, **5**, 2399–2402 (2005).
40. X. Xiong, M. Gungormus, C. Tamerler, M. Sarikaya and B. A. Parviz, Nanoscale Self-Assembly Mediated by Genetically Engineered Gold-Binding Polypeptide, 5th IEEE Conference on Nanotechnology, paper # TU-PS8-3, Nagoya, Japan July 11, 2005.
41. S. R. Whaley, D. S. English, E. L. Hu, P. F. Barbara and A. M. Belcher, Selection of peptides with semiconductor binding specificity for directed nanocrystal assembly, *Nature*, **405**, 665–668 (2000).
42. R. R. Naik, L. L. Brott, S. J. Clarson and M. O. Stone, Silica-Precipitating Peptides Isolated from a Combinatorial Phage Display Peptide Library, *J. Nanosci. Nanotechno.* **2**, 95–100 (2002).
43. S. Brown, Metal-recognition by repeating polypeptides, *Nat. Biotechnol.*, **15**, 269–272 (1997).

44. M. A. Schembri, K. Kjaergaard and P. Klemm, Bioaccumulation of heavy metals by fimbrial designer adhesins, *FEMS Microbiology Letters*, **170**, 363–371 (1999).
45. M. Sarikaya, Biomimetics: materials fabrication through biology, *Proc. Natl. Acad. Sci. USA*, **96**, 14183–14185 (1999).
46. M. Sarikaya, C. Tamerler, A. K.-Y. Jen, K. Schulten and F. Baneyx, Molecular biomimetics: nanotechnology through biology, *Nat. Mater.*, **2**, 577–585, (2003).
47. K. Keren, R. S. Berman, E. Buchstab, U. Sivan and E. Braun, DNA-Templated Carbon Nanotube Field-Effect Transistor, *Science*, **302**, 1380–1382 (2003).

CHAPTER 5

NANOFABRICATION BASED ON SELF-ASSEMBLED ALUMINA TEMPLATES

S. SEN and N. A. KOUKLIN*

Department of Electrical Engineering and Computer Science, University of Wisconsin-Milwaukee, 3200 N Cramer Street, Milwaukee 53211, USA

**nkouklin@uwm.edu*

A newly emerging route for non-lithographic nano-fabrication based on a powerful combination of self-assembly, top-down and bottom-up nano-fabrication paradigms is presented and applied for a controlled engineering of arrayed nanostructures. The approach relies on the use of self-assembled anodized alumina templates as masks for direct and inverse pattern transfer facilitated by metal deposition and dry-etching processing. The low material specificity inherent in this approach uniquely allows engineering of a vast variety of nano-materials ranging from metal dot arrays to compositionally complex three-dimensional arrays of semiconductor quantum dots. The ability to achieve dense packing, excellent uniformity, and ordering across large length scales provided with the electrochemical processing of aluminum, combined with recent advances in dry-etching techniques, enables a new platform to synthesize advanced nano-materials whose primary electronic, magnetic and optical properties can be tailored precisely as a function of their size, morphology and spatial arrangement of individual nanostructures. This new platform enabled by the technique holds particular promise for a broad range of advanced nano-electronic device applications and future nano-materials processing.

Keywords: Self-assembly; alumina; nonlithographic; nanofabrication; array

CONTENTS

1. Introduction 160
2. Anodization of Aluminum 161
   2.1. Two-step fabrication 162
   2.2. Pore growth mechanism 163
3. Properties of AAO Templates — Parameters Controlling Pore Growth and Diameter 165
   3.1. Acid type 165
   3.2. Pore widening and shrinkage (diameter tuning) 166

3.3. Ordering 166
3.4. Mechanical characteristics of AAO 167
3.5. Formation of free standing alumina masks 167
4. Fabrication Methods of Nano Materials Using AAO Templates 168
4.1. Overview 168
4.2. Electrochemical deposition 169
4.3. Sol-gel synthesis of nanowires and nanotubes 169
4.4. Sol-gel electrophoretic deposition 170
4.5. Sol-gel electro-chemical deposition 171
5. Nano-Patterning Using AAO for Controlled Fabrication of Nanostructures 171
5.1. Overview 171
5.2. Metal nanodot arrays by e-beam evaporation 172
5.3. Synthesis of planar arrays of oxide nanoparticles 173
5.4. Site-selective reactive ion etching of GaN 174
5.5. Ultra-dense spatially arranged arrays of InGaAsN/GaAs quantum dots and their photoluminescence properties 175
5.6. Catalyst-assisted VLS growth of highly crystalline ordered arrays of ZnO nanorods 179
5.7. Straight and Y-junction carbon nanotube arrays 181
6. Conclusion 183
References 184

1. Introduction

A continuous evolution of semiconductor device technologies towards smaller dimensions has proven to be a fascinating venture. The physical properties of materials can be altered dramatically when their size approaches deep submicron dimensions, which opens new horizons in realizing low (per unit) cost engineering of devices with novel and dramatically improved performance. Practically speaking, the behavior of the system is expected to change only when its size becomes comparable or less than one of the characteristic lengths, among which are the mean free path, de Broigle wavelength and exciton Bohr radius. Engineering of materials with nanoscale dimension and precision by using photo-lithography represents an insurmountable challenge that the research community has yet to address satisfactorily. Meanwhile, a number of novel fabrication techniques have been recently introduced and developed to push beyond the limits of conventional photolithography, among which are copolymer block lithography, vapor-based deposition methods, Molecular Beam Epitaxy (MBE), colloidal methods, sol-gel, and second order self-assembly techniques employing anodized aluminum oxide (AAO) templates.

Even with today's advances in techniques to synthesize highly crystalline nanostructures such as MBE, Chemical Vapor Deposition (CVD) and colloidal methods,

controlling the organization of matter on larger than atomic scales remains highly difficult due to the lack of long-range interaction between individual nanostructures. This not only affects the extrinsic parameters of the system, but also its intrinsic properties as a result of strong electronic coupling between individual nanostructures with dense arrangement. The effect of electronic coupling is induced by a leak of an electronic wave function into the potential barrier of finite height and small width. The development and introduction of AAO-based techniques provides a cost-effective solution to the current problems of uncontrolled nanofabrication and, compared with other techniques, offers such advantages as low cost, low material selectivity, the possibility of fast and parallel processing, as well as precise size tailoring of nanostructures. In parallel, a use of the templates in MBE, CVD and dry etching has recently emerged as an important non-lithographic route to the fabrication of a variety of nanostructures, which are a part of this review as well.

The concept relies on the implementation of the alumina templates as a mask for secondary processing of materials into nanoscale building blocks ranging from planar ultra-densely packed superlattices of nanodots, nanopillars, nanowires to the arrays of vertically aligned and periodic multi-walled carbon nanotubes and three-dimensionally arranged stoichiometrically complex semiconductor quantum dots. In many cases, the resultant structures are inherent in the order and size of the templates used. Even though the templates can be applied only once, this fabrication pathway shows a high degree of repeatability and reproducibility that is of particular importance for emerging nano-device technologies.

The review presented in the next four paragraphs is organized as follows. First, we discuss the process of the fabrication and key properties of resultant free standing alumina templates. Synthesis of nanostructures by electrochemical and sol-gel deposition in the pores of alumina templates is presented in Section 4. Next, we look at the details of the fabrication of highly ordered arrays of nanostructures in metals, semiconductors and oxides. The review concludes with the growth of highly ordered arrays in both straight and Y-junction nanotubes enabled through the use of the templates.

2. Anodization of Aluminum

Anodization of aluminum is generally referred to as the process of self-driven formation of cylindrical nanoscale diameter pores when aluminum is chemically etched in an acidic bath by applying an electrical current. The process has been known for decades and has already found application for surface decoration with inorganic and organic materials. In 1995, Masuda *et al.* [1] offered a way to dramatically improve the order and diametric distribution of the pores by performing a two-step anodization process. This finding has broadened the range of uses of self-ordered alumina structures towards new areas of applications such as magnetic storage [2], solar cells [3], carbon nanotubes [4], catalysts [5], and metal nanowires [6–7]. Deposition

of a variety of materials inside the nanopores of the anodized aluminum oxide (AAO) layers enabled a large scale synthesis of quality metallic and semiconducting nanowires, nanorods and nanodots with novel and improved electronic characteristics. More recently, the AAO templates have been successfully used in the combination with other additive and subtractive fabrication routes, which has opened new horizons in the controlled synthesis of a variety of nanostructure materials with a large yield and on a large scale as discussed further.

Engineering of morphologically different nanostructures can be accomplished by using well-defined, self-ordered non-lithographic porous alumina with different pore diameter and interpore distance, ranging from tens to hundreds of nanometers [8]. Anodization of aluminum, which can be considered as technologically undemanding and low cost technique for fabrication of nanostructures, is an excellent non-lithographic alternative to other conventional approaches such as imprint and e-beam lithography [9,10] currently used in nanopatterning applications. Among other advantages of using AAO templates for nanoscale processing is the possibility to apply them in a controlled and large-scale synthesis of an almost arbitrary class of materials with a fast throughput. In many cases, the properties of these fabricated nanomaterials have been found to show varying characteristics with respect to the type of deposition/processing implemented, while in certain cases they are also found to directly depend on the structural characteristics of the templates used. The size and interpore distance that change with anodization conditions are among the key parameters that control the electronic properties of nanomaterials through quantum confinement, dielectric confinement and electronic coupling effects. In addition, apart from quantum confinement, the primarily influence comes from the structural characteristics of the materials themselves, such as those related to the grain size, phase, orientation of crystallites and interface, to be discussed further.

2.1. *Two-step fabrication*

The electrochemistry of porous AAO template formation has been a subject of intensive studies for many decades. These studies suggest that the growth of porous anodic alumina happens spontaneously and is a result of two counter-processes that yield a time-continuous formation of a porous oxide film on top of an aluminum base. One of the processes involves the development of an oxide film, while the other one accounts for its inhomogeneous dissolution in the aqueous acid solution. The chemistry of the overall anodization process is described with the following equation:

$$2Al + 3H_2O \rightarrow Al_2O_3 + 3H_2, \quad [\Delta G = -8.65 \times 10^5 J]$$

where ΔG stands for a free Gibbs energy change.

The anodic alumina has been able to attain its successful position in nanoscale engineering due to its widely accepted role as a template for the production of high density arrays in a variety of semiconducting, ceramic, magnetic and metallic

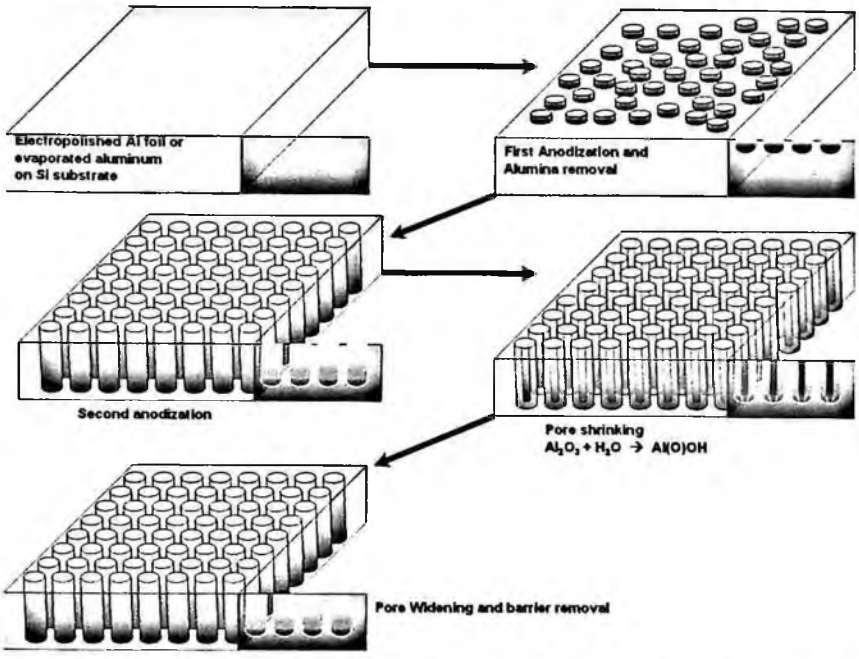

Figure 1. Schematics of alumina nano-template formation based on two-step anodization.

nanomaterials. The set of parameters used to fabricate these nanomaterials is optimized based on the morphology, composition and electrical properties of the nanopores of the alumina templates, which are discussed next.

A typical two step anodization process is schematically presented in Fig. 1. To prepare the films, first an ultra-pure 99.99% aluminum foil is degreased and electrochemically polished in electrolyte, containing perchloric acid, ethanol, butyl cellusolve and de-ionized water. Next, the foil is anodized in sulfuric/oxalic/phosphoric acid using DC current or voltage mode for at least 12 hours. During this step, a porous alumina layer with the thickness of several microns is generated. Stripping the film in a phosphoric acid creates the scallop-like top surface of Al. The anodization can be then repeated under the same conditions. During the second anodization, the pores tend to nucleate according to the scallop pattern. To achieve the desired pore depth and aspect ratio, exact control is required on the second anodization time. Increasing in the number of anodization steps to three or four can further improve uniformity and ordering of the film.

2.2. *Pore growth mechanism*

The time evolution studies on the current density for anodization performed at constant voltage normally reveal a presence of minimum in the current vs. time characteristics. As mentioned earlier, such behavior is attributed to the presence

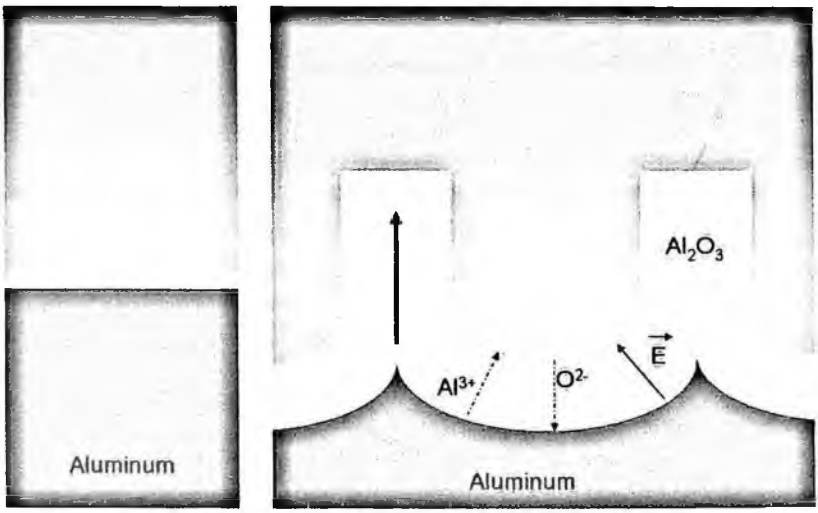

Figure 2. Shows schematically the mechanism of the nanopore formation.

of two types of electrical currents due to: (i) oxide growth and (ii) its dissolution, which balance each other only at the steady-state.

The formation of pores proceeds only in the direction normal to the top surface of the substrate, while the growth area is directly controlled by the size of the anodization cell. The growth of Al_2O_3 takes place only at the thin surface layer due to its low conductivity, which forces the current to drop rapidly as the thickness of the oxide film increases. More specifically, the alumina forms at the bottom of the layer [11] with the height of the sidewalls being equal to the thickness of the barrier layer. As the sidewalls are thin enough for the anions, including OH^-, O_2^- and $C_2O_2^{-4}$, to penetrate into the Al–Al_2O_3 interface, these ions can interact with the Al^{3+} ions, yielding a growth of alumina at the sidewall regions [12]. In general, the process of oxide formation will continue as long as the barrier remains electrically transparent to the anions, as shown in Fig. 2.

The position of the minimum in the anodization curve usually depends on external parameters such as temperature, annealing temperature, anodization voltage, pH of the solution, and surface morphology. At the bottom, the sidewalls are found to be wider than at the top for a short anodization time, in which case the nanopore cross section shows a more V-like shape. This implies that the growth mechanism in the unsteady state is different from that of the steady state. However, for a larger anodization time, the V-shape nanopores become normally U-shaped and the template growth switches to steady state. In general, both the sidewall height and barrier layer thickness are proportional to the anodization time, initially resulting in the rapid current density drop. As the anodization time increases further, the alumina layer at the bottom of the V-shape nanopores will be dissolved, and the V-shape nanopores will gradually transform into U-shape ones.

The disappearance of the alumina part facilitates the penetration of the ions into the Al– Al_2O_3 interface. On the other hand, higher sidewalls will substantially limit the current; therefore the barrier layer thickness cannot increase any further. The increase in current density before the steady state is reached is therefore mainly induced by the dissolution of the alumina layer. At the stable state, the nanopores develop a regular U-shape. The important aspect of the presented analysis is that one can easily fabricate morphologically different nanoporous templates and therefore nanostructures as being of V-shape or U-shape by controlling the anodization time.

The chemical reaction leading to the oxide formation involves migration of oxygen containing ions (O^{2-}/OH^{-}) from the electrolyte through the oxide layer at the pore bottom, while Al^{3+} ions simultaneously drift through the oxide layer and are ejected into the solution at the oxide/electrolyte interface [13]. Al^{3+} ions reaching the oxide/electrolyte interface form Al_2O_3 [14–15]. Some of the Al^{3+} ions are lost to the electrolyte and the phenomenon is a requisite for porous oxide growth. The density of Al^{3+}in alumina is twice as low as in the metallic aluminum. It is the entire pore bottom where the oxidation takes place simultaneously and hence the growth expansion of the material can only take place in the vertical direction, pushing the existing pore walls upwards. The mobile Al^{3+} ions in the oxide can move under the electric field so that part of the oxidized aluminum does not contribute to oxide formation and hence the expansion of aluminum is less than twice the original volume.

Currently, there are many reports on the mechanism of self-assembled growth of nanopores. Recent theories rely on the framework of a repulsive interpore interaction that may arise due to mechanical stress induced by the oxide formation at the metal/oxide interface to explain this phenomenon, although this question still remains open to further explorations.

3. Properties of AAO Templates — Parameters Controlling Pore Growth and Diameter

3.1. *Acid type*

The physical properties of the AAO templates depend on the process conditions like applied voltage, temperature and type and concentration of the electrolyte. As discussed before, the anodization of Al plates leads to hexagonally arranged close-packed arrays of cylindrical pores. The type of acid used determines the diameter of pores of the AAO templates. Sulfuric acid generally gives the smallest pore diameter of ~10 nm, therefore yielding the largest pore density. For oxalic and phosphoric acids, the pore diameters are ~50 nm and ~90 nm, respectively. The standard deviation in the pore diameters normally falls within 10% of their mean values (Table 1). Since hexagon-shaped arrays demonstrate the largest packing densities, electronic systems with device packing densities approaching $\sim 10^{12}$ per cm^2 can potentially be

Table 1. Lists the array of geometrical parameters as a function of the anodization conditions.

Electrolyte	Interpore Distance, D_{int}	Inner Wall Thickness, D_{inner}	Pore Diameter, D_P	Porosity
H_2SO_4 25 V 0.3 M	66.3 nm	7.2 nm	24 nm	12%
$(COOH)_2$ 40 V 0.3 M	105 nm	9.1 nm	31 nm	8%
H_3PO_4 195 V 0.1 M	501 nm	54 nm	458.4 nm	9%

fabricated using AAO templates, which can account for a very high density, closely packed array of nanomaterials to be fabricated within the pores of the templates.

3.2. *Pore widening and shrinkage (diameter tuning)*

The tailoring of materials at a nanoscale to a desired property or specific device function provides an efficient way to build electronic devices with novel functionalities. Diameter tuning of the pore by changing the anodization conditions (such as the type of acid, as discussed above) gives a route to precise tuning of the lateral dimensionality of nanostructures, i.e., their diameter and hence their electronic parameters. The use of different acid types can affect the overall pore density and ordering. Enlargement/narrowing of pores using chemical wet-etching or gold plating techniques is therefore viewed as a more systematic way to modify the lateral size characteristics of the nanostructures which in turn provides a path of diameter-tailoring of the nanowires that can be fabricated inside the pores by using various deposition techniques.

3.3. *Ordering*

The pore ordering has a direct impact on the diameter uniformity, the latter being critical for any application of the templates for nanoscale processing. Highly ordered AAO films can be made by lithographically (stamp imprinting and focused-ion-beam lithography) patterning of the aluminum top surface prior to the anodization process. In general, to assess the ordering, we can define one side (Lx) of the unit cell of the lattice (Fig. 3) while fixing the other (Ly) at L. The ratio $Lx/Ly = \sqrt{3}$ has to be kept to maintain the hcp lattice symmetry. The "lattice mismatch" defined as $f = (L_x - L\sqrt{3})/L\sqrt{3}$ can be minimized to 0% for AAO films by pre-patterning of Al, (Fig. 3) [16].

To improve the aspects of grain size and therefore the ordering, pre-annealing of aluminum can be carried out. The annealing is normally performed at 500°C for a few hours at 10^{-3}Pa vacuum in the presence of nitrogen or argon gases. This is known to enhance the grain size in the melt and help to obtain homogeneous

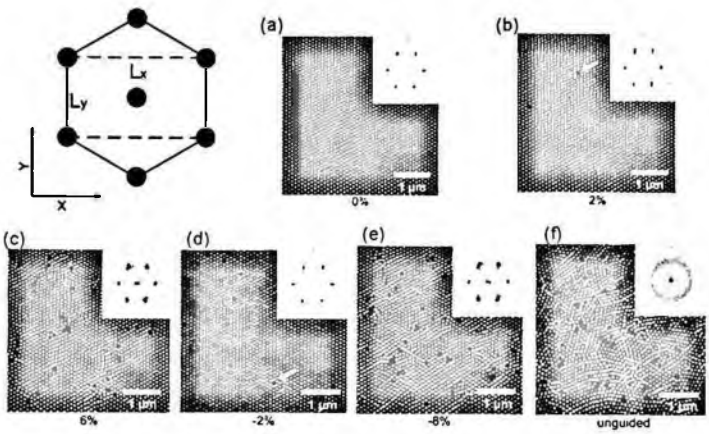

Figure 3. Diagram of an unit cell of the lattice followed by AFM images of the barrier with lattice mismatch = (a) 0%, (b) 2%, (c) 6%, (d) −2%, (e) −8% and (f) a self organized structure with insets showing the 2D power spectra of the corresponding regions of the 10 micron AAO films. White arrows in (b) and (d) indicate point defects in the lattice. [Reproduced with permission from APL 84, No 14 (2004) Pg 2510.]

conditions for pore growth over larger areas. An alternative solution to ordering is to use a mold to press against an aluminum film to create any desired surface pattern. For integration of the nanostructures fabricated by using AAO templates, Al films can be grown by e-beam evaporation on conductive (highly doped) Si wafers with a pre-deposited Ti layer to promote adhesion. Ordering of the nanotemplates will enhance the ordering of the nanomaterials to be grown and hence play an important role behind the performance of future nanodevices.

3.4. *Mechanical characteristics of AAO*

The mechanical properties of AAOs have considerable importance for nanodevice fabrication. Due its amorphous composition, the hardness and the AAO templates have a lower Young's modulus by a factor of $3.1 \sim 3.7$ compared with that of the crystalline bulk Al_2O_3 [17]. The hardness of barrier-type, amorphous alumina determined by nano-indentation measurements is approximately 7.0 GPa. The Young's modulus of anodic alumina is approximately 122 GPa. Studies of the effect of annealing on the mechanical characteristics of the templates using XRD have shown gradual crystallization of AAO with increasing the annealing temperature, leading to improvement in their mechanical characteristics.

3.5. *Formation of free standing alumina masks*

After anodization, the alumina membranes can be further processed into free standing nanoporous masks that can be used in non-lithographic based nano-processing of bulk materials. For this, the membrane is first separated from the Al substrate

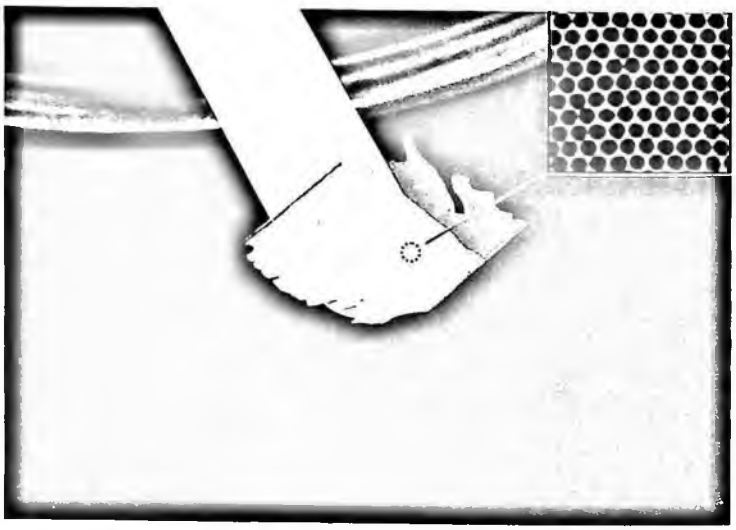

Figure 4. A digital optical image of a free standing ~10 μm thick AAO template (gold plated for better viewing contrast); inset shows its top-view SEM image, scale bar is 200 nm.

by dissolving the latter with $HgCl_2$ solution. The free standing mask is next allowed to air-dry for several hours. A picture of a free standing alumina template is shown in Fig. 4.

4. Fabrication Methods of Nano Materials Using AAO Templates

4.1. *Overview*

A recent advance in the area of controlled fabrication of nanomaterials provides an efficient platform for manipulating and exploiting the properties of otherwise conventional materials that can later lead to engineering of novel multifunctional electronic, mechanical and sensing nanodevices. Mesoscopic materials change their key properties depending on their size parameters, especially when approaching nano and atomic scale ranges. In parallel, many interesting new phenomena and effects are expected when the surface to volume ratio becomes large. These properties have recently sparked substantial interest of scientists and engineers worldwide. In particular, thermal, mechanical, optical, magnetic and ferroelectric properties of nanomaterials are within the focus of the investigations conducted as they can facilitate the development of novel device technologies. In the area of functional nanoceramics, the effects of reduced dimensionality involve lowering of sintering temperatures, increased hardness, stability, diffusion transport and ductility. Likewise, ferroelectric properties of some of the ferroelectric oxide films have been shown to undergo orders of magnitude enhancement as compared with their bulk counterparts [18,19]. Magnetic-related effects are further known to benefit significantly from size reduction. In fact, giant magneto-resistance, high Curie temperatures and

large coercivities are among the factors that were observed to improve when system dimension approaches nanoscale [20]. Gas sensing characteristics and optical response have all been shown to exhibit many fold enhancements in nano-crystaline materials [21]. In many cases, however, the selected nano-fabrication route plays a critical role behind the improvement in the properties observed. Mesoscopic materials produced with the use of self-assembled nanometric alumina templates feature highly uniform diameters, lengths and arrangement. The low material specificity inherent in this approach uniquely allows for synthesizing a vast variety of nanomaterials and their heterojunctions in the form of nanodot, nanowire and nanotube lateral superlattices as well as compositionally complex three-dimensional arrays of semiconductor quantum dots.

4.2. *Electrochemical deposition*

Nanostructures can easily be fabricated electrochemically, i.e., by depositing materials, mostly metals and semiconductors, into the pores of templates. This process yields a formation of high areal density arrays of metallic and semiconducting nanorods and nanowires. The quality of the materials and the structural properties depend on the deposition and processing conditions as well as the properties of the materials such as nature of defects and their energetics. Post deposition processing such as oxidation, for example, of metallic nanostructures can further be used to create nano-oxides. The synthesis of CdS, ZnSe, ZnS and other type semiconducting nanowires and nanodots has been successfully accomplished earlier, and an in-depth review of their properties can be found in reference [22].

4.3. *Sol-gel synthesis of nanowires and nanotubes*

In the area of nanoceramic materials, the use of AAO templates has provided an economical solution to the fabrication of different types of oxide ceramics, mostly in the form of highly ordered arrays of nanowires and nanotubes by the so-called sol-gel methods.

Hydrolysis of a solution of a precursor material to obtain a suspension of colloidal particles (sol) and hence later obtain a gel of the aggregated sol particles is known as the sol-gel process. Thermal treatment of the gels gives the desired material. The advantages of this process are low-temperature, and homogeneous and high quality synthesis of multicomponent systems by mixing different precursor solutions. This process has become one of the ubiquitously used techniques for the preparation of inorganic materials recently since the fabrication of multicomponent oxides by other routes is known to be a highly difficult task.

In the conventional sol-gel template process, the templates are usually dipped directly in the relevant sols for a certain period of time, where a capillary action is employed to fill the pores gradually. The pH and temperature are among the most critical parameters controlling the growth. In general, the sol-gel method is used for

the fabrication of either a nano-tubule or a nano-fibril, which are formed after the heat treatment [23]. The immersion time determines whether the structure will be nano-tubule or nano-fibril, with a longer time yielding fibrils. At the same time, if the pore size is relatively small, then the tubule structure cannot be obtained.

There are certain limitations to this process. Filling up the pores with the sol becomes one of the primary constraints, especially when solutions of higher concentrations are used. As such, lower concentrations are generally preferred as it is easier to fill up the pores. At the same time, this effectively reduces the amount of material that can be deposited, leading to the development of serious cracks and shrinkage after thermal treatment, yielding growth of highly defective nanostructures. Likewise, use of the templates with a small pore diameter for sol-gel deposition is known to be highly difficult.

Several techniques have been developed to eradicate the problems associated with the difficulty of filling up the pores with sol. A general working principle of the alternative approaches employ the idea of allowing the sol formation to take place inside the pores once the solution fills up the pores. In this case, the sol is formed not only inside the pores but in the solution as well. The approach has been successfully used to fabricate Y_2O_3:Eu nanotubes [24].

4.4. *Sol-gel electrophoretic deposition*

Electrophoretic deposition is an assembly process by which small particles move in applied electric fields and attach to an electrode [25]. The technique is essentially a sol-gel process in which an electric field is used in addition to capillary force to facilitate the deposition. Along with excellent stoichiometry and reduced cost provided with a sol-gel method, this approach offers high throughput and extends the range of processing parameters. The electric force plays an important role in cases when increased concentrations of sol are used, making pore filling an extremely difficult task. One interesting aspect of the electrophoretic deposition is that as no electrode reaction takes place, the deposited layer preserves its charge and therefore it can be easily stripped off by alternating the bias polarity. A concurrent deposition of a different species is possible with this technique only if their charge is of the same sign in the solution.

The deposition is sensitive to the surroundings and the solvent used. Water and organic solvents have found their application in electrophoretic deposition. The drawback of aqueous solvents is formation of gas as a result of water hydrolysis, especially when large electric fields, i.e., bias voltages, are applied. For deposition to occur, the particles have to be stably suspended and have to carry an electrical charge. In addition, a binder has to be added to the solution to improve sticking between the particles and to promote uniform deposition. The deposition rate shows a functional dependence on the applied electric field, the suspension concentration, and the mobility of particles in solution. Higher electric fields promote faster

deposition. The produced films can next be sintered at very high temperatures to form a uniform coating.

ZnO nanowires have been grown by the electrophoretic based assembly of nanoparticles in the pores of AAO templates [26]. This process however is very complex and requires special equipments while not all types of oxides can be obtained by this process either.

4.5. *Sol-gel electro-chemical deposition*

Another variation of Sol-gel deposition is the electrochemically induced sol gel synthesis. In this case, a hydroxyl ion is generated due to cathodic reduction, while a further increase in the concentration of OH- ions raises the local pH at the electrode surface, resulting in gel formation within the pores. A diagram of the gel formation inside the AAO pore from the sol particles is explained by the schematics of Fig. 5. The limitation of the electrophoretic sol-gel technique in case of the synthesis of nanoceramic nanowires lies in its failure to produce nanowires with diameter generally less than ~50 nm. The problem is associated with the fact that the transport of clusters is highly restricted in the nanopores. The electrochemically induced sol-gel method overcomes these limitations and can be used to prepare single-crystalline alumina embedded nanowires featuring very small diameters [27].

5. Nano-Patterning Using AAO for Controlled Fabrication of Nanostructures

5.1. *Overview*

A number of techniques for controlled processing of semiconductors have been deployed to suffice the needs of the evolving nano-device technologies. Non-lithographic patterning that relies on the use of AAO templates as a mask has recently emerged as a novel route to large-scale fabrication of nanomaterials.

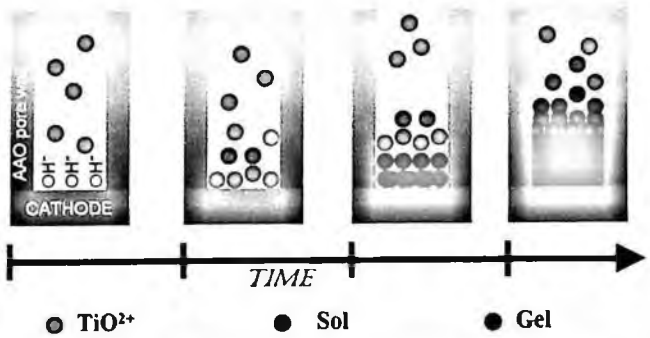

Figure 5. Schematically shows an electrochemically induced sol-gel process (Reproduced with permission of Nano Letters 2 (2002) 787).

This technique takes advantage of excellent thermal and mechanical stability of alumina for the fabrication of highly uniform nanopatterns in conventional semiconductor materials. The technique sometimes becomes the only alternative, especially when the integration of the resultant nanostructures with existing device platforms becomes economically or technologically not feasible. As shown further, the nanopatterning techniques also can be combined with bottom-up paradigms of Vapor-Liquid-Solid (VLS) growth [28] for controlled synthesis of single crystal nanowires in high performance semiconductors and oxides.

Though direct electro deposition of metals and semiconductors into the pores of AAO templates was initially considered as a only use of the templates for the fabrication of diameter and length uniform nanowires and nanodots, more recently the templates have found their application as nanomasks in dry etching and e-beam deposition, which has opened new horizon in non-lithographic based engineering of nano-semiconductors, metals and oxides. The process flow diagram presented in Fig. 6 schematically shows different possibilities for implementation of AAO templates for creating (a) semiconductor nanopore arrays by reactive ion etching (RIE) (b) metal nanodot array with e-beam deposition (c) nanowire arrays by Vapor Liquid Solid (VLS) growth and (d) nanopillar array by RIE.

5.2. *Metal nanodot arrays by e-beam evaporation*

Planar superlattices of metal nanodots have a potential application in many future device technologies ranging from sensor arrays (Surface Plasmon Resonance effect)

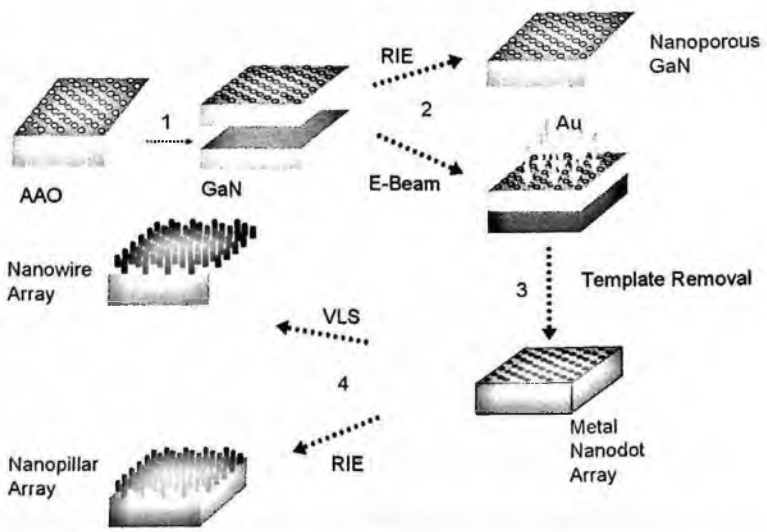

Figure 6. A process flow diagram illustrating the fabrication of lateral superlattices of nanostructures by using AAO templates as discussed in the text.

to high density magnetic storage systems, such as ultra-dense random-access-memory (RAM). Template assisted fabrication offers a possibility for parallel processing of more than 10^{12} single devices in a single fabrication cycle using an electrochemical cell with anodization area of only $\sim 1\,\mathrm{cm}^2$. Direct patterning of semiconductor surfaces provides the advantage of easy integration of the produced structures into electronic devices.

Hexagonal arrays of Ni-dots on GaN have been created by electronic beam evaporation of Ni in a vacuum of $\sim 10^{-6}$ Torr, where a typical metal deposition rate of $\sim 5 \times 10^{-3}$ nm/s is used. Figure 7 shows a top-view SEM image of the resultant array formed by this technique on the top surface of the GaN substrate. An Atomic Force Microscope (AFM) analysis revealed the height and diameter of the dots as being of 20 nm and 55 nm for membrane with a pore diameter of $\sim$60 nm. Apart from Ni, other metals such as Au, Co and Fe have all been successfully deposited on top of cm-size semiconductor wafers using this approach. A general requirement for using this technique is that deposited metal atoms/ions have to have a very narrow angular distribution of velocities, so that the deposits do not clog the pores as a result of a competitive fast growth of thin film on their sidewalls. This requirement can easily be fulfilled using e-beam and pulsed laser deposition techniques, while reducing the aspect ratio of the pores further mitigates this drawback.

5.3. *Synthesis of planar arrays of oxide nanoparticles*

A straightforward approach to the fabrication of oxide nanoparticle arrays with uniform diameter and highly ordered arrangement as mentioned earlier can be realized by performing a thermal oxidation of an e-beam deposited metal nanoparticle array. At the same time, alternatively oxide materials can be directly deposited by laser ablation techniques. In particular, the growth of ZnO nanodots on top of the Si substrate has recently been demonstrated by this route. A ZnO target has been

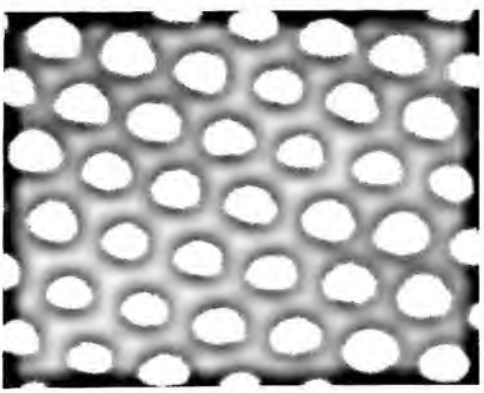

Figure 7. Top view SEM image of Ni mask produced by e-beam deposition using AAO templates as shadow mask, the average diameter of the dots is $\sim$55 nm.

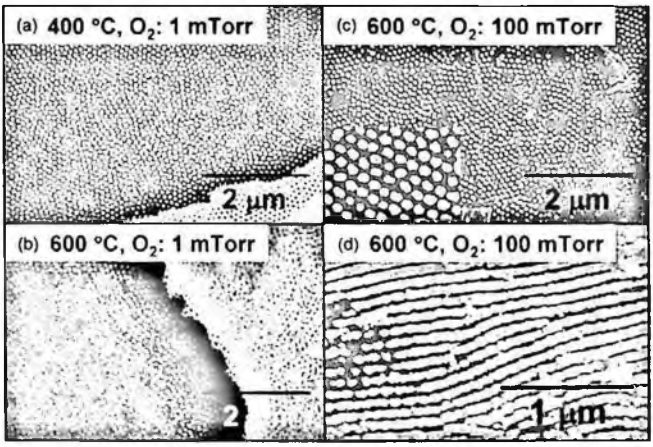

Figure 8. Top-view SEM images of ZnO nanodot arrays grown by PLD at oxygen pressure of 10^{-3} Torr at (a) 400°C and (b) 600°C, respectively. (c) and (d) show SEM images obtained on different spots of samples grown under oxygen pressure of 10^{-3} Torr at 600°C. The inset of figure 1(c) shows a close-view image of the ZnO nanodot arrays. Reproduced with permission of Journal of Nanotechnology.

ablated with a focused Nd:YAG laser operating at UV range, while the growth has been performed at different temperature ranges and O_2 partial pressures, Fig. 8.

Magnetron sputtering has been additionally employed for a controlled synthesis of highly regular hexagonal crystalline nanowires and nanotemplates using AAO templates. Nanostructures of materials that can terminate into two oppositely charged surfaces along a fast growth direction can be generally fabricated.

In hexagonal ZnO, the crystal planes are composed of tetrahedrally coordinated Zn^{2+} and O^{2-} ions that are stacked alternately along the c axis, Fig. 9 (a) and therefore nanostructures in this materials system can be easily produced via magnetron sputtering. In this process, initially, the surface of AAOs that carry a partial negative charge, Fig. 9 (b) will tend to attract Zn^{2+} ions, the process by which the top surface will become positively charged. A subsequent attraction of O^{2-} ions will result in the nucleation and growth of ZnO crystal normal to the AAO top surface, Fig. 9 (c) yielding porous multilayer nanotemplates of ZnO Fig. 9 (d) originating from the top surface of AAOs.

5.4. *Site-selective reactive ion etching of GaN*

Several uses of ordered nanoporous alumina templates for nanopatterning of GaN have been recently explored. Wang *et al.* studied a possibility of direct anodization of an aluminum layer deposited on the top surface of GaN [29]. The formed AAO template has then been used as a mask for site-selective plasma etching of GaN to engineer GaN nanoporous arrays.

Another alternative employs free standing alumina masks instead, thus avoiding a direct deposition of metal on the top surface of the semiconductor and also allowing

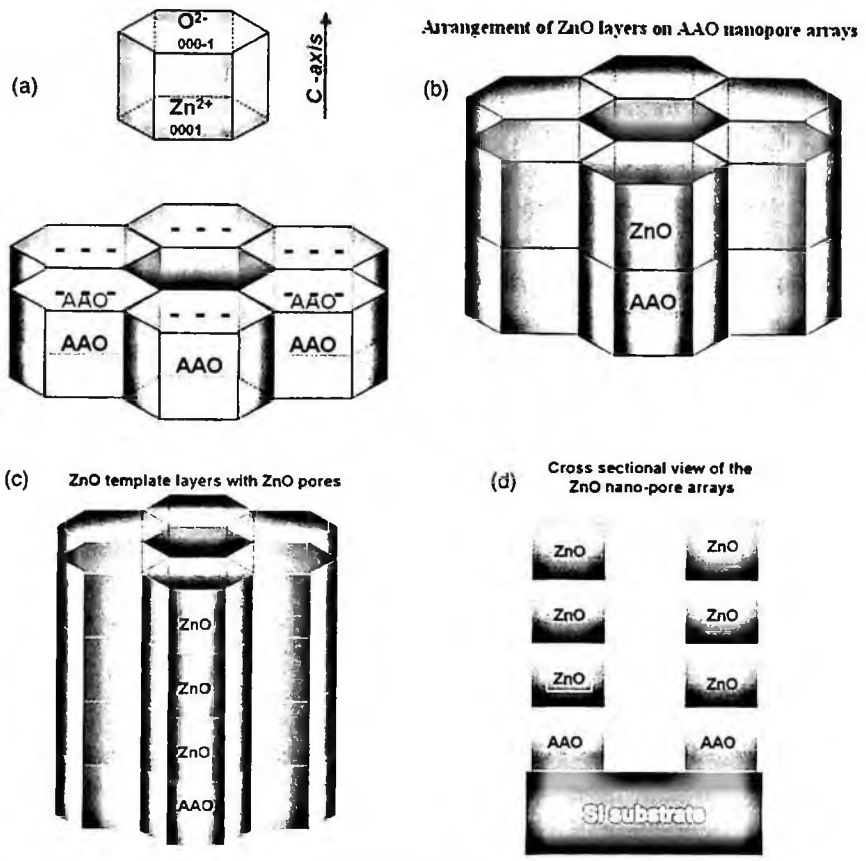

Figure 9. Schematic diagrams of magnetron sputtering growth of the ordered ZnO nanopore arrays by the aid of AAO template.

for a negative pattern transfer. The alumina mask can be separated easily from the semiconductor after the Reactive ion etching (RIE) of GaN by soaking the sample in an aqueous solution with the help of ultra-sound agitation. Figure 10, left shows a typical SEM image obtained on a GaN nanopore array. For a negative pattern transfer, first a planar array of Ni nanodisks was deposited on a GaN substrate by the e-beam evaporation of Ni through the pores of the AAO template as discussed earlier. The template was next lifted-off in ultrasonic bath. As a final sequence, the unmasked parts of GaN were selectively removed with RIE. Figure 11 shows an SEM image of the resultant GaN nanopillar arrays.

5.5. *Ultra-dense spatially arranged arrays of InGaAsN/GaAs quantum dots and their photoluminescence properties*

Highly uniform and ultra-dense arrays of 3D quantum dots in stoichiometrically complex semiconductor materials, such as InGaAsN can be fabricated by using

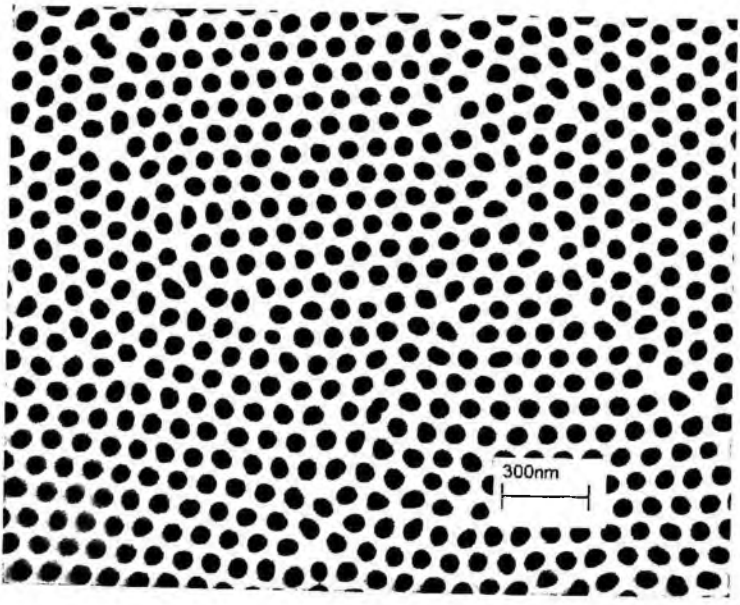

Figure 10. Top view SEM image of resultant GaN nanopore array.

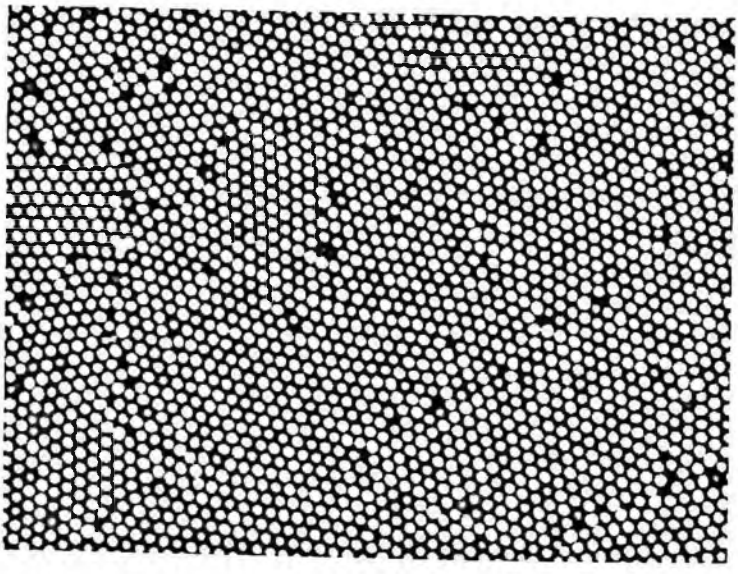

Figure 11. Top view SEM images of resultant GaN nanopillar array, the scale bar is 1.5 μm.

AAO nanotemplates. InGaAsN is a ternary semiconductor that has been proposed recently by Kondow [30] and that has attracted strong attention for its potential for applications in long wavelength communication lasers, optical switches and light detection systems. InGaAsN can be grown lattice matched with GaAs by adjusting

the N with the dislocation density. Significant improvement in the optical properties has been achieved by growing InGaAsN:Sb/GaAs quantum wells by MBE with the addition of Sb as a surfactant [31]. While the first realizations of QW LDs have been successful [32–33], better device performances, in particular, improved temperature stability and low current threshold, could be achieved by using quantum dots instead. Inter-sub-band transitions are another subject of interest in these systems [34]. In general, lattice-matched growth of InGaAsN QDs by the Stranski-Krastanov technique would not be possible, while in the case of lattice-mismatched formation it would be challenging and difficult to produce the level of uniformity, dense packing, and control in the stoichiometry required in achieving optimum optical characteristics. To overcome the aforementioned difficulties a new approach has been developed, based on the use of ceramic AAO templates. The idea is based on the processing of MBE grown high quality multiple-quantum well wafers into highly periodic 3D arrays of QDs.

For the proof of concept demonstration, a self-organized array of nanopore templates with through pore openings of 55 nm diameters was used to deposit a metal nanodot array on top of an MBE grown $In_{0.3}Ga_{0.7}$ $As_{0.992}$ $N_{0.008}$:Sb/GaAs multiple quantum well wafer, after which the nanopore template was ultrasonically removed in alcohol solution. Next, RIE was employed to selectively etch away the unmasked region of the GaAs wafer, as schematically shown in the flow diagram, Fig. 12. The etching of InGaAsN:Sb/GaAs quantum wells were done with BCl_3 gas under the following conditions: pressure of 15 mTorr, 100 W power and a gas flow rate of 20 sccm. The experimentally found etching rate was ~8 nm/min in this case.

The resultant structure is a hexagonal, periodic array of ~55 nm diameter, 6.7 nm thick InGaAsN:Sb quantum dots sandwiched between GaAs layers, as shown in the SEM top view image of the surface on Fig. 12. The diameter uniformity of

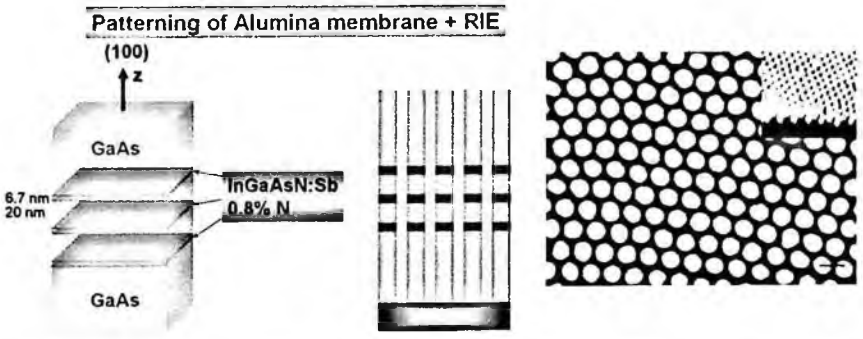

Figure 12. Schematic view of MBE grown InGaAsN:Sb/GaAs quantum wells before and after RIE processing by using anodic membrane template (left), and top surface SEM image of RIE etched InGaAsN:Sb/GaAs quantum dot pillar heterostructures. The inset shows an SEM image taken on tilted array. The scale bar is 100 nm. The length of the pillars is about ~250 nm, diameter 55 nm. (N Kouklin, H Chik, J Liang, M Tzolov, J M Xu, J B Heroux and W.I.Wang, J. Phys. D: Appl. Phys. 36 (2003) 2634–2638)

the pillars, and thus the quantum dots, lies within 10% of its mean value, therefore offering precise control over the dot diameter, periodicity, and density.

The photoluminescence spectra obtained on the InGaAsN:Sb/GaAs dots and unprocessed quantum wells show emission peaks centered at 0.96 eV and 1.01 eV respectively, Fig. 13. A minimum PL peak broadening demonstrates high size uniformity of the dots. An observed small 50 meV red shift in the peak position as opposed to an expected blue shift due to quantum confinement effects in QD systems is explained by the slightly increased concentration of the defects leading to a formation near band-edge defect states; the effect can be viewed similar to that of a temperature increase.

It is interesting to note that the emission from QDs scales up super-linearly with the laser intensity, yielding a slope between 1 and 2 on the log-log plot, implying an increased role of non-radiative recombination induced by increased defect concentrations in as-processed samples. At the same time, stronger hole localization (in the x-y plane) in the dots and PL polarization dependence have been attributed previously to observed good light emission efficiencies of the samples. Due to preferential absorption and emission of light polarized parallel to the pillars of small width/height ratio and big dielectric constant mismatch, stronger PL intensities can be obtained by exciting samples by performing excitation and detection normal to the pillars. This raises the strength of the emission/absorption matrix element, which is proportional to a local electric field and of the highest absolute value when the field is oriented along the pillar axis. This property can enable application of

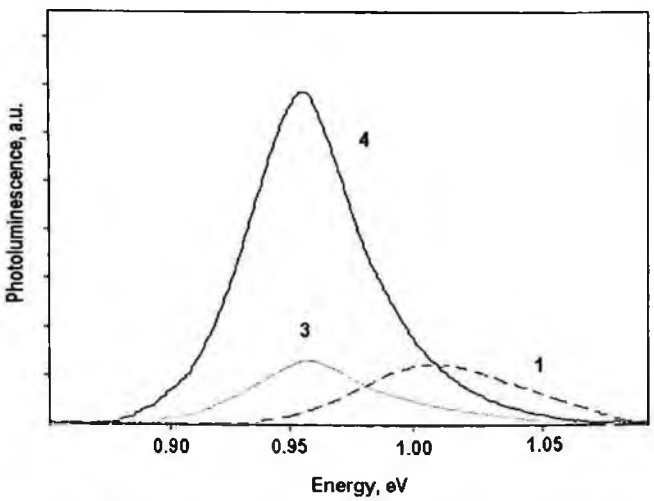

Figure 13. Base-line corrected PL-Raman spectra of Quatum Dots (3) and Quantum Wells (1) The QD peak position is ~50 meV red shifted compared to QW one. QD PL taken and excited normally to pillar axis (4) shows further increase in the integrated PL intensity. All spectra were excited with 1064 nm laser of 25 mW power, the collection spot was of 10 μm diameter.

the fabricated arrays in a polarization sensitive detection in the long-wavelength part of spectrum.

5.6. *Catalyst-assisted VLS growth of highly crystalline ordered arrays of ZnO nanorods*

The relentless drive of down-scaling of traditional electronics towards a new class of devices that operate faster, consume less power and cost less catalyzed development of new fabrication approaches to push beyond the limits of conventional lithography. The VLS mechanism, schematically presented in Fig. 14, has recently emerged as a primary route to a large-scale fabrication of highly crystalline nanowires in semiconductors and oxides. Compared with other approaches, the technique offers several important technological advantages, including fast growth rates, the possibility of direct diameter and length control, and lower cost. As shown, the growth undergoes the following stages: deposition of the catalyst such as Au, formation of binary alloy, the saturation of which results in self-driven growth of oxide crystals in the presence of oxygen.

Controlling the size and position of catalyst islands becomes critical to produce nanowires with reproducible electronic, optical, chemical and mechanical characteristics as the diameter of the nanowire is the same as the size of the solid-liquid interface. To overcome the problems with uncontrolled growth of nanowires and nanorods using VLS, it has been previously proposed to reduce the growth temperature and perform non-lithographic nano-patterning of the catalyst. In non-lithographic nano-patterning combined with VLS growth, an anodized aluminum

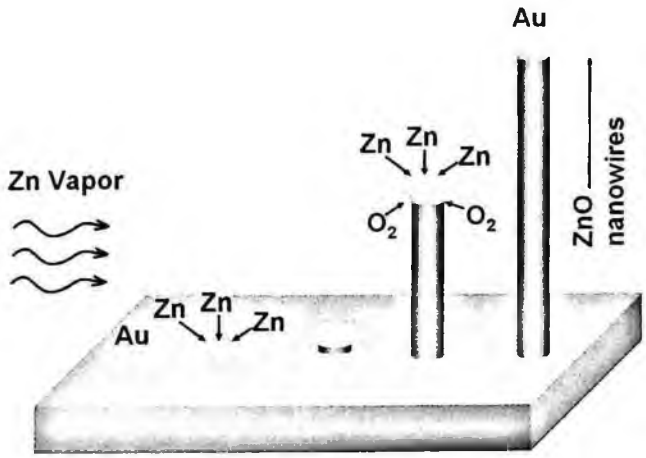

Figure 14. A catalyst-assisted VLS mechanism of ZnO nanorod growth, as shown from left to right: deposition of Au nanoparticle; formation of Au-Zn alloy at T > eutectic point; alloy oversaturated with Zn initiates growth of ZnO nanorod at solid-liquid interface.

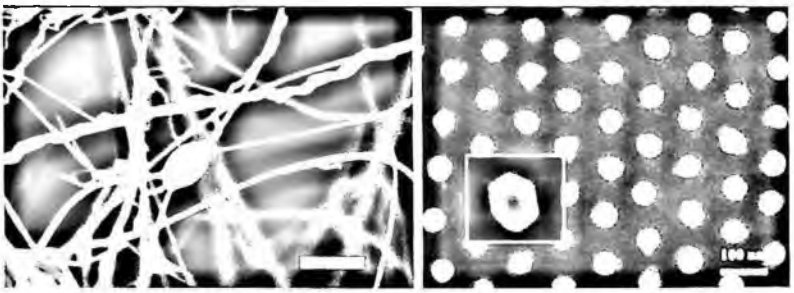

Figure 15. Top view SEM image of uncontrolled (left) and controlled (right) catalyst-assisted VLS growth of ZnO nanorods by combining top-down and bottom-up paradigms. The inset shows the hexagonal shape of the nanorods. The nanorods are ~2 um long.

oxide nanopore membrane is used as an evaporation mask for deposition of the Au catalytic nano-particle array. Figure 15 shows a SEM image of the resultant ZnO array produced by this approach. The detailed XRD, SEM, PL and TEM analysis have confirmed that ultra-dense arrays of single crystal, single diameter and length, uniformly positioned ZnO nanorods can be controllably and reproducibly fabricated on semiconductor substrates such as Sapphire or GaN.

The presence of a secondary broader PL band (Fig. 16) centered at 470 nm for ZnO nanowires grown on top of crystalline (001) Si substrate is attributed to the recombination of photo generated holes with the singly and doubly ionized oxygen

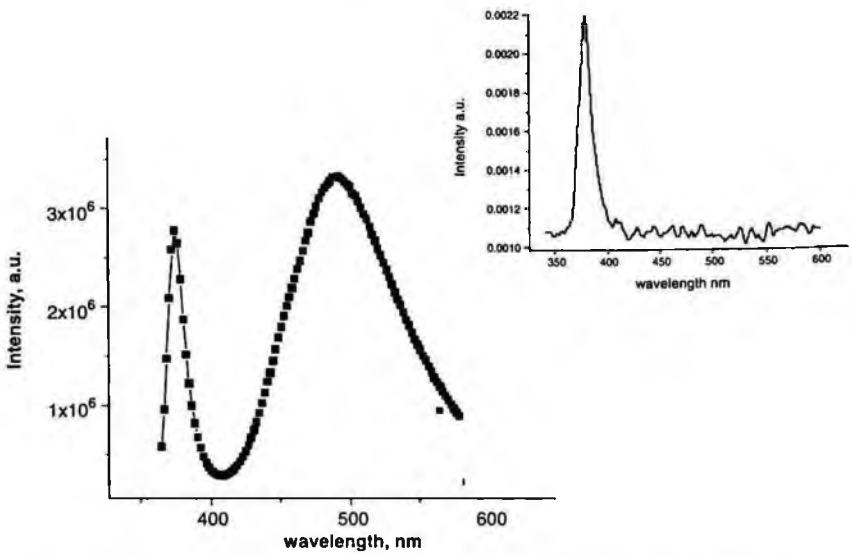

Figure 16. PL spectrum of ZnO nanorods grown on Si(100) showing a very narrow excitonic and broad defect induced visible peak; the inset shows PL spectrum of ZnO nanorods grown on GaN with only excitonic peak present.

vacancies in the ZnO crystal structure [33]. The absence of green emission from nanowires grown on a GaN substrate implies an improved crystal quality of ZnO provided with lattice matching growth conditions.

5.7. *Straight and Y-junction carbon nanotube arrays*

Since the pioneering work of Ijima in 1991, the carbon nanotubes (CNTs) have become a focus of many research efforts because of their unique electronic properties and ability to conduct electric current. These novel materials can potentially replace silicon electronics in the future, although low control in electronic characteristics along with unresolved architectural, interconnect and addressing issues still remain the main obstacles toward mass production of useful nanotube electronic devices in the near term. Here, we review the use of template-assisted method to grow arrayed CNTs as one of the solutions to those limitations, with their biggest impact anticipated on computer memory and logic device sectors. Based on the second order self-assembly technique, both Y-junction and straight cylindrically shaped CNTs can be synthesized predictably as easily accessible highly periodic two-dimensional arrays.

The synthesis of straight CNTs embedded in AAO templates can be accomplished by two different routes: by using a metal catalyst such Ni, Fe or Co or without it, the former has been found to yield nanotubes with fewer structural defects. Catalyst assisted growth is simply accomplished by electrodepositing metal at the bottom of the pores. The growth of the nanotubes is next accomplished by loading the templates into a high temperature Chemical Vapor Deposition (CVD) furnace where pyrolisis of CH_4 gas takes place. The process is schematically presented in Fig. 17.

The fabrication of Y-junction nanotube arrays is analogous to that of straight CNTS in AAO templates with the only difference being the use of templates with Y-shaped pores. The formation of Y-shaped channels is triggered by switching the voltage during the anodization of alumina. Because the pore cell diameter is proportional to the anodization voltage, reducing the voltage by a factor of $1/\sqrt{2}$ results in twice as many pores appearing in order to maintain the original total area of the template, and nearly all pores branch into two smaller-diameter pores. An SEM image of free standing CNT extracted from the template is presented in Fig. 18, confirming its Y-shape morphology and polycrystalline multi-walled structure.

The approach for growing Y-shape nanotubes is not only conceptually novel and interesting from the point of view of fabricating of novel nanomorphologies but also presents a platform for nanoelectronics device engineering. In contrast with the VLS based approaches to produce both n- and p-types of semiconductor nanowires by conventional doping, the diameter modulation of the nanotubes is the key to achieve the intrinsic diode functionalities with a number of advantages.

In particular, the arrays of Y-shaped CNTs that comprise different diameter tubes embedded into alumina feature the same level of periodicity, uniformity and

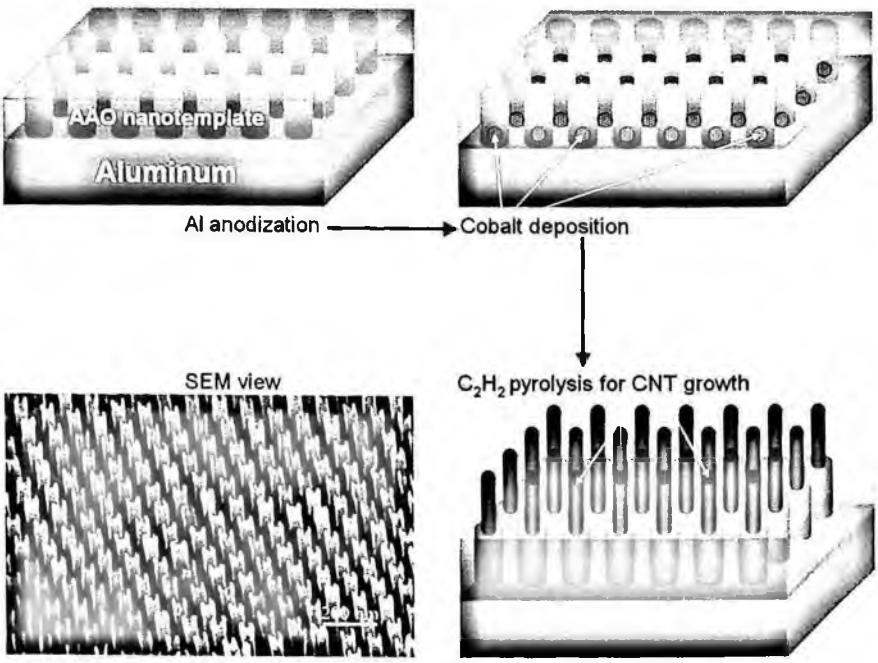

Figure 17. Schematics of catalyst-assisted CNT growth in AAO templates. Below, left a top view SEM image of CNT array is presented. Reprinted with the permission of [C. Papadopoulos, A. Rakitin, J. Li, A. S. Vedeneev, and J. M. Xu, Phys. Rev. Lett. 85, 3476-3479 (2000)].

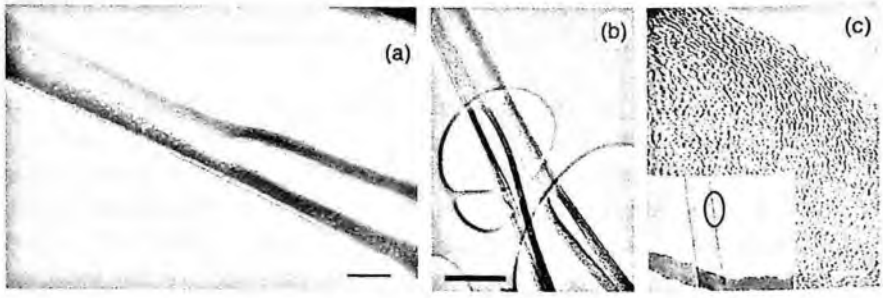

Figure 18. From left to right are shown SEM image of Y-CNT extracted from alumina, its low resolution image and high resolution TEM images. Reproduced with permission of Nature 402, 253–254 (1999).

packing density (by order of magnitude) as that of straight CNTs. Recent transport studies confirmed that single Y-CNTS after being removed from the surrounding alumina or in an array in the alumina matrix can exhibit intrinsic rectification (Fig. 19) similar to conventional diodes at room temperature, which is a highly desirable feature in nanoscale devices [35].

The planar array of Y-CNTs embedded in alumina template represents a 2D array of well-defined, spatially localized and self-insulated diodes with single element

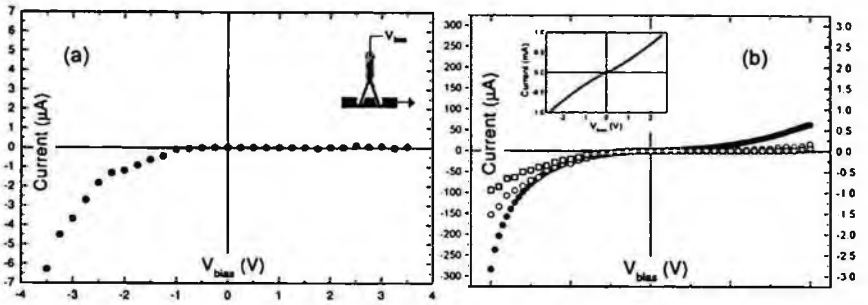

Figure 19. I-V characteristics of Y-CNTs showing rectifying nature (a) for a single isolated Y-junction nanotube of stem/branch (s/b) diameter ratio 50/35 nm (b) for a Y-CNT array of s/b ratio 60/40 nm with current increasing with the number of nanotubes involved. (b inset) for a straight tube array showing nearly linear characteristics. Reprinted with the permission of [C. Papadopoulos, A. Rakitin, J. Li, A. S. Vedeneev, and J. M. Xu, Phys. Rev. Lett. 85, 3476-3479 (2000)].

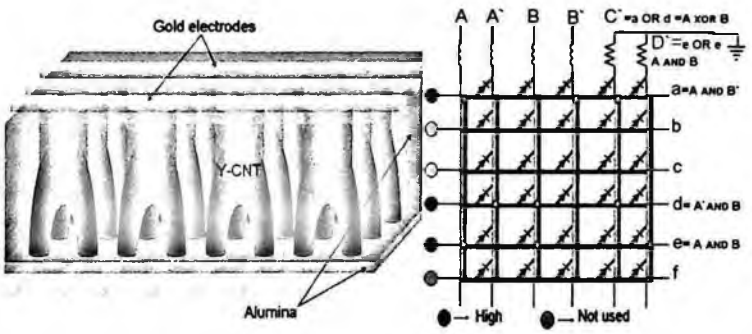

Figure 20. Shows a Y-junction diode array and an example of its use for computation, based on an diode array architecture for molecular electronics (HP-Labs).

access without any architectural complexity. Depending on the contact configurations AND / OR logic gates can be realized, while advancement from a single-device level to a circuit level can be adopted according to the schematics presented in Fig. 20.

6. Conclusion

A general discussion has been presented on the fabrication and use of self-assembled nanometric anodized alumina templates in a large scale and facile engineering of arrays of nano-electronic materials with precisely tailored sizes and arrangement. Combining the use of the nanopatterning techniques with other existing fabrication routes such as MBE, CVD, magnetron sputtering and VLS might enable new opportunities in synthesizing quality nanodots, nanowires and nanotemplates with novel functionalities for a variety of device applications. In general, the AAO based non-lithographic route might provide a low cost solution to many problems in the

emerging fields of Nanoscale Science and Technology as requiring precise and parallel integration of the resultant nano-structures into larger length scale multi-functional architectures. In the near term, the presented approaches should accelerate the conversion of nanotechnological paradigms and the development of new markets of affordable nano-electronic, nano-photonic, nano-mechanical and nano-sensing devices.

References

1. H. Masuda and K. Fukuda, Ordered Metal Nanohole Arrays Made by a Two-Step Replication of Honeycomb Structures of Anodic Alumina, *Science* **268**, 1466–1468 (1995).
2. K. Nielsch, R. B. Wehrspohn, J. Barthel, J. Kirschner, U. Gösele, S. F. Fischer and H. Kronmüller, Hexagonally ordered 100 nm period nickel nanowire arrays, *Appl. Phys. Lett.* **79** 1360–1362 (2001).
3. R. Karmhag, T. Tesfamichael, E. Wackelgard, G. A. Niklasson and M. Nygren, Oxidation Kinetics of Nickel Particles: Comparison between Free Particles and Particles in an Oxide Matrix, *Sol. Energy* **68** 329 (2000).
4. G. Che, B. B. Lakshmi, E. R. Fisher and C. R. Martin, Carbon nanotubule membranes for electrochemical energy storage and production, *Nature* **393** 346–349 (1998).
5. G. Che, B. B. Lakshmi, C. R. Martin, E. R. Fisher and R. S. Ruoff, Chemical vapor deposition based synthesis of carbon nanotubes and nanofibers using a template method, *Chem. Mater.* **10** 260–267 (1998).
6. Z. B. Zhang, D. Gekhtman, M. S. Dresselhaus and J. Y. Ying, Processing and Characterization of Single-Crystalline Ultra fine Bismuth Nanowires, *Chem. Mater.* **11** 1659–1665 (1999).
7. G. Sauer, G. Brehm, S. Schneider, K. Nielsch, R. B. Wehrspohn, J. Choi, H. Hofmeister and U. Gösele, Highly ordered monocrystalline silver nanowire arrays, *J. Appl. Phys.* **91** 3243–3247 (2002).
8. R. B. Wehrspohn, A. P. Li, K. Nielsch, F. Müller, W. Erfurth, U. Gösele, R. S. Lillard and B. R. MacDougall, *Eds., Electrochemical Society: Pennington*, PV-2000-4271 (2000).
9. H. Masuda, H. Amada, M. Atoh and H. Asoh, Highly ordered nanochannel-array architecture in anodic alumina, *Appl. Phys. Lett* **71**, 2770–2772 (1997).
10. A. P. Li, F. Müller and U. Gösele, Polycrystalline and mono crystalline pore arrays with large inter pore distance in anodic alumina, *Electrochem. Solid-State Lett.* **3**, 131–134 (2000).
11. O. Jessensky, F. Muller and U. Gösele, Self-organized formation of hexagonal pore arrays in anodic alumina, *Appl. Phys. Lett.* **72** 1173–1175 (1998).
12. G. Q. Ding, M. J. Zheng, W. L. Xu and W. Z. Shen, Fabrication of controllable free-standing ultrathin porous alumina membranes, *Nanotechnology* **16** 1285–1289 (2005).
13. J. Siejka and C. Ortega, An oxygen-18 study of field-assisted pore formation in compact anodic oxide films on aluminum, *J. Electrochem. Soc.* **124** 883–891 (1977).
14. Y. Xu, G. E. Thompson and G. C. Wood, Mechanism of Anodic Film Growth on Aluminum. (Retroactive Coverage), *Trans. Inst. Met. Finish.* **63** 98–103(1985).

15. K. Shimizu, K. Kobayashi, G. E. Thompson and G. C. Wood, *Philos. Mag. A* **66** 64(1992).
16. C. Y. Liu, A. Datta, N. W. Liu, C. Y. Peng and Y. L. Wang, Order-disorder transition of anodic alumina nanochannel arrays grown under the guidance of focused-ion-beam patterning, *Appl. Phys. Lett.* **84** 2509–2511 (2004).
17. G. Alcalá, P. Skeldon, G. E. Thompson, A. B. Mann, H. Habazaki and K. Shimizu, Mechanical properties of amorphous anodic alumina and tantala films using nanoindentation, *Nanotechnology* **13** 451-455 (2002).
18. X. Y. Zhang, C. W. Lai, X. Zhao, D. Y. Wang and J. Y. Dai, Synthesis and ferroelectric properties of multiferroic BiFeO3 nanotube arrays, *Appl. Phys. Lett.* **87** 143102 (2005).
19. P. Katiyar and D. Kumar, Magnetic properties of self-assembled nanoscale $La_{2/3}Ca_{1/3}MnO3$ particles in an alumina matrix, *Appl. Phys. Lett.* **78** 1327–1329 (2001).
20. S. Bandyopadhyay, N. Kouklin and L. Menon, "Device and circuit applications of electrochemically self-assembled quantum dots and wires", chapter in *"Quantum Dots and Nanowires", copyright ©American Scientific Publishers*, (2003).
21. Kolmakov, Y. Znang, G. Cheng and M. Moskovits, Detection of CO and O_2 Using Tin Oxide Nanowire Sensors, *Adv. Mater.* **15** 997–1000 (2003).
22. B. B. Lakshmi, P. K. Dorhout and C. R. Martin, Sol-Gel Template Synthesis of Semiconductor Nanostructures, *Chem. Mater.* **9** 857–862 (1997).
23. G. S. Wu, Y. Lin, X. Y. Yuan, T. Xie, B. C. Cheng and L. D. Zhang, A novel synthesis route to Y_2O_3:Eu nanotubes, *Nanotechnology* **15** 568–571 (2004).
24. M. S. J. Gani, "Electrophoretic Deposition–A Review," *Ind. Ceram.*, **14** 163–174(1994).
25. Y. C. Wang, I. C. Leu and M. H. Hon, Dielectric property and structure of anodic alumina template and their effects on the electrophoretic deposition characteristics of ZnO nanowires arrays, *J. Appl. Phys.* **95** 1444–1449 (2003).
26. Z. Miao, D. Xu, J. Ouyang, G. Guo, X. Zhao and Y. Tang, Electrochemically Induced Sol-Gel Preparation of Single-Crystalline TiO_2 Nanowires, *Nano Lett.* **2** 717–720 (2002).
27. J. J. Wu and S. C. Liu, Catalyst-Free Growth and Characterization of ZnO Nanorods, *J. Phys. Chem. B* **106** 9546–9551 (2002).
28. Y. Wang, S. Chua, M. Sander, P. Chen, S. Tripathy and C. Fonstad, Fabrication and properties of nanoporous GaN films, *Appl. Phys. Lett.* **85** 816–818 (2004).
29. Chang Hyun Bae, Seung Min Park, Sung Chan Park and Jeong Sook Ha, Array of ultraviolet luminescent ZnO nanodots fabricated by pulsed laser deposition using an anodic aluminium oxide template, *Nanotechnology* **17** 381–384 (2006).
30. X. F. Duan, Y. Huang, Y. Cui, J. F. Wang and C. M. Lieber, Indium phosphide nanowires as building blocks for nanoscale electronic and optoelectronic devices, *Nature*, **409** 66–69 (2001).
31. M. H. Huang, S. Mao, H. Feick, H. Q. Yan, Y. Y. Wu, H. Kind, E. Weber, R. Russo and P. D. Yang, Room-Temperature Ultraviolet Nanowire Nanolasers, *Science* **292** 1897–1899 (2001).
32. J. S. Wang and K. M. Lakin, c-axis inclined ZnO piezoelectric shear wave films *Appl. Phys. Lett.* **42** 352–354 (1983).
33. W. I. Park, G. C. Yi and H. M. Jang, Metalorganic vapor-phase epitaxial growth and photoluminescent properties of Zn1-xMgxO($0 < x < 0.49$) thin films, *Appl. Phys. Lett.* **79** 2022–2024 (2001).

34. K. Vanheusden, W. L. Warren, C. H. Seager, D. K. Tallant, J. A. Voigt and B. E. Gnade, Mechanisms behind green photoluminescence in ZnO phosphor powders, *J. Appl. Phys.* **79** 7983–7990 (1996).
35. M. Huang, S. Ma, H. Feick, H. Yan, Y. Wu, H. Kind, E. Weber, R. Russo and P. Yang, Room-Temperature Ultraviolet Nanowire Nanolasers, *Science* **292** 1897–1899 (2001).
36. C. Papadopoulos, A. Rakitin, J. Li, A. S. Vedeneev and J. M. Xu, Electronic Transport in Y-Junction Carbon Nanotubes, *Phys. Rev. Lett.* **85** 3476–3479 (2000).

CHAPTER 6

NANOWIRE ASSEMBLY AND INTEGRATION

ZHIYONG GU

Department of Chemical Engineering and UML Nanomanufacturing Center of Excellence, University of Massachusetts Lowell, One University Ave, Lowell, MA 01854, USA

DAVID H. GRACIAS*

Department of Chemical and Biomolecular Engineering and Department of Chemistry, Johns Hopkins University, 3400 N. Charles St, Baltimore, MD 21218, USA

Semiconducting, metallic and insulating nanowires are attractive building blocks in nanotechnology due to their small size and anisotropy. Moreover, it is possible to fabricate homogeneous or heterogeneous nanowires with high purity and crystallinity in a parallel and cost effective manner. Strategies have also emerged to position nanowires precisely on substrates to allow integration of nanoelectronic devices. In this chapter, we describe the fabrication and assembly of nanowires to form functional devices. Several fabrication strategies including vapor-liquid-solid (VLS) and electrodeposition in nanoporous templates are discussed. We detail advances made in the bottom-up integration of nanowires using patterned growth and directed assembly. Finally, some functional devices fabricated using nanowires are reviewed, and strategies to reduce errors and improve defect tolerance are discussed.

Keywords: Nanowire (NW); Nanotechnology; Self-assembly; Nano-soldering; Nanoelectronics; Directed assembly; Interconnects; Bottom-up assembly.

CONTENTS

1. Introduction 188
2. Nanowire (NW) Fabrication 189
   2.1. Vapor-liquid-solid (VLS) method 189

*Corresponding author: David H. Gracias, Department of Chemical and Biomolecular Engineering, Johns Hopkins University, 125 Maryland Hall, 3400 N. Charles Street, Baltimore, MD 21218, USA. E-mail: dgracias@jhu.edu

2.2. Solution phase synthesis 190
2.3. Electrodeposition in nanoporous templates 191
2.4. Electrospinning 191
3. Nanowire (NW) Assembly and Manipulation 192
3.1. Controlled or patterned growth 192
3.2. Self-assembly and directed assembly 192
3.2.1. Molecular/Bio-molecular linkers 193
3.2.2. Electrical field-assisted assembly (including DEP) 194
3.2.3. Magnetic assembly 194
3.2.4. Holographic optical traps 195
3.2.5. Langmuir-Blodgett technique 196
3.2.6. Surface tension (capillary forces) based assembly 196
4. Nanowire (NW) Integration 197
5. Nanowire (NW) Applications 199
5.1. Diodes and field effect transistors (FET) 199
5.2. Sensors 200
5.3. Photonics 200
5.4. Solar Cells 201
6. Defects and Errors 201
7. Conclusions and Perspective 204
Acknowledgments 204
References 204

1. Introduction

A nanowire is a nanoparticle whose diameter is much smaller than its length. Nanowires typically have diameters of 10-100 nm or less and lengths of 100 nm to tens of microns. Nanowires can be fabricated out of a wide range of materials including both inorganic and organic electrical conductors, semiconductors and insulators [1–13]. In contrast to other nanoparticle shapes such as polyhedra, rods and spheres, nanowires are long (length >> diameter); this length facilitates relatively easy integration with patterned micro and sub-micron device architectures. The high anisotropy in the properties of nanowires can also be an advantage in facilitating the propagation of electricity and light in specific spatial directions. Nanowires can also be fabricated with multiple heterogeneous segments, spaced precisely along the length of the nanowires. Nanowires have been fabricated of single crystal or amorphous materials, using a variety of methods. Functional devices such as diodes have also been fabricated within a single nanowire [14].

While a single nanowire device is itself a useful component, when positioned precisely on substrates, or when integrated with other nanowires, can result in integrated functional devices. Hence, the nanowire is often treated as a building

block that will be used to construct nanoelectronic, nanophotonic and nanofluidic devices. The idea of using building blocks to fabricate and integrate functional devices from the bottom-up is motivated by the fact that in recent years, the conventional lithographic scaling down of microelectronic, photonic and microelectromechanical systems (MEMS) to the 50–500 nm length scale has encountered severe challenges in the cost-effective, mass production of devices and integrated systems. Hence, there is an increasing need to develop new nano-fabrication technologies to address the challenges of decreasing dimensions, in order to enable the era of nanotechnology.

In this chapter, we review methods to integrate nanowires with each other and with substrates with the end goal of fabricating functional devices from the bottom-up. We will first review non-lithographic methods commonly employed to fabricate nanowires in a cost-effective and parallel manner. We will then discuss some approaches to assemble nanowires into integrated structures and devices. Finally, we will introduce several representative applications of integrated nanowire structures and devices, and some perspectives in the future assembly and integration of products and devices based on nanowires.

2. Nanowire (NW) Fabrication

Several non-lithographic methods are available to fabricate nanowires. The methods usually involve the spontaneous or templated growth of the nanowire using vapor or solution phase chemical reactions. In all cases, growth of the nanowire is directed preferentially along its long axis using chemical (e.g. a catalyst or surfactant) or physical (e.g. a porous membrane) methods. These methods are described below.

2.1. *Vapor-liquid-solid (VLS) method*

The vapor-liquid-solid (VLS) method for growing nanowires involves the chemical reaction between gaseous reactants and a liquid or molten catalyst to form nanowires on a solid substrate. VLS is the most attractive method for growing high purity, single crystal nanowires. As can be seen in Fig. 1(a), the three stages in the VLS growth mechanism are alloying, nucleation and axial growth [15]. The nanowires produced generally have alloy droplets on their tips. The example shown in Fig. 1(b) typifies the process which includes a solid catalyst that forms an alloy with a gaseous reactant at elevated temperatures. The alloy then becomes supersaturated with the reactant, which causes nucleation of the nanowire and preferential axial precipitation (growth) of the nanowire from the liquid alloy surface. Using this process, single crystal nanowires composed of silicon, germanium, ZnO, GaN, and SnO_2 have been fabricated [15–22]. Core-shell nanowires can also be fabricated by this method [23]. Other similar techniques, such as supercritical fluid-liquid-solid (SFLS) or supercritical fluid-solid-solid (SFSS) [24-26], and solution-liquid-solid (SLS) [27,28] methods have also been used to fabricate Si, Germanium, and CdSe nanowires.

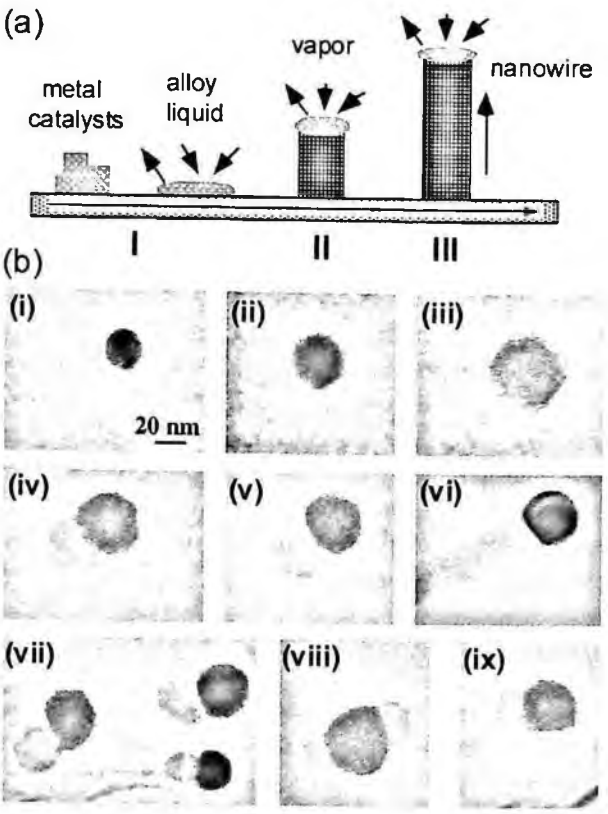

Figure 1. (a) Schematic of vapor-liquid-solid (VLS) germanium (Ge) nanowire growth mechanism including three stages (I) alloying, (II) nucleation, and (III) axial growth. (b) *In situ* TEM images recorded during the process of Ge nanowire growth. (i) Au nanoclusters in solid state at 500°C; (ii) alloying initiates at 800°C, at this stage Au exists in mostly solid state; (iii) liquid Au/Ge alloy; (iv) the nucleation of Ge nanocrystal on the alloy surface; (v) Ge nanocrystal elongates with further Ge condensation and eventually a wire forms (vi). (vii) Several other examples of Ge nanowire nucleation, (viii, ix) TEM images showing two nucleation events on single alloy droplet. Reprinted with permission from [15] by American Chemical Society.

2.2. *Solution phase synthesis*

This process involves the formation of nanowires from a liquid precursor, usually in the presence of a catalyst or molecular template [29–33]. One common example is the reduction of silver or gold salts in the presence of polymers or surfactants such as polyvinylpyrrolidone (PVP) or cetyltrimethylammonium bromide (CTAB). The surfactants adsorb preferentially on specific crystalline faces and enhance or inhibit growth along those faces, thereby resulting in the spontaneous growth of nanowires (along the planes in which growth is preferred). In certain cases, solid crystalline seeds are also added to the solution, to initiate preferential axial growth along specific crystal faces. As an example, gold nanorods were prepared by the addition of ~4 nm gold nanospheres as seeds and the subsequent reduction of metal salt with

a weak reducing agent (ascorbic acid) in the presence of a surfactant to produce nanorods. By adding another component such as ascorbic acid, metal was preferentially deposited at the ends of the rods to from Dog-bone like nanowires [34]. In solution, a variety of parameters such as temperature, concentrations and surfactants can be varied to gain some control over the type of nanowires formed.

2.3. *Electrodeposition in nanoporous templates*

This method employs physical templates to direct the growth of nanowires within nanoporous membranes [35–41]. Nanoporous membranes are fabricated using track etching or anodic electrochemical methods; these membranes are also commercially available with pore sizes ranging from 15 nm to 500 nm and membrane thickness up to 60 μm. Briefly the process (Fig. 2[a]) involves sealing one face of the membrane with a conductive seed layer. This seed layer is usually deposited onto the membrane using thermal or sputter evaporation. Single segment or multisegmented nanowires are then deposited in the membrane using an electrolytic solution containing the appropriate ions. The seed layer and a counter electrode immersed in the solution form the electrolytic cell. The length of the segments within the nanowires is restricted by controlling the current density or voltage, and the duration of electrodeposition process. Electrodeposition in templates is the most attractive method to fabricate nanowires with multiple segments (Fig. 2[b]) and theoretically can be used to fabricate nanowires composed of any material that can be electrodeposited.

2.4. *Electrospinning*

Electrospinning is a simple and efficient way to produce polymeric nanowires, also called nanofibers. The basic set-up utilizes a syringe through which polymer

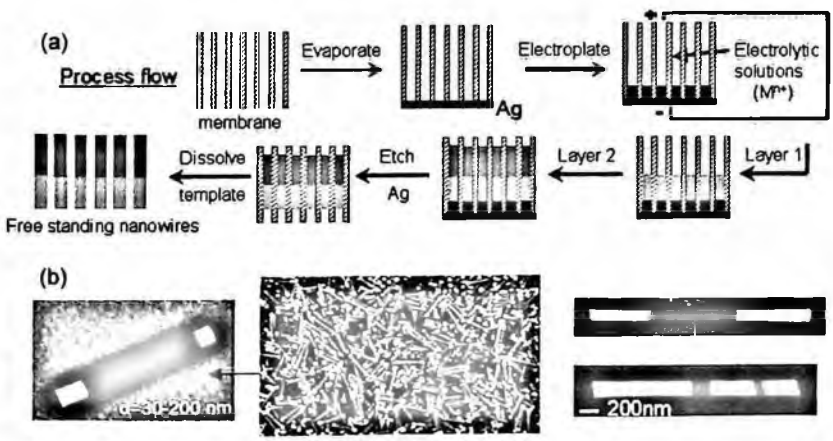

Figure 2. (a) Schematic of nanowire fabrication process using electrodeposition in nanoporous templates. (b) several examples of fabricated multisegment nanowires.

solutions are driven; their surface tension at the tip, under high electric field, can be overcome resulting in the ejection of a charged jet. The electrical forces elongate the jet thousands or even millions of times and the jet becomes very thin, down to nanoscale. After the solvent evaporates, or the melt solidifies, long polymeric nanofibers can be collected on an electrically grounded metal sheet. As compared to other fabrication methods, electrospinning facilitates the formation of extremely long nanowires with well controlled curvature [42–49].

There are other non-lithographic methods that are used to fabricate nanowires including laser ablation and directed growth along step edges or crystal planes [50]. Nanowires can also be fabricated by stringing together particles using dielectrophoresis or biomolecules (viruses) [51–54]. In all cases however the anisotropic growth of the nanowire occurs as a result of preferential growth of a material along one axis.

3. Nanowire (NW) Assembly and Manipulation

Although it is possible to manipulate and position nanowires using nanoscale tools such as scanning probe microscopes [55], these processes are serial, slow and expensive. Hence, strategies need to be developed either to directly integrate the growth of nanowires to form the final device, or to assemble nanowires into functional devices. These strategies or processes need to be highly efficient (high speed and low cost), in order to enable a manufacturable nanoscale process.

3.1. *Controlled or patterned growth*

Since a number of processes used to grow nanowires involve a catalyst or a template, it is conceivable that by patterning the catalyst or template directly on a substrate, it will be possible to grow the nanowires at specific spatial locations so that they grow out of the substrates in specific directions (see Fig. 3[a–b]) [56–72]. This is an attractive strategy that has been explored to form nanoscale vertical or horizontal interconnects. In these cases, the growth of the nanowires occurs between two patterned microstructures and in doing so, the nanowires electrically connect with the substrates (see Fig. 3[c–e]).

3.2. *Self-assembly and directed assembly*

Recently, the strategy of directed assembly has emerged as a highly parallel, cost-effective fabrication methodology that is capable of generating fully 3D structures and integrated systems. Directed assembly of engineered structures is inspired by biological self-assembly; nature is able to mass produce a wide variety of complex 2D and 3D structures with sizes ranging from the sub-nanometer to the millimeter and beyond [73–77]. This methodology involves tumbling chemically patterned components in a fluidic medium, so that they can interact with each other, and form

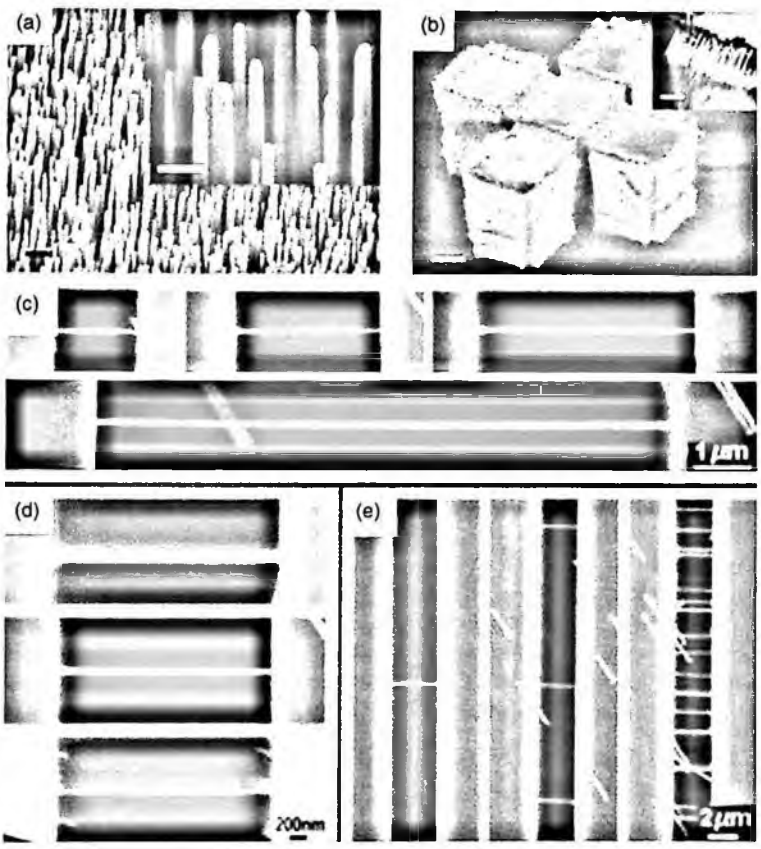

Figure 3. (a) SEM images of vertically aligned Si nanowire arrays grown from Au clusters deposited on Si(111) substrates. Scale bar is 30 nm (b) Laterally aligned Si nanowire arrays grown on Si pillars bounded by (111) sidewalls fabricated on (110) silicon-on-insulator (SOI) substrates. (a) and (b) reprinted with permission from [71] by American Chemical Society. (c) (d) and (e) Control of length (c), diameter (d) and density (e) of Si nanowires in microtrenches. Reprinted with permission from [64] by Wiley.

stable structures with precise function. The chemical patterning of components is engineered using a variety of forces that direct the orientation and binding of the components. This manufacturing paradigm has been largely unexplored in human engineering since the process is generally perceived to be indeterministic and uncontrollable. There are several strategies that have been explored in the past decade to direct the assembly of nanowires with each other and with substrates. We now review some of these strategies.

3.2.1. *Molecular/Bio-molecular linkers*

It is possible to direct the assembly of nanowires using molecular linkers that form chemical bonds with each other. The molecular linkers are first attached to the

nanowires by exposing the nanowires to them (either in solution or vapor phase). Since there are a large variety of molecules that specifically bind to each other such as ligands and receptors, it is possible to incorporate a high degree of specificity to the assembly process. Several groups have also utilized biological molecules such as proteins, DNA, and even viruses to link nanoparticles together in complex architectures [78–86]. The advantage of using biological molecules to direct assembly is that they exhibit complex architectures that facilitate lock-key based recognition, cooperativity and hierarchy.

3.2.2. *Electrical field-assisted assembly (including DEP)*

Dielectrophoresis (DEP) is the motion of neutral particles under the influence of an external non-uniform electric field [87]. DEP arises when the neutral particles get polarized and experience different forces at the ends of the polarized dipole as a result of the non-uniform electric field experienced at these ends. The difference tends to force the polarized particles into regions of differing field strength. Pohl [87] outlines the case of a cylinder of radius a and length L; the force experienced (assuming the cylinder is initially at right angles to the applied field) can be approximated as,

$$F_{\text{cylinder}} = \pi a^2 L \frac{\varepsilon_1[\varepsilon_2 - \varepsilon_1]}{\varepsilon_2 + \varepsilon_1} \nabla |E|^2$$

where E is the magnitude of the field and ε_2 and ε_1 are the dielectric constants of the cylinder and medium, respectively. DEP requires relatively high field strengths and this required field strength depends on the difference in dielectric constant between the particle and medium in which DEP is being carried out. In media of low dielectric constant ($\varepsilon = 2-7$) this is of the order 10^4 V/m, whereas in media of high dielectric constant (water, $\varepsilon \sim 80$) lower fields (500 V/m) are adequate. These fields are easily achievable in microscale gaps even at small voltages, due to high field strengths and can be used to direct the assembly of nanowires. The nanowires are typically suspended in a solvent over contact pads across which a voltage is applied. The nanowires then move, experiencing a force that causes them to orient on the substrates relative to the contact pads. By changing the solvent, aspect ratio of the nanowires, geometry and spacing between the electrodes, and the frequency and field strength it is possible to direct both reversible and irreversible assembly of nanowires in a variety of architectures (Fig. 4) [88–98]. The advantages of DEP are that the strategy can be scaled to the wafer level, such that the nanowires can be incorporated in parallel into many devices, with control over both placement and alignment.

3.2.3. *Magnetic assembly*

Magnetic force is another interaction that can be utilized to assemble and integrate nanowires. In order to facilitate magnetic assembly, either segments within

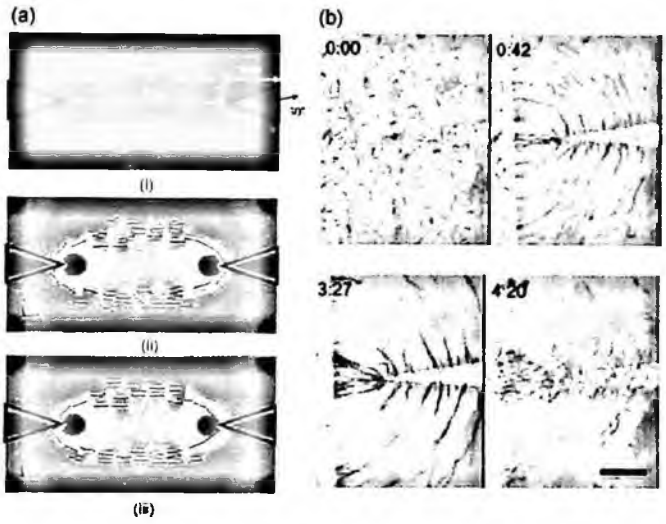

Figure 4. (a) Sequential images of nanowires lining up between triangular-shaped electrodes (angle: 30°). AC field of 5 MHz (0.5V/μm) is applied between electrodes. (i) $t = 0$ s; (ii) $t = 0.5$ s; (iii) $t = 1.0$ s. Reprinted with permission from [96] by American Chemical Society. (b) Reversible silver (Ag) nanowire network formation from a suspension in water, with DEP at 0.2 V and 100 kHz. The frames are labeled with the time (min:s) after the first frame. The first frame is taken just before initiation of DEP, and the third frame is taken just before ending DEP. The scale bar corresponds to 30 μm. Reprinted with permission from [95] by American Institute of Physics.

the nanowire or the entire nanowire itself is constructed from ferromagnetic constituents such as nickel, iron, cobalt or alloys. When magnetized, these segments act like small magnets and orient themselves in an external magnetic field such that the energy is minimized. The nanowires interact with each other and with magnetic substrates such that they assemble into bundles and end to end networks [99–106]. Magnetic forces can also be used to precisely position nanowires on substrates.

3.2.4. *Holographic optical traps*

In this approach, nanowires are dispersed in a fluidic medium on the stage of a light microscope and manipulated by either single or multiple diffraction-limited-optical traps using a holographic optical tweezer. Optical tweezers utilize focused laser beams to apply a radiation force on particles, in order to trap and manipulate them. Optical traps are attractive for nanowire assembly since they can be used to manipulate nanowires in closed chambers with high spatial accuracy (<1 nm); they also are applicable to a wide range of materials. While manipulation with a single optical beam is a serial process, recently *Grier's* group has demonstrated that holographically projected arrays of optical traps can be used to manipulate nanowires in parallel and that semiconductor nanowires can even be rotated, cut and fused to assemble complex structures in 3D using holographic optical traps [107,108].

3.2.5. *Langmuir-Blodgett technique*

The Langmuir-Blodgett method uses the compression of nanowires (capped with surfactants) at a liquid interface, followed by transfer onto solid substrates. Nanowires, capped with surfactants are first dispersed in a fluidic medium, the surfactants cause the wires to float at the fluid-air interface. Solid barriers surrounding the nanowires are made to approach each other in a highly precise and well-controlled manner; the barriers compress the nanowires at the interface causing them to rotate, align and form closed packed ordered arrays. The main highlight of this technique is that it is possible to form ordered arrays of nanowires as large as tens of centimeters in a relatively straightforward manner [109–114].

3.2.6. *Surface tension (capillary forces) based assembly*

Although the aforementioned strategies have been very successful in directing the assembly of nanowires into 2D and 3D integrated structures, in many cases, the structures formed are not permanently bonded to one another, i.e. the assemblies although held together in the fluidic medium in which they are assembled, fall apart when taken out of the medium or during mild sonication. Additionally, in directed assembly between rigid nanocomponents, the strength and the extent of binding is proportional to the overlap area at the binding site between components. Any local roughness of the components (especially when the size approaches 100 nm) reduces the effective binding contact area due to asperities, and consequently decreases the strength and extent of binding. Hence, assemblies often consist of only a few bonded nanocomponents, and large scale integration is extremely challenging. It should be noted that in biological self-assembly, most of the components utilized in the assemblies are soft and deformable which allows the mating surfaces to conform to one another resulting in large contact areas for optimum binding.

Surface tension based assembly involves (i) modification of the surface energy of specific segments of the nanowires using *hydrophobic* organic molecules that attached preferentially to specific segments, (ii) precipitation of a *hydrophobic* or *hydrophilic* liquid layer on the modified segments, and (iii) agitation of the nanowires in a *hydrophilic* or *hydrophobic* medium to facilitate favorable interactions between nanowires, and direct the assembly process. When nanowires patterned with *hydrophobic* liquid layers collide with one another in a hydrophilic liquid, there is a tendency of the liquid layers on different nanowires to fuse with one another on contact, in order to minimize their surface free energy. This surface tension force between liquid layers on colliding nanowires is large enough to hold the wires together in the liquid [115,116]. Since this kind of assembly involved binding between liquid layers (that are soft and deformable) patterned on the nanowires, the roughness of the nanowires does not hamper binding and it is possible to accomplish large scale integration. By patterning different hydrophilic and hydrophobic

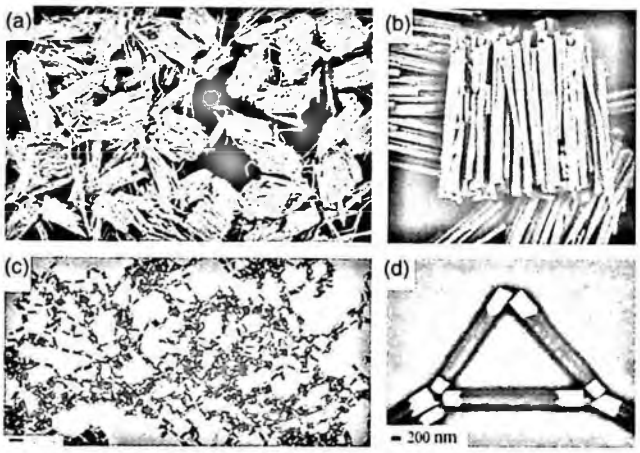

Figure 5. SEM images of (a) and (b) large-scale three-dimensional (3D) Au nanowire bundles bonded by polymeric adhesive. SEM images of (c) large-scale 2D Au-nickel (Ni)-Au nanowire networks and (d) a triangle structure showing end-to-end nanowire connection. (a) Reprinted with permission from [116] by The Minerals, Metals & Materials Society, and (b–d) reprinted with permission from [115] by American Chemical Society.

segments on the nanowire, and precipitating a polymerizable adhesive, it is possible to direct the assembly of nanowires into permanently bonded bundles or 2D end-to-end networks (see Fig. 5).

4. Nanowire (NW) Integration

In order to fabricate a functional device using nanowires, it is often necessary to integrate the nanowires with other components such as contact pads and silicon substrates. It is important to note that although nanoscale components are attractive because their small size facilitates higher packing densities and enhanced functionality, actual devices tend to be on the macroscale (i.e. the scale of the human world). It is thus necessary to interface nanoscale components with micro and finally macroscale components in a hierarchical manner, so that the devices may be functional on the macroscale.

The semiconductor industry has utilized a top-down lithographic approach using patterning, etching, thin film deposition and polishing to fabricate devices with nanowires [117]. In this chapter we do not review this top-down approach, but will mention that there are limitations in terms of the cost-effective, parallel fabrication of devices with nanowires.

There are numerous strategies to integrate nanowires with microfabricated contact pads from the bottom-up. These involve direct growth, imprinting or directed assembly. For electrical devices, after assembly it is often necessary to form a robust electrical contact. When gold contacts are used, this can be done by annealing as gold diffuses relatively easily. However, for other materials this may not be possible.

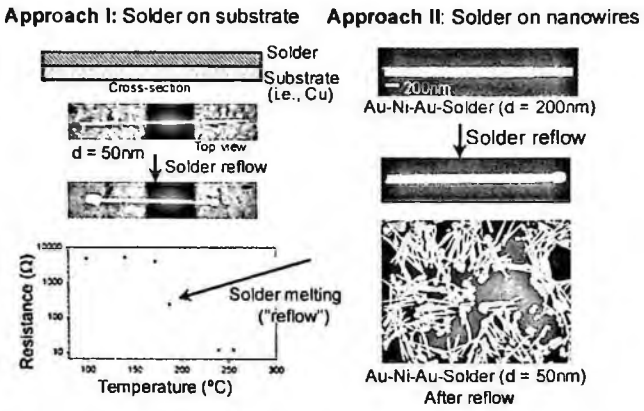

Figure 6. Schematic and SEM images showing two approaches to enable nanoscale soldering. SEM images are reprinted with permission from [105] by the Institute of Electrical and Electronics Engineers, Inc., from [116] by The Minerals, Metals & Materials Society, and from [118] by Wiley.

Our group has focused on investigating and developing the use of solder (low melting point metal or metal alloy) on the nanoscale to form electrical contacts. Soldering technology is one of the most widely used and dominant methods for microelectronics and device integration. Basically our strategy involves the fabrication of nanowires with solder deposited in regions where a robust electrical contact is needed. Figure 6 shows two basic approaches that can be used to solder nanowires to substrates and with each other to form electrically interconnected ordered structures or devices. The first approach is to directly put nanoscale solder onto the substrate, normally through electrodeposition, and then integrate (solder) functional nanowires onto the substrate to form robust electrical contact. Another approach is to fabricate nanoscale solder segments directly onto nanowires, and then solder them at the desired location. Solder reflow (melting) can be carried out in an inert atmosphere to bond nanowires to substrates or to each other, and it may even be

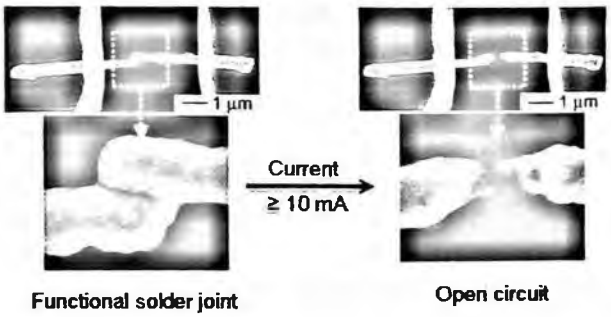

Figure 7. SEM images of contact pads patterned on top of fused nanowires, connected by a solder joint, before (left) electrical testing and after (right) applying a current of approximately 10 mA across the contact pads. The high current caused a break between the nanowires and resulted in an open circuit. Reprinted with permission from [118] by Wiley.

done in a fluidic medium [105,116,118]. When a high current is applied to a functional (electrically-conductive) solder joint, the local heat effect breaks the solder joint resulting in an open circuit (electrically non-conductive), thereby acting as a nanoscale "fuse" (see Fig. 7). These features of nanoscale soldering can be utilized to integrate nanowires into practical devices. As compared to macroscale soldering, however, extra care must be taken to minimize corrosion, diffusion and oxidation of the solder segments during the process.

5. Nanowire (NW) Applications

5.1. *Diodes and field effect transistors (FET)*

Homogeneous semiconducting nanowires have been used as the active semiconductor material and have been integrated within field effect transistor stacks. Since semiconducting nanowires are naturally thin (as well as single crystalline), they eliminate the need for patterning of the active semiconductor layer in these devices. However, considerable lithography is required to integrate these semiconducting nanowires within devices. Recently, the fabrication of nanowire heterostructures has allowed the inclusion of semiconductors, dielectrics and metals within the same nanowire. Park *et al* have fabricated nanowire diodes by electrodepositing segmented nanowires composed of Au-polypyrrole (Ppy)-Cadmium (Cd)-Au [14]. In this case, the nanowire contains the semiconductor and metallic constituents within the same nanowire. Current voltage (I-V) measurements on devices constructed from single Au-Ppy-Cd-Au rods exhibited diode behavior at room temperature (see Fig. 8(a)) [14]. Kovtyukhova *et al* have fabricated nanowires containing semiconducting, metallic as well as insulators to fabricate nanowire transistors [119]. These nanowires composed of metallic Au source and drain electrodes, the CdS (Se) semiconductor and the SiO_2 gate dielectric. The coaxially gated in-wire CdS and CdSe nanowire transistors were fabricated in nanoporous templates using a combination

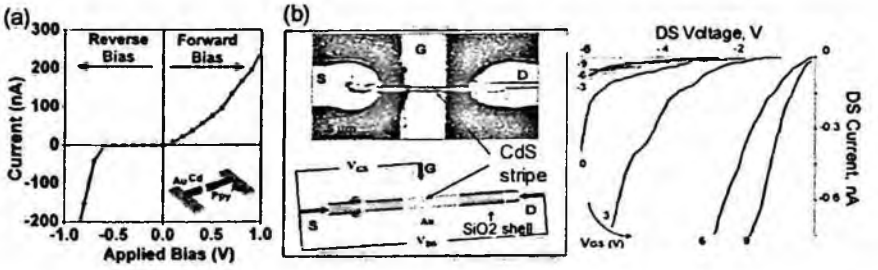

Figure 8. (a) I-V characteristics of a single Au-polypyrrole (Ppy)-cadmium (Cd)-Au nanowire at room temperature. Reprinted with permission from [14] by American Chemical Society. (b) Optical micrograph and schematic drawing of the test structure and a Au/CdS/Au@(SiO_2) nanowire aligned for measurement of electrical properties. Letters S, D and G indicate source, drain and gate electrodes, respectively. The curve shows typical $I_{DS} - V_{DS}$ characteristics of in-wire TFTs for different values of gate voltage (V_{GS}). Reprinted with permission from [119] by American Chemical Society.

of surface sol-gel and electrochemical deposition techniques (Fig. 8(b)). The I-V characteristics of the devices showed a field effect, which was more pronounced at negative drain voltages (See Fig. 8(b)). Other efforts have also been made to fabricate nanowire-based diodes and field-effect-transistors [120–124].

5.2. *Sensors*

Since the diameters of nanowires are small and often comparable to the size of biological and chemical species being sensed, their properties are often dramatically affected on adsorption of certain analytes [125–127]. The electronically switchable properties of semiconductor nanowires offer the possibility for a direct and label-free electronic readout. Sensors with changes in electronic responses are attractive since they can be readily used to trigger alarms, LEDs, readouts etc. *Lieber's* group has pioneered the use of semiconducting nanowires for sensing using a field effect transistor (FET) configuration [128–131]. In the FET, the semiconducting nanowire (with a diameter as small as 2 nm) is placed on top of a gate dielectric (and gate) and bridges source and drain electrodes. The one dimensional morphology of the nanowire ensures that the adsorption of an analyte at the surface of the nanowire leads to large changes in carrier mobility since the surface of the nanowire forms a large fraction of the bulk of the nanowire. Using this strategy, pH, protein, DNA and virus sensors have been fabricated with extremely high sensitivity e.g. electrical detection of 10fM concentration of DNA. For detection of biological moieties such as viruses, it is sometimes necessary to functionalize the nanowire surface using molecular receptors such as antibodies. For example, virus solutions with concentrations of 10^{-18} M bound to p-type Si nanowire devices (modified with the monoclonal antibody for influenza) and produced well-defined discrete detectable conductance changes.

5.3. *Photonics*

Nanowires fabricated with III–V and II–VI direct band gap semiconductors have been used as building blocks to produce multicolor, electrically driven nanophotonic systems [132–140]. Moreover due to their anisotropic geometry, as noted by Duan *et al.* [136], when single crystal nanowires are used with flat ends, the nanowire itself can behave as a Fabry-Perot optical cavity with modes $m\frac{\lambda}{2n_1} = L$, where m is an integer and L is the length of the nanowire. Since the light is constrained to within the nanowire, the nanowires were noted [136] to function as efficient lasing structures. These nanowire lasers were demonstrated using an n-type CdS nanowire laser cavity assembled onto p-Si electrodes (see Fig. 9). The structure produced an n-CdS nanowire/p-Si heterojunction similar to a p-n diode that was used for injection. Images of room temperature electroluminescence produced in forward bias from these hybrid nanowire structures exhibited strong emission with narrow lasing lines. In reverse bias, nanowire light emitting diodes can function as photodiodes which were reported [139] to offer polarization dependent ultrasensitive detection

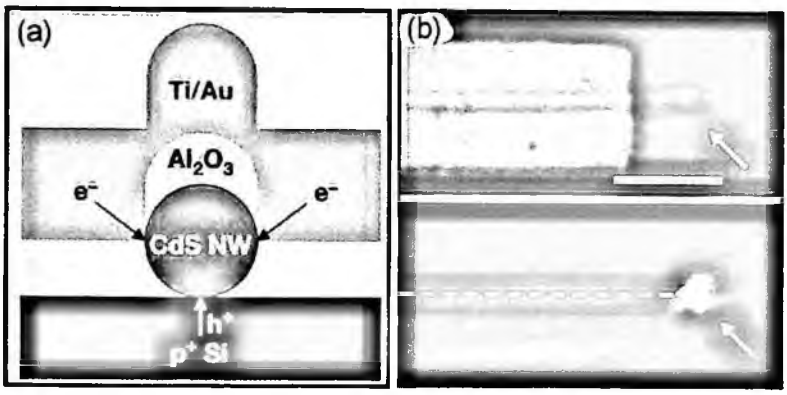

Figure 9. (a) Schematic showing the cross-section of a nanowire electrical injection laser. The devices were fabricated by assembling CdS nanowires on heavily doped p-Si on insulator substrates, followed by electron beam lithography and electron-beam evaporation of aluminium oxide, Ti and Au. One end of the nanowire was left uncovered for emission output from the device. (b) Top panel shows an optical image of a nanowire laser device. The arrow highlights the exposed CdS nanowire end. Scale bar is 5 μm. Bottom panel shows an electroluminescence image recorded from this device at room temperature with an injection current of about 80 mA. The arrow highlights emission from the CdS nanowire end. The dashed line highlights the nanowire position. Reprinted with permission from [136] by Nature Publishing Group.

limits of ~100 photons with unprecedented spatial resolution of 250 nm × 250 nm. As compared to planar devices, a clear advantage of nanowire-based optical structures is the ability to combine ultrapure, single crystalline materials to achieve the required device function. By varying the chemical composition of different nanowires materials and junctions it is possible to create nanoscale light emitting sources and detectors emitting at different wavelengths.

5.4. *Solar Cells*

Dense arrays of oriented, crystalline dye sensitized zinc oxide nanowires have been used to fabricate solar cells (see Fig. 10) [141]. As opposed to thick films of zinc oxide or nanoparticle films, the advantage of using a nanowire film includes high internal surface area and direct electrical connections between nanowires for efficient and rapid carrier collection in the device. The full Sun efficiency of 1.5% was demonstrated. A switch from particles to wires also improved the charge transfer rates at the dye-semiconductor interfaces, due to a high number of single crystal planes, accounting for 95% of the surface area of the wires.

6. Defects and Errors

One of the big issues in self-assembly is that the structures that result have defects in them. At the present time, since the methodology of self-assembly is still in its infancy, quantitative studies on yield and reliability of structures have largely been

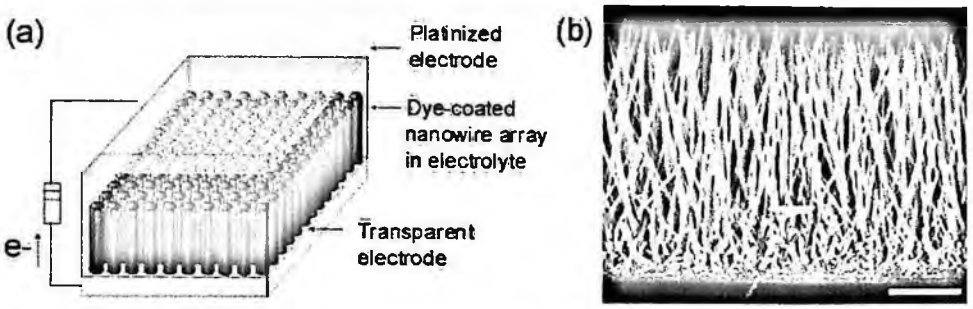

Figure 10. (a) Schematic of the nanowire dye-sensitized cell based on a ZnO nanowire array. Light is incident through the bottom electrode. (b) Typical SEM cross-section of a cleaved nanowire array on F:SnO_2 conductive glass (FTO). The nanowires are in direct contact with the substrate, with no intervening particle layer. Scale bar is 5 μm. Reprinted with permission from [141] by Nature Publishing Group.

ignored. As the methodology of fluidic assembly matures, it will be crucial that yields are quantified. Along with the identification of predominant defect modes, it is necessary to design assemblies that are inherently defect resistant. One strategy involves minimizing unfavorable interactions and maximizing favorable ones. In essence, it is necessary to design energy landscapes that are smooth, with a large funnel shaped global energy minimum, so that erroneous assemblies do not form as a result of the structure being trapped in a weak local minimum. An example of such a design was used in the demonstration of millimeter scale 3D networks by self-assembly [75]. In that case it was necessary to use patterns of solder dots on square faces of polyhedra to form electrical connections. Every pattern of solder dots results in a different energy landscape for the self-assembly. As an example, two patterns investigated are shown in Fig. 11 (a–b). The two patterns have four-fold rotational symmetry, but due to the enhanced local asymmetry of pattern *b*, a much smoother potential energy landscape results. When experiments were done with the pattern in Fig. 11(a), several erroneous attachments were observed including those in which only one dot on the mating faces was bonded. When patterns such as those in Fig. 11(b) were used, perfect assembly was obtained. A simulation of the energy landscape is shown in Fig. 11(c) [142]. There is a large global minimum and relatively weak local minima. It is believed that biological self-assembly such as protein folding, that occurs with incredible fidelity, is based on such funnel shaped potential energy landscapes.

It is possible to have structures function at the system level even in the presence of defects. For example, the fault tolerant system developed at Hewlett Packard [143] had 220,000 defects, demonstrating that it may be feasible to utilize and assemble chemical components with considerable defects, and still construct a functional computational network. Systems and architectures [143–146] that display this feature are called fault or defect tolerant. One of the easiest ways to incorporate defect tolerance into a system is to increase redundancy. This redundancy implies that

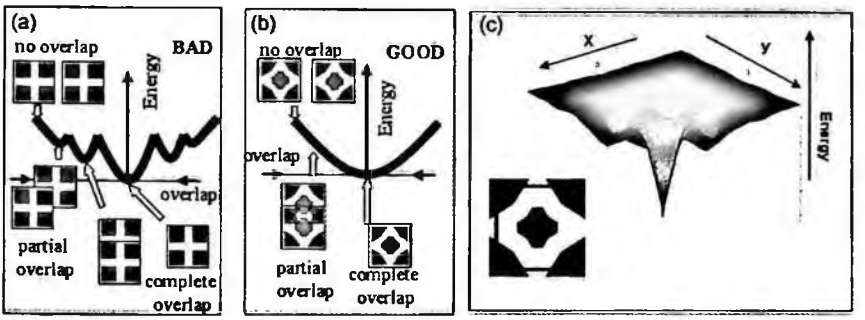

Figure 11. The design of energy landscapes for self-assembly that minimize errors. For binding between solder dots on square faces, a pattern of dots in (b) results in less errors than that shown in (a). This decrease in errors is due to the fact that the potential energy surface that results is smoother, with a larger global minimum and relatively weak local minima. (c) The actual surface energy plotted as a function of displacement in the plane of the pattern for assembly of two faces. Reprinted with permission from [142] by the Institute for Electrical and Electronics Engineers, Inc.. As can be seen, there exists a strong funnel shaped global minimum.

there exist multiple connections that serve the same function. Scale free network architectures are also inherently more robust and defect tolerant (see Fig. 12) [143].

Finally it is also possible to incorporate error correction schemes after integration using pick and place tools. However, it should be noted that this process will be serial and expensive.

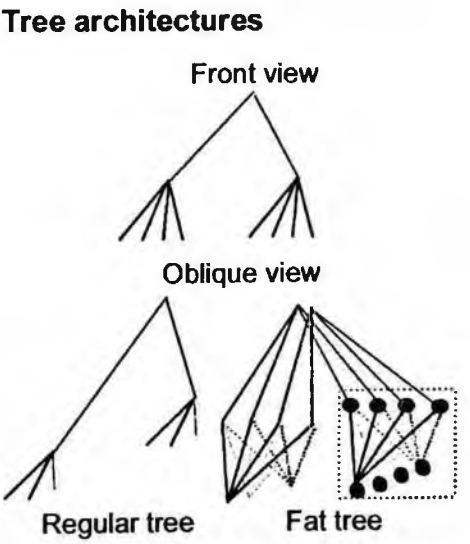

Figure 12. Schematic of a "fat tree" architecture. Reprinted with permission from [147] by The American Association for the Advancement of Science.

7. Conclusions and Perspective

In summary, nanowires are attractive building blocks for the fabrication of nanoscale electronics and devices. Various techniques are available for the facile fabrication of functional nanowire building blocks such as diodes and field effect transistors. Directed assembly and controlled growth are attractive bottom-up strategies to assemble the nanowires into functional devices. The critical challenges involve improving device to device variability, yields and defect tolerance. Moreover, studies need to be done to test reliability of these nanowire devices before they can be fully implemented. However, as an alternative to expensive top down methods for fabricating nanoscale devices, nanowire assembly and integration from bottom-up will continue to offer a promising alternative.

Acknowledgments

We are grateful the financial support from the National Science Foundation (CAREER Award), NSF-IIS and American Chemical Society Petroleum Research Foundation (ACS-PRF).

References

1. J. Hu, T. W. Odom and C. M. Lieber, Chemistry and physics in one dimension: synthesis and properties of nanowires and nanotubes, *Acc. Chem. Res.*, **32**, 435–445 (1999).
2. Y. Wu, H. Yan, M. Huang, B. Messer, J. H. Song and P. Yang, Inorganic semiconductor nanowires: rational growth, assembly, and novel properties, *Chem. Eur. J.*, **8**, 1260–1268 (2002).
3. N. I. Kovtyukhova and T. E. Mallouk, Nanowires as building blocks for self-assembling logic and memory circuits, *Chem. Eur. J.*, **8**, 4354–4363 (2002).
4. P. Yang, Y. Wu and R. Fan, Inorganic semiconductor nanowires, *Int. J. Nanosci.*, **1**, 1–40 (2002).
5. Y. Xia, P. Yang, Y. Sun, Y. Wu, B. Mayers, B. Gates, Y. Yin, F. Kim and H. Yan, One-dimensional nanostructures: synthesis, characterization, and applications, *Adv. Mater.*, **5**, 353–389 (2003).
6. C. Lieber, Nanoscale science and technology: building a big future from small things, *MRS Bull.* **28**, 486–491 (2003).
7. M. Law, J. Goldberger and P. Yang, Semiconductor Nanowires and Nanotubes, *Annu. Rev. Mater. Res.*, **34**, 83–122 (2004).
8. Z. L. Wang, Zinc oxide nanostructures: growth, properties and applications, *J. Phys.: Condens. Matter*, **16**, R829–R858 (2004).
9. Y. Huang and C. M. Lieber, Integrated nanoscale electronics and optoelectronics: exploring nanoscale science and technology through semiconductor nanowires, *Pure Appl. Chem.*, **76**, 2051–2068 (2004).
10. C. J. Murphy, T. K. Sau, A. M. Gole, C. J. Orendorff, J. Gao, L. Gou, S. E. Hunyadi and T. Li, Anisotropic metal nanoparticles: synthesis, assembly and optical Applications, *J. Phys. Chem. B*, **109**, 13857–13870 (2005).

11. P. Yang, The chemistry and physics of semiconductor nanowires, *MRS Bull.*, **30**, 85–91 (2005)
12. J. Goldberger, R. Fan and P. Yang, Inorganic nanotubes: a novel platform for nanofluidics, *Acc. Chem. Res.*, **39**, 239–248 (2006).
13. S. J. Hurst, E. K. Payne, L. Qin and C. A. Mirkin, Multisegmented one-dimensional nanorods prepared by hard-template synthetic methods, *Angew. Chem. Int. Ed.*, **45**, 2672–2692 (2006).
14. S. Park, S.-W. Chung and C. A. Mirkin, Hybrid organic-inorganic, rod-shaped nanoresistors and diodes, *J. Am. Chem. Soc.*, **126**, 11772–11773 (2004).
15. Y. Wu and P. Yang, Direct observation of vapor-liquid-solid nanowire growth, *J. Am. Chem. Soc.*, **123**, 3165–3166 (2001).
16. E. A. Stach, P. J. Pauzauskie, T. Kuykendall, J. Goldberger, R. He and P. Yang, Watching GaN nanowires grow, *Nano Lett.*, **3**, 867–869 (2003).
17. S. Sharma, T. I. Kamins and R. S. Williams, Diameter control of Ti-catalyzed silicon nanowires, *J. Cryst. Growth*, **267**, 613–618 (2004).
18. P. X. Gao and Z. L. Wang, Substrate atomic-termination induced anisotropic growth of ZnO nanowires/nanorods by VLS process, *J. Phys. Chem. B*, **108**, 7534–7537 (2004).
19. S. Sharma, T. I. Kamins and R. S. Williams, Synthesis of thin silicon nanowires using gold-catalyzed chemical vapor deposition, *Appl. Phys. A*, **80**, 1225–1229 (2005).
20. J. H. He, C. S. Lao, L. J. Chen, D. Davidovic and Z. L. Wang, Large-scale Ni-doped ZnO nanowire arrays and electrical and optical properties, *J. Am. Chem. Soc.*, **127**, 16376–16377 (2005).
21. I. Lombardi, A. I. Hochbaum, P. Yang, C. Carraro and R. Maboudian, Synthesis of high density, size-controlled Si nanowire arrays via porous anodic alumina mask, *Chem. Mater.*, **18**, 988–991 (2006).
22. J. H. He, T. H. Wu, C. L. Hsin, K. M. Li, L. J. Chen, Y. L. Chueh, L. J. Chou and Z. L. Wang, Beaklike SnO_2 nanorods with strong photoluminescent and field-emission properties, *Small*, **2**, 116–120 (2006).
23. L. J. Lauhon, M. S. Gudiksen, D. Wang and C. M. Lieber, Epitaxial core–shell and core–multishell nanowire heterostructures, *Nature*, **420**, 57–61 (2002).
24. T. Hanrath and B. Korgel, Supercritical fluid-liquid-solid (SFLS) synthesis of Si and Ge nanowires seeded by colloidal metal nanocrystals, *Adv. Mater.*, **15**, 437–440 (2005).
25. H.-Y. Tuan, D. C. Lee, T. Hanrath and B. A. Korgel, Germanium nanowire synthesis: an example of solid-phase seeded growth with nickel nanocrystals, *Chem. Mater.*, **17**, 5705–5711 (2005).
26. H.-Y. Tuan, D. C. Lee, T. Hanrath and B. A. Korgel, Catalytic solid-phase seeding of silicon nanowires by nickel nanocrystals in organic solvents, *Nano Lett.*, **5**, 681–684 (2005).
27. T. J. Trentler, K. M. Hickman, S. C. Goel, A. M. Viano, P. C. Gibbons and W. E. Buhro, Solution-liquid-solid growth of crystalline III-V semiconductors: an analogy to vapor-liquid-solid growth, *Science*, **270**, 1791–1794 (1995).
28. H. Yu, J. Li, R. A. Loomis, P. C. Gibbons, L.-W. Wang and W. E. Buhro, Cadmium selenide quantum wires and the transition from 3D to 2D confinement, *J. Am. Chem. Soc.*, **125**, 16168–16169 (2003).
29. N. R. Jana, L. Gearheart and C. J. Murphy, Wet chemical synthesis of silver nanorods and nanowires of controllable aspect ratio, *Chem. Commun.*, 617–618 (2001).

30. J. Gao, C. M. Bender and C. J. Murphy, Dependence of the gold nanorod aspect ratio on the nature of the directing surfactant in aqueous solution, *Langmuir*, **19**, 9065–9070 (2003).
31. Y. Sun, B. Mayers, T. Herricks and Y. Xia, Polyol synthesis of uniform silver nanowires: a plausible growth mechanism and the supporting evidence, *Nano Lett.*, **3**, 955–960 (2003).
32. C. Qian, F. Kim, L. Ma, F. Tsui, P. Yang and J. Liu, Solution-phase synthesis of single-crystalline iron phosphide nanorods/nanowires, *J. Am. Chem. Soc.*, **126**, 1195–1198 (2004).
33. T. K. Sau and C. J. Murphy, Seeded high yield synthesis of short Au nanorods in aqueous solution, *Langmuir*, **20**, 6414–6420 (2004).
34. L. Gou and C. J. Murphy, Fine-tuning the shape of gold nanorods, *Chem. Mater.*, **17**, 3669–3673 (2005).
35. C. R. Martin, Membrane-based synthesis of nanomaterials, *Chem. Mater.*, **8**, 1739–1746 (1996).
36. V. M. Cepak and C. R. Martin, Preparation of polymeric micro- and nanostructures using a template-based deposition method, *Chem. Mater.*, **11**, 1363–1367 (1999).
37. S. Demoustier-Champagne and P.-Y. Stavaux, Effect of electrolyte concentration and nature on the morphology and the electrical properties of electropolymerized polypyrrole nanotubules, *Chem. Mater.*, **11**, 829–834 (1999).
38. M. Steinhart, J. H. Wendorff, A. Greiner, R. B. Wehrspohn, K. Nielsch, J. Schilling, J. Choi and U. Gosele, Polymer Nanotubes by Wetting of Ordered Porous Templates, *Science*, **296**, 1997 (2002).
39. Y. Long, Z. Chen, N. Wang, Y. Ma, Z. Zhang, L. Zhang and M. Wan, Electrical conductivity of a single conducting polyaniline nanotube, *Appl. Phys. Lett.*, **83**, 1863–1865 (2003).
40. M. Chen, P. C. Searson and C. L. Chien, Micromagnetic behavior of electrodeposited Ni/Cu multilayer nanowires, *J. Appl. Phys.*, **93**, 8253–8255 (2003).
41. C. Ji and P. C. Searson, Synthesis and characterization of nanoporous gold nanowires, *J. Phys. Chem. B*, **107**, 4494–4499 (2003).
42. P. W. Gibson, H. L. Schreuder-Gibson and D. Rivin, Electrospun fiber mats: transport properties, *AIChE J.*, **45**, 190–195 (1999).
43. I. D. Norris, M. M. Shaker, F. K. Ko and A. G. MacDiarmid, Electrostatic fabrication of ultrafine conducting fibers: polyaniline polyethylene oxide blends, *Synth. Met.*, **114**, 109–114 (2000).
44. J. Kameoka and H. G. Craighead, Fabrication of oriented polymeric nanofibers on planar surfaces by electrospinning, *Appl. Phys. Lett.*, **83**, 371–373 (2003).
45. D. Li, Y. Wang and Y. Xia, Electrospinning nanofibers as uniaxially aligned arrays and layer-by-layer stacked films, *Adv. Mater.*, **16**, 361–366 (2004).
46. X. Lu, Y. Zhao, C. Wang and Y. Wei, Fabrication of CdS nanorods in PVP fiber matrices by electrospinning, *Macromol. Rapid Commun.*, **26**, 1325–1329 (2005).
47. X. Lu, D. Zhang, Q. Zhao, C. Wang, W. Zhang and Y. Wei, Large-scale synthesis of necklace-like single-crystalline PbTiO3 nanowires, *Macromol. Rapid Commun.*, **27**, 76–80 (2006).
48. K. H. Hong and T. J. Kang, Polyaniline–Nylon 6 composite nanowires prepared by emulsion polymerization and electrospinning process, *J. Appl. Polym. Sci.*, **99**, 1266–1286 (2006).
49. Y.-T. Jia, H.-Y. Kim, J. Gong and D.-R. Lee, Electrospun nanofibers of block copolymer of trimethylene carbonate and ε-caprolactone, *J. Appl. Polym. Sci.*, **99**, 1462–1470 (2006).

50. A. M. Morales and C. M. Lieber, A laser ablation method for the synthesis of crystalline semiconductor nanowires, *Science*, **279**, 208–211 (1998).
51. A. Kotlyar, N. Borovok, T. Molotsky, H. Cohen, E. Shapir and D. Porath, Long, monomolecular Gyanine-based nanowires, *Adv. Mater.*, **17**, 1901–1905 (2005).
52. S. Hou, J. Wang and C. R. Martin, Template-synthesized DNA nanotubes, *J. Am. Chem. Soc.*, **127**, 8586–8587 (2005).
53. Q. Gu, C. Cheng, R. Gonela, S. Suryanarayanan, S. Anabathula, K. Dail and D. T. Haynie, DNA nanowire fabrication, *Nanotechnology*, **17**, R14-R25 (2006).
54. K. T. Nam, D.-W. Kim, P. J. Yoo, C.-Y. Chiang, N. Meethong, P. T. Hammond, Y.-M. Chiang and A. M. Belcher, Virus-enabled synthesis and assembly of nanowires for lithium ion battery electrodes, *Science*, **312**, 885–888 (2006).
55. S. Hsieh, S. Meltzer, C. R. C. Wang, A. A. G. Requicha, M. E. Thompson and B. E. Koel, Imaging and manipulation of gold nanorods with an atomic force microscope, *J. Phys. Chem. B*, **106**, 231–234 (2002).
56. Y. Chen, D. A. A. Ohlberg, G. Medeiros-Ribeiro, Y. A. Chang and R. S. Williams, Self-assembled growth of epitaxial erbium disilicide nanowires on silicon (001), *Appl. Phys. Lett.*, **76**, 4004–4006 (2000).
57. Y. Chen, D. A. A. Ohlberg and R. S. Williams, Nanowires of four epitaxial hexagonal silicides grown on Si(001), *J. Appl. Phys.*, **91**, 3213–3219 (2002).
58. R. Ragana, Y. Chena, D. A. A. Ohlberga, G. Medeiros-Ribeirob and R. S. Williams, Ordered arrays of rare-earth silicide nanowires on Si(001), *J. Cryst. Growth*, **251**, 657–661 (2003).
59. P. Nguyen, H. T. Ng, J. Kong, A. M. Cassell, R. Quinn, J. Li, J. Han, M. McNeil and M. Meyyappan, Epitaxial directional growth of indium-doped tin oxide nanowire arrays, *Nano Lett.*, **3**, 925–928 (2003).
60. D. F. Moore, Y. Ding and Z. L. Wang, Crystal orientation-ordered ZnS nanowire bundles, *J. Am. Chem. Soc.*, **126**, 14372–14373 (2004).
61. T. L. Karmins, X. Li and R. S. Williams, Growth and structure of chemically vapor deposited Ge nanowires on Si substrates, *Nano Lett.*, **4**, 503–506 (2004).
62. M. S. Islam, S. Sharma, T. I. Kamins and R. S. Williams, Ultrahigh-density silicon nanobridges formed between two vertical silicon surfaces, *Nanotechnology*, **15**, 15–18 (2004).
63. T. Kuykendall, P. J. Pauzauskie1, Y. Zhang, J. Goldberger1, D. Sirbuly, J. Denlinger and P. Yang, Crystallographic alignment of high-density gallium nitride nanowire arrays, *Nature*, **3**, 524–528 (2004).
64. R. He, D. Gao, R. Fan, A. I. Hochbaum, C. Carraro, R. Maboudian and P. Yang, Si nanowire bridges in microtrenches: integration of growth into device fabrication, *Adv. Mater.*, **17**, 2098–2102 (2005).
65. X. Wang, J. Song, P. Li, J. H. Ryou, R. D. Dupuis, C. J. Summers and Z. L. Wang, Growth of uniformly aligned ZnO nanowire heterojunction arrays on GaN, AlN, and Al0.5Ga0.5N substrates, *J. Am. Chem. Soc.*, **127**, 7920–7923 (2005).
66. S. Sharma, T. I. Kamins, M. S. Islam, R. S. Williams and A. F. Marshall, Structural characteristics and connection mechanism of gold-catalyzed bridging silicon nanowires, *J. Cryst. Growth*, **280**, 562–568 (2005).
67. X. Wen, S. Wang, Y. Ding, Z. L. Wang and S. Yang, Controlled growth of large-area, uniform, vertically aligned arrays of r-Fe_2O_3 nanobelts and nanowires, *J. Phys. Chem. B*, **109**, 215–220 (2005).
68. J. Song, X. Wang, E. Riedo and Z. L.Wang, Systematic study on experimental conditions for large-scale growth of aligned ZnO nanwires on nitrides, *J. Phys. Chem. B*, **109**, 9869–9872 (2005).

69. A. I. Hochbaum, R. Fan, R. He and P. Yang, Controlled growth of Si nanowire arrays for device integration, *Nano Lett.*, **5**, 457–460 (2005).
70. L. E. Greene, M. Law, D. H. Tan, M. Montano, J. Goldberger, G. Somorjai and P. Yang, General route to vertical ZnO nanowire arrays using textured ZnO seeds, *Nano Lett.*, **5**, 1231–1236 (2005).
71. D. Gao, R. He, C. Carraro, R. T. Howe, P. Yang and R. Maboudian, Selective growth of Si nanowire arrays via galvanic displacement processes in water-in-oil microemulsions, *J. Am. Chem. Soc.*, **127**, 4574–4575 (2006).
72. J. H. He, J. H. Hsu, C. H. Wang, H. N. Lin, L. J. Chen and Z. L. Wang, Pattern and feature designed growth of ZnO nanowire arrays for vertical devices, *J. Phys. Chem. B*, **110**, 50–53 (2006).
73. G. M. Whitesides and M. Boncheva, Beyond molecules: self-assembly of mesoscopic and macroscopic components, *Proc. Nat. Acad. Sci. USA*, **99**, 4769–4774 (2002).
74. S. R. J. Oliver, N. Bowden and G. M. Whitesides, Self-assembly of hexagonal rod arrays based on capillary forces, *J. Colloid Interface Sci.*, **224**, 425–428 (2000).
75. D. H. Gracias, J. Tien, T. L. Breen, C. Hsu and G. M. Whitesides, Forming electrical networks in three dimensions by self-assembly, *Science*, **289**, 1170–1172 (2000).
76. H. O. Jacobs, A. R. Tao, A. Schwartz, D. H. Gracias and G. M. Whitesides, Fabrication of a cylindrical display by patterned assembly, *Science*, **296**, 323–325 (2002).
77. S. Park, J.-H. Lim, S.-W. Chung and C. A. Mirkin, Self-assembly of mesoscopic metal-polymer amphiphiles, *Science* **303**, 348–351 (2004).
78. J. K. N. Mbindyo, B. D. Reiss, B. R. Martin, C. D. Keating, M. J. Natan and T. E. Mallouk, DNA-directed assembly of gold nanowires on complimentary surfaces, *Adv. Mater.*, **13**, 249–254 (2001).
79. K. K. Caswell, J. N. Wilson, U. H. F. Bunz and C. J. Murphy, Preferential end-to-end assembly of gold nanorods by biotin-streptavidin connectors, *J. Am. Chem. Soc.*, **125**, 13914–13915 (2003).
80. Z. Deng and C. Mao, DNA-templated fabrication of 1D parallel and 2D crossed metallic nanowire arrays, *Nano Lett.*, **3**, 1545–1548 (2003).
81. A. K. Salem, J. Chao, K. W. Leong and P. C. Searson, Receptor-mediated self-assembly of multi-component magnetic nanowires, *Adv. Mater.*, **16**, 268–271 (2004).
82. A. K. Salem, M. Chen, J. Hayden, K. W. Leong and P. C. Searson, Directed assembly of multisegment Au/Pt/Au nanowires, *Nano Lett.*, **4**, 1163–1165 (2004).
83. A. Gole and C. J. Murphy, Biotin-streptavidin-induced aggregation of gold nanorods: tuning rod-rod orientation, *Langmuir*, **21**, 10756–10762 (2005).
84. Q. Zhang, S. Gupta, T. Emrick and T. P. Russell, Surface-functionalized CdSe nanorods for assembly in diblock copolymer templates, *J. Am. Chem. Soc.*, **128**, 3898–3899 (2006).
85. M. Chen, L. Guo, R. Ravi and P. C. Searson, Kinetics of receptor directed assembly of multisegment nanowires, *J. Phys. Chem. B*, **110**, 211–217 (2006).
86. A. A. Wang, J. Lee, G. Jenikova, A. Mulchandani, N. V. Myung and W. Chen, Controlled assembly of multi-segment nanowires by histidine-tagged peptides, *Nanotechnology*, **17**, 3375–3379 (2006).
87. A. Pohl, *Dielectrophoresis: The Behavior of Neutral Matter in Nonuniform Electric Fields,* Cambridge University Press, Cambridge, New York, 1978.
88. P. A. Smith, C. D. Nordquist, T. N. Jackson, T. S. Mayer, B. R. Martin, J. Mbindyo and T. E. Mallouk, Electric-field assisted assembly and alignment of metallic nanowires, *Appl. Phys. Lett.*, **77**, 1399–1301 (2000).

89. A. Theron, E. Zussman1 and A. L. Yarin, Electrostatic field-assisted alignment of electrospun nanofibres, *Nanotechnology*, **12**, 384–390 (2001).
90. X. Duan, Y. Huang, Y. Cui, J. Wang and C. M. Lieber, Indium phosphide nanowires as building blocks for nanoscale electronic and optoelectronic devices, *Nature*, **409**, 66–69 (2001).
91. D. L. Fan, F. Q. Zhu, R. C. Cammarata and C. L. Chien, Manipulation of nanowires in suspension by ac electric fields, *Appl. Phys. Lett.*, **85**, 4175–4178 (2004).
92. C. Cheng, R. K. Gonela, Q. Gu and D. T. Haynie, Self-assembly of metallic nanowires from aqueous solution, *Nano Lett.*, **5**, 175–178 (2005).
93. O. Englander, D. Christensen, J. Kim, L. Lin and S. J. S. Morris, Electric-field assisted growth and self-assembly of intrinsic silicon nanowires, *Nano Lett.*, **5**, 705–708 (2005).
94. J. J. Boote and S. D. Evans, Dielectrophoretic manipulation and electrical characterization of gold nanowires, *Nanotechnology*, **16**, 1500–1505 (2005).
95. S. J. Papadakis, Z. Gu and D. H. Gracias, Dielectrophoretic assembly of reversible and irreversible metal nanowire networks and vertically aligned arrays, *Appl. Phys. Lett.*, **8**, 233116 (2006).
96. Y. Liu, J.-H. Chung, W. K. Liu and R. S. Ruoff, Dielectrophoretic assembly of nanowires, *J. Phys. Chem. B*, **110**, 14098–14106 (2006).
97. C. S. Lao, J. Liu, P. X. Gao, L. Zhang, D. Davidovic, R. Tummala and Z. L. Wang, ZnO nanobelt/nanowire Schottky diodes formed by dielectrophoresis alignment across Au electrodes, *Nano Lett.*, **6**, 263–266 (2006).
98. K. M. Ryan, A. Mastroianni, K. A. Stancil, H. Liu and A. P. Alivisatos, Electric-field-assisted assembly of perpendicularly oriented nanorod superlattices, *Nano Lett.*, **6**, 1479–1482 (2006).
99. M. Tanase, L. A. Bauer, A. Hultgren, D. M. Silevitch, L. Sun, D. H. Reich, P. C. Searson and G. J. Meyer, Magnetic alignment of fluorescent nanowires, *Nano Lett.*, **1**, 155–158 (2001).
100. M. Tanase, D. M. Silvitch, A. Hultgren, L. A. Bauer, P. C. Searson, G. J. Meyer and D. H. Reich, Magnetic trapping and self-assembly of multicomponent nanowires, *J. App. Phys.*, **91**, 8549–8552 (2002).
101. C. L. Chien, L. Sun, M. Tanase, L. A. Bauer, A. Hulgren, D. M. Silevitch, G. J. Meyer, P. C. Searson and D. H. Reich, Electrodeposited magnetic nanowires: arrays, field-induced assembly and surface functionalization, *J. Magn. Magn. Mater.*,**249**, 146-155 (2002).
102. J. C. Love, A. R. Urbach, M. G. Prentiss and G. M. Whitesides, Three-dimensional self-assembly of metallic rods with submicron diameters using magnetic interactions, *J. Am. Chem. Soc.*, **125**, 12696–12697 (2003).
103. C. M. Hangarter and N. V. Myung, Magentic alignment of nanowires, *Chem. Mater.*, **17**, 1320–1324 (2005).
104. E. Choi, Z. Gu, D. Gracias and A. G. Andreou, Chip-scale magnetic sensing and control of nanoparticles and nanorods, *2006 IEEE International Symposium on Circuits and Systems (ISCAS 2006)*, 1319–1322 (2006).
105. H. Ye, Z. Gu, T. Yu and D. H. Gracias, Integrating nanowires with substrates using directed assembly and nanoscale soldering, *IEEE Trans. Nanotechnol.*, **5**, 62–66 (2006).
106. B. Yoo, Y. Rheem, W. P. Beyermann and N. V. Myung, Magnetically assembled 30 nm diameter nickel nanowire with ferromagnetic electrodes, *Nanotechnology*, **17**, 2512–2517 (2006).

107. R. Agarwal, K. Ladavac, Y. Roichman, G. Yu, C. M. Lieber and D. G. Grier, Manipulation and assembly of Nanowires with holographic optical traps, *Opt. Exp.*, **13**, 8906–8912 (2005).
108. P. J. Pauzauskiel, A. Radenovic, E. Trepagnier, H. Shroff, P. Yang and J. Liphardt, Optical trapping and integration of semiconductor nanowire assemblies in water, *Nature*, **5**, 97–101 (2006).
109. F. Kim, S. Kwan, J. Akana and P.Yang, Langmuir-Blodgett nanorod assembly, *J. Am. Chem. Soc.*, **123**, 4360-4361 (2001).
110. P. Yang and F. Kim, Langmuir-Blodgett assembly of one-dimensional nanostructures, *ChemPhysChem*, **3**, 503–506 (2002).
111. A. Tao, F. Kim, C. Hess, J. Goldberger, R. He, Y. Sun, Y. Xia and P. Yang, Langmuir-Blodgett silver nanowire monolayers for molecular sensing using surface-enhanced raman spectroscopy, *Nano Lett.*, **3**, 1229–1233 (2003).
112. D. Whang, S. Jin, Y. Wu and C. M. Lieber, Large-scale hierarchical organization of nanowire arrays for integrated nanosystems, *Nano Lett.*, **3**, 1255–1259 (2003).
113. P. Yang, Nanotechnology: wires on water, *Nature*, **425**, 243–244 (2003).
114. S. Acharya, A. B. Panda, N. Belman, S. Efrima and Y. Golan, A semiconductor-nanowire assembly of ultrahigh junction density by the Langmuir–Blodgett technique, *Adv. Mater.*, **18**, 210–213 (2006).
115. Z. Gu, Y. Chen and D. H. Gracias, Surface tension driven self-assembly of bundles and networks of 200 nm diameter rods using a polymerizable adhesive, *Langmuir*, **20**, 11308–11311 (2004).
116. Z. Gu, H. Ye and D. H. Gracias, The bonding of nanowire assemblies using adhesive and solder, *JOM*, 60–64 (2005).
117. S. Jin, D. Whang, M. C. McAlpine, R. S. Friedman, Y. Wu and C. M. Lieber, Scalable interconnection and integration of nanowire devices without registration, *Nano Lett.*, **4**, 915–919 (2004).
118. Z. Gu, H. Ye, D. Smirnova, D. Small and D. H. Gracias, Reflow and electrical characteristics of nanoscale solder, *Small*, **2**, 225–229 (2006).
119. N. I. Kovtyukhova, B. K. Kelley and T. E. Mallouk, Coaxially gated in-wire thin-film transistors made by template assembly, *J. Am. Chem. Soc.*, **126**, 12738–12739 (2004).
120. Y. Cui, Z. Zhong, D. Wang, W. U. Wang and C. M. Lieber, High performance silicon nanowire field effect transistors, *Nano Lett.*, **3**, 149–152 (2003).
121. P. Nguyen, H. T. Ng, T. Yamada, M. K. Smith, J. Li, J. Han and M. Meyyappan, Direct integration of metal oxide nanowire in vertical field-effect transistor, *Nano Lett.*, **4**, 651–657 (2004).
122. N. I. Kovtyukhova and T. E. Mallouk, Nanowire p-n heterojunction diodes made by templated assembly of multilayer carbon-nanotube/polymer/semiconductior-particle shells around metal nanowires, *Adv. Mater.*, **17**, 187–192 (2005).
123. J. Goldberger, D. J. Sirbuly, M. Law and P. Yang, ZnO nanowire transistors, *J. Phys. Chem. B*, **109**, 9–14 (2005).
124. J. Goldberger, A. I. Hochbaum, R. Fan and P. Yang, Silicon vertically integrated nanowire field effect transistors, *Nano Lett.*, **6**, 973–977 (2006).
125. Z. Li, B. Rajendran, T. I. Kamins, X. Li, Y. Chen and R. S. Williams, Silicon nanowires for sequence-specific DNA sensing: device fabrication and simulation, *Appl. Phys. A*, **80**, 1257–1263 (2005).
126. D. J. Sirbuly, M. Law, P. Pauzauskie, H. Yan, A. V. Maslov, K. Knutsen, C.-Z. Ning, R. J. Saykally and P. Yang, Optical routing and sensing with nanowire assemblies, *Proc. Nat. Acad. Sci. USA*, **102**, 7800–7805 (2005).

127. A. K. Wanekaya, W. Chen, N. V. Myung and A. Mulchandani, Nanowire-based electrochemical biosensors, *Electroanalysis*, **18**, 533–550 (2006).
128. F. Patolsky and C. M. Lieber, Nanowire sensors, *Mater. Today*, 20–28 (2005).
129. G. Zheng, F. Patolsky, Y. Cui, W. U. Wang and C. M. Lieber, Multiplexed electrical detection of cancer markers with nanowire sensor arrays, *Nat. Biotech.*, **23**, 1294–1301 (2005).
130. F. Patolsky, G. Zheng and C. M. Lieber, Nanowire-based biosensors, *Anal. Chem.*, **78**, 4260–4269 (2006).
131. F. Patolsky, G. Zheng and C. M. Lieber, Nanowire sensors for medicine and the life sciences, *Nanomedicine*, **1**, 51–65 (2006).
132. J. C. Johnson, H. Yan, R. D. Schaller, L. H. Haber, R. J. Saykally and P. Yang, Single nanowire lasers, *J. Phys. Chem. B*, **105**, 11387–11390 (2001).
133. M. H. Huang, S. Mao, H. Feick, H. Yan, Y. Wu, H. Kind, E. Weber, R. Russo and P. Yang, Room-temperature ultraviolet nanowire nanolasers, *Science*, **292**, 1897–1899 (2001).
134. H. Kind, H. Yan, B. Messer, M. Law and P. Yang, Nanowire ultraviolet photodetectors and optical switches, *Adv. Mater.* **14**, 158–160 (2002).
135. J. C. Johnson, H.-J. Choi, K. P. Knutsen, R. D. Schaller, P. Yang and R. J. Saykally, Single gallium nitride nanowire lasers, *Nature Mater.*, **1**, 106–110 (2002).
136. X. Duan, Y. Huang, R. Agarwal and C. M. Lieber, Single-nanowire electrically driven lasers, *Nature*, **421**, 241–246 (2003).
137. Y. Huang, X. Duan and C. M. Lieber, Nanowires for integrated multicolor nanophotonics, *Small*, **1**, 142–147 (2005).
138. D. J. Sirbuly, M. Law, H. Yan and P. Yang, Semiconductor nanowires for subwavelength photonics integration, *J. Phys. Chem. B*, **109**, 15190-15213 (2005).
139. O. Hayden, R. Agarwal and C. M. Lieber, Nanoscale avalanche photodiodes for highly sensitive and spatially resolved photon detection, *Nature*, **5**, 352–356 (2006).
140. P. J. Pauzauskie, D. J. Sirbuly and P. Yang, Semiconductor nanowire ring resonator laser, *Phys. Rev. Lett.*, **96**, 143903 (2006).
141. M. Law, L. E. Greene, J. C. Johnson, R. Saykally and P. Yang, Nanowire dye-sensitized solar cells, *Nature Mater.*, **4**, 455–459 (2005).
142. K. F. Bohringer, U. Srinivasan and R. T. Howe, Modeling of capillary forces and binding sites for fluidic self-assembly, *The 14th IEEE Int. Conf. MEMS*, 369–374 (2001).
143. J. R. Heath, P. J. Kuekes, G. S. Snider and R. S. Williams, A defect-tolerant computer architecture: opportunities for nanotechnology, *Science* **1998**, *280*. 1716–1721.
144. P. J. Kuekes, W. Robinett, G. Seroussi and R. S. Williams, Defect-tolerant demultiplexers for nano-electronics constructed from error-correcting codes, *Appl. Phys. A*, **80**, 1161–1164 (2005).
145. P. J. Kuekes, W. Robinett, G. Seroussi and R. S. Williams, Defect-tolerant interconnect to nanoelectronic circuits: internally redundant demultiplexers based on error-correcting codes, *Nanotechnology*, **16**, 869–882 (2005).
146. G. Snider, P. Kuekes, T. Hogg and R. S. Williams, Nanoelectronic architectures, *Appl. Phys. A*, **80**, 1183–1195 (2005).
147. R. Albert, H. Jeong and A.-L. Barabasi, Error and attack tolerance of complex networks, *Nature*, **406**, 378–382 (2000).

CHAPTER 7

TAPER-DRAWING FABRICATION OF GLASS NANOWIRES

LIMIN TONG

State Key Laboratory of Modern Optical Instrumentation,
Department of Optical Engineering, Zhejiang University,
Hangzhou 310027, China

ERIC MAZUR

Department of Physics and Division of Engineering and Applied Sciences,
Harvard University, 9 Oxford Street,
Cambridge, Massachusetts 02138, USA

A number of techniques have been developed for the fabrication of glass nanowires (*e.g.*, photo- or electron beam lithography, chemical growth, and taper drawing). Of these techniques, the taper drawing technique yields nanowires with the highest uniformity. Using sapphire fibers, flame or laser-heated glass (fibers) can be drawn directly into nanowires with diameters down to tens of nanometers. Nanowires obtained with this technique show extraordinary diameter uniformity, atomic-level surface smoothness, large length, high mechanical strength and pliability for assembling and patterning, making them promising building blocks for the future micro- and nanoscale photonic devices.

Keywords: Taper-drawing method; Glass nanowires; Micromanipulation; Subwavelength; Optical loss; Evanescent wave.

CONTENTS

1. Introduction 214
2. Taper-drawing Fabrication of Glass Nanowires 214
   2.1. A brief introduction to the taper-drawing method 214
   2.2. Fabrication of nanowires by taper drawing of optical fibers 215
   2.3. Direct taper drawing of nanowires from bulk glasses 220
3. Properties of Taper-drawn Glass Nanowires 222
   3.1. Micromanipulation and mechanical properties 222
   3.2. Optical properties 226
4. Applications of Taper-drawn Nanowires 228
   4.1. Micro- and nano-scale photonic components 229

4.2. Nanowire optical sensors 230
4.3. Additional applications 231
References 231

1. Introduction

As one of the fundamental materials in fields ranging from photonics to electronics, and chemistry to biology, glass has a number of advantages over other materials in homogeneity, transparency, ease of fabrication and excellent solvent properties [1–3]. Recently, low-dimensional structures of glasses, especially one-dimensional nanowires, have attracted much interest in a variety of fields, including nanoscale photonics, electronics and mechanics [4–9]. A number of techniques have been reported to date for the fabrication of one-dimensional nanowires of amorphous or glass structures (*e.g.*, photo- or electron-beam lithography, chemical growth, nanoimprint and taper drawing) [6,10–13]. Among these techniques, the taper drawing method described here offers nanowires with unparalleled uniformity [6,14–16]. With the help of sapphire fibers, flame or laser-heated glass fibers or bulk glasses can be drawn into long nanowires with uniform diameters. Furthermore, this kind of top-down fabrication yields nanowires with surface roughness down to atomic level [15,16]. Because of their extraordinary uniformity, taper drawn nanowires have unique properties, including low optical loss for subwavelength waveguiding and high strength for mechanical research and assembly [6,8,14–16].

This chapter begins by describing the taper-drawing fabrication of glass nanowires. Next, the optical and mechanical properties of the as-fabricated glass nanowires are discussed. Finally, a brief overview of current and potential future applications of these nanowires is presented.

2. Taper-drawing Fabrication of Glass Nanowires

2.1. *A brief introduction to the taper-drawing method*

Taper-drawing fabrication of thin glass wires was first reported in the nineteenth century [17,18]. Melted minerals were pulled or drawn at a high speed by a flying arrow or a strong blow of gas to form fine threads, typically several micrometers in diameter. Long uniform wires obtained this way were used for making springs because of their excellent elastic properties, but most of their other properties and applications remained uninvestigated. It was not until a century later, when optical waveguide theory had been well established, that researchers began to investigate the optical applications of silica wires made by drawing high-purity glass fibers from a laser-heated melt [19–23]. With a diameter of more than one micrometer, these glass wires allow multimode waveguiding of visible and infrared light with low optical loss. Submicrometer wires allow single-mode operation, but both theoretical and experimental results show that the laser power required for drawing silica submicrometer- or nanometer-diameter wires with a uniform diameter

is impractically large [20,23]. When drawing from a flame-heated melt, turbulence and convection make it difficult to control the temperature gradient in the drawing region, and consequently size uniformity is difficult to maintain when the wire diameter goes down to the nanoscale regime.

Minimizing the width of optical waveguides is particularly desirable for achieving high-performance and high-density optical circuits [24–26]. However, light guided along subwavelength-width waveguides fabricated by conventional techniques usually is accompanied by high scattering losses due to the large sidewall roughness of the waveguide. Previous research has shown that melt-solidification of glasses yields a surface smoothness much better than all other techniques [27–29]. This high smoothness provided the motivation for adapting the taper-drawing technique to nanofabrication in order to achieve highly uniform nanowires for low-loss single-mode optical wave guiding [6].

2.2. *Fabrication of nanowires by taper drawing of optical fibers*

Recently, glass nanowires have been obtained by direct taper drawing of flame-heated optical fibers (one-step approach) [14,30]. The one-step approach is simple and convenient. However, when drawing fibers directly from a flame-heated melt, the instability of the flame usually makes it difficult to control the temperature gradient in the drawing region, and consequently glass nanowires with diameters of less than 200 nm are difficult to obtain.

In order to maintain a steady working temperature for drawing nanowires with high repeatability, a two-step taper drawing technique was developed. A schematic view of the two-step taper drawing method is illustrated in Fig. 1(a). First, a microfiber with a diameter of several micrometers is taper drawn using standard techniques. Second, in order to maintain steady conditions for further reduction of the fiber diameter, a tapered sapphire fiber with a tip diameter around 100 μm is used to absorb the thermal energy from the flame. The sapphire fiber taper (fabricated using a laser-heating growth method [31]), confines the heating to a small volume and helps maintain a steady temperature distribution via its thermal inertia during the drawing. One end of a micrometer-diameter silica fiber is placed horizontally on the sapphire tip, and the flame is adjusted until the temperature of the tip is just above the drawing temperature (about 2,000 K). Then the sapphire tip is rotated around its axis of symmetry to wind the silica fiber and the fiber coil is moved out of the flame to prevent melting (Fig. 1[b]). When a certain drawing force is applied perpendicular to the axis of the sapphire tip, the fiber is drawn in the horizontal plane at a speed of 1–10 mm/s, forming a silica nanowire. With the technique shown in Fig. 1, the diameter of a silica fiber can be reduced to about 50 nm, which is thin enough for most of optical applications involving single-mode guiding.

To obtain even thinner nanowires, for example for structural and catalytic investigations of silica nanowires [32–34], one can use a self-modulated drawing force

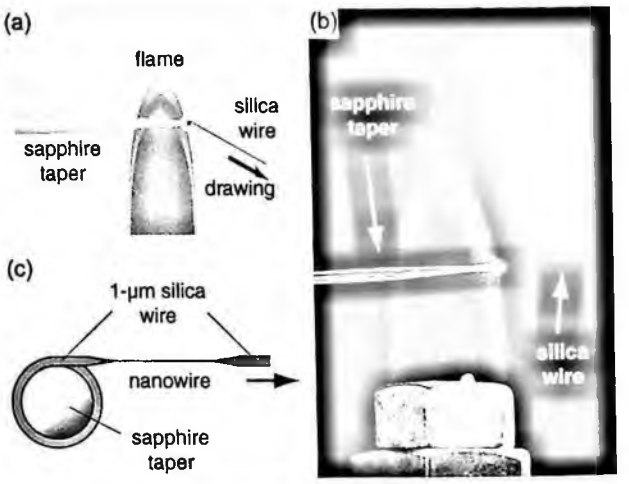

Figure 1. Two-step taper drawing of silica nanowires. After drawing a standard fiber down to a diameter of about 1 μm (step 1), the resulting fiber is wound around a sapphire taper. (a) The coil is heated by the flame and the thermal conduction of the sapphire taper and then a nanowire is drawn (step 2). (b) Close-up photograph of the second-step taper drawing of silica nanowires. (c) Schematic of the nanowires drawing from the silica coil wound around the sapphire taper.

instead of the constant drawing force in the second-step taper drawing process [15]. As shown in Fig. 2, to introduce the self modulation, one introduces an elastic bend around the taper area of the silica fiber by holding the silica fiber parallel to the sapphire taper and tautening the connected microfiber between the silica and the sapphire taper. The tensile force generated by the elastic bend can be used for self modulation, as illustrated in Fig. 2(c). During the initial stage, when drawing a thick fiber that requires a relatively large force, the sharpest bending occurs at the thicker part of the taper. As the fiber is elongated and the fiber diameter decreases, the bend loosens and the bending center moves towards the thin end of the taper, resulting in smaller forces for drawing thinner fibers, which is helpful for drawing uniform fibers with very small diameters. The self-modulation can also instantly smoothen unpredictable undulations such as temperature fluctuations (that may cause large variation in the viscosity of silica) by shifting the bending center to-and-fro to avoid sudden changes in fiber diameter, whereas a constant-force drawing may cause abrupt taper or even breakage of the fiber in these cases.

When the drawing is completed, the nanowire is connected to the starting fiber at one end and free-standing on the other end. Low-carbon fuel such as CH_3OH or hydrogen is used to avoid contamination from incompletely burned carbon particles. When the working temperature is kept below the melting temperature of sapphire (about 2320 K), the sapphire tip can be used repeatedly. In addition, for real-time monitoring the drawing process, a continuous-wave He-Ne laser (633-nm wavelength) is usually launched into and guided along the silica fiber, fiber taper and silica nanowire to illuminate the taper and nanowire, as shown in Fig. 2(b).

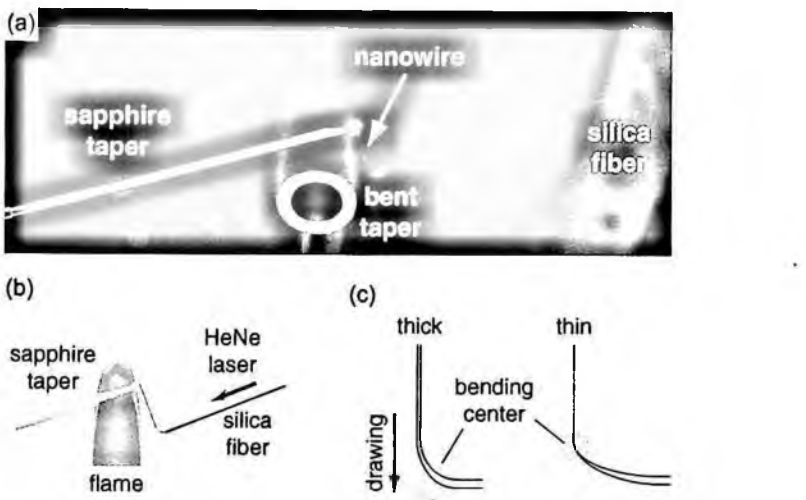

Figure 2. Self-modulated taper drawing of silica nanowires. (a) Close-up photograph of the nanowire drawing. The red light visible around the nanowire and tapers is from a He-Ne laser. (b) Schematic diagram of the self-modulated taper drawing setup. A 3-dimensional stage is used to mount and adjust the silica fiber taper to form a 90° bend and a He-Ne laser is launched into the silica fiber for illuminating the nanowire and monitoring the drawing process. (c) The self-modulation of the drawing force is due to the shifting of the bending center as the fiber is drawn. (Adapted from Ref. [15].)

Generally, the nanowire obtained with a two-step taper drawing technique contains three parts: an obviously tapered start connected to the starting microfiber with a length of millimeters, a uniform nanowire with a length up to tens of millimeters, and an abruptly tapered end that is usually several to tens of micrometers in length. Figure 3 shows SEM images of the three parts of a typical nanowire with a diameter centered around 390 nm. The uniform, main part of the nanowire, is of special interest for using as a subwavelength-diameter waveguide for low-loss optical wave guiding, and the following investigation is focused on this part.

Depending on the experimental conditions (such as drawing temperature, force and speed), diameters of as-drawn silica nanowires range from tens of nanometers

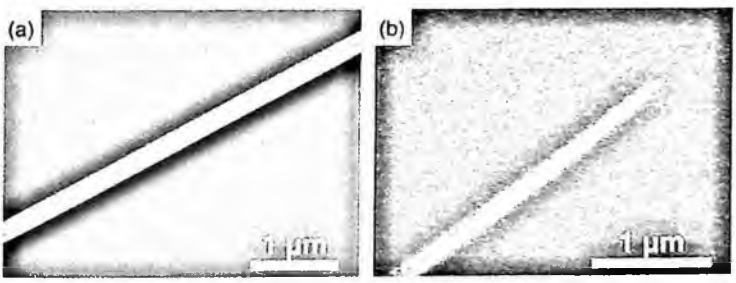

Figure 3. SEM images of the (a) uniform part and (b) end of a silica nanowire with a nominal diameter of 200 nm.

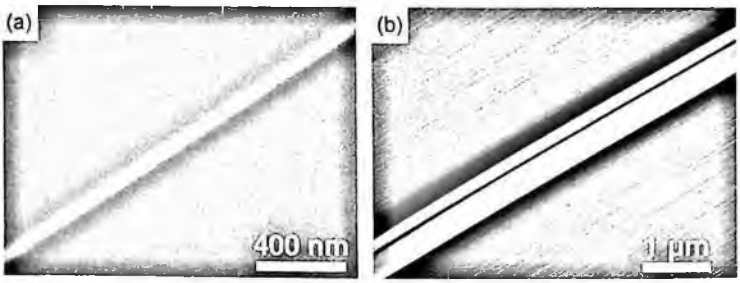

Figure 4. SEM images of (a) a silica nanowire with a diameter of about 50 nm and (b) two parallel 170-nm and 400-nm thick nanowires. (Adapted from Ref. [6].)

to one micrometer. The smallest diameter of a uniform nanowire obtained using self-modulated drawing is 20 nm [15]. Shown in Fig. 4 are SEM images of silica nanowires with diameters of tens to hundreds of nanometers, demonstrating the typical dimension and uniformity of these nanowires.

Because of the surface tension during the melting drawing fabrication, the cross section of the taper-drawn nanowire is circular. Figure 5 shows a SEM image of the circular cross-section of a 480-nm thick nanowire. The cylindrical geometry of the nanowire makes it possible to obtain exact expressions of the guided modes by solving Maxwell's equations analytically [35,36].

The maximum obtainable length of the nanowires depends on their diameters. Generally, for nanowires thinner than 100 nm, the length of the uniform part can be up to 1 millimeter long; nanowires thicker than 200 nm can be as long as 100 millimeters. For example, Fig. 6 shows an SEM image of a 4-mm long nanowire with a diameter of 260 nm; the nanowire is coiled up on the surface of a silicon wafer to show its length.

Figure 5. SEM image of the circular cross section of a 480-nm thick nanowire.

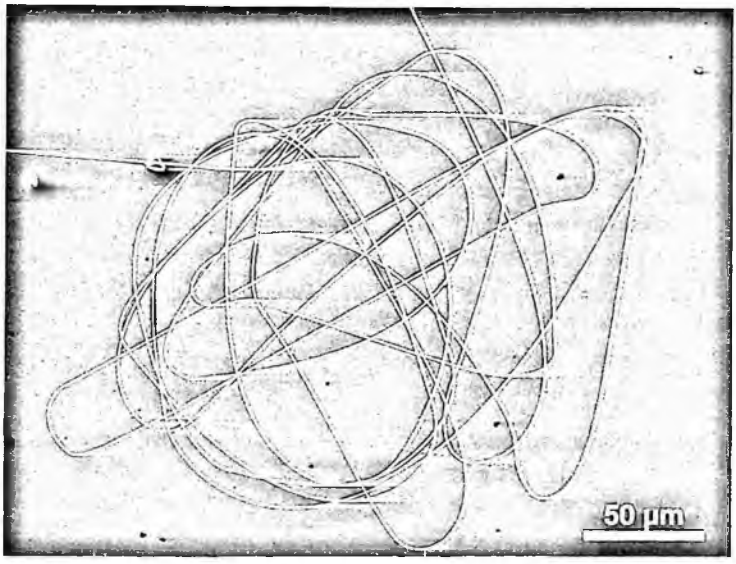

Figure 6. SEM image of a 4-mm long 260-nm thick nanowire coiled up on the surface of a silicon wafer. (Adapted from Ref. [6].)

Besides the large length, taper-drawn nanowires also provide excellent diameter and surface roughness uniformity, as can be seen in Fig. 4. The diameter uniformity of the nanowires can be investigated quantitatively by measuring the diameter variation ΔD along the length L of the nanowire with an electron microscope. Figure 7 shows the measured diameter D and diameter uniformity U_D (defined as $\Delta D/L$) of a thin nanowire with respect to its length (starting from the thin end). Although the nanowire exhibits an overall monotonic tapering tendency, neglecting the obvious

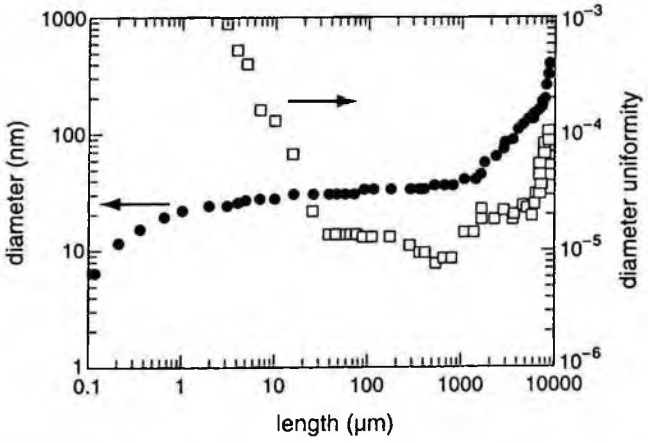

Figure 7. Diameter and diameter uniformity of a taper-drawn silica nanowire measured along its length starting from the distal end. (Adapted from Ref. [15].)

initial and end tapered regions, the uniform part of the nanowire shows a very high uniformity. For example, at $D = 30\,\text{nm}$, $U_D = 1.2 \times 10^{-5}$, which means that, for a 80-μm long nanowire with a diameter centered around 30 nm, the maximum diameter difference between the two ends is less than 1 nm. Thicker nanowires show even better uniformity. For example, for a 260-nm thick nanowire, the maximum diameter variation ΔD is about 8 nm over a 4-mm length, giving $U_D = 2 \times 10^{-6}$. Recently, G. Brambilla *et al.* reported U_D lower than 5×10^{-7} [14].

The small diameter of the nanowire makes it possible to investigate the surface roughness with a TEM. Shown in Fig. 8 is a typical image taken at the edge of a 330-nm thick nanowire. No obvious irregularity and defect can be observed along the sidewall of the nanowire. The typical sidewall root-mean-square roughness of these fibers can be as low as 0.2 nm [15], approaching the intrinsic roughness of melt-formed glass surfaces [28,29]. Considering that the length of the Si-O bond is about 0.16 nm [27], such a roughness represents an atomic-level smoothness of the nanowire surface, and is much lower than those of silica nanowires, tubes or strips obtained using other fabrication methods [10–13].

2.3. *Direct taper drawing of nanowires from bulk glasses*

Although taper drawing optical fibers is a very efficient technique for obtaining nanowires with extraordinary uniformity, it requires an optical fiber as a preform. Therefore, the available materials for drawing nanowires are limited to those that have been drawn into fibers. Recent research shows that, using sapphire fibers, glass nanowires can be drawn directly from bulk glasses [16]. The technique for drawing of nanowires directly from bulk glasses extends the nanowire taper drawing technique to arbitrary shapes and various types of glasses.

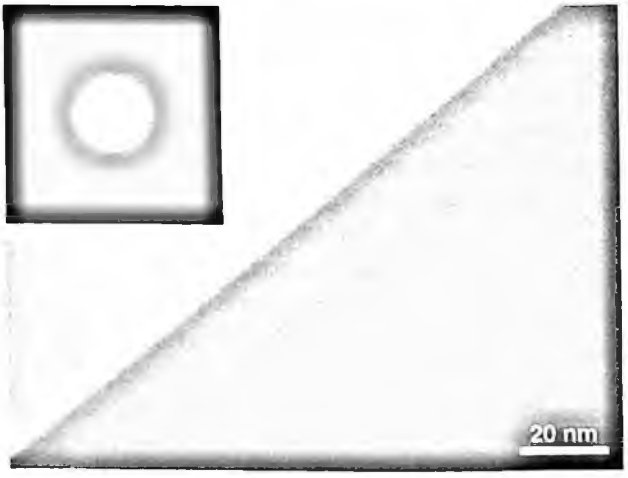

Figure 8. TEM image of the surface of a 330-nm thick silica nanowire. The inset shows the electron diffraction pattern demonstrating that the nanowire is amorphous. (Adapted from Ref. [6].)

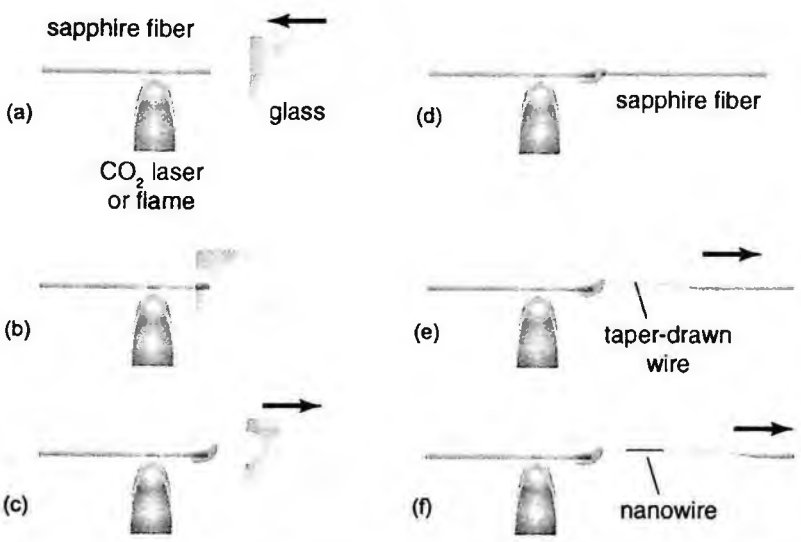

Figure 9. Schematic diagram illustrating the direct draw of nanowires from bulk glasses. (a) A glass is moved towards a sapphire fiber heated by a CO_2 laser or flame. (b) The fiber end is immersed into the glass through local melting. (c) A portion of molten glass is left on the end of the fiber when the glass is withdrawn. (d) A second sapphire fiber is brought into contact with the molten-glass-coated end of the first sapphire fiber. (e) The heating power is reduced and the second sapphire fiber is withdrawn. (f) A nanowire is formed at the freestanding end of the taper drawn wire.

The approach for directly drawing glass nanowires is illustrated in Fig. 9. First, a CO_2 laser or flame is used to heat a sapphire fiber (hundreds of micrometers in diameter) to a temperature high enough for melting the glass, and a piece of glass is moved towards the fiber. After the fiber is immersed into the glass through local melting, the glass is withdrawn leaving a portion of melt behind on the fiber. A second sapphire fiber is then brought into contact with the glass-coated sapphire fiber end and the heating power is reduced to cool down the melt (800–1000 K for phosphate glass). The second sapphire fiber is then withdrawn at a speed of 0.1–1 m/s to draw wires from the melt until breakage of the wire. When the process is finished, a long nanowire is formed at the freestanding side of the taper drawn wire. To draw nanowires from chemically unstable materials such as fluoride glasses, one can use laser heating in an atmosphere of an inert gas (*e.g.*, Argon). This technique can also be applied to pulverized glasses, allowing for adjustments to the properties of the nanowire by tailoring the composition of the initial powder. In addition, nanowires can be drawn using extremely low starting quantities of glass (as little as 1 mg).

Using the technique shown in Fig. 9, a variety of glass materials (*e.g.*, phosphate, fluoride, silicate and tellurite glasses) have been drawn into highly uniform nanowires with diameters down to 50 nm and lengths up to tens of millimeters. Figure 10(a) shows an SEM image of a 100-nm thick tellurite glass (70% TeO_2, 25% ZnO, 5% La_2O_3) nanowire. The uniform diameter and defect-free surface of the

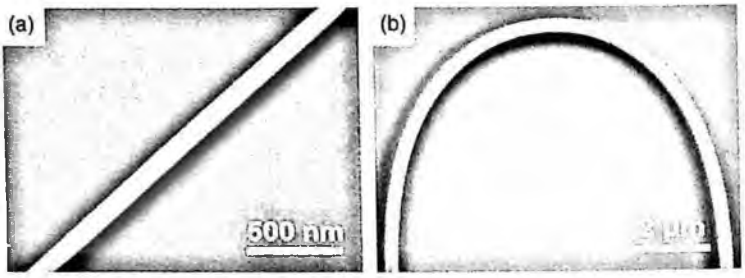

Figure 10. Electron microscopic characterizations of as-drawn glass nanowires. (a) SEM image of a 100-nm thick tellurite glass nanowire. (b) SEM image of an elastically bent 320-nm thick silicate glass nanowire. (Adapted from Ref. [16].)

wire is clearly visible. The high uniformity and integrity give the wires considerable strength and pliability for manipulation. Figure 10(b) shows an elastically bent 320-nm thick silicate glass (Corning 0215) nanowire with a minimum bending radius of 5 μm, the wire shows a tensile strength sufficient for withstanding such a sharp bend. Figure 11 shows a TEM image of the sidewall of a 210-nm thick Er and Yb co-doped phosphate glass (65% P_2O_5, 12% Al_2O_3, 5% Li_2O, 16% Na_2O, 1.5% Yb_2O_3, 0.5% Er_2O_3) nanowire, showing no visible defects or irregularities on the wire surface. The typical sidewall root-mean-square roughness of these nanowires is around 0.3 nm, which is on the same order of the roughness of silica nanowires drawn from optical fibers, approaching the intrinsic roughness of melt-formed glass surfaces [28,29].

3. Properties of Taper-drawn Glass Nanowires

3.1. *Micromanipulation and mechanical properties*

The ability to manipulate nanowires individually is critical for their characterization and for applications. Because of their long length, silica nanowires obtained by the

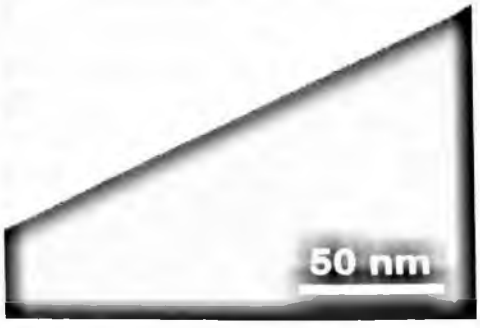

Figure 11. TEM examination of the sidewall of a 210-nm thick phosphate glass nanowire. (Adapted from Ref. [16].)

Figure 12. Optical microscope image of a 60-nm thick silica nanowire supported by a silicon wafer. The image is taken in dark-field reflection mode.

taper drawing method can be easily identified under an optical microscope. For reference, Fig. 12 shows a photograph of a 60-nm thick silica nanowire taken under an optical microscope in dark-field reflection mode. The profile of the nanowire is clearly seen when it is supported on a silicon wafer. This optical visibility makes it possible to manipulate a single nanowire in air, greatly facilitating the handling, tailoring and assembly of these nanowires for various purposes.

A typical experimental setup for micromanipulation of silica nanowires is shown in Fig. 13. The micromanipulation is monitored using an optical microscope objective which images the nanowire onto a CCD camera. Probes from a scanning tunneling microscope (STM) are mounted on micromanipulators and used for holding and manipulating the nanowires, as shown in the captured image in the inset of Fig. 13. Silica nanowires can be either freestanding in air or supported by high-index substrates (e.g., silicon or sapphire wafers) for better visibility.

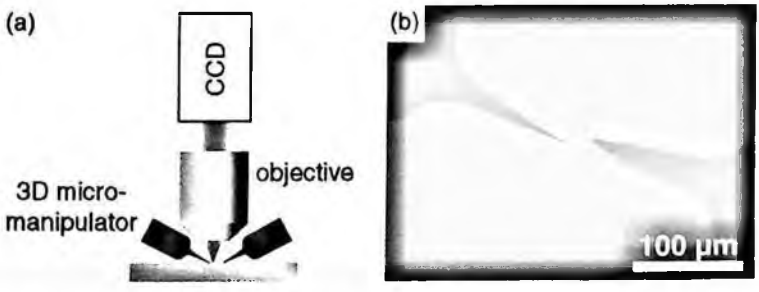

Figure 13. (a) Experimental setup for micromanipulating silica nanowires. (b) Microscope image showing the bending of a silica nanowire using two STM probes.

Using micromanipulation under an optical microscope, silica nanowires can be cut, positioned, bent and twisted with high precision. To cut a nanowire to a desired length, a bend-to-fracture method can be applied by holding the nanowire with two STM probes on a silicon or sapphire substrate and then using a third probe to bend the nanowire to fracture at the desired point. Because of their high integrity and uniformity, taper drawn nanowires usually demonstrate symmetrically flat end faces at the fracture point, as shown in Fig. 14.

To perform the bending and repositioning, the nanowires are first placed on a finely polished substrate (*e.g.*, silicon wafer), which holds them tightly in place by van der Waals or electrostatic attraction between the nanowire and the substrate. They are then pushed by STM probes to a desired bending radius or position. The shape of the elastic bend is maintained after removing the STM probes because of the friction between the nanowire and the substrate. Figure 15 shows a 280-nm thick nanowire bent to a radius of 2.7 μm. Usually, the nanowires do not break when bent and pushed, indicating that they have excellent flexibility and mechanical properties. As shown in Fig. 15, the tensile strength of the nanowires is estimated to be at least 4.5 GPa assuming a Young's modulus equal to that of ordinary silica fibers [37]. The tensile strength of the wires can be determined by bending nanowires to the point of fracture. Figure 16 shows that the measured tensile strength of silica nanowires falls between 4 GPa and 7 GPa, regardless of their diameter. Taper drawn silica nanowires have a tensile strength that is much higher than that of standard glass fibers (about 3 GPa at room temperature and moderate humidity [37,38]), which can be attributed to the lower defect density in materials of lower dimension.

The nanowires can readily be twisted without breaking. Figure 17 shows a rope-like twist formed with a 480-nm thick silica nanowire on a silicon wafer. This

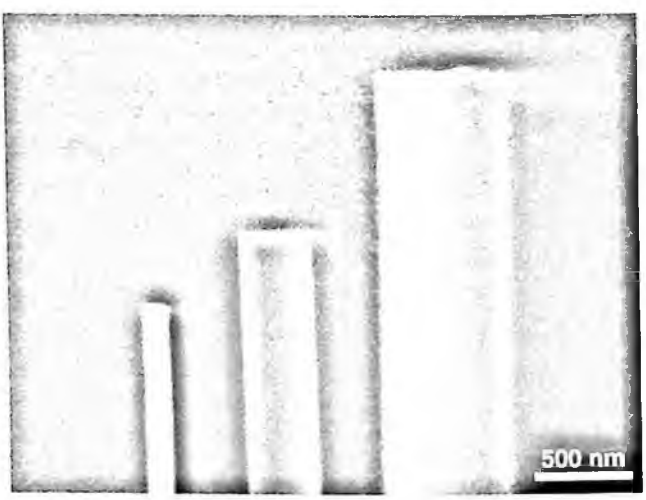

Figure 14. SEM images of the cut end faces of 140-, 420- and 680-nm thick silica nanowires. (Adapted from Ref. [47].)

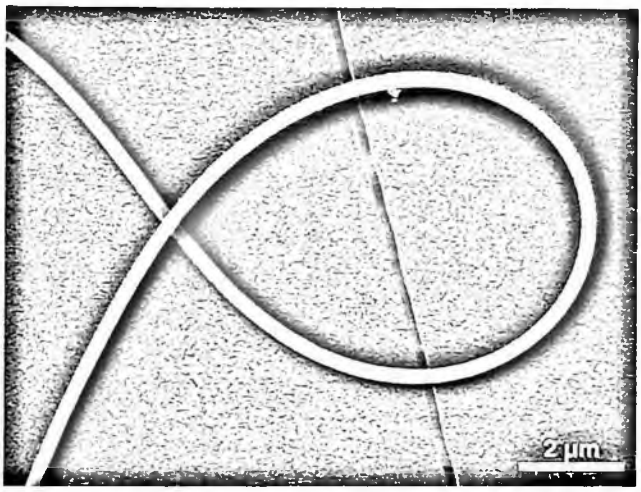

Figure 15. SEM image of a 280-nm thick nanowire elastically bent to a radius of 2.7 μm. (Adapted from Ref. [6].)

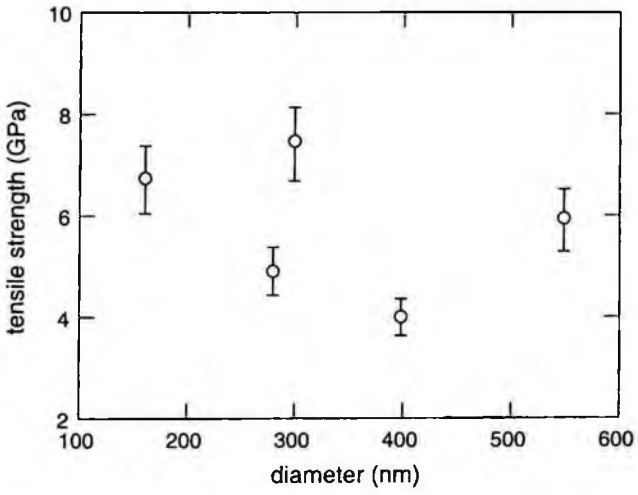

Figure 16. Tensile strength of silica nanowires measured by a bend-to-fracture procedure.

"nanorope" keeps its shape when it is lifted up from the substrate, indicating that the nanowire can withstand shear deformation.

Silica nanowires can also be assembled into complex structures such as nanowire knots. Figure 18 shows a 15-μm wide knot tied in a 520-nm thick silica nanowire. Such a ring-like structure can be developed into micro optical components such as ring resonators.

To avoid long-term fatigue and fracture of an elastically bent nanowire due to bending stress [39,40], an annealing-after-bending procedure can be applied to form

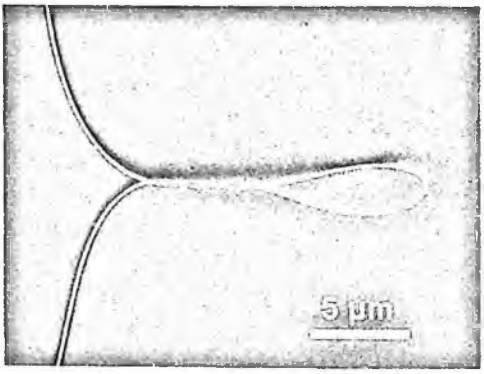

Figure 17. SEM image of a rope-like twist formed with a 120-nm thick silica nanowire. (Adapted from Ref. [15].)

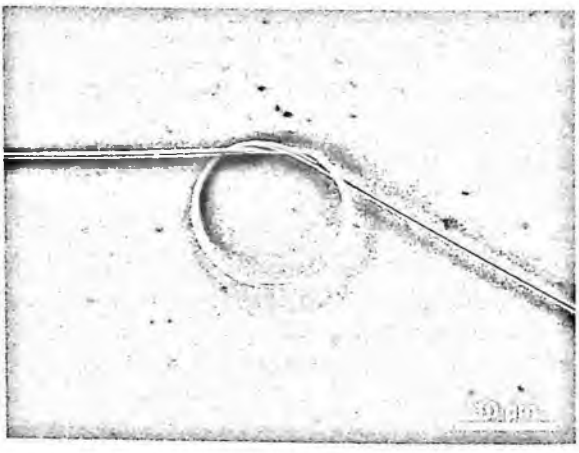

Figure 18. SEM image of a 15-μm diameter knot made with a 520-nm thick silica nanowire. (Adapted from Ref. [6].)

permanent plastic deformation, without change in surface smoothness and diameter uniformity. Shown in Fig. 19 are a spiral plastic bends in an 80-nm thick phosphate glass nanowire (Fig. 19[a]) and sharp bends in a 170-nm thick tellurite glass nanowire (Fig. 19[b]).

3.2. *Optical properties*

The extraordinary uniformity of the taper drawn nanowires makes it possible to use them for guiding light with low optical loss. To investigate the optical guiding properties of silica nanowires experimentally, it is essential to be able to effectively send light into and pick light out of a single nanowire. For a nanowire that is still connected to the starting fiber, light guided in the standard fiber can be squeezed directly into the nanowire through the tapered region connecting the two.

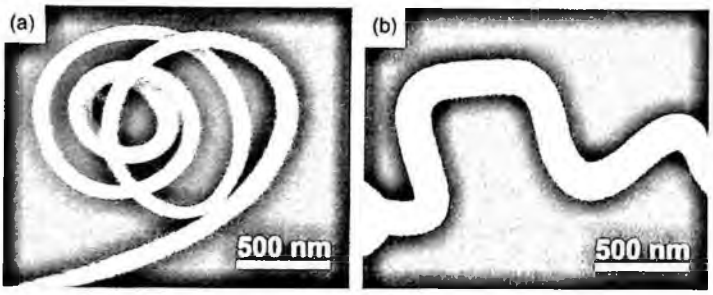

Figure 19. SEM image of plastically bent glass nanowires. (a) A spiral plastic bend in an 80-nm thick Erbium-doped phosphate glass nanowire. (b) A 170-nm thick tellurite glass nanowire with sharp plastic bends. (Adapted from Ref. [16].)

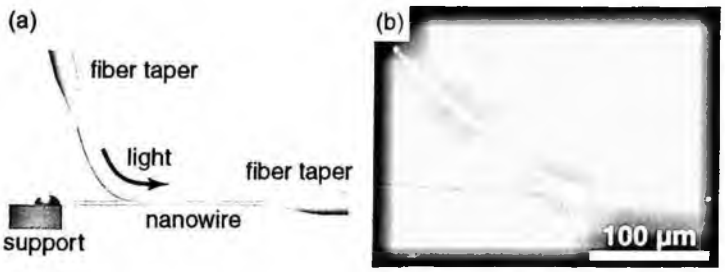

Figure 20. Launching light into a silica nanowire. (a) Schematic diagram for launching light into a silica nanowire using evanescent coupling. (b) Optical microscope image of a 390-nm thick nanowire coupling light into a 450-nm thick silica nanowire. (Adapted from Ref. [6].)

For nanowires with free-standing ends, light can be launched using an evanescent coupling method, as shown in Fig. 20. Light is first sent into the core of a single-mode fiber that is tapered down to a nanowire and the nanotaper is then used to evanescently couple the light into another nanowire by overlapping the two in parallel. Because of electrostatic and van der Waals forces, the nanowires attract one another and form a contact connection. Figure 20(b) shows an optical micrograph of the coupling between a 390-nm thick silica launching taper and a 450-nm thick silica nanowire. The coupling efficiency of this evanescent coupling can be as high as 90% when the fiber diameter and overlap length are properly selected. This method can also be used for picking light out of a single nanowire.

Using evanescent coupling, the optical loss of the silica nanowire can be determined quantitatively by measuring the transmission as a function of the length [6]. Shown in Fig. 21 is the optical loss of silica nanowires taper drawn from optical fibers, as reported by several groups [6,14,30]. Figure 22 shows the optical loss of nanowires directly drawn from bulk glasses [16]. For single-mode operation, the optical loss is typically around 0.1 dB/mm and can be as small as 0.0014 dB/mm, which is much lower than the optical loss of other subwavelength-structures such as metallic plasmon waveguides, nanowires or nanoribbons [41–43]. The increasing

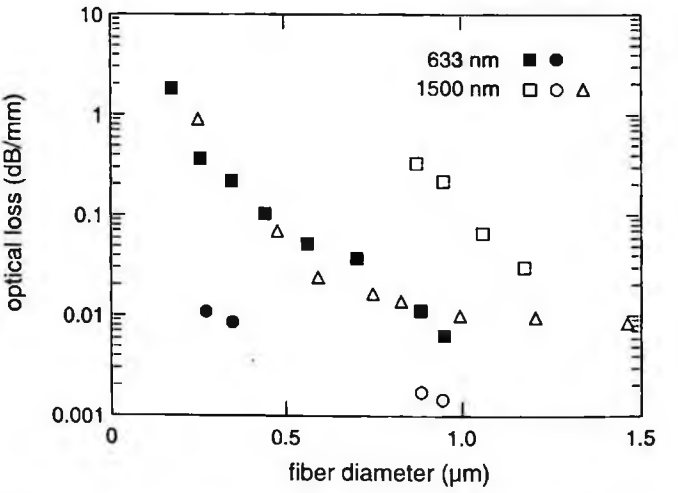

Figure 21. Optical loss in freestanding silica nanowires measured in air at 633 nm (■ [6], ● [30]) and 1550 nm (□ [6], △ [14], ○ [30]).

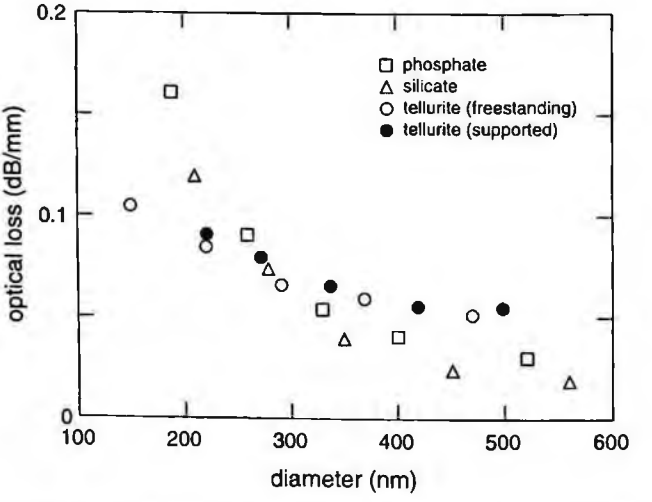

Figure 22. Measured loss of freestanding phosphate, silicate, tellurite and MgF_2-supported tellurite glass nanowires taper drawn from bulk glasses. (Adapted from Ref. [16].)

loss with decreasing wire diameter can be attributed to surface contamination: as the wire diameter is reduced below the wavelength, more light is guided outside the wire as an evanescent wave and becomes susceptible to scattering by surface contamination and/or microbends.

4. Applications of Taper-drawn Nanowires

Because of their low-loss optical wave guiding ability, taper-drawn nano wires are ideal building blocks for various applications in nanophotonics. For example, low

optical loss of the guiding structure is essential to obtain a high Q-factor in an optical microcavity resonator [44], to maintain the coherence of the guided light in optical waveguide/fiber sensors using coherent detection [45], to reduce the noise or cross talk in high-density optical integration, and to reduce energy consumption when many devices are connected in series. So far, taper-drawn glass nanowires have inspired broad interest in a variety of fields, such as photonic components and devices [46–48], nanowire optical sensors [49–51], nonlinear interaction and supercontinuum generation [30,52–60], and atom trap and guidance [61–64]. A brief review of the current and potential applications of these nanowires is presented here.

4.1. *Micro- and nano-scale photonic components*

A variety of micro- or nanoscale photonic components have been assembled using taper-drawn nanowires [46–48]. Because of their small size, low optical loss, evanescent wave guiding and mechanical flexibility, photonic devices assembled from nanowires have a number of advantages over conventional devices.

Figure 23 shows a micro-scale waveguide bend assembled by transferring plastically bent silica nanowires onto the surface of silica aerogel [47]. The 530-nm thick silica nanowire was first bent to a radius of about 8 μm on a sapphire wafer, annealed, and then transferred to silica aerogel (Fig. 23[a]). The aerogel-supported plastic bends show excellent optical wave guiding with good confinement of the light (Fig. 23[b]), demonstrating advantages such as compact overall size, low coupling loss, simple structure and easy fabrication over other types of waveguide bends such as photonic crystal structures [65–67].

The bent waveguides can be used to fabricate optical couplers. Figure 24 shows an X-coupler assembled from two tellurite glass nanowires with diameters of 350 and 450 nm, respectively. When 633-nm wavelength light is launched into the bottom left arm, the coupler splits the flow of light in two, working as a 3-dB splitter with almost no excess loss. The overlap length of less than 5 μm is much shorter than the transfer length required by conventional fused couplers made from larger-diameter fiber tapers [68].

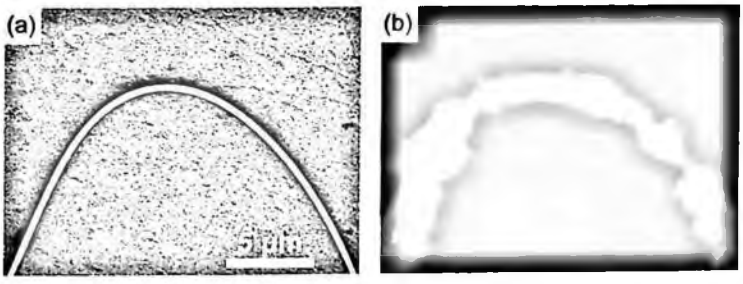

Figure 23. An aerogel-supported 530-nm thick nanowire with a bending radius of 8 μm. (a) SEM image and (b) optical microscopy image showing the guiding light around the bend. (Adapted from Ref. [47].)

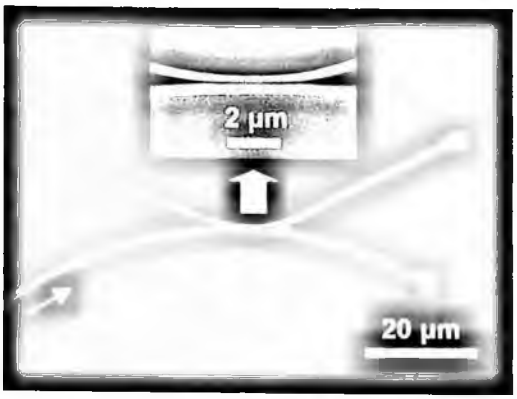

Figure 24. Optical micrograph of an optical coupler assembled using two tellurite glass nanowires (350 and 450 nm in diameter respectively) on the surface of silicate glass. The coupler splits the 633-nm-wavelength light equally. (Adapted from Ref. [16].)

Microring resonators have also been proposed or developed [6,46,48,69–71]. Recently, micro coil/loop resonators with Q-factors of 650,000 have been experimentally realized [71], and a microcoil resonator with self-coupling turns is expected to reach a Q-factor as high as 10^{10} [69].

4.2. *Nanowire optical sensors*

Because of their subwavelength-size, nanowires guide light with a large fraction of the energy in an evanescent wave that is highly sensitive to index change in the environment [36]. At the same time, because of the low optical loss of the taper-drawn nanowires, the coherence of the guided light can be maintained over a considerable length. These excellent guiding properties make these nanowires ideal for high-sensitivity optical sensing at the nanoscale.

Numerical simulations show that when two nanowires are assembled into a Mach-Zehnder interferometer for coherently detecting phase shifts in the guided light in one of the nanowires acting as the sensitive arm, the sensitivity of such a nanowire optical sensor can be over one magnitude higher than that of conventional fiber/waveguide optical sensors of similar design [49]. An important benefit is that the size of the sensing element can be greatly reduced.

Optical sensors based on taper-drawn silica nanowires (nanofibers) have also been experimentally realized. For example, P. Polynkin *et al.* reported a nanofiber optical sensor for measuring the refractive index of liquids propagating in microfluidic channels [50], with an estimated sensitivity of about 5×10^{-4} in the refractive-index. J. Villatoro *et al.* reported a miniature hydrogen sensor that consists of a taper-drawn nanofiber coated with an ultra thin palladium film [51]. Measurements using light of 1550-nm wavelength show that the sensor's response time (about 10 s) is several times faster than that of optical and electrical hydrogen sensors reported so

far. Moreover, the sensor is small, reversible, and suitable for detection of hydrogen around the lower explosive limit.

4.3. *Additional applications*

Additional applications of taper-drawn nanowires have been reported in fields such as nonlinear interaction and supercontinuum generation [30,52–60], as well as atom trapping and guiding [61–64]. Because of the tight mode confinement and strong waveguide dispersion, subwavelength-diameter nanotapers or fibers make it possible to exploit nonlinear properties at relatively low pumping power and short interaction length [30,53]. Another promising application involves the use of silica nanowires for trapping and guiding atoms by the optical force of the evanescent field around the fibers [61–64]. It was shown that the gradient force of a red-detuned evanescent-wave field in the fundamental mode of a silica nanowire can balance the centrifugal force of the atoms [62,63]. In addition, atom traps and waveguides using a two-color evanescent light field around a nanowire can produce a net potential with large depth, coherence time, and trap lifetime [64].

References

1. T. Izawa and S. Sudo, *Optical Fiber: Materials and Fabrication* (Kluwer Academic Publishers, Dordrecht, 1987).
2. M. Yamane and Y. Asahara, *Glasses for Photonics* (Cambridge University Press, Cambridge, 2000).
3. K. Hirao, T. Mitsuyu, J. Si and J. Qiu, *Active Glasses for Photonic Devices: Photoinduced Structures and Their Applications* (Springer-Verlag, New York, 2001).
4. D. P. Yu, Q. L. Hang, Y. Ding *et al.*, Amorphous silica nanowires: Intensive blue light emitters, *Appl. Phys. Lett.* **73**, 3076–3078 (1998).
5. Z. L. Wang, R. P. P. Gao, J. L. Gole and J. D. Stout, Silica nanotubes and nanofiber arrays, *Adv. Mater.* **12**, 1938–1940 (2000).
6. L. Tong, R. Gattass, J. Ashcom, S. He, J. Lou, M. Shen, I. Maxwell and E. Mazur, Subwavelength-diameter silica wires for low-loss optical wave guiding, *Nature* **426**, 816–819 (2003).
7. Z. L. Wang, Functional oxide nanobelts: Materials, properties and potential applications in nanosystems and biotechnology, *Annu. Rev. Phys. Chem.* **55**, 159–196 (2004).
8. E. C. C. M Silva , L. Tong, S. Yip and K. J. van Vliet , Size effects on the stiffness of silica nanowires, *Small* **2**, 239–243 (2006).
9. G. Bilalbegovic, Electronic properties of silica nanowires, *J. Phys.: Condens. Matter* **18**, 3829–3836 (2006).
10. S. Y. Chou, P. R. Krauss and P. J. Renstrom, Imprint lithography with 25-nanometer resolution, *Science* **272**, 85–87 (1996).
11. Y. Xia, J. A. Rogers, K. E. Paul and G. M. Whitesides, Unconventional methods for fabricating and patterning nanostructures, *Chem. Rev.* **99**, 1823–1848 (1999).
12. Z. W. Pan, Z. R. Dai, C. Ma and Z. L. Wang, Molten gallium as a catalyst for the large-scale growth of highly aligned silica nanowires, *J. Am. Chem. Soc.* **124**, 1817–1822 (2002).

13. F. Romanato, D. Cojoc, E. Di Fabrizio, M. Galli and D. Bajoni, X-ray and electron-beam lithography of three-dimensional array structures for photonics, *J. Vac. Sci. Technol.* **B21**, 2912–2917 (2003).
14. G. Brambilla, V. Finazzi and D. J. Richardson, Ultra-low-loss optical fiber nanotapers, *Opt. Express* **12**, 2258–2263 (2004).
15. L. Tong, J. Lou, Z. Ye, G. T. Svacha and E. Mazur, Self-modulated taper drawing of silica nanowires, *Nanotechnology* **16**, 1445–1448 (2005).
16. L. Tong, L. Hu, J. Zhang, J. Qiu, Q. Yang, J. Lou, Y. Shen, J. He and Z. Ye, Photonic nanowires directly drawn from bulk glasses, *Opt. Express* **14**, 82–87 (2006).
17. C. V. Boys, On the production, properties, and some suggested uses of the finest threads, *Phil. Mag.* **23**, 489–499 (1887).
18. Threlfall, R. *On Laboratory Arts*, (Macmillan, London, 1898).
19. J. C. Knight, G. Cheung, F. Jacques and T. A. Birks, Phase-matched excitation of whispering-gallery mode resonances by a fiber taper, *Opt. Lett.* **22**, 1129–1131 (1997).
20. T. E. Dimmick, G. Kakarantzas, T. A. Birks and P. St. J. Russell, Carbon dioxide laser fabrication of fused-fiber couplers and tapers, *Appl. Opt.* **38**, 6845–6848 (1999).
21. M. Cai and K. Vahala, Highly efficient hybrid fiber taper coupled microsphere laser, *Opt. Lett.* **26**, 884–886 (2001).
22. G. Kakarantzas, T. E. Dimmick, T. A. Birks, R. Le Roux and P. St. J. Russell, Miniature all-fiber devices based on CO2 laser microstructuring of tapered fibers, *Opt. Lett.* **26**, 1137–1139 (2001).
23. A. J. C. Grellier, N. K. Zayer and C. N. Pannell, Heat transfer modeling in CO2 laser processing of optical fibers, *Opt. Commun.* **152**, 324–328 (1998).
24. R. E. Kunz, Miniature integrated optical modules for chemical and biochemical sensing, *Sensors and Actuators* **B38**, 13–28 (1997).
25. C. Manolatou, S. G. Johnson, S. Fan, P. R. Villeneuve, H. A. Haus and J. D. Joannopoulos, High-density integrated optics, *J. Lightwave Technol.* **17**, 1682–1692 (1999).
26. P. Domachuk and B. J. Eggleton, Photonics: Shrinking optical fibers, *Nat. Mater.* **3**, 85–86 (2004).
27. N. P. Bansal and R. H. Doremus, *Handbook of Glass Properties*, Academic Press, Orlando, 1986.
28. J. Jackle and K. Kawasaki, Intrinsic roughness of glass surfaces, *J. Phys.: Condens. Matter* **7**, 4351–4358 (1995).
29. E. Radlein and G. H. Frischat, Atomic force microscopy as a tool to correlate nanostructure to properties of glasses, *J. Non-Cryst. Solids* **222**, 69–82 (1997).
30. S. G. Leon-Saval, T. A. Birks, W. J. Wadsworth, P. St. J. Russell and M. W. Mason, Supercontinuum generation in submicron fiber waveguides, *Opt. Express* **12**, 2864–2869 (2004).
31. H. E. Labelle and A. I. Mlavsky, Growth of sapphire filaments from melt, *Nature* **216**, 574–575 (1967).
32. Z. L. Wang, *Nanowires and Nanobelts: Materials, Properties and Devices*, Kluwer–Academic, New York, 2003.
33. T. Zhu, J. Li, S. Yip, R. J. Bartlett, S. B. Trickey and N. H. De Leeuw, Deformation and fracture of a SiO2 nanorod, *Mol. Simul.* **29**, 671–676 (2003).
34. J. T. Hu, T. W. Odom and C. M. Lieber, Chemistry and physics in one dimension: Synthesis and properties of nanowires and nanotubes,*Acc. Chem. Res.* **32**, 435–445 (1999).

35. A. W. Snyder and J. D. Love, *Optical Waveguide Theory*, (Chapman and Hall, New York, 1983).
36. L. Tong, J. Lou and E. Mazur, Single-mode guiding properties of subwavelength-diameter silica and silicon wire waveguides, *Opt. Express* **12**, 1025–1035 (2004).
37. J. T. Krause, L. R. Testardi and R. N. Thurston, Deviations from linearity in the dependence of elongation upon force for fibers of simple glass formers and of glass optical light guides, *Phys. Chem. Glasses* **20**, 135–139 (1979).
38. M. J. Matthewson, C. R. Kurkjian and S. T. Gulati, Strength measurement of optical fibers by bending, *J. Am. Ceram. Soc.* **69**, 815–821 (1986).
39. M. J. Matthewson and C. R. Kurkjian, Static fatigue of optical fibers in bending, *J. Am. Ceram. Soc.* **70**, 662–668 (1987).
40. V. Annovazzi-Ledi, S. Donati, S. Merlo and G. Zapelloni, Statistical analysis of fiber failures under bending-stress fatigue, *J. Lightwave Technol.* **15**, 288–293 (1997).
41. J. Takahara, S. Yamagishi, H. Taki, A. Morimoto and T. Kobayashi, Guiding of a one-dimensional optical beam with nanometer diameter, *Opt. Lett.* **22**, 475–477 (1997).
42. S. A. Maier, P. G. Kik and H. A. Atwater, Observation of coupled plasmon-polarization modes in Au nanoparticle chain waveguides of different lengths: Estimation of waveguide loss, *Appl. Phys. Lett.* **81**, 1714–1716 (2002).
43. M. Law, D. J. Sirbuly, J. C. Johnson, J. Goldberger, R. J. Saykally and P. Yang, Nanoribbon waveguides for subwavelength photonics integration, *Science* **305**, 1269–1273 (2004).
44. K. J. Vahala, Optical microcavities, *Nature* **424**, 839–846 (2003).
45. Z. M. Qi, N. Matsuda, K. Itoh, M. Murabayashi and C. R. Lavers, A design for improving the sensitivity of a Mach-Zehnder interferometer to chemical and biological measurands, *Sens. Actuators* **B81**, 254–258 (2002).
46. M. Sumetsky, Y. Dulashko and A. Hale, Fabrication and study of bent and coiled free silica nanowires: Self-coupling microloop optical interferometer, *Opt. Express* **12**, 3521–3531 (2004).
47. L. Tong, J. Lou, R. Gattass, S. He, X. Chen, L. Liu and E. Mazur, Assembly of silica nanowires on silica aerogels for microphotonic devices, *Nano Lett.* **5**, 259–262 (2005).
48. M. Sumetsky, Y. Dulashko, J. M. Fini and A. Hale, Optical microfiber loop resonator, *Appl. Phys. Lett.* **86**, 161108 (2005).
49. J. Lou, L. Tong and Z. Ye, Modeling of silica nanowires for optical sensing, *Opt. Express* **13**, 2135–2140 (2005).
50. P. Polynkin, A. Polynkin, N. Peyghambarian and M. Mansuripur, Evanescent field-based optical fiber sensing device for measuring the refractive index of liquids in microfluidic channels, *Opt. Lett.* **30**, 1273–1275 (2005).
51. J. Villatoro and D. Monzn-Hernndez, Fast detection of hydrogen with nano fiber tapers coated with ultra thin palladium layers, *Opt. Express* **13**, 5087–5092 (2005).
52. M. A. Foster, K. D. Moll and A. L. Gaeta, Optimal waveguide dimensions for nonlinear interactions, *Opt. Express* **12**, 2880–2887 (2004).
53. Y. K. Lize, E. C. Magi, V. G. Ta'eed, J. A. Bolger, P. Steinvurzel and B. J. Eggleton, Microstructured optical fiber photonic wires with subwavelength core diameter, *Opt. Express* **12**, 3209–3217 (2004).
54. M. Kolesik, E. M. Wright and J. V. Moloney, Simulation of femtosecond pulse propagation in sub-micron diameter tapered fibers, *Appl. Phys.* **B79**, 293–300 (2004).
55. E. C. Magi, H. C. Nguyen and B. J. Eggleton, Air-hole collapse and mode transitions in microstructured fiber photonic wires, *Opt. Express* **13**, 453–459 (2005).

56. J. M. Moison, A. M. Apetrei, J. A. Levenson, G. Melin, P. Pedeboscq, A. Fleureau, S. Lempereur and L. Gasca, Light transmission in multiple or single subwavelength trefoil channels of microstructured fibers, *Opt. Express* **13**, 1193–1201 (2005).
57. G. Brambilla, E. Koizumi, X. Feng and D. J. Richardson, Compound-glass optical nanowires, *Electron. Lett.* **41**, 400–402 (2005).
58. D. K. Qing and G. Chen, Nanoscale optical waveguides with negative dielectric claddings, *Phys. Rev.* **B71**, 153107 (2005).
59. A. Zheltikov, Gaussian-mode analysis of waveguide-enhanced Kerr-type nonlinearity of optical fibers and photonic wires, *J. Opt. Soc. Am.* **B22**, 1100–1104 (2005).
60. R. R. Gattass, G. T. Svacha, L. Tong and E. Mazur, Supercontinuum generation in submicrometer diameter silica fibers, *Opt. Express* **14**, 9408–9414 (2006).
61. F. Le Kien, J. Q. Liang, K. Hakuta and V. I. Balykin, Field intensity distributions and polarization orientations in a vacuum-clad subwavelength-diameter optical fiber, *Opt. Commun.* **242**, 445–455 (2004).
62. V. I. Balykin, K. Hakuta, F. Le Kien, J. Q. Liang and M. Morinaga, Atom trapping and guiding with a subwavelength-diameter optical fiber, *Phys. Rev.* **A70** 011401 (2004).
63. F. Le Kien, V. I. Balykin and K. Hakuta, Atom trap and waveguide using a two-color evanescent light field around a subwavelength-diameter optical fiber, *Phys. Rev.* **A70** 063403 (2004).
64. F. Le Kien, V. I. Balykin and K. Hakuta, State-insensitive trapping and guiding of cesium atoms using a two-color evanescent field around a subwavelength-diameter fiber *J. Phys. Soc. Jpn* **74**, 910–917 (2005).
65. J. D. Joannopoulos, R. D. Meade and J. N. Winn, *Photonic Crystals: Molding the Flow of Light*, Princeton University Press, Princeton, 1995.
66. J. Moosburger, M. Kamp, A. Forchel *et al.*, Enhanced transmission through photonic-crystal-based bent waveguides by bend engineering, *Appl. Phys. Lett.* **79**, 3579–3581 (2001).
67. M. Augustin, H. J. Fuchs, D. Schelle, E. B. Kley, S. Nolte, A. Tunnermann, R. Iliew, C. Etrich, U. Peschel and F. Lederer, High transmission and single-mode operation in low-index-contrast photonic crystal waveguide devices, *Appl. Phys. Lett.* **84**, 663–665 (2004).
68. G. Kakarantzas, T. E. Dimmick, T. A. Birks, R. Le Roux and P. St. J. Russell, Miniature all-fiber devices based on CO2 laser microstructuring of tapered fibers, *Opt. Lett.* **26**, 1137–1139 (2001).
69. M. Sumetsky, Optical fiber microcoil resonator, *Opt. Express* **12**, 2303–2316 (2004) 2303.
70. M. Sumetsky, Uniform coil optical resonator and waveguide: transmission spectrum, eigenmodes, and dispersion relation, *Opt. Express* **13**, 4331–4340 (2005).
71. M. Sumetsky, Y. Dulashko, J. M. Fini, A. Hale and D. J. DiGiovanni, Demonstration of the microfiber loop optical resonator, Optical Fiber Communication Conference, Postdeadline papers, Paper PDP10, Anaheim (2005).

CHAPTER 8

EXTREME ULTRAVIOLET LITHOGRAPHY

HIROO KINOSHITA

Nano Science and Technology Utilizing SR,
Laboratory of Advanced Science and Technology for Industry,
University of Hyogo, NewSUBARU,
1-1-2 Kouto Kamigori Ako-gun, Hyogo, Japan
kinosita@lasti.u-hyogo.ac.jp

This chapter describes an EUVL technology that is expected to be introduced into the manufacturing of the 32 nm-node device from 2009–2011. EUVL consists of a light source of 13.5 nm, a reflective mask, objective optics and wafer. A reflective mask and objective optics with multilayer coating are employed. The reflectivity of multilayer at the wavelength of 13.5 nm is 68%.

The challenging items are high power source, defect-free mask and resist with low LER and high sensitivity. EUV scanner of α-type have delivered and process studies are performed in several institutions. In this chapter, the principle of EUV lithography, concepts of optics design, aspherical mirror fabrication and measurement, mask fabrication process and inspection, recent activities of resist and source are described.

Keywords: Extreme ultraviolet; Mo/Si multilayer; reflection optics; aspherical mirror; laser plasma source.

CONTENTS

1. Introduction 236
2. Principle of Extreme Ultraviolet Lithography 237
3. Optics 241
   3.1. Optics design 241
   3.2. Fabrication and measurement of aspherical mirror 244
4. Source 246
5. Reflection Mask 253
   5.1. Mask structure and mask fabrication process 253
   5.2. Actinic EUV mask inspection system 257
      5.2.1. Observation of finished mask 259
      5.2.2. Observation of phase defects 260

6. Contamination removal 262
6.1. In situ removal of contamination from an EUVL mirror using synchrotron radiation 263
6.2. Removal of contamination from a finished EUVL mask using 172-nm radiation 265
7. Resist 266
8. Exposure Tools and Experiments 270
9. Conclusions 277
References 278

1. Introduction

Soft X-ray reduction lithography using multilayer-coated Schwarzchild (SC) optics was first demonstrated in NTT in 1986 [1,2]. The exposure optics were then refined, and a 0.5-μm pattern was delineated [3] in 1989. However, the next year, the AT&T group demonstrated a pattern with a diffraction-limited size of 0.05 μm [4]. Stimulated by those results, R&D accelerated in both the US and Japan. The past 20 years have seen many technological advances; and EUVL is now the most promising next-generation technology for LSI fabrication.

According to the latest semiconductor road map, EUVL will be introduced for the fabrication of LSIs at the 32-nm node in 2011. Research institutions, equipment makers, and infrastructure makers throughout the world are now accelerating development with the goal of fabricating devices by EUVL. Although the optical system is reflective, employing mirrors covered with a multilayer film, rather than refractive, as in a conventional system, this technology can be considered an extension of conventional ultraviolet lithography. That is, advances in lithography for device fabrication have so far come about by improving the NA of the optical system and shortening the exposure wavelength. Recently, the required minimum feature size has reached one-half the wavelength or less, and the influence of diffraction has become marked. Even so, a conventional refractive system can still be used due to the development of resolution enhancement technologies, such as a phase-shift mask and a ring illumination system, which result from the engineering of optical components. Furthermore, a new technique called ArF immersion technology is making rapid progress.

Ultraviolet lithography employs reduction exposure and a bulk mask, and covers several generations. Any technology worthy of being called a "lithography standard" for device fabrication must satisfy these three conditions. EUVL does satisfy them, and can be considered an extension of ultraviolet lithography. Moreover, a fine pattern less than 30 nm can be replicated without the resolution enhancement or OPC techniques developed for KrF excimer lithography.

In contrast to conventional ultraviolet lithography, which employs refractive optics, EUVL employs a reflective optical system consisting of multilayer-coated

mirrors. Each aspect of this technology (coating, polishing, metrology, vacuum mechanism, etc.) requires an extremely high precision of less than one nanometer, although nanotechnology seems to have grabbed the world's attention lately. On the road to the establishment of a workable technology, solutions to critical problems in each field must be found; and their impact will spread widely into other fields. For example, consider the light source, which is based, for instance, on laser-produced plasma. If a high-intensity light source is realizable, it will lead to improvements in the performance of X-ray microscopes and analytical tools. Progress in optical polishing and figuring will have an impact on the quality of many products. Research on multilayer films promotes the study of the process by which a single atomic layer is formed and also research on the surface interface of materials. Furthermore, the advances in metrology required to make EUVL a practical production tool will revolutionize evaluation methods based on the conventional point diffraction interferometer.

Thus, although difficult problems must be solved in each technology related to EUVL, this research is part of the process by which we are progressing into the nano-scale regime; and this same process will one day carry us into the pico-scale regime. In this sense, the development of EUVL will have a large ripple effect on all fields.

This chapter discusses the principal of EUVL, the current status of the individual technologies, and future prospects.

2. Principle of Extreme Ultraviolet Lithography [3]

Figure 1 illustrates the principle of extreme ultraviolet lithography. The system consists of a source, illumination optics, a mask, an objective lens, and a wafer. The mask, the objective optics, and parts of the illumination optics are coated with a reflective multilayer film. Since the aberration-free area in a reflective system is limited, the exposure area is expanded by synchronously moving the mask and wafer in the optical system.

The diffraction-limited resolution is determined by Fraunhofer diffraction when aberration in the optical system is completely eliminated:

$$d = K1\lambda/(NA). \tag{1}$$

And the depth of focus, D, is given by the Rayleigh equation:

$$D = \lambda/(NA^2), \tag{2}$$

where λ is the wavelength of the X-ray source and NA is the numerical aperture of the objective lens. Table 1 gives estimates of the resolution and depth of focus, assuming a K1 factor of 0.5 and a wavelength of 13.5 nm.

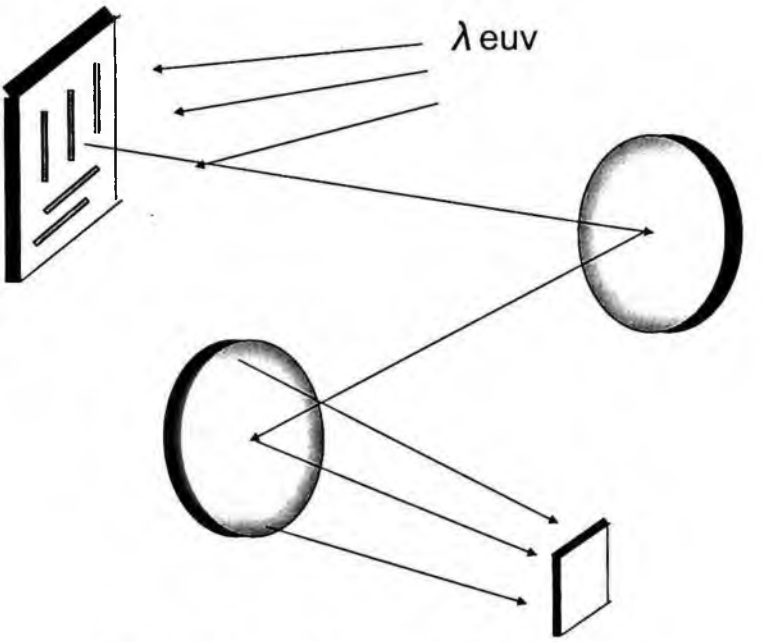

Figure 1. Principle of extreme ultraviolet lithography.

If a K1 factor of 0.4 is permitted, optics with an NA of 0.25 can be used for the 22 nm-node without any narrowing of the depth of focus. This is one of the biggest advantages of EUVL.

At the start of system design, the choice of X-ray wavelength is the most important consideration because many other things (optical characteristics, multilayer reflectivity, resist materials, etc.) depend on it. Figure 2 shows the numerical aperture and X-ray wavelength for the target resolution and depth of focus both in the early stages (1980s) and now. In the early stages, the target resolution was less than 0.2 μm, but it has now become less than 45 nm. In this figure, a larger numerical aperture provides a higher resolution and a smaller depth of focus. However, it is extremely difficult to design optics with a high numerical aperture, such as 0.4. Another way to improve the resolution is to shorten the wavelength; but that reduces the reflectivity of the multilayer and narrows the bandwidth.

Figure 3 shows the reflectivity of multilayer films experimented in the world wide [5]. The shortest wavelength that can be used at normal incidence is around

Table 1. Estimated resolution and depth of focus.

NA	0.25	0.3	0.4
d(nm)	27	22.5	17
Df(nm)	216	150	84

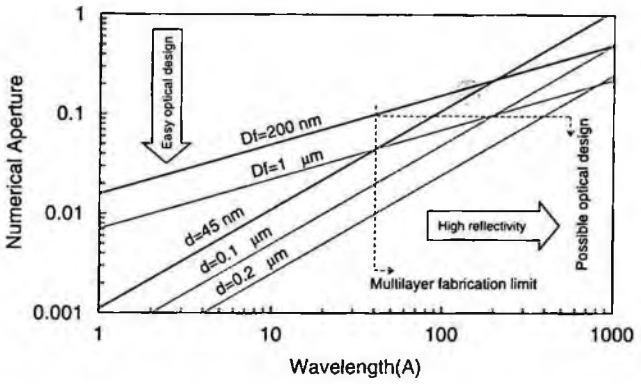

Figure 2. Numerical aperture and X-ray wavelength for the target resolution and depth of focus.

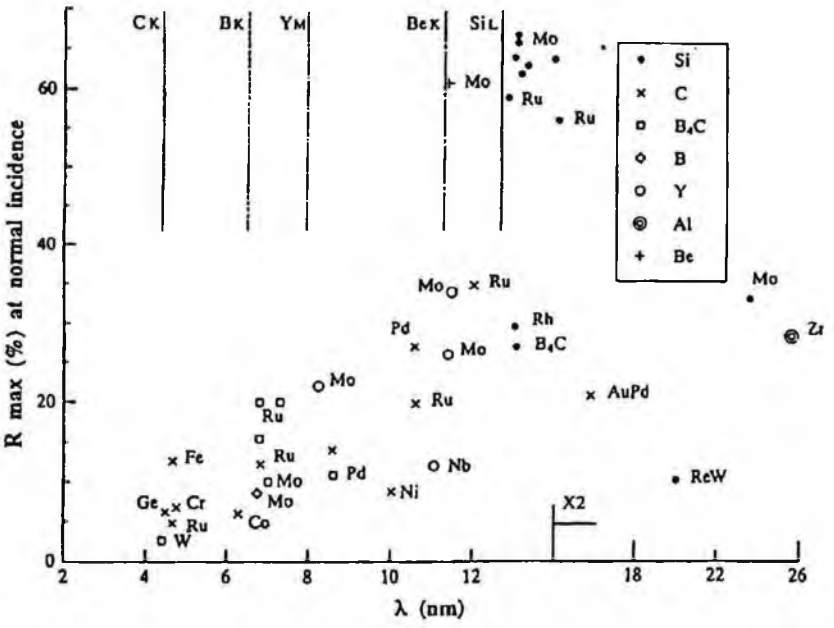

Figure 3. The reflectivity of multilayer films fabricated and measured in the world wide.

4.7 nm, considering the controllability of the period of the thinnest layer on a mirror. Generally, the peak reflectivity is obtained at the wavelength of minimum absorption of the low index material, such as carbon, boron, beryllium or silicon for the wavelength range of 4.0–40 nm. It occurs at a wavelength of 4.47 nm for carbon, 6.7 nm for boron, 11.4 nm for beryllium, and 12.4 nm for silicon. The peak reflectivity and the bandwidth are easily calculated from Fresnel's equations. For instance, assuming that the wavelength is beyond the absorption edge of each material and

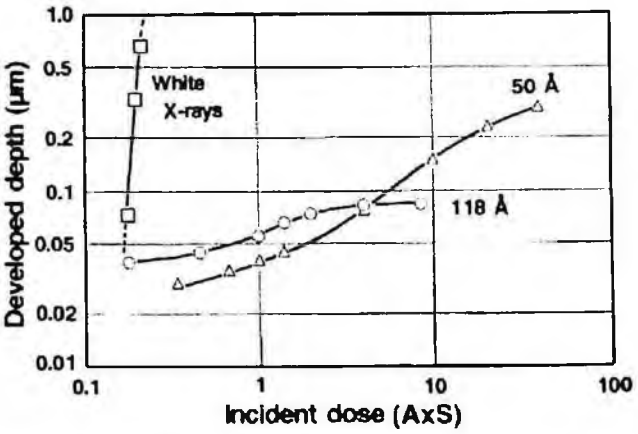

Figure 4. The relationship between the exposure depth of PMMA resist and the incident dose of synchrotron radiation (SR).

also assuming normal incidence, the calculated peak reflectivity is 17% for Cr/C, 33% for Ru/B_4C, 73% for Mo/Be, and 72% for Mo/Si. The experimental reflectivity must be over 65%, from the standpoint of a practical throughput. The values for Mo/Si and Mo/Be satisfy the requirement. Furthermore, since demagnifying optics usually consist of two or more mirrors, a bandwidth of 0.3–0.4 nm is required to adjust the multilayer mirrors to the wavelength of the peak reflectivity. The bandwidths of multilayer mirrors made of Mo/Si (for $\lambda = 13$ nm) and Mo/Be (for $\lambda = 11.4$ nm) satisfy the requirements.

The sensitivity and exposure depth of the resist depend on its X-ray absorption coefficient. Since the characteristics of organic resists depend primarily on the X-ray absorption of carbon, the exposure depth is easily calculated. At a wavelength of 4.47 nm or a little longer, the X-ray absorption of an organic resist is small, which allows a thick resist (thickness $> 0.5\,\mu$m) to be used. For wavelengths longer than 4.47 nm, the X-ray absorption becomes appreciable; and only a thin top layer at the surface is exposed.

Figure 4 shows the relationship between the exposure depth of PMMA resist and the incident dose of synchrotron radiation (SR). Two pairs of Schwarzschild-type multilayer mirrors were used to monochromate the SR source, which was adapted for wavelengths of 5 nm and 11.8 nm. For a wavelength of 11.8 nm, the exposure depth reaches a limit at 0.08 μm; while for 5 nm, it is more than 0.3 μm. So, the use of wavelengths greater than about 10 nm requires the development of either a bilayer resist process or a new resist that permits exposure depths of at least 0.3 μm.

As mentioned above, considering all the factors (required numerical aperture, multilayer reflectivity, resist characteristics, etc.), two wavelength regions appear to be suitable. One is from 4.47 to 7.0 nm, and the other is from 11.4 to 13.0 nm (Fig. 2). The final selection of the wavelength will be decided on the basis of further

Table 2. Critical issues in individual EUVL technologies.

Component	Issue	Goal
Optics	Design	6 mirrors
	Aspherical-mirror fabrication	0.3 nm
	Alignment accuracy of optics	0.5 nm
Source	High power	115–180 W
	Low debris	>5 st
	Large collection angle	$>10^{11}$
	Long life	
Mask	High reflectivity	>67%
	Low defect density	$0.001/cm^2$
Resist	High sensitivity	$2\text{-}5mj/cm^2$
	Low LER	1.5 nm @32 nm
Exposure system	Containmation & temp. control	
	Mask & wafer handling	
	Scan stage	

studies on optical design for a high numerical aperture, the resist process, and the ability to deposit highly reflective multilayers.

Until the target feature size reached 45 nm, a single-layer resist was adequate, since penetration depth did not need to be considered. And the exposure wavelength was set to around 13.5 nm. Table 2 shows the critical issues for EUVL components.

3. Optics

3.1. *Optics design*

To design EUVL optics with a large exposure field, the following factors need to be considered: (i) the construction of optics with the fewest mirrors; (ii) telecentricity on a wafer for easier alignment and a large depth of focus; (iii) a demagnification of 1/4 to 1/5 to make mask fabrication easier; (iv) an MTF of over 70% (it needs to be high enough to provide the required resolution); and (v) a minimum blur of an exposure pattern of less than 0.01% in the scanning mode.

Figure 5 illustrates a two-aspherical-mirror system for the replication of 0.06-μm patterns in a large exposure area demonstrated by NTT [3,6]. The incident angle to the optics is nearly normal (~2°). The focused beam strikes the wafer perpendicularly; that is, the optics are telecentric with respect to the plane of a wafer. The demagnification is 1/5. The numerical aperture is 0.1; and the exposure area has a ring field image 20 mm × 0.4 mm in size, in which the aberration is less than 0.01 μm. The square-wave modulation transfer function for these optics is 75% at 5000 cycles/mm, which yields a resolution of less than 0.1 μm for incoherent 13-nm-wavelength radiation. This design satisfies requirements (i) to (iv) above.

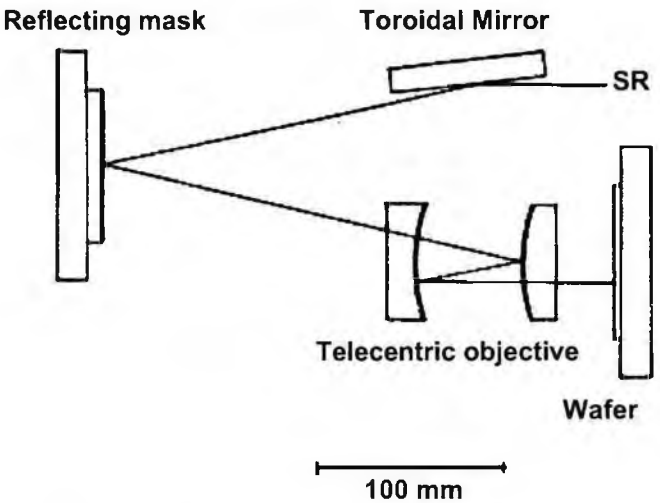

Figure 5. A two-aspherical-mirror system.

This optics design employs two mirrors with the same radius of curvature to compensate for the curvature of the image plane. However, the difference in distortion in the ring field is not negligible. In this case, assuming a distortion of 0.25%, the blur of a pattern is 0.2 μm in a ring field with a size of 20 mm × 0.4 mm on a wafer. A two-mirror system is not good enough to eliminate various types of aberration, especially the distortion in a wide field. However, this design can be considered illustrative of "the principle of an EUVL optical system."

Figure 6 shows a four-mirror ring-field system devised by Tania Jewell *et al.* [7,8]. It satisfies all the requirements for practical 0.1-μm EUV projection lithography. This design is also based on a reflective Cook triplet with a fourth mirror added between the secondary and tertiary mirrors. It is a 4x reduction system with an NA of 0.1 and provides excellent image quality over a ring width of several millimeters. All the mirrors are rotationally symmetric aspherical surfaces with a low asphericity. The radius of the center of the ring field at the side of a wafer is 31.5 mm, which

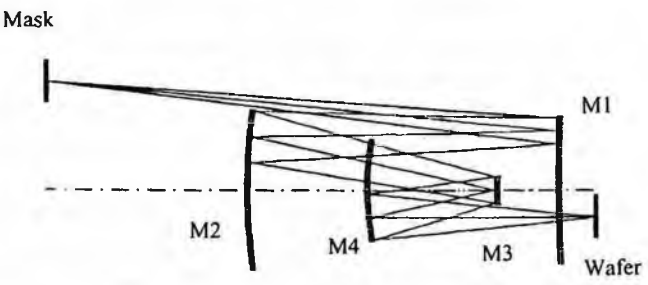

Figure 6. A four-mirror ring-field system devised by Tania Jewell *et al.*

allows the exposure of large chips by scanning. Adding the fold mirror allows several requirements of a practical lithography system to be met: it brings the image to the opposite side of the projection system, thus allowing for unlimited wafer travel; it provides an accessible stop in the system; when power is added to it, it helps to provide a larger back clearance; and it helps to achieve full astigmatic correction over a large field of view, thereby reducing the alignment sensitivity. In a ring-field system, the width of the ring is usually limited by astigmatism. In this design, since the astigmatism is corrected over nearly the entire image field, the width is limited by distortion. For example, the amount of residual distortion for a ring 1.0 mm wide is 7.0 nm in the scan direction and 3.5 nm in the cross-scan direction; while for a ring 2.5 mm wide, the values are larger at 40.0 nm and 20 nm, respectively. An additional feature of this design is an optimum chief ray angle in the object space. During system optimization, the chief ray angle for a mask normal to the incident light is limited to a minimum of 2.5° to allow enough room to bring in the illumination beam for the reflective mask.

A 4-mirror system based on this design has been developed in a DOE program, and it has led to the solution of a basic problem in the development of a stepper [9,10].

Figure 7 shows the characteristics of replicated patterns simulated using SPLAT, assuming a wavelength of 13.5 nm. Increasing NA makes finer hole and elbow patterns. In resolving a 30-nm hole and elbow pattern, the numerical aperture of over around 0.3 is required. On the other hand, influence of σ value does not make a significant change.

Figure 8 shows the 6-aspherical-mirror optics devised by Williamson in 1998 [11]. This system provides even more degrees of freedom to correct residual aberration, enabling a 4 × reduction with an NA in excess of 0.25 and a ring field over 2.0 mm wide on a wafer. For a 2.0-mm-wide ring field, the residual distortion can be reduced

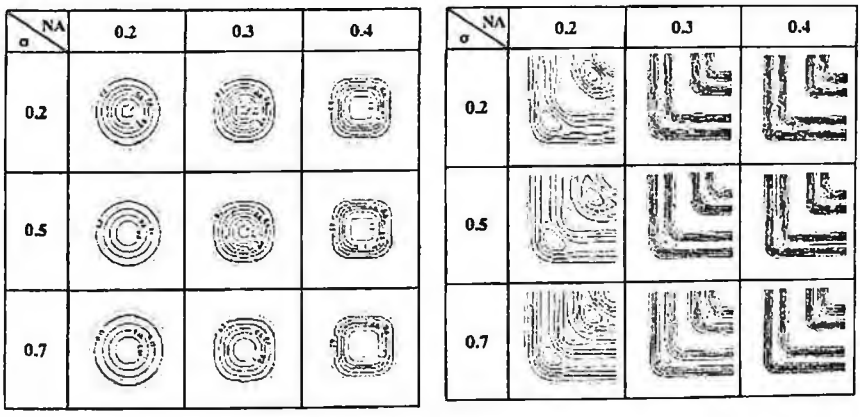

Figure 7. The characteristics of replicated patterns simulated using SPLAT.

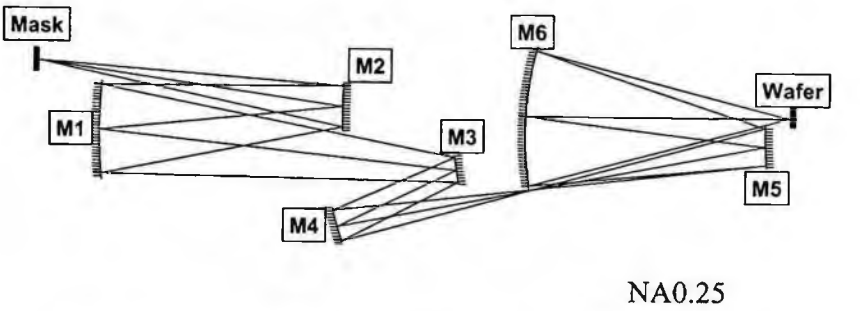

Figure 8. A 6-aspherical-mirror optics devised by Williamson in 1998.

to less than 0.25 nm. This camera enables 20-nm patterns to be replicated [12]. ASML, Nikon, and Canon have developed a practical EUVL system employing this type of optics.

3.2. *Fabrication and measurement of aspherical mirror*

Aspherical mirrors are key optical elements of the imaging optics and require high-precision fabrication. In general, the figure accuracy of one mirror can be obtained from Rayleigh's eq. (3) and Marechal's eq. (4):

$$\sigma = \lambda/4n \quad (\mathrm{P-V}) \tag{3}$$

$$G = \lambda/28\sqrt{n} \quad (\mathrm{RMS}), \tag{4}$$

where n is the number of mirrors. For example, the figure error for each mirror of imaging optics with six aspherical mirrors (Fig. 8) must be less than 0.56 nm P-V and 0.2 nm RMS.

Improvement in the precision of mirror fabrication is due to progress in the technology for measuring figure error. Utilizing computer-controlled polishing and a laser interferometer, to which phase analyzing equipment was added, Tinsley achieved a figure error of 0.3 nm(RMS).

Figure 9 illustrates the fabrication process for aspherical mirrors [13]. First, precision machining with a diamond grinding wheel produces the initial spherical surface to an accuracy of 1–2 μm, as measured with a contact-type profilometer. Second, an aspherical surface meeting the required specifications is fabricated by CCOS(*C*omputer *C*ontrolled *O*ptical *S*urfacing), which employs iterative polishing with substrate polishing tools and a phase-measuring interferometer to measure the shape. The final shape is acquired by repeated polishing and measurement. In 1993, the two aspherical mirrors for the system in Fig. 5 were delivered; but the accuracy was only 1.5 nm for the concave mirror and 1.8 nm for the convex one [14].

A new metrological method was needed to fabricate a mirror with an accuracy of better than 1 nm. Figure 10 shows a Twaiman green interferometer based on CGH, which applies a Fourier transform to the aspherical surface. CGH calculates

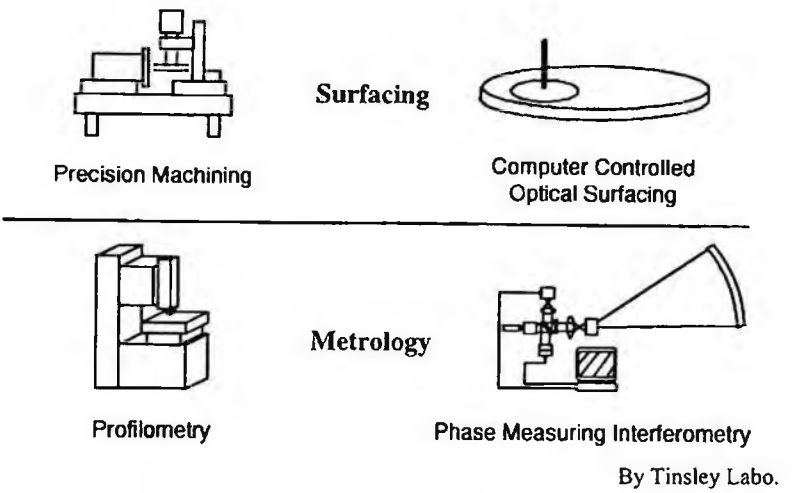

Figure 9. The fabrication process for aspherical mirrors.

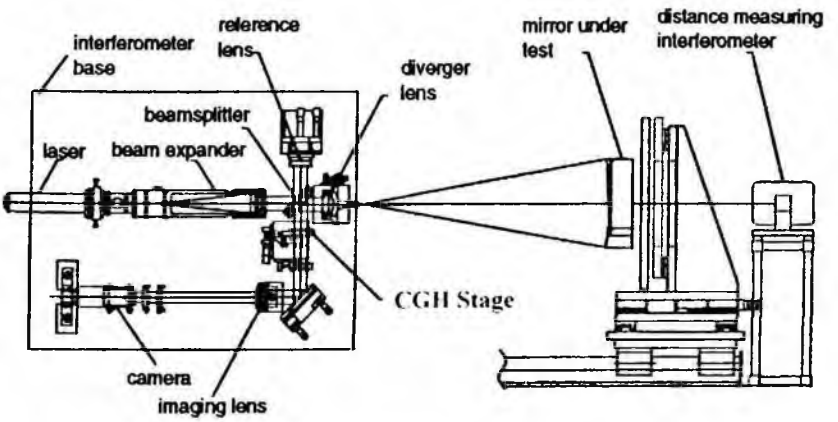

Figure 10. The aspherical mirror measurement using CGH.

interference fringes for actual and ideal wave fronts, and it enabled the precision to reach the required value. That is, this technique of processing the Fourier transform rather than the actual wave front provides an accuracy of 0.5 nm. Figure 11 shows a fabricated aspherical mirror. Further advances in the technology have reduced the roughness in the mid-frequency range, allowing an accuracy of 0.3 nm to be achieved in 2000.

An interferometer is used to measure the surface figure, and the measurement accuracy depends on the accuracy of the optics of the instrument itself. The need to overcome this limitation engendered the concept of a new type of interferometer for

	M1	M2	M3
Diameter	272 mm	116 mm	224 mm
Figure error (rms)	0.58 nm	0.58 nm	0.58 nm
Roughness (rms)	0.28 nm	0.31 nm	0.35 nm

Figure 11. A fabricated aspherical mirror in 1999.

which the accuracy of the instrument optics is not a factor determining measurement accuracy.

Gary E. Sommargren of LLNL considered the spherical wave emitted from a glass fiber and came up with the idea of determining shape from the interference fringes formed by the wave front reflected from the measurement optics and an ideal spherical wave, taking the uniformity of the diameter of the fiber core into account (Fig. 12[a–b]) [15,16]. Up to that time, a processed pinhole had been used, which produced a spherical wave that was far from ideal. The new system was a technological breakthrough that eliminated spatial restrictions on measurements and provided an accuracy in the sub-nanometer region. This method can measure the figure error of single-element optics and the wave-front error of optics with a couple of elements.

The LBNL group has developed a PDI (Fig. 13) using the exposure wavelength of EUV [17–19]. The light source is an undulator, and a transparent diffraction grating increases its intensity. ETS-1 and the MET system were aligned using this system; and a WFE of less than 0.5 nm was obtained over the entire field.

4. Source

Early research on EUVL employed synchrotron radiation (SR)[20]; but it soon became apparent that SR could not provide the required throughput. Thereafter, hopes centered on laser-produced plasma (LPP) because it has a smaller footprint than SR, and an exposure system with LPP is compatible with conventional equipment on a semiconductor production line.

SNL developed the first equipment for forming a Au tape target, which enables continuous irradiation [21]. Au, Sn, Ta, and W can be employed as a solid target to generate 14-nm-wavelength radiation from LPP. However, Sn and Au targets produce a great deal of debris [22,23]. The conversion efficiency (CE) of a solid target is generally over 1%; and for a Sn target, it is over 2%.

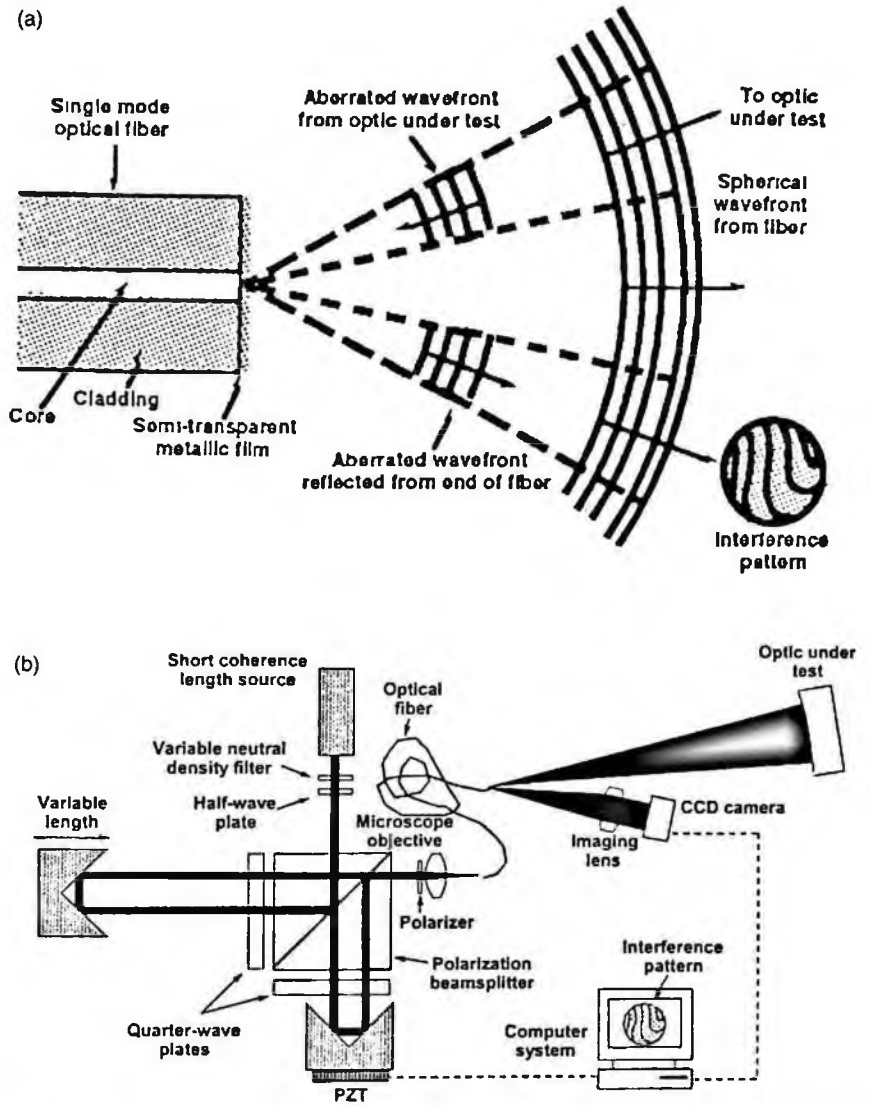

Figure 12. A PDI system devised by Gary E. Sommargren of LLNL: (a) principle of point diffraction interferometer, (b) configuration of spherical mirror test stand.

Various ways of reducing debris and increasing the lifetime of a mirror to 10^{10} shots have been investigated, such as the use of material with a light mass as a target, a helium atmosphere, and a chopper with a rapidly rotating slit. The Nikon has developed the new technologies shown in Fig. 14 [24]. Ways of reducing the amount of debris include the use of a Ta tape target, Kr buffer gas, which has a greater mass than He, and triple shielding. As a result, the amount of debris was reduced below the measurable limit.

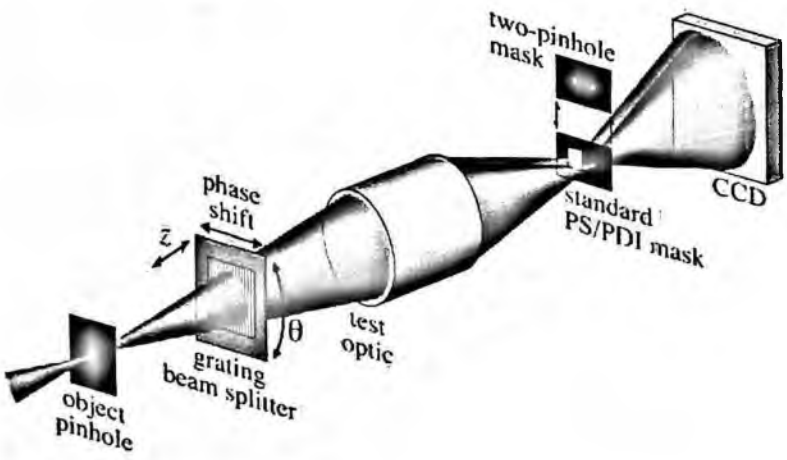

Figure 13. A PDI using the exposure wavelength of EUV developed by LBNL.

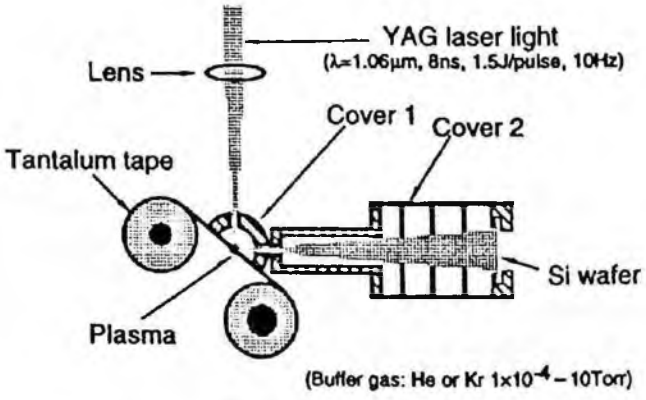

Figure 14. A debris shielding way developed by Nikon.

However, a great deal of debris scatters from a solid target. The use of a gas flow and a rotating chopper reduce the rate at which metal target debris is deposited by a factor of 10^3–10^4; but these methods still cannot extend the lifetime of a mirror to 10^{10}–10^{11} shots, which is required for a commercial system. Cryogenic targets have been proposed as a way of avoiding debris scattering [25]; and a system using a cryogenic target consisting of a Xe pellet irradiated with a 248-nm KrF laser was developed at SNL in 1994. A schematic diagram of the pellet injector and the associated fragmentation imaging apparatus is shown in Fig. 15. A Xe pellet is formed by isolating the pellet-formation tube with a valve, introducing Xe vapor to a pressure of -120 Torr, and allowing the pellet to grow for -20 sec. To inject the pellet, the isolation valve is opened and a 0.4 mm diameter pneumatic punch shears the pellet from the wall of the syringe and accelerates it into the vacuum chamber.

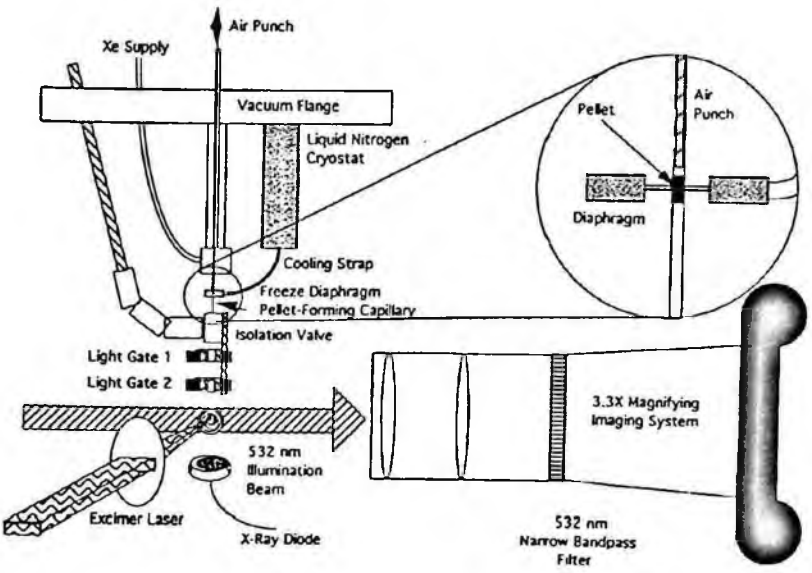

Figure 15. A schematic diagram of the pellet injector and the associated fragmentation imaging apparatus of cryogenic target.

A KrF excimer laser operating at 248 nm was used to irradiate pellets for plasma formation. The pulse energy and pulse width were 0.8 J and 32 ns, respectively, focused to achieve an intensity of 9×10^{10} watt/cm^2 on target. EUV radiation within a 4.5% bandwidth centered at 14.3 nm from the resulting laser plasma was reflected by a Mo/Si multilayer mirror into a calibrated Be-filtered x-ray diode to determine CE.

The peak conversion efficiency of a Xe target is 2.5% at a wavelength of 11 nm, but only 0.8% at a wavelength of 13.4 nm (Fig. 16). Furthermore, Xe fragments damage a multilayer mirror.

In order to avoid damage, a gas-jet target (Fig. 17) was devised [26]. Xe gas is emitted in a pulse from an ultrasonic nozzle into vacuum, and then adiabatic expansion produces a cluster as a target. Irradiating the cluster with a laser yields highly ionized plasma with an electron temperature of several tens of electronvolts. The energetic radiation created by the recombination and de-excitation of these ions is emitted in all directions, collected by a normal incidence mirror (collector), and focused on an intermediate point, from which it is relayed to the scanner optics and ultimately to the wafer. Although the conversion efficiency of Xe gas is about 0.5%, this is a promising method of debris removal.

To build a practical system with 6 aspherical mirrors and a reflective mask, stepper companies (ASML, Nikon, Canon, etc.) carried out simulations to determine the requirements of the source. They found that a source power of 115 W at the intermediate focus point is needed to obtain a throughout of 100 8-inch wafers/h, assuming a resist sensitivity of 5 mJ/cm^2.

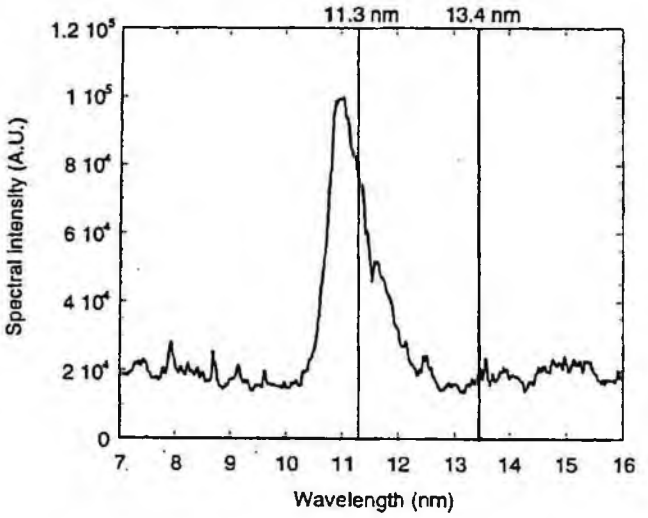

Figure 16. The peak conversion efficiency of a Xe target.

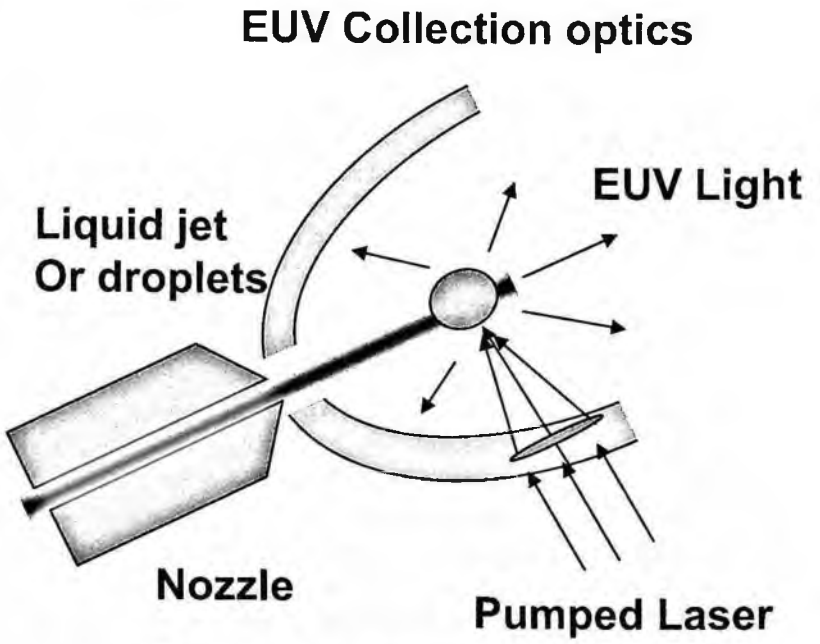

Figure 17. A gas-jet typed laser produced source.

Currently, two types of EUV sources, LPP and discharge-produced plasma (DPP: Fig. 18), are being investigated. In general, LPP has the advantages of collection over a large solid angle, little debris, and a high repetition rate. On the other hand, DPP has the advantages of high power and high efficiency, although ablation

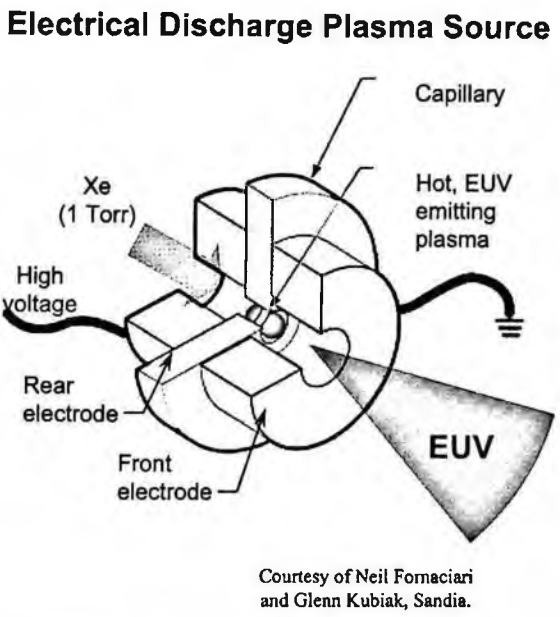

Figure 18. A discharge-produced plasma (DPP).

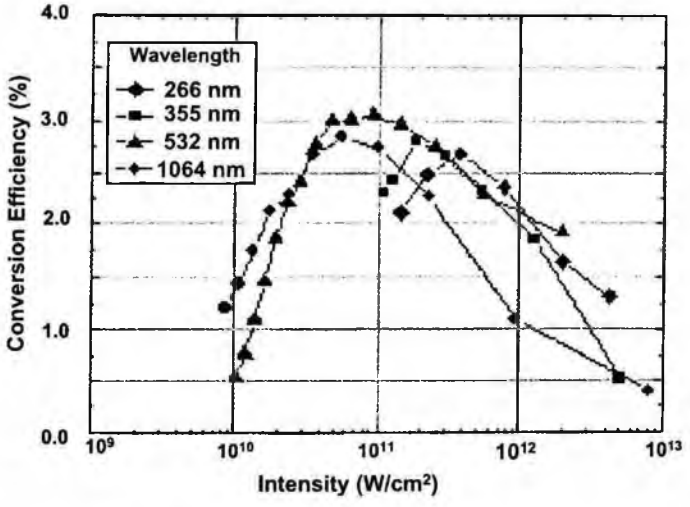

Figure 19. The measured lithium CE as a function of intensity.

of the electrode and the amount of debris are serious problems. DPP directly changes electrical energy into EUV light, while LPP first changes electrical energy into laser energy, which is then converted into EUV light.

Cymer Co. has been developing an LPP source for a practical system [28]. They are carrying out fundamental studies on the emission spectrum and conversion

efficiency of a Sn droplet target and the condensing efficiency of a normal-incidence mirror using a XeF (DUV) driving laser with an output of 800 W and a repetition frequency of 4 kHz. The typical conversion efficiency (CE) of this system is 0.5% into 2% BW and 2π sr. However, the efficient conversion of laser energy into EUV energy is critical to obtaining the required power. Several combinations of laser wavelength and source element CE have been examined. Plans call for the use of a Li rather than a Sn target and a CO_2 laser in a system for high-volume manufacturing (HVM).

Figure 19 shows the measured lithium CE as a function of intensity for 5 different driving laser wavelengths. Even under non-optimized conditions, the lithium CE is quite high, approaching 3%; and it is relatively insensitive to laser wavelength in the wavelength range from 266 nm to 1064 nm.

Figure 20 shows (a) the estimated Sn CE as a function of intensity for different driving laser wavelengths; and (b) the CE of a CO_2 laser as a function of lens position. A longer laser wavelength yields a higher CE; and a CE of 4% can be obtained for a CO_2 laser at a wavelength of 10.6μm. A CE as high as 5% has been reported for a wavelength of 1064 nm. Based on these experimental results, a Sn LPP source appears to be a viable option for an HVM source.

A DPP source for EUVL is potentially much simpler and less expensive than an LPP source. It employs high-voltage, high-current discharge pulses to form a 15-eV to 50-eV plasma in a gaseous medium, such as Xe, Sn or Li vapor. Angle-integrated EUV outputs of 7-mJ/eV pulses and repetition rates of up to 1000 Hz have recently been achieved for a Xe capillary discharge source, suggesting that it may be possible to scale the average power of this source to meet commercial requirements.

Xtreme Co. developed the first commercial Xenon GDPP source in 2003. It is based on the Z-pinch, which generates a power of 35 W within a solid angle of 2π sr. This source has been integrated into micro-exposure tools from Exitech Co., UK. The first tool has produced more than 100 million pulses without visible degradation of the source collection optics. Xtreme Co. has a GDPP source under development with a power of 115 W at the intermediate focus point for an HVM system [29]. It utilizes a Sn source and a rotating disk electrode.

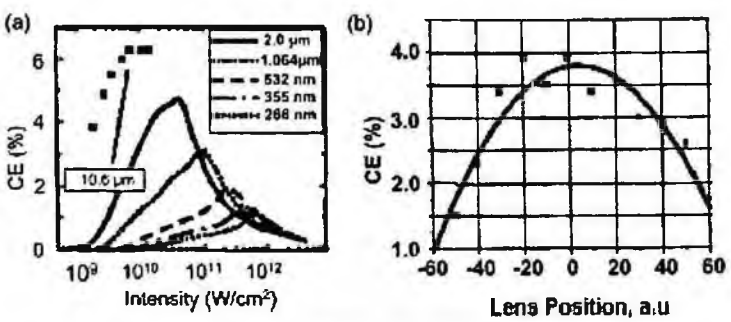

Figure 20. (a) The estimated Sn CE as a function of intensity for different driving laser wavelengths; and (b) the CE of a CO_2 laser as a function of lens position.

The Philips Co. Nova Sn GDPP source uses an electrical input power of over 10 kW and continuously delivers a power of 200 W in the EUV band over a solid angle of 2π sr [30]. 500 million shots have been generated; and the electrode lifetime is estimated to be at least 2 billion shots. The debris mitigation system is based on a two-step method that employs a foil-trap-based stage and a chemical cleaning stage. The total collector lifetime should be over 10 billons shots.

Although both systems have great potential, the best type of system will become clear after a suitable resist has been developed. Moreover, the lifetimes of the condensing efficiency and the condensing mirror are important factors determining conversion efficiency; further studies will be carried out in the future.

5. Reflection Mask

5.1. *Mask structure and mask fabrication process*

The EUV mask is one of the key technologies for establishing EUV lithography, with the production of defect-free substrates and phase defect measurements being critical issues. An EUV mask (Fig. 21) consists of an LTE glass substrate, a multilayer, a capping layer, a buffer layer, and an absorber pattern [31–33]. Table 3 shows the specifications of EUVL mask.

The use of LTE glass for EUV mask substrates is essential for reducing mask distortion caused by thermal loading during EUV exposure [34]. Corning's ULE^{TM} and

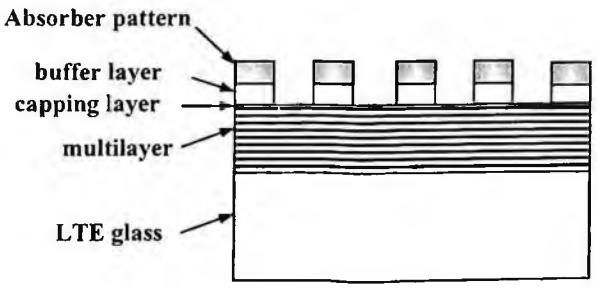

Figure 21. The configuration of EUVL mask.

Table 3. Specification of EUVL mask.

Item	Specification
Substrate size & properties	6025, LTE
Surface roughness of substrate	<0.15 nm(RMS)
Flatness of substrate	<50 nm (P-V)
Defect density of substrate	Zero (for defect size >50 nm)
Defect density of blank	$<0.003/cm^2$ (for 30-nm defects)
Reflectivity of blank	>67%(13.4 nm $\leq \lambda \leq$ 3.5 nm)

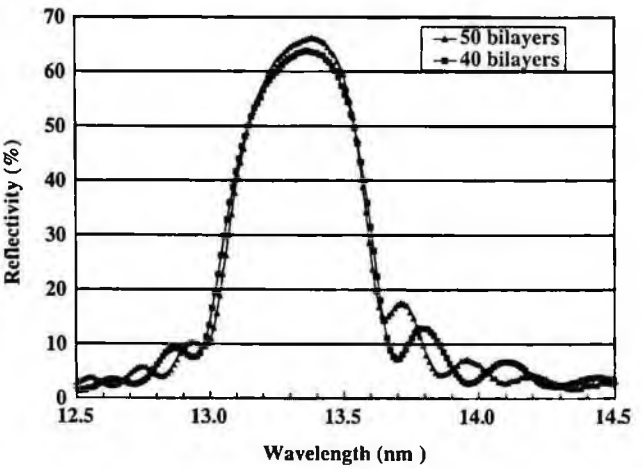

Figure 22. The reflectivity spectrum of typical multilayer blanks measured with the reflectometer at the NewSUBARU SR facility.

Schott's ZERODUR^{TM} are widely used as EUV mask substrates. ULE^{TM} glass is an amorphous SiO_2 glass doped with TiO_2, and has properties similar to those of quartz glass. Smooth surfaces with an RMS roughness of at most 0.15 nm, which meets the surface-finish requirements, have been created on ULE^{TM} glass by mechanical polishing [34]. ZERODUR^{TM} is a crystallized glass, and has several desirable properties for use as an EUV mask substrate due to its high Young's modulus and homogeneity. However, it is difficult to create ZERODUR^{TM} substrates with the required surface smoothness using conventional polishing methods. Some companies have developed new polishing technologies and obtained a flatness of less than 50 nm in tests using ULE^{TM}; further studies are necessary.

A multilayer consisting of Si and Mo has been found to be the most suitable for obtaining a high reflectivity at EUV wavelengths of 13–14 nm. One with 40 bilayers has a peak reflectivity of 69%, which meets the minimum reflectivity requirement of 67%. The reflectivity spectrum (Fig. 22) of typical multilayer blanks was measured with the reflectometer at the NewSUBARU SR facility. The deviation from the theoretical value of around 73% is thought to be due to the formation of interdiffusion layers between the Si and the Mo layers. Improvement of the deposition process should yield a reflectivity of 67% or more. The uniformity of the centroid wavelength (Fig. 23) of a multilayer blank was measured in 5-mm increments in the diagonal direction from the center to a corner. The range from the center to 70 mm corresponds to a 100-mm-square quality area. A centroid wavelength uniformity of ± 0.015 nm was achieved in a 100-mm-square area of a blank, which meets the specification of ± 0.03 nm.

The centroid wavelength and the reflectivity of multilayer blanks must be stable during the various steps of the mask fabrication process, such as cleaning and resist

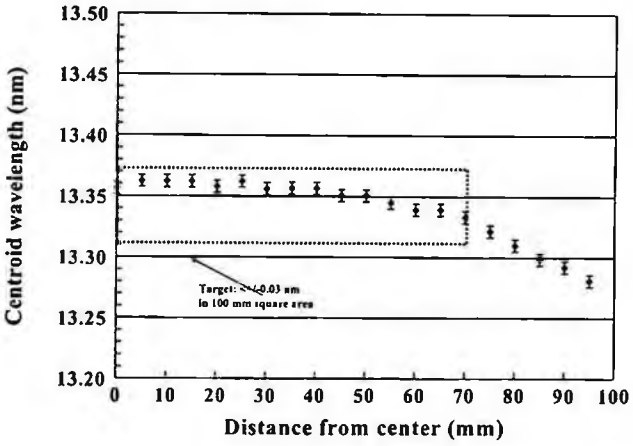

Figure 23. The uniformity of the centroid wavelength of a multi layer blank.

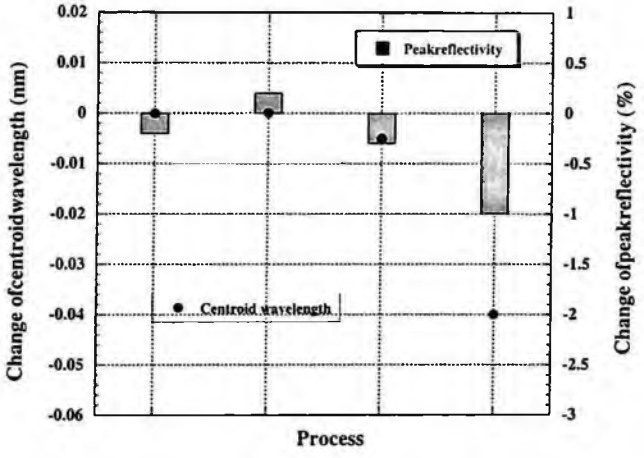

Figure 24. The process-induced damage to multilayer blanks.

baking. In order to investigate process-induced damage to multilayer blanks, blanks were baked in a hot-plate baking system with a 0.2 mm proximity gap in a temperature range of 100–200°C, and were also subjected to acid-based cleaning with either hot sulfuric acid or a solution containing H_2SO_4 and H_2O_2 [35]. Figure 24 shows how this treatment affected the centroid wavelength and peak reflectivity. Neither showed any significant change after acid cleaning or baking up to 150°C. On the other hand, baking at 200°C caused a slight 1% drop in reflectivity and a wavelength shift of 0.04 nm. This wavelength shift might prove unacceptable for the production phase. The change in the multilayer period was similar to the change in the centroid wavelength. It is known that baking at an elevated temperature

accelerates interdiffusion in Mo/Si multilayers, with a corresponding reduction in reflectivity and contraction of the period [36]. From these results, it was concluded that the wavelength shift and reflectivity drop for a multilayer blank was due to a thicker interdiffusion layer caused by thermal loading at 200°C. The results of this study thus indicate that a Mo/Si multilayer blank can withstand the acid-based cleaning and baking used in the conventional mask-making process.

Since the throughput of an EUV lithography system is strongly affected by the EUV reflectivity of the multilayers on the optics and the mask, the multilayers should be as reflective as possible. A peak reflectivity of 67% is required for the multilayer on a mask for the 45-nm node. The uniformity of the centroid wavelength and peak reflectivity of a multilayer blank must be tightly controlled to minimize illumination uniformity errors in the exposure system. According to simulation results, the variation in the multilayer period should be at most around ±0.02 nm to meet the tolerance requirements of the centroid wavelength.

TaN and Cr films have been reported to be the best candidates for the EUV absorber material [37–40]. SiO_2, SiON, C and Ru films are commonly used as repair buffers for a TaN or Cr absorber [41–43]. A buffer layer is required to protect the multilayer from damage during the repair of absorber defects with a focused ion beam (FIB). It needs to be patterned along with the EUV absorber layer as a stack to prevent any degradation in the EUV reflectivity of the multilayer [44–47].

In a typical mask fabrication process (Fig. 25), a Mo/Si multilayer composed of 40 bilayers and an 11-nm-thick Si capping layer are deposited on a ULE glass substrate [48–51]. The RMS surface roughness of an as-deposited multilayer is 0.16 nm in a 5-micron-square area on a polished ULE substrate, as measured with an AFM. A CrN buffer layer and a TaBN absorber are then deposited on the Si capping layer

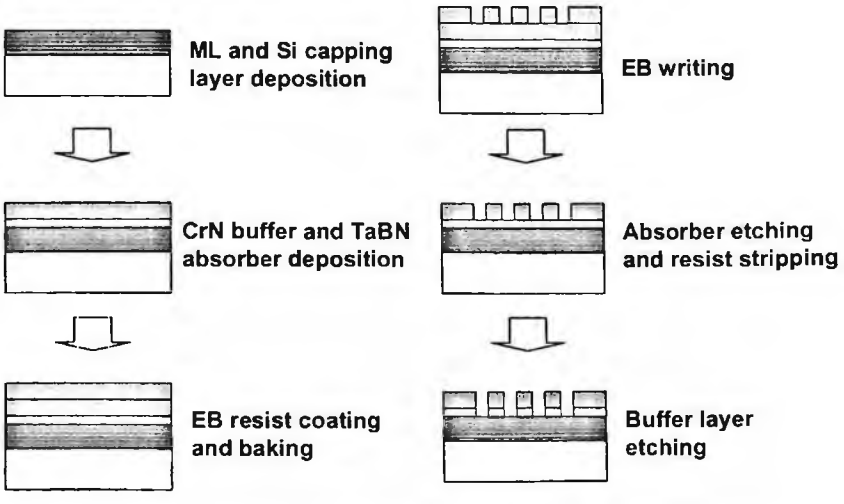

Figure 25. A typical mask fabrication process.

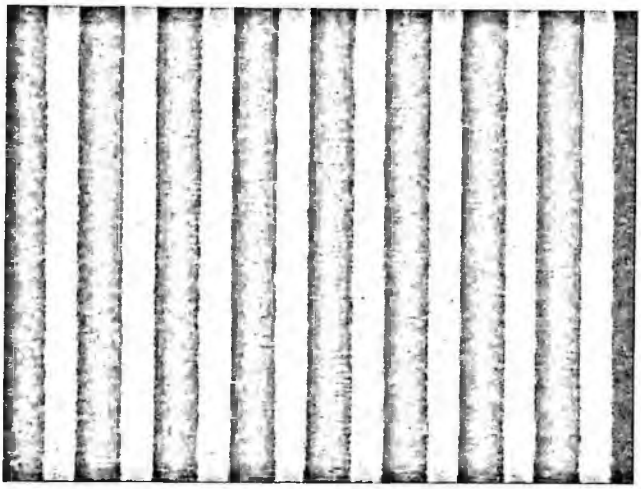

Figure 26. An EUV mask with a minimum feature size of 180 nm (width) for the 45-nm node.

by DC magnetron sputtering. After the lithography process, the TaBN absorber is etched in an ICP etching system using Cl_2 gas; the etching selectivity of TaBN with respect to the CrN buffer layer is around 20:1. Finally, the TaBN absorber pattern acts as a hard mask for the removal of the CrN buffer layer. The CrN buffer layer is etched with Cl_2/O_2 plasma; it has a high etching selectivity of 20:1 with respect to the Si capping layer. The surface roughness shows no change after this processing due to the high etching selectivity between CrN and Si. The Si layer was slightly thicker after the etching process, as measured with low-angle XRD. This is thought to be due to the oxidization of the Si layer by oxygen plasma. EUV masks can be produced without a significant drop in EUV reflectivity by optimizing the mask process and by using newly developed mask blanks. An EUV mask (Fig. 26) with a minimum feature size of 180 nm (width) for the 45-nm node was successfully fabricated using the optimized process.

5.2. *Actinic EUV mask inspection system*

The fabrication of defect-free masks is a critical issue in EUVL. Based on the ITRS, a defect width of less than 25 nm is required at the 32-nm node.

There are two types of defects (Fig. 27) in an EUVL mask: amplitude and phase defects. Amplitude defects are either particles on the surface of the multilayer or flaws in the multilayer. They can be detected directly by measuring the intensity of DUV light scattered from them. On the other hand, phase defects are produced when the multilayer is deposited over a bump or pit on the substrate, which results in swellings or depressions on the surface.

There are two techniques for detecting a small swelling on the surface: using deep ultraviolet (DUV, $\lambda = 257$ nm) light and using EUV light at the exposure

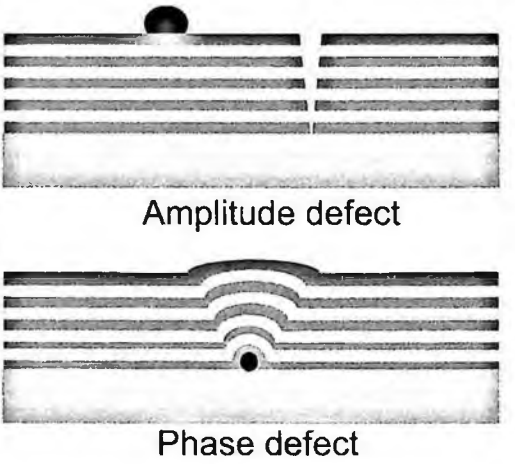

Figure 27. Two types of defects in an EUVL mask.

wavelength. The use of DUV light is the conventional method in optical lithography. However, it is difficult to detect defects on an EUVL mask by this method because the defects that need to be detected are much smaller than the inspection wavelength. That is, it is extremely difficult to detect defects of 50 nm or less using DUV light. Furthermore, since the characteristics of phase defects depend on the exposure wavelength, it is necessary to observe phase defects at the same wavelength as that used for exposure [52–56].

An actinic EUV mask inspection system (Fig. 28), the EUVM, has been installed on the BL-3 beamline of the NewSUBARU SR facility. It consists of Schwarzschild optics, a Mirau interferometer for phase-shift interference measurements, an X–Y sample stage for 6025 substrates, a focus detector, an X-ray zooming tube connected to a CCD camera, and an image processing computer. It is in a vacuum chamber evacuated down to a pressure of 1×10^{-5} Pa, and the vacuum chamber is on a vibration isolation table [57].

The system employs Schwarzschild optics with an NA of 0.3 and a magnification of 30×. Simulations predict that the system can resolve 10-nm-wide isolated lines under practical illumination conditions. The figure error of the mirrors, which are made of Zerodur, is less than 0.4 nm and the mid-frequency surface roughness is less than 0.15 nm. A D-space matching of less than 0.01 nm has been achieved at a wavelength of 13.5 nm. The RMS wavefront error of the Schwarzschild optics was measured with a Fizeau interferometer (ZYGO GPI) after assembly and found to be about 2 nm. The optics are installed in a housing made of Invar to prevent thermal expansion.

The X-ray imaging system is composed of an X-ray zooming tube (Kawasaki Heavy Industries Co., Ltd.), a CCD camera, and an image processing computer. The mask image is projected onto the X-ray zooming tube with electromagnetic

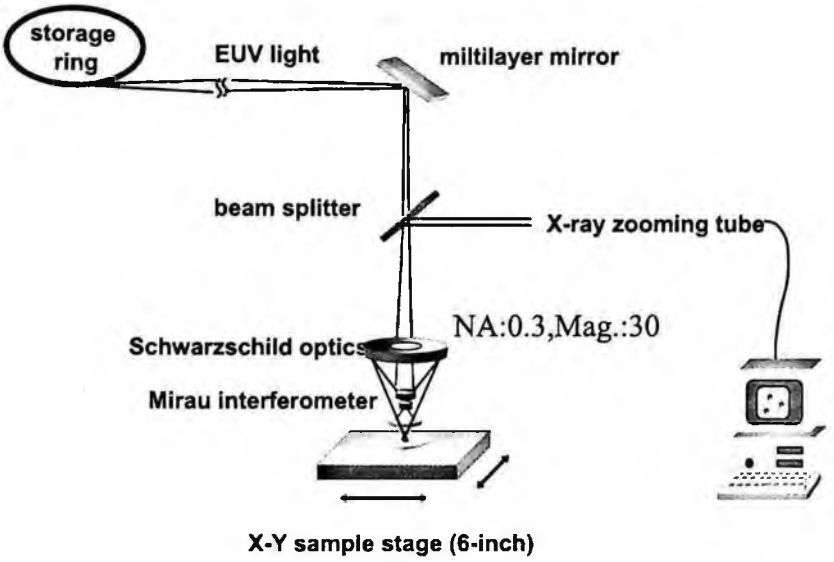

Figure 28. An actinic EUV mask inspection system.

lenses that can be tuned to vary the magnification in the range from 10 to 200. Thus, considering the magnification of the Schwarzchild optics, the total magnification of the microscope system is from 300× to 6000×. The resolution of the X-ray zooming tube is 0.3μm on a CsI photocathode. Defects 10 nm in size are magnified by the Schwarzschild optics to 300 nm. Thus, the resolution of the X-ray zooming tube is sufficient to enable the detection of 10 nm defects and to produce diffraction-limited images of mask patterns. The field of view of the X-ray zooming tube is 1.5 mm square at the CsI photocathode, which corresponds to 50 μm square on a mask surface. The magnified EUVM images are fed into a CCD camera and displayed on the screen of the image processing computer; the image data can be stored in the computer.

5.2.1. *Observation of finished mask* [58,59]

A finished EUVL mask was observed using the EUVM. A mask (Fig. 29) on a 6025-format substrate (ULE glass, Corning Inc.) was fabricated by HOYA Corporation. It has 300-nm-wide isolated lines. The white part is the top Si layer of the Mo/Si multilayer, and the dark part is the TaBN absorber. The EUVM is capable of resolving 300-nm-wide absorber patterns on a mask, which corresponds to 75-nm-wide patterns on a wafer, assuming the typical magnification of 1/4 for commercial exposure tools. The detection resolution estimated from the contrast at the edge of a pattern is 50 nm.

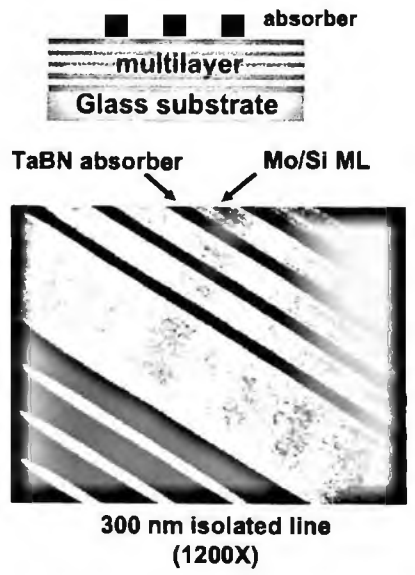

Figure 29. A finished EUVL mask observed using the EUVM.

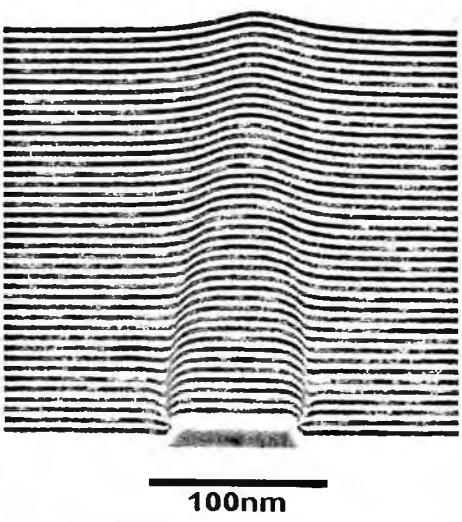

Figure 30. The TEM picture of programmed defect.

5.2.2. *Observation of phase defects* [59–61]

Mask blanks with programmed phase and bump defects were made on ULE glass substrates. The bump defects were made in a CrN layer deposited on a substrate, and the CrN was coated with a Mo/Si multilayer (Fig. 30).

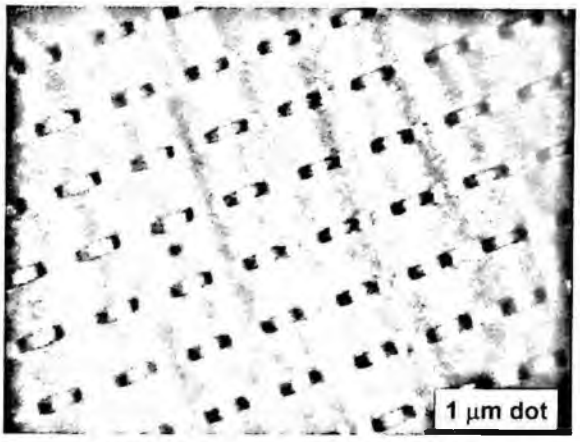

Figure 31. An EUV microscope image of programmed phase defects consisting of dots 1 μm wide and 5 nm high.

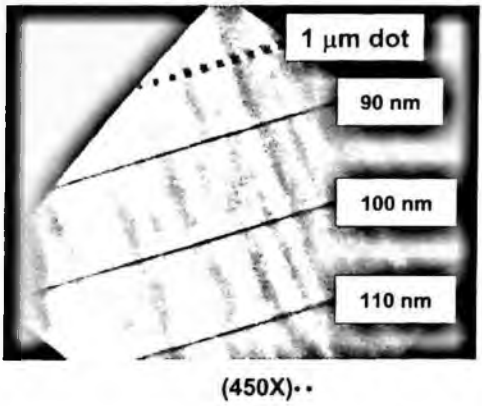

Figure 32. An EUV microscope images consisting of isolated lines with widths of 90 nm, 100 nm, 110 nm.

An EUV microscope image (Fig. 31) of programmed phase defects consisting of dots 1 μm wide and 5 nm high shows that such defects can, in fact, be detected, in spite of the astigmatic aberration of the illumination optics.

EUV microscope images (Fig. 32) were taken of phase defects consisting of isolated lines with widths of 90 nm, 100 nm, and 110 nm. The lines were 5 nm high and 500 μm long. Pit defects are more significant than bump defects because it is possible to remove some types of bump defects by ultrasonic cleaning.

EUVM images (Fig. 33) were also taken of 500-nm-wide lines and spaces and a 100-nm-wide isolated line with 5-nm-deep pit defects. Phase defects with a depth of 5 nm are printable.

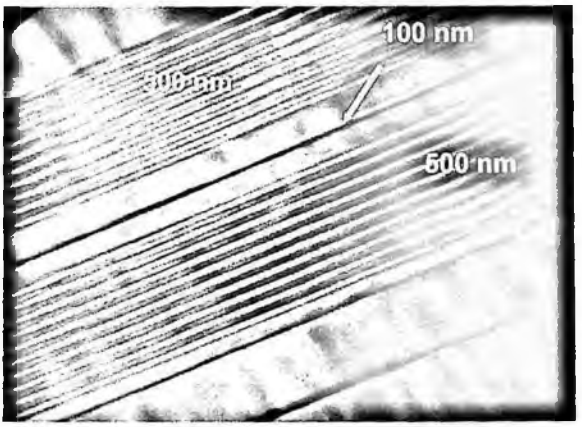

Figure 33. An EUVM images of 500-nm-wide lines and spaces and a 100-nm-wide isolated line with 5-nm-deep pit defects.

Thus, the actinic EUV mask inspection system is capable of detecting topological defects inside a multilayer. These results show that this system can detect internal reflectivity distributions, without depending on surface perturbations.

6. Contamination removal [62,63]

For a throughput of 80 wafers/h, the Mo/Si multilayers used in EUVL require a reflectivity of 67%. This throughput can be maintained as long as the drop in reflectivity is less than 2%, which would be caused by a 3-nm-thick layer of carbon contamination. However, EUV radiation initiates photochemical reactions that cause hydrocarbons to adsorb to the mirror and mask. This contamination degrades the reflectivity of the mask and imaging optics. Thus, a method of contamination removal is essential for a practical EUVL system. In a previous study, UV irradiation in an ozone atmosphere was found to be generally useful for removing contaminants from the glazing mirror of an SR beamline; and to accelerate carbon removal, the mirror is usually heated to a temperature of 150°C. However, since EUVL optics are precisely aligned and the mirrors cannot easily be detached from the exposure tool, cleaning of the imaging optics requires an *in situ* process without heating. This has led to an investigation of the use of synchrotron radiation for *in situ* contamination removal for the mirrors of EUVL tool; and light with a wavelength of 172 nm was found to be effective for masks, which require high-speed cleaning of a large area.

Outgassing in the chamber of an EUVL exposure system produces various species, and their partial pressure was measured as a function of mass number (Fig. 34) with a quadrupole mass spectrometer (M-100QA, ANELVA Co., Ltd.). The total pressure was 1×10^{-5} Pa. The main substances detected were H_2O, CO, N_2 and hydrocarbons. The partial pressure of the hydrocarbons was about 10%.

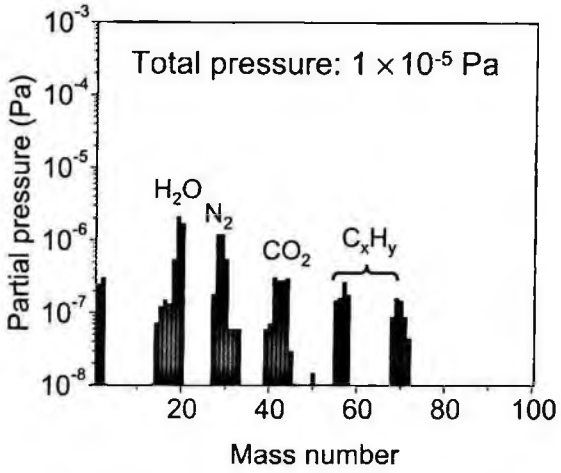

Figure 34. An outgassing in the chamber of an EUVL exposure system.

A sample Mo/Si multilayer was placed on the mask stage of the ETS-1 and irradiated with SR. The thickness was measured with a non-contact optical thickness measurement system (NANOMETRICS M5100A); the surface roughness of a contaminated region was measured with an atomic force microscope (AFM); and the reflectivity was measured with the reflectometer on the BL-10 beamline of the New-SUBARU. The incident angle for the reflectivity measurements was 2.05°, which is same angle employed in an EUVL exposure tool. After cleaning with SR, the thickness and surface roughness of the contaminated region and the multilayer reflectivity were measured again.

6.1. In situ *removal of contamination from an EUVL mirror using synchrotron radiation*

Contamination removal experiments for the cleaning of EUVL imaging optics were carried out on the BL-3 beamline of the NewSUBARU SR facility [6]. The mirror samples were 4-inch-diameter polished-silicon wafers covered with a Mo/Si multilayer. One mirror sample was used for several months in exposure experiments, and the thickness of the contaminants was found to be 170 nm. The SR-irradiated area on a sample was 20 mm in diameter. The oxygen flow rate was regulated with a gas flow controller (STEC). The initial back pressure of the chamber was 5×10^{-5} Pa, and an O_2 flow rate of 6 sccm kept the pressure at that level.

The relationship (Fig. 35) between the thickness of contaminants removed and exposure dose indicates that irradiation at a storage ring current of 130 mA for 7 hours removes a 0.1-μm-thick layer. In this case, the removal rate of 0.24 nm/min was obtained. In the photographs (Fig. 36[a–b]) of the surface of a mirror sample before and after cleaning. The dark region (Fig. 36[a]) is carbon contamination.

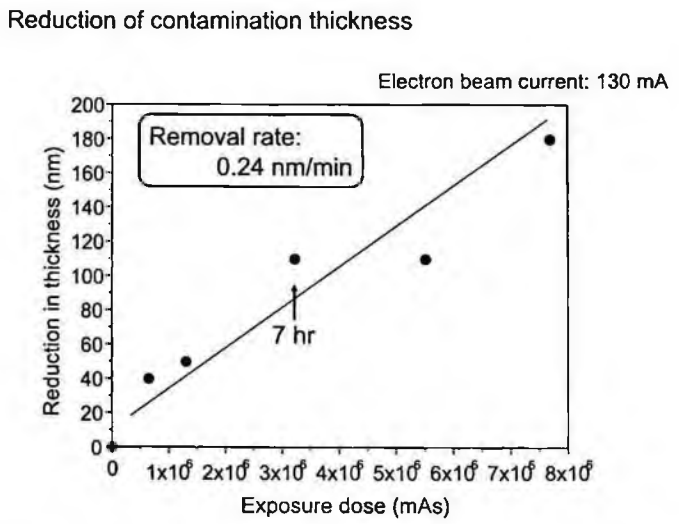

Figure 35. The relation of removal thickness and SR irradiation time.

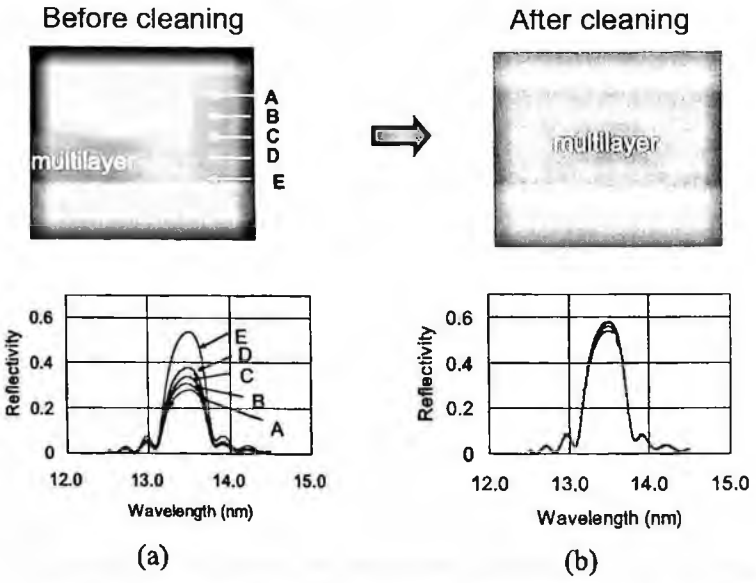

Figure 36. The photographs of the surface and reflectivity of a mirror sample before (a) and after cleaning (b).

Points A to D were covered with contaminants, and E was not contaminated, according to visual observations. Before cleaning, the reflectivity had values of 28%, 32%, 34%, 38% and 54% for Points A–E, respectively. However, cleaning completely removed the contamination (Fig. 36[b]); and the reflectivity was restored to the same

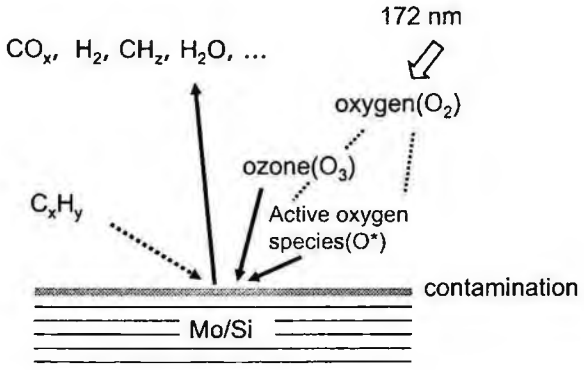

Figure 37. The mechanism of mask cleaning using 172 nm excimer lamp.

level as that of an uncontaminated region. Furthermore, the surface roughness of a cleaned region was found to be the same as that of a region that was not irradiated. Thus, it was found that cleaning using SR irradiation in an O_2-rich atmosphere is an effective way to remove contamination from optics without heating.

6.2. *Removal of contamination from a finished EUVL mask using 172-nm radiation*

The removal of contaminants by irradiation with a 172-nm excimer lamp (Ushio Lamp Co.) was investigated. Unlike 185-nm light, 172-nm light produces active oxygen directly from molecular oxygen because the absorption coefficient of molecular oxygen is 20 times larger at a wavelength of 172 nm than at 185 nm. Thus, a high density of active oxygen species can be produced, which should enable the efficient cleaning of masks (Fig. 37). The system is very simple and consists of just a 172-nm lamp and a sample stage. This makes it easy to install in a mask load-lock chamber. The system can clean an area 8 inches in diameter. In this study, two cleaning environments were investigated: air and a low-pressure environment, which was created with a scroll pump. The initial back pressure was 500 Pa, and an O_2 flow maintained the pressure at 2×10^3 Pa.

The relationship (Fig. 38) between cleaning time and the amount of contaminants removed shows that cleaning for about 40 minutes removes a 20-nm-thick layer of contaminants. The removal rate is higher in the low-pressure environment (2 nm/min.) than in air (0.53 nm/min.) because there is less photoabsorption by ambient gases. Figure 39 shows the reflectivity of a multilayer before and after cleaning for 40 minutes. The contaminated sample had a reflectivity of 50%; but contamination removal in a low-pressure environment restored the value to 60%. The change in surface roughness with cleaning time (Fig. 40) shows that contamination removal in a vacuum is more effective in reducing surface roughness than removal in air. Thus, it has been demonstrated that contamination removal under

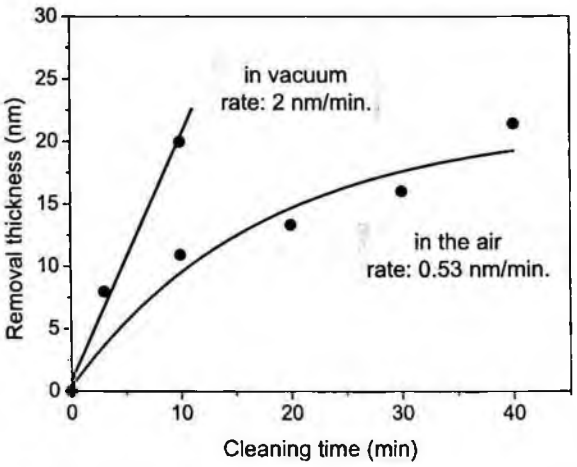

Figure 38. The relation of removal thickness of cabon contamination and irradiation time 172 nm excimer lamp.

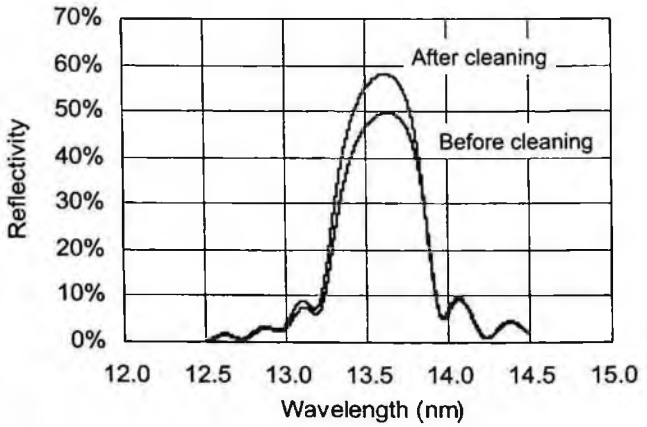

Figure 39. The reflectivity of before and after irradiation of 172 nm excimer lamp.

172-nm light irradiation in a low-pressure environment is an effective method of cleaning masks.

7. Resist

In general, since EUV light interacts strongly with many materials, the sensitivity is higher than that for 193-nm or 257-nm light. On the other hand, the depth of penetration into a resist is estimated to be less than 200 nm. Thus, exposure involves a smaller number of photons and the line edge roughness (LER) due to shot noise is worse.

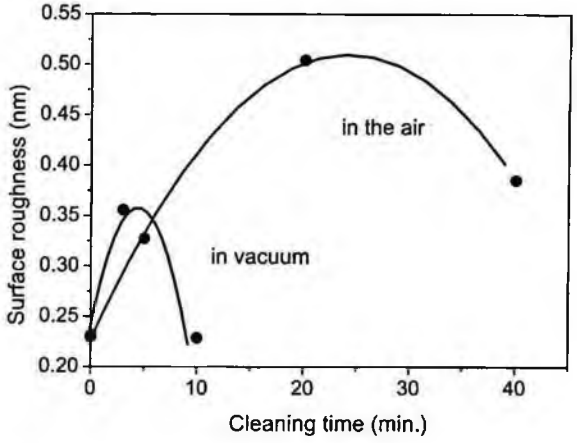

Figure 40. The surface roughness of mask cleaning using 172 nm excimer lamp.

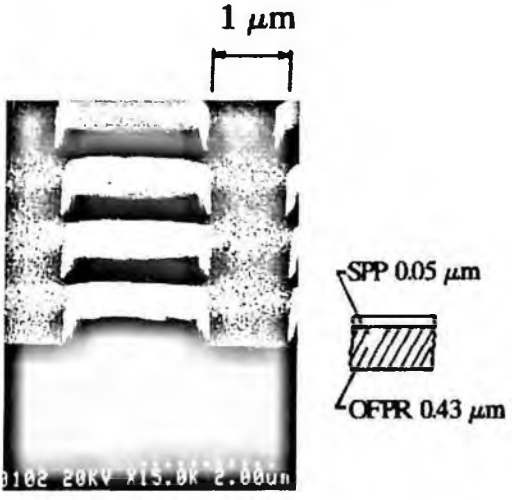

Figure 41. An exposure pattern of bilayer resist of 2 μm using reflection mask and SC optics; upper resit is silicone contained resist SPP and lower resit is OFPR.

In the early stages of this research, the target feature size for EUVL was 0.1 μm or less. And the required penetration depth is 3 times the feature size. Resist development focused on resist materials with a penetration depth of 0.3 μm, a bilayer resist structure (Fig. 41), or a silation process for surface treatment [3,64–66]. However, the target size has now dropped to less than 45 nm, which means that the penetration depth is 0.2μm. This is sufficient for replication using an ordinary resist. And currently, the critical issues for resists are lowering the LER and increasing the sensitivity because of the technical and cost problems with developing a high-power source.

Table 4. Specification of EUV resist for 32-nm node.

Item	Target
Resolution, gate	15 nm
Resolution, half pitch	50 nm
LER (3σ)	1.5 nm
Sensitivity	2–5 mJ/cm^2
Absorbance	1.1 μm^{-1}
DOF	$\geq$0.2 μm
Outgassing	1×10^{-6} pa

According to the ITRS (Table 4), EUV lithography will be introduced in 2009 for patterning at the 32-nm node [67]. The target resolution for the gates of an MPU is 15 nm for isolated lines and 50 nm for dense lines. At these feature sizes, the LER must be at most 1.5 nm (3σ) to avoid impacting device performance. This LER requirement is very challenging, especially when combined with a sensitivity target of $2 \sim 5$ mJ/cm^2. In addition, the absorption of EUV light should be limited so as to produce vertical side wall profiles. And a minimum depth of focus (DOF) of 200 nm is needed for high-volume manufacturing. Furthermore, EUV resists must not produce much outgassing to prevent contamination of the optics. Thus, LER, sensitivity, resolution and outgassing are the biggest issues in the development of EUV resists.

There are three types of EUV light sources: laser-produced plasma (LPP), discharge-produced plasma (DPP), and synchrotron orbital radiation (SOR). The required output power of 115 W at the entrance to the illuminator system in combination with the required lifetimes of the source components and collector optics make the source technology critical for EUV lithography. Currently, for a resist sensitivity of 10 mJ/cm^2 or 20 mJ/cm^2, the required power is 180 W or 200 W, respectively. That means that, to meet the ITRS roadmap for EUV lithography, the EUV source is the most critical issue. Thus, we need an EUV resist with a much higher photosensitivity to mitigate source power requirements. The most aggressive target is reported to be 2–5 mJ/cm^2 for EUV exposure, which is 5–10 times higher than that for KrF or ArF excimer laser lithography.

The LER of MOS transistors is becoming a serious obstacle to the establishment of a mass production technology for the sub-100 nm technology node. The LER of transistor gates causes variations in gate length that degrade device performance. A variation of at most 10% of the feature size of a gate pattern is required to guarantee the performance of LSIs. Many factors influence LER, such as mask roughness, optical-image quality, local variations in photochemical events due to shot noise, the molecular structure of resist polymers, and the degree of mixing of resist components. The reduction of LER is a primary goal of resist development that needs to be achieved for the mass production of advanced LSIs.

Furthermore, the reduction of LER is a great challenge when the sensitivity target for resists is as high as 2–5 mJ/cm^2. An evaluation [68,69] of KrF and EB chemically amplified positive-tone resists showed that sensitivity is inversely proportional to LER. Shot noise is the main factor affecting sensitivity and LER, and acid diffusion is the main factor affecting resolution. That means that it is very difficult to achieve both a higher sensitivity and a lower LER at the same time. Robert L. Braiard *et al.* [70] reported on the relationship between LER and the quantum efficiency of EUV. The LERs for EUV and KrF exposure were compared by plotting LER against E-size for both wavelengths. A rule of thumb is that LER $\propto$ Dose$^{1/2}$, which means that a higher resist sensitivity inevitably leads to a worse LER, regardless of exposure wavelength.

EUV lithography is carried out in a vacuum because most molecules strongly absorb light at EUV wavelengths. In addition, since EUV light has a very high energy, exposure easily induces the decomposition of organic bonds, such as carbon-carbon bonds. This raises the possibility of easing the trade-off between sensitivity and LER, based on the mechanism of non-chemically amplified resists. However, EUV exposure induces decomposition reactions that cause the outgassing of small molecules. The outgassed species not only increase the vacuum pressure, but they also seriously contaminate the reflective optics (mirror, mask), which reduces their reflectivity and produces ablation. To reduce outgassing in EUV lithography, the main consideration is the resist material [base polymer, solvent, photo acid generator (PAG)]. Thus, in the development of EUV resists, it is essential to take the outgassing characteristics of the components into consideration for the practical use of EUV lithography for mass production.

A system (Fig. 42) for evaluating resist outgassing and sensitivity has been installed on Beamline 3 of the NewSUBARU SR facility [71,72]. The system consists of an optics chamber, an exposure chamber, and a load-lock chamber. Seven reflections from Mo/Si multilayer mirrors are employed to monochromate SR light and extract EUV light, which simulates a practical exposure tool. The centroid wavelength is 13.57 nm. The size of the exposure beam is 4 mm square on a sample. A high-sensitivity quadrupole mass spectrometer (Model HAL/3F/PIC 501 RC,

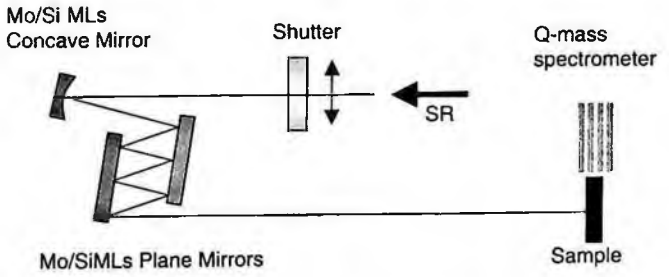

Figure 42. A system for evaluating resist outgassing and sensitivity.

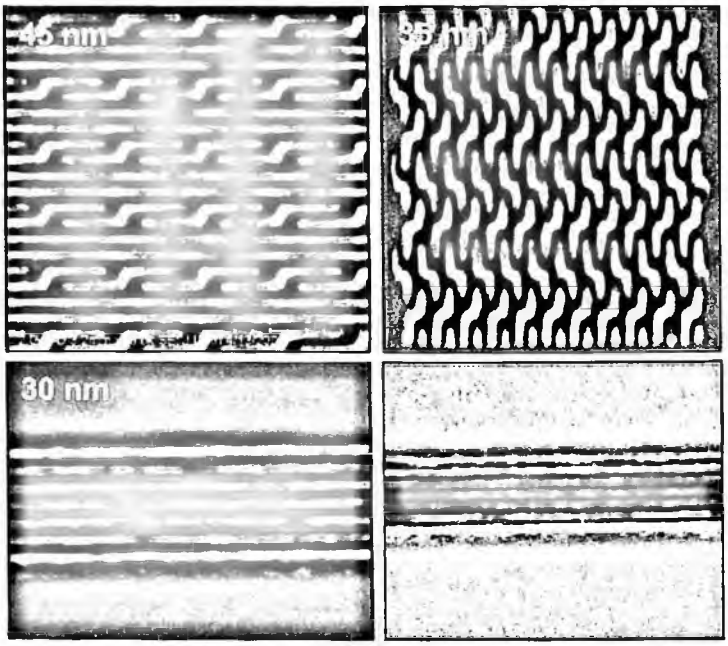

Figure 43. Recent experimental results of MET-2. Courtesy of Patrick Naulleau (CXRO/IBNL).

HIDEN ANALYTICAL Ltd.) connected to this system analyzes outgassed species according to mass number (from 1 to 500). This system enables the identification of the ion species outgassed under EUV irradiation for Eth sensitivity.

The resolution of resists was estimated using the Micro Exposure Tool (MET) systems at Berkeley and ISEMATEC and the HINA-3 system of ASET in Japan. Thus far, a resolution of 25 nm for line-and-space (L&S) patterns has been demonstrated (Fig. 43). Furthermore, 30-nm-wide isolated patterns with an LER of 3 nm have been replicated. A chemically amplified (CA) resist was used because it provides a higher contrast than other types of resists. To improve resist resolution and sensitivity, the addition of an acid generator, for which one photon induces several reactions, is being studied. And to improve the LER and the side wall profile, low-molecular-weight resists are being investigated.

From now on, the research will be accelerated through the use of exposure machines.

8. Exposure Tools and Experiments

In Japan, the NTT, Nikon, SORTEC and Hitachi groups are carrying out exposure experiments using Schwarzchild optics; and patterns with sizes of 0.1-0.05 μm have been replicated (Fig. 44) [75,76]. In the USA, the AT&T, SNL and LLNL groups

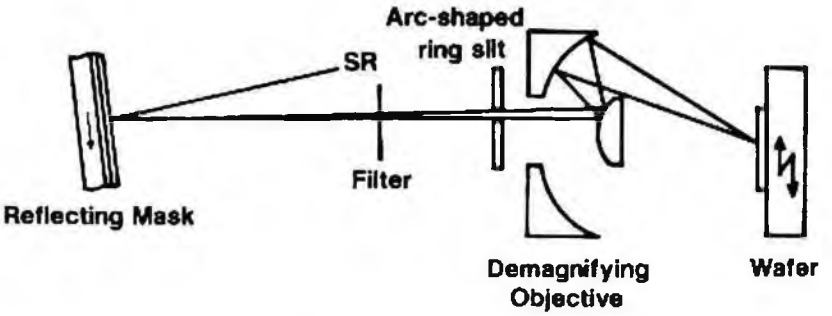

Figure 44. Exposure system developed by NTT in 1989.

Figure 45. The replicated patterns with a size of 0.05 μm replicated by AT&T.

have replicated patterns with a size of 0.05 μm (Fig. 45) [77–83]. Since spherical mirrors, which can easily be fabricated to a high accuracy, are employed for the optics, the resolution obtained (0.05 μm) is close to the diffraction limit. But a practical field size on a wafer is required. Thus, optics with a high resolution and a large field are being investigated.

The NTT group is investigating large-field exposure in an area 20 mm × 0.4 mm in size using a two-aspherical-mirror system; and patterns with a size of 0.15 μm have been replicated at a wavelength of 13 nm. In addition, a large field

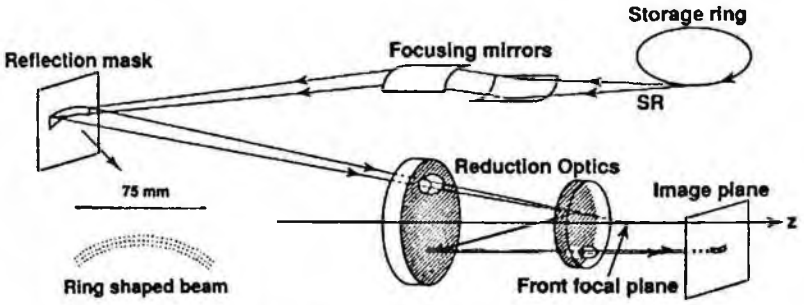

Figure 46. A two aspherical mirror system developed by NTT in 1991.

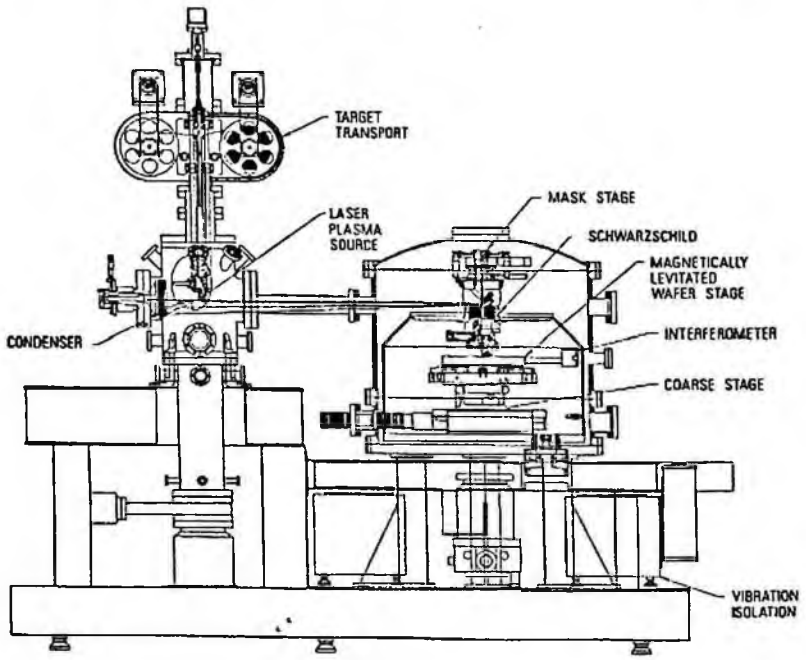

Figure 47. The exposure system developed by SNL, LLNL, LBL, and AT&T groups in 1995.

10 mm × 12.5 mm in size has been achieved using illumination optics and synchronized mask and wafer stages (Fig. 46) [84].

The SNL, LLNL, LBL, and AT&T groups have developed exposure tools (Fig. 47) for laboratory use [85]. They employ a laser-produced plasma X-ray source with a Cu wire target. The amount of debris is reduced to a practical level by using a rapidly rotating slit and a helium atmosphere. The optics, mask, and wafer stage are installed in the exposure chamber. The Schwarzchild optics consist of two aspherical mirrors with a wave-front aberration of less than 1 nm. They have the potential to replicate patterns with a size of 0.1 μm in an exposure area 0.4 mm square. The

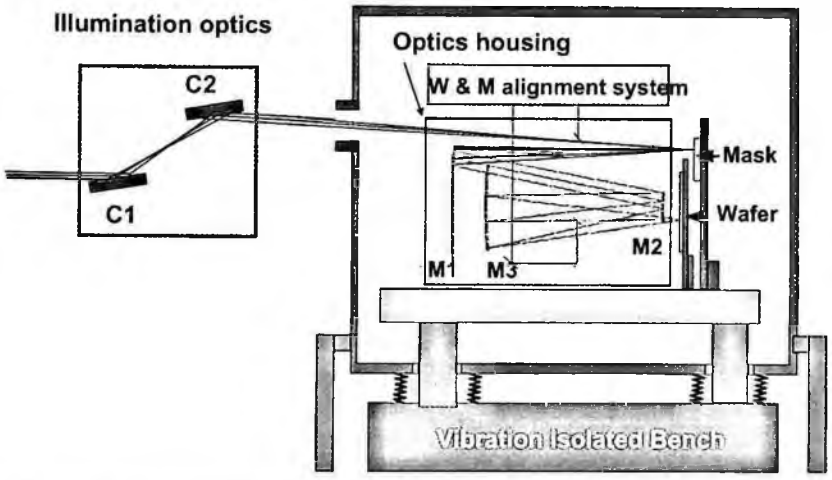

Figure 48. The configuration of a 3-aspherical-mirror system developed by HIT, Nikon and Hitachi.

wafer stage consists of a fine-positioning stage (stroke length: 300 μm) and a coarse-positioning stage (stroke area: 100 mm × 74 mm). The fine-positioning stage has 16 magnetic suspensions, and 6 shafts for repositioning. The alignment between mask and wafer is carried out by matching Moiré interference fringes from Moiré patterns on the mask and wafer through observation of an image from a CCD camera on a display. The measured resolution is 10–15 nm (3σ) for the X- and Y-directions. A wafer is held by an electrostatic chuck, and wafer distortion is measurable to an accuracy of ±0.15 μm by detecting the focus position on a wafer. Since the mask stage, the wafer stage, and the imaging optics are mounted on a vibration isolation table, and the whole system is mounted in a vacuum chamber. Utilizing this exposure tool, 0.1-μm NMOS transistors have been fabricated with an i-line hybrid exposure tool [86].

Figure 48 shows the configuration of a 3-aspherical-mirror system [87–89]. It consists of illumination optics, mask and wafer scanning stages, mask and wafer alignment optics, a reduction camera, and a load-lock chamber for loading wafers. The reduction camera consists of three aspherical mirrors. The magnification of the optics is 1/5. There is a distortion-free area less than 0.01 μm wide in a 1.0-mm-wide ring image field with a chord length of 30 mm on a wafer. So, by moving the mask stage in synchronization with the wafer stage, an exposure area of 30 mm × 38 mm can be achieved. The mask stage has five degrees of freedom. The Y-axis is used for scanning the mask, and the Z-axis is for focus and magnification alignment. The wafer stage consists of coarse- and fine-positioning stages. The course-positioning stage is driven by a pulse motor and a mechanical bearing guide. And the Z-axis of the wafer coarse-positioning stage has a measurement system with a resolution of 0.1 μm. The fine-positioning stage for mask and wafer alignment and focus alignment employs a piezoelectric transducer, which provides a resolution of 1 nm in the X- and Y-directions and 10 nm in the Z-direction. The photograph in Fig. 49 shows

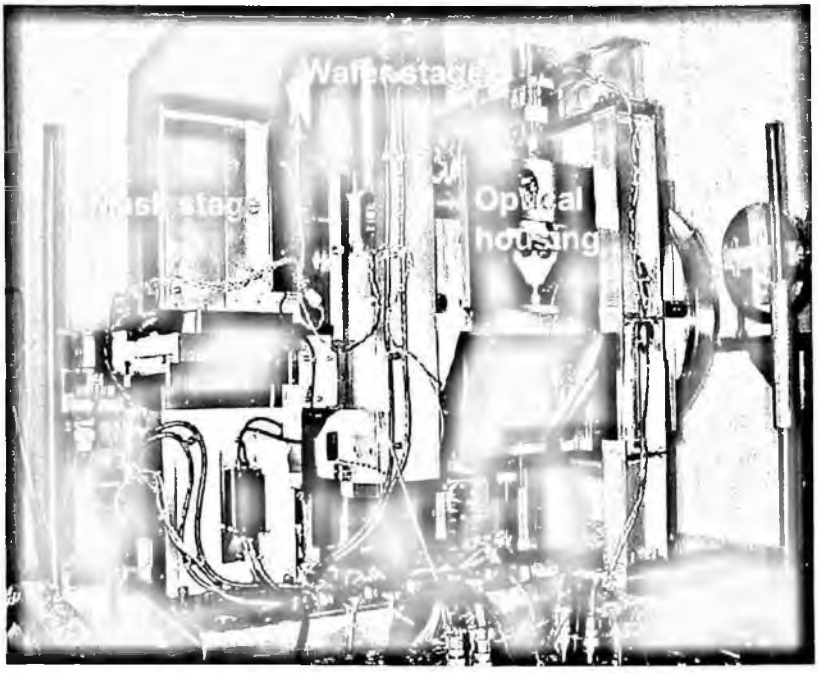

Figure 49. The photograph of overview of the system of a 3-aspherical-mirror system.

an overview of the system. The system is in a thermal clean chamber, in which the temperature is controlled to ±0.1 centidegree. The dimensions of the chamber are approximately 1 m × 1.2 m × 1 m. In 2000, this system was used to clearly observe 60-nm-wide L&S patterns and 40-nm-wide isolated lines in an exposure area 10 mm ×10 mm in size.

Figure 50 shows the ETS-1 developed by EUV-LLC [90]. It is a step-and-scan system with an operating wavelength of 13.4 nm. The POB is a multilayer-coated, four-mirror, ring-field system with a numerical aperture (NA) of 0.1 and an image reduction of 4:1. The field is a 30° sector of a ring field with a radius of 211 mm (chord length of 96 mm × width of 6 mm at the reticle). The reticle is a reflective multilayer-coated ULE substrate with a patterned absorber. The EUV radiation comes from laser-produced plasma generated by focusing a pulsed Nd:YAG beam onto a Xe cluster target. The source has a diameter of approximately 300 μm. It employs a 40-W laser, which delivers an EUV power of 0.11 mW/cm^2 on a wafer.

An experimental projection optics box was assembled and characterized by both visible-light and EUV interferometry. The wave-front error was measured by both techniques at 45 field points throughout the ring field. The mean RMS wave-front error across the field is 1.20 nm ($\lambda/l1$) in a 36-term Zernike polynomial decomposition, and varies between 0.90 nm and 1.4 nm. On average, the difference between the EUV and visible-light measurements was 0.25 nm RMS.

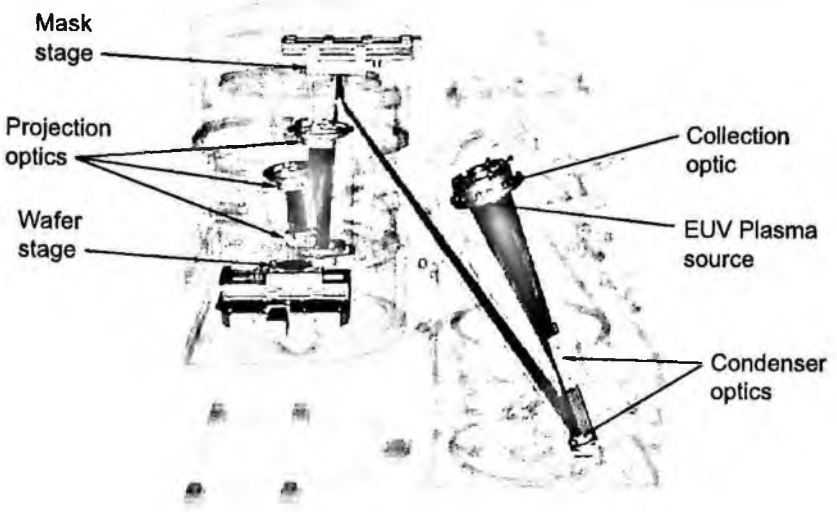

Figure 50. The ETS-1 developed by EUV-LLC.

Scanned images are formed by scanning the reticle at a constant velocity through the illuminated field of the projection optics. The wafer is synchronously scanned at a quarter of the mask velocity so that the scanned image appears stationary on the wafer. Any deviation from true synchronization, either in speed or direction, will blur the printed image. A feedback control system synchronizes the stages and dynamically references their positions to the POB structure. Several full-field scanned images, each measuring 24 mm × 32.5 mm, have been printed. The reticle scan speed was approximately 40 μm/s (limited by the EUV intensity). At velocities of zero and 40 μm/s the RMS jitter of the reticle stage is below 5 nm, and the jitter of the wafer stage is below 10 nm. The stages have also been tested at speeds of 20 mm/s, and were found to have the same jitter performance.

Static resist images of dense 1:1 elbow patterns, ranging in size from 100 to 300 nm, show as-expected image quality across the entire ring field of the projection optics. The 100-nm patterns, including both dense and isolated features, are well resolved throughout the entire field, and 80-nm patterns are well resolved at the center of the field, where aberrations are lowest. Full-field (24 mm × 32.5 mm) scanned images have been acquired. The scanned images of dense 100-nm elbow patterns are almost indistinguishable from the static images, proving that neither stage motion nor the POB static distortion field impacts image quality. Figure 51 shows isolated 3:1 elbow patterns with sizes of 45 nm and 39 nm. Although the system has an NA of 0.1, it has been proven that the NA can be increased to 0.25, which would enable patterns with a size of 32 nm or less to replicated.

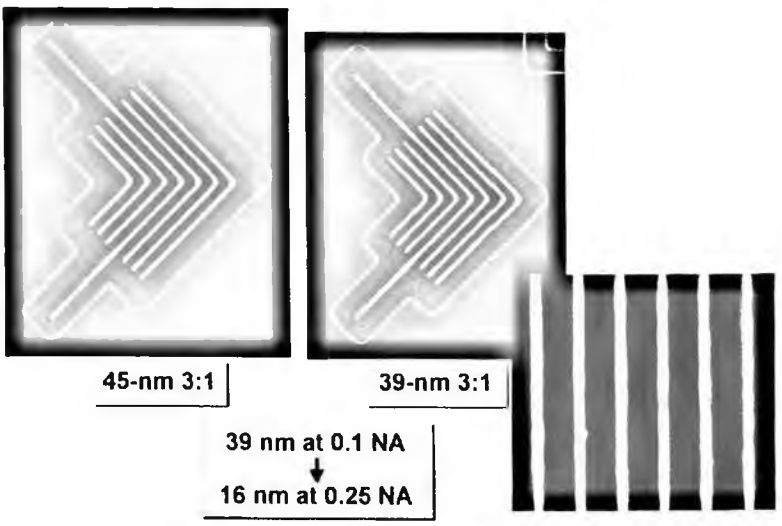

Figure 51. The exposure pattern using ETS-1.

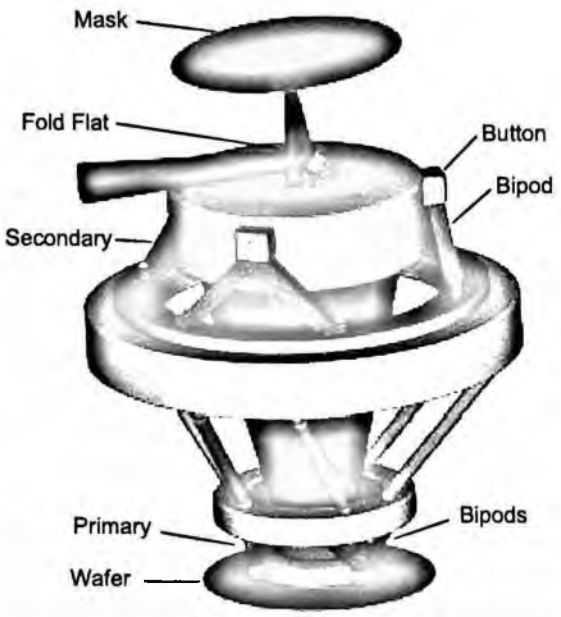

Figure 52. The Micro Exposure Tool (MET).

The Micro Exposure Tool (MET) (NA = 0.3) was built to clarify the minimum feature size of replicable patterns and to promote the development infrastructure in EUV-LLC (Fig. 52) [91]. This technology was subsequently transferred to ASML and a European company. Four systems are now available [92–94]. This system has a

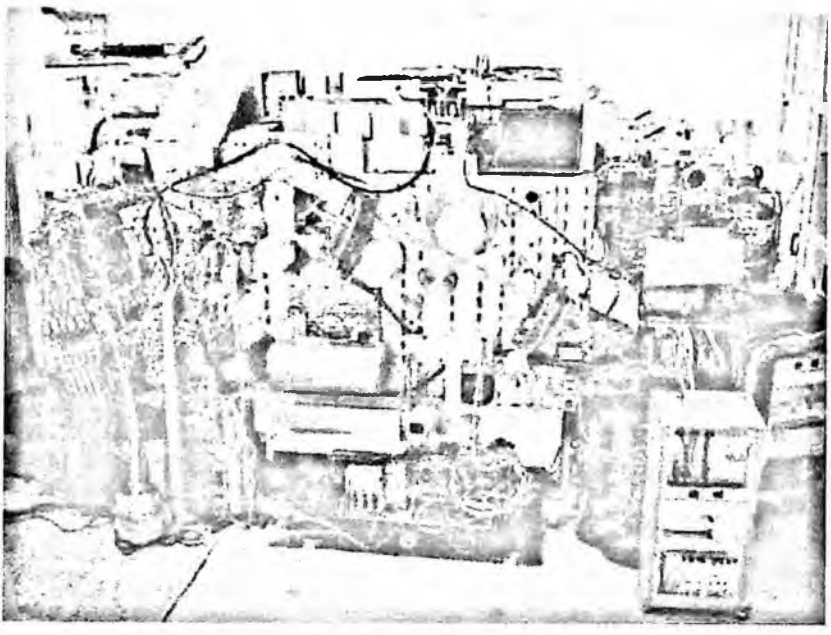

Figure 53. An EUVL α-demo tool developed by ASML.

2-aspherical-mirror system with a numerical aperture of 0.3, and a demagnification of 1/5. The exposure area is 100 μm × 200 μm. This system was used to replicate the 25-nm L&S pattern mentioned in Section 7. Regarding the performance of the optical system, the diffraction limit is 20 nm. Moreover, Exitech developed a commercial system with a DPP source in 2004. The two systems have been delivered and are being used for process studies.

On the other hand, an EUVL α-demo tool developed [95,96] by ASML was used to replicate the pattern in Fig. 53. It has been used to replicate a 40-nm L&S pattern. One feature of the system is that it employs newly developed wafer handling technology. This system will be tested at ISEMATECH this year (2006). Table 5 below shows the specifications.

9. Conclusions

An advanced exposure method has been devised that employs multilayer mirrors in the X-ray optics. The fabrication of the mirrors and multilayer coatings require nanometer-order accuracy. However, US researchers have made intensive efforts to measure and to fabricate aspherical mirrors. Now, the measurement technologies for figure error and the fabrication technologies are close to satisfying the target performance. EUVL is the most promising lithographic technology for device fabrication at the 32-nm node. Furthermore, the need for more advanced ultralarge-scale

Table 5. Specification if EUVL α-demo tool.

Item	Specification
λ	13.5 nm
NA range	0.15–0.25
Field size	26 mm × 33 mm
Wafer size	300 mm
Magnification	4×
Flare	16%
Dense L/S	40 nm
Isolated lines	30 nm
Iso/dense contact	55 nm
Overlay	12 nm
Throughput	10 wph

integrated circuits, such as MPUs, that operate at a high speed requires progress in a number of EUVL technologies. These technologies will become a driving force for progress in many other fields of science and technology.

References

1. H. Kinoshita, T. Kaneko, H. Takei, N. Takeuchi and N. Ishii, Extended Abstracts, The 47th Autumn Meeting, 1986; The Japan Society of Applied Physics, p. 322 [in Japanese].
2. T. Namioka, Current research activities in the field of multilayers for soft X-ray in Japan, *Revue Phys. Appl.* **23**, 1711–1726 (1988).
3. H. Kinoshita, K. Kurihara, Y. Ishii and Y. Torii, Soft x-ray reduction lithography using multiplayer mirrors, *J. Vac. Sci. Technol.* **B7**, 1648 (1989).
4. J. E. Bjorkholm, J. Bokor, L. Eichner, R. R. Freeman, J. Gregus, T. E. Jewell, W. M. Mansfield, A. A. MacDowell, E. L. Raab, W. T. Silfvast, L. H. Szeto, D. M. Tennant, W. K. Waskiewicz, D. L. Windt, R. Wood II and J. H. Bruning, Reduction imaging at 14 nm using multiplayer-coated optics: Printing of features smaller than 0.1μm, *J. Vac. Sci. Technol.* **B8**(6), 1509–1513 (1990).
5. M. Yamamoto. Soft X-ray Multilater, *NEW GLASS*, **10**(2), 43 (1995).
6. K. Kurihara, H. Kinoshita, N. Yakeuchi, T. Mizota, T. Haga and Y. Trii, Two-mirror telecentric optics for soft x-ray reduction lithography, *J. Vac. Sci. Technol.*, **B9**(6), 3189 (1991).
7. T. E. Jewell, M. M. Becker, J. E. Bjorkholm, J. Boker, L. Eichner, R. R. Freeman, W. M. Mansfield, A. A. Macdowell, M. L. O'Malley, E. L. Raah, W. T. Silftvast, L. H. Szeto, D. M. Tennant, W. K. Waskieewicz, D. L. White, D. L. Windt, O.R. Wood II and J. H. Bruning, *Proc. of the SPIE Symp. on Microlithography*, March, San Jose, 1263 (1990).
8. T. Jewell, J. Rodgers and K. Thompson, *J. Vac. Sci. Technol.*, **B8**(6), 1519 (1990).
9. D. A. Tichenor, G. D. Kubiak, S. J. Haney, R. P. Nissen, K. W. Berger, R. W. Arling, A. K. Ray-Chaudhui, K. B. Nguyen, R. H. Stulen, J. B. Wronosky, J. D. Jordan, T. G. Smith, J. R. Darnold, P. M. Kahle, J. E. Bjorkholm, O. R. Wood II, G. N. Taylor and R. S. Hutton, Recent results in the development of a integrated EUVL laboratory tool, *SPIE*, **2437**, 292–307 (1995).

10. D. Tichenor *et al.*, *Proc. SPIE*, **3997**, 48 (2000).
11. Williamson: U.S. Patent 5,815,310 (1998).
12. H. Mailing, J. Benschop, U. Dinger and P. Kurz, Progress of α-RT, the EUVL Alpha Reaearch Tool, *Proc. SPIE*, **4343**, 38 (2001).
13. D. Bajuk and R. Kestner, Fabrication and testing of EUVL optics, JSPE Proceedings of the second US-Japan Workshop on Soft X-ray Optics: Technical Challenges, Mt. Fuji, Nov. 12–14, (1996).
14. H. Kinoshita, K. Kurihara, T. Mizota, T. Haga, H. Takenaka and Y. Torii, Large-area, high-resolution pattern replication by the use of a two-aspherical-mirror system, *Appl. Optics 32*, **34** 7079–7083 (1993).
15. G. Sommergran, Phase Shifting Diffraction Interferometry for Measuring Extreme Ultraviolet Optics, *OSA Trends in Optics and Photonics*, **4**, 108–112 (1996).
16. Gary E. Sommargren, Donald W. Phillion and Eugene W. Campbell, Sub-nanometer Interferometry for Aspheric Mirror Fabrication, *Precision Science and Technology for Perfect Surfaces*, 329–335 (1999).
17. K. A. Goldberg, R. Beguiristain, J. Bokor, H. Medecki, D. T. Attwood, K. Jackson, E. Tejnil and G. E. Sommargren, Progress towards $\lambda/20$ extreme ultraviolet interferometry, *J. Vac. Sci. Technol.* **B13**(6), 2923–2927 (1995).
18. E. Tejnil, K. A. Goldberg, H. Medecki, J. Boker and D. Attwood, Phase-Shifting Point Diffraction Interferometer for At-Wavelength Testing of Lithographic Optics, *OSA Trends in Optics and Photonics*, **4** (1996).
19. K. Goldberg, P. Naulleau, P. Baston, P. Denham, E. Anderson, H. Chapman and J. Bokor, Extreme ultraviolet alignment and testing of a four-mirror ring field extreme ultraviolet optical system, *J. Vac. Sci. Technol.* **B18**(6), 2911–2915 (2000).
20. J. B. Murphy, D. L. White, Alastair A. MacDowell and Obert R. Wood II, Synchrotron radiation sources and condensers for projection x-ray lithography, *Appl. Optics 3234*, 6920–6929 (1993).
21. G. D. Kubiak, D. A. Tichenor, M. E. Malinowski, R. H. Stolen, S. J. Haney, K. W. Berger, L. A. Brown, J. E. Bjorkholm, R. R. Freeman, W. M. Mansfield, D. M. Tennant, O. R. Wood, II, J. Bokor, T. E. Jewell, D. L. White, D. L. Windt and W. K. Waskiewicz, Diffraction-limited soft x-ray projection lithography with a laser plasma source, *J. Vac. Sci. Technol.*, **B9**(6), 3184–3188 (1991).
22. G. D. Kubiak, K. W. Berger, S. J. Haney, P. D. Rockett and J. A. Hunter, Laser Plasma Sources for SXPL: Production and Mitigation of Debris, *OSA Proceedings on soft X-Ray Projection Lithography*, **18**, 127–131 (1993).
23. Paul D. Rockett, John A. Hunter, Glenn D. Kubiak, Kevin Krenz, Harry Shields and Michael Powers, Detailed EUV Characterization of Laser-Plasma Sources for EUV Lithography, *OSA Proceedings on Extreme Ultraviolet Lithography*, **23**, 255–259 (1994).
24. N. Kandaka and H. Kondo, Decreasing debris emitted from a laser produced plasma, *JSPE Proceedings of the 2nd US-Japan Workshop on Soft X-ray optcs* (1996).
25. Glenn D. Kubiak, Kevin D. Krenz, Kurt W. Berger, Timothy G. Trucano, Paul W. Fisher and Michael J. Gouge, Cryogenic Pellet Laser Plasma Source Targets, *OSA Proceedings on Extreme Ultraviolet Lithography*, **23**, 248–254 (1994).
26. G. Kubiak, L. Bernardez, K. Krenz, D. O'Connell, R. Gutowski and A. Todd, Debris-free EUVL sources based on gas jets, *OSA TOPS on Extreme Ultraviolet Lithography*, **4**, 66–71 (1996).
27. G. Kubiak, L. Bernardez and K. Krenz, High-power extreme ultraviolet source based on gas jets, *SPIE*, **3331**, 81–89 (1998).

28. B. Hansson, I. Fomenkov, N. Bowering, A. Ershov, W. Partlo, D. Myers, O. Khodykin, A. Bykanov, C. Rettig, J. Hoffman, E. Vargas, R. Simmons, J. Chavez, W. Marx and D. Brandt, LPP EUV Source Development for HVM, *SPIE*, **6151**, 61510R1–61510R9 (2006).
29. U. Stamm, J. Kleinschmidt, D. Bolshukhin, G. Hergenhan, V. Korobotchko, B. Nikolaus, M. C. Schurmann, G. Schriever, C. Ziener and V. M. Borisov, Development status of EUV sources for use in Beta-tools and high-volume chip manufacturing tools, *SPIE*, **6151**, 61510O1–61510O11 (2006).
30. J. Pankert, R. Apetz, K. Bergmann, M. Damen, G. Derra, O. Franken, M. Janssen, J. Jonkers, J. Klein, H. Kraus, T. Krucken, A. List, M. Loeken, A. Mader, C. Metzmacher, W. Neff, S. Probst, R. Prummer, O. Rosier, S. Schwabe, S. Seiwert, G. Seimons, D. Vaudrevange, D. Wagemann, A. Weber, P. Zink and O. Zitzen, EUV Sources for the Alpha-Tools, *SPIE*, **6151**, 61510Q1–61510Q9 (2006).
31. Andrew m. Hawryluk, Natale M. Ceglio and David P. Gaines, Reflection mask technology for x-ray projection lithography, *J. Vac. Sci. Technol.*, **B7**(6), 1702–1704 (1989).
32. D. M. Tennant, J. E. Bjyokholm, R. M. D'Souza, L. Eichner, R. R. Freeman, J. Z. Pastalan, L. H. Szeto, O. R. Wood II, T. E. Jewell, W. M. Mansfield, W. K. Waskiewicz, D. L. White, D. L. Windt and A. A. MacDowell, Reflective mask technologies and imaging results in soft x-ray projection lithography, *J. Vac. Sci. Technol.*, **B9**(6), 3176–3183 (1991).
33. H. Kinoshita, T. Watanabe, A. Ozawa and M. Niibe, Mask technology of extreme ultraviolet lithography, *SPIE*, **3412**, 358–368 (1998).
34. S. Gianoulakis and A. Ray-Chaudhuri, Themal-mechanical performance of extreme ultraviolet lithography reticles, *J. Vac. Sci. Technol.*, **B16**(6), 3440–3443 (1998).
35. H. Nii, H. Kinoshita, T. Watanabe, Y. Matsuo and Y. Sugie, Studies on EUV mask cleaning by dry and wet processes, *Proceeding of SPIE* **4409**, 687–694 (2001).
36. W. M. Tonh, J. S. Taylor, S. D. Hector and M. K. Shell, Mask substrate requirements and development for extreme ultraviolet lothography (EUVL), *SPIE*, **3873**, 421 (1999).
37. S. Yulin, T. Kuhlmann, T. Feigl and N. Kaiser, Damage Resistant and Low Stress EUV Multilayer Mirrors, *SPIE*, **4343**, 607 (2001).
38. P. Y. Yan, G. Zhang, P. Kofron, J. Powers, M. Tran, T. Ling, A. Stivers and F. C. Lo, EUV Mask absorber. characterization and selection, *SPIE*, **4066**, 116 (2000).
39. P. Y. Yan, G. Zhang, A. Ma and T. Liang, TaN EUVL Mask Fabrication and Characterization, *SPIE*, **4343**, 409 (2001).
40. H. Nii, H. Kinoshita, T. Watanabe, K. Hamamoto, H. Tsubakino and Y. Sugie, Performance of Cr mask for extreme ultraviolet lithography *Proceeding of SPIE*, **4409**, 681–686 (2001).
41. J. Wasson, K. Smith, P. J. S. Mangat and S. Hector, An Infinitely Selective Repair Buffer for EUVL Reticles, *SPIE*, **4343**, 402 (2001).
42. J. R. Wasson, B. Lu, P. J. S. Mangat, K. Nordquist and D. J. Resnick, Writing, repairing, and inspecting of extreme ultraviolet lithography reticles considering the impact of the materials, *J. Vac. Sci. Technol.* **B19**(6), 2635 (2001).
43. B. T. Lee, E. Hoshino, M. Takahashi, T. Yoneda, H. Yamanashi, H. Hoko, M. Ryoo, A. Chiba, M. Ito and M. Sugawara, Approach to Patterning of Extreme Ultraviolet Lithography Masks using Ru Buffer Layer, *Jpn. J. Appl. Phys.*, **40**, 6998 (2001).
44. D. M. tenant, L. A. fetter, L. R. Harriott, A. A. MacDowell, P. P. Mulgrew, W. K. Waskiewicz, D. L. Windt and O. R. Wood II, Detect repair for soft x-ray projection lithography masks, *J. Vac Sci. Technol.*, **B10**(6), 3134–3140 (1992).

45. Andrew M. Hawryluk and Diane Stewart, Repair of opaque defects on reflection masks for soft x-ray projection lithography, *J. Vac. Sci. Tecnol.*, **B10**(6), 3182–3185 (1992).
46. K. Early, D. L. Windt, W. K. Waskiewicz, O. R. Wood II and D. M. Tennant, Repair of soft-x-ray optical elements by stripping and redeposition of Mo/Si reflective coatings, *J. Vac. Sci. Technol.*, **B11**(6), 2926–2929 (1993).
47. Y. Tanaka, K. Fujii, K. Suzuki, T. Iwamoto, S. Tsuboi and Y. Matsui, Fabrication of NIST-format x-ray masks with 4-Gbit DRAM test patterns, *SPIE*, **4409**, 660 (2001).
48. W. M. Tonh, J. S. Taylor, S. D. Hector and M. K. Shell, Mask substrate requirements and development for extreme ultraviolet lothography (EUVL), *SPIE*, **3873**, 421 (1999).
49. P. Y. Yan, G. Zhang, A. Ma and T. Liang, TaN EUVL Mask Fabrication and Characterization, *SPIE*, **4343**, 409 (2001).
50. J. R. Wasson, B. Lu, P. J. S. Mangat, K. Nordquist and D. J. Resnick, Writing, repairing, and inspecting of extreme ultraviolet lithography reticles considering the impact of the materials, *J. Vac. Sci. Technol.*, **B19**(6), 2635 (2001).
51. B. T. Lee, E. Hoshino, M. Takahashi, T. Yoneda, H. Yamanashi, H. Hoko, M. Ryoo, A. Chiba, M. Ito and M. Sugawara, Approach to Patterning of Extreme Ultraviolet Lithography Masks using Ru Buffer Layer, *Jpn. J. Appl. Phys.*, **40**, 6998 (2001).
52. M. Yi, T. Haga, C. Walton and J. Bokor, High sensitivity actinic detection of native detects on extreme ultraviolet lithography mask blanks, *J. Vac. Sci. & Technol.*, **B19**, 2401 (2001).
53. T. Terasawa, Y. Tezuka, M. Ito and T. Tomie, High-speed actinic EUV mask blank inspection with dark-field imaging, *Proc. SPIE*, **5446**, 804 (2004).
54. Y. Tezuka, M. Ito, T. Terasawa and T. Tomie, Actinic detection and screening of multilayer defects on EUV mask blanks using dark-field imaging, *Proc. SPIE*, **5446**, 870 (2004).
55. T. Haga, H. Takenaka and M. Fukuda: *J. Vac. Sci. Technol.*, **B18**, 2916 (2000).
56. T. Haga, H. Kinoshita, K. Hamamoto, S. Takada, N. Kazui, S. Kakunai, H. Tsubakino and T. Watanabe, Evaluation of Finished Extreme Ultraviolet Lithography Masks Using a EUV Microscope, *Jpn. J. Appl. Phys.*, **42**, 3771 (2003).
57. H. Kinoshita, T. Haga, K. Hamamoto, S. Takada, N. Kazui, S. Kakunai, H. Tsubakino, T. Shoki, M. Endo and T. Watanabe, Actinic mask metrology for extreme ultraviolet lithography, *J. Vac. Sci. Technol.*, **B22**, 264 (2004).
58. K. Hamamoto, Y. Tanaka, H. Kawashima, S. Y. Lee, N. Hosokawa, N. Sakaya, M. Hosoya, T. Shoki, T. Watanabe and H. Kinoshita, Actinic Mask Inspection Using an EUV Microscope, *Jpn. J. Appl. Phys.*, **44**(7B), 5474–5478 (2005).
59. K. Hamamoto, Y. Tanaka, S. Y. Lee, N. Hosokawa, N. Sakaya, M. Hosoya, T. Shoki, T. Watanabe and H. Kinoshita, Mask defect inspection using an extreme ultraviolet microscope, *J. Vac. Sci. Technol.*, **B23**(6), 2852 (2005).
60. K. Hamamoto, Y. Tanaka, T. Yoshizumi, N. Hosokawa, N. Sakaya, M. Hosoya, T. Shoki, T. Watanabe and H. Kinoshita, Phase defect Observation Using Extreme Ultraviolet Microscope, *Jpn. J. Appl. Phys.*, **45**(6B), 5378 (2006).
61. K. Hamamoto, Y. Tanaka, T. Yoshizumi, Y. Fukushima, H. Shiotani, N. Sakaya, M. Hosoya, T. Shoki, T. watanabe and H. Kinoshita, Phase defect Observation Using an EUV Microscope, *Proc. of SPIE*, **6151**, 615119-1-7 (2006).
62. K. Hamamoto, Y. Tanaka, T. Watanabe, N. Sakaya, M. Hosoya, T. Shoki, H. Hada, N. Hishinuka, H. Sugawara and H. Kinoshita, Cleaning of extreme ultraviolet

lithography optics and masks using 13.5 nm and 172 nm radiation, *J. Vac. Sci. Technol.*, **B23**(1), 247–251 (2005).
63. Y. Tanaka, K. Hamamoto, H. Tsubakino, T. watanabe and H. Kinoshita, Reducing off Hydrocarbon Contaminants for EUVL, *Jpn. J. Appl. Phys.*, **44**(7B), 5547–5551 (2005).
64. Gary N. Taylor, Richard S. Hutton, David L. Windt and William M. Mansfield, Resist schemes for soft x-ray lithography, *SPIE 1343 X-Ray/EUV Optics for Astronomy, microscopy, Polarimetry, and Projection Lithography*, 258–273 (1990).
65. D. W. Berreman, J. E. Bjorkholm, M. Becker, L. Eichner, R. R. Freeman, T. E. Jewell, W. M. Mansfield, A. A. MacDowell, M. L. O'Malley, E. L. Raab, W. T. Silfvast, L. H. Szeto, D. M. Tennant, W. K. Waskiewicz, D. L. White, D. L. Windt and O. R. Wood II, Use of trilevel resists for high-resolution soft x-ray projection lithography, *Appl. Phys. Lett.*, **56**(22), 2180–2182 (1990).
66. G. Kubiak, E. Keedler, K. Berger and R. Stulen, Resist Characterization at Soft-X-Ray Wavelength, *OSA Proceedings in Soft-X-Ray Projection Lithography*, **12**, 124–128 (1991).
67. Semiconductor Industry Association, *International Technology Roadmap for Semiconductors: 2004 update: Lithography* Austin TX, International SEMATECH.
68. T. Watanabe, H. Kinoshita, H. Nii, K. Hamamoto, H. Hada and H. Komano, *J. Vac. Sci. Technol.*, **B17**, 3112 (1999).
69. Kazuhiko Hamamoto, Takeo Watanabe, Hideo Hada, Hiroshi Komano and Hiroo Kinoshita, *J. Photopolym. Sci. Technol.*, **15**, 361 (2002).
70. Robert L. Brainard, Peter Trefonas, Jeroen H. Lammers, Charlotte A. Cutler, Joseph F. Mackevich, Alexander Trefonas and Atewart A. Robertson, Shot noise, LER, and quantam yields of EUV Photoresists, *Proc. SPIE*, **5374**, 74 (2004).
71. H. Hada, T. Watanabe, H. Kinoshita and H. Komano, Outgassing Analysis in EUV resist, *J. of Photopolymer Sci. & Tech.*, **18**(4), 475–480 (2005).
72. T. Watanabe, H. Hada, S. Lee, H. Kinoshita, K. Hamamoto and H. Komano, Development of Fast-Photospeed Chemical Amplified Resist in Extreme Ultraviolet Lithography, *Jpn, J. Appl. Phys.*, **44**(7B), 5866–5870 (2005).
73. P. Naulleau, J. Chain, E. Anderson, K. Dean, P. Denham, K. Goldberg, B. Hoef and K. Jakson, Characterization of the synchrotron-based 0.3 numerical aperture extreme ultraviolet microexposure at the Advanced Light Source, *J. Vac. Sci. Technol.*, **B23**(6), 2840–2843 (2005).
74. M. Shumway, P. Naulleau, K. Goldberg, J. Boker, Measuring line roughness through aerial image contrast variation using coherent extreme ultraviolet spatial filtering techniques, *J. Vac. Sci. Technol.*, **B23**(6), 2844–2847 (2005).
75. H. Nagata, M. Ohtani, K. Murakami, T. Oshino, Y. Maejima, T. Tanaka, T. Watanabe, Y. Yamashita and N. Atoda, Soft X-ray Projection Imaging using 32:1 Schwerazschild Optics, OSA Proceedings on Soft X-Ray Projection Lithography, **18**, 83–86 (1993).
76. M. Ito, S.Katagiri, H. Yamanashi, E. Seya, T. Ogawa, H. Oizumi and T. Terasawa, Optical Technology for EUV Lithography, *OSA TOPS on Extreme Ultraviolet Lithography*, **4**, 9–12 (1996).
77. W. T. Silfvast and O. R. Wood, II , Tenth micron lithography with a 10 Hz 37.2 nm sodium laser, *Microelectron. Eng.*, **8**, 2–10 (1988).
78. Andrew M. Hawryluk and Lynn G. Seppala, Soft x-ray projection lithography using an x-ray reduction camera, *J. Vac. Sci. Technol.*, **B6**(6), 2162–2166 (1988).
79. D. L. White, J. E. Bjorkholm, J. Bokor, L. Eichner, R. R. Freeman, J. A. Gregus, T. E. Jewell, W. M. Mansfield, A. A. MacDowell, E. L. Raab, W. T. Silfvast,

L. H. Szeto, D. M. Tennant, W. K. Waskiewicz, D. L. Windt and O. R. Wood II, Soft X-ray Projection Lithography: Experiments and Practical Printers, *SPIE 1343 X-Ray/EUV Optics for Astronomy, Microscopy, Polarimetry, and Projection Lithography*, 204–213 (1990).

80. Glenn D. Kubiak, Duane A. Outka, Celeste M. Rohlfing, John M. Zeigler, David L. Windt and Warren K. Waskiewicz, Extreme ultraviolet resist and mirror characterization: Studies with a laser plasma source, *J. Vac. Sci. Technol.*, **B8**(6), 1643–1647 (1990).
81. D. W. Berreman, J. E. Bjorkholm, L. Eichner, R. R. Freeman, T. E. Jewell, W. M. Mansfield, A. A. MacDowell, M. L. O'Malley, E. L. Raab, W. T. Silfvast, L. H. Szeto, D. M. Tennant, W. K. Waskiewicz, D. L. White, D. L. Windt and O. R. Wood II, Soft-x-ray projection lithography: printing of 0.2-μm features using a 20:1 reduction, *Opt. Let.* **15**, 10, 529–531.
82. N. M. Ceglio, A. M. Hawryluk, D. G. stearns, D. P. Gaines, R. S. Rosen and S. P. Vernon, Soft x-ray projection lithography, *J. Vac. Sci. Technol.*, **B8**(6), 1325–1328 (1990).
83. A. A. MacDowell, J. E. Bjorkholm, J. Bokor, L. Eichner, R. R. Freeman, W. M. Mansfield, J. Pastalan, L. H. Szeto, D. M. Tennant, O. R. Wood, II, T. E. Jewell, W. K. Waskiewicz, D. L. White, D. L. Windt, W. T. Silfvast and F. Zernike, Soft x-ray projection lithography using a 1:1 ring field optical system, *J. Vac. Sci. Technol.*, **B9**(6), 3193–3197 (1991).
84. Tsuneyuki Haga and Hiroo Kinoshita, Illumination system for extreme ultraviolet lithography, *J. Vac. Sci. Tecnol.*, **B13**(6), 2914–2918 (1995).
85. D. A. Tichenor, A. K. Ray-Chaudhui, G. D. Kubiak, K. B. Nguyen, S. J. Haney, K. W. Berger, R. P. Nissen, Y. E. Perras, P. S. Jin, L. I. Weingarten, P. N. Keifer, R. H. Stulen, R. N. Shagam, W. C. Sweatt, T. G. Smith, O. R. Wood, II, A. A. MacDowell, J. E. Bjorkholm, T. E. Jewell, F. Zernike, B. L. Fix and H. W. Hauschildt, Progress in the Development of EUV Imaging System, *OSA TOPS on Extreme Ultraviolet Lithography*, **4**, 2–8 (1996).
86. K. B. Nguyen, G. F. Cardinale, D. A. Tichenor, G. D. Kubiak, K. Berger, A. K. Ray-Chaudhui, Y. Perras, S. J. Haney, R. Nissen, K. Krenz, R. H. Stulen, H. Hujioka, C. Hu, J. Bokor, D. M. Tennant and L. A. Fetter, Fabrication of MOS devices with extreme ultraviolet lithography, *OSA TOPS on Extreme Ultraviolet Lithography*, **4**, 208–211 (1996).
87. H. Kinoshita, T. watanabe, M. Ito, H. Oizumi, H. Yamanashi, K. Murakami, T. Oshino, Y. Platonov and N. Grupid, *Three-Aspherical Mirror System for EUV Lithpgraphy*, **3331**, 20–31 (1998).
88. H. Kinoshita, T. Watanabe, Y. Li, A. Miyafuji, T. Oshino, K. Sugisaki, K. Murakami, S. Irie, S. Shirayone and S. Okazaki, Recent advances of 3-aspherical mirror system for EUVL, *SPIE*, **3997**, 70–75 (2000).
89. T. Watanabe, H. Kinoshita, A. Mityafuji, S.Irie, S. Shirayone, S. Mori, E. Yano, H. Hada, K. Ohmori and H. Komano, Lithographic performance and optimization of chemically amplified single layer resists for EUV lithography, *SPIE*, **3997**, 600–607 (2000).
90. D. Tichner, A. Ray-Chaudhuri, W. Repolgle, R. Stulen, G. Kubiak, P. Rocket, L. Klebanoff, J. Wronosky, L. Hale, H. Chapman, J. Taylor, J. Forta and C. Montcalm, System Integration and Performance of the EUV Engineering Test Stand, *SPIE*, **4343** (2001).
91. P. P. Naulleau, K. A. Goldberg, E. Anderson, J. P. Cain, P. Denham, B. Hoef, K. Jackson, A.-S. Morlens, S. Rekawa and K. Dean, EUV microexposures at the ALS using the 0.3-NA MET projection optics, *SPIE*, **5751**, 56 (2005).

92. J. M. Roberts, T. Bacuita, R. L. Bristol, H. B. Coo, M. Chandhok, S. H. Lee, E. M. Panning, M. Shell, G. Zhang and B. J. Rice, One small step: world's first integrated EUVL process line, *SPIE*, **5751**, 64 (2005).
93. M. Booth, 0. Brisco, A. Brunton, J. Cashmore, P. Elbourn, G. Elliner, M. Gower, J. Greuters, P. GrOnewald, R. Gutierrez, T. Hill, J. Hirsch, L. Kling, N. McEntee, S. Mundair, P. Richards, V. Truffert, I. Wallhead, M. Whitfield and R. Hudyma, High-resolution EUV imaging tools for resist exposure and aerial image monitoring, *SPIE*, **5751**, 78 (2005).
94. H. Oizumi, Y. Tanaka, F. Kumasaka, I. Nishiyama, H. Kondo, M. Shiraishi, T. Oshino, K. Sugisaki and K. Murakami, Lithographic performance of high-numerical-aperture (NA = 0.3) EUV small-field exposure tool (HINA), *SPIE*, **5751**, 102 (2005).
95. H. Meiling, V. Banine, N. Horned, B. Blum, ASML Wilton, P. KOrz and H. Meijer, Development of the ASML EUV alpha demo tool, *SPIE*, **5751**, 90 (2005).
96. H. Meiling, H. Meijer, V. Banine, R. Groeneveld, H. Voorma, U. Mickan, B. Wolschrijn, B. Mertens, G. Baars, P. Kurz and N. Harned, First performance results of the ASML alpha demo tool, *SPIE*, **6151**, 6151081–61510811 (2006).

CHAPTER 9

ELECTRON PROJECTION LITHOGRAPHY

TAKAHARU MIURA

Nikon Corporation, 201-9 Miizugahara, Kumagaya, Saitama, 360-8559, Japan
miura.takaharu@nikonoa.net

KAZUAKI SUZUKI

Nikon Corporation, 201-9 Miizugahara, Kumagaya, Saitama, 360-8559, Japan
kzsuzuki@nikongw.nikon.co.jp

HIROSHI ARIMOTO

FUJITSU LIMITED, Akiruno Technology Center, 50 Fuchigami, Akiruno, Tokyo, 197-0833, Japan
arimoto.hiroshi@jp.fujitsu.com

SHINTARO KAWATA

Nikon Corporation, 1-10-1 Asamizodai, Sagamihara, Kanagawa, 228-0828, Japan
kawata.sk@nikon.co.jp

The basic study of EPL has been done under the name of SCALPEL® by AT&T (Lucent Technologies, then Agere Systems) from the beginning of 1990s and the name of PREVAIL for electron optical system by the joint work of IBM and Nikon. The features of EPL are larger sub-field size and higher acceleration voltage of electron for obtaining usable higher electrical current on wafer and a wide deflection width for obtaining higher throughput.

EPL system has such features as a large sub-field size, large deflection width, high electrical current, high acceleration voltage and thin Si stencil mask. EPL has been considered as one of the promising technologies for hp65nm node and beyond.

Nikon has developed the first EPL tool and it was delivered to Selete in Japan. The tool has been used for EPL technology evaluation and process development in the pilot line of Selete. This chapter describes the various aspects of EPL technology from basic concept through technology evaluation and future extendibility.

Keywords: Electron beam lithography; Electron beam projection lithography (EPL); EB stepper; Electron Beam (EB); Scattering contrast; Stencil reticle; Continuous membrane reticle; Proximity effect correction; Stitching; Resist.

CONTENTS

1. Introduction 287
References 288
2. Imaging Concept 288
2.1. Acceleration voltage of electrons 288
2.2. Imaging concept 289
References 291
3. Electron Optics for Imaging and Illumination 292
3.1. Electron optics system 292
3.2. Illumination system 294
3.3. Imaging system 294
3.3.1. Coulomb interactions in the EPL system 295
3.3.2. Chromatic aberration 296
3.3.3. Geometrical aberration and CVAL concept 296
3.3.4. Dynamic correction 297
3.4. Correction for stage position shift (Filter/Predictor) 297
References 298
4. Exposure Concept 299
4.1. Dynamic exposure motion 299
4.2. Dosage control and stage velocities 299
4.3. Proximity effect correction 301
4.4. Sub-field/Complementary stitching 302
References 303
5. Tool System Description 304
5.1. Tool system configuration 304
5.2. Tool system design concept 305
5.3. Reticle and wafer vacuum stages 306
5.4. Vacuum body 310
5.5. Reticle and wafer vacuum loaders 315
5.6. Metrology sensors 316
5.7. Tool control system 316
5.8. Expected tool performance 316
5.9. Actual EPL tool configuration and performance summary 317
References 319
6. EPL Reticle 320
6.1. EPL reticle format 320
6.2. Si stencil reticle fabrication 321
6.3. Scattering reticle 322

6.3.1. Stencil reticle 322
6.3.2. Continuous membrane reticle 324
6.3.3. Summary 324
References 325
7. Mask Inspection and Other Infrastructures 325
7.1. Mask inspection 325
7.2. Repair for mask defects 328
7.3. Mask cleaning 329
7.4. Data processing for masks 330
References 331
8. Process and Application Results 332
8.1. Resist process 332
8.2. Prototyping of Cu two-layer wiring TEG 332
Reference 333
9. Technology Evaluation and Future Extendibility 334
9.1. Next EPL system and Coulomb interaction 334
9.2. EB2 system 337
9.3. EB3 system 338
References 339
10. Summary 340
11. Acknowledgments 340

1. Introduction

Electron beam technology has as long a history as optical instruments and has been used in many areas in the various industries and in fact this technology has been used as a mask making tool in the semiconductor industry. Thanks to EB mask making and some direct writing machine, the resist and data conversion are highly improved up to realistic industry level of EPL, and the basic research for a EPL mask also has been done by 1X X-ray mask and cell projection mask that is already commercialized. Furthermore the EPL system takes over a lot of element from EB mask making or direct writing machine. It is a well-known fact that IBM has established its specialized position about conventional EB technology.

AT&T Bell Laboratories carried out a basic study of EPL technologies and proposed the SCALPEL® system [1]. In parallel, IBM investigated their own electron optics called PREVAIL to realize the large sub-field and large deflection field for EPL [2]. Nikon and IBM worked together for the development of PREVAIL electron optics technology in order to realize the EPL tool.

The electron optics, PREVAIL consists of two variable axis lenses, the excellent large deflection technique introduced by Pfeiffer. VAL technique was already proven

at EL4, high precise mask making machine in IBM. But a new concept, curvilinear variable axis lens, was introduced in order to implement a realistic electron demagnified projection lens.

The teaming of Nikon and IBM is a very good synergic collaboration for EPL lithography tool development, because the high precision scanning stage in vacuum is another key technology coupled with a precise metrology system of auto-focus, interferometer and alignment to realize high throughput production-worthy EPL tool.

EPL is the one of the most promising realistic technologies beyond hp65nm node in terms of resolution extendibility, and also the expected throughput extendibility.

EPL can play a vital role as a complementary technology of optical lithography especially for contacts and gate layers because of its superior resolution and large process margin.

Nikon has developed the first EPL tool, dubbed as Nikon NSR-EB1A, and it was delivered to Selete(Semiconductor Leading Edge Technologies) in Japan. The tool has been used for EPL technology evaluation and process development in the pilot line of Selete for several years. Selete has also taken the vital role in the development of EPL mask, mask inspection, mask repair, resist and other necessary infrastructures.

References

1. S. D. Berger and J. M. Gibson, New approach to projection-electron lithography with demonstated 0.1 μm linewidth, *Appl. Phys. Lett.* **57**, pp. 153–155, 1990.
2. H. C. Pfeiffer, Projection Exposure with Variable Axis Immersion Lenses: A High-Throughput Electron Beam Approach to "Suboptical" Lithography, *Jpn. J. Appl. Phys.* **34**, pp. 6658–6662, 1995.

2. Imaging Concept

2.1. *Acceleration voltage of electrons*

The resolution and throughput enhancement is the most important issue in EPL. Management of Coulomb effect is indispensable for the use of higher beam current in order to obtain higher throughput. The image blur by Coulomb interaction is given by

$$R = k\frac{I^{5/6}L^{5/4}M}{\alpha^{3/5}SF^{1/2}V^{3/2}} = k\frac{L^{5/4}M}{\alpha^{3/5}SF^{1/2}V^{2/3}}\left(\frac{I}{V}\right)^{5/6}, \tag{2.1}$$

where $R, I, L, M, \alpha, SF, V$ are the image blur by Coulomb interaction, the total beam current on wafer, the length between reticle and wafer, magnification, beam half angle, sub-field size and acceleration voltage, respectively [1]. k is a coefficient and its value depends on the design of electron optics. The resist sensitivity is

approximately proportional to the acceleration voltage of electrons. Therefore keeping a throughput (that is an exposure time) constant, a higher acceleration voltage makes beam blur by Coulomb interaction smaller because required beam current is proportional to the acceleration voltage from eq. (2-1). On the other hand, for the specific value of R, large acceleration voltage of electron gives larger beam current, in other words higher throughput. Therefore the acceleration voltage of 100 kV is adopted.

2.2. *Imaging concept*

EPL makes use of the concept of scattering contrast for its image formation. A membrane reticle which has two different areas with electron scattering characteristics is necessary for this concept.

The scattering contrast has been utilized in the area of transmission electron microscopy and was applied to image formation on an actinic film using a master stencil [2]. Then AT&T Bell Laboratories proposed to apply this concept to lithography tool with a continuous membrane type reticle [3]. A bright field is obtained at a membrane itself which works as a transmitter of the electron beam and a dark field is obtained in the area made of large atomic number materials such as heavy metals on a membrane which works as a scatterer. The contrast of this reticle type was well studied and reported by Lucent Technologies [4]. Transmittance of this type reticle with several thickness was measured and reported by Nikon as shown in Fig. 2-1. [5]. Membrane thickness less than 50 nm is required in order to keep the reasonable transmittance.

A silicon stencil reticle was proposed by IBM and Nikon as another type of EPL reticle [6,7,8]. In the case of the stencil reticle, a membrane area works as a scatterer and an aperture through membrane works as a transmitter of the electron beam. An angular distribution of scattered electrons was evaluated as a function of scattered

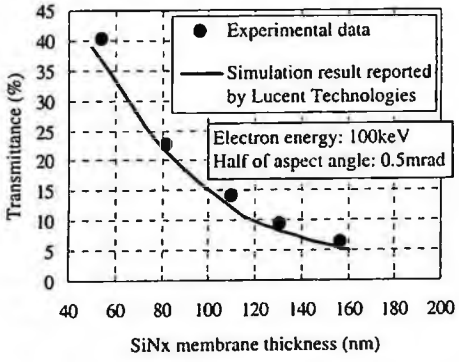

Figure 2-1. Transmittance of 100 keV electrons through SiNx membrane in the case that a half of aspect angle of contrast aperture is 0.5 mrad.

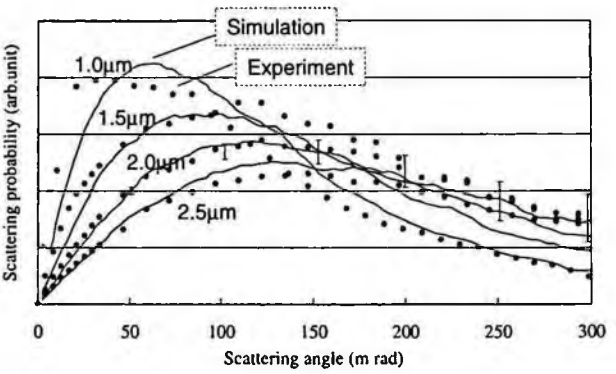

Figure 2-2. Angular distribution of scattered electrons (100 keV) through a silicon membrane. The parameter of these curves is a membrane thickness. The dots represent experimental data and the solid lines represent simulation results.

angle experimentally [9], and compared with Monte Carlo simulation of Screened Rutherford scattering and Bethe's stopping power law with the treatment of the theory of special relativity [10]. The experimental results and simulation results are shown in Fig. 2-2. Figure 2-2 shows the dependency of angular distribution of scattered electrons on the membrane thickness (1, 1.5, 2, 2.5 μm) at the acceleration voltage of 100 kV. The dots represent experimental data and the solid lines represent simulated curves. The measurement results have good agreement with the simulation results.

Figure 2-3 shows the imaging concept of EPL with a stencil reticle. As shown in Fig. 2-3, almost all scattered electrons are obstructed at the column inner wall and the contrast aperture plate in the projection optics and all of transmitted electrons through stencil apertures contribute on the image formation on the wafer plane. Figure 2-4 represents the relationship between silicon membrane thickness and contrast aperture radius (converted to a half of aspect angle onto wafer) which gives a constant contrast value under the condition of the electron energy of 100 keV. The parameter of each curve is scattering contrast C, which is defined as follows:

$$C = 1 - Itr/Iin, \tag{2.2}$$

where Iin and Itr represent the incident electron beam current onto a specific area on a reticle membrane and the transmitted electron beam current through the contrast aperture which comes from such a specific area on the reticle membrane, respectively. Because a beam half angle is less than 10 mrad as explained in another subsection 3.3, the contrast aperture size of 10–20 mrad will be suitable in order to obtain the contrast larger than 99.5%. The silicon membrane thickness larger than 1 μm is also necessary.

Lotus mask proposed by NEC is composed from thin DLC (<50 nm) as a transmitter and thick DLC (>500nm) as a scatterer [11] and was manufactured by

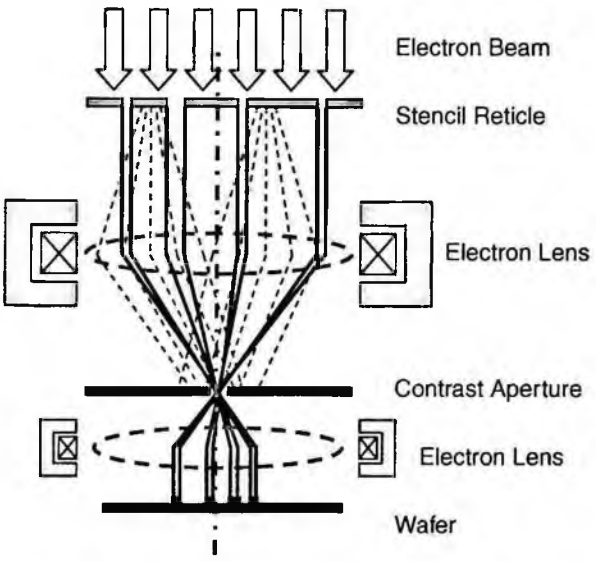

Figure 2-3. Imaging concept of EPL with a stencil reticle.

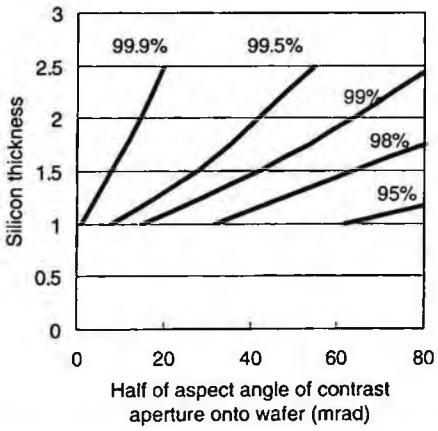

Figure 2-4. Relationship between silicon membrane thickness and a half of aspect angle of contrast aperture onto wafer which gives a constant contract value. Incident electron energy is 100 keV.

HOYA [12]. It is also one of the candidate for a practical continuous membrane reticle.

References

1. W. Stickel, Simulation of Coulomb interactions in electron beam lithography systems — A comparison of theoretical models, *J. Vac. Sci. Technol.* **B16**, pp. 3211–3214, 1998.

2. W. H. P. Koops and J. Grob, Submicron Lithography by Demagnifying Electron-Beam Projection in *Springer Series in Optical Sciences Vol. 43: X-ray Microscopy*, edited by G.Schmahl and D.Rudolph, pp. 119–128, Springer, Berlin, 1984.
3. S. D. Berger and J. M. Gibson, New approach to projection-electron lithography with demonstrated 0.1 μm linewidth, *Appl. Phys. Lett.* **57**, pp. 153–155, 1990.
4. M. M. Mkrtchyan, J. A. Liddle, A. E. Novembre, W. K. Waskiewicz, G. P. Watson, L. R. Harriott and D. A. Muller, Electron scattering and transmission through SCALPEL masks, *J. Vac. Sci. Technol.* **B16**, pp. 3385–3391, 1998.
5. K. Suzuki, T. Fujiwara, K. Hada, N. Hirayanagi, S. Kawata, K. Morita, K. Okamoto, T. Okino, S. Shimizu, T. Yahiro and H. Yamamoto, Nikon EB Stepper: the latest development status, *SPIE* **4343**, pp. 80–87, 2001.
6. H. C. Pfeiffer, R. S. Dhaliwal, S. D. Golladay, S. K. Doran, M. S. Gordon, T. R. Groves, R. A. Kendall, J. E. Lieberman, P. F. Petric, D. J. Pinckney, R. J. Quickle, C. F. Robinson, J. D. Rockrohr, J. J. Senesi, W. Stickel, E. V. Tressler, A. Tanimoto, T. Yamaguchi, K. Okamoto, K. Suzuki, T. Okino, S. Kawata, K. Morita, S. C. Suzuki, H. Shimizu, S. Kojima, G. Varnell, W. T. Novak, D. P. Stumbo and M. Sogard, Projection reduction exposure with variable axis immersion lenses: Next generation lithography, *J. Vac. Sci. Technol.* **B17**, pp. 2840–2846, 1999.
7. S. Kawata, N. Katakura, S. takahashi and K. Uchikawa, Stencil reticle development for Electron Beam Projection System, *J. Vac. Sci. Technol.* **B17**, pp. 2864–2867, 1999.
8. K. Uchikawa, S. Takahashi, N. Katakura, T. Oshino, S. Kawata and T. Yamaguchi, Pattern displacement measurements for Si stencil reticles, *J. Vac. Sci. Technol.* **B17**, pp. 2868–2872, 1999.
9. R. D. Birkhoff, The Passage of Fast Electrons Through Matter, *Handbuch der Physik*, **Vol. 19**, pp. 53–138, 1958.
10. K. Morita, T. Yahiro, S. Shimizu, H. Yamamoto, N. Hirayanagi, T. Fujiwara, S. Suzuki, H. Shimizu, S. Kawata, T. Okino and K. Suzuki, Data of scattered electron characteristics in 100kV EB stepper, *SPIE* **3997**, pp. 703–712, 2000.
11. H. Yamashita, I. Amemiya, E. Momura, K. Nakajima and H. Nozue, High-performance membrane mask for electron projection lithography, *J. Vac. Sci. Technol.* **B18**, pp. 3237–3241, 2000.
12. I. Amemiya, H. Yamashita, S. Nakatsuka, M. Tsukahara and O. Nagarekawa, Fabrication of a continuous diamond-like carbon membrane mask for electron projection lithography, *J. Vac. Sci. Technol.* **B21**, pp. 3032–3036, 2003.

3. Electron Optics for Imaging and Illumination

3.1. *Electron optics system*

The Electron optics (EO) subsystem consists of three groups as shown in Fig. 3-1 [1]: the 100 keV electron gun with a Ta disc cathode [2], the condenser and illumination optics (upper column), and the projection optics (lower column) [3].

The illumination optics is designed to have a highly uniformed intensity distribution on a 1mm-square reticle subfield (SF) on the basis of the critical Koehler illumination principle [4]. The projection optics (the imaging system) is based on the PREVAIL system, which had been developed by IBM and Nikon using the curvilinear variable axis lens (CVAL) concept, as shown in Fig. 3-2 [5,6]. CVAL is a

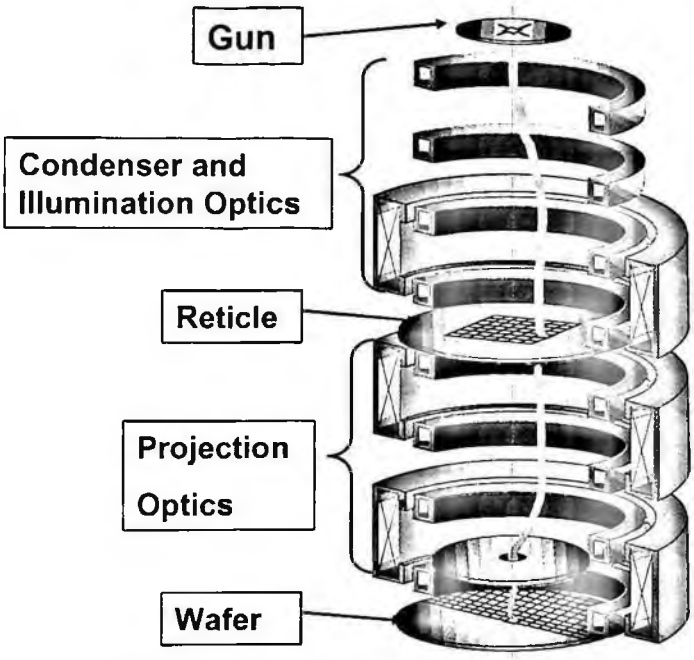

Figure 3-1. Schematic of electron optics of EB stepper.

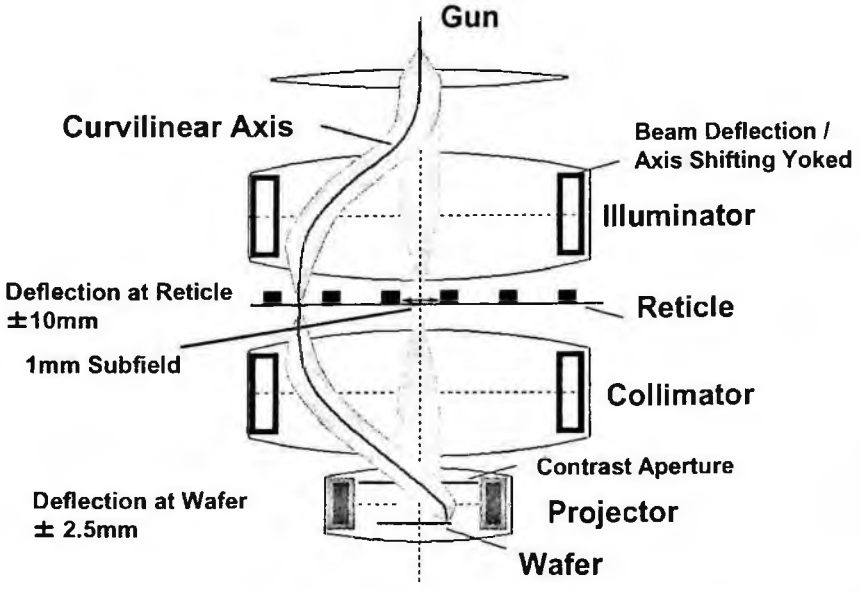

Figure 3-2. Schematic of Curvilinear Variable Axis Lens (CVAL).

highly optimized deflection orbit to minimize the deflection aberrations which are not corrected by the dynamic correction. Compared with conventional EB exposure systems, EPL must cover the wide range of exposure area electron-optically. On a wafer, the exposure SF size is 0.25 mm square and the deflection area is ±2.5 mm × ±0.25 mm. CVAL concept has been considered to match the EPL optics. The scattering contrast is used for the pattern imaging [3,7]. The pattern area (exposure area) on a reticle is a thin membrane where incident electrons are scattered without absorption, as mentioned in the subsection 2. The projection optics has a contrast aperture near the pupil plane to stop the scatted electron beams in the reticle.

3.2. *Illumination system*

The EPL electron source illuminates a large area (1 mm square on reticle) uniformly. The beam semi-angle is in the range of 1.25–2 mrad at reticle. The emittance is high (1.25–2.00 mm mrad.). Despite the high beam current (~100μA), the illumination brightness is low (~10^3 A/cm^{2}Sr) [2].

For the illumination system requirements, the new gun system was designed using diode type with large single Ta crystal cathode, which is ~5 mm in diameter. The Ta surface is fine-polished to obtain uniform electron emission. The gun is operated in the temperature limited emission region (>1000°C). Emission current density uniformity reflects the cathode temperature uniformity. To obtain 1% emission uniformity, the temperature must be uniform to better than 1°C over the electron emission area. The cathode is heated by the electron direct bombardment. The cathode emission current is regulated by controlling the cathode temperature which is regulated by the bombardment current. The gun operation parameters are:

Acceleration voltage 100 kV;
High voltage stability < ± 2.5 ppm (at 100 kV);
Current 100 μA at reticle (max.);
Output current stability < ± 0.1%;
Cathode temperature uniformity <1°C.

The illumination optics is based on the critical Koehler illumination principle, which utilizes the emitting cathode conjugate (or nearly conjugate) relation to the wafer. However, the critical Koehler illumination is very sensitive to the cathode surface condition. To keep less than 2% illumination uniformity for a long time (a long life cathode, > 12 months), a new Non-critical-Koehler illumination system was needed, which uses the relation far from conjugate between the cathode and the wafer. The modified illumination optics provide illumination uniformity ~1% [8].

3.3. *Imaging system*

The CVAL concept has two functions: the improvement of the resolution and the reduction of the nonlinear distortion at the deflection beam position. In the CVAL

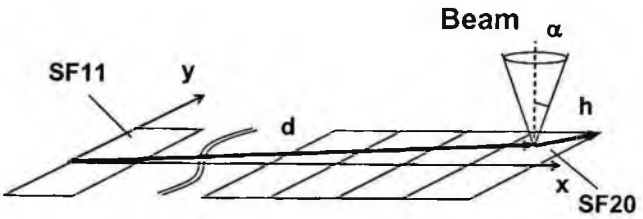

Figure 3-3. EO operating parameters.

concept, deflectors work as correctors for the geometrical aberrations, where the geometrical blur and nonlinear distortion of a deflected beam are decreased as if they are on-axis [9,10]. EO operating parameters in Fig. 3-3 are defined as follows:

$\alpha = \alpha_x + i\alpha_y$: Beam semi-angle,
$h = h_x + ih_y$: Sub-field (SF) vector (position in Subfield),
$d = d_x + id_y$: Main-field (MF) vector (deflection).

3.3.1. *Coulomb interactions in the EPL system*

As it is well known, electron beam blurs are changed by the Coulomb interaction effect between electrons in the beam. The beam blur is defined as the root sum square of the blur due to the Coulomb interaction and the geometrical blur of EO-system. The beam blur due to the Coulomb interaction is determined in good approximation by the following empirical expression (see eq. [2-1] in subsection 2) [11]:

$$\mathrm{Blur_{coulomb}} = k(I^{5/6}L^{5/4}M)/(\alpha^{3/5}SF^{1/2}V^{3/2}), \tag{3.1}$$

where I is the beam current, L is the distance between the reticle plane and the wafer plane (~600 mm), M is the magnification (x 1/4), α is the beam semi-angle at the image plane (6–8 mrad.), SF is the sub-field size, V is the acceleration voltage of the electrons (100 kV) and k is a constant [3,9].

In the EB stepper, these parameters are fixed to obtain the optimum optical properties including the chromatic and geometrical aberrations. In fact, the beam blurs due to the Coulomb interaction depend on the reticle patterns in each SF. In the data processing of EPL reticle, which includes the complimentary data split, the proximity effect correction, and so on, the effects of Coulomb interaction on the electron optics are estimated and the EO correction parameters to compensate these effects are calculated for each SF, too (the plug-in software). The parameters are added to the exposure files, which have EO parameters for all SF exposures and control SF exposures. The EPL data conversion system with the plug-in software for the EO corrections on Coulomb interaction is commercially available.

3.3.2. *Chromatic aberration*

The lowest order of the chromatic aberration is proportional to the beam energy spread ($\Delta V/V$), where ΔV is the beam energy spread ($\sim$3 eV) [12].

The part of the chromatic aberration proportional to h (the SF vector) is completely eliminated under the symmetric magnetic doublet (SMD) condition [13]. EO system in the EB stepper is similar to SMD, so this aberration can be almost zero. Other chromatic aberrations are also proportional to $\Delta V/V$, such as $\alpha\Delta V/V$ and $d\Delta V/V$. Considering that the beam energy is 100 keV, these chromatic aberrations are much smaller than the geometrical aberrations and the blur caused by the Coulomb interaction.

3.3.3. *Geometrical aberration and CVAL concept*

According to the third-order aberration theory, geometrical aberrations are composed of spherical aberration, coma, field curvature, astigmatism and distortion [12]. These aberrations are divided into three groups. One is dependent on the SF size (shaped-beam aberrations). The second is deflection-dependent (MF aberration). The last is the hybrid aberration. Table 3-1 shows the components of the third order normal aberrations. The fourfold aberrations, mainly caused by the mechanical fabrication error of deflectors, are not shown in this table. The suffix 'c' denotes their complex conjugate value.

The aberration 'ddd_c', which is called the main-field distortion, is corrected by adjustment of the deflection position by CVAL deflectors. MF field curvature, MF astigmatism and hybrid distortions such as ddh_c, dhd_c (proportional to d or d_c) can be corrected by dynamic focus coils and dynamic stigmators [14].

The other aberrations are highly dependent on the lens condition and the trajectories of the deflected beam. The SMD condition makes the shaped beam distortion ddd_c zero. In the EB stepper (NSR-EB1A) lens condition, which is similar to the SMD condition, these values are also approximately zero theoretically [13].

CVAL decreases the geometrical aberration of the deflected beam by optimizing the lens fields and deflection fields. This optimization also makes the hybrid distortion small. Particularly, the aberrations, which cannot be corrected by dynamic correction, such as the MF coma, the hybrid field curvature, the hybrid astigmatism and nonlinear distortion, can be optimized.

Table 3-1. 3rd order normal aberrations

	Shaped beam	Hybrid	Main-field
Spherical aberration	$\alpha\alpha\alpha_c$	—	—
Coma	$\alpha\alpha h_c$ $\alpha h\alpha_c$	—	$\alpha\alpha d_c\alpha d\alpha_c$
Field curvature	αhh_c	$\alpha dh_c\alpha hd_c$	αdd_c
Astigmatism	$hh\alpha_c$	$dh\alpha_c$	$dd\alpha_c$
Distortion	hhh_c	$ddh_cdhd_cdhh_chhd_c$	ddd_c

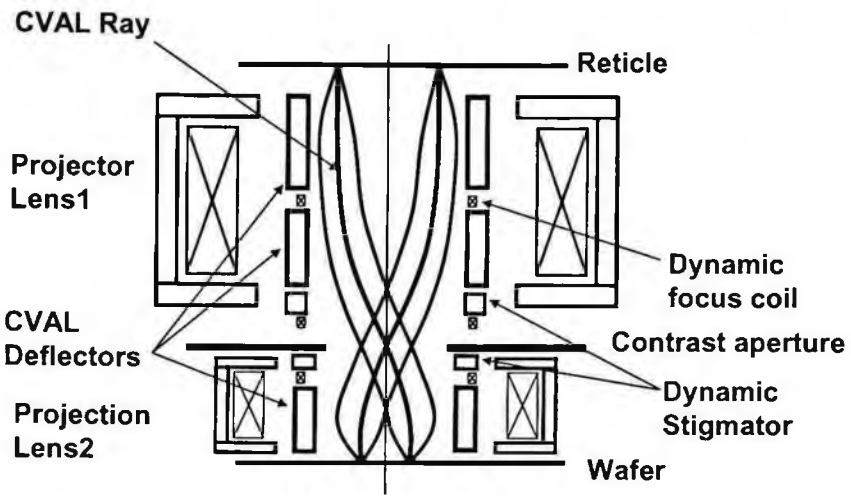

Figure 3-4. CVAL optical components in the projection optics.

NSR-EB1A has four lenses (parameters) for imaging, three of which are used for rotation, magnification and focus adjustment. Another one is used for optimizing other aberrations with CVAL deflector. Each lens current is determined by simulation. Moreover, rotation, magnification and focus have some errors caused by factors such as magnetic field calculation error, magnetic material inhomogeneity and fabrication error. These errors are canceled by the lenses.

There are some CVAL deflectors in the projection section as shown in Fig. 3-4. Each deflector position, size and current is optimized to obtain a small aberration. As a result CVAL deflectors contribute to the projection of an off-axis sub-field (SF) and act as deflection aberration correctors. The same aberration of the on-axis beam must be expected at the deflected position in the CVAL.

3.3.4. *Dynamic correction*

It is possible to minimize the blur and to adjust the shape in each SF, by using three focus coils and two stigmators, dynamically. In actuality, MF curvature (αdd_c), MF astigmatism ($dd\alpha_c$) and hybrid distortion (ddh_c, dhd_c) are eliminated, completely [14].

Third-order fourfold distortion, which is mainly caused by the fabrication errors of deflectors and expressed as $h_c h_c$, can be corrected with special correctors (fourfold corrector) dynamically.

3.4. *Correction for stage position shift (Filter/Predictor)*

The position shifts of the reticle stage and the wafer stage cause the position shift of the beam on the wafer. In the EB stepper, in order to cancel these shifts, a prediction

control system (Filter/Predictor) is applied. Position, velocity and acceleration are measured for both reticle and wafer stage at the time T. Using these values, the positions of both stages are predicted at $t = T + \Delta T$. These position data are transferred to the EO system. Then the beam is moved to the predicted position as if the stages are just at the position when $t = T + \Delta T$.

Thus, the filter/predictor makes it possible to stitch SFs and *in situ* measurement of the distortion and blur.

In this system, the beam shift dependent on the reticle stage position error is corrected by the CVAL deflectors.

The beam shift on the wafer stage is caused by two factors. One is the position error of the reticle stage and the other is the wafer stage position shift. In both cases, the beam shift is corrected by a set of special deflectors in the projection part.

References

1. H. C. Pfeiffer, Projection Exposure with Variable Axis Immersion Lenses: A High-Throughput Electron Beam Approach to "Suboptical" Lithography, *Jpn. J. Appl. Phys.* **34**, 6658–6662 (1995).
2. S. D. Golladay, R. A. Kendall and K. Doran, High emmitance source for the PREVAIL projection lithography system, *J. Vac. Sci. & Technol. B* **17**, 2856–2859 (1999) 2856.
3. H. C. Pfeiffer, R. S. Dhaliwal, S. D. Golladay, S. K. Doran, M. S. Gordon, T. R. Groves, R. A. Kendall, J. E. Lieberman, P. F. Petric, D. J. Pinckney, R. J. Quickle, C. F. Robinson, J. D. Rockrohr, J. J. Senesi, W. Stickel, E. V. Tressler, A. Tanimoto, T.Yamaguchi, K. Okamoto, K. Suzuki, T. Okino, S. Kawata, K. Morita, S. C. Suziki, H. Shimizu, S. Kojima, G. Varnell, W. T. Novak, D. P. Stumbo and M. Sogard, Projection Reduction Exposure with Variable Axis Immersion Lenses: Next Generation Lithography, *J. Vac. Sci. Technol. B* **17**, 2840–2846 (1999).
4. M. Essig and H. C. Pfeiffer, Critical Koehler Illumination for Shaped Beam Lithography, *J. Vac. Sci. Technol. B* **4**, 83–85 (1986).
5. P. F. Petric: U.S. Patent No. 5,635,719.
6. W. Stickel and G. O. Langner, PRIVAIL: Theory of the proof of concept column electron optics, *J. Vac. Sci. Technol. B* **17**, 2847–2850 (1999).
7. S. D. Berger and J. M. Gibson, New Approach to Projection Electron Lithography with Demonstrated 0.1 Micron Linewidth, *Appl. Phys. Lett.* **57**, 153–155 (1990).
8. S. Kojima, K. Nakano, S. Suzuki, S. Takahashi, T. Umemoto, J. Ikeda, A. Yamada, T. Yahiro, M. Hamashima and S. Kawata, Novel Illumination Method for Electron Projection Lithography, to be published in Microelectronic Engineering **67–68** (2003).
9. W. Stickel and G. O. Langner, Application of the generalized curvilinear variable axis lens, *J. Vac. Sci. & Technol. B*, **18**, 3029–3033 (1999).
10. A. Yamada, K. Okamoto, T. Umemoto, H. Shimizu, S. Takahashi, J. Ikeda, S. Kojima, T. Yahiro, S. Shimizu, T. Ujiwara and M. Hamashima, Electron Optics Properties of Electron Beam Stepper, *Jnp. J. Appl. Phys.* **42**, 3822–3826 (2003).
11. W. Stickel, Simulation of Coulomb interactions in electron beam lithography systems – A comparison of theoretical models, *J. Vac. Sci. Technol. B* **16**, 3211–3214 (1998).

12. H. C. Chu and E. Munro, Numerical analysis of electron beam lithography systems III, Optik, **61**, 121–145 (1982).
13. M. B. Heritage, Electron-Projection Microfabrication System, *J. Vac. Sci. Technol.* **12**, 1135–1140 (1975).
14. X. Zhu, H. Liu and E. Munro, Dynamic correction of aberrations in focusing and deflection systems with shaped beams, *Proc. SPIE* **2522**, 66–77 (1995).

4. Exposure Concept

4.1. *Dynamic exposure motion*

As explained in subsection 3.3, the magnification of the projection optics is 1/4, and sub-field size is 0.25 mm × 0.25 mm on wafer. The main field width is 5 mm on wafer obtained from twenty sub-field deflection positions. The 1 mm × 1 mm illumination beam is deflected and controlled by a deflector along one direction for twenty sub-fields. As explained later in subsection 6.1, there is a minor strut and two peripheral membrane areas of 0.3 mm width in total between sub-fields and then a pitch of sub-fields is 1.3 mm on the reticle. Therefore the main field width on reticle becomes 25.7 mm. Reticle stage moves along a cross-beam-deflection direction with a constant velocity. Each sub-field on reticle is irradiated in turn with the combination of the beam deflection and the stage motion. Simultaneously a wafer stage moves in the opposite direction of the reticle stage and patterns on the reticle are projected onto a wafer one after another [1]. Minor struts between sub-fields on reticle are not projected onto a wafer by deflecting a beam to stitch adjacent sub-fields. A 5 mm × 25 mm area from ϕ200 mm reticle can be exposed and this area is called as a stripe. After one stripe exposure, reticle and wafer stages turn around and the next exposure of stripe starts as a scan and stitch stage motion. Finally, 20 mm × 25 mm exposure field can be exposed from four stripes on a ϕ200 mm reticle.

Figure 4-1 shows an actual exposure beam motion on wafer stage coordinate. There are forty different sub-field positions in a main field. It is required that sub-field distortion and resolution are simultaneously adjusted to the best performance at any sub-field position by correcting rotation, orthogonality, x,y-magnification, x,y-translation, focus and astigmatism because different sub-field positions have different linear components of aberration. For this purpose two stigmators, three focus coils and a pair of deflectors are prepared [2]. These correctors can compensate other necessary factors dynamically such as stage position error, etc., too.

4.2. *Dosage control and stage velocities*

Illumination electron beam tracks reticle sub-field along the stage scanning direction during exposure. Dosage control is done by blanking control of this illumination beam. Here $I(\mu A/cm^2)$ is the illumination intensity on the wafer. Then the exposure time ($Texp$) of sub-field for resist sensitivity of $S(\mu C/cm^2)$ represents as follows:

$$Texp = S/I. \tag{4.1}$$

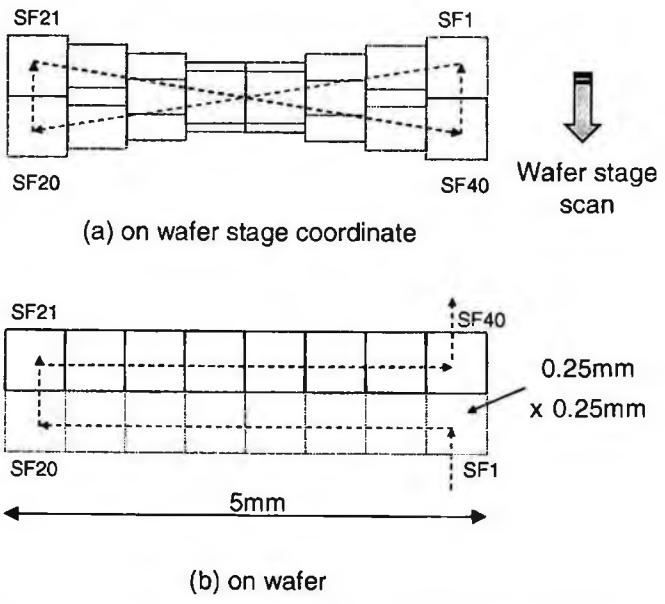

Figure 4-1. Actual exposure beam motion (a) on the wafer stage coordinate, and (b) on wafer.

Then the suitable reticle stage velocity Vr,exp is expressed as follows:

$$Vr, exp = Pr/(n(Texp + Tsettle)), \tag{4.2}$$

where Pr and n represent sub-field pitch (=1.3 mm) on reticle and the number of sub-fields (=20) within one deflection length, respectively. $Tsettle$ represents the beam settling time and other necessary durations. Actual reticle stage velocity Vr is given by

$$Vr = min(Vr, exp, Vr, max), \tag{4.3}$$

where Vr,max is the maximum velocity of the reticle stage.

On the other hand, the wafer stage velocity Vw is given by

$$Vw = Vr/(Pr/Pw), \tag{4.4}$$

where Pw (=0.25 mm) is the pitch of the sub-field on the wafer. Therefore, the ratio of wafer stage velocity to reticle stage velocity is 1/5.2 even though the magnification of the projection optics is 1/4. The difference between the magnification of projection optics and the ratio of reticle and wafer stages will generate an image smear during stage scanning exposure if without any correction. Deflection control of projection lens system will make reticle sub-field image at proper position on wafer in order to avoid image smear.

4.3. *Proximity effect correction*

In the proximity effect caused by electrons with high acceleration voltage such as 100 kV, the influence of backscattered electron from silicon wafer is dominant. The Monte Carlo simulation result of the distribution of backscattered electron from silicon wafer is shown in Fig. 4-2. The number of backscattered electrons becomes about 11% of the number of incident electrons and each backscattered electron has a different energy according to the path length in silicon wafer. The maximum distance between the injection point of incident electrons and the ejection point of each backscattered electron is 55–60 μm.

Reticle pattern shape correction is adopted as a countermeasure for this proximity correction [3]. In order to verify the effectiveness of reticle pattern shape correction, twin lines near a large opening pattern were exposed and those linewidths were measured as a function of the distance between twin lines and the large opening [4]. Negative type resist was used. Figure 4-3 shows the experimental results of Mask bias values which give 100 nm resist images as a function of the distance between twin lines and the large opening. It is confirmed that approximately 50 μm radius is a required correction range, but its feature is continuous and gradual.

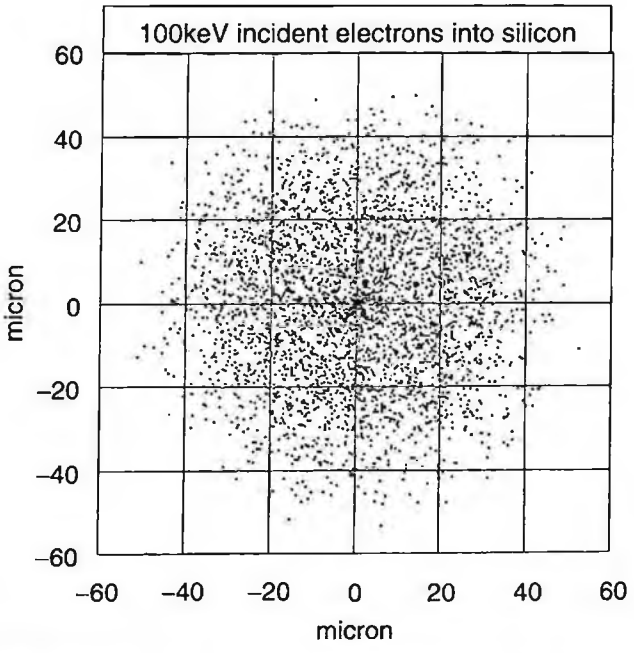

Figure 4-2. Monte Carlo simulation result of the distribution of backscattered electron from silicon wafer. Incident electron energy is 100 keV. The number of incident electron is 30,000.

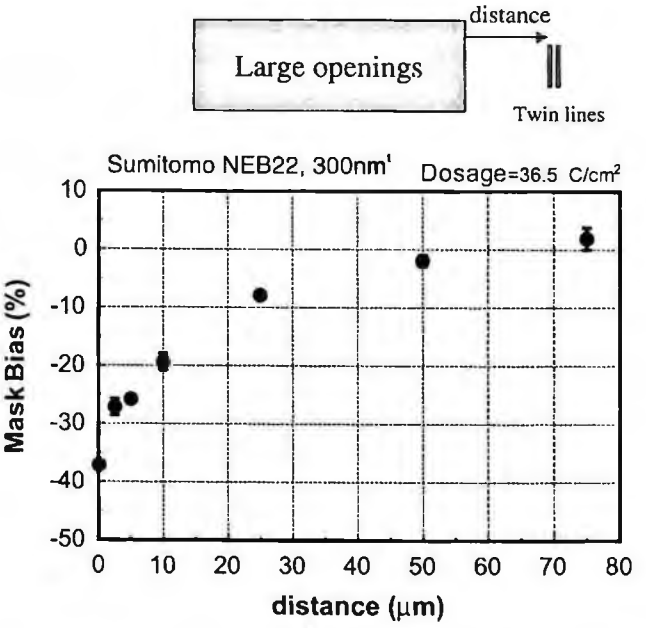

Figure 4-3. Required mask bias in order to obtain 100 nm resist image.

4.4. *Sub-field/Complementary stitching*

The pattern linewidth irregularity occurs when the stitching accuracy between adjacent sub-fields or overlapping complementary sub-fields is not zero. There are two countermeasures in order to avoid or in order to moderate the influence of stitching errors;

(i) Fuzzy boundary around sub-field in order to avoid division of a critical position,
(ii) Reticle pattern edge deformation and overlap exposure.

Figure 4-4 represents the concept of fuzzy boundary. There is a supplementary illumination area out of the nominal sub-field pattern area of 1 mm × 1 mm on a reticle. The patterns in this supplementary area can be exposed properly. Therefore, the division of reticle pattern to adjacent sub-fields can be avoided for patterns within this supplementary area by setting a fuzzy boundary between adjacent sub-fields.

Because the fuzzy boundary concept cannot be used for overlapping complementary subfields, a pattern edge deformation is recommended for stitched patterns. Figure 4-5 shows the effectiveness of the pattern edge deformation. The rectangular shapes of stitched patterns are deformed to a pencil-shape and an inverse-pencil-shape, respectively. The experimental data is consistent with the simulation result and CD irregularity can be moderated within 10 nm (3σ) [5].

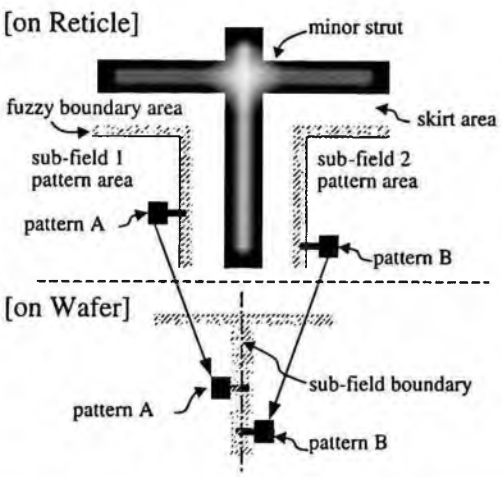

Figure 4-4. Fuzzy boundary concept in order to avoid CD irregularity at sub-field boundary.

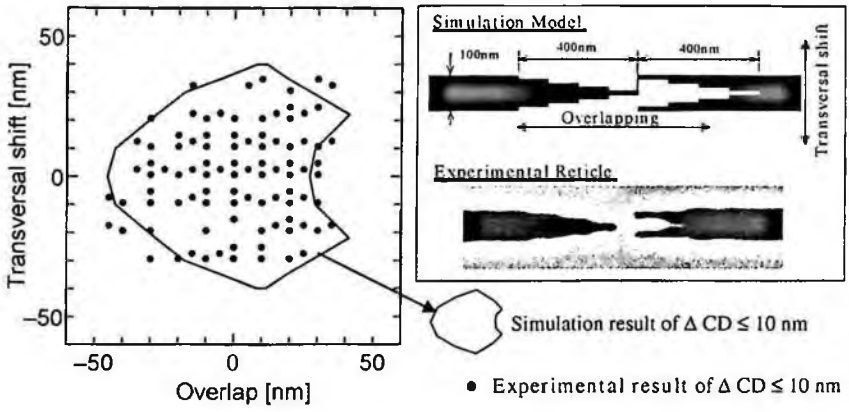

Figure 4-5. Effectiveness of pattern edge deformation on CD irregularity.

References

1. K. Suzuki, T. Fujiwara, K. Hada, N. Hirayanagi, S. Kawata, K. Morita, K. Okamoto, T. Okino, S. Shimizu and T. Yahiro, Nikon EB stepper: its system concept and countermeasures for critical issues, *SPIE* **3997**, pp. 214–224, 2000.
2. S. Kojima, W. Stickel, J. D. Rockrohr and M. Gordon, Electron Optical Image Correction Subsystem in Electron Beam Projection Lithography, *J. Vac. Sci. Technol.* B18, pp. 3017–3022, 2000.
3. T. Okino, K. Suzuki, K. Okamoto, S. Kawata, K. Uchikawa, S. Suzuki, S. Shimizu, T. Fujiwara, A. Yamada and K. Kamijo, Investigation of proximity effect correction in electron projection lithography (EPL), *SPIE* **3997**, pp. 235–244, 2000.
4. K. Suzuki, T. Fujiwara, K. Hada, N. Hirayanagi, S. Kawata, K. Morita, K. Okamoto, T. Okino, S. Shimizu, T. Yahiro and H. Yamamoto, Nikon EB Stepper: the latest development status, *SPIE* **4343**, pp. 80–87, 2001.

5. T. Fujiwara, T. Irita, S. Shimizu, H. Yamamoto and K. Suzuki, High-accurate CD control at stitching region for electron-beam projection lithography, *SPIE* **4343**, pp. 727–735, 2001.

5. Tool System Description

5.1. *Tool system configuration*

In the EPL system, the exposure process is accomplished by directing electron beam through a reticle or mask, and imaging the reticle pattern onto a silicon wafer at magnification of 1/4 as is shown in Fig. 5-1. The electron optics between the reticle and wafer precisely deflects the electron beam to sequential positions on the reticle and wafer, and make corrections to the beam positioning to compensate stage positioning errors. The beam is electronically deflected mainly in the X direction while the stages are scanned in the Y direction, simultaneously correcting for the relative stage motion error and any known position errors in X, Y and Yaw directions [1].

A 5 mm × 25 mm area from ϕ200 mm reticle can be exposed and this area is called as "a mechanical stripe". After one mechanical stripe exposure, reticle and wafer stages turn around and the next exposure of mechanical stripe starts as a scan and stitch stage motion. Finally 20 mm × 25 mm exposure field from ϕ200 mm

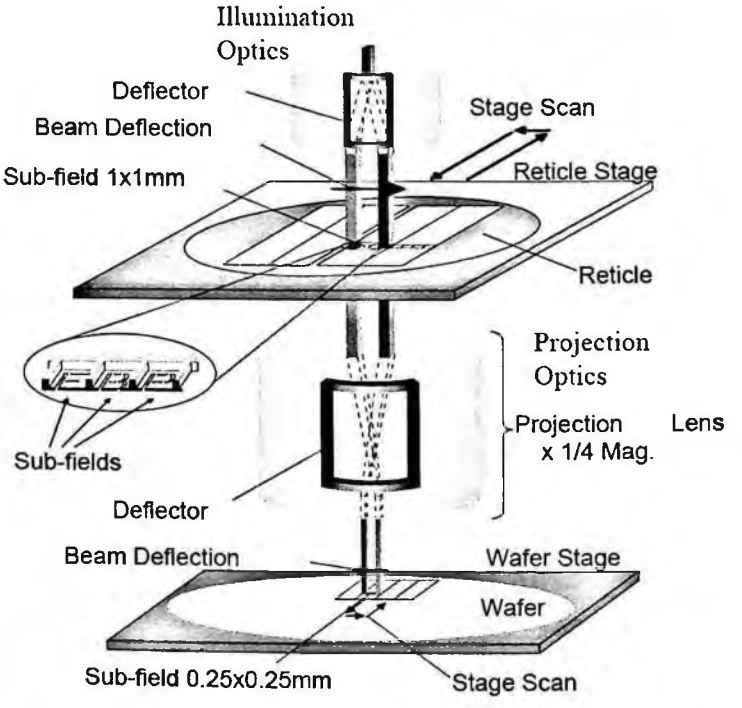

Figure 5-1. EB stepper exposure process.

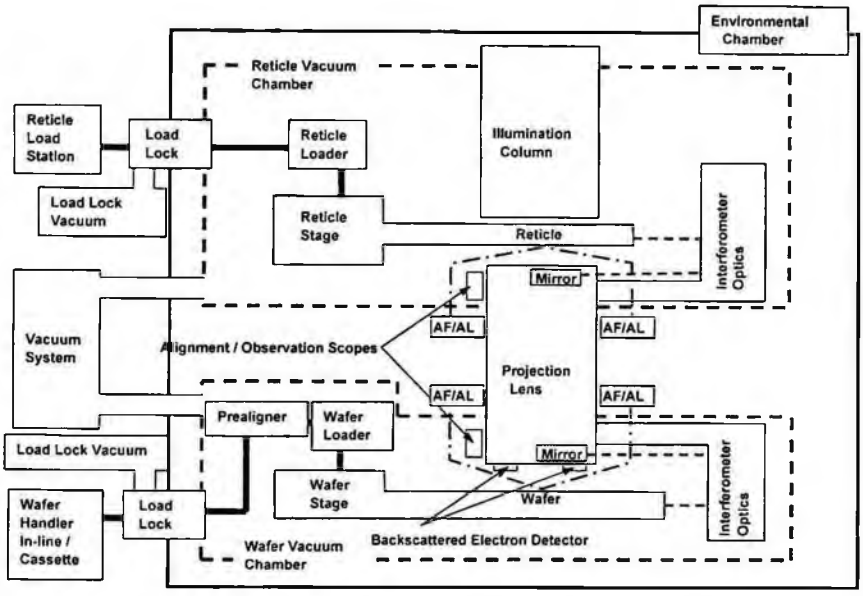

Figure 5-2. System block diagram of EPL tool configuration.

reticle can be exposed. Full size of exposure field was realized using ϕ 200 mm reticle. Typically 115 exposure fields including edge fields are exposed on ϕ 300 mm wafer (44 fields on ϕ 200 mm wafer).

The basic system configuration of EPL tool shown in Fig. 5-2 is similar to conventional optical scanning exposure tool except for its vacuum system and electron optical system including control electronics. Electron beam path in the electron optical system, reticle stage and wafer stage are in vacuum. Reticle and wafer loader systems have load-lock chambers between vacuum chamber and outside air.

5.2. *Tool system design concept*

Other essential requirement as well as higher resolution requirement is the ability to align precisely a pattern being exposed to other patterns already exposed on the wafer, which is called system overlay accuracy. As a general rule, the total alignment tolerance is about 1/3 of the line width being patterned. For hp65 nm technology node, this comes down to about 22 nm total from all error sources. Making system overlay accuracy feasible, each error component in various error categories need to be very small, typically around 1 to 5 nm. This places a severe challenge on design and engineering of all EPL tool modules such as electron optics, vacuum body, vacuum stages, vacuum loaders and total control system. It is also important while considering final system accuracy to take into account two categories of errors. One is the observable errors which can be measured by metrology sensors and the other is the non-observable errors which can not be measured by metrology sensors but

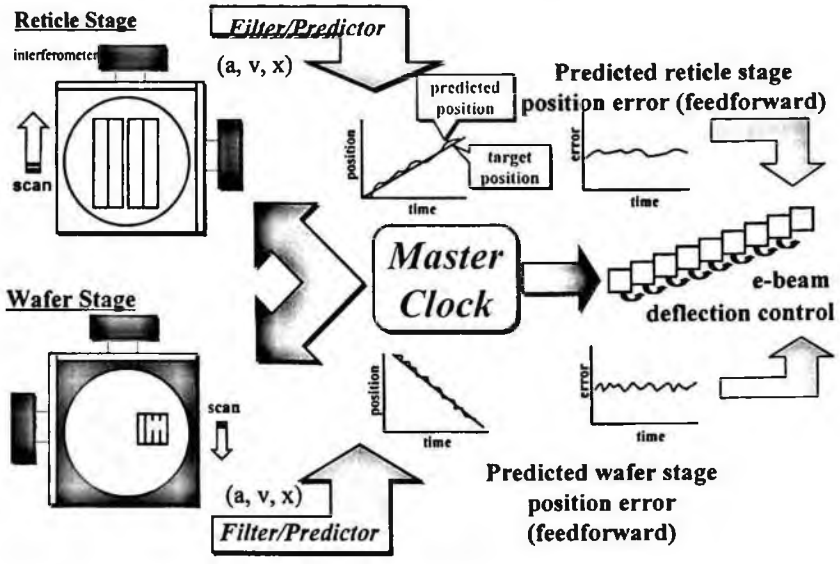

Figure 5-3. Filter/Predictor real time control concept.

should be quantified by other methods. CAE simulation technologies relating to total motion control analysis, structural analysis and magnetic field analysis are effective in estimating those errors. As can be seen in Fig. 5-2, there are many modules which are related to each other and must work synchronously to achieve the required performances and functions. The most remarkable feature of total control system is its dynamic exposure motion combining beam deflection and stage scan. The horizontal position of stage is measured by interferometer system and the vertical position is measured by height sensor. The position errors of both reticle and wafer stages are compensated by adjusting exposure position of each sub-field by electron beam deflection control. Excellent combination control is required for this dynamic image formation [2,3,4].

5.3. *Reticle and wafer vacuum stages*

The wafer and reticle stages are required to move precisely in vacuum environment at high velocities and high accelerations in order for the system throughput to be reasonable, which is an essential requirement for EPL tool to be marketable. In Nikon NSR-EB1A system, the maximum acceleration and maximum velocity of reticle stage are designed to be 0.4 g and 400 mm/s respectively and those of wafer stage are 0.1 g and 100 mm/s respectively. Since no vacuum stage system with such features has ever existed, the new development of high performance EPL vacuum stage systems was required.

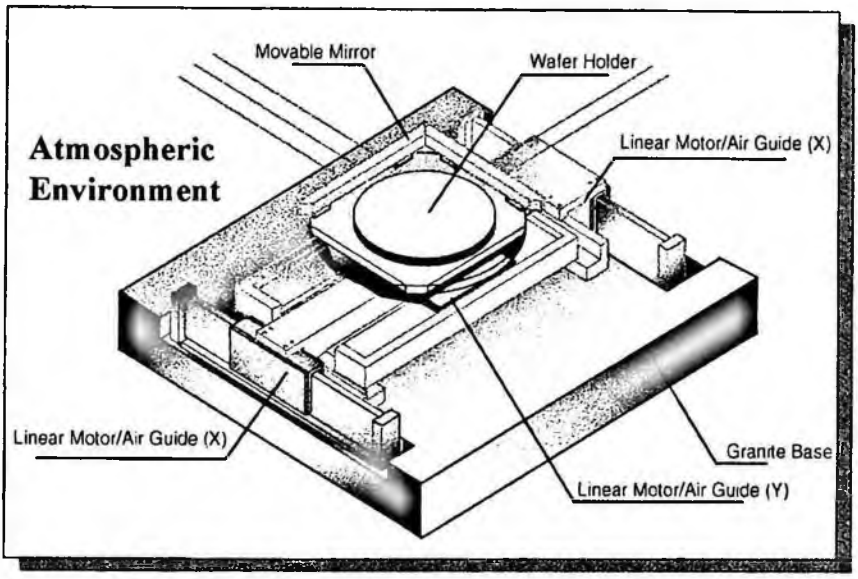

Figure 5-4. Air bearing and linear motor stage concept.

The optical lithography stages have been developed based on air bearing and linear motor technologies in order to get higher control bandwidth and smaller mechanical non-linearity characteristics. Figure 5-4 shows the simplified stage structure of conventional optical lithography tool with air bearing and linear motors. Precision stage development results of optical lithography tools should be utilized. However, the requirements for the EPL stages are very different from and much more difficult than their optical counterparts due to the following reasons.

First of all, the stages must operate in a vacuum and should not cause any deterioration to the vacuum environment because of gas leakage and outgass. Conventional air bearings cannot be used without any elaborate methods to remove effectively the air escaping from the bearing pads and to prevent air release into the vacuum chamber through air gaps by differential-pumping method. The vacuum level of 10^{-4} Pa within stage vacuum chambers should be maintained. Test chamber was built to test and evaluate vacuum compatible air bearing performances [5]. One test fixture is shown in Fig. 5-5. Using this test fixture, gas leak and outgas data were obtained and the results were compared to analytical models. From this result, a vacuum compatible airguide design has been established. These air bearings perform like a conventional air bearing with typical gas flows, air gaps and stiffness. In addition, the pump-out grooves are used to scavenge the air escaping from the bearing pads before it leaks into the stage vacuum chamber. We could verify the differential pumping performance and choose the optimum materials and surface finish treatments. This vacuum compatible requirement causes the stages

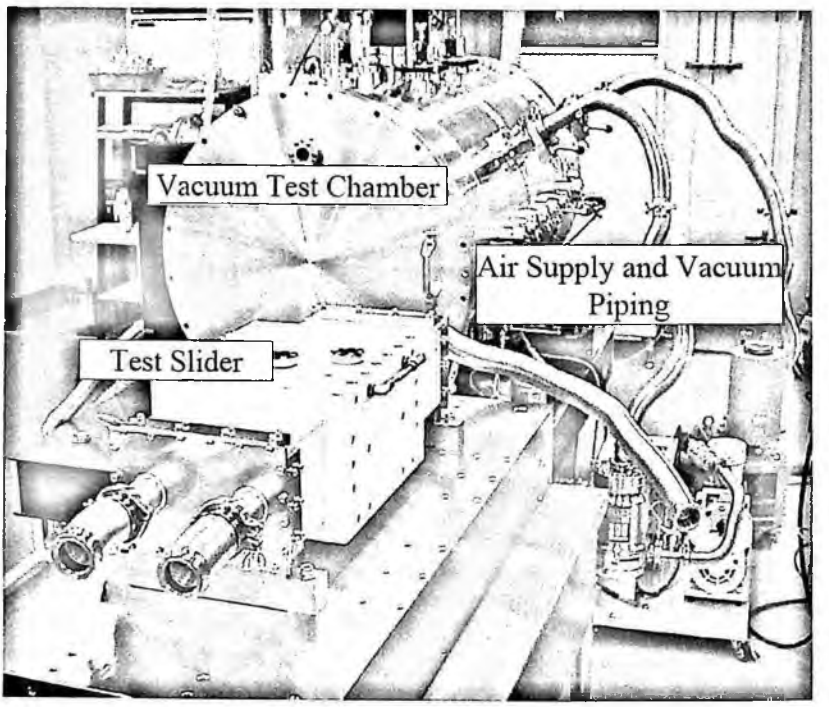

Figure 5-5. Vacuum air guide test fixture.

to be much complicated in structure and to be made of low outgass materials with special surface finish treatment.

The other major reason is that the electron beam is extremely sensitive to magnetic fields, which will shift the X-Y placement of the beam. Any electromagnetic motors or actuators must be well-shielded to prevent stray magnetic fields from letting out of the motors. We had to develop electro-magnetic shield technologies for stage motors. Electromagnetic simulation and actual experimental data were successfully collated and verified through fine collation checks. Very low level of stray magnetic field from the shielded linear motors was achieved. We need non-magnetic type of actuator on the top of the stage very close to electron beam position while printing. Figure 5-6 shows newly developed table leveling unit driven by piezo actuators which is non-magnetic type of actuator.

Although these requirements make the EPL stages much more difficult to design and manufacture compared to the optical counterparts, a key mitigating factor can be found to make the system design requirements reasonable. The ability to deflect the electron beam acts as a high performance fine stage to make precise corrections to the stage positioning errors. Thus the EPL stages can be allowed to have micron level positioning errors which are looser compared to nanometer level positioning errors required on the optical counterparts. Full scale stage development has been

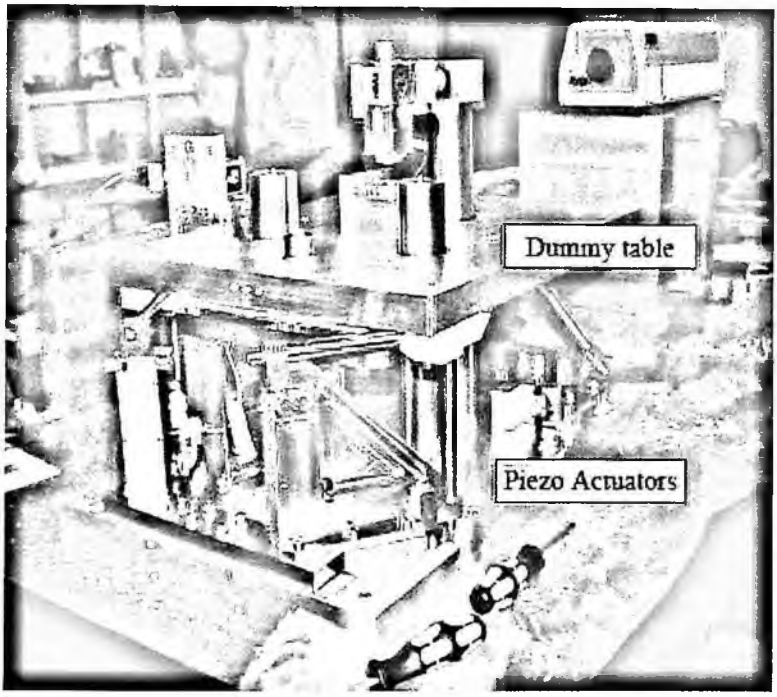

Figure 5-6. Table leveling unit driven by piezo actuators.

carried out for both wafer vacuum stage and reticle vacuum stage and confirmed stage performances. Figure 5-7 and Fig. 5-8 show stage position control response data of the reticle stage in Y scan direction and X direction.

Since electron beams are very sensitive to magnetic fields, the proper body design to prevent the magnetic fields near the electron beam is required. Total system accuracy puts severe limits on allowable beam positioning error, while throughput requirement almost certainly makes stage motors located much closer to EO column and supplied by much more electric current than in previous E-beam systems. These conditions require a system level design approach to magnetic shielding considering that AC fields perturb the e-beam while DC fields can, in principle, be calibrated out. However, DC fields can perturb the e-beam if any magnetically permeable materials (magnetic material) near the column move. When any unit made of magnetic materials changes its position, the DC fields change in position and magnitude, thereby causing the beam to be shifted some amount. If this change is not measured or calibrated out, the result is that the exposed image is then incorrectly aligned on the wafer. The magnetic fields considered can be external ones to the system such as earth magnetic field, local magnetic field from manufacturing equipment, or can come from actuators within the system such as stage linear motors, loader robot, or isolation system (AVIS) actuators. To prevent the DC lens

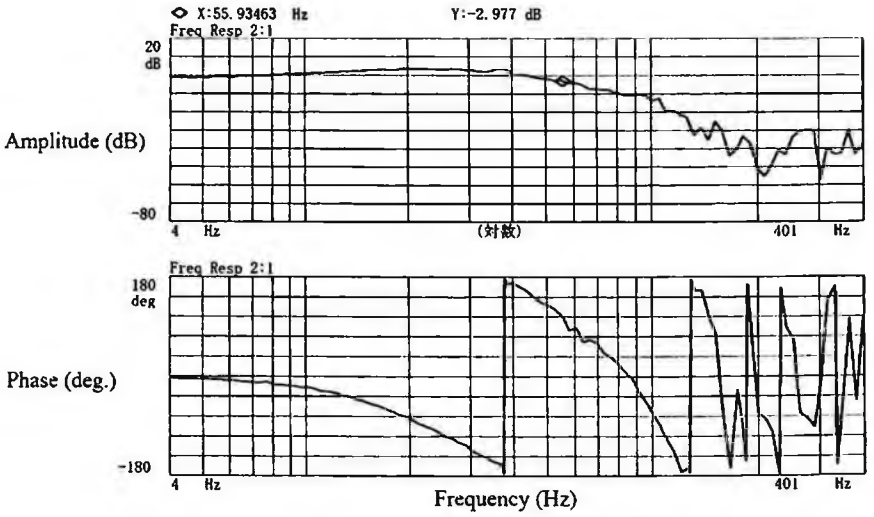

Figure 5-7. Reticle stage control response in X direction.

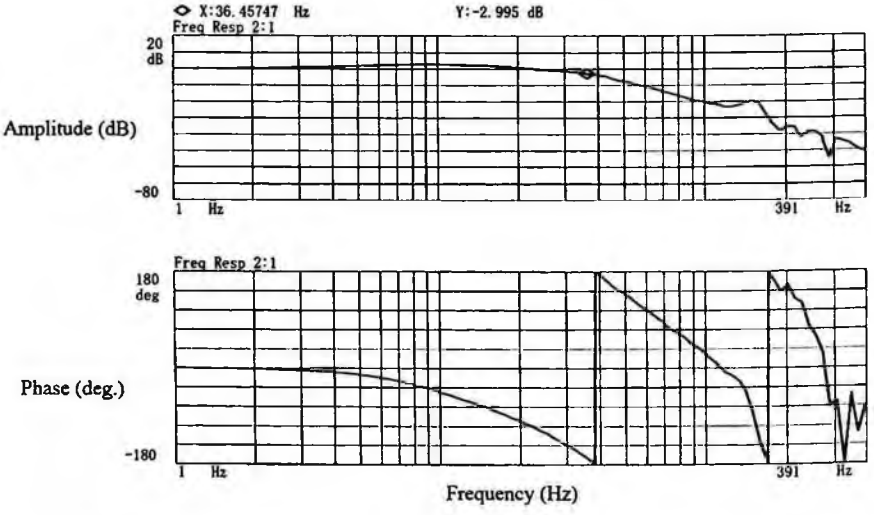

Figure 5-8. Reticle stage control response in Y direction.

fields from being a potential problem, all materials used for stage moving parts should be non-magnetic, which leads to the stage design task being very difficult.

5.4. *Vacuum body*

Figure 5-9 shows internal body arrangement of the electron optics column and the reticle and wafer stages. It is important for vacuum body design that stages and

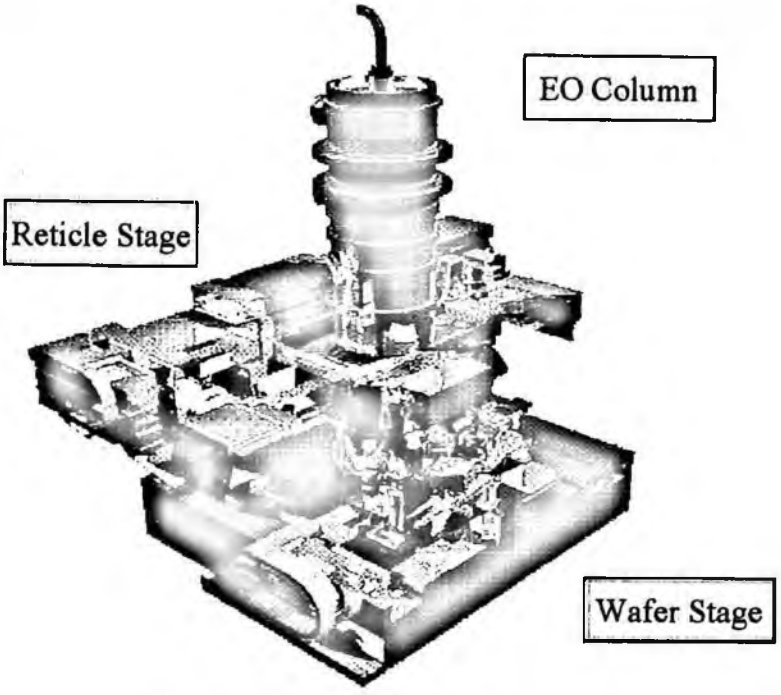

Figure 5-9. EO column and stage arrangement.

EO column are firmly connected to each other to maintain metrology references to be unchanged.

It is also important to establish proper design method to prevent magnetic field problems from total body design point of view. Many component level and total assembly level experiments were carried out. Figure 5-10 shows full scale magnetic shielding setup. Both AC and DC magnetic fields from linear motors have been measured in a total body structure and correlated with computer modeling software (FEA) analysis. These magnetic characteristics have been incorporated into the innovative magnetic shielding designs in both linear motors and internal body structure. One mitigating factor is that during scanning, the stage moves at constant velocity with low currents to the motor windings. Therefore AC fields from the linear motors during scan are expected to be much less than during stage acceleration.

The EPL body structure has been designed to minimize overall deformation variation under vacuum loading changes and stage C.G. shift movement, and particularly in terms of the shifts and tilts at reference positions of the metrology system and stage system. The vacuum chambers containing the stages are accessible for maintenance via panels and other openings. The total structure concept of the main body is shown in Fig. 5-11. It is also supported and isolated from floor vibration by AVIS. The detailed FEA modelings of not only various local unit

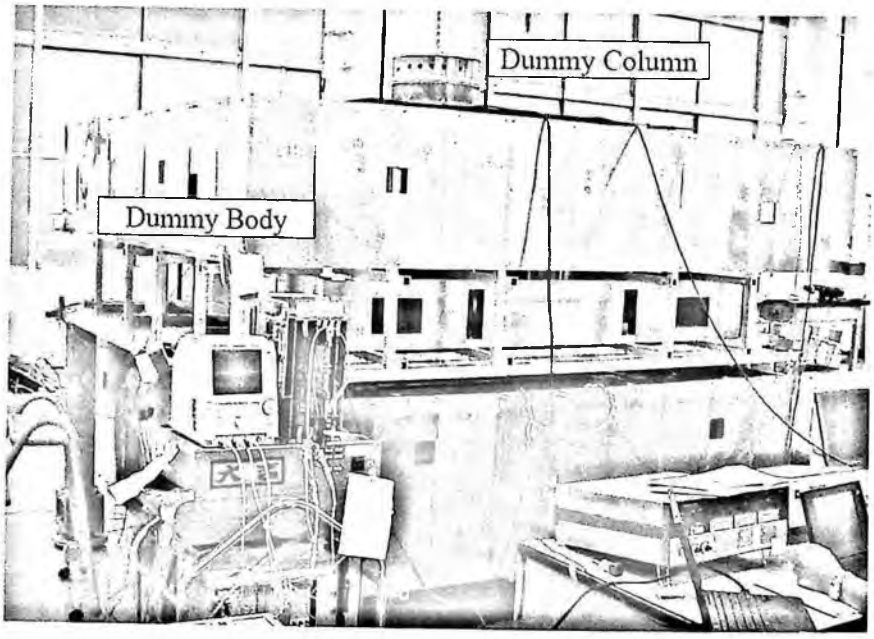

Figure 5-10. Full scale magnetic shield experimental setup.

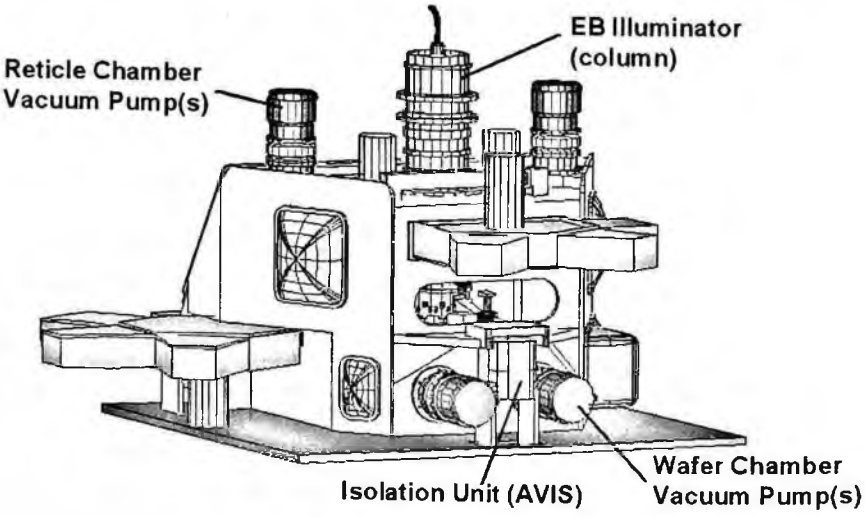

Figure 5-11. EPL total body configuration concept.

structures but also whole structure have been iterated many times to optimize vibration modes, structural rigidity and deformation variation under changing loads. One of most important references are stage mounting reference points. Figure 5-12 and Fig. 5-13 are structural deformation simulation analysis for reticle stage and wafer

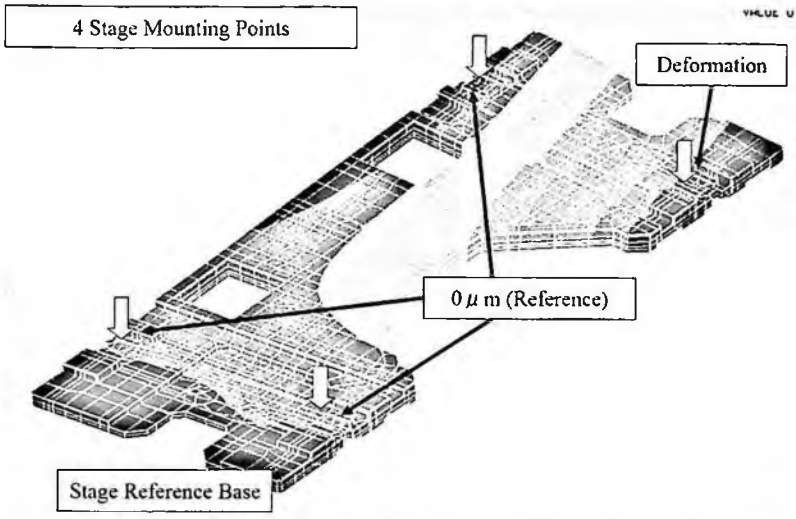

Figure 5-12. Reticle stage support reference points deformation analysis.

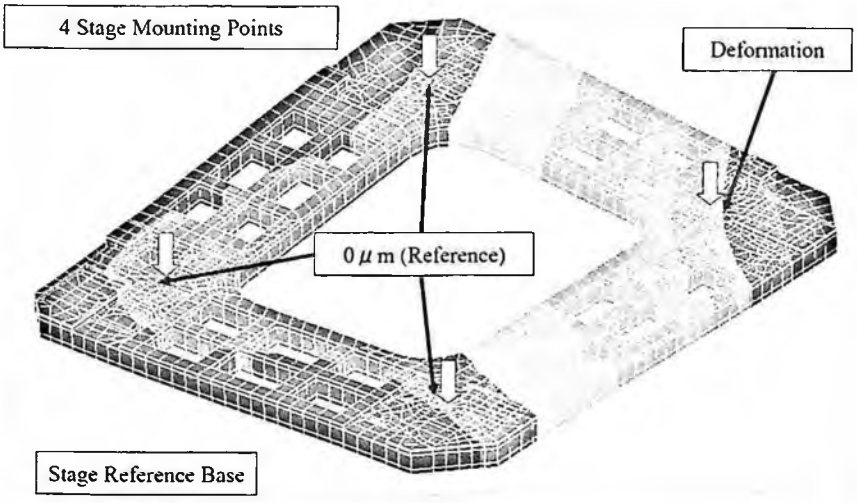

Figure 5-13. Wafer stage support reference points deformation analysis.

stage reference points respectively. Simulation results show several micron level deformations, which correspond to enough body rigidity to keep reference point almost unchanged even while being loaded by huge changing atmospheric pressure loads and stage C.G. shift movement. That range of deformation can keep the stage accuracy unchanged and vacuum compatible air bearing working.

As mentioned earlier, in order for the electron optics to precisely correct the stage X-Y positioning errors, we have to manage properly two categories of error sources, observable errors and non-observable errors. Observable errors consist of

any errors observed by metrology sensor systems such as laser interferometer signals to measure stage positions, whereas non-observable errors are made up of any errors which the metrology sensor systems can not observe directly. Those would be induced by metrology reference deformation, magnetic field variation, thermal expansion, stress distortion due to atmospheric pressure and C.G. shift due to moving stages, internal and external vibration sources, electronic noise, and electronic drift and so on. The system must be able to observe observable errors precisely and determine non-observable errors correctly by nanometer level accuracy. This requires considerable attention in the design of whole body and metrology modules. The laser interferometer system must be extremely stable because it should act as common ultra-precise metrology reference to total control system. EPL total system must be controlled by common reference timing which must be stable and known precisely so that all control modules can cooperate to exercise their functions in timely manner without any timing mismatch which may sometimes cause system performance deterioration.

In order to get printing position accuracy, we need to make the body very quiet by reducing body vibration and deformation. The reaction forces from the wafer and reticle stages should be isolated, and brought out to outside main body. Reaction force path is isolated from the main body and led to floor ground. As the stages accelerate and decelerate, these forces should not vibrate the body containing the metrology and the electron optics modules. Figure 5-14 and Fig. 5-15 show stage synchronization accuracies simulated under the conditions of with and without reaction force management respectively. This result shows that we can not reach required synchronization accuracy without it.

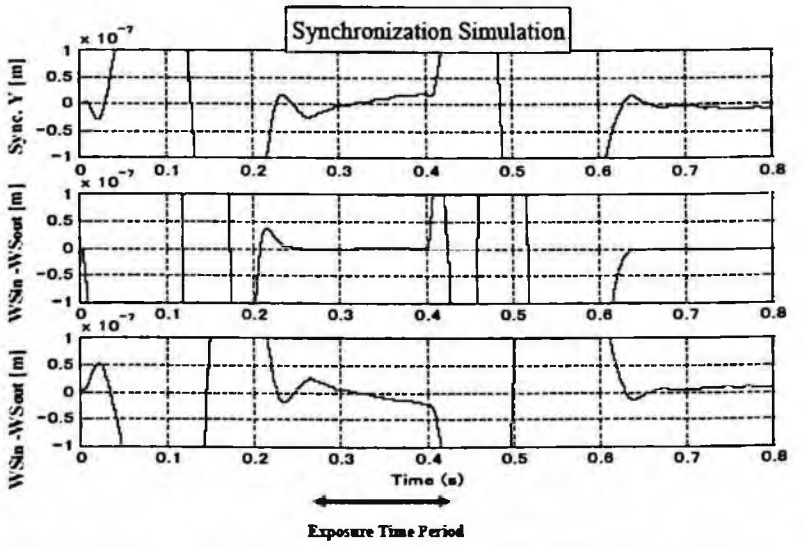

Figure 5-14. Stage synchronization accuracy with reaction force management.

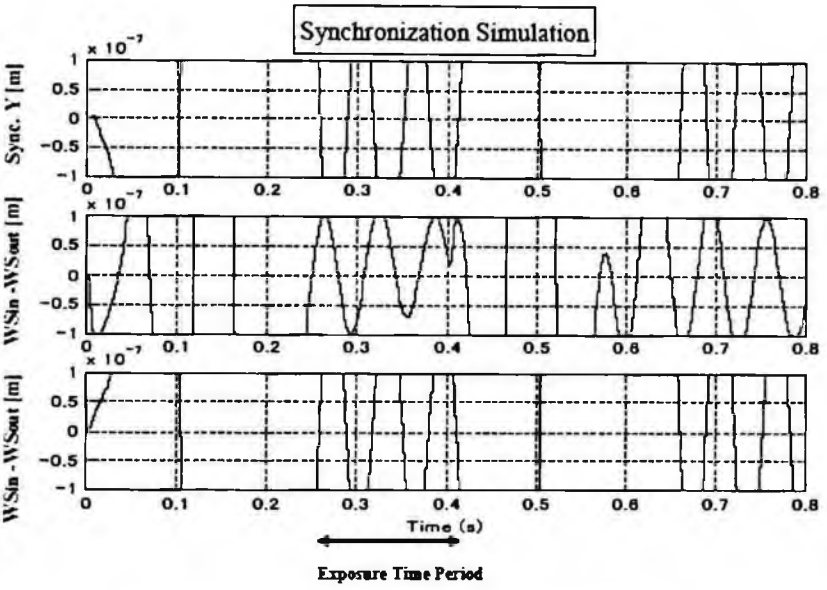

Figure 5-15. Stage synchronization accuracy without reaction force management.

Figure 5-16. Wafer vacuum loader module.

5.5. *Reticle and wafer vacuum loaders*

In addition to the electron optics, the stages and the body, there are other major units, wafer loader and reticle loader. Figure 5-16 shows newly developed vacuum loader module. Reticle and wafer loader modules have load-lock chambers between vacuum chamber and outside air. Almost all subsystems are set in an environmental chamber. We must also consider the temperature control system carefully since vacuum pumping causes the temperature inside the chamber lower.

5.6. *Metrology sensors*

Metrology sensors such as interferometers and focus/leveling sensors are prepared for both reticle and wafer stages. Multiple interferometer axes are adopted for the measurements of X,Y, positions, yaw, pitch and mirror bow. The concept of focus sensor is an oblique incident optical sensor with multiple measurement beams to obtain the height and tilt information of reticle or wafer. Since EPL mask is made of thin 200 mm wafer which is expected to be bent by gravity force, a reticle focus sensor is adopted. During exposure, data from those metrology sensors are used for servo-control of both stages and residual control errors are sent to electron optics for fine compensation control. The off-axis wafer alignment microscope FIA (Field Image Alignment) is prepared as the main alignment sensor.

FIA is a wafer mark image processing system with a bright image field illumination and been adopted considering mix-and-match use. Similar optical microscope is prepared for reticle side to observe reticle patterns. Backscattered electron detector is located at the bottom of the electron projection optics and is used mainly for electron optics calibration and measurement of reticle position by observing fiducial marks.

5.7. *Tool control system*

EPL tool has a master clock system in the electron optics control system, the reticle stage and wafer stage control systems. Under the common master clock system, reticle and wafer stages are servo-controlled to target positions independently. Position error of each stage is measured by interferometers and compensated by the electron beam deflection control. The difference between the magnification of projection optics and the ratio of wafer stage velocity to reticle stage velocity is also compensated by the electron beam deflection control. In order to prevent control delay from interferometer data acquisition to the electron beam deflection control, a unique control concept called "Filter/Predictor" shown in Fig. 5-3 is used for a feed-forward correction. The Filter/Predictor function predicts the stage position at the moment of sub-field exposure by calculating past data of position, velocity and acceleration [6].

5.8. *Expected tool performance*

Table 5-1 shows the target specification of EPL R&D tool for hp65 nm technology node, dubbed as Nikon NSR-EB1A, which was delivered to Selete and used in the pilot line there for the development of EPL technology including reticle evaluation, resist evaluation and trial manufacturing of devices.

Two 200 mm round reticles can be set on the reticle stage. Therefore exposure field size is 40 mm × 25 mm in the case of non-complementary exposure or 20 mm × 25 mm for complementary exposure.

The stitching accuracy of 20 nm is given in order to assure the local CD irregularity at stitching region within a tolerable range.

Table 5-1. Target specification of Nikon NSR-EB1A.

Items	Target Specifications
Electron Beam Energy	100 KeV
Standard Resolution	100 mm node (70 nm gate)
CD Uniformity	±10%
Magnification	x 1/4
Exposure Field Size	20 mm × 25 nm for Complementary 40 mm × 25 mm for Non-Complementary
Sub-field Size	0.25 mm × 0.25 mm
Deflection Length	5 nm
Wafer Size	200 mm
Reticle Size	200 mm round reticle Stencil type as standard
Product Overlay	35 nm ($X + 3\sigma$)
Stitching Accuracy	20 nm ($X + 3\sigma$)

Table 5-2. Achieved performance of Nikon NSR-EB1A performances.

Items	Achieved Performances
Exposure Field Size	20 mm × 25 mm from 200 mm Reticle
Resolution	70 nm L/S, 50 nm 1:2 L/S, 60 nm $CH_{,,}$ 50 nm iso.
CD Uniformity	5% (3s)
Stitching Accuracy	18–22 nm (3s)
Overlay Accuracy	18–22 nm ($X + 3s$)
Throughput	4WPH@300 mm wafer

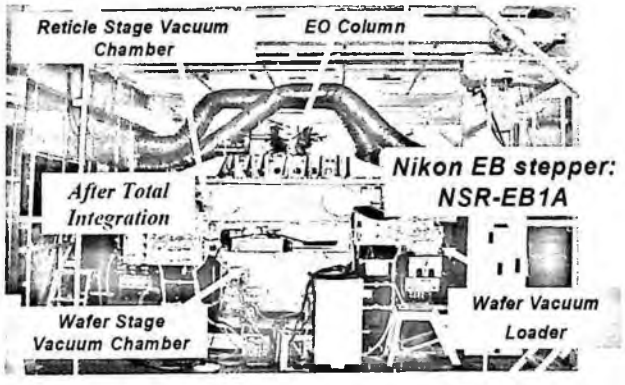

Figure 5-17. EPL R&D tool configuration.

5.9. *Actual EPL tool configuration and performance summary*

Since the first dynamic exposure results were reported in 2003, Nikon NSR-EB1A has been operated to improve resolution, stitching accuracy and overlay accuracy as well as throughput. Figure 5-17 shows the actual picture of total system

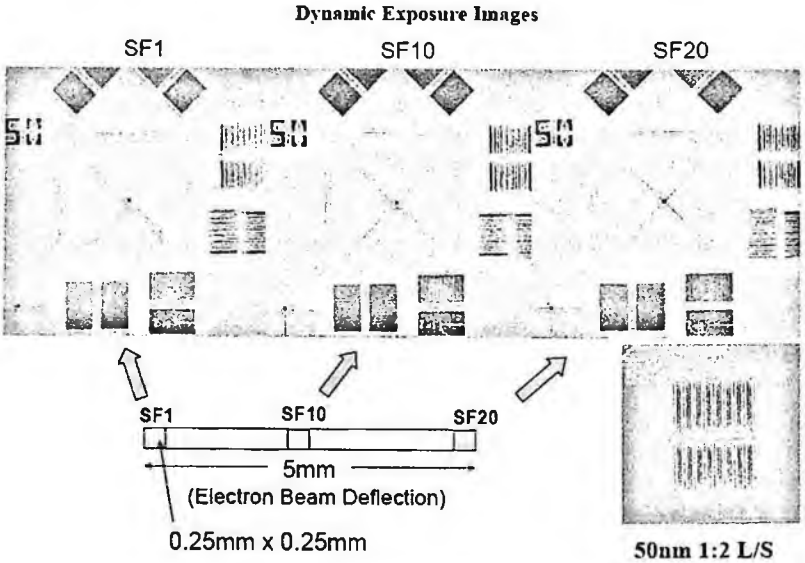

Figure 5-18. 50 nm L/S resolution in dynamic exposure.

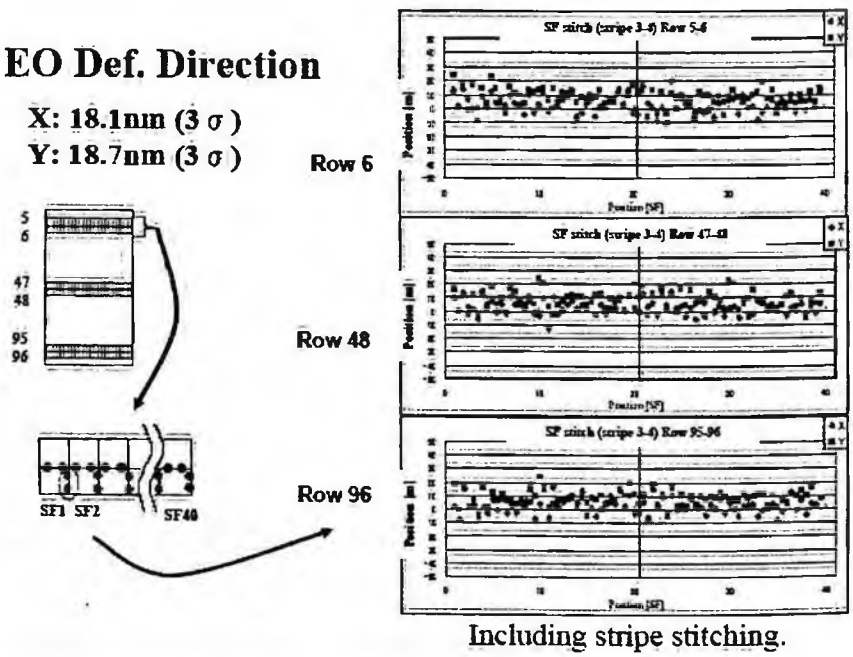

Figure 5-19. Sub-field stitching example data in dynamic exposure.

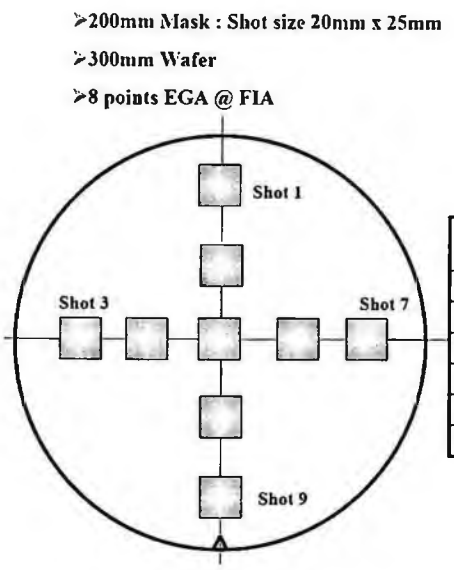

Overlay Data

3wafers
(72points/shot, 9shots/wafer)

nm	Mean	3σ	Mean+ 3σ
X(1st)	6.25	14.66	20.91
Y(1st)	2.03	16.48	18.51
X(2nd)	6.49	14.52	21.01
Y(2nd)	2.57	18.04	20.61
X(3rd)	5.92	16.52	22.44
Y(3rd)	0.68	21.53	22.21

Figure 5-20. Overlay example data in dynamic exposure.

configuration of EPL R&D tool. Figures 5-18 and 5-19 and 5-20 show examples of dynamic exposure performance data achieved in NSR-EB1A. NSR-EB1A has demonstrated dynamic exposures and achieved the required specifications and functions for hp65 nm technology node tool [6].

References

1. K. Suzuki, T. Fujiwara, K. Hada, N. Hirayanagi, S. Kawata, K. Morita, K. Okamoto, T. Okino, S. Shimizu and T. Yahiro, Nikon EB stepper; its system concept and countermeasures for critical issues, *Proc. SPIE* **3997**, pp. 214–224, 2000.
2. T. Miura, Nikon Electron Projection Lithography (EPL) System Tool and Mechanical Technology Development, Proc. 4th International Workshop on High Throughput Charged Particle Lithography 2001.
3. T. Miura, Electron projection lithography tool development status, *J. Vac. Sci. Technol.* **B20**, 2622–2626, 2002
4. T. Miura, T. Sato, M. Miyazaki, K. Hada, Y. Sato and M. Tokunaga, Nikon EPL tool development summary, *Proc. SPIE* **4688**, pp. 527–534, 2002.
5. W. Thomas Novak, Douglas Watson, Yasushi Yoda, Nikon Electron Projection Lithography System: Mechanical and Metrology Issues, ASPE Annual Meeting Proceedings Volume 22, pages 517–520, 2000.
6. T. Miura, S. Kawata, K. Hada, Y. Kakizaki, M. Miyazaki, K. Suzuki, N. Hirayanagi, A. Yamada, J. Ikeda, T. Yahiro, J. Udagawa, H. Takekoshi, T. Umemoto, Y. Ohkubo, T. Shimoda, T. Tanida, Y. Watanabe, K. Ohmori, F. Moro, S. Takemoto, T. Yoshioka and K. Morita, Nikon EPL tool: The latest development status and results, *Proc. SPIE* **5751**, pp. 477–482, 2005.

6. EPL Reticle

6.1. *EPL reticle format*

As a standard EPL reticle (mask), the 200 mm scattering reticle has been used (EPL reticle), as shown in Fig. 6-1. Its format is shown in Fig. 6-2 [1,2]. A reticle pattern area is a thin membrane for the scattering contrast imaging. The membrane

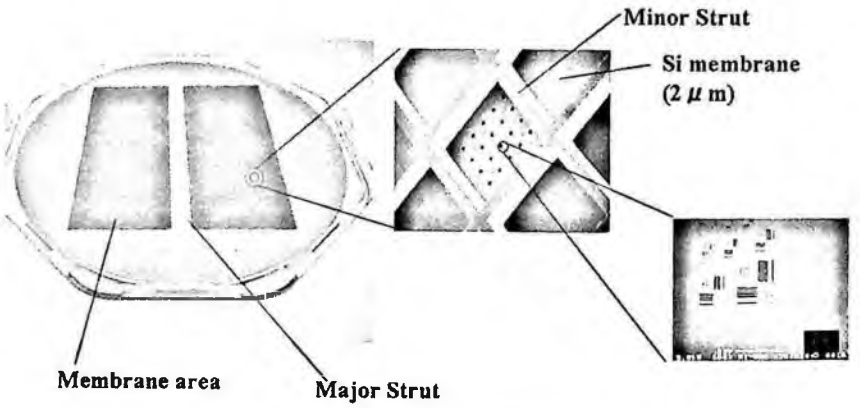

Figure 6-1. 200 mm EPL stencil reticle.

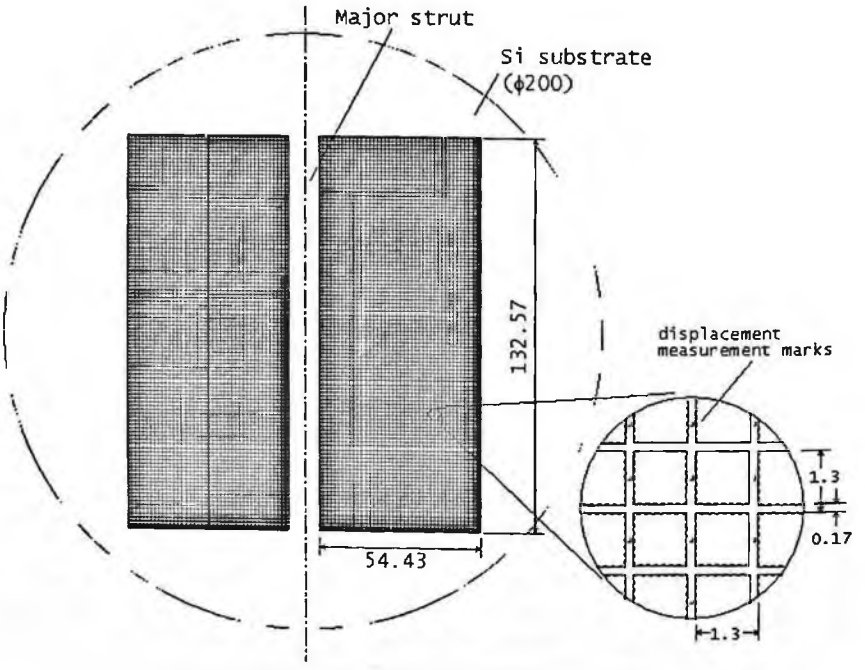

Figure 6-2. EPL reticle format for EB Stepper.

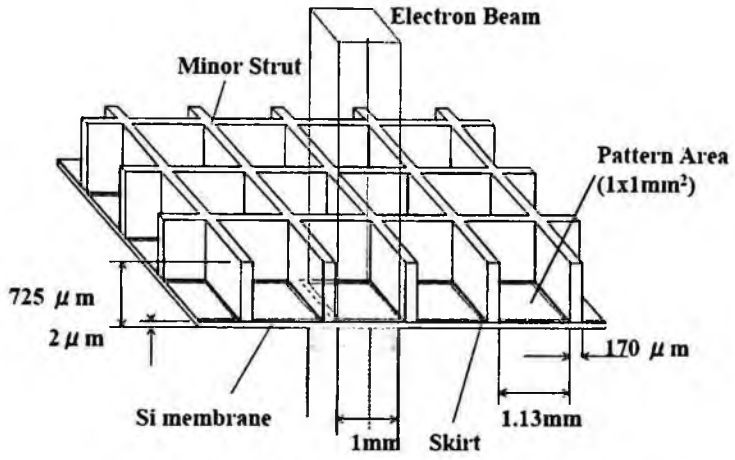

Figure 6-3. Subfield structure of EPL reticle.

is divided to subfield (SF1.13 × 1.13 mm^2 square /the exposure field and peripheral membrane area) by struts to increase mechanical stiffness of the membrane reticle (Fig. 6-3) [1]. In the scattering contrast method, the reticles have no energy deposition due to electron-beam irradiation because most electrons (100 keV) pass through the reticle (membrane) only with scattering but without energy loss, as shown in Fig. 6-4 (see subsection 6.3). Non-scattering stencil reticles (masks) have been used in EB character projection (CP) systems, which have thick Si membranes (10–20 μm) for ~50 keV electron beam and absorb most of electrons in the mask [4,5]. In the CP system, mask heating have been also observed but because of high mask magnification (x20–60), the mask heating does not affect the pattern accuracy. On the other hand, the EPL magnification is low (x4) and exposure current is high (~100 μA), reticle temperature is very sensitive for pattern accuracy. To keep the EPL reticle temperature within a few degrees in EB exposure, the introduction of the scattering reticle was epoch-making in EB exposure system [3,6].

EPL reticles had been developed in phase with EPL development by mask manufacturers. Two type reticles: the stencil reticle and the continuous membrane reticle, are commercially available, as shown in Fig. 6-5 [1,4,7].

6.2. *Si stencil reticle fabrication*

Basic reticle fabrication process is well-known as a Si membrane fabrication process using SOI wafers in Fig. 6-6.

First, an impurity (for example, Boron or Phosphorus) is doped in Si layer of SOI wafer (the top layer) to control silicon membrane internal-stress. The internal stress causes the reticle pattern displacement(IP/Image placement and CD uniformity). In the case of 2 μm Si membrane, the target internal stress may be <5 MPa (tensile stress) [8].

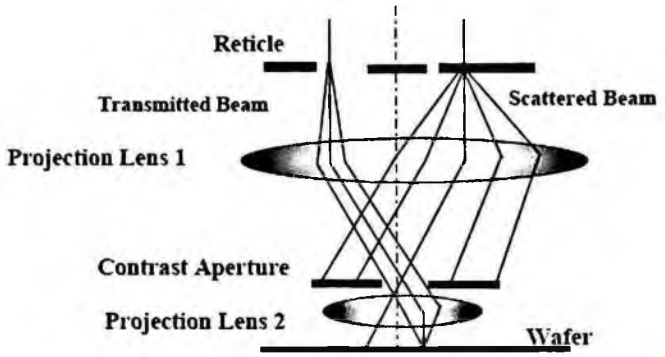

Figure 6-4. Scattering contrast imaging.

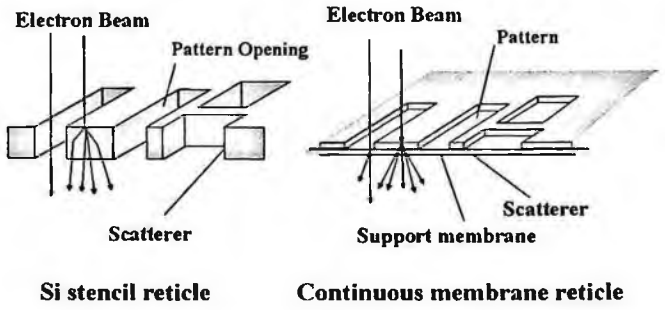

Figure 6-5. EPL reticles.

Next, the reticle blanks are finished by backside dry etching (Vertical strut fabrication). The oxide layer in SOI wafer acts as an etching stop.

The oxide layer of SOI wafer is removed by wet etching.

Lastly the reticle patterns are defined by electron beam writing and the stencil patterns through silicon membrane are etched by dry-etching.

EPL Reticle specifications for 70 nm technology node are listed in Table 6-1.

6.3. *Scattering reticle*

Two type of scattering reticles are reported: Si stencil reticle and continuous membrane reticle. Si stencil reticle is commercially available. Several continuous membrane reticles have been studied but only the SCALPEL mask and the continuous diamond-carbon (DLC) membrane reticle are fabricated in 200 mm-wafer size [3,4,6].

6.3.1. *Stencil reticle*

The stencil pattern consists of the silicon scattering membrane and pattern openings, as shown in Fig. 6-5. Electrons on the patterns of reticle transmit through

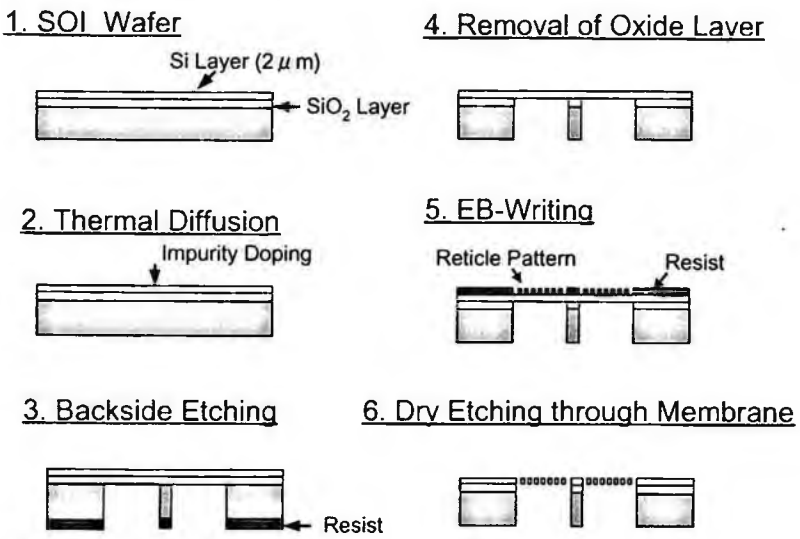

Figure 6-6. Fabrication process flow of EPL reticle.

the pattern openings without scattering, reach a wafer through the imaging lens section, and contribute the pattern imaging by the imaging system. On the other hand, electrons onto the membrane go through the reticle with scattering by the Si membrane, which are stopped at contrast aperture near the pupil plane of the projection optics (Fig. 6-4). The membrane thickness was decided upon after considering the pattern fabrication process, the electron mean free path in the membrane materials (the electron scattering and the energy absorption), the heat conductivity,

Table 6-1. EPL reticle specifications for 70 nm technology node.

Item	Specifications (on Reticle)
Technology Node	70 nm
Magnification	x4
Reticle Size	200 mm Wafer
Membrane Area	55 × 132 mm^2
Pattern Area	2 Membrane Areas
Major Strut	Width: 10 mm
Minor Strut	Grid Grillage type, Pitch: 1.3 mm/Width: 0.17 mm/ Height: 725 μm
Sub-field Size	1 × 1 mm^2
Membrane Size	1.13 × 1.13 mm^2
Membrane Thickness	~2 μm
Minimum Image Size	180 nm (45 nm on wafer)
CD Uniformity	7 nm
Image Placement	15 nm

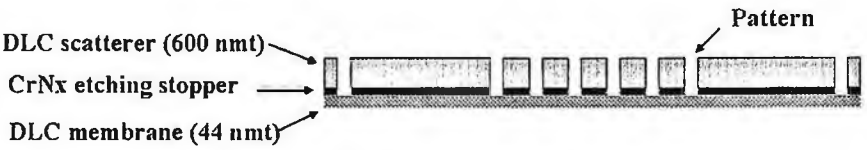

Figure 6-7. DLC continuous membrane reticle.

the mechanical stiffness (crystal or amorphous), and so on. In the case of Si, the membrane thickness is $\leq 2\,\mu$m [4].

6.3.2. *Continuous membrane reticle*

Continuous membrane reticles consist of two or three layers of thin films: the base layer (the support membrane, <100 nm) which supports pattern layer, the pattern layer (the scatterer, <500 nm), and the etch stop layer (if needed, which depends on the fabrication process) (Fig. 6-5).

The combination (150 nm-thick SiN for the support membrane, 10 nm thick Cr for the etch stop, and 50 nm thick W for the scatterer) had been known as the SCALPEL mask. Another candidate is a diamond-like carbon (DLC) membrane. The DLC has high mechanical stiffness and low interaction with electron. It has good material properties as an EPL reticle. DLC continuous scattering performance on EPL was reported [3,7]. The structure, the fabrication process, the electron scattering, and the material parameters of DLC membrane are optimized. Typical membrane thicknesses are DLC 15–40 nm thick for the support membrane and DLC ~500 nm thick for the scatterer as shown in Fig. 6-7.

6.3.3. *Summary*

The two types of scattering reticles have advantages over each other. The Si stencil reticle uses Si-crystal, so the membrane is very stable mechanically and its reticle fabrication process is well-known.

However, the stencil patterns have several restrictions for patterning:

(i) the Donuts problem (the complimentary patterns). In reticle fabrication, the donuts patterns must be split into complimentary patterns. In fact several kinds of pattern split software for complimentary patterns are commercially available. Basically donut patterns need double exposures;
(ii) the pattern aspect ratio (the membrane thickness/the pattern opening size). The stencil reticle has pattern openings. The maximum pattern aspect ratio depends on its fabrication process, which may be 10–20.

The continuous membrane reticle has no stencil patterns, so it doesn't need the data split procedure and double exposures. However, even electrons, which contribute to imaging, must pass through the support membrane. In the membrane,

electrons undergo several interactions. For instance, elastic scattering may result in exposure current loss and additional beam energy dispersion due to inelastic scatterings degrades the optics resolution (the lithographic resolution). The support membrane is 30–100 nm thick. Its mechanical stiffness depends on the fabrication process and the pattern density. We need studies on this new type reticle more.

A choice between the two types of reticles should be made to meet exposure purposes carefully. For finer patterns, thinner membranes (the continuous membrane) have advantages for pattern fabrication process. However, the image resolution is sensitive to the additional energy dispersion of EB through the membrane.

EPL reticle is a wafer-base thin reticle, compared with other optical reticles. For future requirements for reticles— image placement (IP) and other pattern accuracies, the introduction of the support frame of reticle, which is attached on reticle peripheral area, should be considered to increase the stiffness.

References

1. S. Kawata, N. Katakura, S. Takahashi and K. Uchikawa, Stencil reticle development for electron beam projection system, *J. Vac. Sci. & Technol.* **B17**, 2864–2867 (1999).
2. N. Katakura, S. Takahashi, M. Okada, S. Shimizu and S. KAwata, EPL Reticle Technology, *Proceeding of SPIE* **4562**, 893–901 (2001).
3. K. Morita, N. Hitayanagi, S. Suzuki, S. Kawata, H. Mizukami, S. Takahashi and Y. Miki, Thermal Characteristics of Scattering Stencil Reticle for Electron Beam Stepper, *Jpn. J. Appl. Phys.* **38**, 7027–7030 (1999).
4. I. Amemiya, H. Yamashita[1], S. Nakatsuka, T. Sakurai, I. Kimura, M.Tsukahara and O. Nagarekawa, Stencil Mask Technology for Electron-Beam Projection Lithography, *Jpn. J. Appl. Phys.* **42**, 3811–3815 (2003).
5. Y. Nakayama, H. Satoh, N. Saitou, S. Hirasawa, T. Yanagida and H. Todokoro, *Jpn. J. Appl. Phys.* **31**, 4268–42772 (1992).
6. S. D. Berger and J. M. Gibson, New Approach to Projection Electron Lithography with Demonstrated 0.1 Micron Linewidth, *Appl. Phys. Lett.* **57**, 153–155 (1990)
7. H. Yamashita, I. Amemiya, E. Nomura, K. Nakajima and H. Nozue, High-performance membrane mask for electron projection lithography, *J. Vac. Sci. & Technol.* **B18**, 3237–3241 (2000).
8. K. Uchikawa, S. Takahashi, N. Katakura, T. Oshino, S. Kawata and T. Yamaguchi, Pattern displacement measurements for Si stencil reticles, *J. Vac. Sci. & Technol.* **B17**, 2868–2872 (1999).

7. Mask Inspection and Other Infrastructures

7.1. *Mask inspection*

An inspection tool for an EPL mask was developed by TOKYO SEIMITSU CO. LTD. and HOLON CO. LTD. A beta system is now available [1]. The tool produces

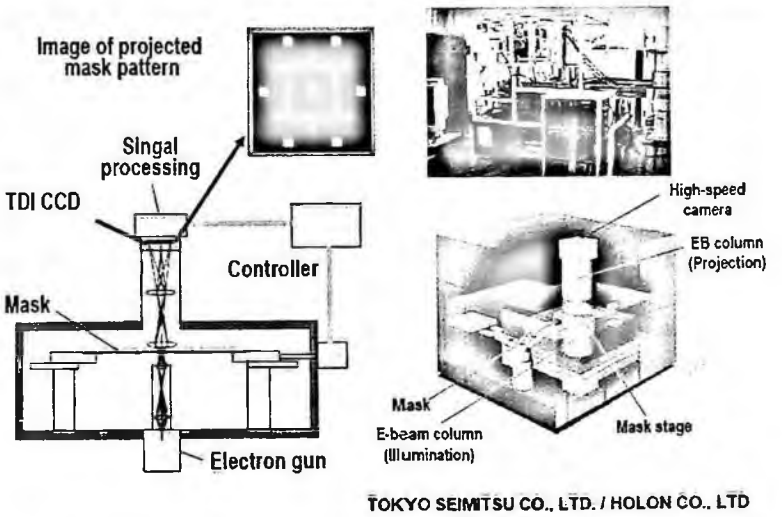

Figure 7-1. EPL mask inspection tool. Acceleration energy of electron beams is 5 keV. The pixel size is 50 nm.

an electron beam projection system capable of inspecting defects on Si stencil masks as shown in Fig. 7-1. Electron beams with an acceleration energy of 5 keV are irradiated from the back of the mask to project a mask pattern onto a time delay integration (TDI) CCD detector, through a magnifying projection lens. To inspect

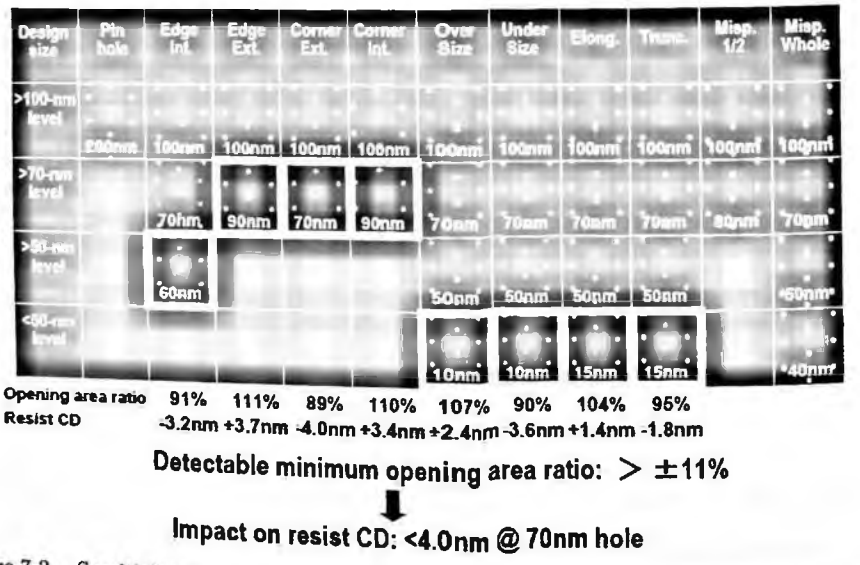

Figure 7-2. Sensitivity of defect detection. Limits of the defect inspection are indicated by white thick frames. When the mask opening area ratio is used as a index, the limits are about 10% and transcribed resist CD is less than 4 nm.

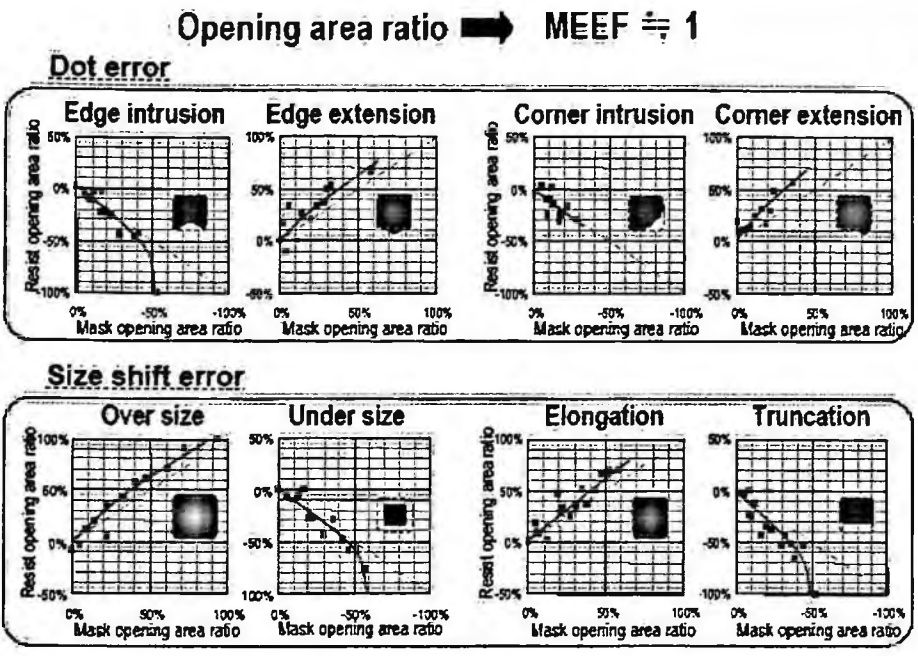

Figure 7-3. Defect printability. Mask defects are transcribed with MEEF = 1 using the ratio of mask opening area of defect pattern to that of the normal one as a new index.

the full mask area, continuous stage movement and stepping are employed. This system detects defects by comparing the mask image obtained with the design data or adjacent cell images. The pixel size is 50 nm. Figure 7-2 shows inspection results for a hole which caused a program defect. The defect size measured by an SEM is shown in the images. The limits of the defect inspection for various defect types indicated by the white thick frames are different from each other. The inspection sensitivities for over-sized or under-sized defects are very high at 10 nm, while those for the edge- or corner-intrusive and -extrusive defects are relatively low at around 100 nm. The sensitivities will be improved by reducing the pixel size to 25 nm. Figure 7-3 shows the defect printability for various programmed defects. In particular, it was found that mask defects concerning holes are transcribed with MEEF=1 using the ratio of the mask opening area of the defect pattern to that of the normal one as a new index [2]. When the new index is used to evaluate the inspection sensitivities, the sensitivities were found to be about 10% of the mask opening area through any types of defect as indicated in Fig. 7-2. This will impact a resist CD of less than 4 nm. Considering that the MEEF of the hole layer is 3 to 5 in the case of optical exposure, the burden on mask manufacturing (mask CD's accuracy and inspection sensitivity) was reduced, so that the superiority of EPL was revealed.

7.2. *Repair for mask defects*

A mask defect repair tool which enables the observation of transparent and surface images by scanning focused Ga ion beams (FIBs) and the measurement of stencil angles was developed by SII Nano Technology Inc. as shown in Fig. 7-4 [3]. FIB repair of defects for EPL stencil masks is similar to that for photomasks, however,

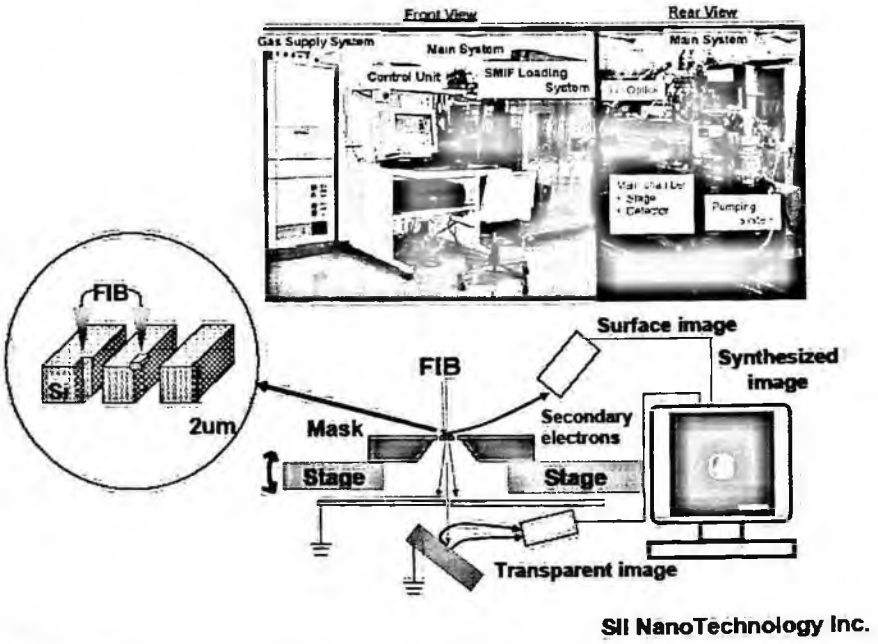

Figure 7-4. EPL mask repair tool. It enables observation of transparent and surface images and the measurement of stencil angles.

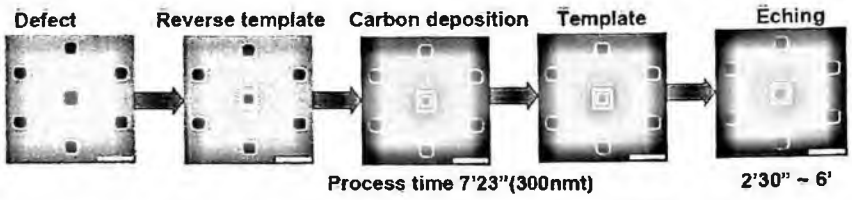

Consistent template method is available for any defect types.

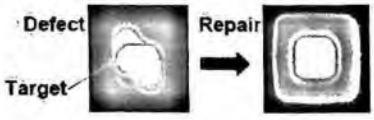

Figure 7-5. Template repair method.

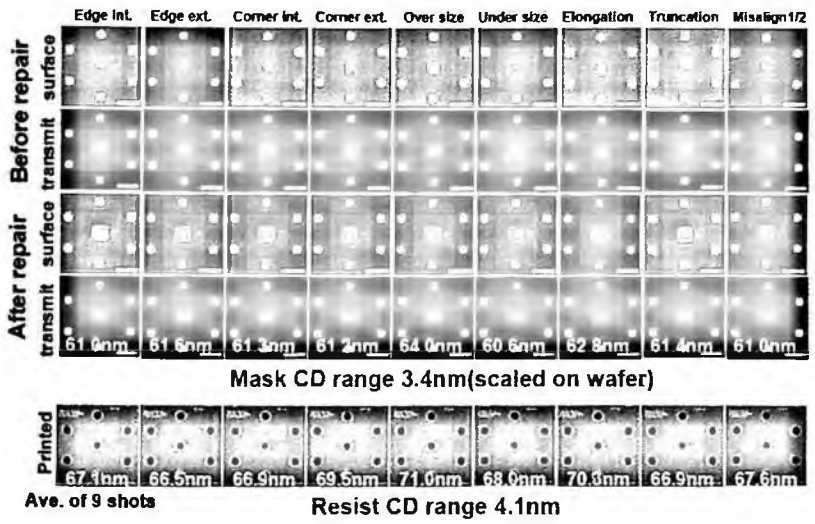

Figure 7-6. Results of repairing with template method. Accuracy of repairing are less than 3.4 nm scaled on a wafer and transcribed resist CD accuracy is less than 4 nm.

EPL stencil masks have unique requirements. Clear defects are repaired by FIB-assisted carbon deposition using a hydro carbon series gas in a hollow area without a substrate. Opaque defects are repaired by FIB-etching 2-μm thick Si with vertical sidewalls using a halogen series gas. Accordingly, a synthesized image of both transparent and surface images produced in the system is very useful to decide if the defects have been repaired completely. A new method which adopts the same deposition and etching recipes using templates has been developed as shown in Fig. 7-5 [4]. This method achieves a very high accuracy in the repair process and the repaired mask was examined by a comparison of the exposure results. Figure 7-6 shows the results of repairing defects for a hole which caused a program defect and its transcribed results. Each defect was repaired with a high accuracy of 3.4 nm scaled on a wafer and transcribed resist CD accuracy of less than 4 nm.

7.3. *Mask cleaning*

An EPL mask cannot use a pellicle as conventional photomasks are provided with. Therefore, mask cleaning technique is very important. An alpha mask cleaning tool that produces a spray using a nitrogen aerosol capable of sweeping particles on the EPL stencil mask away was developed by Sumitomo Heavy Industries, Ltd. [5]. A schematic drawing is shown in Fig. 7-7. A nitrogen aerosol produced by adiabatic expansion is sprayed onto the EPL mask with an accelerated nitrogen gas flow. Figure 7-8 shows SEM images of before and after cleaning. Particles are swept away without destroying the free-standing Si membrane.

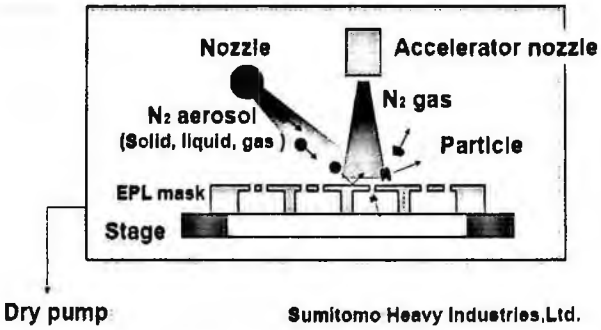

Figure 7-7. A schematic drawing of cleaning tool for EPL masks. A nitrogen aerosol produced by adiabatic expansion is sprayed onto the EPL mask with an accelerated nitrogen gas flow.

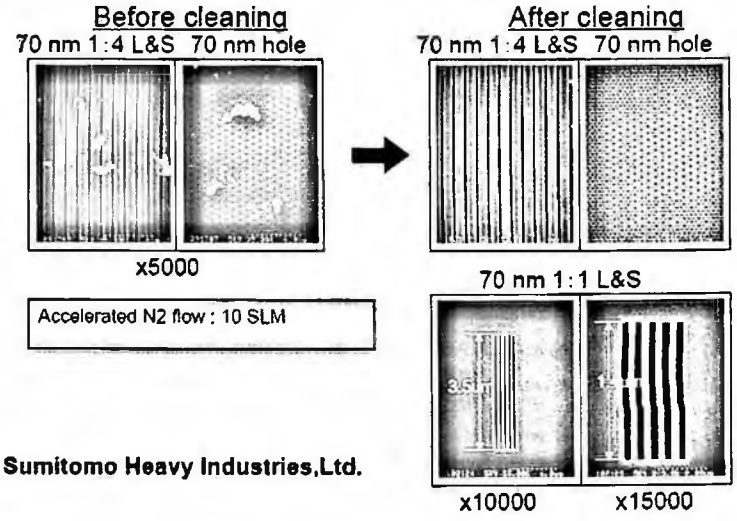

Figure 7-8. Results of EPL mask cleaning.

7.4. *Data processing for masks*

Data processing for the EPL stencil mask involves subfield splitting of layout data, proximity effect correction, and the calculation of correction data for an exposure system to correct the pattern-dependent space charge effect. Conventional flat data processing takes an enormous processing time and produces a huge volume of data. To solve these two problems, a PC-clustered hierarchical data processing system has been developed [5]. GDS design data are split into separate sub-fields, corrected by the proximity effect correction (PEC), verified, and converted into mask layout data to be output as shown in Fig. 7-9. A map of the area density of patterns in the sub-fields, which is calculated by a PEC program, is input into Nikon's space charge effect correction (SCEC) program, and exposure parameters

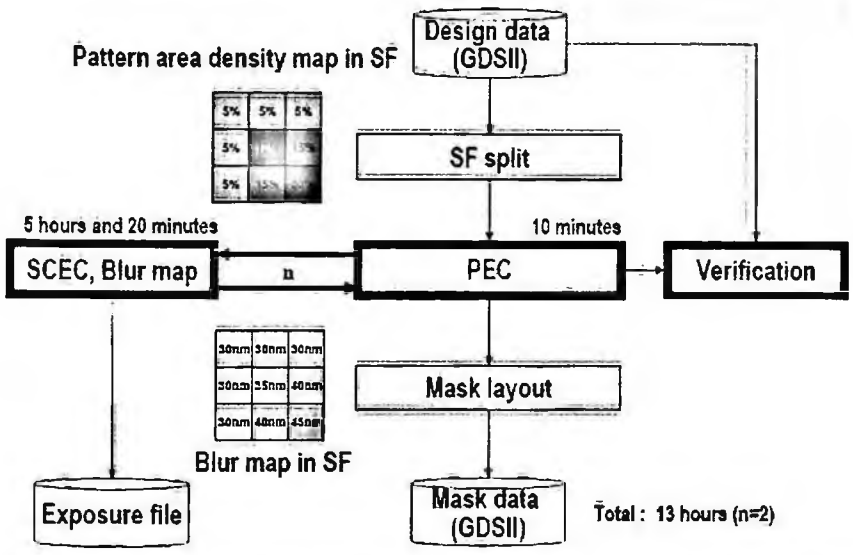

Figure 7-9. Data processing system configuration which involves subfield splitting of layout data, proximity effect correction, and the calculation of the pattern-dependent space charge effect.

such as the refocus volume are extracted and fed back to the EPL system. On the other hand, a blur map which was modified by the Coulomb effect is output by the SCEC program, imported into the forward scattering parameter in the PEC program again, and iterated until the corrected value becomes convergent. Data conversion was evaluated using trial Test Element Group (TEG) data through a flow of whole processes, and data conversion was completed in approximately 13 hours [6].

References

1. J. Yamamoto *et al.*, EPL stencil mask defect inspection system using transmission electron beam, p. 531, *Emerging Lithographic Technologies VII (SPIE)* 2003.
2. J. Yamamoto *et al.*, Defect printability of hole pattern on electron projection lithography, p. 972, *Emerging Lithographic Technologies VII (SPIE)* 2003.
3. J. Yamamoto *et al.*, Development of defect inspection and repair systems for EPL mask infrastructure, p. 1144, *24th Annual BACUS symposium on Photomask Technology* 2004.
4. N. Iriki *et al.*, Preliminary study on EPL mask repair technology for 45-nm node, p. 892, *Photomask and Next-Generation Lithography Mask Technology XII* 2005.
5. M. Yamabe *et al.*, Status and issues of EPL, p. 880, *Photomask and Next-Generation Lithography Mask Technology XI* 2004.
6. H. Yamashita *et al.*, Proximity effect correction using blur map in electron projection lithography, p. 3188, *American Vacuum Society (EIPBN)* 2005.

8. Process and Application Results

8.1. *Resist process*

For the resist, sensitivity has not yet reached the target of $5\,\mu C/cm^2$ which is used in the estimation of EPL throughput. Sensitivity is about $15\,\mu C/cm^2$ for thin-film resist of the line type. Thus, resist development is still an important issue. However, resolution has greatly improved, so that it has become possible to resolve L&S (low density) patterns with a size of 45 nm and micro-hole patterns as shown in Figs. 8-1 and 8-2. Since resist collapse is expected to be a serious problem in forming line patterns for hp45, the tri-layer resist process which transcribes resist patterns on the top layer to the SOG of the medium layer once, and then transcribes them onto the organic film of the bottom layer was developed. The resist thickness should be less than 100 nm based on the results of pattern collapse which may occur at an aspect ratio of less than 2.5. Figure 8-3 shows SEM images of the tri-layer resist process. It was confirmed that L&S patterns up to 45 nm can be successfully processed on Low-k materials.

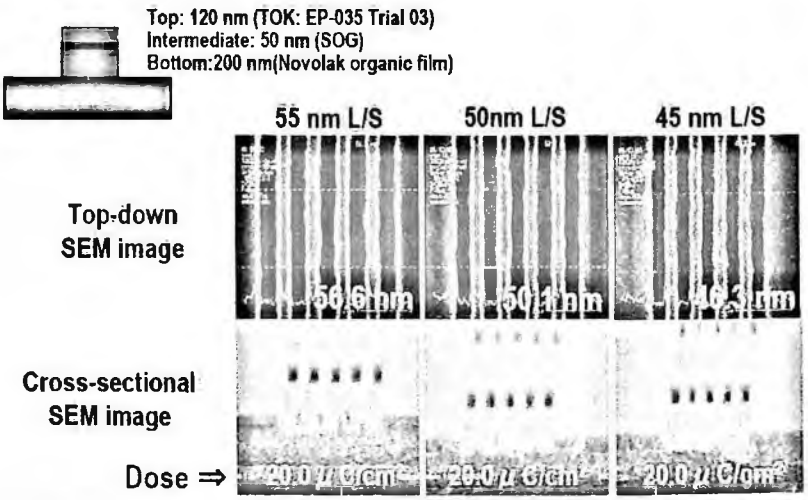

Figure 8-1. SEM images of L&S patterns with a 120-nm thin resist of EP-038Tr1 resist (TOK). Dosage was $20\,uC/cm^2$.

8.2. *Prototyping of Cu two-layer wiring TEG*

A TEG of a via-hole chain consisting of 1st metal, 1st via, and 2nd metal layers was fabricated using F2/EPL mix-and-match lithography [1]. EPL was applied to the via layer. A schematic drawing of the sample structure is shown in Fig. 8-4. The wiring pitch was 140 nm and the via size was 70 nm which meets the technology requirement for intermediate wiring at hp45 stipulated from ITRS shown in the

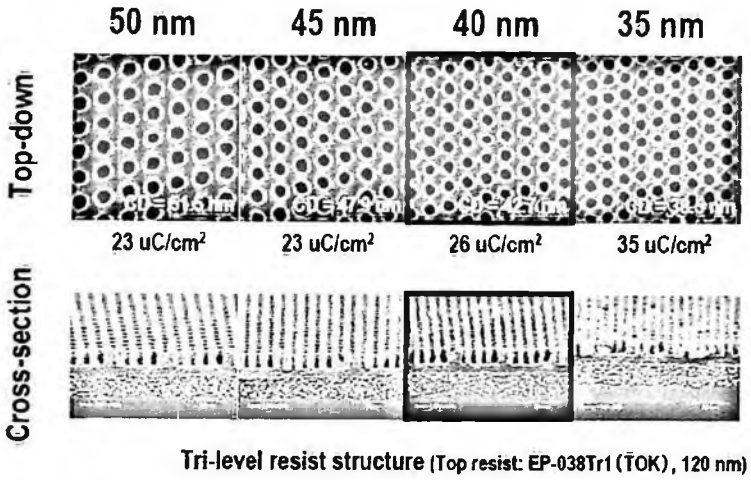

Figure 8-2. SEM images of hole patterns with a 120-nm thin resist of EP-038Tr1 resist (TOK).

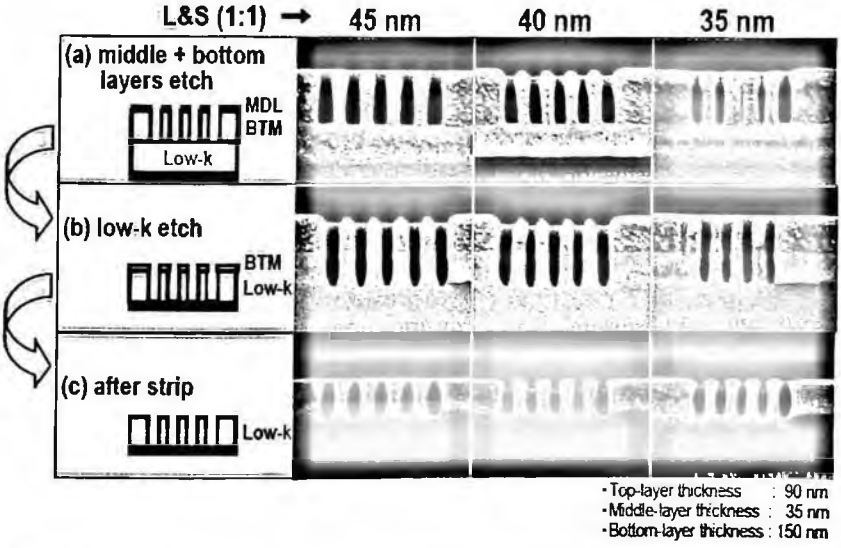

Figure 8-3. Low-k etching using tri-layer resist process. Thicknesses of tri-layer are 90 nm, 35 nm, and 150 nm, respectively. SEM images are after bottom etching of tri-layer resist, after low-k etching and after resist stripping.

figure. In the fabrication, a single damascene process with a low-k insulator and Cu interconnects were used. A 70-nm via-hole was confirmed to be successfully buried from the TEM image as shown in Fig. 8-5. From this trial, applying EPL to hole layers yields denser integration than optical lithography at hp45 and beyond.

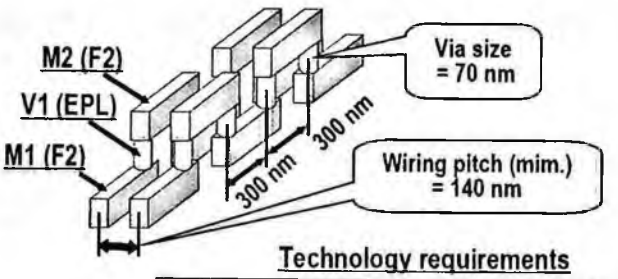

Technology requirements

Technology node	65 nm	45 nm	32 nm
Via size	100 nm	70 nm	50 nm
Intermediate wiring pitch	200 nm	140 nm	100 nm

Figure 8-4. A schematic drawing of via-hole chain device with Cu/low-k. Via size is 70 nm. Wiring pitch is 140 nm.

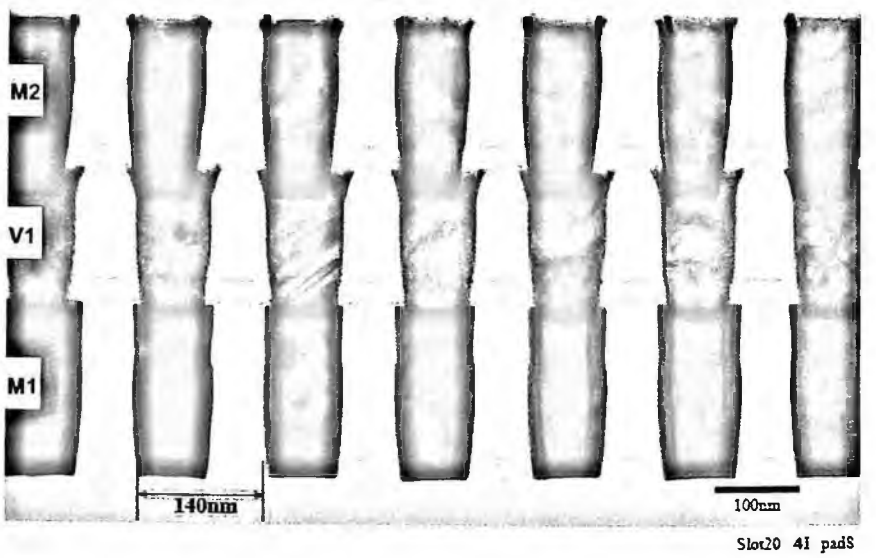

Figure 8-5. TEM image of via-hole chain.

Reference

1. F. Koba *et al.*, "Highly accurate proximity effect correction for 100 kV electron projection lithography", p. 5590, *Japanese Journal of Applied Physics (MNC)* 2004.

9. Technology Evaluation and Future Extendibility

9.1. *Next EPL system and Coulomb interaction*

High resolution and high throughput are indispensable requirements for every exposure tool. However, generally they could be opposite requests. Especially, in

the EB exposure system, they have the physical limitation due to the Coulomb interaction. High beam current for the high throughput always deteriorates its lithographic resolution (the beam blur) due to the Coulomb interaction (See equation [3-1]) [1].

In the EB system, the beam blur is defined as the root sum square of the blur due to the Coulomb interaction and the geometrical blur of EO-system, as previously described. The design of a lithography tool has to take this relationship (the total blur) in account. The geometrical blur can be calculated correctly including the tool condition such as the EO mechanical errors. Knowledge of magnitude and dependencies of the Coulomb interaction effect is essential for EB exposure systems. Coulomb interaction calculations have been studied for probe-forming systems in the literature [2]. However EPL has a large shot-size (SF) which has different pattern distributions and different exposure beam currents. The beam current distribution in the SF affects the magnitude of the Coulomb interaction effect and results in the blur distribution in the SF. To predict the Coulomb interaction effect correctly and take these blur distribution in account for EPL system design, new Coulomb interaction simulation was needed instead of the empirical expression as previously described [1].

EPL (EB1A) was developed as a high throughput EB exposure system (>10 wafers/hour). Its throughput is 4 wafers/hour (300 mm wafer, for 90 nm-node). At that time when EB1A was designed, the Coulomb interaction effect to the beam blur was estimated to be so small that higher throughput would be expected.

The Coulomb interaction consists of the global space charge and stochastic Coulomb effects, which cause defocus and beam blur changes respectively [2]. The

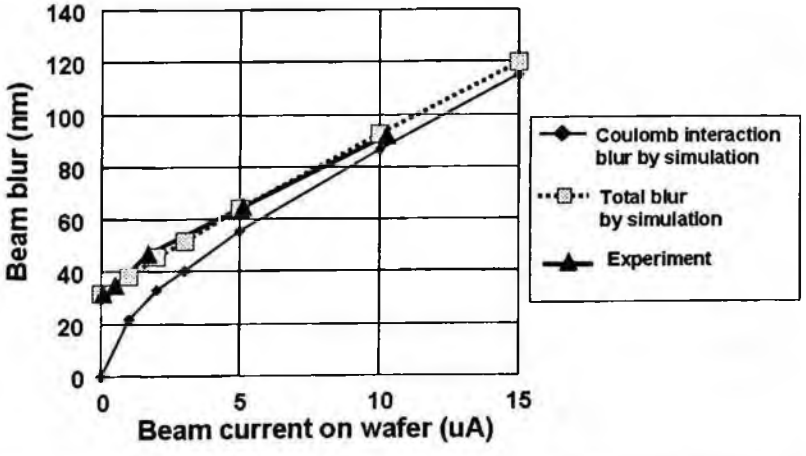

Figure 9-1. Coulomb Interaction effect evaluation of EB1A. Total blur by simulation means root sum square of the simulated blur and the geometrical blur of EO-system (32 nm). Experiment data was measured directly by the aerial image sensing technique.

space charge effect can be corrected by refocusing correction, which is calculated from an average electric field of the electron distribution in the EO column (the lower column) analytically. On the other hand, for the evaluation of the stochastic Coulomb effect due to discrete electron-electron interaction, the Monte Carlo calculation is used rather than the analytical method. Recent studies have shown that beam blurs due to the Coulomb interaction can be calculated using the Monte Carlo calculation on the basis of the EPL exposure condition carefully. Figure 9-1 shows experimental and simulation results of beam blurs due to the Coulomb interaction [3,4]. Total blur by simulation in Fig. 9-1 means root sum square of the simulated blur and the geometrical blur of EO-system (~32 nm). The beam blur was measured directly by the aerial image sensing technique [5]. The experimental results agree well with the simulation. It should be noted that the blur change due to the Coulomb interaction can be calculated correctly even for large field EB now. This simulation method is introduced into the plug-in software in EPL data conversion system.

The EPL base technologies such as hardware design, EO controllers and system controll software for the tool development have been established through the EB1 development. On the basis of EB1A system, we can draw the new EPL system images exactly.

For next EPL systems, the condition, that the Coulomb interaction is the critical and physical phenomenon, is not changed. For the next systems toward the fine patterning (45 nm-node and 32 nm-node), reduction methods of the coulomb interaction should be considered. For the high volume product, two scenarios (systems) are proposed: EB2 and EB3. Their throughputs are shown schematically in Fig. 9-2. Specifications are listed in Table 9-1.

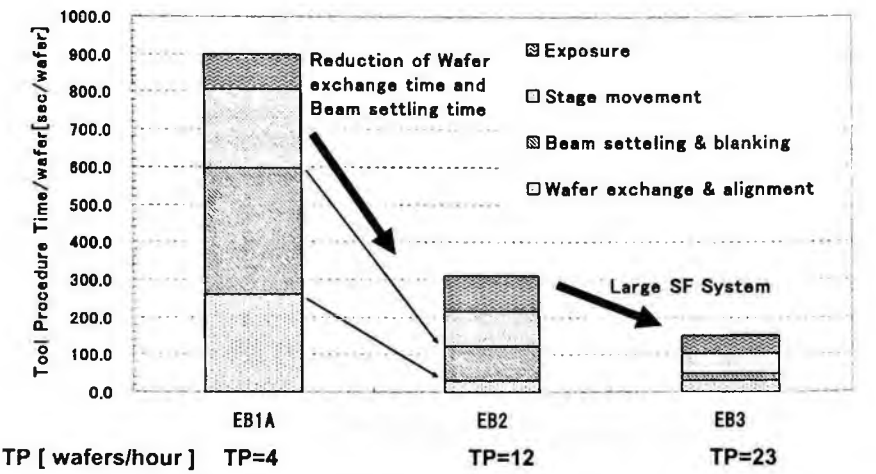

Figure 9-2. EPL tool throughputs. Beam current on reticle: 30 mA (EB1A, EB2), 50 mA (EB3). Resist sensitivity: 5 $\mu C/cm^2$.

Table 9-1. Specifications of EPL tools

	EB1A	EB2	EB3
Technology node [nm]	100	45	45
	70(R&D)	—	32(R&D)
Deflection width [mm]	5.0	2.5	5.0
SF size at wafer (at reticle)[mm]	0.25(1)	0.25(1)	$1 \sim 1.25(4 \sim 5)$
Beam settling [usec]	100	100	100
Beam Half angle [mrad]	3.7	6	0.15–0.3
Beam Truncation angle [mrad]	5.3	4.5	—
TP [WPH](300 mm wafer, NP) (PD 5%)	4	12	23

NP: Non-complimentary pattern, PD: Pattern Density

9.2. *EB2 system*

The EB2 system design is based on EB1A system. To improve the lithographic resolution (the beam blur), the maximum total beam current in one SF (one shot) on a wafer has to be $\sim 1.5\,\mu$A, which depends on the Coulomb interaction, as shown in Fig. 9-1. To achieve a higher throughput, the systematic redundancies for the exposure action in EB1A will be improved or eliminated as described in Fig. 9-2. As the result, a throughput 12 wafers/hour will be expected in EB2 system. The base technologies of EB2 development are established through EB1 development. EB2 system as the tool will be expected to have high cost performances.

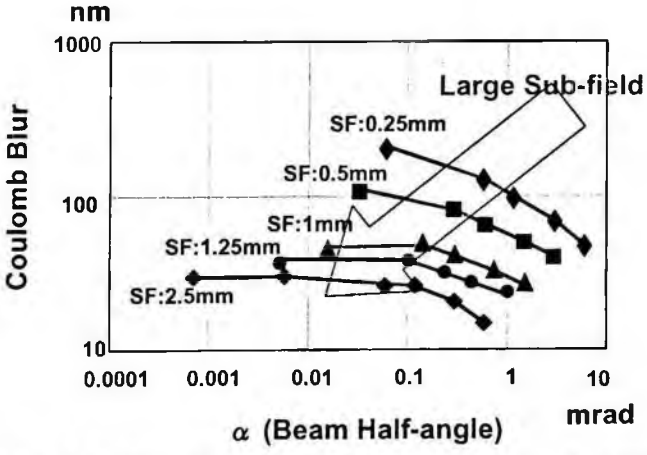

Figure 9-3. Coulomb blur as a function of beam half and SF size.

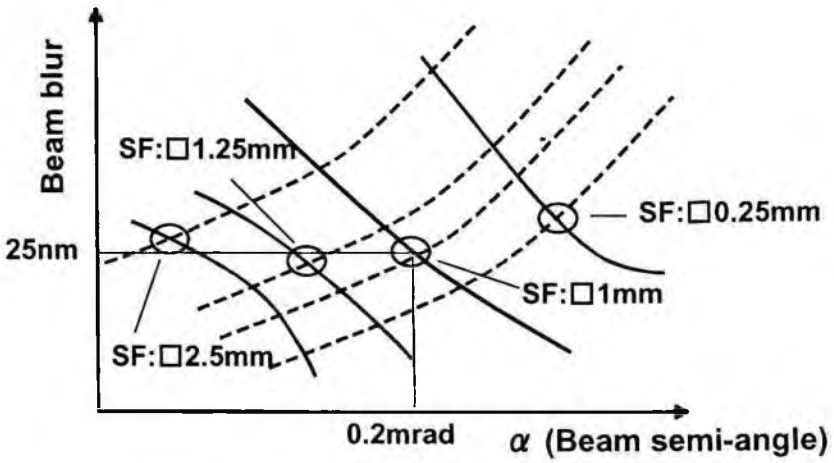

Figure 9-4. Beam blur of EPL with large SF as a function of beam half angle. Solid line: Coulomb blur Monte-Carlo simulation. Dashed line: Geometrical aberrations.

9.3. *EB3 system*

EB3 is a new EPL tool with a large SF size which is 1–1.25 mm square at a wafer (compared to 0.25 mm of EB1A) [6]. The introduction of large SF will be able to reduce the average current density and to increase the total current in one SF. The beam blur due to the Coulomb interaction (the Coulomb blur) is evaluated using the Monte-Carlo simulation with thin lens approximation. The simulation results (the total beam current: $\sim 10\mu$A) in Fig. 9-3 show that at low beam density (large SF) the Coulomb blur keeps small even at small beam angle schematically. Some electron optical designs of EB3 using the large SF have been studied [6]. Figure 9-4 shows the Coulomb blur and the geometric aberrations as a function of the beam half-angle α for SF sizes on EB3 system condition. As previously mentioned, the Coulomb blur becomes smaller with increasing SF size but the geometric aberrations increase with larger SF size. The total blur consisting of the Coulomb blur and the geometric aberrations at an intersection depends on SF size. The total blur becomes the smallest for SF sizes of 1–1.25 mm square. In fact several theoretical solutions for EB3 are found. For example, the imaging section of EB3 will have (Table 9-1) [6]:

Exposure SF size 1–1.25 mm square a wafer;
Deflection width ±2.5 mm;
Beam half angle 0.15–0.3 mrad;
Magnification x4.

For 32 nm-node, maximum current on a wafer can be expected to be $\sim 3\,\mu$A. A new gun for EB3 will be also needed, which has relative high emittance ($\sim$1.00 mm mrad.), high brightness ($\sim 10^5$ A/cm^{2}Sr), and high beam current (50 μA at reticle, the pattern density is assumed to be 5–6%).

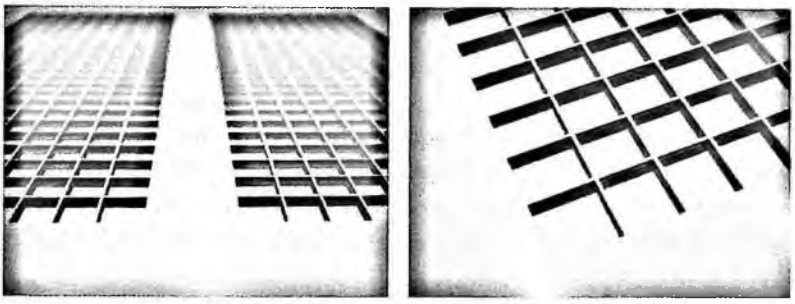

Figure 9-5. EPL reticle for large SF exposure tool (EB3). Tentative Specification. Membrane Size: 4.13 mm × 4.13 mm Strut Width: 0.27 mm Subfield Number: 500 subfields Pattern Area: 100.46 mm × 111.23 mm.

In the optics and the gun developments, key issues are mechanical accuracies of EO system parts (lens, deflectors, and so on) and low noise high speed lens and deflector drivers in the EO control circuits. They require advanced technical levels but are not showstoppers, which are the existing technical levels but not future technology. However, it may take several years to develop fundamental fabrication technique and to complete the new optics.

EB3 will need infrastructure developments, such as reticle and resist, to achieve its specifications. Especially as the reticle format will be changed and SF size will be 4–5 mm square, the fabrication possibility of large SF reticle have to be evaluated. In fact, its development has started. A large SF reticle is already fabricated and used for exposure as shown in Fig. 9-5. It is worthwhile noting that EO designs and the experiments show technical potentialities for EB3 and the future direction of EPL.

References

1. W. Stickel, Simulation of Coulomb interactions in electron beam lithography systems — A comparison of theoretical models, *J. Vac. Sci. Technol. B*, **16**, 3211–3214 (1998).
2. G. H. Jansen, Coulomb Interaction in Particle Beams (Academic, New York, 1990).
3. J. Yamamoto, H. Yamashita, H. Arimoto, J. Ikeda, S. Suzuki and S. Kawata, Direct measurements and analyses of the Coulomb effects in electro projection lithography, *J. Vac. Sci. Technol. B*, **23**, 3182–3187 (2005).
4. T. Yahiro, S. Suzuki, T. Irita, N. Hirayanagi, H. Shimizu, S. Kojima, K. Morita, S. Kawata, T. Okino and K. Suzuki, Direct measurement of Coulomb effects in electron beam projection lithography, *J. Vac. Sci. Technol. B*, **19**, 2468–2473 (2001).
5. T. Yahiro, N. Hirayanagi T. Irita, H. Shimizu and K. Suzuki, High-accuracy aerial image measurement for electron beam projection lithography, *J. Microlith. Mircofab. Microsyst.* **1**, 136–143 (2002).
6. S. Fukui, H. Shimizu, W. Ren, S. Suzuki and K. Okamoto, Novel electron optics for large sub-field electron beam projection lithography (EPL), *Proc. SPIE* **5037**, 512–520 (2003).

10. Summary

EPL is a realistic technology for 65 nm node and below, as a complementary technology of optical lithography especially for contacts and gate layers because of its high resolution and large process margin. Cheaper mask cost is also expected compared with that of optical lithography which gives the same resolution. Nikon's first generation EB stepper; dubbed as NSR-EB1A, was developed for 65 nm node R&D tool. It was delivered to Selete and has been used for the EPL technology development considering EPL application for hp45 nm node technology.

NSR-EB1A has demonstrated dynamic exposure results and achieved the required specifications and functions for hp65 nm technology node. EPL technical issues for hp45 nm technology node application was also considered and conducted basic experiments using NSR-EB1A and feasibility studies.

The issues and their assessments are addressed as follows;

— Overlay accuracy 18 nm is feasible.
— Throughput 23 WPH is feasible with large sub-field electron optics.
— Mask IP accuracy (Global IP 8 nm, Local IP 8 nm) is feasible.
— Resist sensitivity 5 $\mu C/cm^2$ is feasible.
— EPL Mask inspection and Repair tools are feasible.

EPL lithography is judged to be feasible for hp45 nm technology node device production and expected to be used in mix and match with optical lithography tools such as ArF immersion and EUVL.

11. Acknowledgments

The authors would like to thank Selete, Nikon, infrastructure relating makers and other organizations for their support and technical contributions in EPL development program.

CHAPTER 10

ELECTRON BEAM DIRECT WRITING

KENJI YAMAZAKI

NTT Basic Research Laboratories, NTT Corporation,
3-1 Morinosato-Wakamiya, Atsugi, 243-0198, Japan
yamazaki@aecl.ntt.co.jp

Electron beam (EB) lithography has been mainly used for patterning on masks and reticles in the semiconductor industry and has progressed according to the scaling up of circuit integration and the miniaturization of patterns. Among the various techniques in EB lithography, EB direct writing has played an important role in developing advanced devices because it offers higher resolutions and shorter turn-around time, though its patterning speed has not been high enough for mass-production use. Cutting-edge applications in advanced fields have always been investigated and developed using EB direct writing, and future devices and devices for scientific research, such as various quantum devices, which of course require high resolutions, have also been investigated using the technique.

In this chapter, interactions between electrons and materials, EB direct writing apparatuses, and calculation/measurement of EB diameter are discussed in Section 2. The accuracies of patterning dimensions and positioning in EB lithography are discussed in Section 3. The former includes roughness on pattern edges, and the proximity effect due to electron scatterings and its correction, and the latter is for mainly overlay accuracy. Resist materials, fine patterning, and some applications, including the creation of three-dimensional structures are discussed in Section 4.

Keywords: Gaussian beam; variable shaped beam; Monte Carlo simulation; EID (Exposure Intensity Distribution); latent image; mean free path; proximity effect (correction); wave optics; aberration (coefficient); overlay (accuracy); stitching (accuracy); (fast) secondary electrons; LER (line-edge roughness); single-electron transistor/device/circuit.

CONTENTS

1. Introduction 342
2. Fundamentals of Electron Beam Direct Writing 343
   2.1. Interaction between electrons and material 343
   2.2. Apparatus and technology trends 347

2.3. Measurement of beam diameter 350
2.4. Calculation of EB diameter and shape 352
3. Accuracy of EB Lithography 354
3.1. Pattern-size accuracy and proximity effect 354
3.2. Pattern-edge roughness 359
3.3. Positioning accuracy 361
4. Nanopatterning and Applications 362
4.1. EB resist and nanopatterning 363
4.2. Application to nanodevices 366
4.3. Three-dimensional fabrication for nanotechnology applications 369
5. Conclusion 372
Acknowledgments 373
References 373

1. Introduction

Patterning using an electron beam (EB) goes back to the early 1960's [1]. At that time, the systems were modified electron microscopes that used Gaussian beams (which are converged as much as possible and are so named because their shape is Gaussian. They are also called point beams). The patterns were directly written on substrates/films without using masks. The resolution was already under 1 μm, and applications to the fabrication of circuits began soon.

The most important issue in EB direct writing has been writing speed (or throughput). Among the various EB direct writing techniques that have been devised to improve it are variable-shaped-beam lithography [2], cell-projection (or character-projection) lithography, [3], electron projection lithography [4,5], and low-energy electron-beam proximity projection lithography [6]. These techniques have indeed improved writing speed and are mainly intended for mass production. Some of them using masks are described in Chapter 9. In this chapter, Gaussian beam (and variable shaped beam) techniques are mainly described. The newer techniques provide higher throughput, but their resolutions are not as high as those attainable with Gaussian beams (and variable shaped beams). Moreover, they use large complicate masks, which have become more expensive and more time-consuming to make as feature sizes shrink and integration scales increase. EB direct writing techniques without using masks have advantages of high resolution and short turn-around time. Lithography using Gaussian beams can provide resolutions of 10 nm or less and is the only practical way to arbitrarily pattern with the resolutions and a reasonable speed, while the other approaches such as nanoimprinting [7], which uses molds fabricated mainly by EB lithography with Gaussian beams, are under development. Because of these advantages, Gaussian beams are used in the research and development of advanced devices, which generally require higher resolutions of patterning and short turn-around time. They

are also used in specific areas of production that require such advantages, where the target is to produce small batches of a variety of products consisting of high-performance devices, which are known as Systems on Chips. EB direct writing is used to form very small patterns in the production of, for instance, high-frequency devices made of compound semiconductors, for which other techniques can not be easily used. The other important target is research/development of advanced devices.

The main focus in research on EB direct writing is how to improve resolution (to extend the advantage for creating new devices) and accuracy. To discuss techniques with resolutions near the limit, we first have to cover some physical fundamentals in detail. This chapter therefore starts with the interaction between the EB and materials. Pattern-size accuracy and some techniques for improving it from some aspects are mainly described, and accuracies in pattern positioning are also discussed to some extent. Next, the ultimate patterning with resolutions of less than 10 nm using some kinds of resist materials is reviewed, and some specific applications using the advantages of EB direct writing are introduced. As a current topic in the evolution of EB direct writing, three-dimensional (3D) EB lithography is also introduced.

2. Fundamentals of Electron Beam Direct Writing

This section first discusses the interaction between EBs and materials (i.e., resists and substrates), which is quantitatively simulated using Monte Carlo calculations of electron scattering, and comparing the results with experiments. The interaction is directly related to pattern-size accuracy or the proximity effect, which is covered in subsection 3.1. Next, apparatuses of EB writing are described. For direct writing, considering that Gaussian beams and variable shaped beams are mainly used, the apparatuses for these EBs and their associated technology trends are described. Focusing on the Gaussian beams, the metrology and calculation for fine EBs are also discussed in this section.

2.1. *Interaction between electrons and material*

As EB lithography uses phenomena where a resist is chemically (or physically) modified by exposure to electrons, it is very important to well understand the interactions between the electrons and resist materials. For precise patterning, the amount of this change in resist has to be quantitatively understood and predicted or calculated as spatial distributions. This spatial distribution of the quantitative amount of change in a resist is the key to understanding the patterning in detail and the distribution is sometimes called a latent image. For organic resists, the principle of exposure (change in resist) is the large exposure dependency of resolving speed, which, in most cases, is due to cutting of main chains in the resist polymers (positive resist)

or to cross-linking of the polymers (negative resist). The cutting or cross-linking of the polymers occurs because of the dissipation of energy of more than about 5 eV (in the case of organic resists) from electrons, mainly secondary electrons scattered by the incident electrons. Then, polymers with smaller molecular weights dissolve in the developer, whose shape follows the writing. The amount of change in the resist is directly related to the density of the cutting or cross-linking of polymers, which is generally proportional to the total energy deposited by electrons. (The amount of the change in some inorganic resists may not be so simple because the change depends on the energy in each deposition process.) Since the energy deposited (and dissipated) in resist material on exposure adds up (accumulates) as the amount of the chemical changes, such as the cutting/cross-linking of polymers, the total deposited energy, which can be physically simulated, is used instead of the amount of chemical changes. The indirect exposure due to electrons scattered in the resist and in the substrate is known as the proximity effect, where the part of interest in resist is exposed slightly by scattering electrons due to exposure on some other adjacent parts as well as due to direct exposure on that part. The total amount of energy deposited has to therefore be considered to understand the precise patterning in the lithography. The proximity effect will be discussed detail in subsection 3.1. Here, the calculation of energy deposited by electrons using Monte Carlo simulation of electron scattering is described.

The energy deposited in a material by electrons can be calculated and analyzed as the energy the electrons lose as they scatter in the material, and some models have been proposed since many years ago [8–11]. Among them, elastic scattering using the theory of Rutherford scattering (or its modifications) and stopping power (how much energy is deposited along the electron trajectories owing to inelastic scatterings) using the Bethe-Bloch formula had been used for many years [11]. These enable us to obtain the distribution of the energy deposited in a resist by Monte Carlo simulation of electron scattering. However, relatively recent investigations have revealed that more detailed calculations and models for elementary excitations are necessary for accurate simulations, which are required for simulating nanopatterning with high enough accuracy [12,13]. Here, a relatively new kind of simulation is described, which has two important features. One is that it follows all of the incident (primary) electrons and secondary electrons until the energy of each electron becomes small enough. (In this chapter, "secondary electrons" mean all of the scattered electrons – in a cascading shower – except the incident ones.) The other feature is a calculation for each scattering process of energy loss (energy deposition) as the elementary excitation processes instead of stopping power, which is a little more abstract than each concrete physical phenomenon of inelastic scattering. The elementary processes are excitations of plasmons, conduction-band electrons, valence-band electrons, inner-shell electrons, phonons and so on. Although such precise simulations take longer time than the conventional method, they clearly follow physical phenomena and provide higher accuracy. Moreover, recent progress in

semiconductor technology has made it easy to simulate three-dimensional distributions of deposited energy with reasonable speed and accuracy.

For elastic scattering, the simulation uses partial wave expansion. This method uses plane waves connected to the wave function around the atomic potential, and has been proven to provide a better approximation even for electrons of very low energies than the conventional screened Rutherford method [14]. The differential scattering cross-section is given by

$$\frac{d\sigma_m}{d\Omega} = |f_k(\theta)|^2 \tag{1}$$

$$f_k(\theta) = \frac{1}{k}\sum_l (2l+1)\exp(i\delta_l)\sin\delta_l P_l(\cos\theta), \tag{2}$$

where σ_m is cross-section of elastic scattering for the target atom m, Ω is the scattering cubic angle, $f_k(\theta)$ is the scattering amplitude, k is the wave number of the (incident) electron, θ is scattering angle, δ_l is the phase shift of the lth partial wave, and $P_l(\cos\theta)$ is the Legendre function. The phase shift δ_l is derived by solving the Schrödinger equation for the wave function with the quantized angular momentum $\hbar\sqrt{l(l+1)}$ and atomic potential, which can be approximately described [15]. The total scattering cross-section σ_m and the mean free path Λ is obtained by integrating (1) as

$$\begin{aligned}\sigma_m &= \int \frac{d\sigma_m}{d\Omega} d\Omega \\ &= \frac{4\pi}{k^2}\sum_l (2l+1)\sin^2\delta_l \end{aligned} \tag{3}$$

$$\Lambda = 1/\sum_m N_m\sigma_m, \tag{4}$$

where N_m is the number of atoms m in unit volume.

The scattering angle θ and azimuth ϕ are derived using the differential scattering cross-section (1) and uniform random numbers.

For excitation processes (i.e., inelastic scatterings), Gryzinski formula is used in the simulation to derive the differential scattering cross-sections for inner-shell-electron and valence-band-electron excitations [12]. The formula is

$$\begin{aligned}\frac{d\sigma_{mi}}{d\Delta E} = n_{mi}\frac{\pi e^4}{\Delta E^3}\frac{E_{mi}}{E}\left(\frac{E}{E+E_{mi}}\right)^{3/2}\left(1-\frac{\Delta E}{E}\right)^{E_{mi}/(E_{mi}+\Delta E)} \\ \times\left\{\frac{\Delta E}{E_{mi}}\left(1-\frac{\Delta E}{E}\right)+\frac{4}{3}\ln\left[2.7+\left(\frac{E-\Delta E}{E_{mi}}\right)^{1/2}\right]\right\},\end{aligned} \tag{5}$$

where σ_{mi} is the inelastic scattering cross-section, ΔE is lost (deposited) energy, n_{mi} is the number of electrons in orbital i of atom m, E_{mi} is the averaged binding

energy of electrons in orbital i of atom m, and E is the energy of the (incident) electron. In the case of valence-band-electron excitation, electrons in orbital i should be replaced with valence-band electrons. The scattering cross-section and mean free path for the excitation are

$$\sigma_{mi} = \int_{E_{mi}}^{E} \frac{d\sigma_{mi}}{d\Delta E} d\Delta E \tag{6}$$

$$\Lambda = 1/\sum_{m} \left(N_m \sum_{i} \sigma_{mi} \right), \tag{7}$$

The lost (deposited) energy E_1 is derived using uniform random number R (0-1) from

$$R = \int_{E_{mi}}^{E_1} \frac{d\sigma_{mi}}{d\Delta E} d\Delta E / \sigma_{mi} \tag{8}$$

The scattering angles and energies of incident and scattered electrons can be derived using the classical collision model. It should be noted that the energy of scattered electrons is to be defined considering the biding energy and the energy of the Fermi level.

For conduction-band-electron and plasmon excitations, the differential scattering cross-sections can be derived using the Lindhard dielectric function $\varepsilon(q, \omega)$. For conduction-band-electron excitation, the differential scattering cross-section is described as [16]

$$\frac{d\sigma}{d(\hbar\omega)} = \frac{1}{\pi a_0 E} \int_{q-}^{q+} \frac{dq}{q} \mathrm{Im}\left[\frac{-1}{\varepsilon(q, \omega)} \right], \tag{9}$$

where $\hbar\omega$ is the energy loss of the (incident) electron, a_0 is the Bohr radius, and $\hbar q$ is the transferring momentum on the interaction. The $\varepsilon(q, w)$ is the Lindhard dielectric function based on random-phase approximation [17].

As phonon excitation has smaller scattering cross-section than the other processes described above, omitting it does not seem to cause large errors. The total cross-section for all scattering processes is obtained by adding cross-sections for each process and the mean free path for all processes is derived to be the inverse of the sum of inverse mean free paths for each process. Figure 1 shows mean free paths for Al, derived by the method above and their experimental values [18]. Table 1 lists calculated mean free paths for Si and polymethylmethacrylate (PMMA). Another comparison for more complicated electron scatterings is given in subsection 3.1.

The Monte Carlo simulation, which shows good approximation, is only outlined here owing to the limited space for this section. Details of the calculation methods can be found in the references.

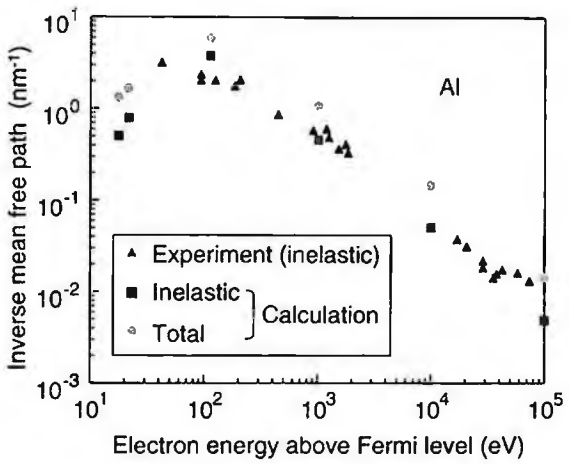

Figure 1. Inverse mean free path of electrons in Al; experiment [18] and calculation.

Table 1. Calculated inverse mean free path (nm^{-1}) of electrons in Si and PMMA.

Energy	Si			PMMA		
(eV)	Elastic	Inelastic	Total	Elastic	Inelastic	Total
10	1.72	13.2	14.9	6.72	2.65	9.37
100	1.80	9.07	10.9	1.35	7.29	8.64
1,000	0.414	1.17	1.59	0.239	0.959	1.20
10,000	0.0880	0.141	0.229	0.0310	0.114	0.145
100,000	0.00893	0.0165	0.0254	0.00296	0.0132	0.0161

2.2. *Apparatus and technology trends*

As mentioned in the introduction in this chapter, direct writing mainly uses Gaussian beams and variable shaped beams. Figure 2 shows schematic drawings of electron optics systems for a variable shaped beam and a Gaussian beam. The electron sources used to be thermal emitters made of LaB_6, but thermal field emitters (Schottky emitters) using Zr/O/W are mainly used now because they provide more stable beams with smaller sizes and/or larger current. Magnetic lenses are mainly used, having mostly replaced electrostatic lenses. A high-resolution objective lens is essential to obtain a nanometer-size EB, and high-performance lenses have been developed. These lenses are unipolar, but lenses with multipole systems have also been recently developed for transmission electron microscopes (TEM), which significantly reduce spherical aberrations and thus provide higher resolutions. An EB lithography apparatus with a high-resolution multipole lens would provide finer EBs and thus higher resolutions in EB direct writing, but such an apparatus has not been developed yet. Magnetic deflectors are mainly used, though electrostatic

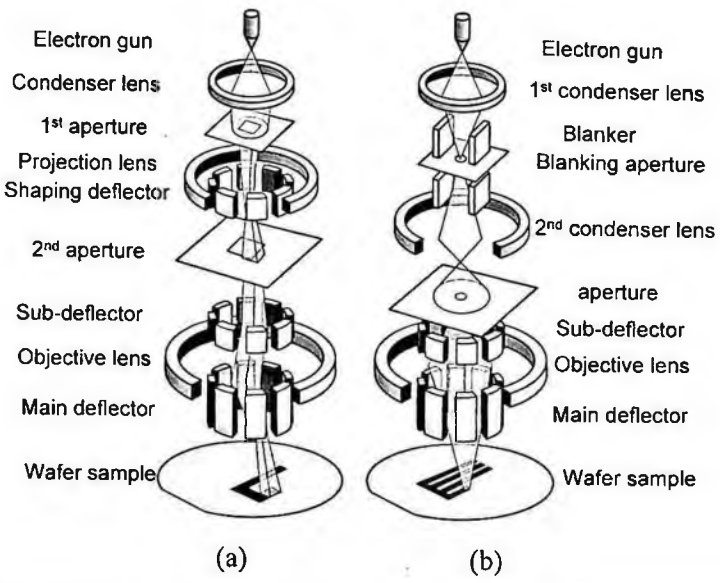

Figure 2. Schematic drawings of electron optics systems for (a) a variable shaped beam and (b) a Gaussian beam.

deflectors are still used to some extent for very-high-speed deflection. (Electrostatic deflectors allow us to easily obtain deflection frequencies as high as 100 MHz, but they usually cause large noise or drifts in EBs compared with magnetic deflectors.) Magnetic deflectors have therefore become predominant and high-frequency magnetic deflectors operating close to 100 MHz have been developed recently. The field sizes of the main deflection are generally 500-μm square or more, which is sufficient for most purposes of direct writing.

Figure 3 shows a more detailed electron optics system for a Gaussian beam [19]. This system is equipped with a two-step main-deflector and a two-step sub-deflector, which reduce the deviations of beam size in the main- and sub-deflection fields of 500-μm square and 20-μm square in size, respectively. The acceleration voltage is 100 kV. Acceleration voltages for EB direct writing used to be ten to several ten kilovolts, but most of them are now 50–100 kV. The advantages of higher acceleration voltages are that they enable smaller beam sizes (i.e., higher patterning resolutions) and higher beam stability (i.e., smaller deflection noise and drift). Moreover, a higher acceleration voltage reduces pattern widening due to forward-scattering electrons in resist film. These advantages are very important for precise high-resolution patterning. A higher voltage also causes longer mean free paths and thus longer ranges of electron scattering, which is significantly related to the proximity effect (See subsection 3.1). This means proximity effect correction has to include a wider area (a larger number of patterns), and which increases the amount of calculation. However, the amount of total energy deposited in proximity areas does not significantly

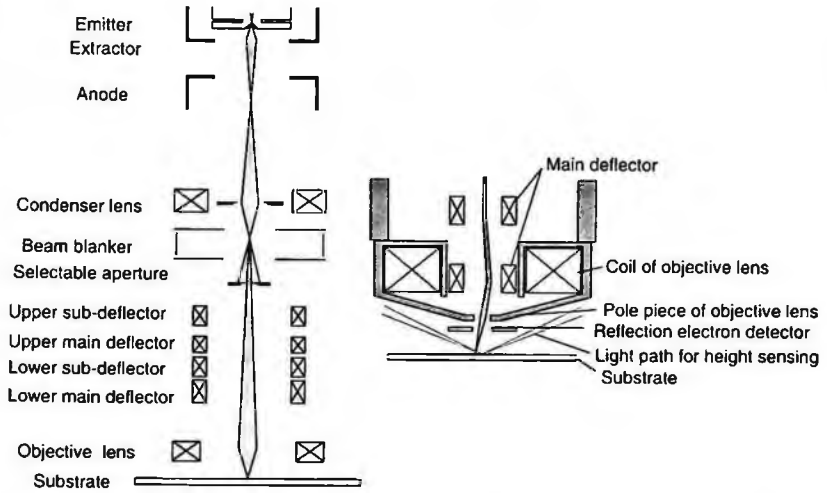

Figure 3. A high-resolution electron optics system (left) for a Gaussian beam (Reprinted with permission from [19] by IPAP) and some details around the objective lens (right).

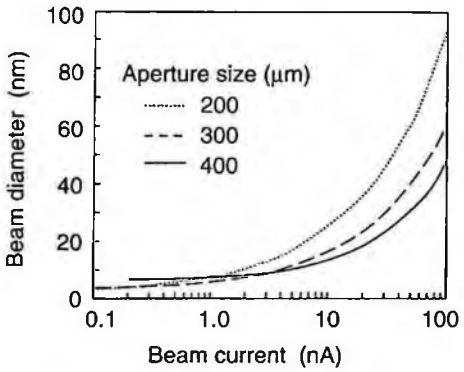

Figure 4. A relationship between beam current and diameter of a Gaussian beam for various aperture sizes.

depend on the voltage. A high voltage is therefore not disadvantagous for maintaining high resolutions even when fine dense patterns are delineated in large areas. On the other hand, higher voltages result in a smaller interaction between electrons and resist, which leads to a reduction of resist sensitivity. They also cause lower throughput, which is serious for mass production, and are related to the writing conditions of beam current, beam step and so on as described next.

Figure 4 shows an example of the relationships between the beam current and the size of a Gaussian beam for various aperture sizes. It is clear that the higher throughput (larger beam current) and higher resolution (smaller beam size) are mutually exclusive. Another important relationship is that among the beam current,

beam step, and resist sensitivity. As the maximum deflection frequency depends on EB apparatus, the smallest beam step is limited by the frequency, beam current, and resist sensitivity. As the beam step should generally be smaller than the minimum feature size in order to obtain smooth pattern edges, the beam current may have to be reduced because of this relationship. The maximum beam current I_b has a simple relationship with the beam step d, maximum deflection frequency f_M, and area dose on exposure D (mainly decided by the resist sensitivity), i.e., $I_b = Df_M/d^2$. This means that even when very-high-sensitivity resist is used, small beam currents can limit throughput, depending on the beam step and maximum deflection frequency. Following the improvement of resolution and sensitivity of resist and considering new requirements for applications in the near future, direct writing apparatuses will be expected to have higher deflection frequency and smaller beam step as well as smaller beam size, higher acceleration voltage, and so on.

2.3. *Measurement of beam diameter*

Accurate measurement of the diameter of Gaussian beams and keeping the diameter constant are essential for reproducible patterning with high pattern-size accuracy. The minimum beam sizes of direct-writing apparatus have become as small as from two to ten nanometers, and it is not very easy to accurately measure the diameters of such small EBs. For an analytical apparatus like a scanning transmission electron microscope (STEM), the conventional knife-edge method [20], or observation of a magnified image of the beam spot, may be satisfactory ways to measure the EB diameter. On the other hand, as it is difficult to equip EB lithography systems with large parts below the focal plane because of the stage system for wafers, it is not very easy to precisely measure the EB diameter in them. In order to measure the diameter in such systems, various knife-edges, such as anisotropically etched crystal Si [21], cleaved GaAs crystal, a gold wire [22,23], and an X-ray mask, have been used. The measurement itself using a knife-edge is simple: the signal of transmission electrons upon scanning the EB across the edge indicates the integrated beam profile (Fig. 5). Although its differential, in principle, indicates the shape of the EB, the diameter is usually derived from scanning positions cutting certain thresholds to avoid effects from noises. For example, 12% and 88% thresholds provide the full width at half maximum (FWHM), assuming the beam shape to be Gaussian. Among the knife-edges mentioned above, gold wires are often used because gold is less affected by contamination, though we may have to look for and use a sharp part on the wire for accurate measurement. With this kind of knife-edge measurement, errors are introduced due to electrons scattering at the knife-edge. The scattered electrons should be reduced as much as possible by using an aperture set below the knife-edge, and this requires precise alignment. Figure 6 shows the relationship between measurement errors and the detection semi-angles defined by the aperture radii, which was obtained by Monte Carlo simulations. The diameter of a smaller beam

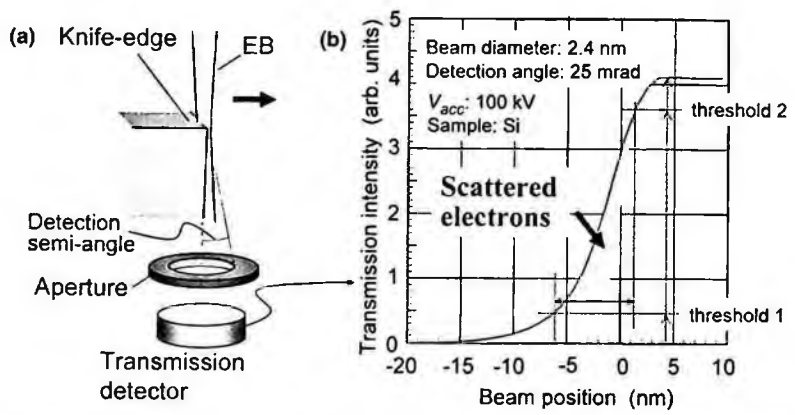

Figure 5. (a) Illustration of setup for beam size measurement using a knife-edge and (b) transmission intensity profile obtained by Monte Carlo simulation. (Reprinted with permission from [19] by IPAP.)

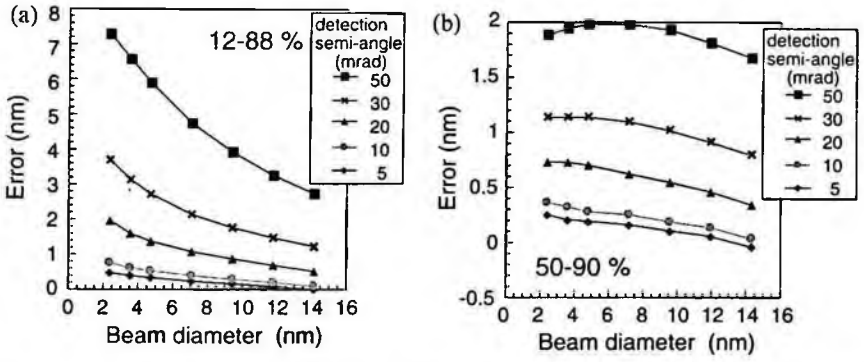

Figure 6. Errors of beam size measurement, depending on detection semi-angle, beam diameter and thresholds (See text for details). These results are for a sharp Si knife-edge with an EB at 100 kV and were obtained by Monte Carlo simulation. (Reprinted with permission from [19] by IPAP.)

(at a higher acceleration voltage) tends to be more difficult to measure accurately, and the measurement error can be reduced using smaller detection angle. A Si knife-edge combined with an aperture made of Ta has been developed that allows us to use the optimal detection angle and to perform the alignment very easily [24]. Moreover, using thresholds at higher transmittances (e.g. 50% and 90%) allows us to reduce the measurement error (Fig. 6[b]). This is easy to understand when we consider that the signal at lower transmittance involves a larger number (ratio) of electrons scattered at the edge (Fig. 5[b]). Another method is to use the cross-section of a multilayer film [25], which allows us to derive the beam diameter from the transmission intensities for a few slits (made of a light element) in the cross-section, assuming the beam shape is Gaussian. This method significantly reduces the

errors due to deflection noise and suppress the degradation due to contamination on the knife-edge, although absolute measurement would not be easy owing to electron scattering in the film.

As there are merits and demerits for each method, it may be good to select one or more of them depending on the purpose, while considering factors such as accuracy, reproducibility, affection from contamination, easiness of use and so on.

2.4. *Calculation of EB diameter and shape*

Theoretical calculation and estimation of the size of EB are very important for EB lithography with nanometer-order resolution because the EB diameter mainly decides the resolution of patterning. Factors limiting EB diameter are aberrations in the objective lens, diffraction, the finite size of EB source, and Coulomb interactions in the EB. In this subsection, the beam diameter on the axis without Coulomb effects is mainly discussed. Coulomb interactions, which can be classified into the space charge effect and stochastic interactions caused when (two) electrons approach each other, become significant for EBs with large current and/or at low acceleration voltages, i.e., under high-throughput conditions. On the other hand, they are not very serious under the conditions for high-resolution direct writing with small beam current at high acceleration voltages.

The following conventional formula based on geometrical optics has been mainly used to calculate the EB diameter (FWHM) on the axis:

$$\begin{aligned} D_{total} &= \sqrt{D_d^2 + D_s^2 + D_c^2 + D_g^2} \\ D_d &= 0.75\frac{1.496}{\alpha\sqrt{V}}(nm) \\ D_s &= \frac{1}{2}C_s\alpha^3 \\ D_c &= \frac{1}{2}C_c\frac{\Delta V}{V}\alpha \\ D_g &= \sqrt{\frac{4I}{\pi^2\beta}}\frac{1}{\alpha}, \end{aligned} \tag{10}$$

where D_d, D_s, D_c, and D_g are diameters for diffraction, spherical and chromatic aberrations, and the finite size of electron source (demagnified source size), respectively, V(V) is the acceleration voltage, $e\Delta V$ is the broadening of the energy of electrons, C_S and C_C are the spherical and chromatic aberration coefficients, respectively, α (rad) is the beam semi-angle, I is the beam current, and β(A/m^2/sr) is the brightness of the electron source. Figure 7 shows the calculated diameter of an EB on the axis using the formula. The energy broadening $e\Delta V$ is estimated to be less than 1 eV from the root mean square of the broadenings due to the high temperature of the electron emitter (0.6 eV), instability of the acceleration voltage (0.2 eV), and the Coulomb effect on energy broadening (the so-called Boersch effect, 0.5 eV).

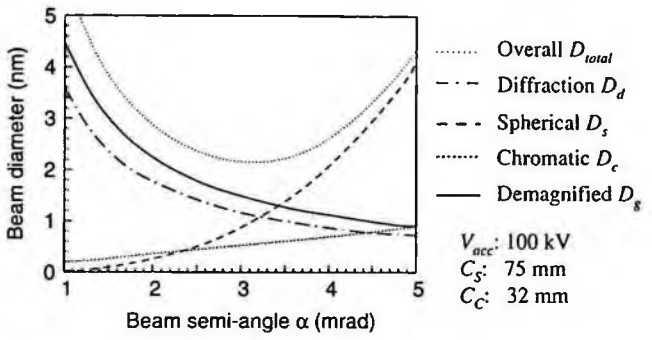

Figure 7. Beam diameter calculated by root-sum-square method.

Although the formula based on geometrical optics is a simple and easy way to derive the beam diameter, it has been pointed out that its accuracy is not good [26]. A method including wave optics has been reported to provide a more precise calculation of beam diameters [27]. Electrons, of course, interfere as waves, so that methods including the effect of the interference should provide better results, even though the actual beams used in EB lithography do not usually provide high coherency as the total beam. The formula for deriving beam intensity $I(r)$ on the basis of wave optics is as follows.

$$I(r) = |\mathcal{F}\{A(\theta)\}|^2 * C(z) * G(x, y) \tag{11}$$

$$A(\theta) = \exp\left\{\frac{i\pi}{\lambda}\left(z\theta^2 + \frac{1}{2}C_s\theta^4\right)\right\}H(\theta), \tag{12}$$

where $A(\theta)$ is a transmission function of the objective lens and aperture, $C(z)$ and $G(x, y)$ are Gaussians corresponding to chromatic aberration ($\sigma = (C_C/4.70) \times (\Delta V/V)$) and broadening due to the demagnified source size ($\sigma = D_g/2.35$), λ is the wavelength of the electron, and $H(\theta)$ is the aperture function, which is unity within the aperture. The transmission function and its two-dimensional Fourier transform just follow wave optics. The convolution along the z direction is for chromatic aberration and that along the x and y directions is for the demagnified source size. These convolutions are performed because these effects are out of coherency. These effects are assumed to be Gaussians as they are in the geometrical optics method. This method provides the beam shape (intensity distribution) along the x, y and z directions. This means the depth of focus, which is derived from the broadening of the beam diameter along the z direction, can also be obtained from the calculation result. Figure 8 shows intensity distributions and beam diameter calculated from the distributions. While fringes due to interferences are seen before the convolutions (Fig. 8[a]), they blur with the convolutions (Fig. 8[b]). Although this method requires a larger amount of calculation than the conventional one, it provides more accurate beam diameters and detailed beam shapes.

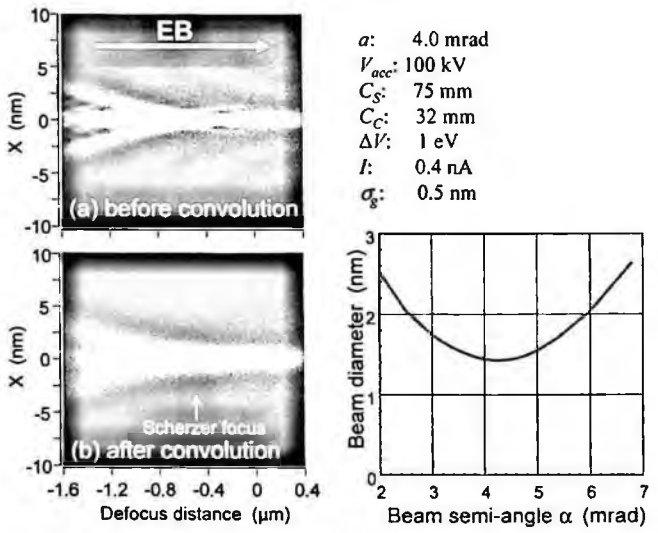

Figure 8. Beam shape calculated by using wave optics method (See text for details) and the relationship between beam diameter and beam semi-angle.

3. Accuracy of EB Lithography

Generally speaking, the important accuracies in EB lithography are that of the delineated pattern size and that of the pattern position. The former is significantly influenced by proximity effect and includes the roughness of pattern edges. The latter mainly concerns the overlay of different layers and stitching between different deflection fields in EB direct writing. These issues and techniques for improvement are described in this section.

3.1. *Pattern-size accuracy and proximity effect*

Although the pattern size accuracy is related to the writing pattern shape, the dose of the writing, EB size, the properties of resist materials, and so on, the most important factor to obtain high accuracy is the proximity effect, which means additional energy deposited by electrons scattered in the resist and/or substrate. Patterns demonstrating the proximity effect are shown in Fig. 9. Even though the same dose and writing pattern size are used, it is clear that the developed patterns are affected by the additional energy due to exposures of surrounding patterns. The quantitative basis for estimating/correcting the proximity effect is the exposure intensity distribution (EID) function. As the EID is the spatial distribution of energy deposited by point exposure at a unit dose, it is easy to obtain experimentally. After exposing and developing many points with various high doses that are N_i times the standard predefined dose, we can obtain the EID by plotting the values of the inverse of N_i at the radii of the developed circle. Strictly speaking, we have to use a beam of zero in size for this, but when the beam size is small, results should be good enough for

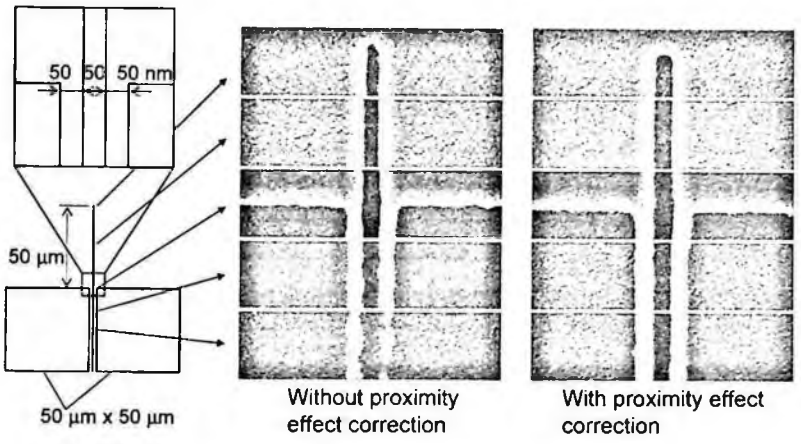

Figure 9. Micrographs of patterns showing the proximity effect and its correction.

deriving the proximity effect. Figure 10 shows an example of EID functions at an acceleration voltage of 70 kV [13], which includes both experimental and simulation results. The beam diameter is about 7 nm, and the Gaussian with this diameter was convoluted with the result obtained by the Monte Carlo simulation described in subsection 2.1. The simulation results show good agreement with experimental ones. Although the EID was thought to mainly consist of two Gaussians: one for forward scattering in resist films and one for backscattering from substrates, the resulting EID is far from the summation of these Gaussians. This mismatch is larger under the conditions for high-resolution lithography (i.e., higher acceleration voltage and thinner resist film) and can be roughly compensated using a third Gaussian [28]. Although the triple Gaussian still has some errors with respect to the actual EID, Gaussians make it easy to calculate correction for obtaining patterns with precise dimensions despite the proximity effect (so called, proximity effect correction). The cause of the mismatch can be explained by the results of Monte Carlo simulation. In the middle radial-distance, the contribution from secondary electrons is much larger than that from primary (incident) electrons, compared with the backscattering region (See Fig. 10). This means that the mismatch is mainly caused by so-called fast secondary electrons [29], which have higher energy than most of the other secondary electrons, which have energies of 5–50 eV.

Although the EID at radial distances larger than 0.1 μm is much smaller than that from zero to a few ten nanometers, the contribution from the distances is not negligible in actual patterning because the exposure area is two-dimensional. Figure 11(a) shows the radial distribution of the maximum contribution (with uniform dose) from areas of similar troidal shapes having various radii (Fig. 11[b]). This distribution is derived by multiplying the EID function (Fig. 10) by r^2 because the areas are proportional to r^2. The contributions of the forward-scattering region and backscattering region are large, and the region of fast secondary electrons between

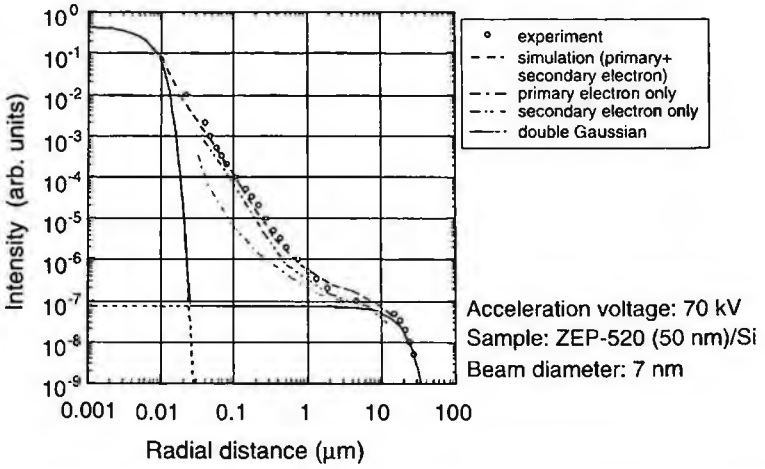

Figure 10. An exposure intensity distribution function. (Reprinted with permission from [13] by IPAP.)

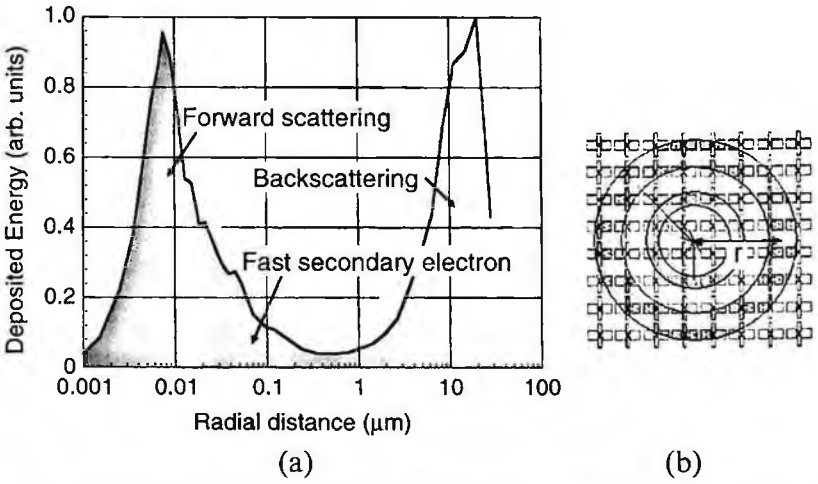

Figure 11. (a) Exposure intensity distribution function (Fig. 10) multiplied by r^2 and (b) similar troidal areas to understand the maximum contributions. (See text for details.)

them is not negligible. Of course, the contributions from backscattering and fast secondary electrons depend on the ratio of the exposed area, but we have to consider them to obtain accurate pattern sizes, especially for dense patterns.

Many methods have been investigated or developed for proximity effect correction. Three major ones are introduced here. The first one involves correcting the dose for each pattern [30] or for each piece of a pattern after dividing the pattern to pieces (Fig. 12[b]). This method was used for the pattern in Fig. 9. Resizing of each pattern (Fig. 12[c]) can also be included in this method by assigning a dose

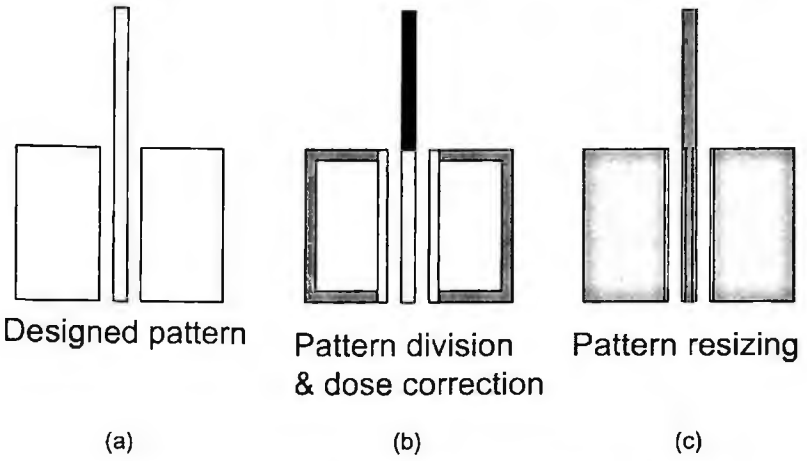

Figure 12. Schematic drawings showing (a) the designed pattern and (b, c) the proximity effect correction for it.

of zero to some outer pieces of the pattern. The ways to divide the pattern may be a little complicated but proper dose assigned to each piece can be derived by calculations of the proximity effect from many surrounding patterns. Although this method can provide precise corrections to obtain accurate pattern sizes, the amount of calculation becomes quite large. In order to reduce the amount of calculation, easier methods have been developed. One is called GHOST [31], which exposes an additional defocused pattern that is complementary to the distribution of the energy produced by backscattered electrons. As shown in Fig. 13, the complementary exposure makes uniform latent images for each pattern independent of the surrounding patterns. This method can drastically reduce the amount of calculation. However, since additional exposure reduces the contrast of the latent image, patterning resolution and edge roughness become worse. The remaining method is similar to the first one and corrects the dose for each pattern considering the amount of backscattering electrons from surrounding patterns as a value derived from the area densities of the patterns [32]. This method can be implemented into hardware on circuit boards in the EB apparatus and thus be used for real-time correction.

For delineating patterns with minimum feature size of less than several ten nanometers, more accurate proximity effect correction is necessary in order to obtain good uniformity of pattern sizes. The above fast methods have limits for this purpose. Moreover, it has been reported that another effect reduces the size uniformity/control of small patterns even good distribution of deposited energy has been obtained by proximity effect correction. While the rate of dry etching for small patterns is known to depend on the size of patterns, which is called aspect-ratio dependent etching (or microloading effect), a similar dependency is observed for developed patterns in EB lithography [13]. However, this effect in EB lithography is more difficult to quantitatively analyze than it is in etching because the effect shows

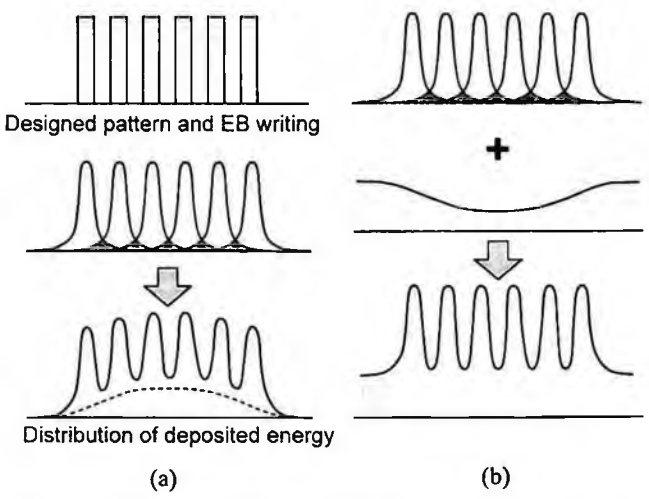

Figure 13. Schematic drawings showing dense patterning (a) without proximity effect correction and (b) with correction by the GHOST method.

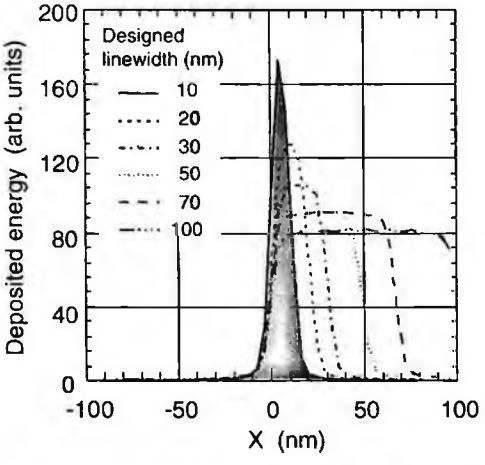

Figure 14. Distributions of energy deposited in resist for different designed linewidths and the same development rate. These were calculated using experimentally obtained doses. (Reprinted with permission from [13] by IPAP.)

characteristics similar to the proximity effect within short ranges. However, from precise simulation of the proximity effect as described above, it is possible to quantitatively measure the pattern-size dependence of the development rate. Figure 14 shows simulated distributions of energy deposited in resist for patterns of various linewidths that have the same development speed. It is clear that the energy causing the same development speed depends on the linewidth. The dependence of the energies with the same development speed on linewidth and background energy (which simulates the energy due to proximity effect for dense patterns) is shown in Fig. 15.

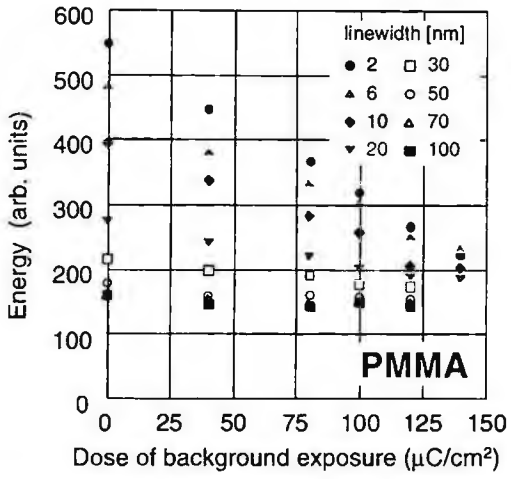

Figure 15. The dependence of deposited energy showing the same development rate on the designed linewidth and background energy. (Reprinted with permission from [13] by IPAP.)

Together with the proximity effect, this pattern-size dependent development has to be considered when we delineate small patterns in the range of a few ten nanometers or less with precise control of pattern size. The pattern-size dependent development can be dealt with more simply using the quasi-beam-profile method, which includes the effects of development and so on that are outstanding for small patterns, and should be considered together with the actual beam size [33].

For detailed investigations such as various background energies, however, we should take care for such nonlinear effects as shown in Fig. 15.

3.2. *Pattern-edge roughness*

When we delineate device patterns, the roughness of pattern edges should be reduced as much as possible. This is especially important when we delineate line patterns for electronic devices with the minimum feature size of less than 10–20 nm, where we may need line-edge roughness (LER) in three sigma (3σ) for one side to be as small as one nanometer or less because the roughness for the devices is generally required to be 5–8% of the linewidth.

In high-speed EB lithography using high-sensitivity resist, stochastic events can cause the edge roughness. Stochastic fluctuation on the incident position and scattering of each electron causes roughness, which together are known as shot noise effects. Moreover, fluctuations in the reaction and diffusion of acid produced by electrons affect the roughness of chemically amplified resist [34]. Under the conditions for high-resolution EB direct writing, however, the main cause of the roughness is material inhomogeneity in resist film. Many electrons for low-sensitivity non-chemically-amplified resist (at a high acceleration voltage) result in small enough

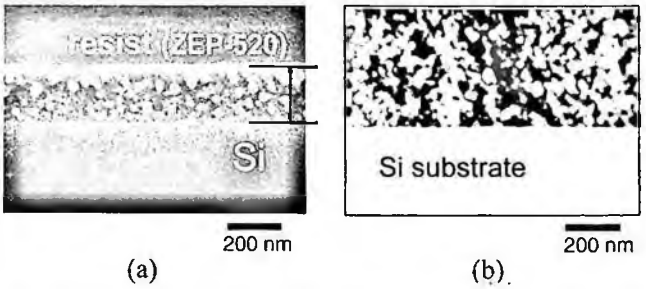

Figure 16. (a) SEM micrograph of cleaved cross-section of resist film (Reprinted with permission from [35] by IPAP) and (b) AFM image of the sidewall of the resist after patterning (Reprinted with permission from [42] by IPAP).

stochastic fluctuations, but higher-order structures from a few to a few ten nanometers in size in the resist film can cause inhomogeneous dissolution in developer. Problematic higher-order structures in the film of resist are aggregates of the resist polymer, which are known to cause LER [35]. The nonlinear effect of pattern-size dependent development described in the previous subsection can also be explained by such higher-order structures in resist.

Figure 16(a) is an SEM image of aggregates in a cross-section cleaved after resist (ZEP-520, Nippon Zeon) had been coated on a substrate. Similar structures are also observed on the sidewall of developed resist for a line pattern (Fig. 16[b]). Similar shapes have been observed for various resist materials [36], suggesting that the aggregates are the main cause of LER in high-resolution patterning. Some approaches to reducing the roughness have focused on improving the resist materials. The uses of a smaller polymer/molecule having small molecular weight [37], a cage structure [38,39] or a ring structure [40], and cross-linking among aggregates [41] have been reported to be effective ways to reduce the roughness. Patterns obtained using some of these are described in subsection 4.1. Moreover, a method of EB writing can also reduce the roughness due to the aggregates [42]. This method writes along the outline of a pattern with a much higher area-dose than usual and thus breaks up the aggregates there. Figure 17 shows an example of the (calculated) distributions of energy deposited in resist for this edge-enhancement method. The measured LER of conventional resist (ZEP-520) was actually reduced by 20%. Applying this method to two-dimensional patterns is easy, and as shown in Fig. 18, precise shape control of corners can be achieved. Although this method is similar to that used to improve the contrast of the latent image at the edge [43], it is also an effective way to improve the controllability of pattern size/shape and latitude in process conditions.

The smallest LER attained using these improvement techniques is still more than 1 nm in 3σ for one side. Although it is reported that dry etching of substrates can reduce LER compared with the original resist pattern [36], more improvement of resist patterns in lithography is needed for delineation with 10-nm resolution.

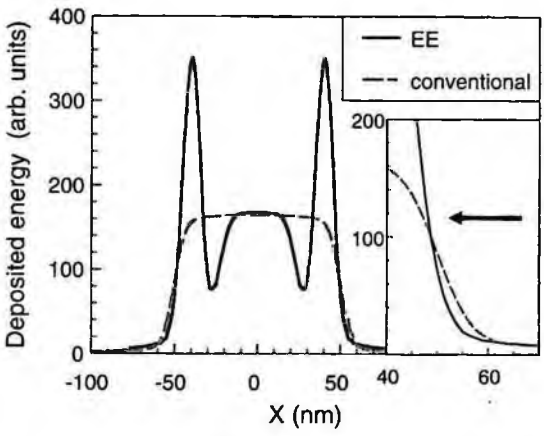

Figure 17. Calculated distribution of energy deposited in resist for the edge-enhancement (EE) method. (Reprinted with permission from [42] by IPAP.)

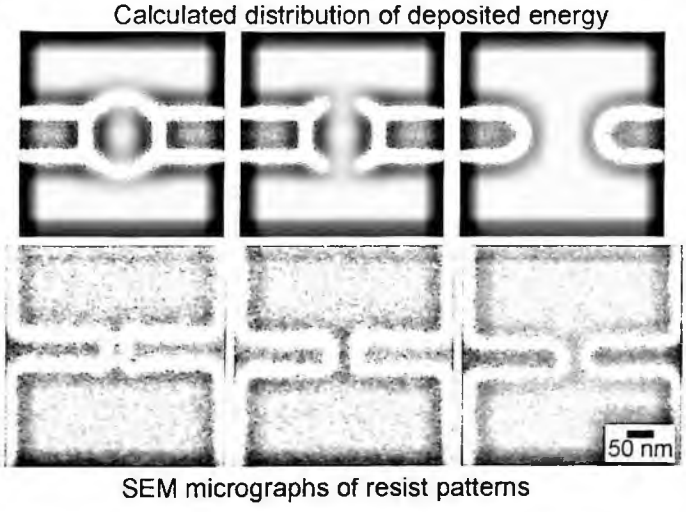

Figure 18. Example showing two-dimensional shape control for an unexposed fine line and corners using the edge-enhancement writing method.

3.3. *Positioning accuracy*

The accuracy of pattern positioning is very important for overlay in EB direct writing. Since most (electronic) devices made using direct writing have a layered structure, the positioning of structures relative to each other layer requires accuracies as high as the resolutions (i.e., several to a few ten nanometers). For example, fine gate electrodes formed on fine channels in field-effect devices require overlay accuracy smaller than the channel size. Recent developments have achieved positioning

Table 2. Factors for achieving high accuracy and example values (for fine patterning).

Small deflection noise (after feedback for stage position error)	<3 nm
Small blanking drift (small effect by charge up)	<3 nm/min
Small stage vibration (before feedback, with stiff structure between column and stage)	$<20\,\mathrm{nm}_{p-p}$
High stage-locating resolution	0.62 nm ($\lambda/1024$)
Small deflection distortion	<10 nm
Stable deflection	<10 nm/30 min
Stable environmental temperature	<0.1 K
Low environmental magnetic field	<0.5 mG (AC)
Smooth mark edge	<20 nm (rms)
Small beam step	1–4 nm
Sufficient beam current	0.2–1 nA
Stable gun (emission)	<0.4%/h
Small stitching error	<5 nm

accuracy as high as 10 nm (in 3σ), which will be sufficient for most applications of EB direct writing for a while.

The positioning accuracy of EB direct writing has improved with progress in EB apparatus technology. A high accuracy can only be achieved by totally refining all aspects of an apparatus, environment and fabrication, such as deflection noise, noise from power source, beam drift, mechanical vibration, and fabrication of overlay marks. Even with good performance of most aspects, the accuracy can become significantly worse owing to degradation of only one factor. Some of the more technically important factors that should be considered to achieve high accuracy are listed in Table 2, which includes their example values (for fine patterning). These (and other) factors allow us to obtain small beam drift, high mark-locating accuracy, and positioning stability with stage movement, which are a few nanometers or less for/within writing patterns in one chip, resulting in overlay accuracy as high as 10 nm [44]. For direct writing, small beam drift over many hours is not as important a concern as it is for mask writing; the stability just has to be sufficient for the time to write patterns (and mark-locating) in one chip.

The stitching accuracy, which is the positioning accuracy across the boundary between adjacent deflection fields, is also important because it affects the shape and performance of the device to be fabricated. The improved stability achieved by the factors mentioned above and the calibration of deflections with high accuracy are resulting in small stitching errors.

4. Nanopatterning and Applications

Nanopatterning with resolutions as high as a few to 5 nanometers using EB direct writing has been desired for the fabrication of advanced devices. For example, single-electron devices/circuits [45] working at room temperature require the total capacitance of each single-electron island to be 1 aF or less, which corresponds to a

diameter of less than 5 nm for Si islands surrounded by SiO_2 [19]. So, a 5-nm resolution is necessary for such devices/circuits. In addition, in order to obtain a voltage gain of more than unity at room temperature, further reduction of the capacitance as well as smaller capacitance between the island-source/drain than that between the island-gate are required [46]. Therefore, a higher resolution on nanopatterning (with sufficient reproducibility and positioning accuracy) is desired for making such single-electron circuits.

Nanopatterning with such ultimate resolutions requires a very fine EB and a high-resolution resist material. For the high-resolution resists used in direct writing, other properties, such as sufficient sensitivity, etching durability, cleanness for devices to be fabricated, and small pattern-edge roughness, are also important. In this section, some high-resolution resist materials and their nanopatterning are described first. Next, some applications of nanopatterns to single-electron devices and a new technique using EB direct writing for three-dimensional (3D) fabrication are introduced.

4.1. *EB resist and nanopatterning*

Although nanopatterning using inorganic resists (AlF_3, etc.) achieved the resolution of 2–3 nm many years ago [47], inorganic resists have not been practical because of their low sensitivities (on the order of Coulombs per square centimeter). Such resists are not only time-consuming to use but also result in noise and drift of the EB during long writing time and thereby cause poor accuracy of patterning. Chemically amplified resists with high sensitivities on the order of 1–10 $\mu C/cm^2$ are used for high-throughput EB writing. However, the useful resists for EB direct writing with high resolutions of a few ten to several nanometers generally have sensitivities of 0.1–10 mC/cm^2. Of course, high-sensitivity resists with a higher resolution would be very useful, but physical limits, such as pattern-edge roughness due to shot noise, could degrade the patterning. Moreover, high sensitivity and high resolution are thought to be contradictory. In fact, most of reported resists roughly satisfy the linear relationship in a log-log plot; higher resolution resists have lower sensitivities. Therefore, it may be difficult to get a resist with both high resolution and high sensitivity.

PMMA and its derivatives are used as standard resists in fine EB direct writing, and 3–4-nm patterning of PMMA has been reported [48,49] as shown in Fig. 19. While PMMA is a positive resist, some phenol-based resists such as NEB (Sumitomo Chemical) are often used as negative resists, which are chemically amplified resists and thus have lower resolutions. The principle of patterning with positive/negative resists is large exposure dependency of resolving speed of resist in developer. This means that developers as well as resist materials are important. For example, the contrast of developed/undeveloped areas of ZEP-520 resist (a PMMA derivative having higher sensitivity and etching durability than PMMA) can be improved by selecting an appropriate developer [50]. The contrast of a resist (γ) is defined as the

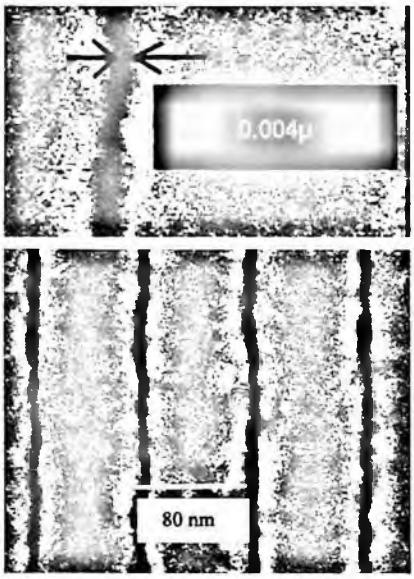

Figure 19. Micrograph of nano-lines of PMMA resist. (Reprinted with permission from [49] by AIP.)

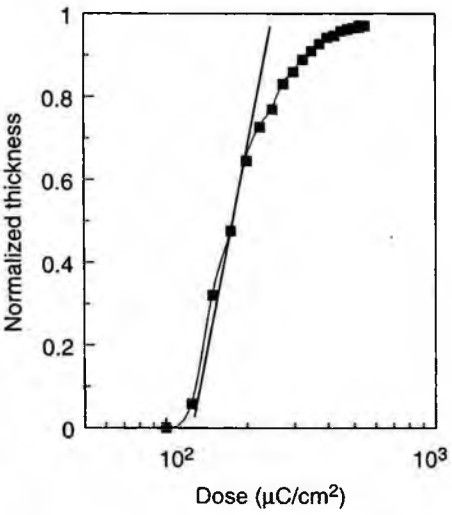

Figure 20. Sensitivity curve of HSQ resist at 100 kV.

slope of the sensitivity curve on a semi-log scale as shown in Fig. 20. High contrast is a very important because it generally allows us to obtain smoother pattern edges and higher resolutions.

As a way to improve the resolution and reduce pattern-edge roughness, the miniaturization of resist polymers/molecules has been investigated. Hydrogen

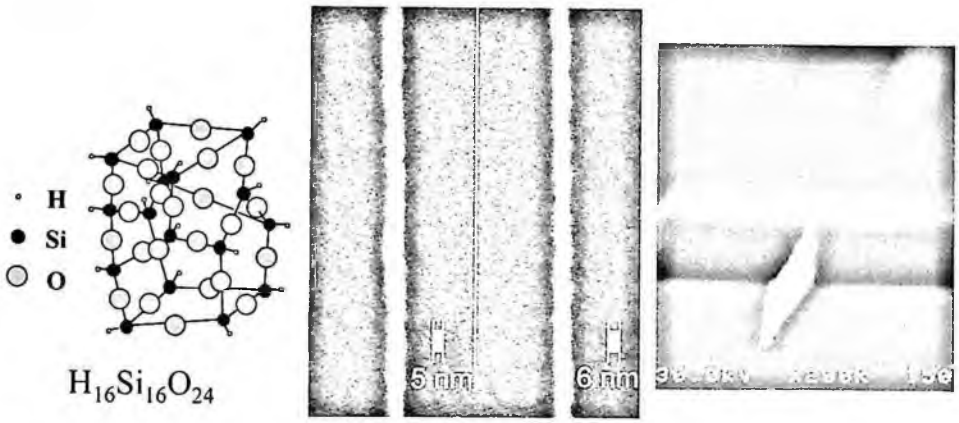

Figure 21. Schematic drawing of low-molecular-weight HSQ (left) and micrographs of nano-lines of HSQ resist. (Reprinted with permissions from [19,51] by IPAP and AIP.)

silsesquioxane (HSQ) is a kind of siloxane with a small cage structure (Fig. 21(left)) and acts as a high-resolution EB resist. (Although siloxane is inorganic by definition, the reaction of HSQ on exposure is similar to that of organic resists.) This polymer with small molecular weight has enabled nanopatterning of 5–7 nm in size and small LER of 1–1.5 nm (Fig. 21) [19,38,51]. Patterning of 23-nm pitch dense lines of HSQ is also reported [52]. Some kinds of calixarenes and their derivatives, which are circular molecules about 1 nm in size, provide 7–10 nm resolution and small LER of 1–1.5 nm (Fig. 22) [40,53]. Another approach to obtaining high resolution uses hybridizing inorganic and organic materials [54]; i.e., the inorganic part improves resolution and the organic part improves sensitivity. This hybrid resist is based on a new principle of patterning, where resist molecules decomposed by EB exposure become "more inorganic" and thus have lower solubility in developer. With this resist, 5–7-nm patterning has been achieved.

The resolutions of organic resists and resists with organic parts that react on exposure are generally limited by traveling of secondary electrons produced by incident electrons in resist film. This is because the reaction energy of the organic parts is generally less than the energies of the secondary electrons. Most of the secondary electrons have energies of several to several ten electronvolts and travel about 1–2 nm in resists, as shown by Monte Carlo simulation (Fig. 23). Therefore, the resists are thought to have a resolution limit of 2–3 nm even though an EB of 1 nm or less in size is used for writing. In order to exceed this limit, the discovery of a new principle of reactions in resist or a significantly high contrast is probably necessary. As properties desired for new resist materials, small pattern-edge roughness of delineated patterns, a high resolution, sufficient sensitivity, and so on, are very important. Advances in resist material for EB direct writing with high resolutions are expected.

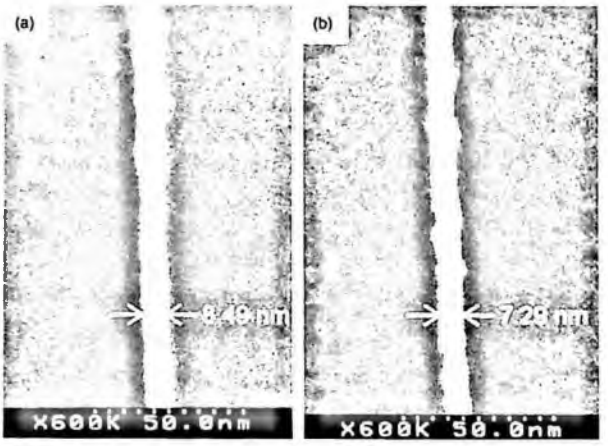

Figure 22. Micrographs of nano-lines of *p*-chloromethyl-methoxy-calix[4]arene resist. (Reprinted with permission from [53] by IPAP.)

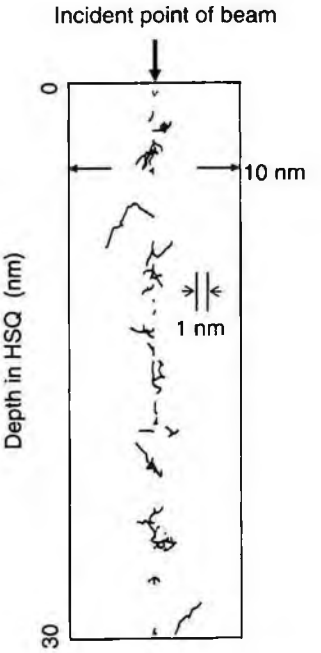

Figure 23. Trajectories of secondary electrons in HSQ resist with an incident beam at 100 kV, obtained by Monte Carlo simulation.

4.2. *Application to nanodevices*

The application fields of EB direct writing include fabrications for various micro/nanoelectronics technologies, micro/nano-optical/photonic devices, metrological devices, nanoelectromechanical systems, biotechnology/biology, material science/technologies (such as metamaterials), and applied/pure physics using, for example, quantum or superconductivity devices. Reviewing all of these fields is not possible here. As described in the beginning of this section, highly accurate high-resolution patterning using EB direct writing is very important for making single-electron devices. Therefore, as examples of advanced applications of EB direct writing, we will look at single-electron transistors with precise dimensions [55] and single-electron device fabricated with high overlay accuracy [56].

In order to integrate single-electron transistors/devices, reproducible fabrication with precise dimensions with minimum feature sizes of 5–10 nm, is desired even for low-temperature operation. The fabrication procedure for the single-electron transistors made of Si introduced here includes an oxidation process (pattern-dependent oxidation [57]) that shrinks the island size. Thus 10–30-nm wide wires on silicon-on-insulator (SOI) substrates can be used to make single-electron transistors working at

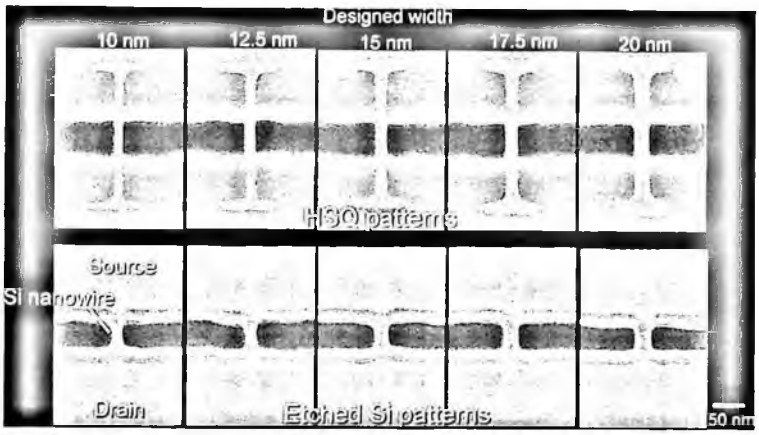

Figure 24. Micrographs of dimension controlled HSQ patterns and Si wires for single-electron transistors. (Reprinted with permission from [55] by AIP.)

a low temperature. Moreover, the oxidation of a fine Si wire between two pads automatically produces two tunneling barriers and a potential island between the barriers, i.e., a single-electron transistor. Improvements of oxidation conditions, LER, and so on, as well as further miniaturizing of the device, will lead to operation at room temperature. Figure 24 shows the HSQ resist lines and Si wires formed using EB direct writing. The linewidths strictly follow the designed widths with 2.5 nm steps. Although the Si wires were fabricated to have cross-sections of trapeziums (i.e., narrower top and wider bottom) because of the slightly short over-etching time, the actual (averaged) width of the Si wires follow the resist linewidths, while only the bottom edges are clearly visible in the micrographs. These Si wires become single-electron transistors after they are oxidized and covered with gate electrodes. Figure 25 shows examples of the electrical characteristics of the transistors, i.e., the linewidth dependence of the Coulomb blockade, which is a blockade of electric current caused by potential change due to changes in the number of electrons in the island. As the width becomes larger, the Coulomb blockade oscillation is less clear because the island becomes larger. This kind of consistency between the characteristics and designed dimensions is clearly seen in Fig. 26, which shows the map of the characteristics depending on the linewidth, length and oxidation duration. These results indicate that EB lithography can provide good consistency and reproducibility on the order of one nanometer and thus controllability of the characteristics of this kind of nanoelectronic devices.

Figure 27 shows another type of single-electron device made of Si. This device has a T-shaped nanowire and three single-electron islands are formed at the center of the branches after oxidation. Two fine gate electrodes were fabricated on two of these islands by using overlay lithography with sub-10-nm accuracy. Therefore, the electrostatic potential of each island can be freely controlled by using the two fine gates and an additional wide upper gate. Figure 28 shows how the signals of electric

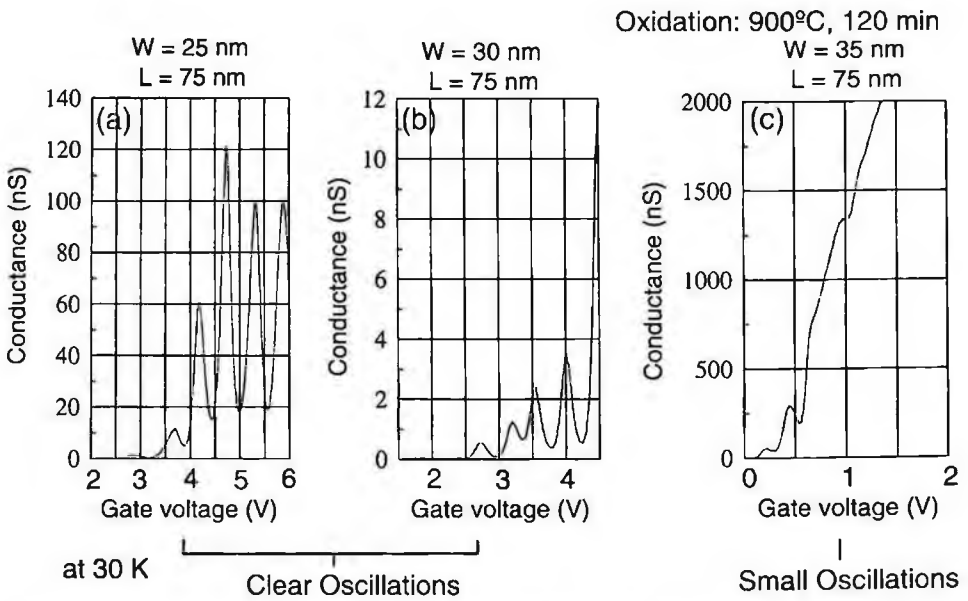

Figure 25. Typical characteristics of single-electron oscillation. (W: width, L: length of designed pattern. Reprinted with permission from [55] by AIP.)

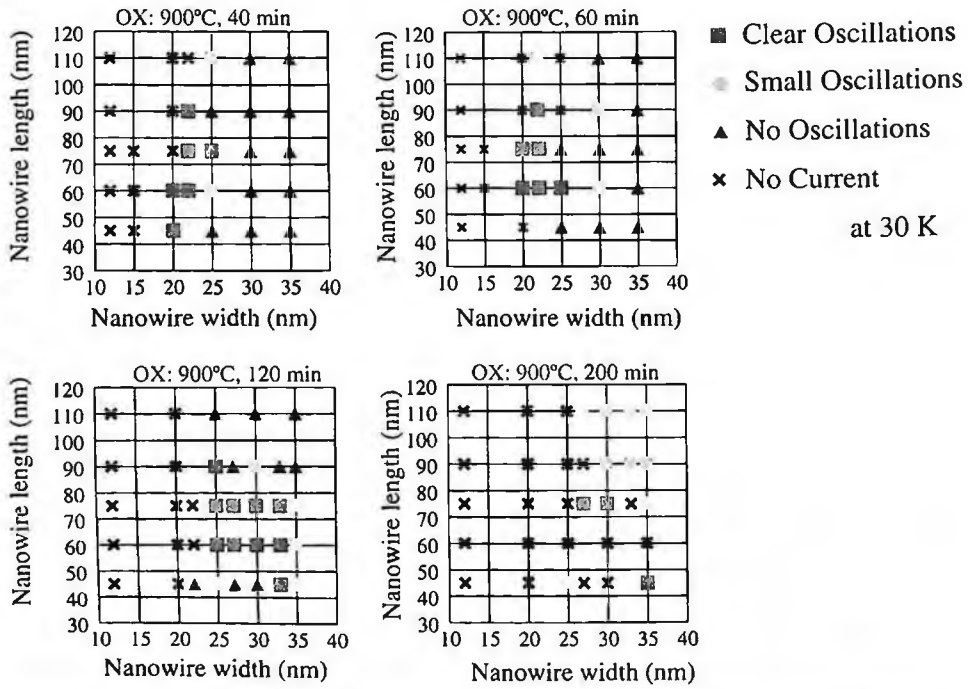

Figure 26. Map of single-electron oscillation depending on dimensions and oxidation condition. (Reprinted with permission from [55] by AIP.)

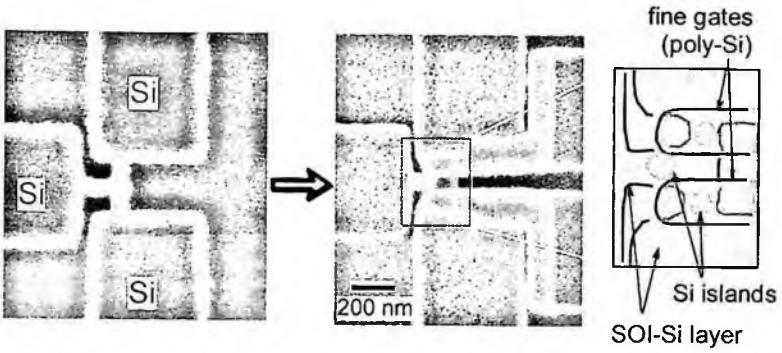

Figure 27. Micrographs of the single-electron device with the T-shaped branch; (left) before and (right) after overlaying fine gate electrodes made of poly-Si. (Reprinted with permission from [44] by IPAP.)

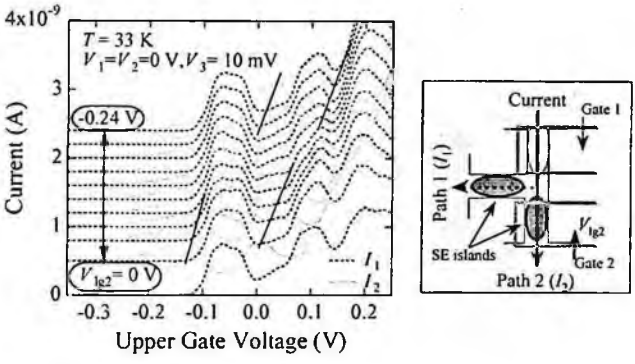

Figure 28. Electrical characteristics of the single-electron device with the T-shaped branch. (Reprinted with permission from [56] by IEEE.)

current along two paths depend on the voltages of the upper gate and one of the fine gates (lower one). The signals indicate good (independent) controllability of the potential of each island, and, moreover, the capacitance coupling between the two islands, which is important to construct functional single-electron devices, is observed [56].

The good dimension controllability with a high resolution and the high overlay accuracy in EB direct writing are very useful for making highly advanced devices. Further advances in device design using these advantages and lithography promise progress in electronic devices and many other fields.

4.3. *Three-dimensional fabrication for nanotechnology applications*

EB lithography is expected to be a key aspect of the fabrication of various nanostructures for many nanotechnology applications. Considering the many applications in the various fields, the adaptation of EB direct writing to 3D fabrication should

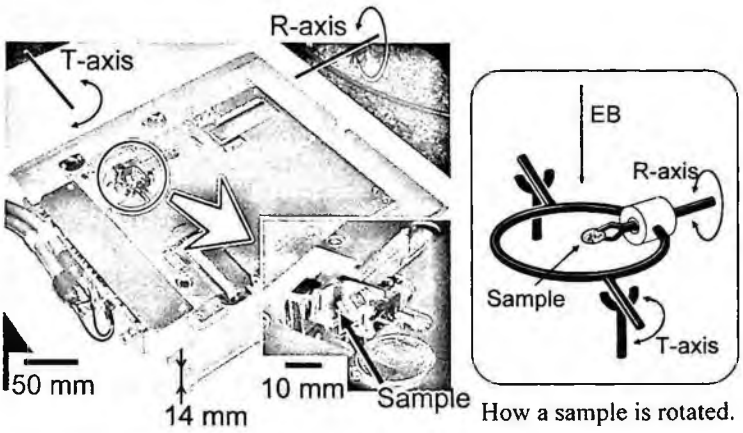

Figure 29. Rotation drive system for 3D nanofabrication using EB lithography. (Reprinted from [58] Copyright (2004) with permission from Elsevier.)

spur progress in the fields. Here, as a new success in the evolution of EB direct writing, 3D nanofabrication using EB lithography is introduced. Since the resolution of EB lithography is close to the size of many molecules, polymers and other nano-materials such as carbon nanotubes, 3D structures interacting with such materials in sizes of nanometers would open up a new field in nanotechnology. 3D-EB lithography is the promising technology for such purposes.

Figure 29 shows the drive rotating a sample (<5 mm in size) in an EB lithography apparatus. The drive was developed for 3D nanofabrication and was built on a pallet to be easily loaded into the apparatus [58]. Rotating a resist sample and writing on it with an EB from various directions enable us to obtain various 3D structures after development. The rotation accuracy of the drive is 1–3 mrad, which is thought to be sufficient for many applications. To use the rotation drive in 3D nanofabrication, new techniques for focusing of the EB and positioning of the writing patterns on 3D or rotated samples were developed. For positioning along x and y directions, conventional EB lithography for flat wafers uses marks consisting of a trench or metal, which changes the intensity of backscattered electrons. However, it is very difficult to use them for this purpose when the sample rotates. The positioning technique for 3D samples uses transmission electrons and is based on the projected image (outline) of the 3D sample, which result in high accuracy in beam positioning. The overlay accuracy using this method, measured by writing vernier patterns on a sphere, is 20–30 nm [59]. In the case of EB focusing, the conventional method for flat wafers cannot be used for 3D samples because it employs an optical lever method and thus the optical beam can not reflect from the 3D sample surface into the photo detector set in the apparatus. For this purpose, a height measurement system consisting of a confocal laser microscope and XY stage is used. Using this system, the height map of a 3D sample can be obtained as that relative to the height of the marks on the pallet so that the EB can be focused on the sample surface

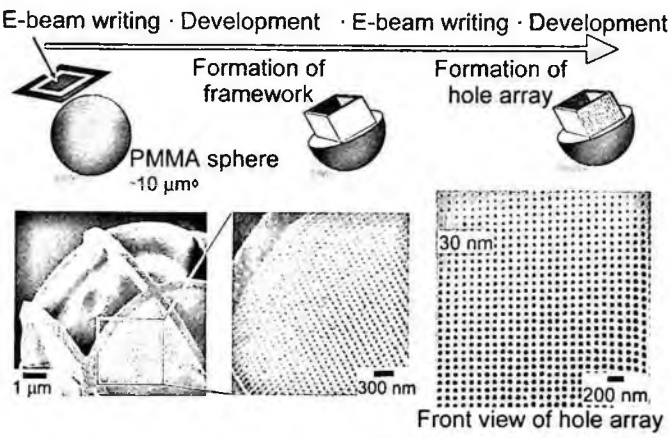

Figure 30. Micrographs of the nano-filter (bottom) and illustration showing its fabrication process (top). A demonstration of deep nanostructures fabricated by 3D-EB lithography. (Reprinted with permission from [59] by IEEE.)

using calculated heights. Although the microscope itself has a height resolution of 0.1 μm or less, sample transferring causes height errors of 1–2 μm. However, this is not a problem because the depth of focus of the EB is more than 5 μm for a small beam semi-angle, which was confirmed by a calculation of the beam shape (See subsection 2.4) [60].

Figure 30 shows a 3D structure fabricated by the 3D-EB lithography [59]. This is a nano-filter made of PMMA, which has 3D frame structures and arrays of holes as small as about 30 nm in size. This nano-filter was fabricated by repeating EB lithography and development. The first exposure and development delineated the deep square frame structure and the second exposure and development delineated the hole array. This clearly demonstrates that this technique can fabricate 3D structures and that it has a 10-nm-order resolution. This kind of deep fabrication of resist samples is limited by electron scattering in the sample. The resolution becomes lower when deeper structures are formed in one step, as shown by the simulated electron trajectories and distribution of deposited energy (Fig. 31). Figure 32 shows another demonstration [60]. This is the world's smallest globe of the earth. The world map pattern was written on a PMMA sphere 60-μm in diameter. This nano-globe displays coastlines and rivers, and the land areas have contrast to sea areas due to dense line patterns. The linewidth is as small as 10 nm over the whole sample. The total exposure time for the whole world map, besides the time for sample rotation, development and so on, was less than 2 min. This means that the 3D-EB lithography enables us to pattern on 3D samples with 10-nm resolution and reasonably high speed.

Although the nano-filter and nano-globe were made of resist material, this technique can be extended to 3D nanofabrication for various materials by coating resist on 3D samples [61] and 3D etching the samples from various directions. This kind of

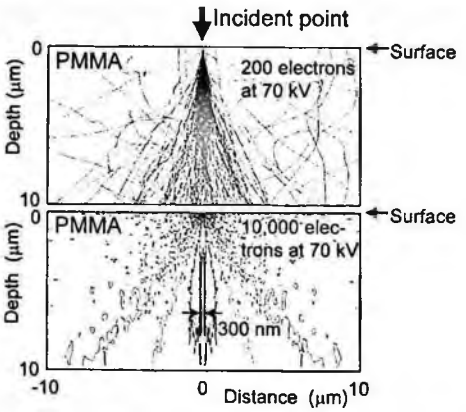

Figure 31. Electron trajectories (above) and distribution of energy deposited in PMMA resist (below), obtained by Monte Carlo simulation.

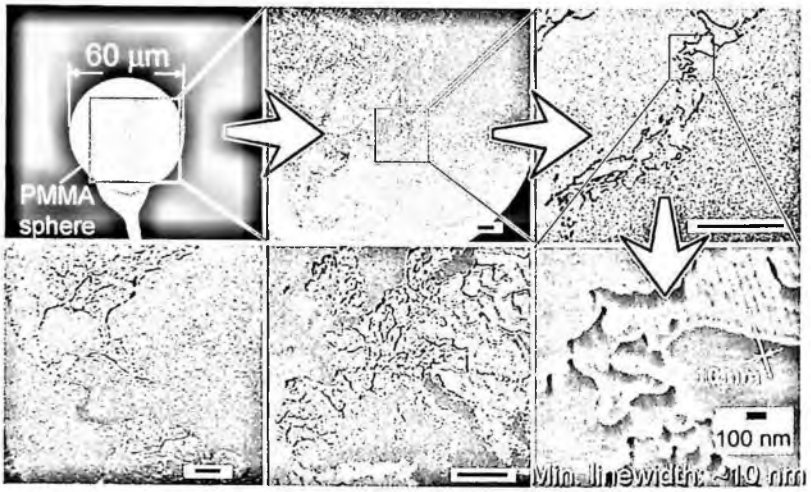

Figure 32. Micrographs of the world's smallest globe; a demonstration of the 10-nm resolution and reasonable patterning speed of 3D-EB lithography. The unlabeled scale bars indicate 3 μm.

3D nanofabrication using EB lithography is expected to open up a new field of 3D nanotechnology, which should be very useful for various fields in nanotechnology.

5. Conclusion

Although EB direct writing has not become a major technology in mass production or industry, it has been able to use the benefits from various developments made in EB mask writers and high-throughput apparatuses, which are widely used or being developed for mass production. This has made it possible to use EB direct writing for the development of the next generation of devices, for research on the

devices of the future, for the fabrication of devices for scientific research, and so on. Considering the main advantage of high resolution in EB direct writing, the development of high-resolution resist (providing small edge roughness) and lithography apparatuses featuring high-resolution lenses (with a multipole system) are expected. On the other hand, nanotechnology is expected to play very important roles in various industries in this century. While bottom-up nanotechnology will also be very important in the various nanotechnology fields, I believe that top-down nanotechnology, including EB direct writing, will be essential for developments in most of the fields. Therefore, as EB direct writing technology evolves further, its importance in various fields of nanotechnology/nanoscience will increase.

Acknowledgments

The author would like to thank Dr. Kenji Kurihara for discussion of the review. He also thanks all of the publishers and authors who allowed him to use their materials in this chapter.

References

1. G. Möllenstedt and R. Speidel, Newer developments in microminiaturization, *Proceedings of 3rd Symposium on Electron Beam Technology*, pp. 340–357, 1961.
2. H. C. Pfeiffer, Variable spot shaping for electron-beam lithography, *J. Vac. Sci. Technol.*, **15**, 887–890 (1978).
3. H. C. Pfeiffer, Recent advances in electron-beam lithography for the high-volume production of VLSI devices, *IEEE Trans. Electron Devices*, **ED-26**, 663–674 (1979).
4. S. D. Berger, J. M. Gibson, R. M. Camarda, R. C. Farrow, H. A. Huggins, J. S. Kraus and J. A. Liddle, Projection electron-beam lithography: A new approach, *J. Vac. Sci. Technol. B*, **9**, 2996–2999 (1991).
5. H. C. Pfeiffer and W. Stickel, PREVAIL — An e-beam stepper with variable axis immersion lenses, *Microelectron. Eng.*, **27**, 143–146 (1995).
6. T. Utsumi, Low-energy e-beam proximity lithography (LEEPL): Is the simplest the best?, *Jpn. J. Appl. Phys.*, **38**, 7046–7051 (1999).
7. S. Y. Chou, P. R. Krauss and P. J. Renstrom, Imprint of sub-25 nm vias and trenches in polymers, *Appl. Phys. Lett.*, **67**, 3114–3116 (1995).
8. T. H. P. Chang, Proximity effect in electron-beam lithography, *J. Vac. Sci. Technol.*, **12**, 1271–1275 (1975).
9. J. S. Greeneich, Impact of electron scattering on linewidth control in electron-beam lithography, *J. Vac. Sci. Technol.*, **16**, 1749–1753 (1979).
10. N. Samoto, R. Shimizu, H. Hashimoto, I. Adesida, E. Wolf and S. Namba, Exposure and development simulations for nanometer electron beam lithography, *J. Vac. Sci. Technol. B*, **1**, 1367–1371 (1983).
11. F. Rohrlich and B. C. Carlson, Positron-electron differences in energy loss and multiple scattering, *Phys. Rev.*, **93**, 38–44 (1954).
12. N. Samoto and R. Shimizu, Theoretical study of the ultimate resolution in electron beam lithography by Monte Carlo simulation, including secondary electron generation: Energy dissipation profile in polymethylmethacrylate, *J. Appl. Phys.*, **54**, 3855–3859 (1983).

13. K. Yamazaki, K. Kurihara, T. Yamaguchi, H. Namatsu and M. Nagase, Novel proximity effect including pattern-dependent resist development in electron beam nanolithography, *Jpn. J. Appl. Phys.*, **36**, 7552–7556 (1997).
14. M. Kotera, K. Murata and K. Nagami, Monte Carlo simulation of 1-10-KeV electron scattering in a gold target, *J. Appl. Phys.*, **52**, 997–1003 (1981).
15. R. A. Bonham and T. G. Strand, Analytical expressions for potentials of neutral Thomas-Fermi-Dirac atoms and for the corresponding atomic scattering factors for X rays and electrons, *J. Chem. Phys.*, **39**, 2200–2204 (1963).
16. M. Kotera, R. Ijichi, T. Fujiwara, H. Suga and D. B. Wittry, A simulation of electron scattering in metals, *Jpn. J. Appl. Phys.*, **29**, 2277–2282 (1990).
17. M. Cailler and J. P. Ganachaud, A simulation model for secondary electron emission from metals. Application to the study of the Auger electron emission of aluminium, *in part I*, O. Johari (Ed), Proceedings of Scanning Electron Microscopy 1983, pp. 85–97, Scanning Electron Microscopy, Inc. 1983.
18. C. J. Tung, J. C. Ashley and R. H. Ritchie, Electron inelastic mean free paths and energy losses in solids II, *Surf. Sci.*, **81**, 427–439 (1979).
19. K. Yamazaki and H. Namatsu, 5-nm-order electron-beam lithography for nanodevice fabrication, *Jpn. J. Appl. Phys.*, **43**, 3767–3771 (2004).
20. J. R. Michael, Probe size measurement in a field-emission STEM, *in Proceedings of Microbeam Analysis 1988*, D. E. Newbury (Ed), (San Francisco Press, Inc. 1988) pp. 60–64.
21. S. A. Rishton, S. P. Beaumont and C. D. W. Wilkinson, Measurement of the profile of finely focused electron beams in a scanning electron microscope, *J. Phys. E*, **17**, 296–303 (1984).
22. H. Hiroshima, S. Okayama, M. Ogura, M. Komuro, H. Nakazawa, Y. Nakagawa, K. Ohi and K. Tanaka, Nanobeam process system: An ultrahigh vacuum electron beam lithography system with 3 nm probe size, *J. Vac. Sci. Technol. B*, **13**, 2514–2517 (1995).
23. D. M. Tennant, R. Fullowan, H. Takemura, M. Isobe and Y. Nakagawa, Evaluation of a 100 kV thermal field emission electron-beam nanolithography system, *J. Vac. Sci. Technol. B*, **18**, 3089–3094 (2000).
24. K. Yamazaki and H. Namatsu, Electron-beam diameter measurement using a knife edge with a visor for scattering electrons, *Jpn. J. Appl. Phys.*, **42**, L491–L493 (2003).
25. K. Kurihara, K. Iwadate, H. Namatsu, M. Nagase, H. Takenaka and K. Murase, An electron beam nanolithography system and its application to Si nanofabrication, *Jpn. J. Appl. Phys.*, **34**, 6940–6946 (1995).
26. J. E. Barth and P. Kruit, Addition of different contributions to the charged particle probe size, *Optik*, **101**, 101–109 (1996).
27. C. Mory, M. Tence and C. Colliex, Theoretical study of the characteristics of the probe for a STEM with a field emission gun, *J. Microsc. Spectrosc. Electron.*, **10**, 381–387 (1985).
28. J. A. McMillan, S. Johnson and N. C. MacDonald, Simulation of electron beam exposure of submicron patterns, *J. Vac. Sci. Technol. B*, **7**, 1540–1545 (1989).
29. K. Murata, D. F. Kyser and C. H. Ting, Monte Carlo simulation of fast secondary electron production in electron beam resists, *J. Appl. Phys.*, **52**, 4396–4405 (1981).
30. M. Parikh, Self-consistent proximity effect correction technique for resist exposure (SPECTRE), *J. Vac. Sci. Technol.*, **15**, 931–933 (1978).
31. G. Owen and P. Rissman, Proximity effect correction for electron beam lithography by equalization of background dose, *J. Appl. Phys.*, **54**, 3573–3581 (1983).

32. F. Murai, H. Yoda, S. Okazaki, N. Saitou and Y. Sakitani, Fast proximity effect correction method using a pattern area density map, *J. Vac. Sci. Technol. B*, **10**, 3072–3076 (1992).
33. M. Yoshizawa and S. Moriya, Edge roughness evaluation method for quantifying at-size beam blur in electron beam lithography, *in Emerging Lithographic Technologies IV*, E. A. Dobisz (Ed), Proceedings of SPIE Vol. 3997, pp. 301–308, The International Society for Optical Eng., 2000.
34. M. Kotera, T. Yamada and Y. Ishida, Line edge roughness of developed resist with low-dose electron beam exposure, *Jpn. J. Appl. Phys.*, **41**, 4150–4156 (2002).
35. T. Yamaguchi, K. Yamazaki, M. Nagase and H. Namatsu, Line-edge roughness: Characterization and material origin, *Jpn. J. Appl. Phys.*, **42**, 3755–3762 (2003).
36. H. Namatsu, M. Nagase, T. Yamaguchi, K. Yamazaki and K. Kurihara, Influence of edge roughness in resist patterns on etched patterns, *J. Vac. Sci. Technol. B*, **16**, 3315–3321 (1998).
37. T. Yoshimura, H. Shiraishi, J. Yamamoto and S. Okazaki, Correlation of nano edge roughness in resist patterns with base polymers, *Jpn. J. Appl. Phys.*, **32**, 6065–6070 (1993).
38. H. Namatsu, Y. Yamaguchi, M. Nagase, K. Yamazaki and K. Kurihara, Nanopatterning of a hydrogen silsesquioxane resist with reduced linewidth fluctuations, *Microelectron. Eng.*, **41/42**, 331–334 (1998).
39. H. Namatsu, Y. Takahashi, K. Yamazaki, T. Yamaguchi, M. Nagase and K. Kurihara, Three-dimensional siloxane resist for the formation of nanopatterns with minimum linewidth fluctuations, *J. Vac. Sci. Technol. B*, **16**, 69–76 (1998).
40. J. Fujita, Y. Ohnishi, Y. Ochiai and S. Matsui, Ultrahigh resolution of calixarene negative resist in electron beam lithography, *Appl. Phys. Lett.*, **68**, 1297–1299 (1996).
41. T. Yamaguchi, H. Namatsu, M. Nagase, K. Yamazaki and K. Kurihara, A new approach to reducing line-edge roughness by using a cross-linked positive-tone resist, *Jpn. J. Appl. Phys.*, **38**, 7114–7118 (1999).
42. K. Yamazaki, T. Yamaguchi and H. Namatsu, Edge-enhancement writing for electron beam nanolithography, *Jpn. J. Appl. Phys.*, **42**, 3833–3837 (2003).
43. H. Nakata, T. Kato, K. Murata, Y. Hirai and K. Nagami, The effect of extra doses at the pattern edges on negative electron resist profiles, *J. Vac. Sci. Technol.*, **19**, 1248–1253 (1981).
44. K. Yamazaki, A. Fujiwara, Y. Takahashi, H. Namatsu and K. Kurihara, Sub-10-nm overlay accuracy in electron beam lithography for nanometer-scale device fabrication, *Jpn. J. Appl. Phys.*, **37**, 6788–6791 (1998).
45. Y. Takahashi, Y. Ono, A. Fujiwara and H. Inokawa, Silicon single-electron devices, *J. Phys.: Condens. Matter*, **14**, R995–R1033 (2002).
46. P. Hadley, G. Lientschnig and M. J. Lai, Single-electron transistors, *in Compound Semiconductors 2002*, M. Ilegems, G. Weimann and J. Wagner (Ed). Institute of Physics Conference Series Vol. 174, (Institute of Physics Publishing, 2003) pp. 125–132.
47. A. Muray, M. Scheinfein and M. Isaacson, Radiolysis and resolution limits of inorganic halide resists, *J. Vac. Sci. Technol. B*, **3**, 367–372 (1985).
48. D. R. S. Cumming, S. Thoms, S. P. Beaumont and J. M. R. Weaver, Fabrication of 3 nm wires using 100 keV electron beam lithography and poly (methyl methacrylate) resist, *Appl. Phys. Lett.*, **68**, 322–324 (1996).
49. S. Yasin, D. G. Hasko and H. Ahmed, Fabrication of < 5 nm width lines in poly(methylmethacrylate) resist using a water:isopropyl alcohol developer and ultrasonically-assisted development, *Appl. Phys. Lett.*, **78**, 2760–2762 (2001).

50. H. Namatsu, M. Nagase, K. Kurihara, K. Iwadate, T. Furuta and K. Murase, Fabrication of sub-10-nm silicon lines with minimum fluctuation, *J. Vac. Sci. Technol. B*, **13**, 1473–1476 (1995).
51. H. Namatsu, Supercritical resist drying for isolated nanoline formation, *J. Vac. Sci. Technol. B*, **19**, 2709–2712 (2001).
52. K. A. Lister, B. G. Casey, P. S. Dobson, S. Thoms, D. S. Macintyre, C. D. W. Wilkinson and J. M. R. Weaver, Pattern transfer of a 23 nm-period grating and sub-15 nm dots into CVD diamond, *Microelectron. Eng.*, **73-74**, 319–322 (2004).
53. M. Ishida, J. Fujita, T. Ogura, Y. Ochiai, E. Ohshima and J. Momoda, Sub-10-nm-scale lithography using *p*-chloromethyl-methoxy-calix[4]arene resist, *Jpn. J. Appl. Phys.*, **42**, 3913–3916 (2003).
54. M. S. M. Saifullah, K. R. V. Subramanian, D. J. Kang, D. Anderson, W. T. S. Huck, G. A. C. Jones and M. E. Welland, Sub-10 nm high-aspect-ratio patterning of ZnO using an electron beam, *Adv. Mater.*, **17**, 1757–1761 (2005).
55. H. Namatsu, Y. Watanabe, K. Yamazaki, T. Yamaguchi, M. Nagase, Y. Ono, A. Fujiwara and S. Horiguchi, Fabrication of Si single-electron transistors with precise dimensions by electron-beam nanolithography, *J. Vac. Sci. Technol. B*, **21**, 1–5 (2003).
56. A. Fujiwara, Y. Takahashi, K. Yamazaki, H. Namatsu, M. Nagase, K. Kurihara and K. Murase, Double-island single-electron devices — a useful unit device for single-electron logic LSI's, *IEEE Trans. Electron Devices*, **46**, 954–959 (1999).
57. Y. Takahashi, M. Nagase, H. Namatsu, K. Kurihara, K. Iwadate, Y. Nakajima, S. Horiguchi, K. Murase and M. Tabe, Fabrication technique for Si single-electron transistor operating at room temperature, *Electron. Lett.*, **31**, 136–137 (1995).
58. K. Yamazaki and H. Namatsu, Two-axis-of-rotation drive system in electron-beam lithography apparatus for nanotechnology applications, *Microelectron. Eng.*, **73–74**, 85–89 (2004).
59. K. Yamazaki and H. Namatsu, Three-dimensional nanofabrication (3D-NANO) down to 10-nm order using electron beam lithography, *in Technical Digest of 17th IEEE International Conference on Micro Electro Mechanical Systems 2004*, pp. 609–612, IEEE 2004.
60. K. Yamazaki, T. Yamaguchi and H. Namatsu, Three-dimensional nanofabrication with 10-nm resolution, *Jpn. J. Appl. Phys.*, **43**, L1111–L1113, (2004).
61. K. Yamazaki and H. Namatsu, Three-dimensional resist-coating technique and nanopatterning on a cube using electron-beam lithography and etching, *Jpn. J. Appl. Phys.*, **45**, L403–L405 (2006).

CHAPTER 11

ELECTRON BEAM INDUCED DEPOSITION

KAZUTAKA MITSUISHI

National Institute for Materials Science,
3-13 Sakura, Tsukuba, Ibaraki, 305-0003, Japan
mitsuishi.kazutaka@nims.go.jp

The electron beam induced deposition (EBID) originated contamination writing as early as 1934, and many studies have been carried out using scanning electron microscopes for various gases and conditions, and the technique was found to be very successful for a number of applications making variously shaped nano-structures. Therefore, EBID is recognized as a very promising nanofabrication technique and the amount of work devoted to this field is rapidly increasing. In this chapter, fundamentals and an overview of EBID are given in [Section Number of FUNDAMENTALS]. Recent progress is discussed in [Section Number of RECENT RESEARCH ACTIVITIES] which includes consideration of resolution improvement using 200 kV scanning transmission electron microscopy, the Monte Carlo-based calculation of a deposit shape, nanowiring and electron conductivities, three-dimensional structure fabrication, magnetic material deposition, and further trials to improve the range of material choices and the fabrication speed.

Keywords: Electron beam induced deposition EBID; scanning transmission electron microscopy STEM; Monte Carlo; precursor; $W(CO)_6$; secondary electron; dissociation cross-section; scanning electron microscopy; Dynamic Monte Carlo profile simulation; annular dark field (ADF) STEM; high-resolution electron microscopy; ultra high-vacuum (UHV) TEM; nanowiring; conductivity of deposits; $Fe(CO)_5$; ion milling; spherical aberration (Cs) corrector.

CONTENTS

1. Introduction 378
2. Fundamentals 379
   2.1. The column 379
   2.2. The precursor introduction 380
   2.3. Dissociation cross-section 381
   2.4. Electron trajectories inside the substrate and the deposit 382

3. Recent Research Activities 383
3.1. Resolution limit Of EBID 383
3.2. Nanowiring and electron conductivity for device applications 385
3.3. Three dimensional nanofabrication 387
3.4. Nanosize magnetic materials fabricated using EBID 389
3.5. Combination with low-energy ion etching 390
3.6. A multi-electron-beam source and an aberration corrector 391
3.7. Other applications and research activities 393
4. Conclusions 393
References 393

1. Introduction

Electron-beam induced deposition (EBID) is a nanofabrication technique in which a precursor gas is introduced to a sample, where it is decomposed by a focused electron beam, so that a nanosize structure is fabricated in the irradiated regions of the surface (Fig. 1). For example, in the case of a carbonyl precursor gas such as $W(CO)_6$, the electron irradiation decomposes the gas into W, CO, C, O and various molecular species, and W deposition occurs while the volatile materials are pumped out. If the electron beam used is well-focused, this technique produces literally nanosize deposits. The deposit grows upwards from the surface when the beam is stationed at one point, and by moving the beam, a line is produced. In reality, the size of the deposit becomes larger than that of the focused electron-beam used for several reasons, and the composition and the structure of the deposit can be degraded by

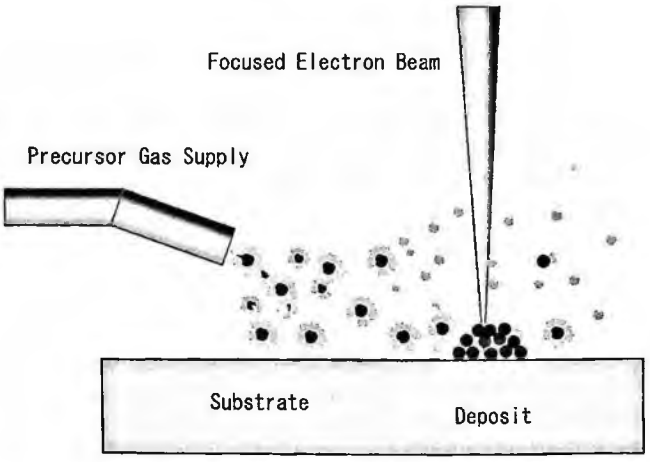

Figure 1. A schematic illustration of EBID. A precursor gas is introduced to a solid sample, and is decomposed by a focused electron beam, so that a nanosize structure is fabricated in the irradiated regions.

many factors (these features of EBID will be explained more in detail in the following chapters). However, EBID is recognized as a very promising nanofabrication technique and the amount of work devoted to this field is rapidly increasing.

The key features of EBID can be summarized as follows:

(i) The technique uses direct writing. In contrast to lithography techniques that use resist, it does not require complicated processing steps such as lift-off.
(ii) The achievable writing size is very small.
(iii) The instrumentation required is rather simple.
(iv) Three-dimensional structure fabrication is also possible.

On the other hand, the current drawbacks of EBID amount to the following:

(i) The deposit is, in many cases, an aggregation of nanocrystallites or an amorphous mixture of various oxides and carbides.
(ii) The materials available for writing are limited by the existence of appropriate precursor gases for EBID.
(iii) In comparison with resist lithography, the EBID process is slow, and so it is not suitable for a large area wiring.
(iv) Due to the high penetration depth of the high-energy electrons employed, the degree of three-dimensional fabrication possible is restricted.

Of course, many courses of action have been pursued in an effort to overcome these difficulties, as we will see in the following sections. Before introducing these efforts we will review the fundamentals of the EBID process.

The EBID method originated contamination writing as early as 1934, and so has a long history. Therefore, in this book, references are selected as new as possible. The reader can easily refer to earlier works in the comprehensive review by Koops [1].

2. Fundamentals

2.1. *The column*

The main tool used for EBID has been the scanning electron microscope (SEM) with an accelerating voltage up to 30 kV. This is because, as is discussed later, the deposition is produced mainly by low-energy electrons, such as secondary electrons, and their spatial distribution becomes wider as the primary electron energy increases. Therefore it was thought that, although the size of the probe electron beam itself shrinks for higher energy electrons, such as those used in a transmission electron microscope (TEM), the resulting deposit would be larger [2,3]. Needless to say, because of the cost and larger size of the microscope itself, and the severity of the high-voltage isolation problem in the higher voltage regime, there were few attempts to use TEM for this purpose.

For a pillar structure which is fabricated by stationing a beam at a point, the lateral size (the radius of the pillar) is dictated by the escape distance of the secondary

electrons, which is several tens of nm. An nm-size electron probe can easily be obtained by field emission (FE) SEM, therefore such an instrument is a reasonable choice for many applications. Recently, several groups have reported results that suggest that the achievable resolution by EBID can be improved by using TEM at an early stage of the deposition process [4–9].

2.2. *The precursor introduction*

The very first instances of EBID resulted from vacuum contamination, so a microscopy column with a poor quality vacuum can be used as a precursor for EBID, and many practitioners of EBID still use these contaminants as a precursor for simplicity [10–15]. However, in order to control the process more precisely, one needs to introduce a gas in a more controlled manner. The usual method used is a gas introduction system that consists of a precursor vessel, leak-valve, pipes and a nozzle (Fig. 2). The precursor tank can be heated to produce an appropriate vapor pressure which is high enough to provide an the appropriate speed of the EBID process, but is still low enough to be safely introduced to the vacuum chamber of an SEM or TEM. For a liquid or a gas phase precursor with relatively high vapor pressure, the flow can be limited by the leak valve. The nozzle directs the gas to a sample in order to keep the pressure at the sample region sufficiently high, while keeping the total amount of gas introduced small. The pipe and the nozzle are also heated to several tens of degrees above ambient to avoid the condensation of the precursor in the pipe.

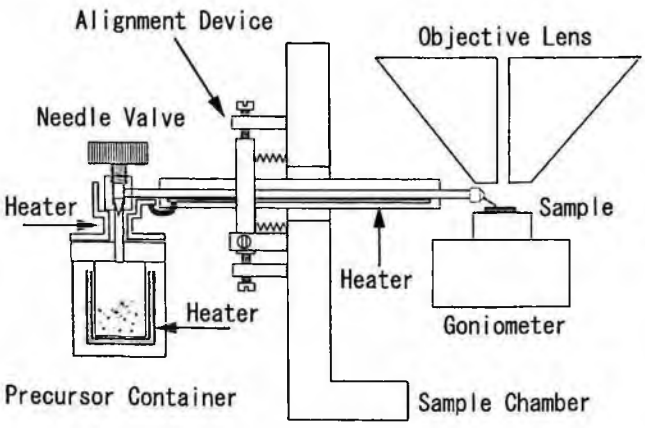

Figure 2. An illustration of a gas introduction system for EBID. The system consists of a precursor vessel, leak-valve, pipes and a nozzle. The precursor tank can be heated to provide an appropriate vapor pressure. The nozzle directs the gas to a sample in order to keep the pressure at the sample region sufficiently high, while keeping the total amount of gas introduced into the system low. To avoid condensation of the precursor in the pipe, it and the nozzle are also heated to several tens of degrees above ambient.

A simpler gas introduction system is by means of a reservoir, which is essentially a container with a small hole directed at the sample. This approach is not suitable for liquid or gaseous source, because the flow cannot be accurately controlled, however, it is still acceptable for solid sources such as $W(CO)_6$. In some applications, even bare precursor material is just placed on a sample and the depositions are performed at adjacent regions [16]. In these techniques, the precursor vapor pressure may vary with time so accurate control of the deposition condition is difficult. However, since it does not require the modification of the SEM or TEM itself, it is still used by many researchers, although precautions must be taken to avoid damage to the microscope.

2.3. *Dissociation cross-section*

The dissociation cross-section is a parameter which indicates the probability of dissociation as a function of electron energy. The shape of the dissociation cross-section is well-known for simple gases, such as, H_2, N_2, CHy, CF, etc. for the gases often used in CVD [17]. Knowledge of the cross-sections for the gases often used in EBID is still limited [18–20], but, commonly, the dissociation cross section has the shape shown in Fig. 3. In the low-energy limit, there is a threshold for dissociation, followed by a peak at several tens to 100 eV, and then a rapid decrease as the electron energy increases. Because the dissociation cross-section peaks in the low energy region, low-energy electrons, such as secondary electrons, play an important role in the EBID process, and the knowledge of the secondary electrondistribution is critical. Many studies have been performed to describe the secondary electron distribution using the Monte Carlo method [21], as described in the next section. Recently, however, the importance of the role of primary electrons has been recognized [22]. The mean free path of a low energy electron is small, so that it does not affect the deposit shape, as we shall see in the following section. Quite recently, the

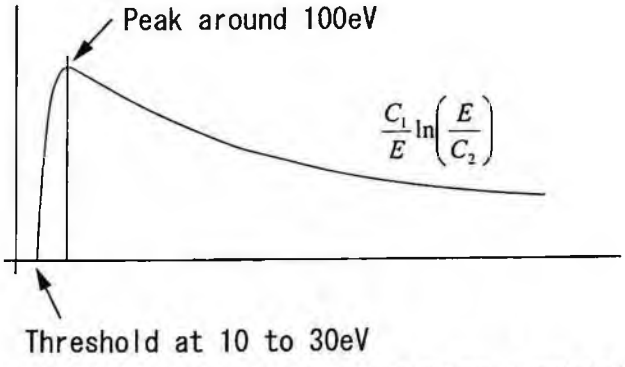

Figure 3. A schematic of the dissociation cross section, showing a typical shape. There is a threshold for dissociation at a few tens of eV, then a peak appears at around 100 eV, followed by a rapid decrease with increasing electron energy. The exact shape of the curve depends largely on precursor material used.

dissociation cross-section of WF_6 has been deduced from its ionization cross-section and the roles of primary, backscattered and secondary electrons re-examined. It was concluded that primary electrons are also playing an important role, especially in the early stages of deposition [20]. This example illustrates that a full knowledge of the energy distribution of electrons, and the dissociation cross-section is necessary.

2.4. *Electron trajectories inside the substrate and the deposit*

Primary electron injected into a substrate is scattered elastically and/or inelastically. Elastic scattering is important because, while it does not generate secondary electrons, it alters the shape of the secondary distribution. The spatial distribution of secondary electrons will be shifted to greater depth for a higher acceleration voltage of the primary electrons. There are also electrons that backscatter to the top surface, then are inelastically scattered and generate secondary electrons which emerge from the surface and contribute to the EBID process (Fig. 4). These scattering processes are complicated so that it requires some sort of simulation to understand and reproduce them. The generation of secondary electrons from materials has long been a subject of research in connection with the imaging mechanism of SEM. The simulation of these processes is usually performed by the Monte Carlo method using the fast secondary model [21]. Recently, a Dynamic Monte Carlo profile simulation was proposed by Silvis-Cividjian *et al.* [23,24] to simulate deposition by including the electron scattering inside the already-grown deposit structure. Figure 5 shows a schematic illustration of the program display window during calculation. In order to simulate the dynamic growth of a deposit, it is modeled as an aggregation of

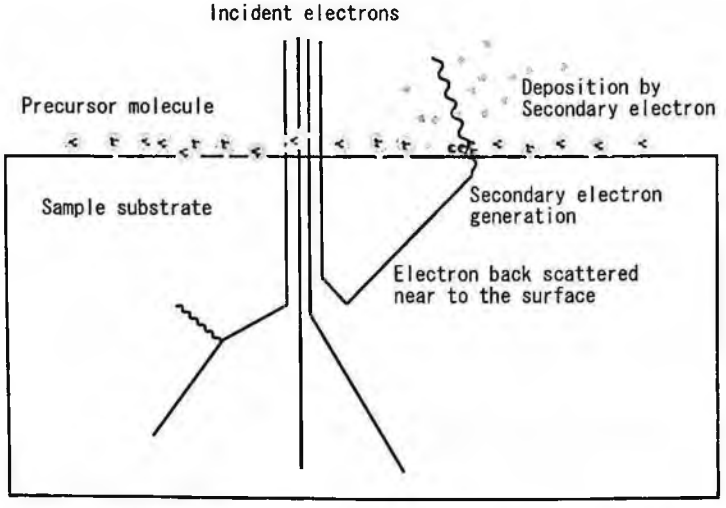

Figure 4. A schematic illustration of secondary electron emission processes that affects the deposit shape.

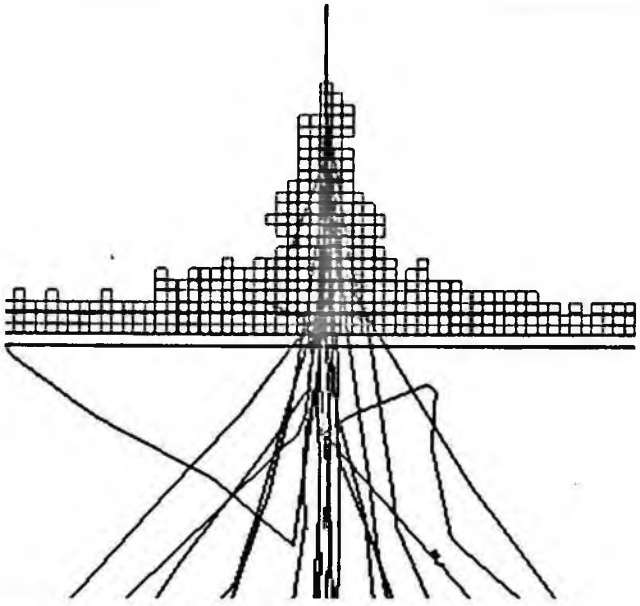

Figure 5. A schematic illustration of the EBID simulation processes. The deposit is considered as an aggregation of cubes. The electron trajectories are calculated by the Monte Carlo method; when an electron exits any of these cubes, a new cube is added with certain probability determined by the dissociation cross-section. Some of the trajectories are also shown.

cubes. In each step of the Monte Carlo calculation, the position of an electron is checked to see whether it is inside or outside any of the cubes. When an electron exits from the cubes, the interface from which the electron exits is decided by the electron's trajectory. Deposition occurs at the interface with a certain probability determined by the dissociation cross section discussed previously. This technique is used to understand various phenomena in EBID and an example will be shown later.

3. Recent Research Activities

3.1. *Resolution limit Of EBID*

Scanning transmission electron microscopy (STEM) is a technique using a TEM apparatus, in which an electron beam is focused to less than 0.2 nm at the sample position and scanned. It has attracted wide attention in the electron microscopy field because, in combination with an annular detector (which called annular dark field [ADF] STEM), an image in which the contrast corresponds to the atomic number can be obtained [25]. STEM is used by several groups to explore the resolution limit of EBID. Figure 6 (left) is an example of such an experiment in which the effect of the deposition period was examined by depositing an array of dots for various deposition times [9]. The nominal deposition time was increased from 1 ms at the upper left to 2.5 s at the lower right increasing with a 25 ms step. Figure 6 (right)

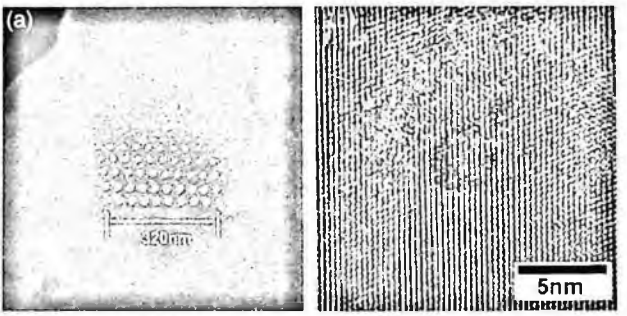

Figure 6. An example of a resolution experiment using STEM; (left): the nominal deposition time was increased from 1 ms at the upper left to 2.5 s at the lower right increasing with a 25 ms step, (right): a high-resolution electron microscopy (HREM) image of a W nanodot which was deposited for 275 ms. The observation of (200) and (111) lattice fringes of Si allows the size of the dot to be estimated as 3.5 nm. Reprinted with permission from ref. [9]. Copyright 2003, American Institute of Physics [1493790822123].

is a high-resolution electron microscopy (HREM) image of a W nanodot which was deposited for 275 ms. In the figure, (200) and (111) lattice fringes of Si are also seen. The separations of these fringes are known to be 0.27 and 0.31 nm, respectively, so the size of the dot can be calibrated accurately, and is found to be 3.5 nm. In the HREM image, no moiré like contrasts due to the interference between Si and W lattice fringes are observed. This means that the nanodots are amorphous under this deposition condition.

Tanaka *et al.* [8] used an ultra high-vacuum (UHV) TEM, and obtain a W 1.5-nm dot. By using UHV condition, the volatile materials are more efficiently pumped out, thereby reducing oxide and/or carbide contaminations in the deposit. This results in a smaller deposit size with a tighter control of the deposition period. In Fig. 7 (upper) the dots are deposited at the intersection of the lines, however the dots are so small that it is hard to distinguish them form the amorphous substrate by HREM (lower left). Only by the ADF-STEM method mentioned above can the deposit be imaged (lower right). W.F. van Drop did similar experiments [6] and obtained a minimum deposit size of 0.7 nm at full-width half maximum(FWHM). In that work, the image was also obtained by ADF-STEM, allowing the imaging of EBID deposits at a resolution level that is hard to achieve by the usual methods of electron microscopy.

It appears counter-intuitive that high-energy electrons can produce a smaller structure in spite of its wider secondary electron distribution on the sample surface. This question has been studied by simulating the deposit shapes for two different acceleration voltages of 20 and 200 kV using the Dynamic Monte Carlo simulation [22] described in the previous section. The primary electron trajectories and outlines of deposit are shown in Fig. 8. It is interesting to note that for both cases of 20 and 200 kV, the deposit profile is well overlapped by the primary electron trajectories. It is argued by many authors [3] that the deposition is mainly caused by secondary

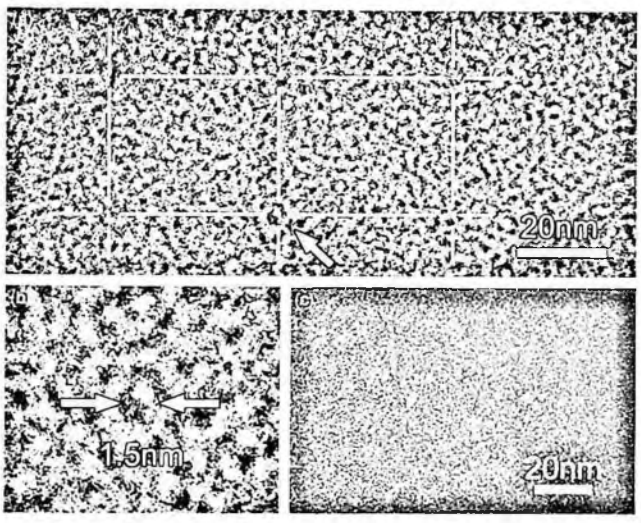

Figure 7. An example of a resolution experiment using a UHV-TEM system. The UHV condition enables the fabrication of smaller structures by reducing the amount of oxide and/or carbide contaminations in the deposit. (Upper): the dots are deposited at the intersection of the lines. (Lower left): The deposited dots are so small that it is difficult to distinguish them from the amorphous substrate. (Lower right): The resolution of the EBID method is at a level that is hard to image by the usual HREM methods and only ADF-STEM can clearly image the deposit. Reproduced with permission from ref. [8] by John Wiley & Sons Limited.

electrons generated by primary electrons. This is reasonable in view of the energy dependence of dissociation cross section. However, such low energy electrons will not travel a long distance due to their short mean free paths, although they have a high dissociation cross-section. Therefore, the overall distribution such generated low energy secondary electron is almost overlapped by the distribution of primary electrons. This means that the shape of the deposit can be roughly estimated by the trajectories of the high energy primary electrons.

3.2. *Nanowiring and electron conductivity for device applications*

EBID is a rather slow process; therefore electron beam lithography has a great advantage for a large structure. However, EBID has a "point-and-shoot" capability, so that a wiring can be made at an arbitrary desired point with nm accuracy. This ability has broadened the technique's range of application to include constructing wiring to nanosized structures fabricated by different techniques, such as dispersed carbon nanotubes (CNTs), in order to measure their properties [26,27]. In such applications, the point-and-shoot capability is crucial because the positions of the dispersed CNTs are not known in advance. A related application is to fabricate wiring to a single quantum dot or ring made by a self-assembled (SA) growth technique [28]. Figure 9 is an example of such nanowiring fabricated between a InAs quantum ring made by the SA technique and Au electrodes made by optical

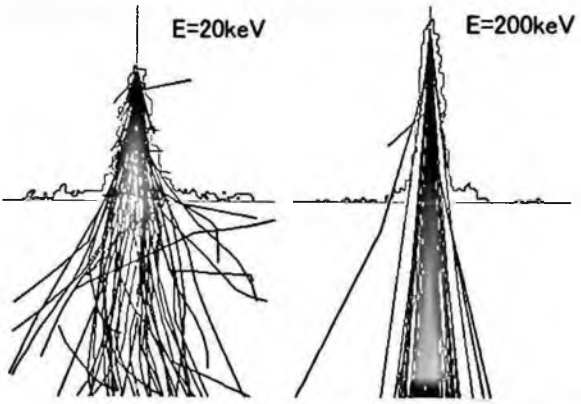

Figure 8. Dynamic Monte Carlo simulation results of the deposit s shapes for two different acceleration voltages of 20 and 200 kV. The deposit profiles and the primary electron trajectories are shown and coincide with each other for both acceleration voltages.

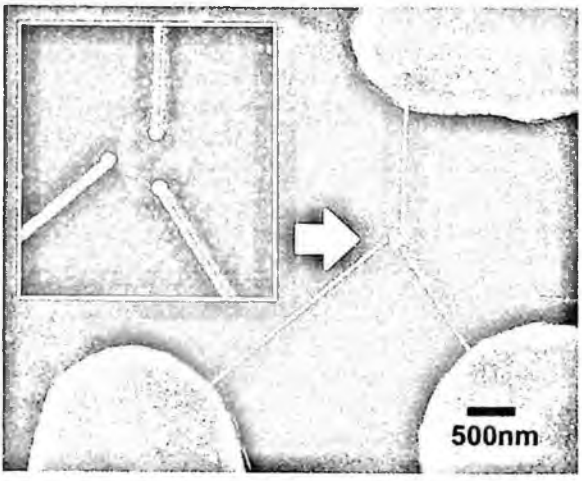

Figure 9. An example of nano-wiring fabrication between an InAs quantum ring fabricated by the SA technique and Au electrodes made by optical lithography. This arrangement is intended to allow the evaluation of the properties of a single quantum structure.

lithography. The properties of these quantum rings had previously been evaluated optically because it was not possible to contact to one single dot. Therefore the property measured was the average of a large number of quantum rings. By using EBID, it should be possible to evaluate the behavior of a single quantum structure, and even an integrated device might be possible in the near future.

The conductivity of deposits made by EBID has been studied by many authors. The best resistivity value reported for EBID deposits is one order of magnitude higher than those usually reported for bulk values. Recent references in are summarized in Table 1. A similar table for earlier works is given in the review by Koops [1].

Table 1. Electron conductivities of deposits fabricated by various precursors.

	Material	Precursor	Conductivity	Reference
1.	W	$W(CO)_6$	0.01 Ω cm	[29,30]
2.	W	WF_6	600 μΩ cm	[31]
3.	Au	$Me_2Au(tfac)$	0.01 Ω cm	[32]
4.	Au	$AuClPF_3$	22 μΩ cm	[33]
5.	Cu	HFA · ECu · EVTMS	3.63 Ω cm for 50 keV	[34]
6.	Pt	$CpPtMe_6$	1 Ω cm	[33]
7.	Co	$Co_2(CO)_8$	2 k Ω cm	[35]

Table 2. References to deposits exhibiting non-Ohmic conductivity.

	Material	Precursor	Conductivity	Reference
1.	Au/Pt	$Me_6Au(tfac)/CpPtMe_6$	Poole-Frenkel Formula	[37]
2.	Pt	$C_6H_{16}Pt$	Variable Range hopping	[38]
3.	Pt	Me_3Me	Variable Range hopping	[39]
4.	Pt	$CpPtMe_3$	Coulomb blockade	[40]

The values obtained are strongly dependent on the deposition conditions, such as the beam current, and also depend on the quality of the vacuum in the system. For example, Hiroshima *et al.* reported that the conductivity can further be improved by reducing the contamination level by O_2 plasma cleaning [36]. Besides deposits showing metallic conductivity, the preparation of non-metallic EBID deposits are starting to be reported and are summarized in Table 2.

Recently, it is was reported that deposition also occurred along the periphery the beam raster area and this was evaluated by time-of-flight secondary ion mass spectrometery (TOF-SIMS). [41]. These delocalized deposits will cause a leakage of current, and may become crucial as the size decreases. These effects need to be evaluated concurrently for EBID to become a nanowiring tool.

3.3. *Three dimensional nanofabrication*

As mentioned in an earlier section, stopping the beam at one position on the sample produces a pillar structure aligned along the beam direction. This occurs because the deposit acts as a substrate for incoming electrons, so that further growth occurs on top of previously deposited material. Effectively, once the deposit has started to form, the substrate is no longer needed. A typical example of this behavior is shown in Fig. 10, where the beam is scanned from a substrate into a vacuum region but deposition continues as the deposit acts as the substrate for the further deposition [42,43]. The lateral shape of it can be controlled freely, as shown in this figure,

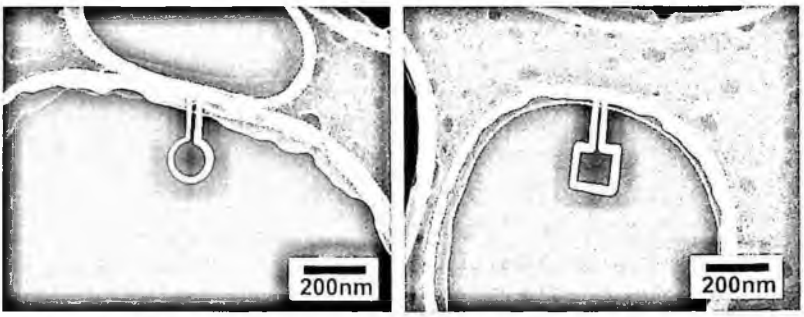

Figure 10. Self supporting nanostructures fabricated by a lateral beam scan from a carbon substrate. (Right: reprinted with permission from ref. [42] by Blackwell Publishing; Left: reprinted with permission from ref. [43] by AVS The Science & Technology Society [1493781336679].

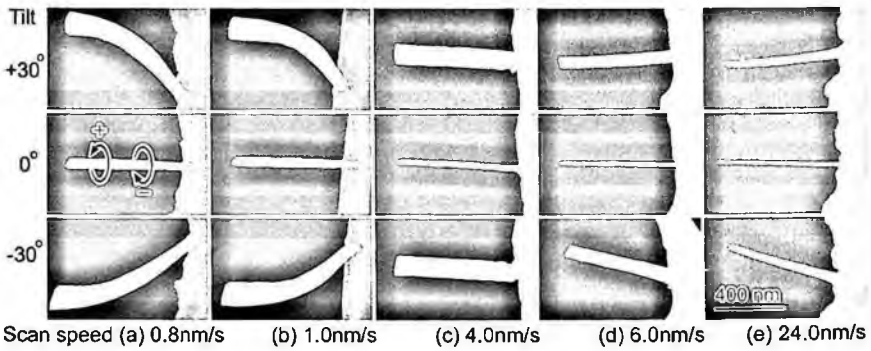

Figure 11. The growth angle dependence on the beam scan speed. SE images of the deposit by 200 kV STEM with various scan rate with 30 degree tilted images. As the scan rate increases, the lessens and eventually becomes negative in accordance with the initial downward growth due to high-energy electrons. Reprinted with permission from ref. [42]. Copyright 2004, American Institute of Physics [1493790591191].

where a circle and a square was formed. When the scan speed is slow, the deposit also grows upward. The growth angle is determined by the lateral scan speed and the vertical growth rate [44–46]. The vertical growth rate is complicated by the fact that for high-energy electrons, a deposit initially grows downwards due to the high penetration depth of the electrons. It is also affected by the precursor supply which, if it is surface diffusion limited, results in a deposition rate that is initially high and then gradually reduced falls, as seen in Fig. 11(a).

When the beam is slowly scanned on a substrate, the pillar growth of a deposit happens at the same time as that of a new deposit on the sample surface produced by the highly penetrating primary electrons. This deposit grows in the angled manner described above as the deposition proceeds while the growth angle of the initial deposit lessens. Eventually, it forms a periodic structure, such as that reported and studied by Bert *et al.* [47].

3.4. *Nanosize magnetic materials fabricated using EBID*

The patterning of nanometer-sized magnetic structures has attracted much attention because of its potential applications, such as ultrahigh density magnetic recording, nanometer-sized magnetic devices and memory cells. Furthermore, for fundamental understanding of magnetic properties in nanostructures, the fabrication of desired shapes with nanometer scale accuracy is quite important. For these purposes, gases such as, $Co_2(CO)_8$, $Fe(CO)_5$ are used. Boero *et al.* [35] used $Co_2(CO)_8$ to make a Co wire deposit which consisted of Co nanoparticles placed between Au electrodes spaced 5 μm apart to make a sub-micrometer Hall device. Lau *et al.* [48] also used $Co_2(CO)_8$ to make Co-containing nanostructures and measured their current-voltage (I-V) characteristics together with magnetic properties by means of the magnetic force microscopy (MEM) mode of scanning probe microscopy (SPM). They observed some domains that appear to be related to topographical features of the sample. Takeguchi *et al.* [49,50] reported that deposition using $Fe(CO)_5$ followed by a 600°C heat treatment produces a single crystalline alpha-iron magnetic deposit, and they also measured its magnetic properties by an electron holography technique. Due to the high spatial resolution of electron holography, the relationship between the magnetic field and the deposit shape is clearly seen in Fig. 12. This example indicates that it is possible to fabricate a magnetic material in any shape with 10-nm resolution, and further shows that electron holography is the

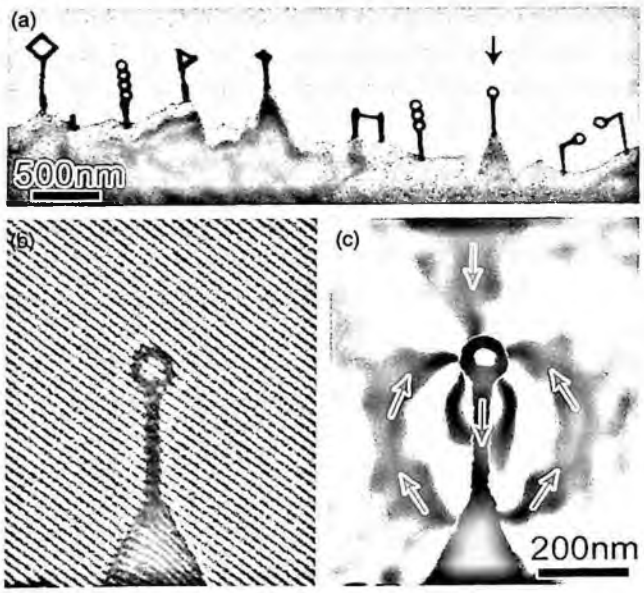

Figure 12. Nano-magnetic structures fabricated using a $Fe(CO)_5$ precursor. (A): an SEM images of the deposits. (b) an electron holography image of one deposit. (c) a reconstructed image of (b) indicating the clear relationship between magnetic field and the deposit shape. Reprinted with permission form ref. [48] by IOP Publishing Limited.

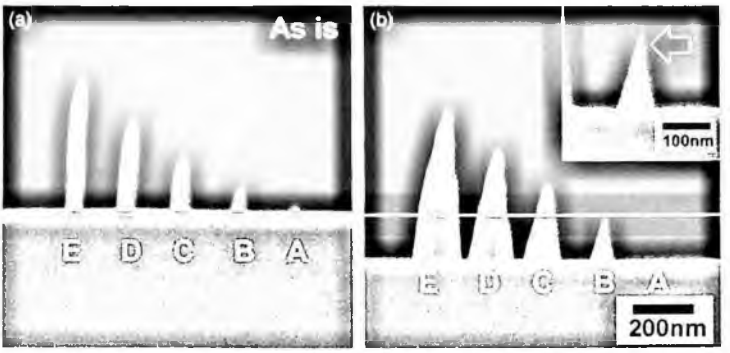

Figure 13. (a) Side view of W pillar deposited on GaAs substrate before low energy ion milling. W masks with different heights were fabricated by changing the deposition time: A, 30 s; B, 60 s; C, 90 s; D, 120 and E, 150 s. (b) The same region after a total of 10 min of ion milling at 2 kV. The white line indicates the position of the initial GaAs substrate surface, showing that the uncovered GaAs region was milled away by ion milling while the masked region remained. (Inset): Magnified image of pillar B after 10 min of ion milling. The size of the interface of the W mask and GaAs is about 8.5 nm, which is achieved by stopping the ion milling the correct time. Reprinted with permission from ref. [52] by The Institute of Pure and Applied Physics.

perfect tool to measure the magnetic properties of nanosize deposits fabricated by EBID.

3.5. *Combination with low-energy ion etching*

As we have seen, with respect to the ability to control the size and position of the deposit, EBID is achieving a sufficient level of performance. However, the use of a particular material in EBID still largely depends on the existence of an appropriate precursor gas. The gas needs to have an appropriate vapor pressure to introduce into a vacuum and, for safety, a low toxicity level and low flammability are desirable. The structure of a deposit is usually an amorphous or amorphous/polycrystalline mixture made of various oxides and carbides when tungsten carbonyl is used as the precursor gas [51], and is an aggregation of diamond-like carbon when phenanthrene ($C_{14}H_{10}$) is used [52]. Although these deposits have some electron conductivity, they are not suitable for device applications which require well controlled, highly crystalline materials. One possible approach to overcome this difficulty is to use a nanofabrication technique combining EBID and low-energy ion milling. The impetus for this idea was rooted in work in which the EBID deposits are used as a mask for reactive ion etching (RIE) [29,30,53]. In one example [54], nanosize deposits fabricated on top of a crystalline substrate by EBID are used as masks for low-energy ion milling, so that the substrate region covered with the deposits forms nanostructure. Figure 13(a) illustrates the side view of W nano-pillars fabricated on GaAs by EBID. These pillars were used as masks for low-energy ion milling, and were fabricated by changing the deposition time; A 30 s B 60 s, C 90 s D 120, and E

150 s, respectively. Figure 13(b) illustrates the same region after a total of 10 min. of ion milling at 2 kV. The white line indicates the position of the initial GaAs substrate surface showing that the uncovered GaAs region was milled away by the ions while the masked region remained intact. In order to obtain a nanostructure, the important parameter to consider is the time to stop the ion milling, not the size of the W mask, nor the height of the mask used. The inset in Fig. 13 is a magnified image of the pillar B at 10 min. ion milling, indicating that the interface of the W mask and GaAs is about 8.5 nm. This structure was achieved by stopping the ion milling at appropriate time starting with a larger diameter W mask. The use of a smaller mask diameter is still very important in order to make small structures that are very close to each other. For example, two fine nanodots that are close to each other cannot be resolved without a fine mask of a similar spacing. However, it is also significant that a nanostructure, such as a nanopillar that is less than 10 nm in diameter, can be fabricated by this method with a much larger diameter W mask if the milling process is terminated at the correct time.

3.6. *A multi-electron-beam source and an aberration corrector*

The structures fabricated by EBID we have examined so far are mainly for research purposes, and hence the relatively slow fabrication speed has not been a serious problem. However, considering that this technology has the potential to become a viable lithography technique for a fabrication node featuring less than 20 nm node in the near future, the improvement of the fabrication speed of EBID will soon become a crucial problem. To overcome this difficulty, Bruggen *et al.* [55] have studied a multi-electron-beam source. In that system, a Schottky FEG gun electrode configuration is changed such that the gun lens is replaced by one that includes an aperture/lens array making 100 beams traveling through a single column to fabricate sub-10 nm structures simultaneously.

Another way of solving the fabrication speed problem is to increase the beam current. The lenses of probe forming system suffer from spherical aberration (Cs). This sets a limit to the relationship between the beam current and the probe size. By correcting the Cs, a much wider area of the objective lens can be made usable without the effect of aberrations, meaning that a much larger aperture is available for a higher current beam, while keeping its probe size even smaller. Such a Cs correction for STEM has been established at several laboratories, and exciting results are being produced [56–58]. Recently, an ultrahigh-vacuum third-order Cs corrector for a STEM was installed at the National Institute for Materials Science (NIMS), Japan, for the purpose of EBID. The Cs corrector is of the dual hexapole type, often called the Rose/Haider type [59,60], which is commercially available (CEOS GmbH). A schematic drawing of the corrector is shown in Fig. 14. It consists of two 12–poles with different dimensions, two transfer lenses, and two sets of deflectors. The 12-pole makes rotatable hexapole-field that creates negative Cs when it

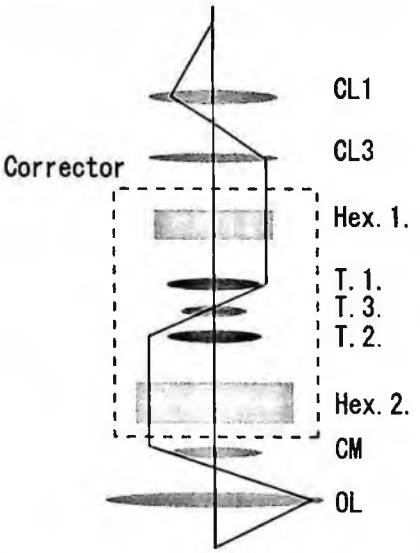

Figure 14. A schematic drawing of the Cs corrector for the probe-forming system of a STEM. It consists of two 12 poles that make hexapole fields, connected by a transfer lens doublet.

deforms the beam into three-fold shape. Another 12 pole brings the beam back to the original shape while the negative Cs remains. The application of the instrument to EBID has not yet taken place, but, as Table 3 summarizes, the expected improvement in the beam current performance is about a factor of 10 times higher, giving us hope that the machine will become a promising tool for EBID.

Table 3. A comparison of estimated probe currents between Cs-corrected and non Cs-corrected STEM at 200 kV for various probe sizes.

	Cs corrected probe current			uncorrected probe current		
Prob size(Å)	2	5	10	2	5	10
FWHM(Å)	2.2	5.2	10	2.6	5.6	10
D50(Å)	2	4.8	9.8	2.6	5.4	10.2
D75(Å)	2.6	6.8	14	4	7.8	14.6
D90(Å)	3.4	8.8	18	5.4	10.2	19
D95(Å)	3.8	9.8	20	6.4	12	21.8
Prob Current						
7×10^8 A/Strcm^2	1.6	9.9	39.8	0.143	0.895	3.85
1×10^8 A/Strcm^2	0.23	1.41	5.69	0.02	0.13	0.55
			Cs = 1μ m			Cs = 0.5 mm
			α = 40 mrad			α = 12 mrad
			Df = −1.9 nm			Df = −42.5 nm
			Cc = 1.1 mm			Cc = 1.1 mm
			ΔE = 0.7 eV			ΔE = 0.7 eV

3.7. *Other applications and research activities*

The applications of EBID are spreading widely, however, due to the page restriction, only a few examples were mentioned in earlier sections. Lithography mask repair is one of the oldest applications of EBID, and is still being improved. It is now used for mask generation for the 32-nm technology node [61]. Another typical application is as a field emission source [62]. Other newly-developed uses of EBID include wiring to a single molecule [63] to measure the conductive property of the material, soldering of CNTs [64], making photonic crystals [65,66], single electron transistors [67], and free electron lasers [68]. Details of these applications can be found in the appropriate references.

4. Conclusions

In this chapter, an overview and recent applications of EBID are briefly outlined. The technique has a long history. However, recent advances using SEM and TEM/STEM equipment have broadened the potential of the method in nanotechnology, and the number of applications is rapidly increasing in various fields. Just a glance at the applications already demonstrated leaves one with no doubt that EBID will advance vigorously into the future.

References

1. H. W. P. Koops, J. Kretz, M. Rudolph, M. Weber, G. Dahm and K. L. Lee, Characterization and application of materials grown by electron beam induced deposition: a review paper, *Jpn. J. Appl. Phys.* **33**, 7099–7107 (1994).
2. N. A. Kislov, I. I. Khodos, E. D. Ivanov and J. Barthel, Electron-beam-induced fabrication of metal-containing nanostructures, *Scanning* **18**, 114–118 (1996).
3. T. E. Allen, R. R. Kunz and T. M. Mayer, Monte-Carlo calculation of low-energy electron-emission from surfaces, *J. Vac. Sci. Technol.* **B6**, 2057–2060 (1988).
4. W. F. van Drop, B. van Someren, C. W. Harge, P. Kruit and P. A. Crozier, Statistical variation analysis of sub-5-nm-sized electron-beam-induced deposits, *J. Vac. Sci. Technol.* **B24**, 618–622 (2006).
5. N. Silvis-Cividjian, C. W. Hagen and P. Kruit, Spatial resolution limits in electron-beam-induced deposition, *J. Appl. Phys.* **98**, 084905-1-12 (2005).
6. W. F. van Drop, B. van Someren, C. W. Hagen, P. Kruit and P. A. Crozier, Approaching the resolution limit of nanometer-scale electron beam-induced deposition, *Nano Lett.* **5**, 1303–1307 (2005).
7. M. Tanaka, M. Shimojo, K. Mitsuishi and K. Furuya, The size dependence of the nano-dots formed by electron-beam-induced deposition on the partial pressure of the precursor, *Appl. Phys.* **A78**, 543–546 (2004).
8. M. Tanaka, M. Shimojo, M. Han, K. Mitsuishi and K. Furuya, Ultimate sized nanodots formed by electron beam-induced deposition using an ultrahigh vacuum transmission electron microscope, *Surf. Interface Anal.* **37**, 261–264 (2005).
9. K. Mitsuishi, M. Shimojo, M. Han and K. Furuya, Electron-beam-induced deposition using a subnanometer-sized probe of high-energy electrons, *Appl. Phys. Lett.* **83**, 2064–2066 (2003).

10. M. Nishio, S. Sawaya and S. Akita, Density of electron-beam-induced amorphous carbon deposits, *J. Vac. Sci. Technol.* **B23**, 1975–1979 (2005).
11. O. Guise, J. Ahner, J. Yates and J. Levy, Formation and thermal stability of sub-10nm carbon templates on Si(100), *Appl. Phys. Lett.* **85**, 2352–2354 (2004).
12. H. Tanaka, S. Akita, L. Pan and Y. Nakayama, Instability of field emission from a standalone multiwalled carbon nanotube with an insulator barrier, *Jpn. J. Appl. Phys.* **43**, 1651–1654 (2004).
13. T. Djenizian, B. Petite, L. Santinacci and P. Schmuki, Electron-beam induced carbon deposition used as a mask for cadmium sulfide deposition on Si(100), *Electrochimica Acta* **47**, 891–897 (2001).
14. W. Fritzsche, J. M. Köhler, K. J. Böhm, E. Unger, T. Wagner, R. Kirsch, M. Mertig and W. Pompe, Wiring of metallized microtubules by electron beam-induced structuring, *Nanotechnology* **10**, 331–335 (1999).
15. N. Miura, T. Numaguchi, A. Yamada, M. Konagai and J. Shirakashi, Single-electron tunneling through amorphous carbon dots array, *Jpn. J. Appl. Phys.* **36**, L1619–L1621 (1997).
16. W. Ding, D. A. Dikin, X. Chen, R. D. Piner, R. S. Ruoff, E. Zussman, X. Wang and X. Li, Mechanics of hydrogenated amorphous carbon deposits from electron-beam-induced deposition of a paraffin precursor, *J. Appl. Phys.* **98**, 14905-1-7 (2005).
17. H. F. Winters and M. Inokuti, Total dissociation cross-section of CF_4 and other fluoroalkanes for electron-impact, *Phys. Rev.* **A25**, 1420–1430 (1982).
18. P. Seuret, F. Cicoira, T. Ohta, P. Doppelt, P. Hoffmann, J. Weber and T. A. Wesolowski, An experimental and theoretical study of $[RhCl(PF_3)_2]_2$ fragmentation, *Phys. Chem. Chem. Phys.* **5**, 268–274 (2003).
19. T. Ohta, F. Cicoira, P. Doppelt, L. Beitone and P. Hoffmann, Static vapor pressure measurement of low volatility precursors for molecular vapor deposition below ambient temperature, *Chemical Vapor Deposition* **7**, 33–37 (2001).
20. J. D. Fowlkes, S.J.Randolph and P.D. Rack, Growth and simulation of high-aspect ratio nanopillars by primary and secondary electron-induced deposition, *J. Vac. Sci. Technol.* **B23** 2825–2832 (2005).
21. D. C. Joy, *Monte Carlo Modeling for Electron Microscopy and Microanalysis* (Oxford Series in Optical and Imaging Sciences, Oxford Univ. Press. 1995).
22. K. Mitsuishi, Z. Q. Liu, M. Shimojo, M. Han and K. Furuya, *Dynamic profile calculation of deposition resolution by high-energy electrons in electron-beam-induced deposition, Ultramicrosocopy* **103**, 17–22 (2005).
23. N. Silvis-Cividjian, C. W. Hargen, P. Kruit, M. A. J. v.d. Stam and H. B. Groen, Direct fabrication of nanowires in an electron microscope, *Appl. Phys. Lett.* **82**, 3514–3516 (2003).
24. N. Silvis-Cividjian, C. W. Hargen and P. Kruit, Spatial resolution limits in electron-beam-induced deposition, *J. Appl. Phys.* **98**, 84905-1-12 (2005).
25. S. J. Pennycook and D.E. Jesson, High-resolution incoherent imaging of crystals, *Phys. Rev. Lett.* **64**, 938–941 (1990).
26. T. Brintlinger, M. S. Fuhrer, J. Melngailis, I. Utke, T. Bert, A. Perentes, P. Hoffmann, M. Abourida and P. Doppelt, Electrodes for carbon nanotube devices by focused electron beam induced deposition of gold, *J. Vac. Sci. Technol.* **B23**, 3174–3177 (2005).
27. V. Gopal, V. R. Radmilovic, C. Daraio, S. Jin, P. Yang and E. A. Stach, Rapid prototyping of site-specific nanocontacts by electron and ion beam assisted direct-wirte nanolithography, *Nano Lett.* **4**, 2059–2063 (2004).

28. T. Mano and N. Koguchi, Nanometer-scale GaAs ring structure grown by droplet epitaxy, *J. Cryst. Growth* **278**, 108–112.
29. K. T. Kohlmann-von Platen, L.-M. Buchmann, H.-C.Petzold and W. H. Brünger, Electron-beam induced tungsten deposition: Growth rate enhancement and applications in microelectronics, *J. Vac. Sci. Technol.* **B10**, 2690–2694 (1992).
30. P. C. Hoyle, J. R. A. Cleaver and H. Ahmed, Electron beam induced deposition form $W(CO)_6$ at 2 to 20 keV, *J. Vac. Sci. Technol.* **B14** (1996) 662–673.
31. M. Komuro and H. Hiroshima, Lateral tunnel junction produced by electron-beam-induce deposition, *J. Vac. Sci. Technol.* **B15**, 2809–2815 (1997).
32. H. W. P. Koops, A. Kaya and M. Weber, Fabrication and characterization of platinum nanocrystalline material grown by electron-beam induced deposition, *J. Vac. Sci. Technol.* 2400–2403 (1995).
33. I. Utke, P. Hoffmann, B. Dwir, K. Leifer, E. Kapon and P. Doppelt, Focused electron beam induced deposition of gold, *J. Vac. Sci. Technol.* **B18**, 3168–3171 (2000).
34. Y. Ochiai, J. Fujita and S. Matsui, Electron-beam-induced deposition of copper compound with low resistivity, *J. Vac. Sci. Technol.* **B14**, 3887–3891 (1996).
35. G. Boero, I. Utke, T. Bert. N. Quack, M. Todorova, S. Mouaziz, P. Kejik, J. Brugger, R.S. Popovic and P. Hoffmann, Submicrometer Hall device fabricated by focused electron-beam-induced deposition, *Appl. Phys. Lett.* **86**, 42503-1-3 (2005).
36. H. Hiroshima, N. Suzuki, N. Ogawa and M. Komuro, Conditions for fabrication of highly conductive wires by electron-beam-induced deposition, *Jpn. J. Appl. Phys.* **38**, 7135–7139 (1999).
37. H. W. P. Koops, C. Schössler, A. Kaya and M. Weber, Conductive dots, wires, and supertips for field electron emitters produced by electron-beam induced deposition on sample having increased temperature, *J. Vac. Sci. Technol.* **B14**, 4105–4109 (1996).
38. P. G. Li, A. Z. Jin and W. H. Tang, Pt/Ga/C and Pt/C composite nanowires fabricated by focused ion and electron beam induced deposition, *Phys. Stat. Sol.* **203**(a), 282–286 (2006).
39. Z.-M. Liao, J. Xun and D.-P. Yu, Electron transport in an array of platinum quantum dots, *Phys. Lett.* **A345**, 386–390 (2005).
40. L. Rotkina, J.-F. Lin and J. P. Bird, Nonlinear current-voltage characteristics of Pt nanowires and nanowire transistors fabricated by electron-beam deposition, *Appl. Phys. Lett.* **83**, 4426–4428 (2003).
41. V. Gopal, E. A. Stach and V. R. Radmilovic, Metal delocalization and surface decoration in direct-write nanolithography by electron beam induced deposition, *Appl. Phys. Lett.* **85**, 49–51 (2004).
42. M. Shimojo, K. Mitsuishi, M. Tanaka, M. Han and K. Furuya, Application of transmission electron microscopes to nanometre-sized fabrication by means of electron beam-induced deposition, *J. Microscopy* **214** (2004) 76–79.
43. M. Shimojo, K. Mitsuishi, A. Tameike and K. Furuya, Electron induced nanodeposition of tungsten using field emission scanning and transmission electron microscopes, *J. Vac. Sci. Technol.* **B22** (2004) 742–746.
44. Z. Q. Liu, K. Mitsuishi and K. Furuya, Features of self-supporting tungsten nanowire deposited with high-energy electrons, *J. Appl. Phys.* **96**, 619–623 (2004).
45. Z. Q. Liu, K. Mitsuishi and K. Furuya, The growth behavior of self-standing tungsten tips fabricated by electron-beam-induce deposition using 200 keV electrons, *J. Appl. Phys.* **96**, 3983–3986 (2004).
46. Z. Q. Liu, K. Mitsuishi and K. Furuya, Three-dimensional nanofabrication by electron-beam-induced deposition using 200-keV electrons in scanning transmission electron microscope, *Appl. Phys.* **A80**, 1437–1441 (2005).

47. T. Bert, I. Utke, C. Gaillard and P. Hoffmann, Periodic structure formation by focused electron-beam-induced deposition, *J. Vac. Sci. Technol.* **B22**, 2504–2510 (2004).
48. Y. M. Lau, P.C.Chee, J.T.L.Thong and V. Ng, Properties and applications of cobalt-based material produced by electron-beam-induced deposition, *J. Vac. Sci. Technol.* **A20**, 1295–1302 (2002).
49. M. Shimojo, W. Zhang, M. Takeguchi, M. Tanaka, K. Mitsuishi and K. Furuya, Nanodot and nanorod formation in electron-beam-induced deposition using ion carbonyl, *Jpn. J. Appl. Phys.* **44**, 5651–5653 (2005).
50. M. Takeguchi, M. Shimojo and K. Furuya, Fabrication of magnetic nanostructures using electron beam induced chemical vapor deposition, *Nanotechnology* **16**, 1321–1325 (2005).
51. M. Han, K. Mitsuishi, M. Shimojo and K. Furuya, Nanostructure characterization of tungsten-containing nanorods deposited by electron-beam-induced chemical vapour decomposition, *Phil. Mag. 21*, **84**(12), (2004) 1281.
52. M. Ishida, J. Fujita, T. Ichihashi, Y. Ochiai, T. Kaito and S. Matsui, Focused ion beam-induced fabrication of tungsten structures, *J. Vac. Sci. Technol.* **B21**, (2003) 2728.
53. H. W. P. Koops, R. Weiel and D. P. Kern, High-resolution electron-beam induced deposition, *J. Vac. Sci. Technol.* **B6**, (1988) 477–481.
54. K. Mitsuishi, M. Shimojo, M. Tanaka, M. Takeguchi and K. Furuya, Resolution in new nanofabrication technique combining electron-beam-induced deposition and low-energy ion milling, *Jpn. J. Appl. Phys.* **44** (2005) 5627–5630.
55. M. J. van Bruggen, B. van Someren and P. Kruit, Development of a multi-electron-beam source for sub-10 nm electron beam induced deposition, *J. Vac. Sci. Technol.* **B23** (2005) 2833–2839.
56. P. E. Batson, Aberration correction results in the IBM STEM instrument, *Ultramicroscopy* **96**, (2003) 239–249.
57. M. van der Stam, M. Stekelenburg, B. Freitag, D. Hubert and J. Ringnalda, A new aberration-corrected transmission electron microscopy for a new era, *Microsc. Microanal.* **19**, (2005) 13–15.
58. H. Sawada, T. Tomita, M. Naruse, T. Honda, P. Hambridge, P. Hartel, M. Haider, C. Hetherington, R. Doole, A. Kirkland, J. Hutchison, J. Titchmarch and D. Cockayne, Experimental evaluation of a spherical aberration-corrected TEM and STEM, *J. Electron Mircoscopy* **54** (2005) 119–121.
59. M. Haider, S. Uhlemann, E. Schwan, H. Rose, B. Kabius and K. Urban, Electron microscopy image enhanced, *Nature* **392**, (1998) 768–769.
60. M. Haider, S. Uhlemann and J. Zach, Upper limits for the residual aberrations of a high-resolution aberration-corrected STEM, *Ultramicroscopy* **81**, (2000)163–175.
61. T. Liang, E. Frendberg, B. Lieberman and A. Stivers, Advanced photolithographic mask repair using electron beams, *J. Vac. Sci. Technol.* **B23** (2005) 3101–3105.
62. K. Murakami and M. Takai, Characteristics of nano electron source fabricated using beam assisted process, *J. Vac. Sci. Technol.* **B22** (2004) 1266–1268.
63. W. Fritzsche, K. Böhm, E. Unger and J. M. Köhler, Making electrical contact to single molecules, *Nanotechnology* **9**, (1998) 177–183.
64. M. Wang, J. Wang, Q. Chen and L.-M. Peng, Fabrication and electrical and mechanical properties of carbon nanotube interconnections, *Adv. Funct. Mater.* **15**, (2005) 1825–1831.

65. A. Perentes, A. Bachmann, M. Leutenegger, I. Utke, C. Sandu and P. Hoffmann, Focused electron beam induced deposition of a periodic transparent nano-optic pattern, *Microelectron. Eng.* **73–4**, (2004) 412–416.
66. H. W. P. Koops, O. E. Hoinkis, M. E. W. Honsberg, R. Schmidt, R. Blum, G. Bottger, A. Kuligk, C. Liguda and M. Eich, Two-dimensional photonic crystals produced by additive nanolithography with electron beam-induced deposition act as filters in the infrared. *Microelectron. Eng.* **57–8** (2001) 995–1001.
67. H. Hiroshima and M. Komuro, Fabrication of conductive wires by electron-beam-induced deposition, *Nanotechnology* **9**, (1998) 108–112.
68. F. Floreani, H. W. Koops and W. Elsäßer, Concept of a miniaturized free-electron laser with field emission source, *Nucl. Inst. Methods* **A483**, (2002) 488–492.

CHAPTER 12

HIGH-RESOLUTION ELECTRON-BEAM-INDUCED DEPOSITION

P. A. CROZIER*

Center for Solid State Science and School of Materials, Arizona State University, Tempe, Arizona 85287-1704, USA

C. W. HAGEN

Delft University of Technology, Faculty of Applied Sciences, Particle Optics Group, Lorentzweg 1, 2628 CJ Delft, The Netherlands

This article gives an introduction to the principles and practices of high-resolution electron-beam-induced deposition (EBID). In EBID, a small focused electron beam is used to locally dissociate a precursor onto the surface of a substrate giving rise to a small deposit. Recently it has been discovered that the size of the deposited structure can be as small as one nanometer allowing EBID to be used to fabricate very small nanostructures of arbitrary shape. EBID provides an alternative to more traditional fabrication methods such as electron beam lithography (EBL) and ion beam induced deposition (IBID). EBID is a direct write technique requiring no pre-deposited resist or development and it can be applied to planar and nonplanar surfaces. This article reviews all aspects of the technique including instrumentation, gas-solid reactions, electron-beam specimen interaction, deposition parameters and deposit composition. Special attention is devoted to factors that must be understood and controlled in order to achieve a resolution of 1 nm. Examples of very small nanostructures fabricated by performing EBID with high-energy subnanometer focused electron beams (200 kV) are demonstrated. The chapter compares and contrasts EBID with other fabrication techniques and discusses current and future applications for the technique.

Keywords: Electron-beam-induced deposition; nanofabrication; gas-solid reactions; environmental cell; fabrication; electron probe; probe formation; precursors; deposit; composition of deposit; electron-specimen interactions; secondary electrons; elastic scattering; inelastic scattering; dissociation.

*Corresponding author: Center for Solid State Science and School of Materials, Arizona State University, Tempe, Arizona 85287-1704, USA; crozier@asu.edu

CONTENTS

1. Introduction and Background 400
2. Basic Principles and Examples 401
3. Instrumentation 405
4. Factors Determining the Resolution of EBID 407
   4.1. Formation of subnanometer electron probes 407
   4.2. Interaction of electrons with molecular precursors on surfaces 409
   4.3. Interaction of electron probe with substrate 411
5. Deposition Parameters for High Resolution EBID 415
6. Deposit Composition 417
7. EBID Applications 424
8. Comparison with Other Techniques and the Future of EBID 424
Acknowledgments 426
References 426

1. Introduction and Background

In electron-beam-induced deposition (EBID), a small focused electron beam is used to dissociate a gaseous precursor adsorbed on a substrate surface. The precursor molecule can fragment into a volatile and nonvolatile component giving rise to local mass deposition. A similar technique, using a focused ion beam, is known as ion beam induced deposition (IBID) and is used routinely in focused ion beam (FIB) systems for inspection and repair of devices in the semiconductor industry. When 157 nm lithography was being developed, it was found that the gallium ions implanted in the IBID mask repair process were absorbing UV light. This problem led to an interest in EBID as an alternative mask repair technique. The technique has not been widely used for device fabrication and until recently it was assumed that the EBID resolution was limited to 10–15 nm. However, recent experimental and theoretical work has shown that, if high-energy electron beams are employed, structures as small as 1 nm can be created with this approach. Compared to the demonstrated resolution of resist-based lithography of about 10 nm, this is an improvement of an order of magnitude. Moreover, the possibility of employing multiple electron beams in parallel may make large-scale parallel processing more feasible within reasonable times [1,2]. EBID is a direct write technique requiring no pre-deposited resist or development and it can be applied to any surface. These advantages have stimulated renewed interest in EBID because of the potential applications for high resolution nanofabrication.

Electron-beam-induced deposition has always taken place inside electron beam instruments as a result of the interaction of the electron beam with the hydrocarbon vapors associated with vacuum pumps. The effect was usually unintentional and is often referred to as contamination. Contamination has been a source of considerable irritation to electron microscopists because the growing layer of deposited

material can significantly hinder sample observation. The first reports giving the correct interpretation of contamination in the electron microscope were published by Watson [3,4]. He recognized that contamination was caused by hydrocarbon adsorbed onto a substrate with subsequent polymerization by the electron beam as had been reported earlier during electron and ion irradiation [5]. Essentially the electron beam dissociated hydrocarbon vapors from the microscope pumping system leaving deposits on the sample. Though considered an annoyance for materials characterization, it was recognized that such an effect could be exploited to fabricate small structures. Christy used the technique to deposit thin insulating polymer films in the presence of a silicone oil vapor [6] and superconducting tin films from a Stannous chloride precursor [7]. Others followed and used the technique to fabricate a variety of small structures [8–10].

Since this early work, there has been ongoing research exploring and developing EBID as a direct writing technique [e.g. 11–14]. Most of the work has been carried out with electrons in the energy range 10–20 kV in instruments with architectures based on the scanning electron microscope (SEM). However, there are still many outstanding scientific questions that must be explored before EBID can be fully exploited as a tool for routine nanofabrication. The purpose of this article is to introduce the reader to the basic concepts of EBID and to illustrate its application to the fabrication of nanostructures. The article gives special emphasis to high-resolution EBID and explores some of the fundamental issues associated with fabricating structures smaller than 10 nm. A comprehensive review of EBID has been prepared by one of the authors and readers who seek more in depth treatment of the topic are referred to this review [15].

This article has been arranged to emphasize the critical issues involved in high resolution fabrication. Examples are presented demonstrating the ability of EBID to fabricate small structures of arbitrary shape. The primary requirement for high resolution fabrication is the ability to form a small focused electron beam. The critical factors in electron probe formation are described and illustrated. The dissociation processes taking place when electrons interact with adsorbed precursor molecules are discussed. Secondary electron generation and emission processes play a major role in determining the deposition rate and the resolution of the deposition process. The relationship between the spatial distribution of emitted secondary electrons and the spatial resolution of the deposit is described. The influence of deposition parameters on the deposition rate and composition are also considered.

2. Basic Principles and Examples

Electron-beam-induced deposition takes place when an electron beam dissociates a gaseous precursor resulting in the deposition of solid material onto the surface of a substrate. It is a special form of chemical vapor deposition where the location of the deposition is controlled by a focused electron beam rather than the substrate

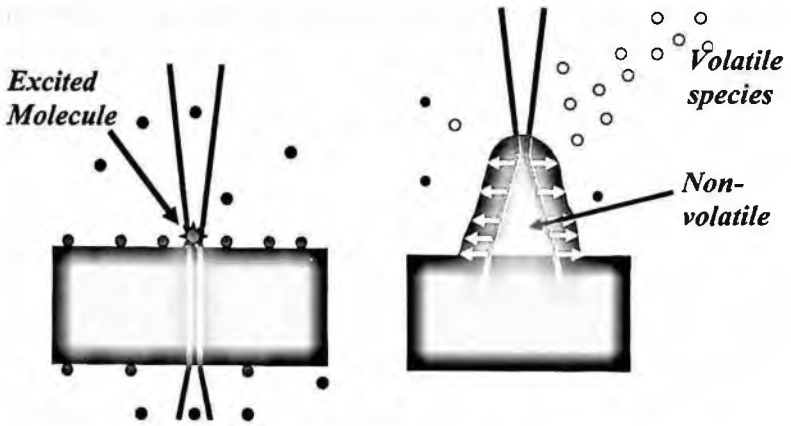

Figure 1. Schematic diagram of electron beam induced deposition. The focused fast electron excites an adsorbed precursor molecule (left panel). The excited molecule dissociates into volatile and non-volatile components. The volatile component escapes and leaves behind the non-volatile deposit (right panel).

temperature. A schematic diagram of the process is shown in Fig. 1. Precursor molecules may adsorb onto the surface of a support with a surface density per unit area of N. During electron irradiation, there is a finite probability that an adsorbed molecule in or directly around the electron beam will enter an excited state as shown by the star in Fig. 1. This excited molecule will be unstable and may relax through a dissociation process generating a volatile and non-volatile component. The volatile component escapes into the vacuum and the non-volatile component remains on the substrate surface. This process can then repeat as new precursor molecules are dissociated by additional electrons allowing the thickness of the deposit to increase. If the electron beam is highly localized (as shown in the Fig. 1), the resulting deposit will also be highly localized allowing structures to be fabricated with nanometer resolution.

One advantage of EBID is that it is easy to control the location and dwell time of the electron beam making it well suited for fabricating nanostructures of arbitrary shape. Figure 2 shows an example of nanowriting in which the Arizona State Unversity logo has been written on a 30 nm thick Si_3N_4 substrate with 2 nm dots of Pt containing deposits. The precursor used to fabricate this structure was $Pt(CH_3)_3CH_3C_5H_4$ and the letters were written with a 200 kV electron beam focused to about 0.3 nm. These structures were generated in an environmental scanning transmission electron microscope (ESTEM) equipped with a field emission electron source [16]. Each letter is only 20 nm wide and the entire logo is well resolved. More complex structures of variable height are possible on any substrate. Figure 3 shows an example of a map of the world (the "nanoworld") fabricated with a tungsten-based precursor on a Si_3N_4 substrate. The nanoworld is only 230 nm across and the writing algorithm was programmed to increase the

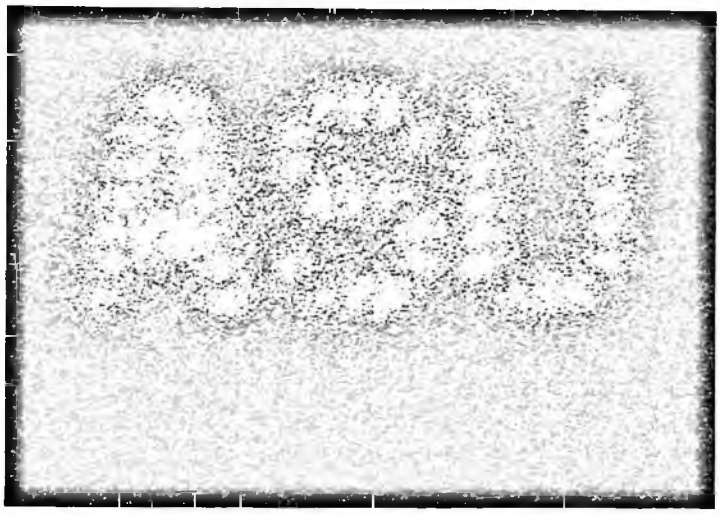

Figure 2. Z-contrast image of Arizona State University logo (ASU) drawn with a Pt-based precursor in which letters of 20 nm are clearly resolved. The letters are formed with 2 nm dots.

Figure 3. Nanoscale topographic map of the world drawn using EBID and a W precursor. The structure is imaged in Z-contrast STEM and the temperature color scheme is used to represent amount of mass deposited (black = no mass, white is greatest mass). Note the map shows the Himalayas, Rockies and Andes mountain ranges.

vertical height of the structure for selected mountain ranges. The image has been color coded to indicate the height of the structures and nicely demonstrates the presence of the Himalayas, the Andes and the Rocky mountains in the nanoworld. Fabrication of self supporting structures and deposition onto non-planar substrates has also been demonstrated [17–20].

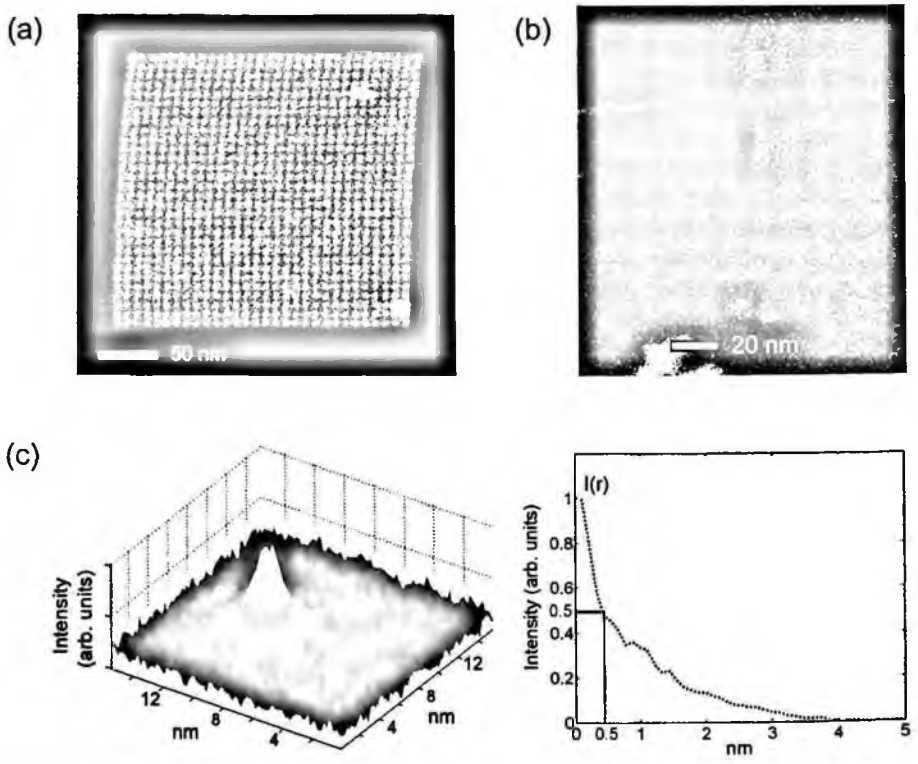

Figure 4. Z-contrast images showing arrays of 4.0 nm (a) and (b) 1.0 nm W containing dots fabricated with a $W(CO)_6$ precursor. For the smallest dots, a variation in size and position is visible. (c) Average image (left) from the dots in (b) with arbitrary units along the z-axis. The average intensity profile (right) through the center of the dot has a radius at full width half maximum (FWHM) is 0.5 nm corresponding to 1 nm dot size. (Reprinted with permission from [22] by American Chemical Society).

Recent experiments and calculations have shown that remarkably high resolution can be achieved if EBID is performed under the correct conditions. Carbon contamination dots as small as 3.5 nm have been fabricated in an SEM using a 20 kV electron beam [21]. Going to higher accelerating voltage can yield subnanometer dots. Figure 4 shows Z-contrast STEM images of periodic arrays of W containing dots fabricated with EBID. Detailed analysis of the deposits in Figure 4b shows that they have an average size of about 1 nm with the smallest deposits being about 0.7 nm [22]. Such features are an order of magnitude smaller than features fabricated with more conventional EBID instrumentation. Moreover, even though the precursor pressure and deposition time were constant, there is a significant fluctuation in the image intensity of the deposits. This fluctuation arises from the Poisson statistics associated with the small number of precursor molecules dissociating under the electron beam during the short exposure time required to make such a small object [23].

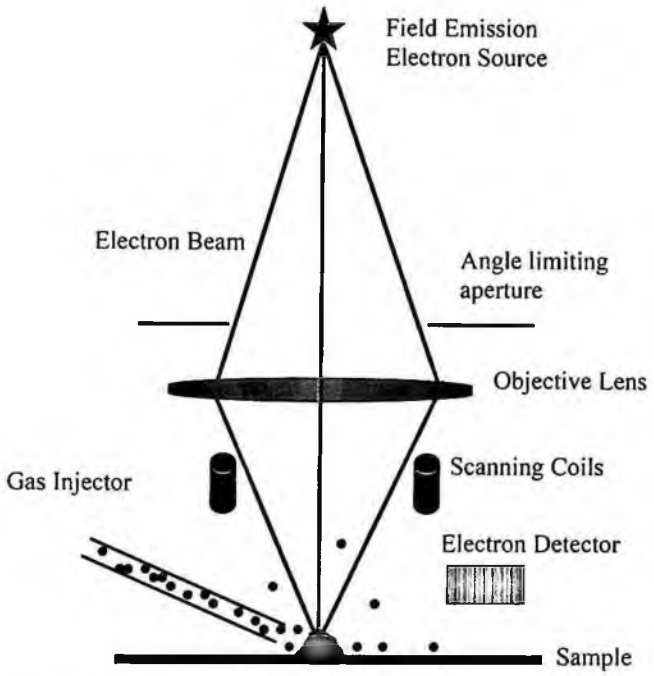

Figure 5. Basic schematic diagram of typical EBID instrumentation showing important components.

3. Instrumentation

Instrumentation for performing high-resolution EBID relies essentially on the electron optical architectures developed for high-resolution electron microscopes modified to allow gaseous precursors into the region around the sample. A simplified schematic diagram of a typical arrangement is shown in Fig. 5. It consists of an electron source, a focusing lens, a gas source, a scanning system and electron detection and imaging systems. The instrument must be operated under high vacuum conditions and for high-resolution EBID, it should be equipped with a high-brightness field-emission gun and a high-resolution objective lens. A flexible beam positioning and blanking system is also required so that patterns of arbitrary shape can be easily generated. In practice, modern systems are much more complicated with many electron lenses and alignment coils being necessary to ensure high electron optical performance. Many EBID systems are modified scanning electron microscopes (SEM) operating at accelerating voltages of 10–20 kV. The imaging detectors on such instruments are capable of detecting secondary electrons and backscattered electrons allow the morphology of the EBID structures to be visualized after fabrication [24]. The instrument may also be equipped with an energy-dispersive x-ray spectroscopy (EDX) permitting elemental analysis to be performed on the deposit

[25]. These detectors provide important tools for characterizing the deposit and provide important feedback for optimizing the deposition conditions.

The highest resolution EBID work is currently being conducted on scanning transmission electron microscopes (STEMs) [e.g. for discussion of STEM see 26,27]. These instruments typically operate at 100–300 kV and are capable of forming probes as small as 0.1 nm in size. The imaging detectors on such instruments usually detect the scattered transmitted electrons and these signals are used to form atomic-resolution bright-field or Z-contrast images. (The Z-contrast image in STEM and the backscattered image in SEM are sensitive to atomic number changes in the samples). The STEMs are usually equipped with EDX and electron energy-loss spectroscopy (EELS). EELS is particularly well suited to light element analysis and is very useful for monitoring the carbon content of deposits provided that thin film substrates are employed [28]. The powerful nanocharacterization techniques available in modern STEMs are critical for developing a deep understanding of the fundamental processes taking place during high-resolution EBID.

There are many different systems for introducing precursor gases into the region around the substrate. A critical requirement for all gas systems is that they maintain a reasonably high gas pressure around the writing area while at the same time minimizing the gas pressure reaching the field-emission electron sources. In many EBID instruments, gas is often introduced using injection systems similar to those used in focused ion beam instruments (see Fig. 5). An injection needle is brought into close proximity with the substrate surface and the precursor is allowed to flow from the tip of the needle into the sample area [29]. This approach is advantageous because it introduces a relatively small volume of gas into the system and usually does not require extra pumping capacity. One disadvantage is that the exact pressure across the sample is not well known and it varies with distance from the injection point. However, the pressure does not vary by much within a distance of several microns of the injection point making the gas pressure essentially constant over the areas typically used to fabricate nanostructures. In practice, even though in principle the deposition rate can be calculated from the gas pressure, it is usually determined empirically so that it is not really necessary to know the true pressure at the writing area. Another disadvantage is that the non-cylindrical symmetry of the syringe-type gas supply system causes the growth of 3D-structures to be dependent on the scan direction of the electron beam with respect to the gas flow direction [30].

Other methods for creating an environmental cell around the sample involve the use of differential pumping systems and windowed cells [31]. The FEI F20 Tecnai environmental STEM used to generate many of the high resolution EBID patterns shown here is based on a differentially pumped system [16]. This system is more flexible and allows the substrate to be exposed to higher gas pressures although it is a more expensive configuration. The Tecnai operates at 200 kV and is capable of forming electron probes as small as 0.2 nm. It is equipped with a Gatan Imaging Filter for EELS analysis and a Z-contrast detector and is ideally suited to the *in situ*

study of high resolution EBID. Other gas handling systems are described elsewhere [11,32,33].

4. Factors Determining the Resolution of EBID

To develop a deeper understanding of high-resolution EBID, it is necessary to consider the fundamental processes taking place in more detail. The properties of the deposit are strongly influenced by the complex electron-solid-gas interactions taking place in the deposition chamber. Although low-resolution EBID (10–15 nm or larger scale) has been discussed extensively in the literature there are many outstanding questions about the physical processes taking place during high-resolution EBID. These questions are still the subject of ongoing investigations in many laboratories around the world but a physical picture is emerging that may help to point the way forward for control of fabrication. Although many processes take place simultaneously during EBID, it is helpful to consider each process separately in order to develop an appreciation for the critical parameters controlling the fabrication of nanostructures. Interactions, between the gas layer and the solid, such as adsorption, desorption, and diffusion are not discussed in this section, as they will have more impact on the growth rate than the resolution. Three important processes controlling the resolution of the deposit are discussed in this section: electron probe formation, electron precursor interactions and electron substrate interactions.

4.1. *Formation of subnanometer electron probes*

The ultimate limit on the size of the EBID feature is determined by the electron probe size. Consequently high-resolution EBID can be performed only on instruments capable of forming small, intense beams of electrons. For much of the work described in this chapter, the electron probes are typically in the size range 0.3–2 nm and carry currents from 0.03–1 nA. The formation of such intense probes requires the use of a high-brightness electron source and at present only field-emission guns (FEG) can fulfill this requirement [34]. The brightness of the electron source determines the amount of current that can be put into the small probe and this current may control the deposition rate in the sample. Ideally we want to have a very high beam current in order to fabricate structures as rapidly as possible.

For EBID applications, the electrons emitted from the source are typically accelerated to between 20–200 kV and then focused onto a substrate. The spatial extent of the electron probe is controlled primarily by the focusing lens (usually called the objective lens) and a probe forming aperture. A schematic illustration of a typical arrangement is shown in Fig. 6(a). In order to calculate the current distribution within the electron probe it is necessary to use a wave mechanical treatment for the electrons. To simplify the mathematics, we assume that the field emission source is infinitesimally small and far enough away from the illumination aperture allowing the electron wave striking the aperture to be approximated as a plane wave. In this

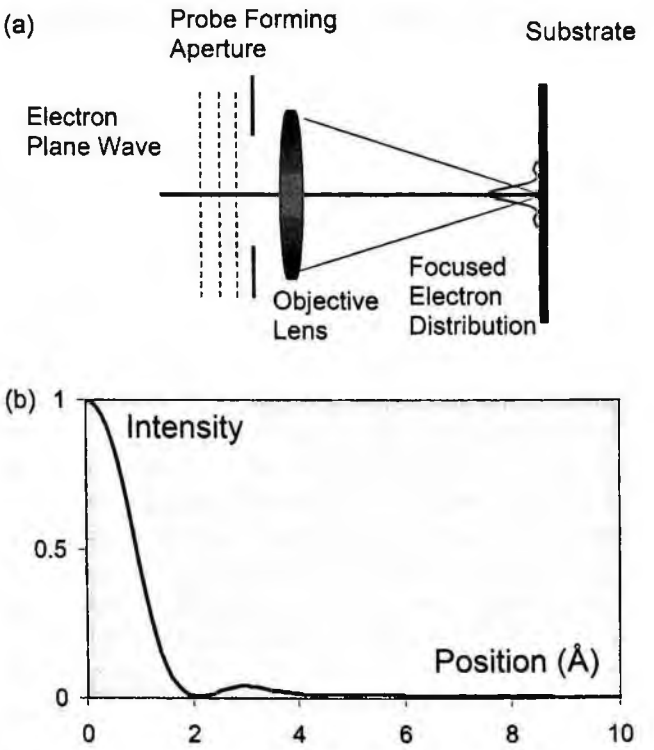

Figure 6. (a) Schematic diagram of electron probe formation and (b) intensity distribution calculated using a wave mechanical model for typical conditions in a modern STEM. Important parameters for calculation are electron energy of 200 kV and spherical aberration coefficient = 1.2 mm.

picture, the electron wavefunction W striking the aperture can be written as

$$W = Ae^{-ik.r}, \tag{1}$$

where **k** is the electron wavevector, **r** the position of the electron and **A** is a normalization constant [35]. The electron wavevector is given by $2\pi/\lambda$ where λ is the electron wavelength. After passing through the aperture, the electron propagates through the objective lens and is focused onto the object. The lens introduces phase shifts into the electron wave resulting in the generation of a convergent wave which comes to focus on the substrate. The wave function at the substrate Ψ_s is related to the electron current distribution **I**(r) through

$$I(r) = \Psi_s \Psi_s^*, \tag{2}$$

where the *stands for the complex conjugate.

A cross section through a current distribution for typical conditions used for ultra-high-resolution EBID is plotted in Fig. 6(b). Notice that the probe consists of a central maximum and a more extended tail consisting of maxima and minima.

Although most of the current is contained in the central maximum, a significant fraction may be present in the tails. Calculations show several important factors about the electron probe distribution which are relevant to EBID:

(i) There is an optimum aperture size required to minimize the diameter of the central maxima. The optimum aperture size is controlled by the aberrations in the objective lens (usually spherical aberration).
(ii) Increasing the aperture size will give higher beam current but will also transfer a greater fraction of electron intensity into the probe tails and thus increase non-local deposition in nanofabrication.

At present the smallest focused probes are formed in instruments with high accelerating voltages (about 200 kV) and high performance objective lenses (spherical aberration coefficients of 1 mm or less). These conditions are typically found in transmission electron microscopes and to date the smallest EBID structures of about 1 nm have been fabricated in these instruments [22,36–38]. Aberration correctors are currently available for modern TEMs and the smallest probe created to date is about 0.07 nm [27]. More traditional EBID systems based on SEM architectures, operate at much lower accelerating voltages (typically 5–20 kV) and produce electron probes in the range 2–5 nm. Modern SEMs equipped with field-emission electron sources are now capable of forming probes of 1 nm in size and EBID structures down to 3.5 nm have been fabricated [21]. In the next section, it will be shown that extremely small probes (less than 0.5 nm) may not improve the resolution of EBID because the broader spatial distribution of emitted secondary electrons strongly influences the size of the EBID deposit. However, aberration correction will permit dramatic increases in the current which can be put into subnanometer probes and offers the potential to significantly reduce the deposition time. Aberration correctors are also being developed for SEM type instruments and should permit similar improvements in spatial resolution and deposition rates.

4.2. *Interaction of electrons with molecular precursors on surfaces*

In order for solid material to deposit on the surface of the substrate, the gaseous precursor must dissociate into fragments with at least one non-volatile component. The primary electron beam initiates the process that leads to this dissociation although it is now widely recognized that only a small fraction of dissociations will result from direct collisions between the primary electron and the precursor molecule. In simulation and modeling of EBID, it has generally been assumed that dissociation takes place after ionization of the precursor. Figure 7 shows the ionization cross section for the common precursor germane (GeH_4) plotted as a function of incident electron energy [39]. The ionization cross sections for gas molecules typically follow a Bethe type behavior [40] with no ionization taking place below the ionization potential and the cross section reaching a maximum between 50–100 eV (for data on molecular

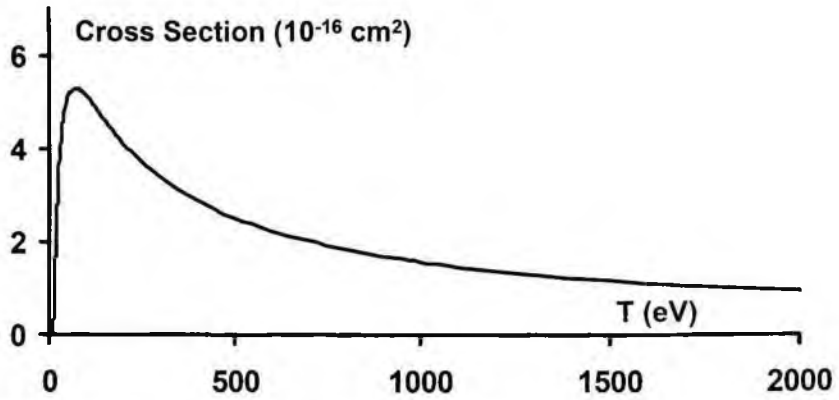

Figure 7. Ionization cross section as a function of electron energy T for germane (GeH_4) molecules calculated using the binary encounter model. Behavior is typical of many gas scattering experiments showing a peak in the ionization cross section in the range 50–100 volts. See reference [39] for details. Data available on NIST website at *http://physics.nist.gov/PhysRefData/Ionization/Xsection.html*.

ionization cross sections see *http://physics.nist.gov/PhysRefData/Ionization/Xsection.html*). The behavior shown in Fig. 7 is typical of most gas molecules, they show the same behavior with the maximum in the range 50–100 eV.

Beyond the maximum, the Bethe ionization cross section falls as approximately ln(E)/E, where E is the electron energy. Consequently, the cross section for ionization by a 200 kV electron will be as much as 3 orders of magnitude lower than the value obtained at the maximum of about 50–100 eV. The substrate emits low-energy secondary electrons in response to irradiation by the primary electron beam (as discussed in the next section). These low-energy electrons are much more likely to dissociate the precursor molecule than the high-energy primary electrons because of their high dissociation cross sections. (This is why the first step in simulating the EBID process requires detailed knowledge of the distribution in space and energy of secondary electrons leaving the surface of the substrate).

While there is general agreement that low-energy electrons play a significant role in direct precursor dissociation, there is considerable uncertainty over the dominant mechanism for dissociation. So far we have assumed that data from electron-gas scattering experiments can provide guidance for the dissociation processes taking place during EBID. However, in EBID, observations performed at different temperatures show that almost all of the deposited material comes from dissociation of *molecules adsorbed on the surface of the substrate* [41]. It is not clear how applicable the data derived from gas scattering is to molecular dissociation on substrates. Surface science studies suggest that ionization of the precursor molecules may not be a necessary step for molecular dissociation to take place. For example, dissociative electron attachment occurs when a low-energy electron attaches to a molecule and triggers dissociation [42,43]. Such processes can take place with electrons of energy

less than 5 eV. Moreover, the high local density of adsorbed molecules on the surface can result in fragments created in this electron excitation process having further collisions with neighboring adsorbates leading to additional molecular fragmentation. Recent work on organic films shows that significant dissociation takes place with low-energy electrons and UV light [44]. The cross sections for molecular dissociation from these mechanisms are comparable with or greater than the ionization cross sections and suggest that secondary electrons with energy below the ionization potential may play a significant role in precursor dissociation. This would be consistent with the observation of photo-enhanced CVD where it has been demonstrated that light can significantly accelerate the deposition process [45]. Further fundamental work is required to elucidate the various mechanisms by which low-energy electrons can dissociate adsorbed molecular precursors.

4.3. *Interaction of electron probe with substrate*

The primary electrons have energies of 20–200 kV and travel with velocities up to 0.8 times the speed of light. As these electrons approach and enter the substrate they interact with matter and various excitation and relaxation processes take place. Typically after the primary electron is scattered, the concomitant relaxation processes taking place in the substrate can result in electron, photon or atom emission from the surface. A schematic diagram of the more important processes taking place when the fast electron enters the substrate is given in Fig. 8.

When the electron enters the sample it can undergo two fundamentally different scattering processes [24,28]. With elastic scattering, the electron interacts with the atomic nucleus or crystal lattice and relatively small energy transfers take place because of the large mass difference. Elastic scattering is the process that gives rise to electron diffraction, phonon scattering and backscattering. With inelastic scattering, the electrons can also be scattered by the electrons in the solid and in this case, because the masses are equal, very large energy transfers can take place. Inelastic scattering events excite the atoms of the solid and give rise to ionization. The ionized or excited atoms are unstable and relax through either emission of photons (light or x-rays) or through emission of additional electrons (e.g. secondary or Auger electrons).

Elastic scattering has a larger angular distribution compared to inelastic scattering and it is the main process through which spreading of the primary beam occurs as the focused electron beam propagates through the substrate. Electronic excitations resulting from inelastic processes play an important role in EBID in two distinct ways. First, as described in the previous section, electronic excitation of precursor molecules is the primary path for dissociation. Secondly, electronic excitation of atoms in the substrate gives rise to the emission of low-energy secondary electrons from the surface which have a much higher probability for dissociating precursor molecules than high-energy primary electrons. Consequently the secondary electrons

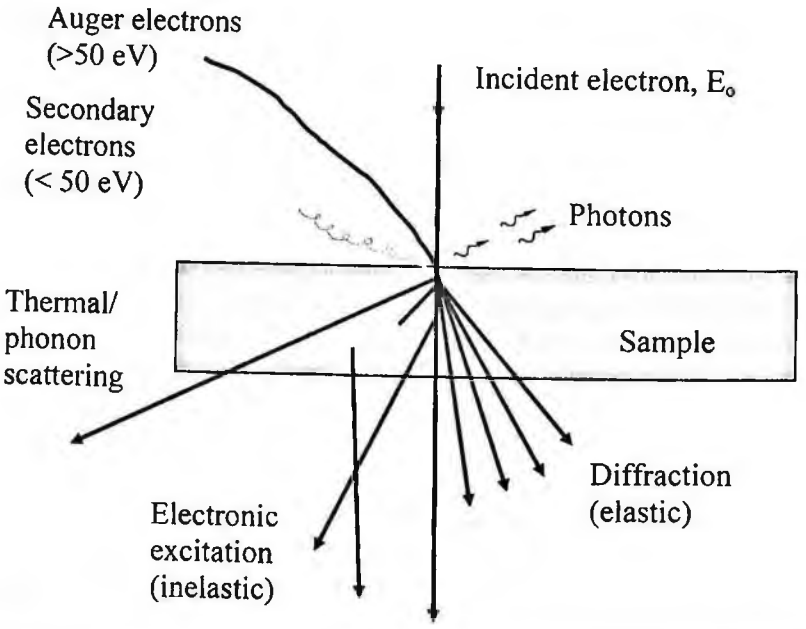

Figure 8. Schematic illustration of typical beam-specimen interactions taking place when a fast electron penetrates the substrate.

emitted from the surface of the sample are responsible for most precursor dissociation. For this reason, it is critical to have information about the spatial distribution of secondary electrons emitted from the surface since this will strongly influence the spatial resolution of the deposit.

Developing an understanding of the spatial distribution of secondary electrons is not easy but some qualitative insights can be gained by consideration of the energy dependence of both the electron mean free paths in solids and the dissociation cross sections. For simplicity it can be assumed that the dissociation cross section has a maximum for electrons with energies in the range 10–50 eV. Figure 9(a) shows the energy dependence of the mean free path for an electron traveling through a solid based on the the universal curves of Seah and Dench [46]. These curves show that the mean free paths for low-energy electrons are typically less than a nanometer. Figure 9(b) shows a possible geometry for a dissociation event. Only those secondary electrons traveling close to the surface will participate in dissociation. Secondary electrons traveling parallel to surface are likely to travel up to one mean free path from the primary beam before being scattered out of the surface. This suggests that the spatial extent of secondary emission of most importance for EBID will be on the order a few mean free paths on either side of the primary beam (i.e. a few nanometers or less).

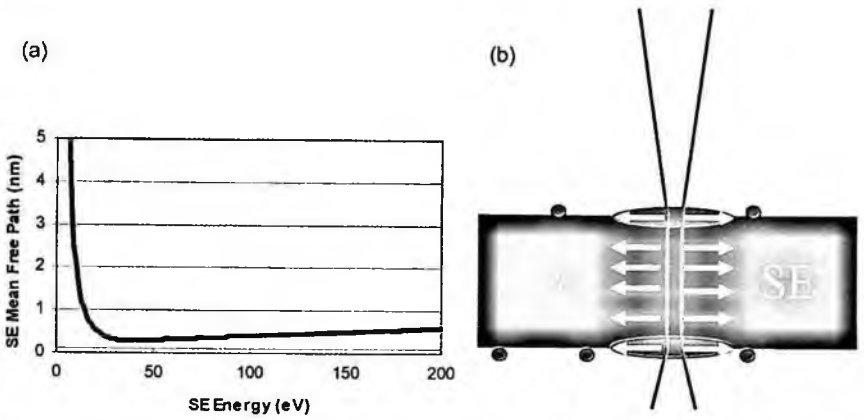

Figure 9. (a) Mean free path of electron traveling through a solid as a function of electron energy (after Seah and Dench, 1979). (b) Schematic diagram illustrating relationship between spatial distribution of emitted secondary electrons and the secondary electron mean free path.

To obtain a more fully quantitative representation of the spatial extent of the deposit and the likely deposition rate it is necessary to perform Monte Carlo simulations in which multiple scattering processes are taken into account. A detailed treatment of Monte Carlo methods is beyond the scope of this chapter and the reader is referred to the many good articles and books on this subject for EBID and SEM applications [47–52]. In the Monte Carlo treatments, a possible trajectory of an individual electron is generated from knowledge of the relative scattering probabilities for the different processes that can take place. The electron is allowed to scatter many times until almost all of the incident electron energy is depleted and its trajectory is tracked in the computer. Secondary electrons generated by the primary scattering events are tracked in a similar manner. This process is repeated for many incident primary electrons until a statistically relevant picture of the spatial scattering distributions are obtained.

Most of the Monte Carlo simulations available for electron scattering have been developed to predict the resolution of SEM images and excitation volumes generating x-ray spectra. However, for EBID it is necessary to know the energy distribution of the electrons leaving the surface since the dissociation cross sections are strongly dependent on electron energy. It is usually assumed that the secondary electrons generated during the exposure process are generated at the same location where the inelastic electron interaction took place. In reality, however, this interaction process is a de-localized process, with the delocalization being inversely proportional to the energy loss. As a result, all processes initiated by this energy loss, like the dissociation of a precursor molecule by a secondary electron, are also delocalized. Its effect on the EBID fabrication resolution was quantified by Silvis-Cividjian et. al and it was found that the delocalization does not broaden the spatial secondary electron

profile by more than 0.05 nm and therefore does not impose a fundamental limit to the EBID resolution [51].

Several treatments have been developed in order to simulate the EBID process over a range of accelerating voltages and substrate thicknesses [50–52]. Here we quote from a recent publication from one of the authors. Figure 10 shows the simulated spatial distribution of emitted secondary electrons and dissociated hydrocarbons on the surface of a Cu film. The calculation assumes that the film is perfectly smooth and thicknesses of 10 and 1000 nm have been considered (i.e. the thin film

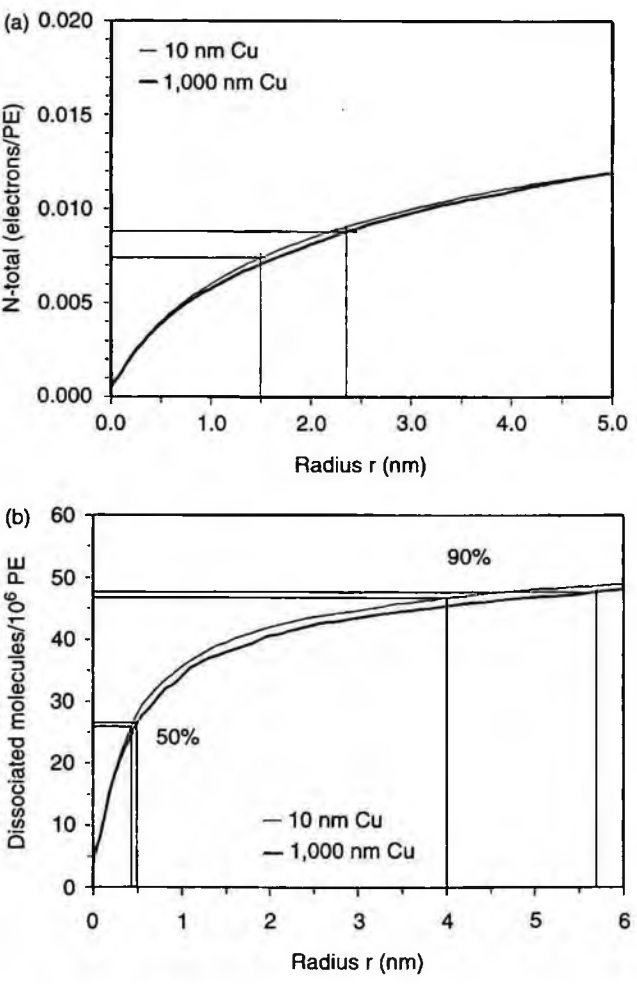

Figure 10. (a) Monte Carlo simulation showing the spatial distribution of emitted secondary electrons from a smooth Cu surface with a 200 kV electron beam of infinitely small size for a 10 nm (thin line) and 1000 nm (thick line) Cu film. (b) shows the number of dissociated molecule/primary electron (PE) as a function of position from the primary beam. 50% of the deposited mass lies within a diameter of 1 nm in both cases. (Reprinted with permission from [52] by FAMS, Inc., Mahwah, N.J., USA.)

and bulk cases). These calculations were undertaken specifically to explore the resolution limit of EBID so 200 kV electron were employed. The analysis shows that 50% of the secondary electron emission is contained in diameters of 3 and 4.7 nm for 10 and 1000 nm thick samples respectively. Similarly, 50% of the deposited mass is contained in disks of diameters of 0.86 and 1 nm respectively (Fig. 10[b]). This calculation gives a more rigorous explanation of how 1 nm resolution can be achieved using high-energy electron beams. It also demonstrates that the high resolution is not only present in thin foils used in TEM experiments but should also be achievable in bulk films. The diameter of the disk containing 50% of the mass increases by only about 15% in going from a thin film to a bulk substrate although the tail in the distribution is more pronounced in the thicker sample. Experimental measurements with 200 kV electrons comparing the size of dots deposited on thin and thick films have also shown that the size is not a strong function of substrate thickness [36].

The lack of a strong dependence of the deposit size on substrate thickness can be understood by noting that the high-energy electron beam penetrates deep below the substrate surface before significant spreading takes place. This means that the primary electron beam remains very small close to the substrate surface. The majority of the secondary electrons leaving the surface are generated within a few mean free paths of the surface. Consequently, when high-energy primary electrons are used, the spatial distribution of emitted secondary electrons should not have a strong thickness dependence provided that the sample is significantly thicker than a few mean free paths.

5. Deposition Parameters for High Resolution EBID

The rate at which material is deposited in EBID will be influenced mainly by precursor pressure, beam current, substrate temperature and secondary electron emission characteristics. The deposition rate R at position x on the substrate, expressed as volume per unit area per second, can be written as:

$$R(x) = \int_0^E f(x, E)\sigma(E)VN(x)dE, \tag{3}$$

where N(x) is the density of adsorbed precursor molecules on the surface, σ(E) is the dissociation cross section for electrons of energy E and V is the volume of the non-volatile component of the dissociated precursor species. The term f(x,E) is the flux of electrons with energy E at position x and includes the flux of primary electrons and the flux of emitted secondary and backscattered electrons. In principle, the energy integration is performed up to incident electron energy E_o but because of the strong peaking of σ(E) at lower energies, the high energy tail does not make a large contribution to the deposition rate.

Practical application of eq. (3) to simulate real EBID structures requires accurate knowledge of the physical quantities involved. As we saw in the previous section, accurate prediction of the secondary electron contribution to f(x,E) requires the use

of Monte Carlo techniques. However, the terms involved in eq. (3) can provide a basis for exploring the role of different experimental parameters on the EBID process especially in the early stages of deposition. The initial density of precursor molecules on the surface N(x) will be determined by the partial pressure of precursor in the gas phase and the temperature of the substrate. The sticking coefficient will depend on the interactions between the precursor and substrate and it will determine the average time that a precursor molecule will reside on the surface. For many precursors employed in EBID, the sticking coefficient drops with increasing temperature decreasing the density of precursor molecules on the surface. The reduction in N(x) associated with increasing temperature can be offset by increasing the pressure in the cell.

For a flat substrate, the secondary electron emission flux is directly proportional to the primary electron flux. Consequently the probability of precursor dissociation depends directly on the beam current. For example, the Monte Carlo simulations of Fig. 10(b) show that approximately 50 precursor molecules are dissociated for every 10^6 primary electrons. This is roughly in agreement with experimental values, which range from 10^5 to 10^7 electrons needed to dissociate 50 precursor molecules, depending on the precursor gas used. In a typical high resolution EBID experiment, the electron beam current is 0.01–0.1 nA. Assuming a primary electron arrival rate of 10^8 per second yields an approximate dissociation rate of 5000 molecules/s. For a nanometer sized deposition feature, such a dissociation rate would rapidly deplete the local supply of adsorbed precursor in the irradiated area. However, the concentration gradient resulting from local dissociation will result in fresh precursor diffusing into the irradiated area. The depleted area can also be replenished directly from the gas phase. For example, the number of molecules bombarding a unit area per second, φ, is readily obtained from [53]

$$\varphi = 3.513 \cdot 10^{22} \frac{p[in\ Torr]}{\sqrt{MT}} (in\ cm^{-2}\, s^{-1}), \tag{4}$$

where p is the precursor pressure in Torr, M the molecular weight, and T the gas temperature in K. For a typical precursor pressure of 0.01 Torr, and $W(CO)_6$ as a precursor (M = 352) at room temperature, this results in each nm^2 of the surface being bombarded approximately 11000 times/second. So the local bombardment rate should be sufficient to replenish the precursor species and effectively keep N(x) constant provided the sticking coefficient is above 0.5. However, at this gas pressure, increasing the beam current by more than a factor 2 may not cause the deposition rate to increase by the same factor because the precursor species will be dissociated at a greater rate than they can be replaced from the gas phase. In this case, the deposition rate is limited by the supply of precursor and significant increases in the deposition rate require corresponding increases in precursor pressure.

As the deposition continues at one point, the deposit will grow vertically and develop into a pillar. At this stage, secondary electrons can also be emitted from

the sides of the pillar causing the deposit to grow laterally as well as horizontally. The rate of mass deposition significantly increases because growth occurs over a much larger area. This pillar continues to broaden and is ultimately limited by the secondary electron escape depth for the deposited material. In practice this gives rise to the formation of pillars 10–20 nm in diameter [54].

6. Deposit Composition

The most important parameter controlling the composition of the deposit is the choice of precursor. The requirements for EBID precursors are very similar to those employed in traditional chemical vapor deposition. The molecules should be designed to dissociate into volatile and non-volatile components. If the precursor comes directly from a solid or liquid source, the vapor pressures should be high enough to ensure adequate mass transport from the precursor vessel into the deposition chamber. As described in the previous section, vapor pressures of about 0.01 Torr allow depositions to be performed at adequate speed under typical conditions. They should be easily decomposed by electron irradiation but their thermal decomposition temperatures should be greater than 200°C so that EBID depositions can be performed on moderately heated substrates to reduce contamination. Ideally the precursor should be safe to handle and should not corrode or damage the inside of the instrument. The precursor should have a reasonable sticking coefficient on the substrate but should also be relatively easy to pump out of the system when the deposition is complete. Table 1 gives a list of commonly used EBID precursors (along with their vapor pressures).

The molecular design of CVD precursors has received considerable attention in the literature because of its importance in the fabrication of compound semiconductors [e.g. 55]. Many of the considerations that apply to thermal dissociation also apply to dissociation via electron irradiation. Ideally, the molecule should be designed so that it breaks into only two components; a nonvolatile component with the desired deposit composition and a volatile component which carries away all other species in the gas phase. Some CVD precursors work very well in EBID and seem to yield products that are similar during both electron and thermal dissociation. For example, D_2GaN_3 can be successfully used to grow almost completely pure GaN deposits through the reaction [38]

$$D_2GaN_3 + e^- \rightarrow GaN(\text{solid}) + D_2 + N_2.$$

Figure 11 shows a Z-contrast image of a two dimensional periodic ordered array of GaN dots on a Si substrate fabricated using this precursor. The dots have a full width half maximum of about 4 nm and an approximate height of about 5 nm. High spatial resolution electron energy-loss spectra taken from these deposits show the presence of only Ga and N. The near-edge structure on the EELS ionization edges can be used to fingerprint the electronic structure of a compound. The EELS

Table 1. Typical Precursors Used in EBID/IBID Chemical formulae and corresponding names for EBID/IBID precursors, vapor pressure at room temperature (unless otherwise stated), and its phase (liquid L, solid S, gas G).

Material	Precursor chemical formula	Precursor name	Vapor pressure at 293 K	Phase
Al	$Al(CH_3)_3$ or $AlMe_3$	trimethyl aluminum, TMA	8.4 m bar	L
	$Al(C_4H_9)_3$	tri-isobutyl aluminum	< 1 m bar	L
	$AlCl_3$	aluminum trichloride	0.004 mbar at 323 K	S
Au	$(CH_3)_2Au(hfac)$ or Me_2Au (hfac)	dimethyl gold hexafuuoroacetylacetonate, DMG(hfac)	700 mTorr	L
	$Me_2Au(acac)$		8 mTorr	
	$Me_2Au(tfac)$	dimethyl fold acetylacetonate	40 mTorr	
	$AuCl_3$	dimethyl gold trifluoroacetylacetonate		
	PF_3AuCl	gold trichloride gold trifluorophosphine cholride		G
C	C_2H_4	ethylene		G
	C_8H_8 or $C_6H_5CH{=}CH_2$	styrene	10-25 Torr	
	$C_{16}H_10$	pyrene		
	$C_{16}H_34$	hexadecane		
	$C_{12}H_{26}$ to $C_{18}H_{38}$	liquid paraffin		L
	CH_2O_2	formic acid		L
	$C_2H_4O_2$	acetic acid		L
	$C_3H_4O_2$	acrylic acid		L
	$C_3H_6O_2$	propionic acid		L
	$C_5H_8O_2$	methyl methacrylate (MMA)		
Co	$Co_2(CO)_8$	dicobalt octacarbonyl		
Cr	$Cr(CO)_6$	chromium hexacarbonyl	10 Torr	L
Cu	$Cu(hfac)_2$	copper bis-hexafluoroacetylacetonate	0.004 mbar	G
	Cu(hfac)(DMB)	DMB = dimethylbutene	1.3 mbar	
	Cu(hfac)(MHY)	MHY = 2-methyl-1-hexen-3-yne	0.2 mbar	
	Cu(hfac)(VTMS)	VTMS = vinyltrimethylsilane	0.1 mbar	G

Fe	$Fe(CO)_5$	iron pentacarbonyl	3 Torr	G/L
	$Fe(C_5H_5)_2$	ferroceneor biscyclopentadienyl iron	0.04 mbar at 313 K	S
GaAs	$Ga(CH_3)/AsH_3$	timethyl gallium/arsine		
Ga	D_2GaN_3	perdeuterated gallium azide		
Mo	$Mo(CO)_6$	molybdenum hexacarbonyl	78 mTorr	G
Ni	$Ni(CO)_4$	nickel tetracarbonyl	10 Torr	S
	$Ni(C_5H_5)_2$	nickelocene	17 mTorr	
Os	$Os_3(CO)_{12}$	triosmium dodecacarbonyl		
Pd	$Pd(OOCCH_3)_2$	Pd-Ac, palladium acetate		
	$Pd(C_3H_5)(C_5H_5)$	palladium allylcyclopentadienyl		
Pt	$(C_5H_5)Pt(CH_3)_3$ or $CpPtMe_3$	cyclopentadienyl trimethyl platinum	54 mTorr	G
	$(CH_3C_5H_4)Pt(CH_3)_3$	methylcyclopentadienyl trimethyl platinum	54 mTorr	G
	$Pt(PF_3)_4$	trifluorophosphine platinum		
Re	$Re_2(CO)_{10}$	dirhenium decacarbonyl		
Rh	$[RhCl(CO)_2]_2$	di-μ-chloro-tetracarbonyl-dirhodium	0.25 Pa	
	$[RhCl(PF_3)_2]_2$	di-μ-chloro-tetrakis-trifluorophosphine-dirhodium	55 mTorr	S
Ru	$Ru_3(CO)_{12}$	triruthenium dodecacarbonyl		
Si	SiH_2Cl_2	dichlorosilane		
SiO_2	$Si(C_2H_5O)_4$	tetraethoxysilane (TEOS)	1.5 Torr	
SiO_x	$Si(OCH_3)_4$	tetramethoxysilane (TMS)	420 Torr	L
W	$W(CO)_6$	tungsten hexacarbonyl	17 mTorr	G
	WF_6	tungsten hexafluoride		
	WCl_6	tungsten hexachloride		

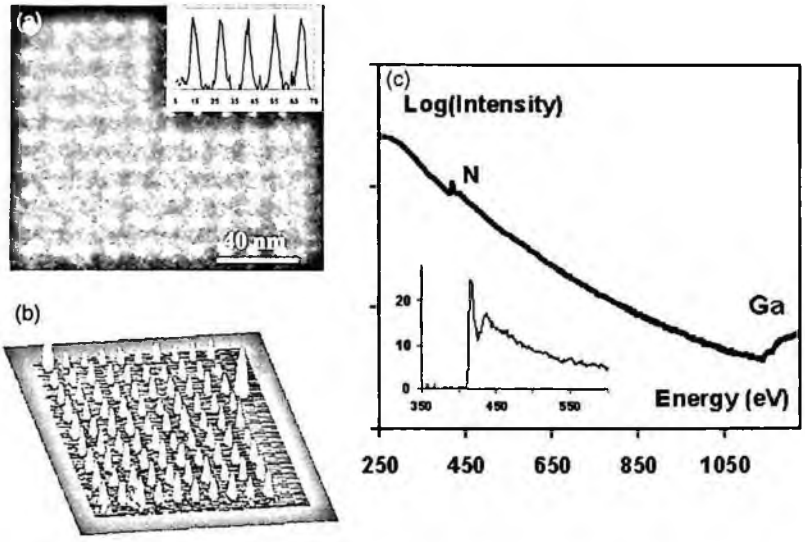

Figure 11. (a) Z-contrast image of a two-dimensional periodic array of GaN dots. Insert shows line profiles through the Z-contrast images showing FWHM of 4 nm. (b) Surface plot of array of dots showing the height of dots derived from the ADF image intensity. Average dot height 5 nm. (c) High spatial resolution electron energy-loss spectrum taken from deposit showing presence of Ga and N. Insert shows near edge structure on nitrogen K-edge which matches that of GaN. No evidence of impurity species such as carbon are present. (Reused with permission from P.A. Crozier, Applied Physics Letters, 84, 3441 (2004). Copyright 2004, American Institute of Physics.).

nitrogen signal shows a near-edge structure which matches that of GaN [56]. There is no evidence for the presence of impurity species such as carbon. A similar reaction accompanies the dissociation of digermane i.e.

$$Ge_2H_6 + e^- \rightarrow 2Ge(solid) + 3H_2$$

to yield solid Ge [57]. These precursors are ideal in the sense that the dissociation products during electron irradiation are similar to those produced by thermal dissociation.

Unfortunately, many other precursors that give pure deposits during thermal dissociation give rise to undesirable additional material in the nonvolatile component during electron dissociation. This is particularly true of precursors containing carbon. For example, $W(CO)_6$ will undergo thermal decomposition through the following reaction

$$W(CO)_6 + \text{heat} \rightarrow W(CO)_{6-n} + nCO$$

The carbonyl groups remaining in the film are easily removed through relatively gentle heating to 200°C to yield a reasonably pure film of W. However, during electron irradiation, the non-volatile component contains a very high concentration of carbon (typically greater than 80% carbon). This carbon is not in the form of

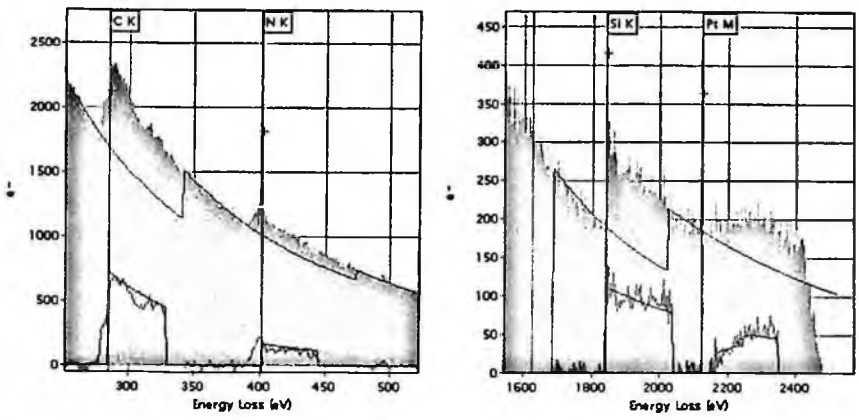

Figure 12. Electron energy loss spectra recorded from Pt deposits on a thin film of Si^3N^4. The spectrum shows the presence of carbon and Pt in the deposit and Si and N from the substrate. EELS is a convenient method to determine the carbon content of small deposits.

simple carbonyl groups and cannot be removed through heating. This phenomenon of forming a tenacious carbon compounds in the deposit seems to be almost universal when carbonaceous precursors are used. Figure 12 shows the energy-loss spectra recorded from deposits created with $Pt(CH_3)_3CH_3C_5H_4$ onto a Si_3N_4 support. The spectra show not only the expected Pt, N and Si signals but also a large C signal indicating that approximately 90% of the deposit is C. This is very similar to the C/Pt ratio in the original precursor molecule of 9:1. The high carbon content is related to the ability of the electrons to aggressively excite and activate many of the atoms in the precursor molecule making it easy to create stable forms of amorphous carbon with a high graphene component. The non-selective nature of the excitation processes taking place during electron irradiation makes it very difficult to control the formation of these energetically favorable forms of carbon.

In high-resolution EBID, even when precursors are used that do not contain carbon, significant carbon content may be found when the deposits are analyzed. This carbon comes from hydrocarbon species present in the vacuum system and on the surface of the substrate. These hydrocarbons effectively provide a second source of precursor and are also easily dissociated by the electron beam giving rise to the formation of carbon containing deposits. A focused electron beam is very effective at concentrating this form of carbon and the effect gets increasingly more pronounced as the probe size decreases. Controlling hydrocarbon contamination is essential in order to reduce the fraction of carbon in high-resolution EBID deposits. If composition control is important, an ideal solution to reduce this carbon contribution is to work only with clean substrates in ultrahigh vacuum (UHV) conditions with a fully bakeable system. In many practical cases, a UHV system is not available but every effort should be made to keep the vacuum system free from hydrocarbon contamination. This can be achieved by using oil free pumps, baking the system or purging

Table 2. Carbon concentration of Pt deposit under different conditions

Extra Gas	Temp (°C)	C/Pt Ratio
none	150	10
H_2	150	10
H_2	200	10
H_2	250	10
H_2	300	5
H_2	310	No deposition

with ultrapure nitrogen. Hydrocarbons can be removed from the substrate surface by heating in vacuum and plasma cleaning. Many of the hydrocarbons responsible for contamination are volatile and will easily desorb from the surface during heating. For this reason, lower carbon concentrations will often be obtained if deposition is carried out on a substrate heated to 150°C or higher. In addition to cleaning the substrate by heating in vacuum, it may also be beneficial to heat in reactive gases such as hydrogen or water.

The composition of the deposit can be modified by combining the precursor with an additional reactive gas or through post-deposition processing. Table 2 shows the carbon concentration of platinum containing deposits synthesized with $Pt(CH_3)_3CH_3C_5H_4$ and H_2 at different temperatures. The C/Pt concentration is determined using high spatial resolution EELS as shown in Fig. 12. For low-temperature deposition, the presence of hydrogen does not change the carbon content of the deposit (which is close the carbon concentration in the original precursor molecule). However, the carbon content drops by a factor of two when the deposition temperature reaches 300°C, presumably because hydrogen starts to gasify the carbon. Unfortunately, for this particular precursor, this high temperature is also accompanied by a significant reduction in the deposition rate because the surface residence time is shortened causing a drop in the average density of precursor molecules on the surface. This is dramatically illustrated in the last entry of Table 2 where increasing the deposition temperature to 310°C reduces the deposition rate to zero.

Post deposition processing can also be employed to modify the composition of the deposit. Electron irradiation has been used to selectively remove carbon from EBID-grown Pt nanowires [58]. Thermal treatments in oxidization environments can also be employed to remove carbon. However, great care has to be exercised when using post deposition processing on high-resolution nanostructures. Such structures can be easily modified with aggressive heating or irradiation techniques. Figure 13 shows the changes that take place in the ASU logo during aggressive heat treatment in air to remove carbon. The structure was fabricated under the conditions used for Fig. 2 and had a carbon content of 90%. Low temperature post-deposition treatments

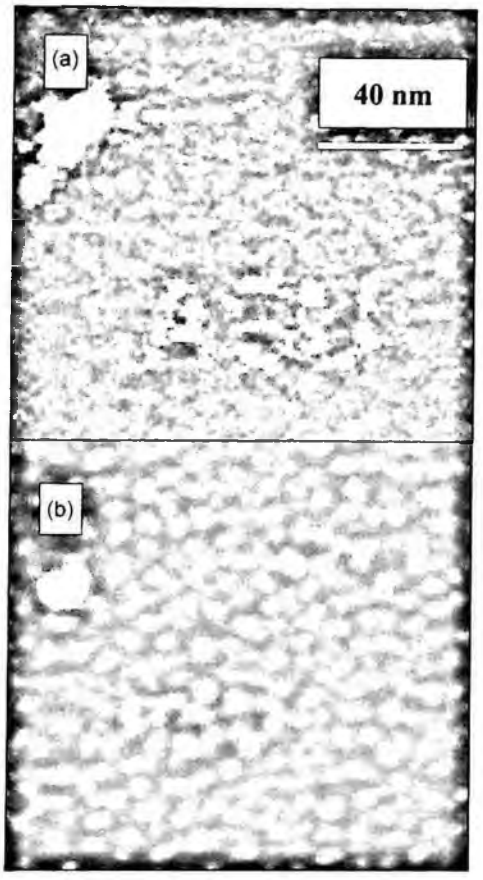

Figure 13. Morphological changes taking place in ASU logo during thermal treatment in air at 800°C after (a) 10 minutes and (b) 20 minutes.

did not prove effective for removing the carbon presumably because of the high percentage of graphitization that was present. Treatment in air at 800°C successfully removed all carbon and transformed the deposit into pure Pt. However, as Fig. 13(a) shows, even after 10 minutes of heating at 800°C the nanostructure undergoes significant coarsening and is substantially degraded. After a further 10 minutes, the nanostructure is completely destroyed by Ostwald ripening of the remaining Pt metal. Sometimes post thermal processing can also lead to the formation of compounds such as carbides in the deposits [59,60].

Composition control remains an important topic of ongoing research in the EBID community and the above discussion demonstrates that many different approaches can be adopted to modify the composition of the deposits. However, more experiments are required to map out the influence of experimental conditions for each combination of substrate and precursor.

7. EBID Applications

Most applications of EBID are found in mask repair and in the fabrication of nanostructures for nanoscience. With the continuing miniaturization of devices, the price of lithography masks is increasing exponentially. And with the feature sizes on the masks getting smaller it is inevitable that they contain defects. Therefore it is of major importance to have techniques to repair these defects. IBID has been used extensively for mask repair, but in specific applications the unavoidable implantation of gallium ions is problematic and EBID may offer an attractive alternative. But also where sub-20 nm features are wanted, EBID might be preferred over IBID because of its superior fabrication resolution. EBID has been used occasionally for mask fabrication in reactive ion etching processes. Craighead and Mankiewich [61], for instance, made such masks in contamination lithography using a 2 nm electron probe, and obtained arrays of 7 nm silver particles and 10 nm gold-palladium particles.

EBID has also been used for the fabrication of scanning probe microscopy tips, field emitters and field emitter arrays, electrical contacts, resistors, and templates. For example, the fabrication of small diameter, and high-aspect ratio, tips for scanning tunneling microscopes (STM) [62] and the fabrication of supertips on commercially available pyramidal Si_3N_4 atomic force microscopy (AFM) tips to improve imaging of narrow and steep features on surfaces [63]. Utke *et al.* successfully used EBID from a $Co_2(CO)_8$ precursor to deposit high-aspect ratio magnetic tips on AFM tips, for magnetic force microscopy [64]. Field emission tips have been made by Schössler *et al.* [65] and later Schössler and Koops [66] even fabricated a nanostructured integrated reliable high-brightness field-emission electron source, including the emitter, a resistor and the extraction electrode. A combination of FIB etching and EBID has been used to make field emitter arrays (FEA) of Pt tips deposited in gate holes [67]. High-resolution EBID can be used to make tiny electrical contacts to single molecules [68,69], or make templates for the growth of controlled arrays of semiconductor quantum dots [21]. A single electron transistor composed of three EBID dots with 20 nm spacings was reported by Komuro and Hiroshima [70,71].

What other applications could one think of for EBID? The technique may be useful in the controlled fabrication of catalysts, in nanosoldering, and in the fabrication of stamps for nanoimprint lithography.

8. Comparison with Other Techniques and the Future of EBID

What are the prospects for EBID? To answer that question one has to compare EBID with other available lithography techniques, mainly resist-based electron beam lithography (EBL) and IBID in dual beam systems.

The best resolution obtained in EBL is about 6 nm. It has been demonstrated that EBID can do better, even down to sub-nm. However, there is not really a

fundamental difference between EBL and EBID. In EBL a polymer resist layer is used, but if this layer is sufficiently thin, there is not much difference anymore with an adsorbed monolayer of precursor molecules. Consequently, in future, EBL and EBID should eventually have the same resolution.

It is usually believed that the writing speed in EBL is much faster than in EBID, being an advantage for EBL. Typical exposure doses are 1 mC/cm^2 in PMMA-based EBL for 10 nm features and 1 C/cm^2 for EBID of 1 nm features. However, when smaller structures are exposed the shot noise, i.e. the statistical variation in the number of electrons in the beam, becomes important. The signal-to-noise ratio S/N is proportional to the square root of the number of electrons in the beam, which can be expressed as $S/N = (D^*A/e)^{1/2}$, where D is the exposure dose, A the area of the beam spot and e the elementary charge. The S/N ratio decreases with decreasing spot size A and therefore, to keep the S/N ratio sufficiently large, e.g. >100, the dose has to increase correspondingly to compensate for the smaller area A. For a 1 nm area, the minimum dose to stay away from the shot noise limit is about 0.2 C/cm^2. This is more than two orders of magnitude larger than the usual EBL doses and it is not too far away from the typical doses used in EBID. Thus, for nanostructures the writing speeds of EBL and EBID are not too different.

EBID has the advantage of the direct deposition, where EBL consists of a large number of process steps (resist spinning, bake-out, exposure, development, deposition, lift-off) before the actual structure is obtained. Also, EBID can do 3D lithography on any substrate topography. EBL is limited to flat substrates only. EBID also allows *in situ* inspection of the fabricated structures, where EBL-made structures can be inspected only after all process steps have been completed. A clear advantage of EBL is that the composition of the resulting structures is well defined, whereas this is certainly not the case yet in EBID.

Now EBID is compared to its other contender, IBID. Both can fabricate 3D structures on any kind of substrate, and therefore they are quite comparable in that sense. EBID can achieve sub-nm resolution whereas the resolution of IBID is typically 10–20 nm. This is mainly due to the probe size of the focused ion beam, which is typically 7 nm in imaging mode, i.e. at very low currents. To obtain more current it is necessary to increase the probe size. Milling speed is usually considered more important than resolution, and therefore FIB systems are not optimized for high-resolution work. However, ion probe sizes in FIB's are not limited by diffraction, so in principle a sub-nm spot is possible, except that the current in such a small probe would be extremely small. That would change, though, if higher-brightness ion sources become available, and at present considerable research is being performed to develop such sources. So, there is no fundamental difference in resolution between EBID and IBID, it is only that the latter technique has not been fully developed yet.

EBID has the advantage that there are no heavy ions involved, to be implanted in the substrate. For some applications, the implanted gallium ions in FIB processing

turn out to be a real problem. However, if one could develop high-brightness gas-ion sources (for example, with Ar, or He ions) this problem would be solved and this advantage disappears. Of course using heavy ions can also be an advantage, because it enables physical sputtering of substrates, something that cannot be done with electrons. In EBID one could also remove material, but only by chemical etching using precursor etching gases. The deposition speed of IBID is approximately 10 times higher than in EBID for reasons that are not really understood at present. This is an advantage of IBID compared to EBID as long as EBID is not parallelized by using multiple beams [1,2]. Another poorly understood observation is that IBID usually results in higher-purity deposits than EBID.

What will be the far future of EBID lithography? In the long run EBID and EBL will have the similar resolutions and writing speeds. EBL will probably be the most important lithography technique for 2-dimensional structures on flat substrates, but EBID will be useful for 3-dimensional lithography on other topographic surfaces. If the fundamental limit on the resolution of IBID is imposed by the ion probe size, this can be solved by improving the ion sources and the ion optics. The gallium contamination problems can be eliminated by the development of gas-ion sources. Then there will be no fundamental difference between IBID and EBID.

At present, however, EBID has a higher resolution than EBL and IBID and it is capable of fabricating 3-dimensional structures with the extreme resolution of 1 nm, free of gallium, on any kind of substrate. The main challenge, for now and for the far future, is to improve the purity of the deposits. It is of major importance to develop a few key processes for EBID which result in pure deposits. But considering how long it took to develop PMMA-based EBL for the semiconductor industry, there is hope to develop EBID also into a full-grown lithography technique.

Acknowledgments

We are very grateful to P. Kruit for sharing his thoughts with us on the future of EBID (presented at the First International Workshop on EBID, Delft, The Netherlands, June 2006). We gratefully acknowledge the use of the environmental electron microscope in the Center for Solid State Science at Arizona State University.

References

1. M. J. van Bruggen, B. van Someren and P. Kruit, Development of a multi-electron-beam source for sub-10 nm electron beam induced deposition, *J. Vac. Sci. Technol. B* **23**, 2833–2839 (2005).
2. M. J. van Bruggen, B. van Someren and P. Kruit, Multibeam electron source for nanofabrication using electron beam induced deposition, *Microelectron. Eng.* **83**, 771–775 (2006).
3. J. H. L. Watson, An effect of electron bombardment upon carbon black, *J. Appl. Phys.* **18**, 153–161 (1947).

4. J. H. L. Watson, Specimen contamination in electron microscopes, *J. App. Phys.* **19** 110–111 (1948).
5. R. L. Stewart, Insulating films formed under electron and ion bombardment, *Phys. Rev.* **45**, 488–490 (1934).
6. R. W. Christy, Formation of thin polymer films by electron bombardment, *J. Appl. Phys.* **31**, 1680–1683 (1960).
7. R. W. Christy, Conducting thin films formed by electron bombardment of substrate, *J. Appl. Phys.* **33**, 1884–1888 (1962).
8. R. Speidel, Elektronenoptischer mikroschreiber mit magnetischer strahlablenkung unter electronenmikroskopischer arbeitskontrolle, *Optik* **23**, 125–144 (1965/1966).
9. G. Möllenstedt, R. Schief and R. Speidel, Fernsehgesteurte elektronenstrahlmikroaufzeichnung, *Optik* **27**, 488–491 (1968).
10. K.-H. Müller, Elektronen-mikroschreiber mit geschwindigkeitsgesteuerter strahlfuhrung, *Optik* **33**, 296–311 (1971).
11. H. W. P. Koops, R. Weiel, D. P. Kern and T. H. Baum, High-resolution electron-beam induced deposition, *J. Vac. Sci. Technol. B* **6**, 477–481 (1988).
12. K. I. Schiffmann, Investigation of fabrication parameters for the electron-beam-induced deposition of contamination tips used in atomic force microscopy, *Nanotechnology* **4**, 163–169 (1993).
13. K. T. Kohlman-von Platen, J. Chlebek, M. Weiss, K. Reimer, H. Oertel and W. H. Brünger, Resolution limits in electron-beam-induced tungsten deposition, *J. Vac. Sci. Technol. B* **11**, 2219–2223 (1993).
14. U. Hübner, R. Plontke, M. Blume, A. Reinhardt and H. W. P. Koops, Online nanolithography using electron beam-induced deposition technique, *Microelectro. Eng.* **57-58**, 953–958 (2001).
15. N. Silvis-Cividjian and C. W. Hagen, Electron-beam-induced nanometer scale deposition, Adv. Imag. Elec. Phys. 43, Elsevier Academic Press, ed. P. W. Hawkes, 1–235 (2006).
16. R. Sharma, P. A. Crozier, R. Marx and K. Weiss, An Environmental Transmission Electron Microscope for in-situ observation of chemical processes at the nanometer level, *Microsc. Microanal.* **9**, Supplement 02, 912–913 (2003).
17. V. V. Aristov, A. Yu Kasumov, N. A. Kislov, O. V. Kononenko, V. N. Matveev, V. A. Tulin, I. I. Khodos, Yu A. Gorbatov and V. I. Nikolaichik, A new approach to fabrication of nanostructures, *Nanotechnology* **6**, 35–39 (1995).
18. Z. Q. Liu, K. Mitsuishi and K. Furuya, Effect of focus change on the fabrication of tungsten nanowire by electron beam induced deposition, *Nanotechnology* **15**, S414–S419 (2004).
19. Z. Q. Liu, K. Mitsuishi and K. Furuya, Features of self-supporting tungsten nanowire deposited with high-energy electrons, *J. Appl. Phys.* **96**, 619–623 (2004).
20. G. Q. Xie, M. Song, K. Mitsuishi and K. Furuya, Selective tungsten deposition into ordered nanohole arrays of anodic porous alumina by electron-beam-induced deposition, *Appl. Phys.* **A 79**, 1843–1846 (2004).
21. O. Guise, J. Ahner, J. Yates and J. Levy, Formation and thermal stability of sub-10 nm carbon templates on Si(100), *Appl. Phys. Lett.* **85**, 2352–2354 (2004).
22. W. F. van Dorp, B. Someren, C. W. Hagen, P. Kruit and P. A. Crozier, Approaching the resolution limit of nanometer-scale electron beam induced deposition, *Nanolett.* **5**, 1303–1307 (2005).
23. W. F. van Dorp, B. Someren, C. W. Hagen, P. Kruit and P. A. Crozier, Statistical variation analysis of sub-5 nanometer sized electron beam induced deposits, *J. Vac. Sci. Technol.* **B 24**, 618–622 (2006).

24. L. Reimer, Scanning Electron Microscopy, Springer Series in Optical Sciences 45, Springer, Heidelberg, 1998.
25. D. C. Joy, A. D. Romig Jr and J. Goldstein, (Eds), Principles of Analytical Electron Microscopy, Springer (Plenum Press, New York, 2001).
26. S. J. Pennycook and P. D. Nellist, Impact of Electron and Scanning Probe Microscopy on Materials Research, 161–207 (Eds. D. G. Rickerby *et al*), 1999 Kluwer Academic Publishers.
27. S. J. Pennycook, M. Varela C. J. D. Hetherington and A. I. Kirkland, Materials advances through aberration-corrected electron microscopy, *MRS Bulletin* **31**, 36–43 (2006).
28. R. F. Egerton, Electron Energy-Loss Spectroscopy in the Electron Microscope, 2nd edn.(Plenum Press, New York, 1996).
29. K. T. Kohlmann, M. Thiemann and W. H. Brünger, E-beam induced X-ray mask repair with optimized gas nozzle geometry, *Microelectron. Eng.* **13**, 279–282 (1991).
30. T. Bret, I. Utke and P. Hoffmann, Influence of the beam scan direction during focused electron beam induced deposition of 3D nanostructures, *Microelectron. Engi.* **78–79**, 307–313 (2005).
31. R. Sharma and P. A. Crozier, "Environmental transmission electron microscopy in nanotechnology", in Handbook of Microscopy for Nanotechnology (Editors: N. Yao and Z. L. Wang), Kluwer Academic Publishers, New York, 531–563 (2005).
32. K. L. Lee and M. Hatzakis, Direct electron-beam patterning for nanolithography, *J. Vac. Sci. Technol.* **B 7**, 1941–1946 (1989).
33. S. Matsui and K. Mori, New selective deposition technology by electron- beam induced surface reaction, *J. Vac. Sci. Technol.* **B 4**, 299–304 (1986).
34. L. Reimer, Transmission electron microscopy; physics of image formation and micro-analysis, Springer Series in Optical Sciences 36, Springer-Verlag, Berlin, New York, 1984.
35. E. J. Kirkland, Advanced Computing in Electron Microscopy (Plenum Press, New York, 1998).
36. K. Mitsuishi, M. Shimojo, M. Han and K. Furuya, Electron-beam-induced deposition using a subnanometer-sized probe of high-energy electrons, *Appl. Phys. Lett.* **83**, 2064–2066 (2003).
37. N. Silvis-Cividjian, C. W. Hagen, P. Kruit, M. A. J. v.d. Stam, and H. B. Groen, Direct fabrication of nanowires in an electron microscope, *Appl. Phys. Lett.* **82**, 3514–3516 (2003).
38. P. A. Crozier, J. Tolle, J. Kouvetakis and Cole Ritter, Synthesis of uniform GaN quantum dot arrays via electron nanolithography of D_2GaN_3" *Appl. Phys. Lett.* **84**, 3441–3443 (2004).
39. M. A. Ali, Y.-K. Kim, W. Hwang, N. M. Weinberger and M. E. Rudd, Electron impact total ionization cross sections of silicon and germanium hydrides, *J. Chem. Phys.* **106**, 9602–9608 (1997).
40. M. Inokuti, Inelastic collisions of fast charged particles with atoms and molecules – Bethe theory revisited, *Rev. Mod. Phys.* **43**, 297–350 (1971).
41. W. Li and D. C. Joy, Study of temperature influence on electron beam induced deposition, *J. Vac. Sci. Technol.* **A 24**, 431–436 (2006).
42. E. Garand and P. Rowntree, The mechanism for hydrogen formation induced by low-energy irradiation of hexadecanethiol self-assembled monolayers, *J. Phys. Chem.* **B 109**, 12927–12934 (2005).
43. L. Sanche and L. Parenteau, Surface reactions between O_2 and hydrocarbons induced by dissociative electron attachment, *J. Chem. Phys.* **93**, 7476–7482 (1990).

44. M. N. Hedhili, B. V. Yakshinskiy, T. W. Schlereth, T. Gouder and T. E. Madey, The interactions of thiophene with polycrystalline UO_2, *Surf. Sci.* **574**, 17–23 (2005).
45. E. Maayan, O. Kreinin, D. Veinger, A. Thon, G. Bahir and J. Salzman, The role of the substrate in photoenhanced metalorganic chemical vapor deposition, *Appl. Phys. Lett.* **66**, 296–298 (1995).
46. M. P. Seah and W. A. Dench, Quantitative electron spectroscopies of surfaces: a standard data base for electron inelastic mean free paths in solids, *Surface Interface Anal.* **1**, 2–11 (1979).
47. R. Gauvin and G. Lesperance, A monte Carlo code to simulate the effect of fast secondary electrons on k_{AB} factors and spatial resolution in the TEM, *J. Microsc.* **168**, 153–167 (1992).
48. D. C. Joy, Monte Carlo Modeling for electron microscopy and microanalysis, (Oxford University Press, New York 1995).
49. N. Silvis-Cividjian, C. W. Hagen, L. H. A. Leunissen and P. Kruit, The role of secondary electrons in electron-beam-induced deposition spatial resolution, *Microelectron. Eng.* **61–62**, 693–699 (2002).
50. K. Mitsuishi, Z. Q. Liu, M. Shimojo, M. Han and K. Furuya, Dynamic profile calculation of deposition resolution by high-energy electrons in electron-beam-induced-deposition, *Ultramicroscopy* **103**, 17–22 (2005).
51. . N. Silvis-Cividjian,, C. W. Hagen and P. Kruit, Spatial resolution limits in electron-beam-induced deposition, *J. Appl. Phys.* **98**, 084905 (2005).
52. C. W. Hagen, N. Silvis-Cividjian and P. Kruit, Resolution limit for electron beam-induced deposition on thick substrates, *Scanning* **28**, 204–211 (2006).
53. A. Roth, Vacuum technology, second edition, North Holland, p. 36 (1982).
54. T. Ichihashi and S. Matsui, In situ observation on electron beam indiced chemical vapor deposition by transmission electron microscopy, *J. Vac. Sci. Technol.* **B 6**, 1869–1872 (1988).
55. J. Tolle, R. Roucka, A. V. G. Chizmeshya, P. A. Crozier, David J. Smith, I. S. T. Tsong and J. Kouvetakis, Novel synthetic pathways to wide bandgap semiconductors in the Si-C-Al-N system, *Solid State Sci.* **4/11–12**, 1509–1519 (2002).
56. N. D. Browning, I Arslan, P. Moeck and T. Topuria, Atomic resolution scanning transmission electron microscopy, *Phys. Stat. Sol.* **B 227**, 229–245 (2001).
57. S. Ketharanathan, R. Sharma, P. A. Crozier and J. S. Drucker, Electron beam induced deposition of pure nanoscale Ge, *J. Vac. Sci. Technol.* **B 24**, 678–681 (2006).
58. S. Frabboni, G. C. Gazzadi, L. Felisari and A. Spessot, Fabrication by electron beam induced deposition and transmission electron microscopic characterization of sub-10-nm freestanding Pt nanowires, *Appl. Phys. Lett.* **88**, 213116 (2006).
59. M. Takeguchi, M. Shimojo, K. Mitsuishi, M. Tanaka and K. Furuya, Nanostructures fabricated by electron beam induced chemical vapor deposition, *Superlattic. Microst.* **36**, 255–264 (2004).
60. M. Shimojo, M. Takeguchi, M. Tanaka, K. Mitsuishi and K. Furuya, Electron beam-induced deposition using iron carbonyl and the effects of heat treatment on nanostructure, *Appl. Phys.* **A 79**, 1869–1872 (2004).
61. H. G. Craighead and P. M. Mankiewich, Ultra-small particle arrays produced by high resolution electron beam lithography, *J. Appl. Phys.* **53**, 7186–7188 (1982).
62. B. Hübner, H. W. P. Koops, H. Pagnia, H. Sotnik, J. Urba and M. Weber, Tips for scanning tunneling microscopy produced by electron-beam-induced deposition, *Utramicroscopy* **42–44**, 1519–1525 (1992).
63. D. J. Keller and C. Chih-Chung, Imaging steeep, high structures by scanning force microscopy with electron beam deposited tips, *Surf. Sci.* **268**, 333–339 (1992).

64. I. Utke, P. Hoffmann, R. berger and A. Scandella, High-resolution magnetic Co supertips grown by a focused electron beam, *Appl. Phys. Lett.* **80**, 4729–4794 (2002).
65. C. Schössler, A. Kaya, J. Kretz, M. Weber and H. W. P. Koops, Electrical and field emission properties of nanocrystalline materials fabricated by electron-beam induced deposition, *Microelectron. Eng.* **30**, 471–474 (1996).
66. C. Schössler and H. W. P. Koops, Nanostructured integrated electron source, *J. Vac. Sci. Technol.* **B 16**, 862–865 (1998).
67. M. Takai, T. Kishimoto, H. Morimoto, Y. K. Park, S. Lipp, L. Lehrer, H. Frey, A. Ryssel, A. Hosono and S. Kawabuchi, Fabrication of field emitter arrayusing focused ion and electron beam induced deposition, *Microelectron. Eng.* **41–42**, 453–456 (1998).
68. A. Bezryadin and C. Dekker, Nanofabrication of electrodes with sub-5 nm spacing for transport measurements on single molecules and metal clusters, *J. Vac. Sci. Technol.* **B 15**, 793–797 (1997).
69. W. Fritzsche, J. M. Köhler, K. J. Böhm, E. Unger, T. Wagner, R. Kirsch, M. Mertig and W. Pompe, Wiring of metallized microtubules by electron-beam-induced structuring, *Nanotechnology* **10**, 331–335 (1999).
70. M. Komuro and H. Hiroshima, Lateral junction produced by electron-beam-induced deposition, *J. Vac. Sci. Technol.* **B 15**, 2809–2815, (1997).
71. M. Komuro, H. Hiroshima and A. Takechi, Miniature tunneljunction by electron-beam- induced deposition, *Nanotechnology* **9**, 104–107 (1998).

CHAPTER 13

FOCUSED ION BEAMS AND INTERACTION WITH SOLIDS

TOHRU ISHITANI*, TSUYOSHI OHNISHI, and TOSHIE YAGUCHI

Nanotechnology Products Business Group,
Hitachi High-Technologies Corporation, 882 Ichige,
Hitachinaka-shi, Ibaraki-ken, 312-8504, Japan
**ishitani-tohru@naka.hitachi-hitec.com*

A focused ion beam (FIB) was successfully applied to prepare cross-sectional samples for transmission electron microscopy (TEM), scanning TEM (STEM), scanning electron microscopy (SEM), and scanning ion microscopy (SIM). The FIB milling has been prospectively applied also to nanofabrication. The FIB allows to mill with high accuracy in positioning, being in contrast with a broad ion beam with poor accuracy. Controlling beam conditions of ion pixel-dose (or pixel dwell time) and FIB scanning direction/velocity, and sample tilt/rotation, we can extend the FIB milling from cross-sectioning to three-dimensional (3D) fabrication. We review inherent characteristics of the FIB milling such as positioning accuracy, milling speed, uniformity of cross-section, beam damage, and secondary electron emission. Discussions are mainly held from a viewpoint of interaction of ion beam with solids.

Keywords: Focused ion beam (FIB); scanning ion microscope (SIM); sputtering; elastic collision; inelastic collision; cross-sectioning; beam damage; channeling; and microsampling.

CONTENTS

1. Introduction 432
2. Focused Ion Beam 434
3. General Aspect of Ion-Solid Interaction 436
   3.1. Elastic collision 436
   3.2. Inelastic collision 440
4. Sputtering 442
5. FIB Milling 444
   5.1. Cross-sectioning and planar milling 444
   5.2. Tilt of FIB-milled section 445
   5.3. Curtain structure formed on cross sections 448

5.4. Milling speed and milling yield 449
5.5. Micro(μ)-sampling method 453
6. Beam Damage 455
7. Secondary Electron Emissions 458
7.1. SIM contrast 458
7.2. Channeling contrast 461
8. Three-Dimensional Microfabrication 463
9. Conclusion 464
Acknowledgments 465
References 465

1. Introduction

Focused ion beam (FIB) is a focused beam (in diameter from a few nm to a few μm, with currents from 1 pA to several tens of nA) of positive ions with energies ranging from a few keV – 50 keV. The FIB plays a role of primary beam in scanning ion microscope (SIM), which produces images of sample surfaces using secondary electrons emitted from the sample, like an electron beam in scanning electron microscope (SEM). The SIM imaging plays an important role in a whole series of processes from specifying the milling area, to monitoring the milling in real-time, and to visually confirming the completion of milling. Being 'stress-free' in addition to 'site-specific', the FIB-milling has been successfully applied to prepare cross-sectional samples for electron microscopes such as transmission electron microscope (TEM), scanning TEM (STEM), and SEM.

FIB-assisted deposition (FIB-AD) and FIB-assisted etching (FIB-AE), which bring about material deposition and enhanced material removal, respectively, are similar in that the FIB interacts with a gas phase chemical precursor adsorbed on the sample surface. For device repair, the FIB-AD and the FIB milling have been actively used to wire conductive lines and disconnect them, respectively.

FIB-milled sections are typically shown in Figs. 1(a)–(d) for the following various samples: (a) and (b) a silicon (Si) device, (c) a diatom [1], and (d) a human hair [2]. Another example is about 0.1 μm-thick sample preparation at specified position for TEM and STEM. Figure 2 shows an STEM image of the thin section prepared at the just center of one particle with X-ray mapping images taken using an EDX (Energy Dispersive X-ray) spectrometers. The particles are color magnetic stratified particles for color printers. There are no technique to cut out thin samples with such a high positional accuracy and stress-free except for the FIB milling. Main characteristics of the FIB milling are itemized below.

(i) Site-specific milling or cross-sectioning with high positional accuracy
(ii) Stress-free milling
(iii) Non-thermal and directional milling using ion beam sputtering

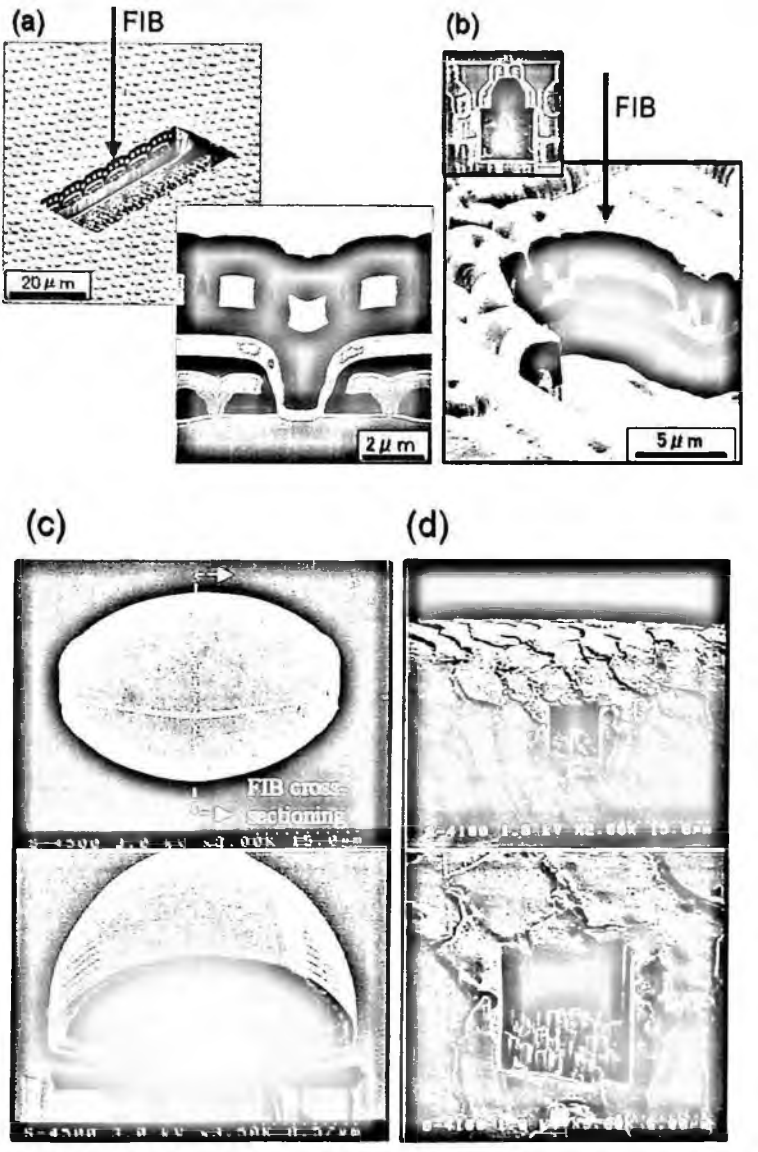

Figure 1. Typical examples of the FIB-milled sections for various samples: (a) and (b) a silicon (Si) device, (c) a diatom (Courtesy of T. Nagumo of The Nippon Dental University), and (d) a human hair.

(iv) Little restriction on sample materials (i.e., hard/soft and/or fragile/ flexible materials)

Visual processing from the set of milling area to the confirmation of milling performed in one FIB apparatus.

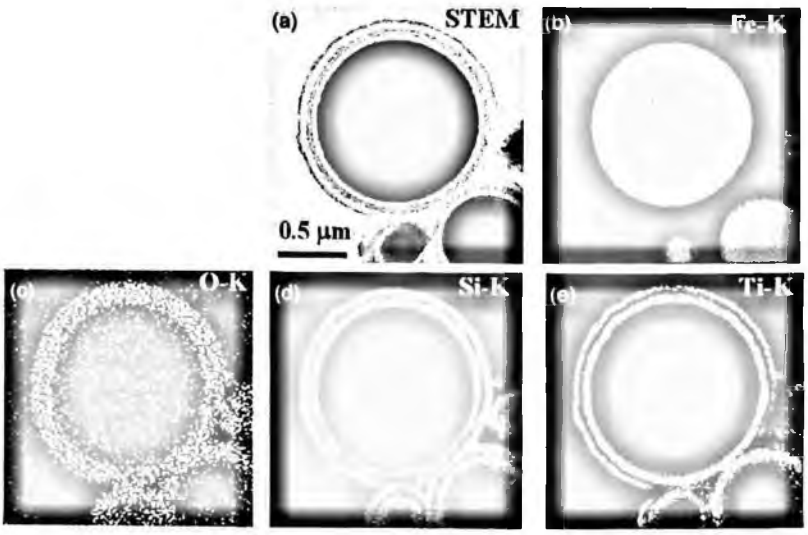

Figure 2. STEM specimen (about 0.1 μm in thickness) FIB-prepared from one of color magnetic particles used in color printers: (a) STEM image and (b)–(e) X-ray (Fe-K, O-K, Si-K, and Ti-K) mapping images taken using an EDX (Energy Dispersive X-ray) spectrometers (probe diameter ≈0.5 nm, acquisition time = 8 min, and beam accelerating voltage = 200 kV): The particles were embedded in a resin and one of the particles was sectioned just at the center of the particle using FIB-milling.

All the processes of FIB-milling, imaging, and material deposition are strongly managed by nature of the ion–solid interactions. We review inherent characteristics of the FIB milling such as positioning accuracy, milling speed, uniformity of cross-section, and beam damage. Discussions are mainly held from a viewpoint of interaction of ion beam with solids. On the FIB technologies and their applications, there are other valuable review articles [3–7], special issues [8], and books [9,10].

2. Focused Ion Beam

The FIB optical system [11] basically consists of a liquid metal ion source (LMIS), two electrostatic lenses (i.e., condenser and objective lenses), beam limiting aperture, and beam deflector as shown schematically in Fig. 3. The ion source is a needle-type LMIS (see Fig. 4), of which the needle tip is 2–5 μm in radius and is wetted with the molten source material of gallium (Ga). When positive voltage applied to the needle with regard to the extractor electrode rises to several kV, a high electric field is formed at the wetted needle tip and causes the liquid Ga to form a point source in the shape of a "Taylor cone." The conical shape results from a balance between the electrostatic and surface tension forces. The source material is extracted as ions from the cone top under the high electric field of about 10^{10} V/m. The liquid Ga flows from the source reservoir to the needle top to continuously replace the evaporated ions. The gallium is most popularly used as the

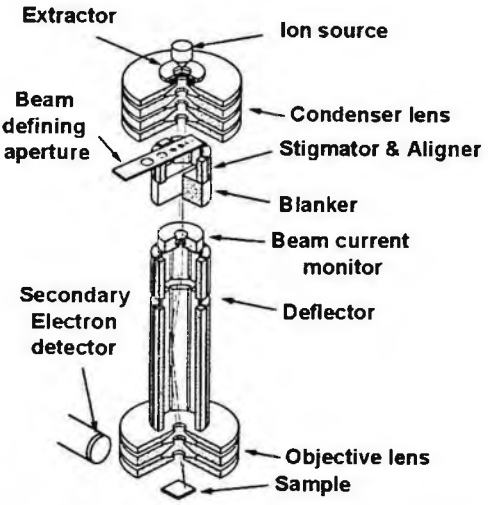

Figure 3. Schematic diagram of an FIB optical system.

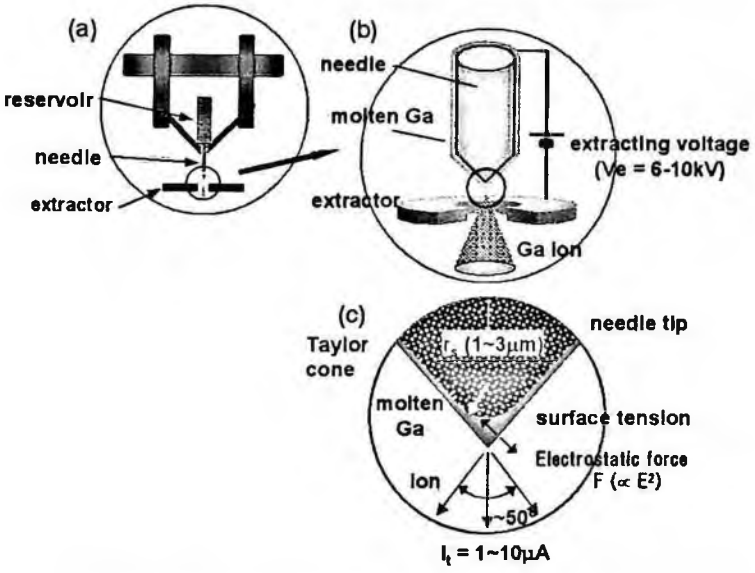

Figure 4. Schematic diagram of a needle-type LMIS.

source material because of the following reasons: the low melting point of 29.8°C, the low vapor pressure ($<10^{-6}$ Pa) at the melting point, the good wet-ability with tungsten (W) needle, little chemical reaction with the W needle, and the easy handling. Another reason is the atomic mass of 69.72 amu, of which ion is enough heavy to sputter away the target atoms. But, implantation of the Ga ions brings to an elemental contamination.

Two electrostatic lenses are adjusted so as to form a high current-density beam at each beam-limiting aperture. The 30–40 keV FIBs (for a set of apertures of various diameters) vary from 5 nm to 1 μm in diameter (about 2.5 orders) and vary from 1 pA to 50 nA in current (about 4.5 orders) for the corresponding apertures. The beam deflector deflects or scans the FIB at the preset scanning speed (or the preset dwell time on the pixel) in the specified area on the sample. As to the ion beam focusing, diffraction effect accompanied with the electron focusing in SEM is negligible in practical use.

3. General Aspect of Ion-Solid Interaction

Ion beam irradiation on a solid target sputters target atoms and generates secondary electrons and ions. The sputtering is used for ion milling. The secondary electrons are detected to form SIM images. The secondary electrons, which are generally far larger generated than the secondary ions, are mostly used in the SIM imaging. Interaction of ion or electron beams with solid samples is complex. Before stopping in the sample or escaping from the sample, each incident particle may undergo many scattering events, distributed between elastic and inelastic processes. While elastic collisions result from collisions of energetic ions or electrons with nuclei of the target atoms and alter their undergoing directions, inelastic collisions result in transfer of their energies to the target, leading to generation of secondary electrons, Auger electrons, photons, and so forth. (Here, elastic and inelastic collisions are defined as the collisions satisfying and unsatisfying the energy and momentum conservation rule, respectively.) The Monte Carlo (MC) method using a stepwise simulation of various scatting events is useful to both macro- and microscopically understood beam interactions [12–15 and 16–19 for the ion and electron impacts, respectively]. MC programs allow also estimating the various signals, their yield, and their spatial/angular/energy distributions.

Figures 5(a) and (b) show MC-simulated trajectories of 30 keV Ga ions and 10 keV electrons in Silicon (Si) and tungsten (W) targets, respectively, using the MC programs [20]. Here, Si and W are chosen as typical lighter and heavier atomic mass elements relative to Ga (i.e., atomic mass M = 28.1, 69.7 and 183.9 amu (atomic mass unit; g/mole) for Si, Ga and W, respectively). A mass ratio of the strike to struck particles much governs an elastic scattering as discussed later. The 30 keV-Ga ions penetrate about 40 nm and 20 nm for the Si and W targets, respectively (see Fig. 5). These ion ranges are shallower by one order of magnitude than those of even 10 keV-electrons. Shallowness of the interaction depth is one of characteristics of the Ga-FIB.

3.1. *Elastic collision*

When the incident particle of mass M_1 (amu) is elastically scattered by the target atom of mass M_2 (amu) through an angle θ relative to the direction of motion of

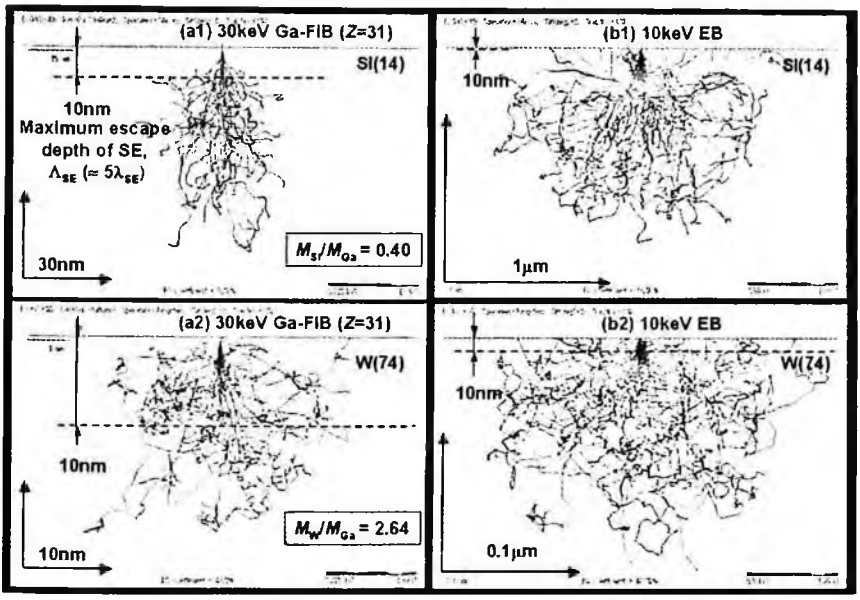

Figure 5. Monte Carlo (MC) simulated 100-trajectories of 30 keV Ga ions and 10 keV electrons in Silicon (Si) and tungsten (W) targets.

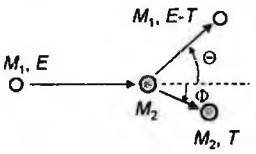

Figure 6. A collision of two particles in a laboratory system: M_1 = incident or moving ion/electron mass, M_2 = struck particle mass, E = kinetic energy of the incident particle before the collision, and T = energy transferred from the moving particle to the struck particle through the collision.

the center of mass (CM) (see Fig. 6), the incident particle with kinetic energy E loses energy T due to the energy transfer to the target atom [13,21],

$$T = T_{\max} \cdot \sin^2(\theta/2), \tag{1}$$

$$T_{\max} = 4 \cdot \frac{A}{(1+A)^2} \cdot E, \tag{2}$$

where $A = M_1/M_2$. This energy loss is equal to post-collision energy of the struck atom. The T value is maximum at $\theta = 2\pi$ (i.e., a head-on collision) to be $T = T_{\max}$.

Only when T is larger than atom displacement energy E_d (≈ 25 eV for metals) in ion-atom collisions, target atoms are knocked out from their lattice positions. When struck atoms have sufficient kinetic energies enough to generate secondary collisions, they initiate a cascade of atomic collisions to cause sputtering and knock-on damage. For the collision of Ga ion with a Si atom, for example, the value of

T_{max}/E is 0.82 and the T_{max} value at $E = 10\,\mathrm{keV}$ is as large as $8.2\,\mathrm{keV}$ ($\gg E_d$). The direction of motion of the post-collision struck atom at angle Φ (in the laboratory system) to the locus of CM is given by

$$\Phi = (\pi - \theta)/2. \tag{3}$$

The scattering angle in the CM system is converted to the scattering angle Θ in the laboratory system using a simple relationship,

$$\cos\Theta = \frac{1 + A \cdot \cos\theta}{\sqrt{1 + 2A \cdot \cos\theta + A^2}}. \tag{4}$$

In Eq. (3), when $\theta = 0$, $\Theta = 0$, and when $\theta = \pi$, $\Theta = 0$ or π, depending on whether $A < 1$ or $A > 1$. The incident ion, which is heavier than the struck atom (i.e., $A < 1$), is always scattered forward in the laboratory system (i.e., $0 \leq \Theta \leq \pi/2$). On the other hand, collisions for $A > 1$ cover a full range of angles (i.e., $0 \leq \Theta \leq \pi$) so that the backward scattering (i.e., $\pi/2 \leq \Theta \leq \pi$) can also occur. Scattering with larger Θ shortens the trajectories of post-collision ions due to more momentum transfer as observed in Fig. 5(a).

The nuclear stopping power depends on the cumulative effect of statistically independent elastic scattering of the incident particle and the target atom.

$$-\frac{dE}{dR} = N \cdot S_n(E) = N \cdot \int_{T_{min}}^{T_{max}} T d\sigma, \tag{5}$$

where N is the number of target atom per unit volume and $S_n(E)$ is the stopping cross-section, which can be thought of as the energy-loss rate per scattering center. The form of $d\sigma$ is the energy-transfer differential cross section as a function of Z_1, Z_2, M_1, M_2, E, and θ. For screened Coulomb potentials, the equation of $d\sigma$ defined in reduced notation, i.e., a universal one-parameter differential cross-section, is expressed as [13,21]

$$d\sigma = \frac{-\pi a_{TF}^2}{2} \frac{f(t^{1/2})}{t^{3/2}}, \tag{6}$$

$$a_{TF} = \frac{0.8854 a_B}{(Z_1^{2/3} + Z_2^{2/3})^{1/2}} \text{(Tohmas-Fermi radius)}, \tag{7}$$

where $a_B = 0.0529\,\mathrm{nm}$ (Bohr radius), t is a dimensionless collision parameter defined by

$$t \equiv \varepsilon^2 \frac{T}{T_{max}} = \varepsilon^2 \sin^2\left(\frac{\theta}{2}\right), \tag{8}$$

ε is the dimensionless energy defined as

$$\varepsilon = \left(\frac{a_{TF}}{Z_1 Z_2 e^2} \frac{M_2}{M_1 + M_2} \right) E, \tag{9a}$$

$$= \left(\frac{0.03255}{Z_1 Z_2 (Z_1^{2/3} + Z_2^{2/3})} \frac{M_2}{M_1 + M_2} \right) E(eV), \tag{9b}$$

and $f(t^{1/2})$ is a scaling function. The general form is

$$f(t^{1/2}) = \lambda t^{1/2-m} [1 + (2\lambda t^{1-m})^q]^{-1/q} \tag{10}$$

where λ, m and q are fitting variables, e.g., with $\lambda = 1$, $m = 1/3$, and $q = 2/3$ for the Thomas-Fermi version for an interatomic screening function.

Equation (5) can be written in a more universal format by introducing a reduced stopping cross-section $S_n(\varepsilon)$ and a reduced length ρ as

$$S_n(\varepsilon) = \frac{d\varepsilon}{d\rho}, \tag{11}$$

and

$$\rho = (4\pi a^2 N) \frac{M_1 M_2}{(M_1 + M_2)^2} \cdot R. \tag{12}$$

A relationship between (dE/dR) and $(d\varepsilon/d\rho)$ is given by

$$-\frac{dE}{dR} = N \cdot S_n(E) = -\frac{d\varepsilon}{d\rho} \left(\frac{dE}{d\varepsilon} \cdot \frac{d\rho}{dR} \right). \tag{13}$$

Using the ZBL universal nuclear stopping cross-section, the expression of universal stopping power is given by [13]

$$S_n(\varepsilon) = \frac{\ln(1 + 1.1383\varepsilon)}{2(\varepsilon + 0.01321\varepsilon^{0.21226} + 0.19593\varepsilon^{0.5})}, \tag{14}$$

for $\varepsilon \leq 30$. The $S_n(\varepsilon)$ curve shows a maximum plateau at $\varepsilon^{1/2} \approx 0.5 - 0.6$. In the high-energy regime,

$$S_n(\varepsilon) = \frac{\ln(\varepsilon)}{2\varepsilon} \tag{15}$$

for $\varepsilon \geq 30$. The reduced energy ε in Eqs. (14) and (15) is calculated using the following universal screening radius a_U instead of a_{TF} in Eq. (9a),

$$a_U = \frac{0.8854 a_B}{(Z_1^{0.23} + Z_2^{0.23})} \tag{16}$$

Values of ε/E, ρ/R, and κ for typical combinations of Ga ion and Si and W targets are shown in Table 2. The nuclear stopping powers for Ga ions in Si and W targets are plotted in Fig. 7 with the electronic stopping power discussed later. For the

Table 1. Source characteristics of Ga-LMIS, field-emission (FE) electron source, and Schottoky electron source.

	Ga-LMIS	FE electron source W(310)	Schottky electron source Zr-O/W
Brightness B [A/m^2 sr]	10^{10}	10^{13}	5×10^{12}
Virtual source size ρ [nm]	50	3	15
Angular emission current dI/dΩ [μA/sr]	15 ~ 20	50 ~ 100	10 ~ 1000
Energy spread ΔE [eV]	5 ~ 8	0.2 ~ 0.5	0.3 ~ 0.7

Table 2. Values of ε/E, ρ/R, and κ for combinations of Ga ion and Si and W targets.

Target element	Atomic number Z	Atomic mass M [amu]	Mass ratio M/M(Ga)	Density [g/cm^3]	LSS parameters		
					ε/E[keV]	ρ/R[μm]	κ
Si	14	28.086	0.403	2.33	5.33E-03	17.3	0.113
W	74	183.84	2.64	19.25	2.10E-03	14.5	0.318

Ga: Z = 31 and M = 69.72

present ion - target combinations, the nuclear stopping is dominant in the energy loss.

Let us consider electron-target atom collisions at $E <$ several tens keV. Both $T \approx 0$ and $\Theta \approx \theta$ are satisfied at any θ because of $A \gg 1$. In other words, electrons can change their directions without losing their kinetic energies through elastic collisions. No target atoms are knocked out from their lattice positions to result in no physical sputtering. For a Si target, for example, the value of $T_{\max}/E$ is 7.8E-5 and the $T_{\max}$ value at $E = 10\,\mathrm{keV}$ is as small as 0.78 eV ($\ll E_\mathrm{d}$). In the same manner, no displacement of carbon atoms for a carbon nanotube (CNT) requires electron irradiation of $E < 82\,\mathrm{keV}$ [22] when $E_d = 15\,\mathrm{eV}$.

3.2. *Inelastic collision*

Regarding the approach to ion inelastic scattering, the continuous slow-down approximation has been widely used. An inelastic stopping power $(-\mathrm{d}E/\mathrm{d}R)$ increases from zero, passes through a maximum when the ion velocity V is of the order of orbital velocities of lattice electrons ($= Z_2^{2/3} V_B$, where $V_B = 2.2\mathrm{E}+6\,\mathrm{m/s}$ is the velocity of Bohr electron in the hydrogen atom), and finally falls off inversely as the first power of energy. The ion energy E converted from the ion velocity of $V = Z_2^{2/3} V_B$ is given by E [keV] $\approx 25 \cdot Z_1^{4/3} M_1$ [amu], which corresponds to 25 keV for hydrogen ion and 170 MeV for Ga ion. In the lower velocity region (i.e., $V < Z_1^{2/3} V_B$ and $Z_2^{2/3} V_B$, a V-proportional stopping power is derived [13,21]. The velocity of $V = Z_1^{2/3} V_B$ is converted to energy of E [keV] $\approx 25 \cdot Z_1^{4/3} M_1$ [amu],

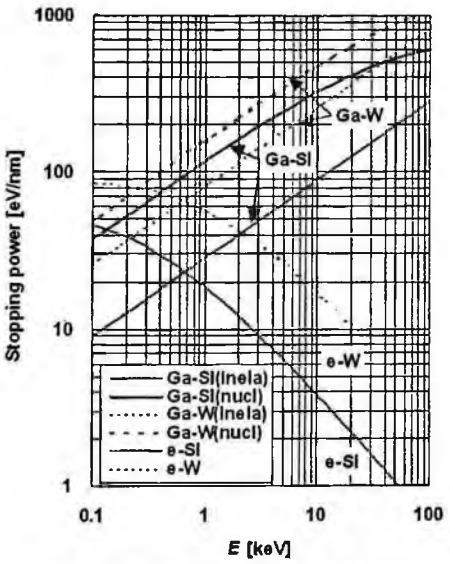

Figure 7. Comparison of stopping power between electron and ion; (a) electron stopping powers for Au and Cu targets and (b) ion stopping powers.

which corresponds to 25 keV for H ion and 170 MeV for Ga ion. Using the dimensionless energy ε and distance R, V-proportional electronic stopping power $S_e(\varepsilon)$ is described as [13,21]

$$S_e(\varepsilon) \equiv \left(-\frac{d\varepsilon}{d\rho}\right)_{electronic} = \kappa\varepsilon^{1/2}, \tag{17}$$

where

$$\kappa = \xi_e \cdot 0.0793 \frac{Z_1^{1/2} Z_2^{1/2}}{(Z_1^{2/3} + Z_2^{2/3})^{3/4}} \frac{(M_1 + M_2)^{3/2}}{M_1^{3/2} M_2^{1/2}} (\xi_e \approx Z_1^{1/6}). \tag{18}$$

At high ion velocities (i.e., $V \gg Z_1 V_B$), inelastic energy loss to lattice electrons through excitation and ionization dominates and electronic stopping power is given by Bethe formula [15]:

$$\left(-\frac{dE}{dR}\right)_{electronic} = \left(\frac{8\pi Z_1^2 e^4}{(4\pi\varepsilon_0)^2 \cdot J \cdot \varepsilon_B}\right) \cdot N \cdot \ln\left(\varepsilon B + 1 + \frac{C}{\varepsilon_B}\right), \tag{19a}$$

$$\left(-\frac{dE}{dR}\right)_{electronic} = 4 \times (7.85 \times 10^3)\left(\frac{Z_1^2}{J \cdot \varepsilon_B}\right) \cdot \left(\frac{D}{M_2}\right) \cdot \ln\left(\varepsilon_B + 1 + \frac{C}{\varepsilon_B}\right)(eV/nm), \tag{19b}$$

where

$$\varepsilon_B = (2m_e V^2/J) = 4(m_e/m_1)(E/J). \tag{20}$$

m_e is the electron mass, m_1 is the ion mass, D the mass density (g/cm^3), R is the path length (nm), E is the energy [eV], and J is the mean ionization energy (eV) given by [17,23]

$$J = 9.76Z_2 + 58.5/Z_2^{0.19} \quad [eV] \quad \text{for } Z_2 \geq 13; \tag{20a}$$

$$J = 11.5Z_2 \quad [eV] \quad \text{for } Z_2 \leq 12. \tag{20b}$$

Here, $C = 5$ and, especially, $C = 100 \cdot (Z_1/Z_2)$ for $Z_1 < 3$. The $(-dE/dR)_{electronic}$ curves for Ga → Si and W targets also are plotted in Fig. 7.

The stopping of an energetic particle in solid results from a sum of the two components, i.e., the nuclear (or elastic) and electronic (or inelastic) stopping, which may be taken in good approximation as independent of each other, and the total stopping power is given by

$$\left(-\frac{dE}{dR}\right)_{total} = \left(-\frac{dE}{dR}\right)_{nuclear} + \left(-\frac{dE}{dR}\right)_{electronic}. \tag{21}$$

As to the electron stopping power, the nuclear term in Eq. (21) is negligible because of $m_2/m_e \gg 1$. The stopping power has a maximum plateau of 60–100 eV/nm at $E = 0.01$–0.1 keV. Bethe's expression is used for the inelastic loss rate at sufficiently high energies of $E > 3$ keV and is modified by Joy and Luo [23] to be more accurate at lower energies E [16],

$$\left(-\frac{dE}{dR}\right) = \left(\frac{2\pi Z_2 e^4 N}{(4\pi\varepsilon_0)^2 E}\right) \cdot \ln\left(\frac{1.166(E + 0.85J)}{J}\right), \tag{22a}$$

$$= 7.85 \times 10^3 \cdot \left(\frac{DZ_2}{M_2 E}\right) \cdot \ln\left(\frac{1.166(E + 0.85J)}{J}\right) \quad (eV/nm). \tag{22b}$$

The electron inelastic stopping powers for Si and W targets are over-plotted in Fig. 7. A big differences in the inelastic stopping power $(-\mathrm{d}E/\mathrm{d}R)$ between electrons and ions at $E >$ several keV is their E-dependencies, i.e., $(-\mathrm{d}E/\mathrm{d}R) \propto 1/E$ for electrons and $(-\mathrm{d}E/\mathrm{d}R) \propto E^{1/2}$ for ions. In a classical explanation, inelastic interactions become to be strongest when a velocity of the incident (electron or ion) is comparable to that of representative electrons in the target. The stopping power for electrons at $E = 1 - 50$ keV are smaller by $1 - 2$ orders of magnitude than those (= nuclear + inelastic stopping powers) for Ga ions. This explains that Ga ion ranges are shorter by $1 - 2$ orders of magnitude than electron ranges under the same incident energies.

4. Sputtering

On the collision cascade within several nm in depth, a fraction of struck target-atoms reach the target surface and escape from the surface when normal components of their kinetic energies are greater than the surface binding energy E_s (= a few eV). This atomic ejection as a result of momentum transfer is called simply "sputtering"

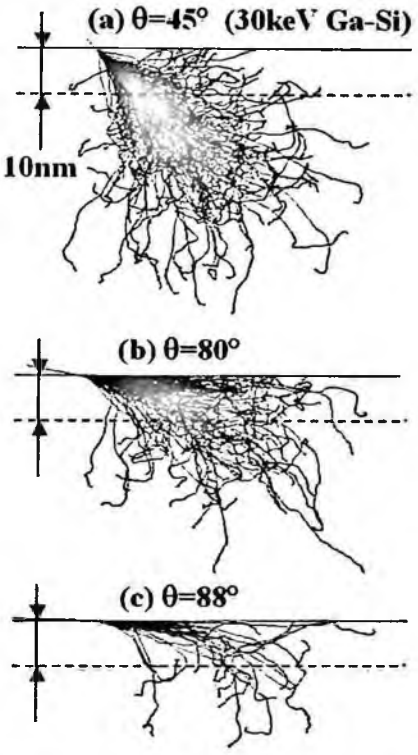

Figure 8. MC-simulated 30 keV 200 Ga-ion trajectories in Si at various incident angles of $\theta = 45$, 80 and 88°.

or "physical sputtering", which is distinguished from "chemical" sputtering defined the sputtering assisted with chemical reaction (discussed later). The most essential parameter governing to the ion milling is a sputtering yield S, which is defined as a number of sputtered atoms per one incident ion. The collision cascade model predicts that the S value is proportional to the nuclear stopping power $(-\mathrm{d}E/\mathrm{d}R)_{\mathrm{nuclear}}$ and inversely to E_s. Typical experimental S values for 30–40 keV Ga ion bombardments are 1–15 atoms/ion, being larger for the targets with lower E_s.

Figure 8 shows typical MC-simulated trajectories of 30 keV Ga ions penetrating into the Si targets at various incident angles (with respect to the surface normal), i.e., $\theta = 0$, 45, 80 and 88°. Since sputtering is an emission of the recoiled target atoms as a result of a collision cascade generated along the incident ion path, $S(\theta)$ at slightly glancing angles θ is in general related to $S(0)$ as

$$S(\theta)/S(0) = \{\cos(\theta)\}^{-f}, \tag{22}$$

where the exponent f is a function of mass ratio of the target atom and the ion, and approximately ranges from 1 to 2 [21], as shown in Fig. 9. This is because, in a straight penetration approximation, the ion path length within the surface layer

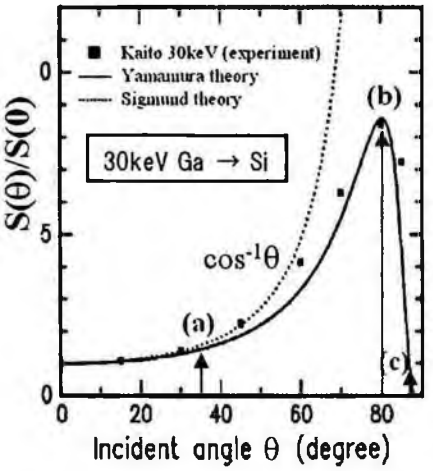

Figure 9. Sputtering yield $S(\theta)$ as a function of angle θ of the incidence.

(of several nm in depth) increases inversely proportional to $\cos(\theta)$ and the ions deposit more energy expressed by $(-\mathrm{d}E/\mathrm{d}R)$ to generate collision cascade. Here, the collision cascade mostly within the surface layer produces the sputtered atoms. For the increase of θ from 0 to 90°, a maximum in $S(\theta)$ is reached at $\theta_{\max} = 70$–$80°$ for most materials; generally the $\theta_{\max}$ value increases with decreasing Z_2 and increasing beam energy. Then, with increasing θ from $\theta_{\max}$ to 90°, $S(\theta)$ starts to decline because more ions are backscattered and they lose less of their kinetic energies in the samples to generate smaller collision cascade [12]. Finally, S approaches 0 at $\theta = 90°$ via the point $S(\theta_c) = S(0)$. Experimental $S(\theta)$ values for Ga-FIB bombardments have been measured as a function of θ by several groups [24,25].

Since the FIB-milling is governed by the ion sputtering based on atomic momentum transfer, material selectivity in the FIB milling is far less as compared with chemical etching, including an FIB-assisted etching (FIB-AE) discussed later. Besides, the FIB milling is stress-free and is essentially different with mechanical milling accompanying with sharing stress. If we use hydrogen (H) or helium (He) ions instead of Ga ions, sputtering is minimum because recoil atoms do not receive enough energy to generate a collision cascade due to $M_1 \ll M_2$.

5. FIB Milling

5.1. *Cross-sectioning and planar milling*

The FIB milling is classified into two types, i.e., cross-sectioning and plane-milling, as shown in Fig. 10. The former milling prepares the cross sections of interest in parallel to the FIB direction using the FIB's round-side, while the latter milling prepares the planes perpendicularly to the FIB direction using the FIB's head. On the planar FIB-milling, three-dimensional (3D) milling is performed by controlling

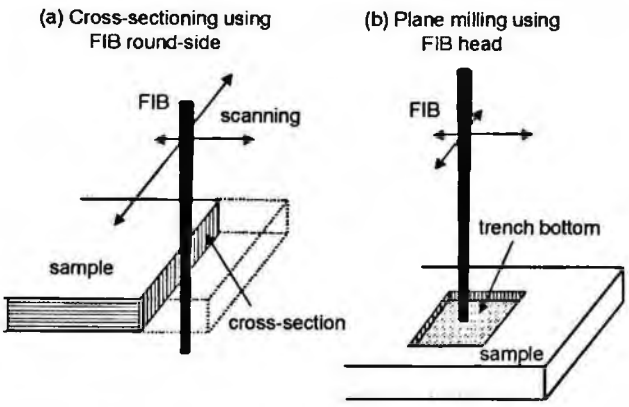

Figure 10. Two types of FIB-milling: (a) cross-sectioning using the FIB's round-side and (b) plane-milling using the FIB's head.

the pixel ion-dose or pixel dwell-time. In the milling evolution, we must take into the consideration that θ varies with milling time as well as the milling position and the S value also varies with the corresponding θ. There are other following additional effects to the practical milling: crystal grain dependency of S, redeposition of sputtered atoms, and the FIB intensity profile. Choice of fast or slow FIB-scanning also largely changes the practical milling speed as discussed later.

Let us consider surface-contour during FIB milling using fast-and-repeated scanning FIB. Here, the fast and repeated FIB-scanning is approximated as the ion bombardment with uniform broad beam. As the first example, a sample surface is originally a one-dimensional rectangular-wave form as shown in Fig. 11(a). Analytical models based on ray-tracing for surface evolution predict that top corners of the rectangle surface are gradually sputtered away to form slopes with the stable gradient angle β_m ($= 90° - \theta_m$; see Fig. 11[b]), and the slopes in a pair approach each other and form cones as shown in Fig. 11(a). The cones shrink with milling time and finally disappear. It is worthy of note that a uniform-beam milling inherently decreases surface roughness for homogenous rough samples [4]. Regarding the model's validity, a minimum wavelength in smoothing is a size of collision cascade on the surface per ion-impact, i.e., about a few nm at $E = 20$–$40\,\mathrm{keV}$. A wave front reconstruction model [26] also allows describing the evolution of surface topography. Figure 11(c) shows the typical staircase milled using the fast FIB-scanning, where a rectangular-wave form on the original surface gradually disappears with increasing milling depth to form the flat bottom.

5.2. *Tilt of FIB-milled section*

For device failure analysis, in general, cross sections to be inspected must be prepared at a right angle with respect to surfaces of the devices (wafer or die in type). However, FIB-milled cross-sections (as shown in Figs. 12[a] and [b]) are not perfectly

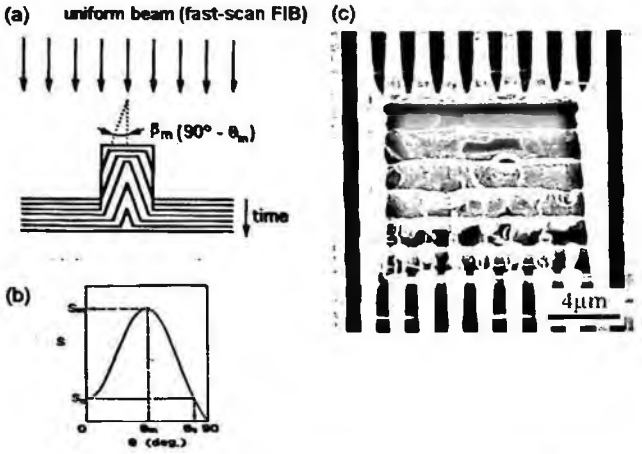

Figure 11. (a) Surface-contour evolution of a rectangle wave sample under fast-scan FIB (approximately regarded as uniform ion bombardment), (b) sputtering yield as a function of angle of the incidence, and (c) FIB-milled staircase: The rectangular-wave form on the original surface gradually disappear with increase of milling depth.

parallel to the FIB incident direction, but incline by a small angle β_s (typically 1.5–4°) depending on both the material. Cross-sectional TEM samples, which are prepared by two-box (trench) milling so as to leave a narrow strip (about 0.1 μm in width) as shown in Fig. 12(a), are fabricated in taper shape as shown in Fig. 12(b) at sample tilt angle $T = 0°$. This shape is off its right one of uniform thick and flat.

Figure 12(c) shows surface development of trench-milling simulated using a fast-scan FIB with Gaussian intensity-profile [3,4]. The trench sidewall steepens with increasing depth and finally reaches a stable angle of θ_s (see Fig. 12[c]). The curves of C, C' and C" shown in Fig. 12(c) correspond to the followings: curve C: a relative accumulated dose profile for the repeated fast-scan Gaussian beam, curve C': an upside-down curve of the curve C, and curve C": an expanded C'-curve, of which top and bottom meet with the trench top and bottom, respectively. The important result is that the θ_s value is roughly equal to θ_c satisfying $S(\theta_c)/S(0) = 1$ in Fig. 12(d). Although the C"-curve has continuity in its gradient, the sharp edges regarded as discontinues points are generated at the bottom of FIB-milled trench (see Figs. 12[a] and [c]). Roundness near the trench top (observed in Fig. 12(c)) is due to sputtering by the Gaussian beam tail. The β_s values tend to increase with increasing Z_2 and decreasing beam energy. To make the cross-sections stand vertically, the sample must be tilted by β_s so as to compensate the taper angle during the final FIB-polishing (see Fig. 12(b)). TEM/STEM samples with nearly parallel sides (or uniform thick) are fabricated by tilting the sample by $\pm T(\approx \pm\, \beta_s)$ during the final FIB-polishing of front and backsides of the TEM/STEM thin samples, respectively [3,4,27–31], where $\beta_s = 90° - \theta_s$ and $\theta_s \approx \theta_c$. Since the θ_m values are typically 70–80°, being larger with increase E and decreasing Z_2, the β_s values decrease with increase E and decreasing Z_2.

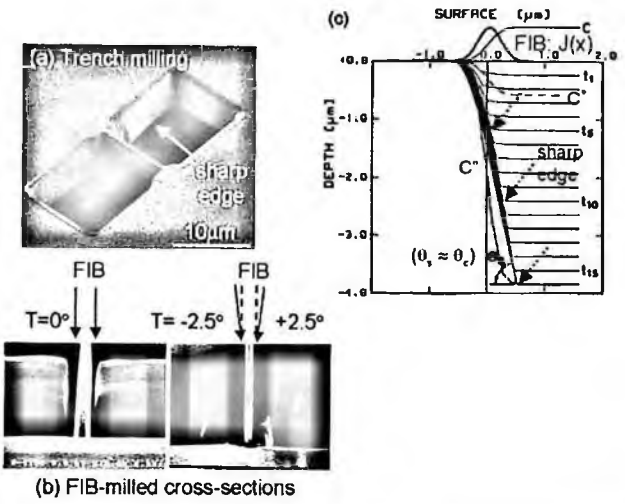

Figure 12. (a) Two-trench FIB-milling so as to leave a film, (b) FIB-milled cross-sections with or without sample tilt of $\pm T(\approx \pm\beta_s)$, where $\beta_s = 90° - \theta_s$ and $\theta_s \approx \theta_c$, and (c) surface development of trench-milling using a fast-scan FIB with Gaussian intensity-profile; curve C: a relative accumulated dose profile for the repeated fast-scan Gaussian beam, curve C': an upside-down curve of the curve C, and curve C": an expanded C'-curve, of which top and bottom meet with the trench top and bottom, respectively. The trench sidewall steepens with increasing depth and finally reaches a stable angle of θ_s ($\approx \theta_c$ in Fig. 12(c)).

Another interesting point is how flat and uniform the FIB-prepared cross-sections are. Recent applications of electron holography using TEM require very flat and uniform samples [32–34], e.g., typically less than several nm in roughness over a 10 μm square size. This is because the phase difference $\Delta\varphi$ between the electron waves passing through a thin specimen and a vacuum is proportional to the product of the mean inner potential Vip of the specimen and the fluctuation (Δt) in the specimen thickness.

$$\Delta\varphi = C_E \cdot V_{ip} \cdot \Delta t, \tag{23}$$

where

$$C_E = \left(\frac{2\pi}{\lambda E}\right)\left(\frac{E + E_o}{E + 2E_o}\right) \quad \text{(a sample independent constant)} \tag{24}$$

E is the electron beam energy, E_o is the rest energy (≈511 keV), and λ is the wavelength of the incident electron. For example, the value $\Delta\varphi$ at $\Delta t = 1$ nm for Si sample is about $2\pi/73$ at $E = 200$ keV.

Such flat and uniform cross sections of $\Delta t = 1$–2 nm are achievable by scanning the FIB so as to make the ion dose uniform over the intervals between the beam scan pixels. One of effective ways is a superimposition of a small x-scan signal with a high frequency on a standard large x-scan signal with a low frequency.

5.3. *Curtain structure formed on cross sections*

Most TEM/STEM specimens exhibit 3D-structure composed of various materials. On their FIB-milled cross-sections in TEM/STEM images as shown in the later Fig. 14(b), curtain or vertical stripes sometimes appear as light and dark contrasts. The curtain stripes originate from a change in milling speed V_{mill} due to differences in specimen topography and/or in material, as schematically shown in Fig. 13. For the FIB cross-sectioning of layered samples, the upper layer composed of smaller (or larger) S material works as a strong (or weak) mask for the lower layer. Gradient angles θ_s of the cross-sections vary with the material as discussed before.

Several ways have been proposed to reduce the curtain effect [3]. For samples surfaced with uneven structures, it is effective to planarise the surface using FIB-assisted deposition (FIB-AD). The deposited-layers of low-S metals protect also as against undesired sputtering of a top portion of the cross-sections due to the beam-tail. However, the planarizing process using FIB-AD damages utmost sample-surfaces (with the depth of ion range) at the beginning of FIB-AD process. To solve this problem, other soft processes such as thermal evaporation, plasma coating, etc. are used before or instead of the FIB-AD process. Beam conditions such as beam scanning speed, beam current, and beam size, subtly influence the growth or decline of curtain structure through the $S(\theta)$ characteristics. Another solution is cut-off of the potential curtain-source regions before the FIB milling if those regions are not intended for the observations.

Deposition of hard metals provides a bonus effect for the TEM lamella preparation. Intrinsic stress can warp the FIB-thinning lamella to curve its top edge. The metal stripes are effective to restrain the lamellas from being warped. Another way to solve the warp problem is to cut one side-end of the lamella to release the

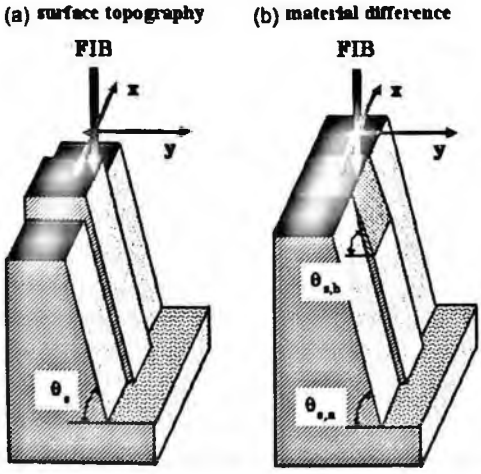

Figure 13. Origins of curtain structure appeared on the FIB-milled sections: (a) difference in surface topography and (b) difference in material difference.

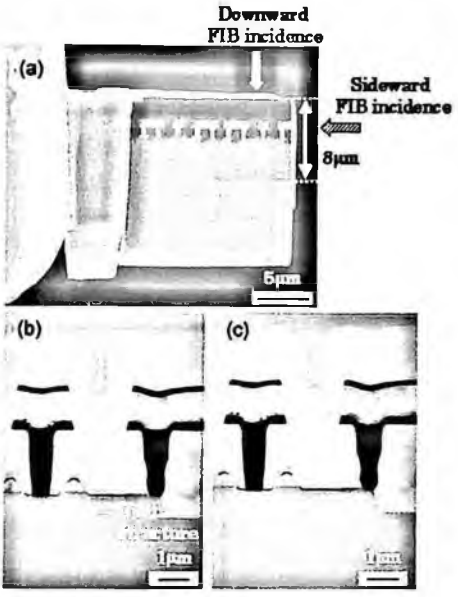

Figure 14. SEM images of the μ-sample: (a) the low magnification image after the final milling using sideward incident FIB to remove the curtain structure, (b) and (c) high magnification images before and after the final milling using sideward incident FIB, respectively.

intrinsic stress before the start of warping. The metal deposition is effective also to reduce charging up of insulator samples.

The best way to avoid the curtain effect is a change or modulation of the FIB incident direction within the cross-sectional plane [3]. The reason is that the curtain stripes always point downstream with respect to the beam direction. Figure 14 shows usefulness of this way. For the μ-sample fixed to a TEM grid, final FIB-milling was performed using the sideward incident FIB and successfully reduced the curtain structures. Since nothing surrounds the μ-samples except for the TEM grid, we can employ various directions of the FIB incidence, i.e., downward, sideward, upward, and other directions, by using 3D FIB/STEM compatible sample holder shown in later Fig. 19(a). FIB-AD was employed to fix the μ-sample to the TEM grid. For magnetic μ-samples, the FIB-AD fix works well to keep the μ-samples on the TEM grids against the attracting power caused by the strong magnetic lens field. This fix is effective also to secure a dissipation path for heat generated by TEM/STEM inspection beams.

5.4. *Milling speed and milling yield*

Let us consider several important parameters, i.e., the milling speed V_{mill} defined as the milled volume per unit time, the milling rate R_{mill} defined as the milling speed per unit beam current, an ion beam current I_p, and the sputtering yield S defined

as a number of the sputtered atoms per incident ion. By practically expressing V_{mill}, R_{mill}, I_p, and S in $\mu m^3/s$, $\mu m^3/s{\cdot}nA$, and atoms/ion, respectively, we obtain V_{mill} as

$$V_{mill} = R_{mill} \cdot I_p, \tag{25}$$

$$R_{mill} = (1/e)\cdot(S/N), \tag{26a}$$

$$R[\mu m^3/nA{\cdot}s] = \{S[atoms/ion]/N[atoms/mm^3]\} \times \{1.0E-9/1.6E-19[ions/nA{\cdot}s]\}, \tag{26b}$$

where e is the elementary electric charge (=1.602E-19 C), and N is the sample's atomic density. Typical R_{mill}-values for normal-incidence of 30–40 keV Ga-FIB are 0.2–4 $\mu m^3/nA{\cdot}s$, depending on the sample material. Solutions to fasten V_{mill} (or to improve the milling throughput) are only the increases of I_p and/or S.

FIB-milling is carried out typically at 30–40 keV in energy, several tens pA – 50 nA in current (i.e., four orders of magnitude), 10 nm – 1 μm in diameter (i.e. two orders of magnitude), and 0.1–40 A/cm^2 in current density. Positional accuracy of the cross-sectioning is mainly determined by the FIB diameter, while the milling speed is determined by the FIB current. As the higher current beams are generally the larger in diameter, the following two or three stages are usually employed: rough box-milling using high-current FIB, medium box-milling using medium-current FIB, and fine milling to finish the cross section using a fine beam. In practice, shorter milling times are desired not only to improve milling throughput, but also to minimize drifts of the FIB and sample stage. Auto-milling software has been developed to correct for these drifts in day and night operations, where the corrections are carried out at pre-set intervals by referring to a mark formed next to the cross sections to be fabricated.

A scanning FIB forms a locally sloped topography at the time of bombarding [3,4,35]. The FIB scanned at slower speed (V_x) forms a steeper slope with angle (θ_{slope}) as schematically shown in Fig. 15. For a simple model of steady state sputtering where redeposition is neglected, the angle of θ_{slope} satisfies the equation

$$J/V_x = 10^2 \cdot tan(\theta_{slope})/R_{mill}, \tag{27}$$

where J is the beam current density (A/cm^2), R_{mill} is the milling rate ($\mu m^3/nA{\cdot}s$), and V_x is expressed in μm/ms. The R_{mill} value for fast scanning (i.e. $\theta_{slope} \approx 0°$) of 30–40 keV Ga-FIB ranges from 0.2 to 4 $\mu m^3/nA{\cdot}s$, depending on the sample material. For example, the V_x value to form the slope of $\theta_{slope} = 45°$ is as slow as 0.05 μm/ms when $J = 10\,A/cm^2$ and $R_{mill} = 0.5\,\mu m^3/nA{\cdot}s$. For $x - y$ (or frame) scanning, a y-component of the local slope must also be taken into consideration. Thus, R_{mill} is strongly affected by the θ_{slope} value through the S characteristics. A drawback of the FIB box milling under high θ_{slope} is redeposition of milled (or

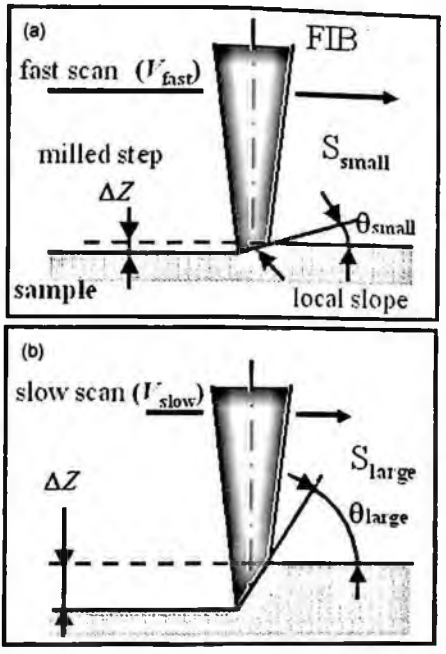

Figure 15. Locally sloped topography formed at the time of FIB-bombarding; The slower scanning FIB produces the sharper slope.

sputtered) atoms on the sidewall facing the local slope. Sputtered atoms are approximately emitted in a cosine distribution (with respect to the slope normal). The V_x-dependencies on both milling rate and redeposition have been evidenced by the experiments [36].

For FIB cross-sectioning using the "slow" $x - y$ scanning, we ought to choose the y-scanning direction (taken as normal to the cross section to be milled) so as to approach the cross-section from the opposite sidewall [3], i.e., "one-way", not "shuttle" y-scanning. Figure 16(a) shows typical trenches milled in μ-sampling (discussed later) using the repeated "one-way" slow y-scan FIB (dwell time $t_d = 50\,\mu s$). The bottoms sloped up toward outer sidewalls were formed by the redeposition in "one-way" slow y-scan mode. Although the value of V_y (or t_d) was not completely optimized, the milling time was favorably shortened to about 10 min, which was about half that for the fast scan mode ($t_d = 3\,\mu s$) combined with the staircase-milling mode as shown in Fig. 16(b). (No other FIB conditions were changed.) Here, the staircase milling diminishes a volume of the original box to be milled by half. The milling time is reducible by a factor of 2–4 by optimizing the value of θ_{slope} (or t_d) according to sample material, beam size and current, box (or trench) size, and sample-depth to be milled out.

Figure 17 shows another experimental and simulated results for the "one-way" slow y-scan FIB trench-milling. Trenches were milled with only two frame (or x-y)

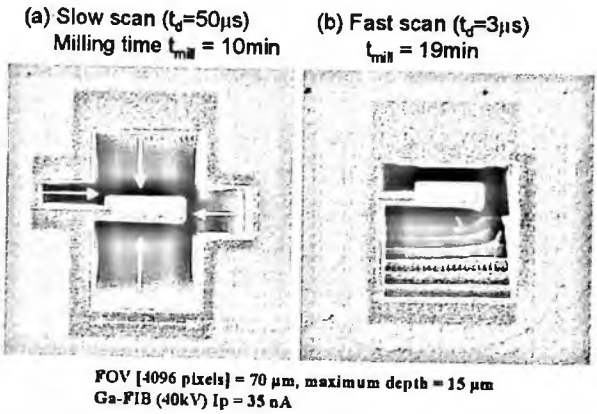

Figure 16. SIM images of typical trenches milled in a μ-sampling using two FIB-scanning modes: (a) a slow-scan mode (dwell time $t_d = 50\,\mu s$) combined with repeated one-way y-scans and (b) a fast-scan mode ($t_d = 3\,\mu s$) used in a staircase milling. The FIBs in both modes were identical except for the scanning speed, i.e., 40 kV Ga-FIB with 35 nA in current.

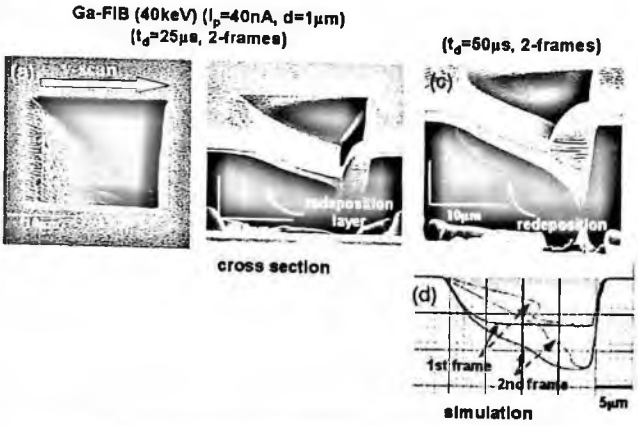

Figure 17. Trenches milled with only two frame (or x-y) scan using slow-scan FIB with $t_d = 25$ or $50\,\mu s$: Here, the FIB y-scan is done only from left to right as shown in Fig. 17(a): (b) and (c) tilt views (at 45°) of the trench bottoms showing arc-like bottoms and significant redeposition on them, and (d) simulated bottom-profiles after the 1st and 2nd frame millings with $t_d = 50\,\mu s$.

scan using slow y-scan FIB with $t_d = 25$ and $50\,\mu s$, where the FIB y-scan were done only from left to right. Tilt views (at 45°) of the trench bottoms are shown in Figs. 17(b) and (c). Here, the bright top-surfaces correspond to the carbon (C) layer deposited using FIB-AD to protect the FIB-tail milling before the FIB cross-sectioning. Middle-brightness regions between the protection layer and the dark substrates correspond to the redeposition layers of interest. The trench bottoms were milled to be arc-like and sputtered atoms significantly deposited on them. Figure 17(d) shows simulated shapes of the bottom after the 1st and 2nd frame-scan millings with $t_d = 50\,\mu s$, where redeposition of the sputtered atoms emitted under a cosine law is taken into consideration. Although the sputtered atoms redeposit on

the just-milled bottom to form a down-slope, the cross-sections milled at the end of y-scan have little chance to be redeposited and stand at the deepest position.

Another way to improve the milling rate is FIB gas-assisted-etching (FIB-GAE), which enhances the milling rate by a factor of 2 or more [27–29,37]. The FIB-GAE, which converts the sputtered material into a volatile compound, is based on chemical reactions and provides strong selectivity in milling materials. It is very useful for high aspect ratio milling for device editing and for significantly enhanced milling of substrates such as Si and GaAs, but it is unsuitable for fine milling to flatten multi-layered cross sections composed of different materials. The FIB trench-milling with "one-way" slow y-scan mode have been positively employed in the μ-sampling method as discussed later.

5.5. *Micro(μ)-sampling method*

FIB μ-sampling method has been successfully used to make selected site-specific TEM/STEM specimens available directly from bulky samples [38–43]. Failure analysis of semiconductor devices often requires sectional and plan views simultaneously. Three functions of FIB milling, fixing, and visualization are fully utilized in the method. Figure 18 shows a series of the μ-sampling process; (a) formation of a W protection layer using the FIB-AD, (b) deep trench FIB-milling of the peripheral area, (c) bottom cutting, (d) bonding of a manipulator probe onto the μ-sample, (e) cutting the μ-bridge and lifting the μ-sample, (f) transferring and mounting on the a sample carrier, (g) and (h) final FIB-milling of the μ-sample.

Typical size of the μ-sample is 15 μm width × several μm width × 15 μm high for the sectional STEM/TEM observation, but largely varies with the application. The μ-sampling requires about 30 min. The sample carrier is mounted on

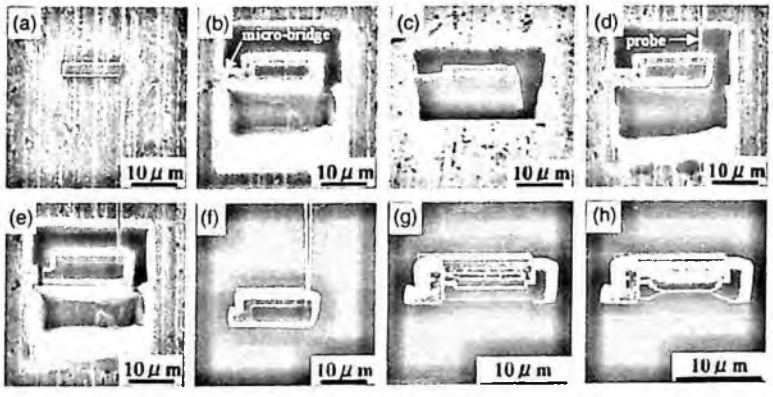

Figure 18. A series of the μ-sampling process; a) formation of a W protection layer using the FIB-AD, b) deep trench FIB-milling of the peripheral area, c) bottom cutting, d) bonding of a manipulator probe onto the μ-sample, e) cutting the micro-bridge and lifting the μ-sample, f) transferring and mounting on the a sample carrier, g) and h) final FIB-milling of the μ-sample.

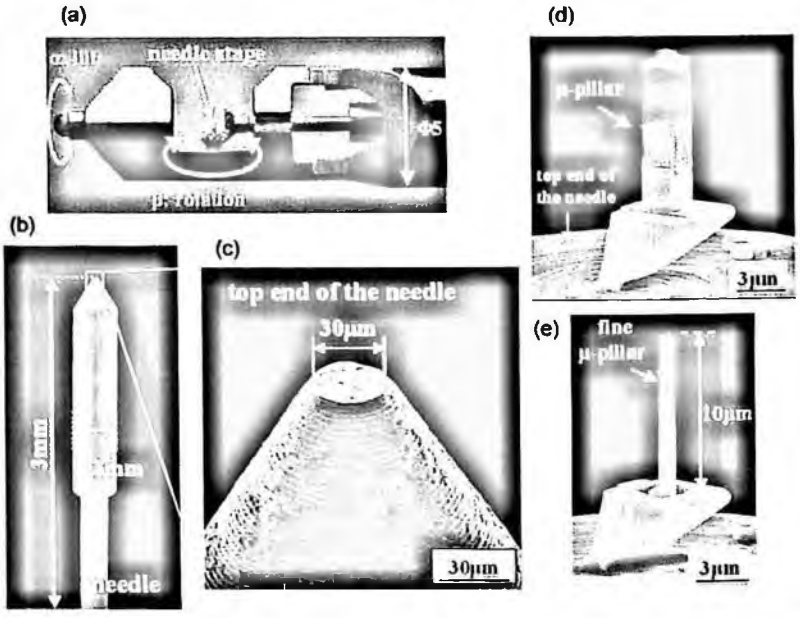

Figure 19. (a) a 3D-FIB/STEM compatible sample holder, (b) a needle stub, (c) top end of the needle, (d) a μ-pillar mounted on the top end of the needle, and (e) a μ-pillar sample trimmed from the μ-pillar shown in Fig. 19(d).

the FIB/STEM/TEM compatible sample holder. The sample transfer from FIB to STEM/TEM systems and vice versa is simply carried out by pulling out the sample holder from one system and pushing it in the other system. No demount and remount of the sample for the sample transfer between the systems is required. Recently, μ-pillar specimens have been prepared for three-dimensional (3D) STEM. Figure 19 shows the 3D-FIB/STEM compatible sample holder and a typical μ-pillar sample [40]. The μ-pillar sample is mounted on the needle stage and is rotatable along the needle axis. Figure 19(d) and (e) shows 200 kV SEM images of the μ-square-pillar and the more FIB-trimmed pillar samples, respectively (using an STEM system: Hitachi HD-2300). Advantages of the μ-sampling are itemized as following:

(i) Possible for additional FIB-milling after TEM/STEM observation
(ii) Possible to extract plural μ-samples in adjacent areas
(iii) Observable also for magnetic materials
(Sample-size reduction for magnetic materials significantly reduces their interference in a TEM/STEM magnetic lens-field.)
(vi) Reducible in beam heating due to securing a heat conduction path using FIB-AD welding
(v) No film to support the sample (Background noise originated from the conventional support film is no more generated in TEM/STEM observations.)

(vi) Possible for sequential cross-sectional and plan views, or vice versa, in TEM/STEM observations

6. Beam Damage

When the target material is bombarded with moderately energetic ions, some of the ions are implanted and retained in the target and the target surface is simultaneously eroded due to sputtering. The implanted ion depth-profile $P(z)$ is characterized by a Gaussian-like curve. As the ion dose increases, sputtering erodes the target surface and the ions implanted underneath the sputtered layer are accumulated as shown in Fig. 20. Ion bombardment ultimately creates a steady-state condition between ion implantation and ion removal by sputtering [44]. Under the steady-state condition

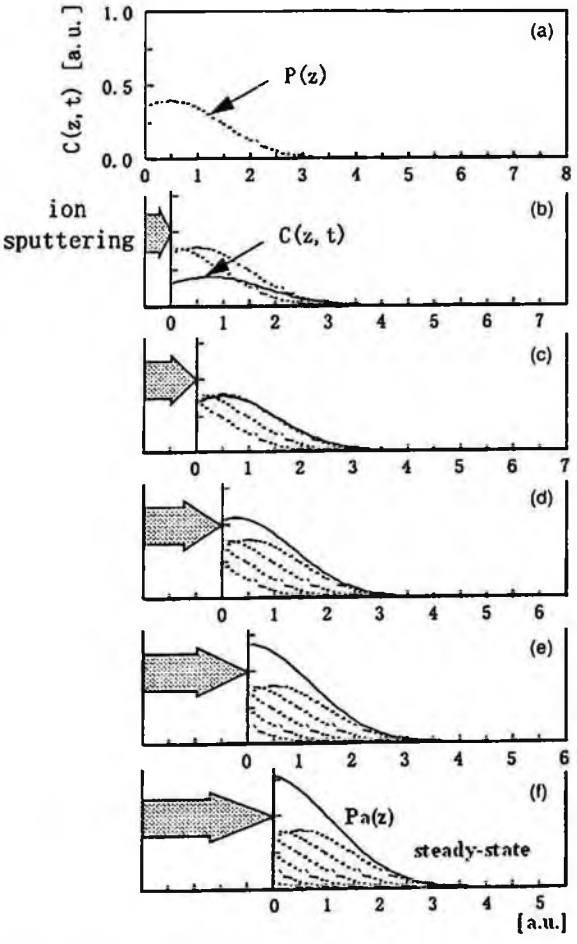

Figure 20. Schematic modification of implanted ion depth profile due to ion sputtering.

the accumulated ion depth-profile $P_a(z)$ has a maximum at $z = 0$ and falls off over a distance of the initial ion range. This phenomenon is schematically shown in Fig. 20. The atomic percent concentration $C(z)$ of implanted atom is converted from $P_a(z)$ as

$$C(z)[at\%] = (100/S) \cdot P_a(z), \tag{28}$$

$$C(0)[at\%] = (100/S) \cdot Y_{imp}, \tag{29}$$

where

$$P_a(z) = \int_0^\infty P(z + z')dz', \tag{30}$$

and Y_{imp} is an ion implantation yield.

During the final polishing of a TEM specimen by FIB almost steady-state sputtering conditions are reached in which the rate of Ga implantation balances the rate of Ga sputtering. The model of ion retention during steady-state sputtering has provided a good agreement with experimental results [44]. The Ga implantation is an elemental contamination itself in the sample preparation. Most implanted Ga ions were within a very near surface layer (<10 nm in depth) of the cross sections and their calculated surface concentrations C_{Ga} were about 4 and 9 at% for the Si and W cross sections prepared by 30 keV FIB. Since the TEM sample prepared using 30 keV Ga-FIB has both sides of Ga-implanted layers, their calculated average contaminations into the 0.1 μm-thick specimen are reduced to 0.7 and 1.1 at% for Si and W specimens, respectively. These values agree with the experimental ones within a factor of 2. The model also predicted that C_{Ga} decreased in reversal proportion to S. Therefore, the FIB-GAE is an effective way to reduce the C_{Ga} value.

The collision cascade under Ga ion bombardment results in also ion damage to crystalline samples. Many authors have investigated the depth of damage (i.e., an amorphous layer) for FIB-milled cross sections. Experimental values [3,28,29,45,46] on depth of the damage to the Si samples caused by 10–40 keV Ga-FIBs are plotted in Fig. 21. The values are well followed with the MC-simulated ones (i.e., 6.0, 9.3, 14.7, 20.0, and 25.7 nm for 5, 10, 20, 30, and 40 kV, respectively [3]), which provide the representative depths of the accumulated vacancy profiles under the steady-state sputtering of the sidewalls.

The following several ways have been studied to reduce the damage depth; lowering the beam energy, broad ion beam (BIB) milling at grazing incidence [3,4,27–29,47–49], and FIB-GAE polishing [27–29,37]. The milling at 5–10 keV of ion energy and 5–10° of sample tilt can remove the thin layer of damage left by higher energy ions. Although the lower beam energy certainly makes the damaged regions shallower, it reduces the milling rate and increases the beam size to deteriorate the site-specificity. The surplus Ga atoms are condensed on the surface because of the non-volatile property. The BIB milling using gas ions of <3 keV at grazing incidence

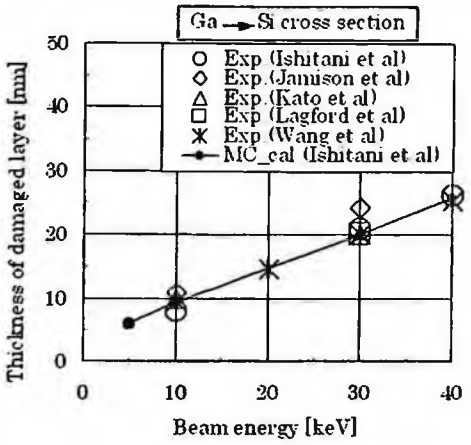

Figure 21. Depth of the damage to the Ga FIB-milled Si cross sections plotted as a function of the ion energy: experiments [3,28,29,44,45] and Monte Carlo simulations [3].

is an effective way to clean TEM membranes of less than 50 nm in thickness. Care has to be taken not to sputter material from the bottom of the milled trenches onto the sidewalls. There are reports that BIB-milling using an argon (Ar) beam formed amorphous layers of about 1 nm thick for Si by 0.25 keV beam energy at a grazing angle of 5° [48] and about 2.6 nm thick for GaAs by (0.2 keV, 30°) [47]. Recently, a system of the BIB milling (Gentle Mill, Technoorg Linda) combined with the 3D-FIB/STEM compatible sample rotation holder (shown in Fig. 19[a]) has been developed to mill the pillar-shape μ-sample at various rotation angles [49], where the damage is reduced to about 1.2 nm for Si sample by 0.2 kV Ar-BIB milling.

The FIB-GAE also is useful to reduce the damage quantity. The damage reduction improves the contrast in lattice imaging for TEM observations. Once the final thinning has been completed, it is important not to take the SIM image of the milled TEM cross sections at any beam current. The FIB incident on the cross sections at the lower angle (closer to normal incidence) produces more damage in both quantity and depth as expected from their simulated trajectories (see Fig. 1).

As to the amorphization behavior (such as vacancy generation, extinction, diffusion, and congregation) under the Ga-FIB bombardment, there are distinct differences between metals and semiconductors. For example, a channeling contrast in SIM images (discussed later) is observed for metal samples (Al, Cu, Ni, Au, etc) even after bombardment of a large dose, but not for semiconductor samples of Si, GaAs, etc. at any stage of the ion bombardment. A plausible explanation for these differences is that many metals remain crystalline as a result of fast recrystalization process under ion bombardment at room temperature, being in contrast with semiconductors. In a recent experimental study, interesting observation has shown that for $Al_xGa_{1-x}As$ TEM sample preparation using 5–30 keV Ga FIB-milling, the damage thickness decreases with an increase of Al concentration x [50].

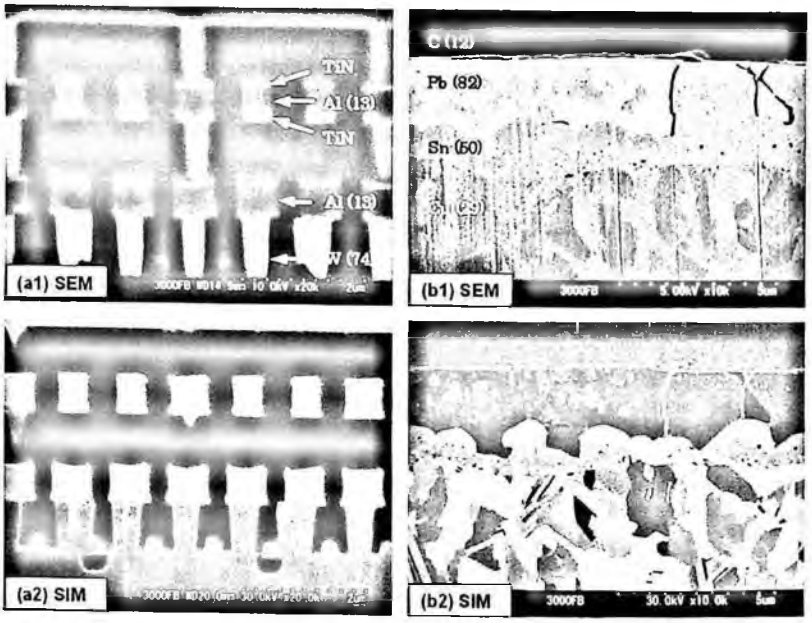

Figure 22. Comparison of image contrast between 30 keV Ga SIM and 5 or 10 keV SEM images of FIB cross-sectioned samples (a) Si SRAM device and (b) solder (Pb-Sn) on Cu base: (The solder sample is covered with a carbon (C) layer.)

7. Secondary Electron Emissions

7.1. *SIM contrast*

Contrast mechanisms in SIM and SEM images are mainly categorized into material contrast, topographic contrast and channeling contrast. Although the SIM contrast mechanism is similar to the SEM one, there are some differences between them [51–53]. For example, Figs. 22(a) and (b) show SIM (for 30 keV Ga ion impact) and SEM (for 5 or 10 keV electron impact) images from the identical FIB cross-sectioned sample fields [53]: (a) Si-device (static random access memory; SRAM) and (b) solder (Pb-Sn) on Cu base. (A protection layer of carbon (C) was deposited on the solder sample before the FIB milling.) Black-and-white contrast among materials is roughly opposite between the SIM and SEM images. As to another experimental data, relative secondary electron (SE) intensities for 8 metals (i.e., Al, Si, Cr, Fe, Ni, Cu, Ag, and Pt) for both 5 keV SEM and 30 keV Ga-SIM are plotted as a function of the atomic number Z_2 of the samples in Fig. 23. MC-simulated SE yields, δ (for 5 keV electron impacts) and γ (for 30 keV Ga ion impacts), for 17 metals including the above 8 metals also are overlaid in the figure. (The MC simulation model is described below.) The experiments show that the SE intensities for Ga-SIM roughly decrease with increasing Z_2, being in contrast to those for SEM.

Monte Carlo (MC) simulations have been employed to study the image characteristics of secondary electrons (SEs) in SIM [53–58], comparing with SEM. The

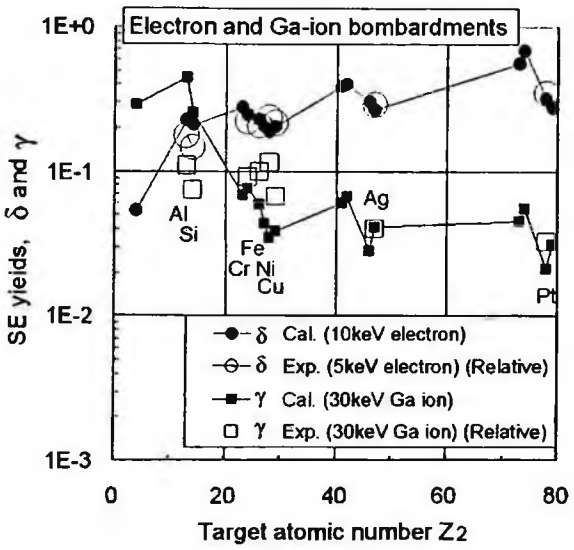

Figure 23. Comparison in relative SE intensities between SEM and SIM: δ (for 5 keV SEM) and γ (for 30 keV Ga-SIM): Experimental data for 8 metals (i.e., Al, Si, Cr, Fe, Ni, Cu, Ag, and Pt) and MC-simulated data for 17 metals including the above 8 metals (i.e., Be($Z_2 = 4$), Al(13), Si(14), V(23), Cr(24), Fe(26), Co(27), Ni(28), Cu(29), Nb(41), Mo(42), Pd(46), Ag(47), Ta(73), W(74), Pt(78), and Au(79)).

emphasis has been placed on the similarities and differences between the SIM and SEM images.

Ion-induced SE emission may proceed via two independent processes, i.e., potential emission (PE) and kinetic emission (KE), which differ by the mechanism of the energy transfer from the incoming ion to the electrons of the solid. In the PE, if the potential energy of the ion is twice (or more) the work function Φ_{WF} of the solid, SE emission may proceed via resonance neutralization and subsequent Auger de-excitation or Auger neutralization. Ga ion bombardment will not lead to potential emission because of its low ionization potential (about 6 eV); the Φ_{WF}-value for normal metals is 4–5 eV. In the KE, on the other hand, the SEs are excited within the solid by direct transfer of kinetic energy from the impinging ion. The SEs that are excited near the surface may eventually be emitted if the SE energies are high enough to overcome the surface barrier. The KE is the major or only source of SEs at medium and high impact energies.

The ion-induced KE is strikingly similar to electron-induced SE emission. The emission of SEs is described by a three-stage process: (i) SE production within a solid, (ii) migration of some of these SEs to the surface, and (iii) eventually, escape through the surface. The big difference between the ion- and electron-induced SE emissions is the SE production stage. In the ion-induced SE emission, the SEs are excited by three types of collision process [53–58]; one due to collisions between projectile ions and target electrons, one due to collisions between recoiled target

atoms and target electrons, and one due to collisions between excited SEs and other target electrons.

Figures 24(a) and (b) shows the MC-calculated partial SE yields for 10 keV electron and 30 keV Ga ion impacts, respectively, on 17 metal targets [54]. For electron impacts, the electron backscattering coefficient increases with increasing Z_2 under the electron impact, and then the SE yields of high-Z_2 metals are dominated by the additional electron excitation by the reflected or backscattered electrons (BSEs) on their way out. As a result, the increase in the SE yield with increasing Z_2 is mainly caused by the increase in the number of SEs excited by the BSEs.

For Ga ion impacts, on the other hand, the projectile ions lose much energy through elastic collisions to create the recoiled target atoms. The recoiled atoms of heavier element transfer less energy to the target electrons, thus leading to a poorer electron-multiplication in a cascade process. Partial SE yields resulted from three types of electron excitation by projectile ions, recoiled material atoms, and electron cascades for 30 keV Ga ion bombardment are plotted as a function of Z_2 in Fig. 24(b). The partial SE yield by the projectile ion, which dominates the total SE yield, generally decreases with increasing Z_2 while showing a fine structure. The reason is that Ga ions in the heavier target atoms lose their energies more sharply

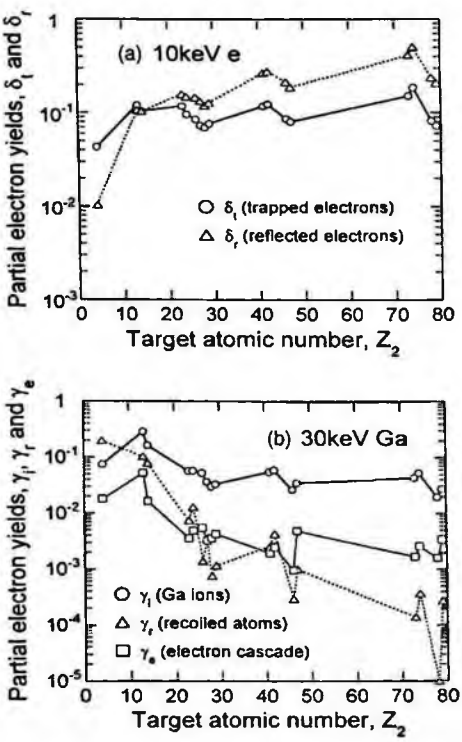

Figure 24. MC-calculated partial SE yields: (a) 10 keV electrons and (b) 30 keV Ga ion impacts on 17 metal targets.

after their incidences as expected from the stopping power shown in Fig. 7. On the inelastic collisions to excite SEs, a velocity of the incident is more important than its kinetic energy. The lower-velocity ions have the less potential in SE excitation. Since the excitation energies decrease with increasing mass M_2 of the recoiled atoms, the partial SE yield by recoiled target atoms decreases with increasing M_2 or Z_2. The partial SE yield by the electron cascade is less important for heavy ion impacts. As a result, the Ga ion bombardment brings to a strong decrease in the total SE yield with increasing Z_2. Fine structures observed on the SE yields for both of electron and ion impacts correlate with the density of conduction band electrons in the targets. The calculated results of Z_2-dependent SE yields for ion and electron impacts roughly explain the reversal in the black-and-white contrast between SIM and SEM images as observed in Fig. 22.

Another interesting topics are a comparison in spatial spreads of SE information between SIM and SEM. Most of SEs are produced in the surface layer of about 5λ in depth (λ: the mean free path of SEs; typically a few nm), being independent of the incident probe. Under 10 keV electron impacts, the SE_I (SE excited by the primary electrons) has a small spatial spread of about 5λ, but the SE_{II} (SE excited by the backscattered electrons) has a large spatial spread of several ten to several hundred nm, decreasing with increasing Z_2. Under 30 keV Ga ion impacts, on the other hand, the spatial spread of SE information is roughly as small as 10 nm, decreasing with increasing Z_2. The reason is that the ion ranges are rather shorter than the electron range. Backscattering yield for the Ga ion impacts is rather smaller than the electron impacts and no BSE is generated for the ion impacts. Besides, the inelastic stopping power, which contributes the SE excitation, is proportional to $1/E$ for the electron impacts, but to $E^{1/2}$ for the ion impacts as shown in Fig. 7. This means that the SE excitation by Ga ions is largest at the impact point and sharply decreases with their penetrations. The 30 keV Ga-SIM imaging is better in spatial resolution than the 10 keV SEM imaging for structure/material measurements when zero-size probes are assumed. A difference in the SE information volume-size between Ga-SIM and SEM has brings also the difference in topography contrast between them [56].

7.2. *Channeling contrast*

Typical SIM images showing channeling (or grain) contrasts are shown in Figs. 25(a) and (b). Their samples are the FIB cross-sectioned Au bonding wire and the Al film deposited on Si substrate, respectively. (Characters of "HITACHI" in Fig. 25(b) were milled by FIB.) SIM image contrasts of the Cu region in Fig. 22(b2) are due to the channeling. Dark grain regions (low SE intensity) represent significant channeling of the primary ions. Such a clear grain contrast for the Al film sample is observable after removing a surface layer of native oxide with high SE yield. The channeled grains lower also the sputtering yield S because the channel ions transfer a little momentum to the target atom.

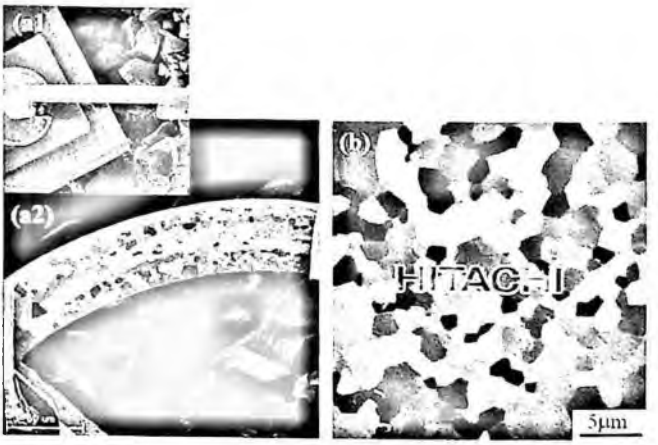

Figure 25. Channeling contrast of SIM images: (a) FIB cross-sectioned Au bonding wire (milling time ≈ 30 min using 30 nA-FIB in HITACHI FB-2100) and (b) Al film deposited on Si substrate.

Figure 26(a) shows a typical measured SE intensity with respect to tilt angle for the iron (Fe) single crystal sample under 30 keV Ga-FIB bombardment, where the tilting direction is from (001) to (111) [59]. Intensity minima observed at the beam incidence normal to the low index planes, i.e., (001), (113) and (111) are attributed to the channeling of the Ga ions as schematically shown in Fig. 26(b). Non-channeling fraction of the incident ions, χ_{uvw}, is given as

$$\chi_{uvw} = N \cdot d_{uvw}^{3/2} \cdot F(Z_1, Z_2, E), \tag{31}$$

where N is the atomic density, d_{uvw} is the distance between two neighboring atoms along the direction of $[u\ v\ w]$, and $F(Z_1, Z_2, E)$ is the factor dependent on Z_1, Z_2, and E. Half-width ψ_c of the minima approximately accords with the Lindhard critical channeling angle [60]

$$\Psi_c \propto \left(\frac{Z_1 Z_2}{E}\right)^{1/2}. \tag{32}$$

The experimental ψ_c values mostly range from several to about 10 degrees (i.e., several 10–200 mrad), which are sufficiently larger than the FIB focusing semi-angles of a few mrad. Since the wide angles in ψ_c produce various contrast levels corresponding to channeling orientations, the SIM image is practically useful to visually evaluate the grain sizes. Here, a channeling contrast in SIM images is observed only for metal samples, but not for semiconductor samples as mentioned. A plausible explanation is that many metals remain crystalline as a result of fast recrystalization under ion bombardment at room temperature.

On SEM images, on the other hand, grains in polycrystalline specimen are seen with BSE and/or SE_{II} (SE excited by BSE) (as shown in the Cu region shown in Fig. 22[b1]), which sensitively depend on the specimen tilt. This sensitivity results

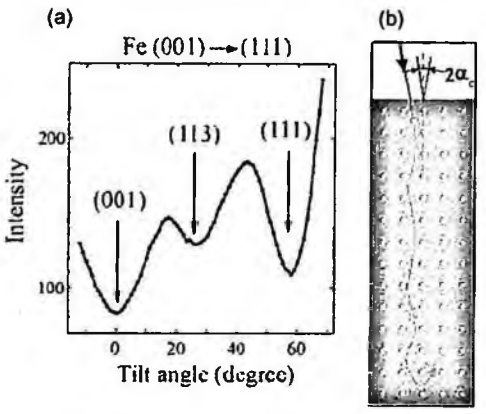

Figure 26. (a) Typical SE intensity with respect to tilt angle for the iron (Fe) single crystal sample under 30 keV Ga-FIB bombardment, where the tilting direction is from (001) to (111) [Reprinted with permission from [59] by Oxford University Press] and (b) schematic diagram of the ion channeling in the crystal solid.

from the dependence of the BSE yield η on the orientation of the primary beam relative to the lattice plane and is caused by a primary Bloch wave field [17]. Due to the sensitivity of the η variation on the surface, the channeling contrast can decrease with an increasing electron-probe focusing angle that should not exceed about 10 mrad. The depth of average channeling varies with Z_2, but for most elements, the additional contribution to the contrast is very small from the depths >50 nm. The channeling contrast is also very sensitive, either on an amorphous surface oxide layer or on multiple scattering in the crystal.

8. Three-Dimensional Microfabrication

An FIB shows its ability to add great value through a small volume of FIB-milling such as site-specific cross-sectioning, drilling and carving. The reason is that the milling time is approximately reciprocal with the FIB fineness. Typical examples are 3D-shaped micro body structures [61], micro tools [62], microlens mold [63,64], and nanoimprint [62]. Another ability is assembling of 3D-shaped micro parts using FIB-AD as "attacher". Using FIB-milling and FIB-AD as "cutter" and "attacher", respectively [35], we can utilize an FIB system as a micro machine shop.

Figure 27 shows a micro universal-joint: Each of the parts is FIB-fabricated from a 25-μm diameter Al wire and is sequentially assembled with each other using a manipulated needle. Another example is a micro diamond ring [65] shown in Fig. 28. The diamond was FIB-cut from a rough one of 10 μm in diameter is as small as five billionth carats, where 1 carat = 0.2 g. The ring was FIB-milled from a 20 μm-diameter W wire. Device transplantation [35] also is another future application using the "cutter" and "attacher" technique.

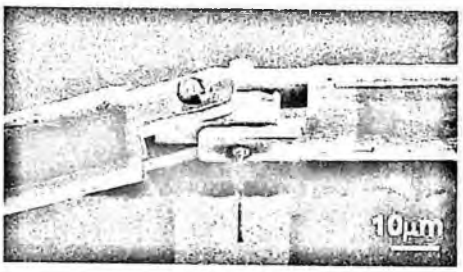

Figure 27. Micro universal-joint: Each of the parts is FIB-fabricated from a 25-μm diameter Al wire and is sequentially assembled with each other using both the manipulated needle (belonging to a μ-sampling units of Hitachi FIB system FB-2100) (Courtesy of T. Tanaka of Osaka Sangyo University).

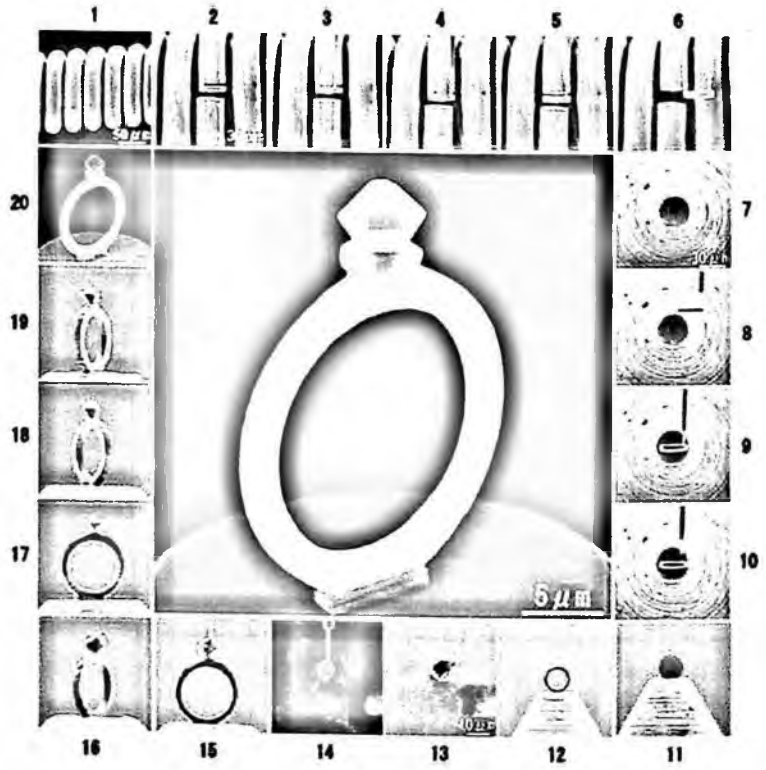

Figure 28. Micro diamond ring: The diamond was FIB-cut from a rough one of 10 μm in diameter is as small as five billionth carats, where 1 carat = 0.2 g. The ring was FIB-milled from a 20 μm-diameter W wire.

9. Conclusion

Gallium-FIB milling has been successfully applied to prepare cross-sectional samples at specific-site for SEM and TEM/STEM observations. It does not matter whether the samples are soft or hard, and/or fragile or flexible. The FIB plays also a role of

primary beam in scanning ion microscope (SIM) like an electron beam in scanning electron microscope (SEM). The SIM imaging plays an important role in a whole series of processes from specifying the milling area, to monitoring the milling in real-time, and to visually confirming the completion of milling. Using the FIB milling and FIB-AD as "cutter" and "attacher", respectively, we will utilize the FIB system as a micro machine shop, which allows milling, welding, and assembling for micro parts.

In the present study, we have reviewed inherent characteristics of the FIB milling such as sputtering, positioning accuracy, milling rate, uniformity of the cross-sections, and beam damage, and contamination. These milling characteristics are basically interpreted using the characteristics of sputtering yield $S(\theta)$ as a function of beam incident angle θ. Since the scanning FIB forms a locally sloped topography at the time of bombarding, the beam scanning speed (or pixel dwell time) in addition to the beam size and current are important parameters to control the milling rate and the redeposition of sputtered atoms.

We have referred also origins of opposite Z_2-contrast between SIM and SEM images. SIM imaging, the larger-Z_2 (or heavier) material shows the lower secondary electron (SE) yield. In the ion-induced SE emission, the SEs are excited by three types of collision process; one due to collisions between projectile ions and target electrons, one due to collisions between recoiled target atoms and target electrons, and one due to collisions between excited SEs and other target electrons. Monte Carlo simulations of the SE emission in SIM and SEM have well follow these Z_2-contrasts.

Acknowledgments

The authors would like to thank our colleagues in Hitachi High-Technologies Corporation for developing FIB systems and their applications over the years, especially Takeo Kamino, Mine Nakagawa, and Yuichi Madokoro. We would especially like to thank Kaoru Ohya, The University of Tokushima, for the joint research on ion-induced secondary electron emission.

References

1. T. Ishitani and H. Tsuboi, Objective comparison of scanning ion and scanning electron microscope images. *Scanning* **19**, 489–497 (1997).
2. T. Ishitani, H. Hirose and H. Tsuboi, Focused-ion-beam digging of biological specimens. *J. Electron Microscopy* **44**, 110–114 (1995).
3. T. Ishitani ,K. Umemura, T. Ohnishi, T. Yaguchi and T. kamino, Improvements in performance of focused ion beam cross-sectioning: aspects of ion-sample interaction, *J. Electron Microscopy* **53**, 443–449 (2004).
4. T. Ishitani and T. Yaguchi, Cross-sectional sample preparation by focused ion beams: A review of ion-sample interaction, *Microsc. Res. Techn.* **35**, 320–333 (1996).
5. S. Matusi and Y. Ochiai, Focused ion beam applications to solid state devices, *Nanotechnology* **7**, 247–258 (1996).

6. B. I. Prenitzer, C. A. Urbanik-Shannon, L. A. Giannuzzi, S. R. Brown, R. B. Irwin, T. L. Shofner and F. A. Stevie, The correlation between ion beam/material interactions and practical FIB specimen preparation, *Microsc. Microanal.* **9**, 216–236 (2003).
7. A. A. Tseng, Recent developments in micromilling using focused ion beam technology, *J. Micromech. Microeng.* **14**, R15–R34 (2004).
8. *J. Electron Microscopy* **53**, Special No. 5: Focused Ion Beam, 441–536 (2004).
9. J. Orloff, M. Utlaut and L. Swanson, *High Resolution Focused Ion Beams: FIB and Its Application* (Kluwer Academic/Plenum Publishers, New York, 2003).
10. L. A. Giannuzzi and F. A. Stevie, *Introduction to Focused Ion Beams: Instrumentation, Theory, Techniques, and Practice* (Splinger-Verlag, New York, 2004).
11. T. Ishitani, Focused-ion-beam system, *Electron Microscope* **32**, 28–32 (1997) (in Japanese).
12. T. Ishitani, Monte Carlo simulation of ion bombardment at low glancing angles, *Jpn. J. Appl. Phys.* **34**, 3303–3306 (1995).
13. J. F. Ziegler, J. P. Biersack and U. Littmark, The Stopping and Range of Ions in Solids (Pergamon Press, New York 1985).
14. J. F. Ziegler, The Stopping and Range of Ions in Matter (SRIM); (http://www.srim.org/).
15. J. P. Biersack and L. G. Haggmark, A Monte Carlo computer program for the transport of energetic ions in amorphous targets, *Nucl. Instrum. & Methods* **174**, 257–269 (1980).
16. D. C. Joy, *Monte Carlo modeling for electron microscopy and microanalysis* (Oxford University Press, Inc., New York, 1995).
17. L. Reimer, *Scanning Electron Microscopy* (Springer-Verlag, Heidelberg, 1998).
18. *Scanning* **17**, Special Issue on Electron Beam/Specimen Interaction Modeling for Metrology and Microanalysis in the Scanning Electron Microscope Part I and II, No. 4 and 5, 199–329 (1995).
19. Z.-J. Ding and R. Shimizu, A Monte Carlo modeling of electron interaction with solids including cascade secondary electron production, *Scanning* **18**, 92–113 (1996).
20. K. Kanda (Programs of "Ion Microscope: Monte Carlo Simulation" and "electron Microscope: Monte Carlo Simulation" are available at http://www.vector.co.jp/soft/win31/edu/se059367.html and http://www.vector.co.jp/soft/win31/edu/se059369.html, respectively.)
21. M. Nastasi, J. W. Mayer and J. K. Hirvonen, *Ion-Solid Interactions: Fundamentals and applications* (Cambridge University Press, Cambridge, 1996).
22. V. Krasheninnikov, F. Banhart, J. X. Li, A. S. Foster and R. M. Nieminen, Stability of carbon nanotubes under electron irradiation: Role of tube diameter and chirality, *Phys. Rev.* **B 72**, 125428 (2005).
23. D. C. Joy and S. Luo, An empirical stopping power relationship for low-energy electrons, *Scanning* **11**, 176–180 (1989).
24. X. Xu, A. D. D. Ratta, J. Sosonkina and J. Melngailis, Focused ion beam induced deposition and ion milling as a function of ion incidence, *J. Vac. Sci. Technol.* **B 10**, 2675–2680 (1992).
25. M. J. Vasile, J. Xie and R. Nassar, Depth control of focused-ion-beam milling from a numerical model of the sputter process, *J. Vac. Sci. Technol.* **B 17**, 3085–3090 (1999).
26. G. Carter, M. J. Nobes and I. V. Katardjiev, The theory of ion beam polishing and machining, *Vacuum* **44**, 303–309 (1993).

27. L. A. Giannuzzi and F. A. Stevie, A review of focused ion beam milling techniques for TEM specimen preparation, *Micron* **30**, 197–204 (1999).
28. R. M. Langford and A. K. Petford-Long, Preparation of transmission electron microscopy cross-section specimens using focused ion beam milling, *J. Vac. Sci. Technol.* **A 19**, 2186–2193 (2001).
29. N. I. Kato, Y. Kohno and H. Saka, Side-wall damage in a transmission electron microscopy specimen of crystalline Si prepared by focused ion beam etching, *J. Vac. Sci. Technol.* **A 17**, 1201–1204 (1999).
30. T. Ishitani, H. Tsuboi, T. Yaguchi and H. Koike, Transmission electron microscopy sample preparation using a focused ion beam, *J. Electron Microscopy* **43**, 322–326 (1994).
31. Y. Hata, R. Etoh, H. Yamashita, S. Fujii and Y. Harada, Microstructure analysis technique of specific area by transmission electron microscopy, *IEICE Trans. Electron*, E77-C, 590–594 (1994).
32. A. Tonomura, H. Kasai, O. Kamimura, T. Matsuda, K. Harada, T. Yoshida, T. Akashi, J. Shimoyama, K. Kishino, T. Hanaguri, K. Kitazawa, T. Matsui, S. Tajima, N. Koshizuka, O. L. Gammel, D. Bishop, M. Sasase and O. Okayasu, Observation of structures of chain vortices inside anisotropic high-Tc superconductors, *Phys. Rev. Lett.* **88**, 237001-1–237001-4 (2002).
33. Z. Wang, T. Kato, T. Hirayama, K. Sasaki, H. Saka and N. Kato, Focused-ion-beam preparation of wedge-shaped cross sections and its application to observing p-n junctions by electron holography, *J. Vac. Sci. Technol.* **B 21**, 2155–2158 (2003).
34. A. C. Twitchett, R. E. Dunin-Borkowski and P. A. Midgley, Quantitative electron holography biased semiconductor devices, *Phys. Rev. Lett.* **23**, 238302-1–238302-4 (2002).
35. T. Ishitani, T. Ohnishi, Y. Madokoro and Y. Kawanami, Focused-ion-beam "cutter" and "attacher" for micromachining and device transplantation, *J. Vac. Sci. Technol.* **B 9**, 2633–2637 (1991).
36. D. Santamore, K. Edinger, J. Orloff and J. Melngailis, Focused ion beam sputter yield change as a function of scan speed, *J. Vac. Sci. Technol.* **B 15**, 2346–2349 (1997).
37. A. Yamaguchi and T. Nishikawa, Low-damage specimen preparation technique for transmission electron microscopy using iodine gas-assisted focused ion beam milling, *J. Vac. Sci. Technol.* **B 13**, 962–966 (1995).
38. T. Ohnishi, H. Koike, T. Ishitani, S. Tomimatsu, K. Umemura and T. Kamino, A new focused-ion-beam microsampling technique for TEM observation of site-specific areas, *Proc. 25th Int. Symp. Testing and Failure Analysis*, 449–453 (1999).
39. T. Kamino, T. Yaguchi, Y. Kuroda, T. Ohnishi, T. Ishitani, Y. Miyahara and Z. Horita, Evaluation of TEM samples of an Mg-Al alloy prepared using FIB milling at the operating voltage of 10 kV and 40 kV, *J. Electron Microscopy* **53**, 459–463 (2004).
40. T. Kamino, T. Yaguchi, M. Konno, T. Ohnishi and T. Ishitani, A method for multi-directional TEM observation of a specific site at atomic resolution, *J. Electron Microscopy* **53**, 583–588 (2004).
41. M. Sugiyama and G. Shigesato, A review of focused ion beam technology and its applications in transmission electron microscopy, *J. Electron Microscopy* **53**, 527–536 (2004).
42. Z. Wang, T. Kato and T. Hirayama, Side-milling of preparing device cross-sections for electron holography based on a focused ion beam micro-sampling system, *J. Electron Microscopy* **53**, 489–491 (2004).

43. H.-J. Eo, J.M. Yang, T.-S. Park, J.-P. Lee, W. Kim, J.-C. Park and S.-Y. Lee, Chemical junction delineation of a specific site in Si devices, *J. Electron Microscopy* **53**, 277–280 (2004).
44. T. Ishitani, H. Koike, T. Yaguchi and T. Kamino, Implanted gallium-ion concentration of focused-ion-beam prepared cross sections, *J. Vac. Sci. Technol.* **B 16**, 1907–1913 (1998).
45. R. B. Jaminson, A. J. Mardinly, D. W. Susnitzky and R. Gronsky, Effects of ion species and ion energy on the amorphization of Si during FIB TEM sample preparation as determined by computational and experimental methods. *Microsc. Microanal.* **6** (Suppl 2: Proc.) 526–527 (2000).
46. Z. Wang, T. Kato, T. Hirayama, N. Kato, S. Sasaki and H. Saka, Surface damage induced by focused-ion-beam milling in a Si/Si p-n junction cross-sectional specimen, *Appl. Surface Sci.* **241**, 80–86 (2005).
47. T. Matsutani, K. Iwamoto, T. Nagatomi, Y. Kimura and Y. Takai, Flattening of sputter-etching with low-energy ions, *Jpn. J. Appl. Phys.* **40**, L481–L483 (2001).
48. A. Barna, B. Pécz and M. Menyhard, Amorphization and surface morphology development at low-energy ion milling, *Ultramicroscopy* **70**, 161–171 (1998).
49. T. Yaguchi, Y. Kuroda, M. Konno, T. Kamino, K. Kaji and M. Watanabe, A method for 3 dimensional structural and compositional imaging of nano-materials, *Microsc. Microanal.* **12**(suppl. 2), 528–529 (2006).
50. Y. Yabuuchi, S. Tametou, T. Okano, S. Inazato, S. Sadayama, Y. Yamamoto, K. Iwasaki and Y. Sugiyama, A study of the damage on FIB-prepared TEM samples of AlxGa1–xAs, *J. Electron Microscopy* **53**, 471–477 (2004).
51. M. Kudo, Y. Sakai and T. Ichinokawa, Dependencies of secondary electron yields on work function for metals by electron and ion bombardment, *Appl. Phys. Lett.* **78**, 3475–3477 (2000).
52. T. Suzuki, N. Endo, M. Shibata, S. Kamasaki and T. Ichinokawa, Contrast differences between scanning ion and electron microscope images, *J. Vac. Sci. Technol.* **A 22**, 49–52 (2004).
53. T. Ishitani, Y. Madokoro, M. Nakagawa and K. Ohya, Origins of material contrast in scanning ion microscope images, *J. Electron Microscopy* **51**, 207–213 (2002).
54. T. Ishitani and K. Ohya, Comparison in spatial spreads of secondary electron information between scanning ion and scanning electron microscopy, *Scanning* **25**, 201–209 (2003).
55. K. Ohya and T. Ishitani, Comparative study of depth and lateral distributions of electron excitation between scanning ion and scanning electron microscopes, *J. Electron Microscopy* **52**, 291–298 (2003).
56. K. Ohya and T. Ishitani, Monte Carlo simulations of topographic contrast in scanning ion microscope, *J. Electron Microscopy* **53**, 229–235 (2004).
57. K. Ohya and T. Ishitani, Imaging using electron and ion beam, *in Focused Ion Beam Systems: Basics and Applications*, N. Yao (Ed), (Cambridge University Press, Cambridge, 2007). (In press)
58. K. Ohya and T. Ishitani, Monte Carlo study of secondary electron emission from SiO_2 induced by focused gallium ion beams, *Appl. Surface Sci.* **237**, 606–610 (2004).
59. Y. Yahiro, K. Kaneko, T. Fujita, W. -J. Moon and Z. Horita, Crystallographic orientation contrast associated with Ga^+ ion channeling for Fe and Cu in focused ion beam method, *J. Electron Microscopy* **53**, 571–576 (2004).
60. J. Lnidhard, Influence of crystal lattice on motion of energetic charged particles, *K. Dan. Vid. Selsk. Mat.-Fys. Medd.* **34**, No.14 (1965).

61. M. Murakawa, H. Noguchi and S. Takeuchi, Fabrication of 3D shaped micro body structures of diamond by use of focused ion beam, Proc. 7th Applied Diamond Conf./3rd Frontier Carbon Technology Joint Conference (ADC/FCT) 185–190 (2003).
62. D. P. Adams, M. J. Vasile, G. Benavides and A. N. Campbell, Micromilling of metal alloys with focused ion beam-fabricated tools, *Precision Engineering* **25**, 107–113 (2001).
63. Y. Fu, Investigation of microlens mold fabricated by focused ion beam technology, *Microelectronic Engineering* **56**, 333–338 (2001).
64. K. Watanabe, T. Morita, R. Kometani, Hoshino, K. Kondo, K. Kanda, Y. Haruyama, T. Kaito, J. Fujita, M. Ishida, Y. Ochiai, T. Tajima and S. Matsui, Nanoimprint using three-dimensional microlens mold made by focused-ion-beam chemical vapor deposition, *J. Vac. Sci. Technol.* B **22**, 22–26 (2004).
65. Micro diamond ring (http://www.hitachi-hitec.com/em/nanoart/2004/index.html)

CHAPTER 14

NANO/MICROSTRUCTURING OF CERAMIC SURFACES BY UNCONVENTIONAL LITHOGRAPHIC METHODS

ROBERTO C. SALVAREZZA

Instituto de Investigaciones Fisicoquímicas Teóricas y Aplicadas, INIFTA CONICET, CC. 16 Suc. 4, (1900) La Plata, Argentina
robsalva@inifta.unlp.edu.ar

OMAR AZZARONI*

Max Planck Institute for Polymer Research
Ackermannweg 10-55128 Mainz, Germany
azzaroni@mpip-mainz.mpg.de

Design of reproducible, simple and efficient nanofabrication routes has become a frontier topic in the emerging field of nanotechnologies. In this chapter we discuss the "state of the art" of ceramics micro- and nanofabrication techniques. We pay special attention to progress in this field made during the last five years.

In this chapter we will discuss about the progress on the use of lithographic tools to create nanoscale ceramic patterns or the potential of soft lithography to create ceramic structures by means of liquid ceramic precursors. The chapter also describes advances on the use of self-assembly and self organization to achieve nanostructured ceramic surfaces. In the final part, we discuss about the possibility of combining physical vapour deposition with micromolding techniques to obtain nanostructured ceramic subtrates.

Keywords: Ceramics; lithography; sol-gel; self-assembled monolayers, nanostructuring.

CONTENTS

1. Introduction 472
2. Writing Ceramic Patterns with the Aid of Lithographic Tools 472
3. Monolayer–Directed Patterned Deposition of Ceramic Thin Films 476

*Corresponding author

4. Soft Lithographic Patterning of Ceramic Surfaces Using Molecular Precursors and Solution Chemistry. 480
5. Fabrication of Nanopatterned Ceramic Substrates Directed by Self-Assembly 484
6. Self-organization as a Route to Fabricate Nanopatterned Ceramic Substrates 487
7. Physical Vapor Deposition Meets Micromolding Techniques 488
8. Summary and Outlook 492
Acknowledgments 493
References 493

1. Introduction

The design and development of new and reproducible strategies for nano- and microscale patterning of materials surfaces has become one of the most relevant topics in the emerging nanotechnology. Physicists, engineers and materials scientists are being continuously challenged to discover new routes for creating small scale features in an efficient and accurate manner [1]. Pursuing this goal, different patterning methods with varying degrees of accuracy have been developed during the last decade. Moreover, researchers involved in the application and development of ceramic-based technologies work with the aim of minimizing the extremely high costs associated with the design, development and large production of ceramic-based micro- and nanodevices. Interaction between industry and academia provided the means for the creation of new strategies to be used as nanofabrication routes. However, many interesting patterning approaches did not reach the presumed technological impact as a consequence of lacking the required combination of reproducibility, accuracy, simplicity, and more important, suitability for large-scale fabrication.

This turned research on nanopatterning and nanomachining of ceramics and hard materials into a frontier topic of the current nanotechnologies. Ceramic materials combine unique properties [2] that make them extremely well suited for manufacturing diverse miniaturized devices, such as the microelectromechanical systems.

In this chapter, we will discuss the "state of the art" of ceramics micro- and nanofabrication techniques. In particular we emphasize the progress made in this area over the past five years, when nanostructuring ceramic surfaces was studied employing different techniques.

2. Writing Ceramic Patterns with the Aid of Lithographic Tools

Lithographic tools play a leading role in processing methods in the semiconductor industry. In the case of conventional lithography, a thin radiation-sensitive polymer layer is used as a resist [3]. Then a determined patterned region is exposed to the radiation in order to alter its solubility and remove it from the substrate using a

chemical developer. Apart from the well-known photolithography using photoresists, they exist a vast range of lithographic methods and techniques with a varying degree of accuracy and sophistication. When making a choice between different hard lithographic tools, a typical problem is to find the compromise between four main variables: resolution, process complexity, costs and time. Working with lithographic tools in the nanoscale (<100 nm) often implies a sudden increase in process complexity, cost and time. Optical lithography is a very well-established tool commonly used in many laboratories. However, resolution of optical lithography is nearly the wavelength of the radiation thus limiting the use of optical lithography with nanolithographic purposes. Moreover, other problems that make the choice even more difficult concerns on the reproducibility, uniformity and suitability for large scale fabrication. Industry and academia converged to develop new members of the lithographic family in order to bring other alternatives fulfilling the demands of the ever growing nanotechnology-based industries. One clear example is the laser holographic printing [4] enabling the formation of gratings with a significant printing speed but lacking on the required versatility to be used as a general patterning method.

The final variable, and central to our chapter,is the material. Ceramics are commonly referred as "hard to machine" materials due to difficulties to transfer, write or print patterns onto their surfaces. Traditionally the problem for patterning ceramic surfaces was on the microscale. However, during the last few years different groups have started to explore novel and clever strategies using electron and ion beam lithography for patterning ceramics with nanoscale resolution. These techniques do not require mask making capability and the resolution is mainly determined by the spatial distributionof the deposited energy and the contrast of the developer.

Focused ion beam in combination with chemical vapour deposition (FIB CVD) has demonstrated to be very useful technique for the fabrication of 3D structures. Morita *et al.* [5] used this approach to fabricate nanostructures of diamond-like carbon materials with a very large Young's modulus (600 GPa). These authors used phenanthrene as the precursor to synthesize the diamond-like material. The experimental setup comprised two gas sources, in order to increase the gas pressure and to achieve uniformity around the sample, and a beam with perpendicular incidence to the substrate. Well-defined three dimensional structures were obtained by combining the lateral growth mode with the beam scanning.

Another very interesting approach was reported by Ruda and co workers [6]. These authors used electron beam lithography (EBL) with processible high resolution resists with high metal content, highly metallized cobalt-clusterized polyferrocenylsilane. The resists operate in a negative tone mode. The exposed regions witnessed a chemical change turning them insoluble in the developing medium. In other words, the regions exposed to the e-beam remains firmly adhered to the substrate while the unexposed metallopolymer is removed. The possibility of manipulating high concentrations of Co and Fe with a well defined stoichiometry was exploited for creating well-defined nanopatterned ferromagnetic ceramics. In the

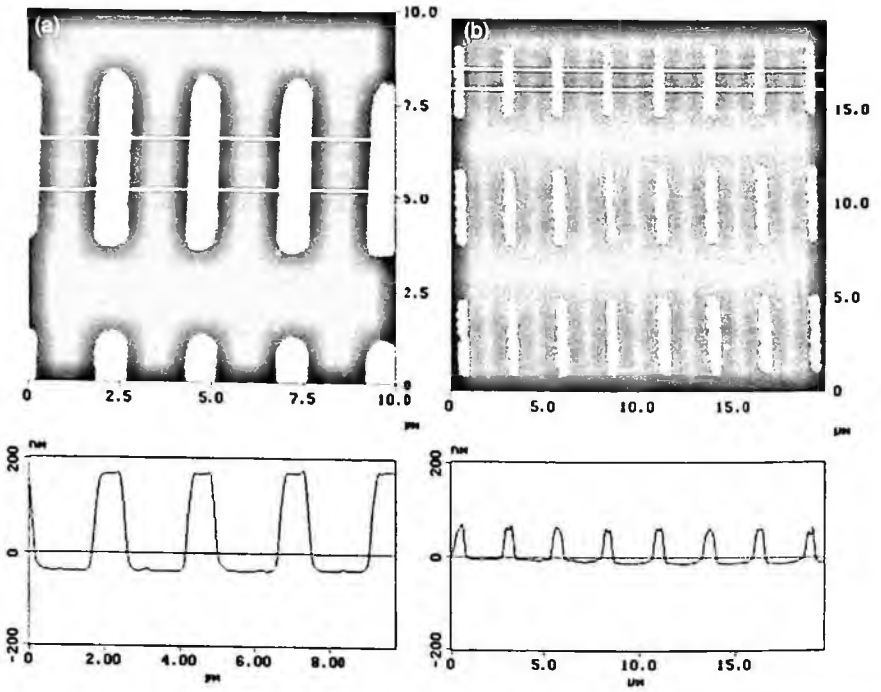

Figure 1. AFM imaging including cross-sectional analysis corresponding to lithographically patterned bars (A) before pyrolisis and (B) following 5 h the pyrolysis at 900 C. Reprinted with permission from [6] by VCH-Wiley.

case of the metallopolymer resist, the negative tone behaviour may result from crosslinking of polymer chins induced by e-beam. After EB nanopatterning, the substrate was pyrolized at 900°C during 5 h under a nitrogen atmosphere in order to obtain ceramics nanostructures containing Fe/Co nanoparticles. Thermal treatment did not introduce shape distortions but promoted an expected shrinkage in average height from 210 to 74 nm and in average width from 736 to 521 nm (Fig. 1).

On the other hand, Donthu *et al.* [7] used a different approach to fabricate ZnO nanostructures using e-sensitive polymers and sol-gel precursor. Firstly, a bilayer consisting of a high sensitivity methyl methacrylate-methacrylic acid (MMA-MAA) copolymer (at the bottom) and a low sensitivity PMMA (on top) was spincoated on the substrate. The polymer-coated substrates were irradiated and treated with oxygen plasma to improve the wettability of the subtrates. Then, a solution containing the sol-gel ceramic precursors was spincoated onto the patterned polymer surfaces and thermally treated at 150°C during 10 min. Finally, the substrates were soaked in acetone to dissolve the polymer resist and lift off the material deposited outside the patterned regions. This strategy enabled the fabrication of continuous and well-defined ceramic nanostructures with lateral resolution close to 40 nm (Fig. 2). A similar approach using this "soft EBL" approach has been recently reported for the fabrication of radially stacked heterostructures of multifunctional oxides [8].

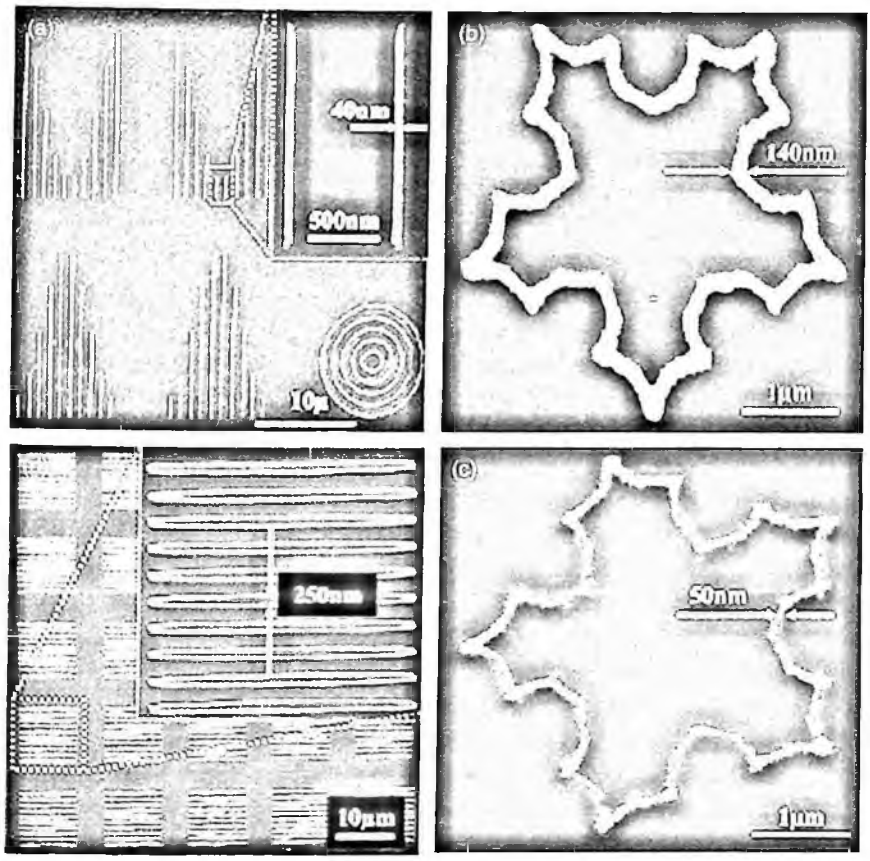

Figure 2. (a) Backscattered electron image of ZnO patterns on SiO_2 substrates annealed in air at 700 C for 20 min (b) secondary electron image before annealing, (c) secondary electron image after annealing at 700 C for 20 min in air and (d) secondary electron image of annealed patterns over large area. Reprinted with permission from [7] by American Chemical Society.

Well-defined nanorings of lead zirconate titanate were fabricated on a variety of substrates. These nanorings were used as nanoreservoirs and filled with a sol gel precursor of $CoTe_2O_4$ to generate radially stacked composite ceramic heterostructures.

Another rapidly growing fabrication method consists of laser processing of ceramic materials [9]. The main motivation for exploring this lithographic strategy was centered on finding a cost effective alternative for ceramic processing based on laser precision microfabrication. The principle lying behind this approach is based on the ablation of the substrate by the laser pulses [10]. When a determined surface is irradiated with an ultrafast laser, the irradiated substrate is melted and evaporated almost instantaneously. Submicrometer structuring of $LiNbO_3$ with periods of about 360 nm can be created by using picosend or femtosecond UV laser pulses [11]. This technique has been increasingly used for patterning a wide variety of substrates [12–22].

However, conventional UV, visible or IR lasers often promote significant damage in the hard material. The thermal stress built up in the materials during irradiation and the extensive cracking and exfoliation are deleterious effects of intense ns pulse laser irradiation. To overcome these problems, different approaches were developed. One is the use of vacuum ultraviolet and femtosecond lasers that has proven to be useful for high quality patterning of fused silica substrates [14]. Another novel approach for high quality patterned ablation is based on using hybrid lasers. In this case, another medium is introduced in the conventional nanosecond laser ablation system. The role of the medium is to enhance the absorption of the nanosecond laser beam by the materials. Sugioka and co-workers reported that simultaneous irradiation with the VUV laser beam which possess extremely small laser fluence and the UV laser beam has resulted in the accurate ablation of hard materials (VUV-UV multiwavelength excitation process) [23–25].

In this technique, the substrate is simultaneously irradiated by VUV and UV laser. The energy density of the VUV is only several tens of J/cm^2. In contrast, the energy density of the irradiated UV laser beam is nearly J/cm^2. The micropatterning process involves the irradiation of an unpatterned VUV beams on a broad area and the localized irradiation with the UV laser.

Another novel technique involving hydrid laser processing technique is laser-induced plasma – assisted ablation (LIPAA). In this technique, a single conventional pulsed laser lead to an effective ablation of transparent materials by coupling the laser beam to plasma generated from a metal target by the same laser [26,27]. An homogeneized beam is projected to the fused silica substrate. Since the silica is transparent in the UV range, the laser beam travels through the substrate and is absorbed by the Ag target placed behind the substrate. The interaction between the generated plasma and the laser beam produces and enhanced patterned ablation at the rear surface of the substrate.

Later on, Hosono and co-workers developed an holographic laser approach for patterning hard materials [28,29]. When two femtosecond pulses collide spatio-temporarily (overlapped region) the imprinting interference pattern results in the encoding of grating structures into the materials. This technique has been used to generate grating-like patterns on hard materials like diamond or sapphire. This is a promising technique which allows encoding gratings in almost all kinds of materials, irrespective of the photosensitivity.

3. Monolayer–Directed Patterned Deposition of Ceramic Thin Films

Modification of substrates with organic monolayers has been used as a very simple and powerful tool in the materials science community devoted to developing patterning strategies [30]. Currently, patterning self-assembled monolayers on a solid substrate is a routine procedure that can be accomplished in the laboratory without

using expensive equipment [31]. Common procedures to achieve this goal in micrometer range are microcontact printing or masked photodegradation of the organic film. Self-assembled monolayers are used to introduce surface functional groups with the aim of influencing the interactions between the deposited ceramic oxides and the substrate.

On the other hand, soft solution processing provides a simple method for synthesizing ceramic materials with a determined structure, size, shape and orientation. In this approach surface chemistry plays a determinant role on achieving the patterning of the desired material. Deposition of ceramic oxides onto SAM-covered surfaces is governed by an interplay between the interfacial chemistry related to the SAM-particle system and the colloidal chemistry referred to the particle-solution system.

In most of the cases, ceramic oxides in solution are charged because of the adsorption of charged species on their surfaces and this determines characteristics like morphology, size and the charge of the depositing particles [32].

On the other hand, the substrate is modified with functional groups deliberately introduced in order to tailor the interaction between the particles and the surface. The functional groups provide a mean for triggering a controlled heterogeneous nucleation and growth of the ceramic film on the pre-patterned regions of the substrate. A clear example is the deposition of TiO_2 using titanium dichloride diethoxide precursors onto methyl/silanol patterned domains. The silanol domains present a high selectivity for the nucleation and growth of the films leading to the formation of well-defined TiO_2 patterned domains (Fig. 3).

However, it must be noted that initial homogeneous nucleation of ceramic particles occur in solution where the solid phase is originated from the inorganic polycondensation derived from the hydrolysis of metal ions and the condensation of hydroxylated complexes [32]. The occurrence of these two processes, heterogeneous and homogeneous nucleation, is regulated by the net interfacial energy of the system. In other words, when the interaction between the ceramic particle and the substrate represents a system with a lower net interfacial energy, the system evolves in the direction of heterogeneous nucleation instead of the homogeneous nucleation. As a consequence, deposition from solution demands an accurate control of the reactive process in such a way of inducing nucleation and growth on the surfaces rather than in solution. Homogeneous nucleation can be suppressed working in a low supersaturation region, that is low solution temperatures or low concentration of metal ions can decrease the degree of supersaturation. On the other hand, heterogeneous nucleation can be achieved in an intermediate supersaturation region.

This strategy exploiting the versatility of solution chemistry in combination with chemically patterned substrates has been successfully used for patterning a wide range of materials such as: TiO_2 [33,34], ZrO_2 [35,36], SnO_2 [37,38], Y_2O_3 [39], ZnO [40,41], La_2O_3 [42], Ta_2O_3 [43], and different iron oxides [44–46]. In most of these cases, the ceramic films were synthesized by inorganic polycondensation and the growth from the substrate was induced using self-assembled monolayers

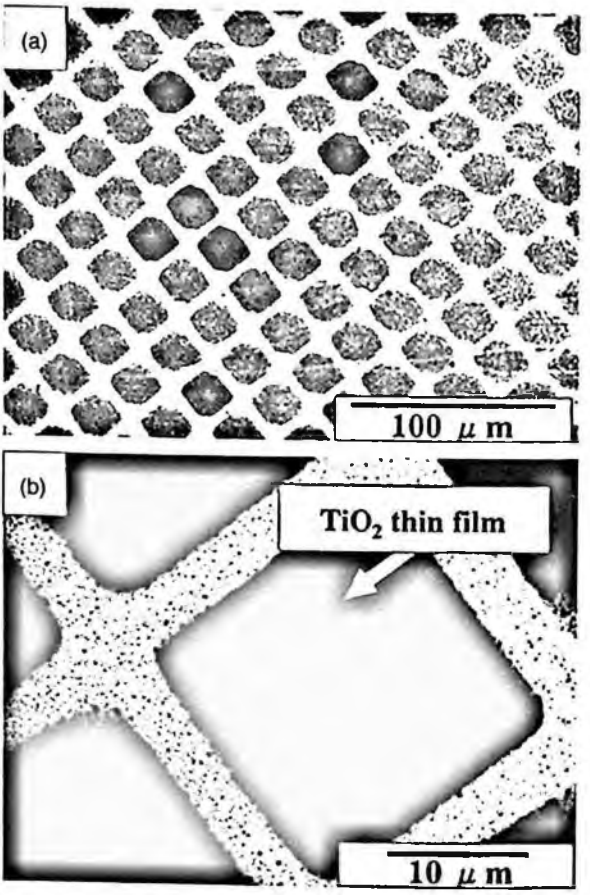

Figure 3. SEM micrographs of (a) a micropattern of TiO_2 thin films and (b) a magnified area of (a). Reprinted with permission from [33] by American Chemical Society.

functionalized with amino, phenyl or sulfonate terminal groups. The surface functional groups can strongly influence the deposition process due to the possible interactions between the depositing ceramic particles and the many different chemical entities on the substrate. A clear example is the growth of iron oxyhydroxide films onto SAM-modified substrates. It has been demonstrated that film growth is sensitively improved by using SAMs with sulfonate terminal groups in clear contrast with other surfaces modified with OH, CH_3, COOH and NH_2 terminal groups [47].

Another nice example is the growth of PbS films on different SAMs by using the chemical bath deposition method. The method consists on depositing PbS films by using a solution containing $Pb(ClO_4)_2$ and thiourea at room temperature. Interestingly, in this case the film formation is mainly governed by the pH. At low pH, the PbS film is preferentially deposited on SAMs with COOH and SO_3H terminal groups. Conversely, at high pH the film can be formed on surfaces bearing different terminal groups [48].

On the other hand, Koumoto *et al.* developed a method which consists of locally inducing supersaturation by using site-selective growth from a catalytic surface.

The authors used this strategy for patterning ZnO films on phenyl/ hydroxyl surfaces [41]. Initially, Pd catalyst is selectively immobilized from a Pd/Sn colloid solution on the phenyl groups domains on the surface. Then, the substrate is immersed in an aqueous solution containing $Zn(NO_3)_2$ and dimethylamineborane (DMAB) at 60°C. The catalyst induces the generation of hydroxyl ions near the substrate surface increasing the local saturation and promoting the heterogeneous nucleation. This approach has proven to be a useful procedure to create ZnO patterns with 1 μm in lateral resolution (Fig. 4).

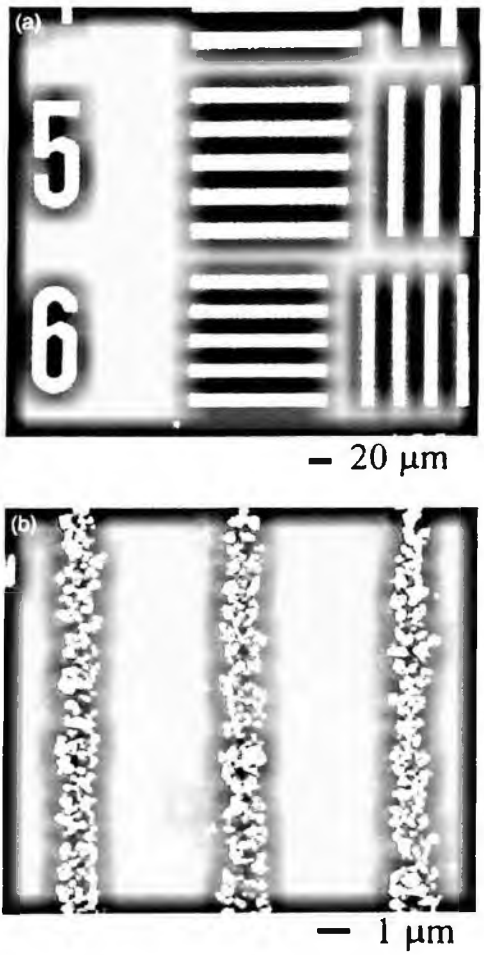

Figure 4. SEM images of the patterned ZnO. a) Large feature sizes area and b) 1 μm lines. Deposited particles are about 0.2 μm in diameter. Reprinted with permission from [41] by VCH-Wiley.

4. Soft Lithographic Patterning of Ceramic Surfaces Using Molecular Precursors and Solution Chemistry.

One of the main outstanding features of sol gel chemistry is its ability to elaborate solid materials beginning from molecular precursor [49]. The combination of inorganic polymerization process with organic chemistry offers a versatile alternative for materials synthesis. Currently, through soft chemistry processes, it is possible to design and control properties in ceramic materials in a predictable manner [49].

Sol gel techniques correspond to a process called hydrolytic polycondensation, where leaving groups at the metal are substituted by nucleophilic attack of H_2O. This process occurs at many metal centers in presence of many different leaving groups like halide, sulphide, alkoxide or nitride. Then, this process is followed by the elimination of the leaving group and formation of the metal hydroxide. This process leads to metal oxide bonds either by homo or heterocondensation. Finally, the solid phase is formed after a set of very complex steps involving precursors, oligomers, polymers, colloids, sol and gel [49]. Sol gel techniques have been employed as a cost effective and fast route to obtain ceramic materials with engineered properties. This choice is also based on their low temperature characteristics and good quality of the obtained films. For example, silica films, prepared by sol gel chemistry possess low optical loss and adjustable refractive index [50].

The first attempts to create patterned ceramic substrates using sol gel chemistry were based on the use of patterned substrates with different chemical domains. Nuzzo *et al.* used surfaces modified with patterned self-assembled monolayers for directing the deposition of Ta_2O_5 from sol gel precursors (tantalum ethoxide in absolute ethanol) onto different technologically important substrates [51]. These authors exploited the poor adhesion of ceramic films onto methyl terminated surfaces allowing delamination of oxide film from the functionalized regions. Sol gel deposition of Ta_2O_5 onto the functionalized substrates was followed by thermal treatment at 700 C and then by mild nonabrasive polishing. This process produced high quality patterned oxide on the patterned unfunctionalized regions.

Moreover, the antiadherent properties of SAMs have been exploited for direct patterning oxides surfaces by electrochemical oxide deposition [52]. The oxide film was deposited onto an alkanethiolate-modified Cu master from a plating bath and by applying a constant potential value at the electrochemical interface. After releasing the electrodeposited oxide film from the master, an accurate pattern transfer in the submicrometer scale was observed.

In order to fabricate ceramic microstructures from molecular precursor many research groups exploited the versatility and low cost of soft lithographic techniques. Soft lithography is a set of techniques that relies on molding and printing with an elastomeric stamp, polydimethylsiloxane (PDMS). This includes microtransfer molding, microcontact printing, and micromolding in capillaries (MIMIC) [53–55].

With soft lithography any material that can be derived from liquid precursor can be patterned, provided that the solvent used does not swell the elastomeric mold.

This makes soft lithography an outstanding alternative for molecular precursors to fabricate a wide range of complex ceramic architectures without using etching procedures.

Whitesides and co workers exploited this combination for patterning ceramic materials for high temperature applications. In particular, they worked with borosilicon carbonitride quaternary ceramics synthesized from several preceramic polymers [56]. A PDMS mold was filled with the preceramic and then a silicon wafer was pressed against the filled PDMS. After curing the preceramic during 1 hour at 200 C the mold was removed. The obtained polymeric microstructures were placed on top of a silicon wafer and transferred into a furnace and thermally treated at 1050 C. After thermal treatment samples evidenced a lateral shrinkage of 30%. The same research group following a similar strategy succeeded on achieving high quality accurate patterning of glass microstructures [57] (Fig. 5).

Cao *et al.* used a similar route to synthesize patterned complex oxide materials with important physical properties such as ferroelectricity, piezoelectricity or pyroelectricity. They synthesized the $Sr_2Nb_2O_7$ sol from inorganic precursors like strontium nitrate and niobium pentachloride using ethylene glycol as a cross linking agent and ethanol as a solvent [58].

Then they used a technique called micromolding in capillaries where the fluid is patterned by spontaneous filling of PDMS mcrochannels. When the elastomeric molds is placed in conformal contact with a clean silicon substrate, the channels of

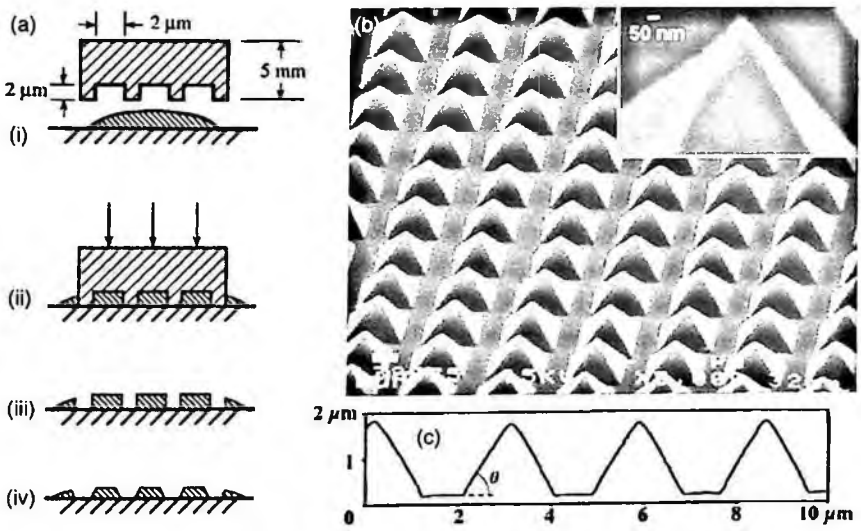

Figure 5. (A) Schematic describing the molding method to fabricate structures supported on a flat susbtrate. A droplet of precursor is compressed between the stamp and the surface (a,b). The high interfacial free energy of the solution promotes dewetting of the precursor where the stamp and the substrate were in contact (c,d). (B) SEM image and its AFM-derived analysis of a patterned piece of silica. Reprinted with permission from [57] by VCH-Wiley.

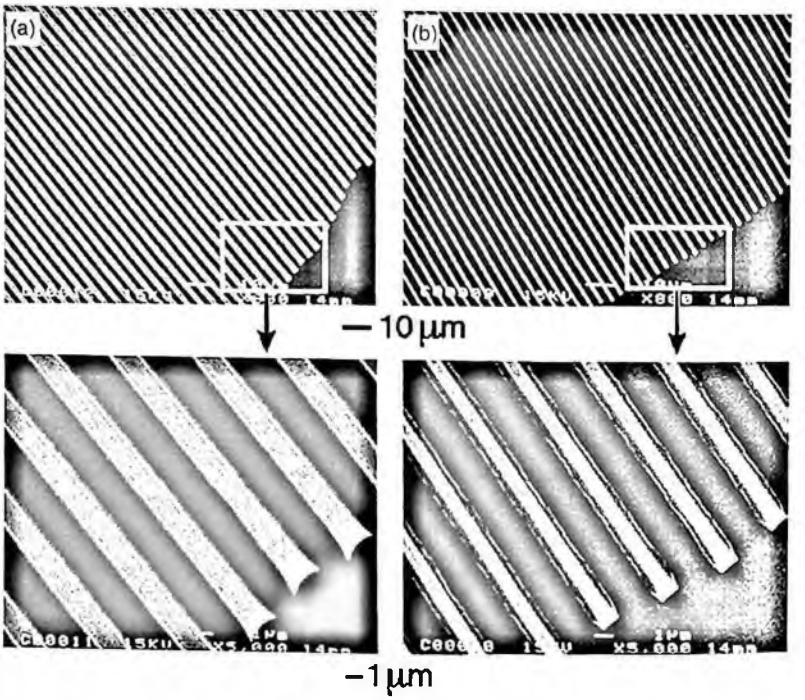

Figure 6. SEM images of MIMIC-patterned microstructures on a silicon substrate using an ethanol solution of the polymeric precursor to ZrO_2: (A) Prior thermal treatment firing, (B) after thermal treatment at 460 C for 4 h. Reprinted with permission from [59] by Materials Research Society.

the mold form capillaries with the substrate. The sol was deposited at the open end of these capillaries. Then the solvent was evaporated by placing the molds and the substrate in a drying oven at 100 C during one day. This process induces the condensation reaction promoting the cross linking and leading to the sol-gel transition. Finally, the molds were removed and the patterned samples were thermally treated at a 700–800 C for 30 min. The features evidenced a 46% shrinkage after densification by thermal treatment. Similar approaches were also applied for patterning other oxide ceramics such as zirconia and tin oxide [59], as shown in Fig. 6.

However, some problems may be present when dealing with MIMIC. Even considering that the filling process by capillary forces is thermodynamically favorable, infiltration kinetics can introduce some limitations for surface patterning by MIMIC [60].

Ideally the solutions suitable for MIMIC are powder free chemical solution with low viscosity and low solid loading. Within this scope we find liquid prepolymers and sol–gel precursors. In spite of lacking on these requirements, particulate fluids were used as a good alternative to obtain ceramic films by soft lithographic techniques.

Gauckler and coworkers used MIMIC for patterning 10 μm lines of SnO_2 ceramics using a 40 vol % suspension [61]. In most of the cases MIMIC patterning with

ceramic suspensions involved the use of low concentration solutions with low viscosity in order to use the capillary forces to fill the channels [62,63].

To overcome this limitation, Moon *et al.* introduced a technique called vacuum-assisted microfluidic lithography [60]. A PDMS microfluidic device is used to fabricate ceramic microstructures employing ceramic suspensions of relatively high solid loadings, 42 vol %. The microfluidic device loaded with the suspensions is then placed in a vacuum chamber. The lower overall pressure allows releasing the gas contained within connected volumes of the channel networks. When the pressure is returned to atmospheric level, the suspensions flow in to fill the voids left in the channels. This technique also permits simultaneous pattern generation of multiple materials on the same substrate. Using mFL with suspensions of Al_2O_3 and NiO it is possible to fabricate interdigitated ceramic microstructures composed of two different materials on the substrate (Fig. 7).

Finally, Chou and co workers reported direct nanoimprinting of sol gel films for the fabrication of SiO_2-TiO_2 gratings [64]. The nanoimprinted samples shows excellent uniformity and smooth pattern profiles having 300 nm pitch and 80 nm linewidth. A 600 nm thick sol film was spin coated onto silicon substrates. Imprints were carried out immediately. During the imprinting process the mold and the gel

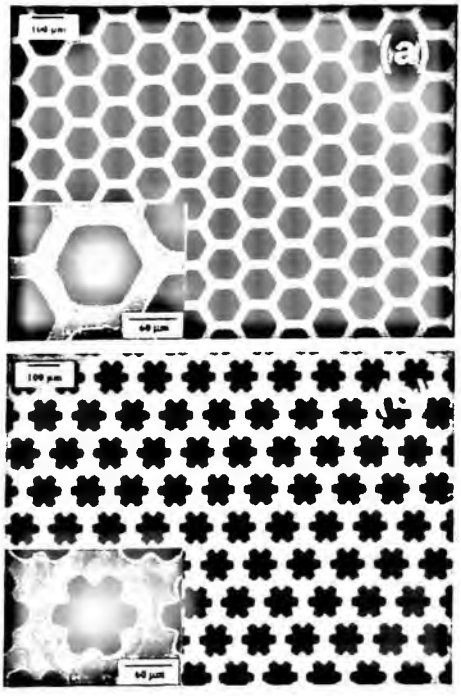

Figure 7. Optical micrographs of different patterned structures of Al_2O_3 on a Si substrate obtained by vacuum-assisted microfluidic lithography. The height of the structure was 25 mm. Reprinted with permission from [60] by Blackwell Publishing.

film were heated from 17 to 200 C. After releasing the mold, the patterned gel was thermally treated at 400 C evidencing a 61% shrinkage in the film thickness. The shrinkage was in the direction perpendicular to the substrate with no obvious shrinkage observed in the direction parallel to the wafer substrate. Similarly, Park *et al.* used nanoimprint lithography for patterning SiC-based ceramic patterns on Si substrates. In this case, a viscous polyvinylsilane was used as a ceramic precursor, followed by pyrolysis at 800 C under nitrogen atmosphere [65].

In most cases, the micromolding of pre-ceramics or ceramic suspensions shows considerable isotropic or ani- sotropic shrinkage after thermal treatment. Recently, Martin and Aksay [66] demonstrated that the micromolding of sol–gel films could produce unintended topographical distortions. This is as a consequence that during thermal treatment, a non-uniform shrinkage across the micromolded film is observed. In spite of the versatility of the method, this fact should limit the potential applications of the technique. Moreover, shrinkage has shown deleterious effects on micromolding ceramic suspensions where high drying shrinkage can lead to partial destruction of the patterned sample. This deleterious effect can be reduced (for patterning above the micrometer scale) by colloidal isopressing [67], a technique in which a pre-consolidated slurry is injected into an elastomeric mold and isopressed to rapidly convert the slurry into an elastic body that can be released from the mold without any distortion.

5. Fabrication of Nanopatterned Ceramic Substrates Directed by Self-Assembly

Most of the approaches discussed along this chapter consist of the so-called top down strategies. These are based on miniaturizing existing techniques which are already available at larger scales. An interesting alternative to these strategies is the bottom up approach. The philosophy of the bottom up strategies is the creation of nano- and microstructures through the use of smaller building blocks. These building blocks generate the desired structure through self-assembly without any external intervention when the process is carried out in the appropriate conditions [54].

The concept of self-assembly is very familiar to disciplines like biology. Different building blocks like molecules, macromolecules or nanoparticles spontaneously organize giving origin to well-defined structures stabilized by non covalent supramolecular interactions. Many biological processes, like membrane formation using phospholipids as building blocks, are based on the self-assembly principle [54].

One very important feature relies on the fact that the stabilized self-assembled structures are close to the thermodynamic equilibrium. As a consequence supramolecular aggregate present a very low level of defects. Biology has demonstrated that self-assembly is able to generate very complex and very small architectures. With this focus different researchers explored the use of self-assembly as a route to achieve well-defined patterned nanostructures [54].

Aksay and co-workers synthesized nanostructured ceramic materials by exploiting the templation effect of complex fluid systems [68]. These complex fluids, which are based on amphiphilic building blocks like surfactants, biomembrane lipids or block copolymers, can generate unique features in the 1–100 nm range through spontaneous self-assembly. By controlling the size of the building blocks and the interaction strength between them, self-assembly can be a very versatile strategy for the manipulation and generation of nanostructures at temperatures <100 C. Higher temperatures can lead to coarsening that is a strong limitation to retain the pre-designed nanostructured features [68].

This approach is based on exploiting to the weak interactions that determine the architecture of the supramolecular aggregates of the amphiphiles. Then by using inorganic precursors, the strategy relies on replicating the structures of the complex fluids into an organic/inorganic nanostructured composite material. Later the complex fluid portion is removed through solvent extraction or pyrolysis, converting the organic-inorganic hybrid into a 100% ceramic nanostructure. Materials obtained by this procedure received the name of self-assembled ceramics.

Chan *et al.* produced porous and relief ceramic nanostructures from self-assembling block copolymer (polyisoprene and poly (pentamethyldisilylstyrene)) precursors in a single step at low temperature [69]. In this case, the key factor is the careful selection of the relative volume fraction and phases. These authors showed that block copolymers can produce precursor materials with different symmetries and structures giving origin to highly ordered and complex nanostructures. The process consisted of a bifunctional oxidation to both selectively remove a hydrocarbon block and convert a remaining silicon-containing block to a silicon oxycarbide ceramic. Interestingly, the obtained nanoarchitectures only depend only on the volume fraction of the hydrocarbon block relative to the silicon-containing block in the block copolymer precursor. Moreover, double gyroid and inverse double gyroid morphologies were obtained by using two triblock copolymer precursors. However, treatments like ozonolysis or ultraviolet irradiation can affect the selective removal of the hydrocarbon block and the conversion of the silicon-containing block to a silicon oxycarbide ceramic. This strategy has been successfully used to synthesize nanorelief ceramic structures with interfacial areas of 40 square meters per gram.

Cooperative self-assembly of organic and inorganic materials can lead to a vast range of ordered morphologies. The combination of self-organization and soft lithography has been exploited as a simple route to generate hierarchically ordered ceramic materials over several length scales. Stucky *et al.* reported the preparation of porous silica, niobia, and titania with three-dimensional structures patterned over multiple length scales [70]. These materials show hierarchical ordering over several discrete and tunable length scales ranging from 10 nanometers to several micrometers (Fig. 8).

Another clear example where self-assembly and self-organization can lead to nanostrutured ceramics is the use of incompatible diblock copolymers. Diblock

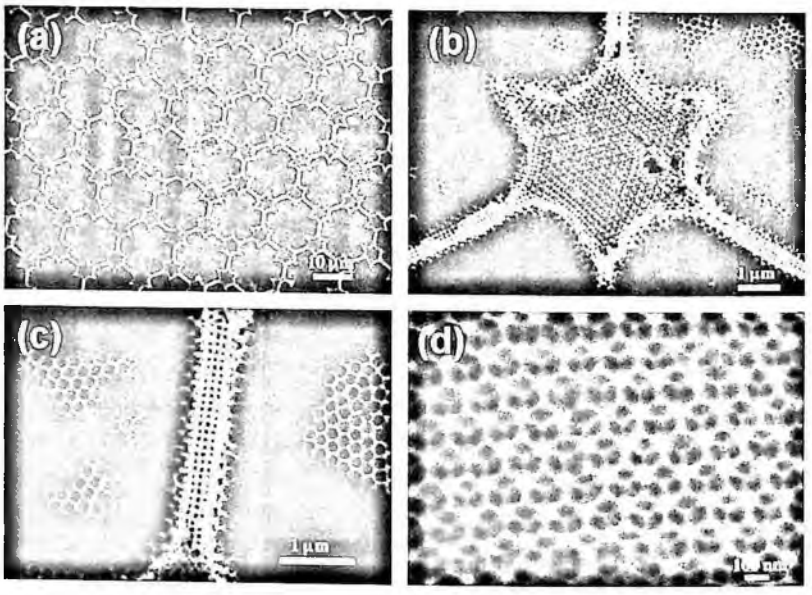

Figure 8. (A to D) SEM images, at different magnifications, of hierarchically ordered mesoporous silica displaying organization over three discrete characteristic dimensions. Reprinted with permission from [70] by American Association for the Advancement of Science.

copolymers are two chemically different polymer chains held together through covalent bond. The interplay between the connectivity constraints and the incompatibility between the blocks, leads to self-assembly into microphase-separated molecular–scale domains with ordered morphologies [71]. These macromolecular architectures can be supported on solid substrates forming a large variety of well ordered structures of molecular dimensions.

Following this framework, Park *et al.* proposed self-assembly in synthetic materials as a route for nanopatterning ceramic surfaces [72]. These authors fabricated dense periodic arrays of holes and dots on silicon nitride-coated silicon wafers using a method called block copolymer lithography. A monolayer of ordered microdomains was deposited on the surface by spin coating. These films consisted of diblock copolymer thin films, polystyrene-polybutadiene (PS-PB) and polystyrene-polyisoprene (PS-PI), with well ordered spherical or cylindrical microdomains.

Initially, the microdomain monolayer was exposed to ozone to selectively degrade and remove the PB spherical domains before treatment with reactive ion etching (RIE). Ozone attacks the double bonds in the PB domains producing a region that can be dispersed in water. This results in an array of voids in the PS matrix. Later, the sample was exposed to RIE producing holes in the substrate. The hexagonally ordered holes were 20 nm in diameter with a separation of 40 nm apart with polygrain structure. The fabrication of dots consisted of using the same microdomain monolayer but the PB domains were stained with OsO_4. Osmium-stained domains present a reduced etching rate during treatment with RIE. As a consequence, the

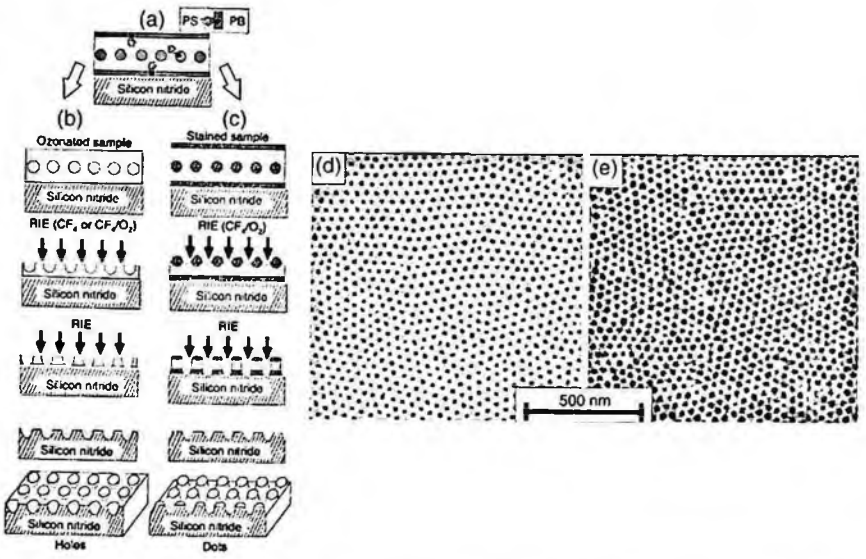

Figure 9. (A) Block copolymer film deposited on the silicon nitride substrate. (B) Schematic of the process producing holes in the silicon nitride. (C) Schematic of the process producing dots in the silicon nitride. (D) SEM image of a partially etched, ozonated monolayer film of spherical microdomains. (E) SEM image of hexagonally ordered arrays of holes in silicon nitride on a thick silicon wafer. The pattern was transferred from a copolymer film such as that in (D). The darker regions represent 20-nm-deep holes etched out in silicon nitride. Reprinted with permission from [72] by American Association for the Advancement of Science.

regions underneath the PB domains were partially masked from the RIE process, resulting in the fabrication of dots (Fig. 9).

6. Self-organization as a Route to Fabricate Nanopatterned Ceramic Substrates

Previously we have described different approaches for exploiting self-assembly in soft matter as a route to generate templates for nanofabrication. The spontaneous formation of different nanostructured materials through self-organization phenomena has attracted increasing interest through the last decade. Self-organization is now being examined extensively for large scale patterning at scales below 100 nm [73]. Concerning this latter, special emphasis was placed on using naturally occurring self-organization processes on hard matter leading to well-defined nanostructured solids.

A typical example is aluminum anodic oxidation producing self-ordered nanochannel arrays. This technique is a very promising self-organization method to obtain highly ordered and high aspect ratio periodic structures arrays in the nanometer scale. Anodic porous alumina is prepared by the anodic oxidation of aluminium in an acidic electrolyte. Recent improvements in the degree of ordering obtainable for a hole array has increased even more the attractiveness of such materials for nanofabrication [73].

Masuda *et al.* pioneered this very successful approach using nanostructured alumina as a host or template for fabrication [74]. The potential of this approach relies on the preparation of large area nanostructures with high aspect ratios. During the last years, nanostructured alumina has been widely used as a template for nanostructuring materials, including ceramics and other hard materials.

Takahagi *et al.* achieved the pattern transfer of an alumina template containing nanohole arrays to a Si substrate by RIE. Treating a nanostructured porous alumina/SiO_2/Si substrate with RIE using chlorine plasma is a very effective route for pattern transfer to Si [75].

On the other hand, Masuda *et al.* used a nanostructured alumina to fabricate nanoholes on a diamond substrate [76]. The nanostructured membranes were laid on top of the synthetic diamond films, and then deep holes were etched into the films using an oxygen plasma treatment. This approach leads to the fabrication of ordered diamond nanostructures over 1 cm^2 areas. The versatility of the method to fabricate different diamond surface architectures is based on the capability for electrochemically nanostructuring the membrane that is used as etching mask. It must be noted that anodic alumina has high resistance to oxygen plasma etching being able the generation of high-aspect ratio features.

7. Physical Vapor Deposition Meets Micromolding Techniques

Molding technology could be interpreted as a primary strategy to replicate features by sequential pattern transfer steps. This is commonly used to transfer surface-relief patterns on diverse functional materials. In spite of its simplicity, molding technology is still at the forefront as a simple and valuable tool for the next generation nanotechnologies. Different research groups have demonstrated how easily molding techniques can be applied in the nanoworld [77,78].

The molding and replication approach (micro- nanomolding) presents distinctive outstanding features: simplicity, high-resolution, low cost and high throughput. However, in spite of these advantages for transferring surface-relief patterns, micromolding strategies have been mainly focused on using polymeric materials.

By simple physical contact, the micromolding process is carried out by casting a pre-polymer or polymer against a master surface. Then, after polymerization or solvent evaporation, the polymer film is released from the master. In the case of replication, it involves two consecutive "relief-transfer" processes.

Molding and replication on polymer materials is widely used on large-scale fabrication of diffraction gratings or compact discs. Extending the concept of molding and replication to ceramic materials brings a straightforward route for patterning "hard to micromachine" materials.

In order to achieve this goal Auger *et al.* explored the direct micromolding of ceramic materials deposited by physical methods onto micromolds with no need for post-patterning treatments [79]. In this strategy, the relevant step of the molding

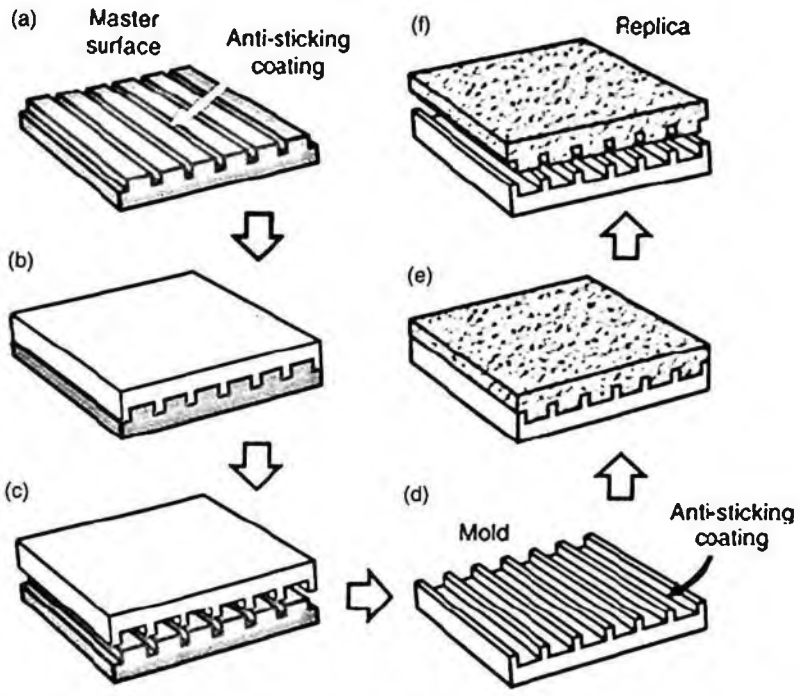

Figure 10. Schematic describing the molding and replication procedure used for transferring surface-relief patterns onto ceramic surfaces. A master surface (a) modified with an antisticking coating is used to fabricate the corresponding metallic mold (b) by thermal evaporation (c). Then, this negative replica (d) is used as a mold for the physical vapour deposition of the ceramic film (e). After detaching the deposited film a replica of the original surface is obtained (f). Reprinted with permission from [79] by VCH-Wiley.

process is to provide molds with good anti-sticking properties (Fig. 10). A low surface-energy layer on mold surfaces helps sensitively the release process and increases the mold lifetime by preventing further surface contamination. In this case, fluorine- or methyl-terminated self-assembled monolayers (SAMs) are the most commonly used anti-sticking layers [80]. These layers are built up by simple self-assemby on the surface. In addition, the molecular thickness of the monolayer enables pattern transfer of nanoscale feature due to the release layer itself.

However, direct micromolding of ceramic materials by depositing onto surface-modified molds is not so straightforward. It is well known that deposition conditions like temperature or particle energy, required to grow high-quality ceramic films, can introduce failure on the release process due to degradation of the anti-sticking coating.

These limitations can be avoided by introducing slight changes in the deposition conditions. For example, ceramic deposition by reactive sputtering involves the formation of high-energy species. Collision of these energetic species with the modified substrate produces immediate degradation of the SAM in the early stages of

deposition. These detrimental effects can be overcomed by increasing the substrate-target distance (d), and by introducing an inert gas into the sputtering chamber, in such a way of "thermalizing" the energetic species arriving at the SAM-coated substrate.

Following this route micromolding of aluminum nitride surfaces deposited by reactive sputtering on metallic micromolds has been recently reported. Aluminum nitride (AlN) is a ceramic material that exhibits a wide bandgap with potential applications in constructing arrays of electro-optical and photonic devices. In spite of the promising properties of this ceramic material, little progress has been reported on the design of cost-effective and reproducible routes for the surface patterning of AlN.

Ceramic films were deposited onto surface-modified Cu micromolds by dc reactive sputtering of a pure aluminum target under specific experimental conditions. By the direct micromolding (deposition and release) of sputtered ceramic films well defined AlN gratings were obtained. In addition, ceramic gratings present a very low roughness (Fig 11).

Other techniques for depositing ceramic films involve the evaporation of the ceramic material itself, such as electron-beam evaporation. In those cases, temperature is a relevant factor that could affect the stability of the anti-sticking coating. The evaporated particles arriving at the substrate are low-energy particles, so the integrity of the antisticking coating is not at risk. By using the micromolding technique in combination with electron beam evaporation it was possible to fabricate patterned B_4C substrates from Au micromolds. The Au micromolds can be easily obtained by micromolding thermally evaporated gold films using copper micromolds as master surfaces. In the case of electron beam evaporation an incident 110 mA e-beam biased at 7 kV with a 1 cm^2 spot size was used to evaporate the B_4C films under vacuum conditions. Detrimental thermal effects on antisticking coating stability can be minimized by increasing the evaporating source-substrate distance. This change influences the growing rate of the evaporated ceramic material but no damage to the antisticking coating is promoted, thus promoting a successful relief transfer (Fig. 11).

Another very useful technique for depositing ceramic materials is pulsed laser deposition (PLD). The combination of PLD with micromolding techniques enlarged even more the variety of ceramic materials that can be micromolded using physical vapour deposition. One example has been recently reported by Zaldo *et al.* on the deposition of micropatterned ZnO films [81]. PLD was performed in a vacuum chamber at room temperature. A KrF laser ($\lambda = 248$ nm) was used to ablate sintered ZnO (99.99%) ceramic targets rotating at 50 rpm. The laser fluence J on the target was 10 J cm^{-2} and the pulse repetition frequency was 10 Hz. The target-substrate distance was 6 cm. One remarkable feature of PLD is that the kinetic energy of the species in the laser plasma can be easily controlled by introducing an inert gas on the deposition chamber. In order to avoid degradation of the antisticking coating,

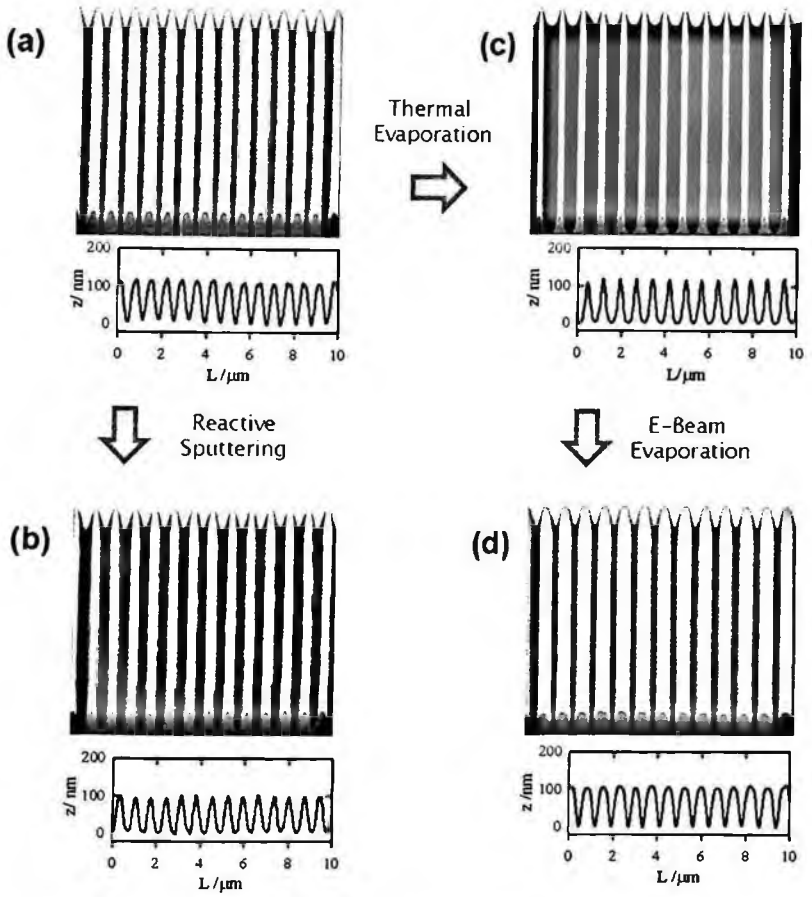

Figure 11. 3D AFM images ($10 \times 10\,\mu m^2$) and their corresponding cross sections showing: (a) a Cu micromold; (b) a micromolded AlN surface obtained by reactive sputtering onto the Cu micromold depicted in (a); (c) a Au micromold obtained by thermal evaporation using the copper surface depicted in (a) as a master; (d) a micromolded B4C surface obtained by electron-beam evaporation onto the Au micromold depicted in (b). Reprinted with permission from [79] by VCH-Wiley.

these authors introduced Ar as a background gas to thermalize the plasma. By using Cu micromolds grating-like patterned ZnO substrates were easily obtained.

One remarkable fact of using physical deposition techniques is that micromolded surfaces do not show significant shrinking effects. The amplitude of the sinusoidal relief structures transferred from the micromold to the ceramic film suffers a shrinkage of $< 5\%$, and the pitch shows only slight variations ($< 2\%$). This is a clear advantage of the direct micromolding procedure if we consider that in most cases, the micromolding of pre-ceramics or ceramic suspensions shows considerable isotropic or anisotropic shrinkage after thermal treatment.

Physical deposition methods can easily produce deposits with small grain sizes (< 30–$40\,nm$). Larger grain sizes can be serious limitation when it is intended to

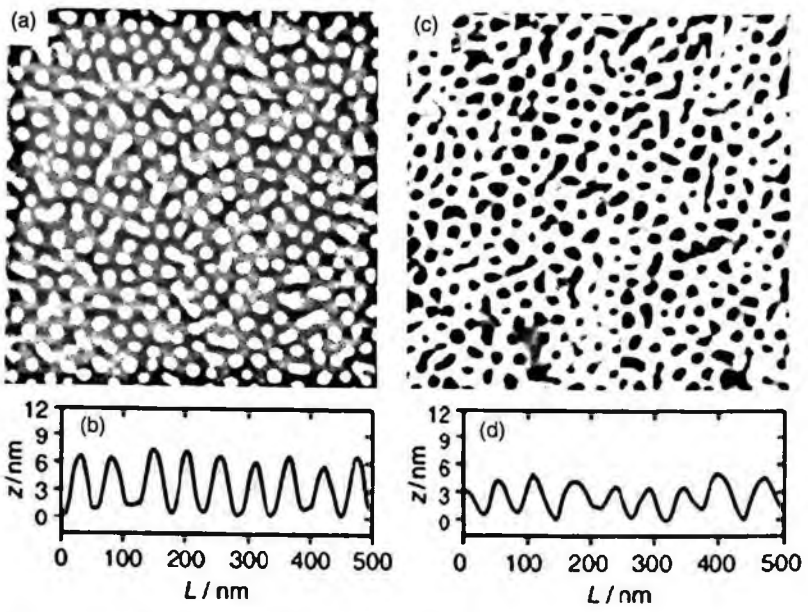

Figure 12. Top view AFM images ($1 \times 1\ \mu m^2$) with their corresponding cross-sectional analysis of a nanostructured SiO_2/Si surface (a,b) and a nanopatterned TiN surface (c,d). Reprinted with permission from [79] by VCH-Wiley.

downsize the micromolding scale with ceramic materials. In the case of ceramics micromolded by physical deposition methods, nanoscale resolution is easily obtained. A clear example is direct molding of nanostructured TiN surfaces deposited by reactive sputtering (Fig. 12).

8. Summary and Outlook

The research area related to the study of new patterning techniques suitable for ceramic materials is a growing field that has attracted the attention of a number of research groups. In contrast to polymer patterning, ceramics patterning still requires a considerable effort and creativity to find new methods capable of fulfilling all the industry demands. As is well-known, reproducibility, accuracy, simplicity and suitability for large-scale fabrication are very important features of the method to be developed. So far, there are no techniques fulfilling all these requirements. Hard lithographic techniques, like e-beam lithography, are very accurate but unsuitable for large scale fabrication as a consequence of being a time-consuming technique. Soft lithographic techniques in combination with sol gel chemistry are a very simple and inexpensive route. However, the significant shrinkage upon thermal treatment makes the approach unsuitable for accurate nanoscale patterning. On the other hand, micromolding in combination with physical vapour deposition enables accurate nanoscale patterning but the range of materials that can be patterned is rather limited. Self-assembly and self-organization seem to be a very powerful alternative.

However, much effort should be placed on achieving different predictable architectures in order to use them as reliable templates for large-scale serial fabrication.

All these efforts are completely justified if we consider the enormous implications of ceramic-based nanotechnologies on the production of high added value products. This review chapter describes with special emphasis the advance in the field during the last five years. It can be clearly seen that "true" nanoscale resolution can be reached by different methods. New high resolution resists, different families of self-assembling molecules, and many other approaches are supporting this point of view. The combination between complimentary disciplines and the creativity of scientific community will pave the way to different affordable techniques and methods for reliable accurate nanoscale patterning of different ceramic materials.

Acknowledgments

We acknowledge financial support from Agencia Nacional de Promoción Científica y Tecnológica (Argentina), Consejo Nacional de Investigaciones Cientificas y Técnicas (Argentina), Fundación Antorchas (Argentina). O.A. acknowledges financial support from the Alexander von Humboldt Stiftung (Germany).

References

1. C. M. Sotomayor Torres, *Alternative lithography: unleashing the potentials of nanotechnology* (Kluwer Academic, New York, 2003).
2. M. Cain and R. Morell, Nanostructured ceramics: a review of their potential, *Appl. Organome. Chem.* **15**, 312–330 (2001).
3. G. Timp, *Nanotechnology* (American Institute of Physics, New York, 1998).
4. K. i. Kawamura, N. Sarukura, M. Hirano and H. Hosono, Holographic encoding of fine-pitched micrograting structures in amorphous SiO_2 thin films on silicon by a single femtosecond laser pulse. *Appl. Phys. Lett.* **78**, 1038–1040 (2001).
5. T. Morita, K. Watanabe, R. Kometani, K. Kanda, Y. Haruyama, T. Kaito, J.-I Fujita, M. Ishida, Y. Ochiai, T. Tajima and S. Matsui, Three-dimensional nanoimprint mold fabrication by focused ion beam chemical vapor deposition, *Jpn. J. Appl. Phys.* **42**, 3874–3976 (2003).
6. S. B. Clendenning, S. Aouba, M. S. Rayat, D. Grozea, J. B. Sorge, P. M. Brodersen, R. N. S. Sodhi, Z. H. Lu, C. M. Yip, M. R. Freeman, H. E. Ruda and I. Manners, Direct writing of patterned ceramics using electron beam lithography and metallopolymer resists, *Adv. Mater*, **16**, 215–219 (2004).
7. S. Donthu, Z. Pan, B. Myers, G. Shekhawat, N. Wu and V. Dravid, Facile scheme for fabricating slid-state nanostructures using e-beam lithography and solution precursors, *Nano Lett* **5**, 1710–1715 (2005).
8. Z. X. Pan, S. K. Donthu, N. Q. Wu, S. Y. Li and V. P. Dravid, Directed fabrication of radially stacked multifunctional oxide heterostructures using soft electron-beam lithography, *Small* **2**, 274–280 (2006).
9. K. Sugioka and K. Midorikawa, Novel technology for laser precision microfabrication of hard materials, *RIKEN Rev.* **32**, 36–42 (2000).
10. L. V. Zhigilei, P. B. S. Kodali and B. J. Garrison, A microscopic view of laser ablation, *J. Phys. Chem. B*, **102**, 2845–2853 (1998).

11. K. Chen, J. Ihlemann, P. Simon, I. Baumann and W. Sohler, Generation of submicron surface gratings on $LiNbO_3$ by ultrashort UV laser pulses, *Appl. Phys. A* **65**, 517–518 (1997).
12. V. Oliveira, O. Conde and R. Vilar, UV laser micromachining of ceramic materials: formation of columnar topographies, *Adv. Eng. Mater.* **3**, 75–81 (2001).
13. K. Zimmer, R. Bohme, A. Braun, B. Rauschenbach and F. Bigl, Excimer laser induced etching of sub micron surface relief gratings in fused silica using phase gating projection *Appl. Phys. A* **74**, 453–456 (2002).
14. J. Ihlemann, S. Muller, S. Puschmann. D. Schafer, M. Wei, J. Li and P. R. Herman, Fabrication of submicron gratings in fused silica by F_2-laser ablation. *Appl. Phys. A* **76**, 751–753 (2003).
15. T. Kim, H. S. Kim, M. Hetterich, D. Jones, J. M. Girkin, E. Bente and M. D. Dawson, Femtoseconglaser machining of gallium nitride, *Mater. Sci. Eng B*, **82**, 262–264 (2001).
16. F. Beinhorn, J. Ihlemann, P. Simon, G. Marowsky, B. Maisenholder, J. Edlinger, D. Neuschafer and D. Anselmetti, Sub-micron grating formation in Ta_2O_5 waveguides by femtosecong UV laser ablation *Appl. Surf. Sci.* **138–139**, 107–110 (1999).
17. O. Yavas, C. Ochiai and M. Takai, Substrate-assisted laser patterning of indium tin oxide thin films. *Appl. Phys. A* **69**, S875–S878 (1999).
18. T. V. Konomenko, V. V. Konomenko, V. I. Konov, S. V. Garnov, A. V. Tishchenko, A. M. Prokhorov and A. V Khomich, Formation od antireflective surface structures on diamond films by laser patterning, *Appl. Phys. A* **68**, 99–102 (1999).
19. E. Vanagas, I. Kudryashov, D. Tuzhilin, S. Juodkazis, S. Matsuo and H. Misawa, Surface nanostructuring of borosilicate glass by femtosecond nJ energy pulses, *Appl. Phys. Lett.* **82**, 2901–2903 (2003).
20. Y. Hirayama, H. Yabe and M. Obara, Selective ablation of AlN ceramic using femtosecong, nanosecond and microsecond pulsed laser, *J. Appl. Phys.* **89**, 2943–2949 (2001).
21. J. W. Glesener and R. J. Tonucci, Micropatterned diamond substrates, *J. Appl. Phys.* **74**, 5280–5281 (1993).
22. K. Venkatakrishnann, B. K. A. Ngoi, P. Stanly, L. E. N. Lim and N. R. Sivakumar, Laser writing techniques for photomask fabrication using a femtosecond laser. *Appl. Phys. A.* **74**, 493–496 (2002).
23. J. Zhang, K. Sugioka and K. Midorikawa, Precise microfabrication of wide band gap semiconductors (SiC and GaN) by VUV–UV multiwavelength laser ablation, *Appl. Surf. Sci.* **127**, 793–799 (1998).
24. J. Zhang, K. Sugioka, S. Wada, H. Tashiro and K. Toyoda, Direct photoetching of single crystal SiC by VUV-266 nm multiwavelength laser ablation, *Appl. Phys. A* **64**, 367–371 (1997).
25. J. Zhang, K. Sugioka, S. Wada, H. Tashiro and K. Toyoda, Dual-beam ablation of fused quartz using 266 nm and VUV lasers with different delay-times *Appl. Phys. A* **64**, 477–481 (1997).
26. J. Zhang, K. Sugioka and K. Midorikawa, High-speed machining of glass materials by laser-induced plasma-assisted ablation using a 532-nm laser, *Appl. Phys. A.* **67**, 499–501 (1998).
27. J. Zhang, K. Sugioka and K. Midorikawa, Laser-induced plasma-assisted ablation of fused quartz using the fourth harmonic of a Nd^+:YAG laser *Appl. Phys. A* **67**, 545–549 (1998).

28. K. Kawamura, T. Ogawa, N. Sarukawa, M. Hirano and H. Hosono, Fabrication of surface relief gratings on transparent dielectric materials by two beam holographic method using infrared femtosecond laser pulses. *Appl. Phys. B*, **71**, 119–121 (2000).
29. M. Hirano, K. I. Kawamura and H. Hosono, Encoding of holographic garting and periodic nanostructure by femtosecond laser pulse, *Appl. Surf. Sci.* **187–198**, 688–698 (2002).
30. J. C. Love, L. A. Estroff, J. K.Kriebel, R. G. Nuzzo and G. M. Whitesides, Self-Assembled Monolayers of Thiolates on Metals as a Form of Nanotechnology, *Chem. Rev.* **105**, 1103–1170 (2005).
31. B. D. Gates, Q. Xu, M. Stewart, D. Ryan, C. G. Willson and G. M. Whitesides, New Approaches to Nanofabrication: Molding, Printing, and Other Techniques, *Chem. Rev.* **105**, 1171–1196 (2005).
32. Y. Gao and K. Koumoto, Bioinspired ceramic thin film processing: present status and future perspectives, *Cryst. Growth Des.* **5**, 1983–2017 (2005).
33. Y. Masuda, W. S. Seo and K. Koumoto, Selective deposition and micropatterning of titanium dioxide on self-assembled monolayer from gas phase, *Langmuir* **17**, 4876–4880 (2001).
34. R. J. Collins, H. Shin, M. R. Guire, A. H. Heuer and C. N. Sukenik, Low temperature deposition of patterned TiO_2 thin films using photopatterned self-assembled monolayers, *Appl. Phys. Lett.* **69**, 860–862 (1996).
35. J. Q. Wang, S. R. Yang, X. H. Liu, S. L. Ren, F. Guan and M. Chen, Preparation and characterization of ZrO_2 thin film on sulfonated self-assembled monolayer of 3-mercaptopropyl trimethoxysilane, *Appl. Surf. Sci.* **221**, 272–280 (2004).
36. H. Z. Yu, A. W. Rowe and D. M. Waugh, Templated Electrochemical Deposition of Zirconia Thin Films on "Recordable CDs" it Anal. Chem. **74**, 5742–5747 (2002).
37. N. Shirahata, Y. Masuda, T. Yonezawa and K. Koumoto, Control over Film Thickness of SnO_2 Ultrathin Film Selectively Deposited on a Patterned Self-Assembled *Monolayer Langmuir* **18**, 10379–10385 (2002).
38. S. Sipothina and M. R. DeGuire, T Characterization of SnO_2 thin films grown from aqueous solutions, *Thin Solid Films* **371**, 1–9 (2000).
39. M. Agarwal, M. R. DeGuire and A. H. Heuer, Synthesis of yttrium oxide thin films with and without the use of organic self-assembled monolayers, *Appl. Phys. Lett.* **71**, 891–894 (1997).
40. N. Saito, H. Haneda, W. S. Seo and K. Koumoto, Selective Deposition of ZnF(OH) on Self-Assembled Monolayers in Zn-NH_4F Aqueous Solutions for Micropatterning of Zinc Oxide, *Langmuir*, **17**, 1461–1469 (2001).
41. N. Saito, H. Haneda, T. Sekiguchi, N. Ohashi, I. Sakaguchi and K. Koumoto, Low-Temperature Fabrication of Light-Emitting Zinc Oxide Micropatterns Using Self-Assembled Monolayers, *Adv. Mater.* **14**, 418–421 (2002).
42. Y. F. Gao, Y. Masuda and K. Koumoto, Micropatterning of lanthanum-based oxide thin film on self-assembled monolayers *J. Colloid. Interface. Sci.* **274**, 392–397 (2004).
43. Y. Masuda, S. Wakamatsu and K. Koumoto, Site-selective deposition and micropatterning of tantalum oxide thin films using a monolayer, *J. Eur. Ceram. Soc.* **24**, 301–307 (2004).
44. H. Shin, J. U. Jeon, Y. E. Park, H. Im and E. S. Kim, Formation and characterization of crystalline iron oxide films on self-assembled organic monolayers and their in situ patterning, *J. Mater. Res.* **16**, 564–569 (2001).

45. M. Nagtegaal, P. Stroeve, J. Ensling, P. Gutlich, M. Schurrer, H. Voit, J.Flath, J. Kashammer, W. Knoll and W. Tremel, Soft-Chemical Growth of γ-FeO(OH) Films on Self-Assembled Monolayers of Substituted Alkylthiols on Gold(111), *Chem. Eur. J.* **5**, 1331–1337 (1999).
46. M. Nagtegaal, J. Kuther, J. Ensling, P Gutlich and W. Tremel, Hydrothermal deposition of small α-Fe_2O_3 (hematite) particles on ordered zirconium phosphonate multilayer SAMs on gold, *J. Mater. Chem.* **9**, 1115–1120 (1999).
47. M. Nagtegaal, P. Stroeve and W. Tremel, Growth of FeO(OH) crystals on self-assembled monolayers on gold, *Thin Solid Films*, **327**, 571–575 (1998).
48. F. C. Meldrum, J. Flath and W. Knoll, Chemical Deposition of PbS on Self Assembled Monolayers of 16-Mercaptohexadecanoic Acid, *Langmuir*, **13**, 2033–2049 (1997).
49. R. J. O. Corriu, Ceramics and nanostructures from molecular precursors, *Angew. Chem. Int. Ed.* **39**, 1376–1398 (2000).
50. Franc, D. Blanc, A. Zerroukhi, Y. Chalamet, A. Last and N. Destouches, Organosilica–titania nanocomposite elaborated by sol–gel processing with tunable optical properties, *Mater. Sci. Eng. B* **129**, 180–185 (2006).
51. P. G. Clem, N.-J. Jeon, R. G. Nuzzo and D. A. Payne, Monolayer-mediated deposition of tantalum (V) oxide thin film structures from solution precursors, *J. Am. Ceram. Soc.* **80**, 2821–2827 (1997).
52. P. L. Schilardi, P. Dip, P. C. Dos Santos Claro, G. A. Benítez, M. H. Fonticelli, O. Azzaroni and R. C. Salvarezza, Metal Electrodeposition on Self–Assembled Monolayers: New Insights in Micro– and Nanofabrication, *Chem. Eur. J.* **12**, 38–49 (2006).
53. B. D. Gates, D. Xu, C. Love, D. B. Wolfe and G. M. Whitesides, Unconventional lithography, *Annu. Rev. Mat. Res.* **34**, 339–372 (2004).
54. Y. Xia, J. A. Rogers, K. E. Paul and G. M. Whitesides, Unconventional methods for fabricating and patterning nanostructures, **99**, 1823–1848 (1999).
55. Y. Xia and G. M. Whitesides, Soft lithography, *Angew. Chem. Int. Ed.* **37**, 550–575 (1998).
56. H. Yang, P. Deschalets, S. T. Brittain and G. M. Whitesides, Fabrication of high oerformance ceramic microstructures from a polymeric precursor using soft lithography, *Adv. Mater.* **13**, 54–58 (2001).
57. C. Marzolin, S. P. Smith, K. E. Paul and G. M. Whitesides, Fabrication of glass microstructures by micro-molding of sol-gel precursors, *Adv. Mater.* **10**, 571–574 (1998).
58. S. Seraji, Y. Wu, N. E. Jewell Larsson, M. J. Forbess, S. J. Limmer, T. P. Chou and G. Cao, Patterned microstructures of sol-gel derived complex oxides using soft lithography, *Adv. Mater.* **12**, 1421–1424 (2000).
59. W. S. Beh, Y. Xia and D. Qin, Foermation of patterned microstructures of polycrystalline ceramics from precursor polymers using micromolding in capillaries, *J. Mater. Res.* **14**, 3995–4003 (1999).
60. S.-J. Ahn and J. Moon, Vacuum-assisted microfluidic lithography of ceramic microstructures, *J. Am. Ceram. Soc* **88**, 1171–1174 (2005).
61. M. Heule and L. J. Gauckler, Gas Sensors Fabricated from Ceramic Suspensions by Micromolding in Capillaries, *Adv. Mater.* **13**, 1790–1793 (2001).
62. M. Heule, S. Vuillemin and L. J. Gauckler, Powder based meso and microscale fabrication process, *Adv. Mater.* **15**, 1237–1245 (2003)
63. M. Heule, U. P. Schonholzer and L. J. Gauckler, Patterning colloidal suspensions by selective wetting of microcontact printed surfaces, *J. Eur. Ceram. Soc.* **24**, 2733–2739 (2004).

64. M. Li, H. Ta, L. Chen, J. Wang and S. Chou, Large area nanoimprinting of SiO_2-TiO_2 gel gratings for optical applications, *J. Vac. Sci. Technol. B* **21**, 660-663 (2003).
65. K. H. Park, J. H. Park and D. P. Kim, Fabrication of nanoscale SiC-based ceramic patterns with near-zero residual layers by using imprinting technique and reactive ion etching, *Mater. Sci. Forum.* **510–511**, 766–769 (2006).
66. C. R. Martin and I. A. Aksay, Topographical Evolution of Lead Zirconate Titanate (PZT) Thin Films Patterned by Micromolding in Capillaries, *J. Phys. Chem. B* **127**, 4261–4268 (2003).
67. Z. Zhang and F. F. Lange, Patterning ceramic surfaces by colloidal isopressing, *Adv. Eng. Mater.* **4**, 294–295 (2002).
68. D. M. Dabbs and I. A. Aksay, Self-assembled ceramics produced by complex-fluid templation, *Annu. Rev. Phys Chem.* **51**, 601–622 (2000).
69. V. Z. H. Chan, J. Hoffman, V. Y. Lee, H. Iatrou, A. Avgeropoulos, N. Hadjichristidis, R. D. Miller and E. L. Thomas, Ordered Bicontinuous nanoporous and nanorelief ceramic films from self assembling polymer precursors, *Science* **286**, 1716–1719 (1999).
70. P. Yang, T. Deng, D. Zhao, P. Feng, D. Pine, B. F. Chmelka, G. M. Whitesides and G. D. Stucky, Hierarchically ordered oxides, *Science* bf 282, 2244–2246 (1998).
71. G. Krausch and R. Magerle, Nanostructured thin films via a self-assembly of block copolymers, *Adv. Mater.* **14**, 1579–1583 (2002).
72. M. Park, C. Harrison, P. M. Chaikin, R. A. Register and D. H. Harrison, Block copolymer lithography: periodic arrays of $\sim 10^{11}$ holes in 1 square centimeter, *Science*, **275**, 1401–1404.
73. H. Chik and J. M. Xu, Nanometric superlattices:non-lithographic fabrication, materials and propects, *Mater. Sci. Eng. R* **43**, 103–138 (2004).
74. H. Masuda and K. Fukuda, Ordered metal nanohole arrays made by a two-step replication of honeycomb structures of anodic alumina, *Science* **268**, 1466–1468 (1996).
75. S. Shingubara, O. Okino, Y. Murakami, H. Sakaue and T. Takahagi, Fabrication of nanohole array on Si using self-organized porous alumina mask, *J. Vac. Sci. Technol. B* **19**, 1901–1904 (2001).
76. H. Masuda, M. Watanabe, K. Yasui, D. Try, T. Rao and A. Fujishima, Fabrication of a Nanostructured Diamond Honeycomb Film, *Adv. Mater.* **12**, 444–447 (2000).
77. Younan Xia, Jabez J. McClelland, Rajeev Gupta, Dong Qin, Xiao-Mei Zhao, Lydia L. Sohn, Robert J. Celotta and George M. Whitesides, Replica molding using polymeric materials: A practical step toward nanomanufacturing, *Adv. Mater.* **9**, 147–149 (1997).
78. B. D. Gates and G. M. Whitesides, Replication of Vertical Features Smaller than 2 nm by Soft Lithography, *J. Am. Chem. Soc.* **125**, 14986–14987 (2003).
79. M. A. Auger, P. L. Schilardi, I. Caretti, O. Sanchez, G. Benitez, J. M. Albella, R. Gago, M. Fonticelli, L. Vazquez, R. Salvarezza and O. Azzaroni, Molding and Replication of ceramic surfaces with nanoscale resolution, *Small* **1**, 300–309 (2005).
80. R. Maboudian, W. R. Ashurst and C. Carraro, Self-assembled monolayers as anti-stiction coatings for MEMS: characteristics and recent developments, *Sens. Actuators A: Physical* **82**, 219–223 (2000).
81. O. Azzaroni, P. L. Schilardi, R. C. Salvarezza, J. Manuel-Herrero, C. Zaldo and L. Vazquez, Surface–Relief Micropatterning of Zinc Oxide Substrates by Micromolding Pulsed–Laser–Deposited Film, *Appl. Phys. A* **81**, 1113–1116 (2005).

CHAPTER 15

ALTERNATIVE NANOFABRICATION APPROACHES FOR NON-CMOS APPLICATIONS

C.V. COJOCARU, F. CICOIRA and F. ROSEI*

INRS-EMT, University of Québec, 1650 Blvd. Lionel Boulet, Varennes, J3X 1S2, Québec, Canada

rosei@emt.inrs.ca

In the race to downsize the features of components in integrated electronics, nanostructure fabrication is a primary challenge. Semiconductor technology has always relied on the top-down approach such as conventional CMOS technology for surface structuring and patterning. The most remarkable example is the amazing miniaturization of transistors and data storage components by ever more sophisticated lithographic techniques. Nevertheless, the so far unbeaten nanofabrication techniques such as deep-UV (DUV), extreme-UV (EUV) or electron-beam lithography (EBL) are particularly dedicated for patterning motifs in photo or electron-beam resists, spin-coated on planar, ultra-flat semiconductor surfaces. Alternative fabrication processes for growth of integrated novel nanostructured functional materials are already foreseen in related areas such as micro/nano-electro mechanical systems (MEMS/NEMS), sensors and actuators, optoelectronics, bio-chips, plastic or molecular electronics, etc. In other words, appropriate patterning methods are explored for creating and positioning structures with nanometer dimensions (<100 nm) on non-planar (e.g. curved or rough) surfaces or other functionalized and often fragile surfaces (membranes, cantilevers, organic layers). In this context, a variety of other forms of parallel lithography such as molding, stamping, imprinting or stenciling are revisited for their potential as nanofabrication alternatives that alleviate conventional lithography limitations. Thus, fabrication of functional structures with controlled size and shape, precisely positioned on a substrate of choice, using a minimal number of processing steps, becomes a central issue in nanotechnology. Furthermore, growth of novel nanostructured complex materials with functionality represents a big challenge for materials development. Probing new routes to prepare these materials and understand the relationship between their size/structure and their properties is also essential to the development of related technologies.

Significant advances in defining nano-patterns have been made by *nanoimprint lithography* (NIL). NIL is able to deliver features well below 100 nm, rapidly and with

*Corresponding author: INRS-EMT, University of Québec 1650 Blvd. Lionel Boulet, Varennes, J3X 1S2, Québec, Canada; rosei@emt.inrs.ca

high accuracy, at least compared to advanced optical lithography methods. Either by hot embossing technique (HET) or its related variant, step and flash imprint lithography (S-FIL) nanoimprint shows great potential for the semiconductor industry and has been already placed on the International Technology Roadmap for Semiconductors (ITRS) for the next years. Another promising approach, although less investigated to date, is *nanostenciling*, known also as controlled growth of nanostructures through a shadow-mask. This process has been proposed both in static or dynamic mode and projected as a suitable method to locally grow patterned nanoscale structures, in a single, resist-less, deposition step. While offering a high degree of freedom in choosing the physical vapor deposition method, nanostenciling is in principle applicable to the deposition of arbitrary materials on almost any substrate. It drastically reduces the number of processing operations with respect to resist–based lithography and therefore represents a promising "universal tool" for local deposition of high-resolution and high-purity 3D nanostructures under high or ultra high vacuum (UHV) conditions.

We provide fundamental and extensive descriptions of stenciling and imprint processes and outline the main concepts used for the fabrication of both stencil-masks and molds. Then, through a couple of detailed examples we will emphasize the importance of several particular parameters involved in these processes (e.g. geometry and methods of deposition for stenciling, molds, resists, tools in the case of imprinting). Finally we will present a couple of examples where either nanostenciling or nanoimprint have been successfully used for device applications and in conclusion offer our perspective on future potential applications (prototyping) in areas where other forms of lithography are much less suitable.

Keywords: Nanofabrication; nanopatterning; lithography; alternative approaches; nanoimprint; nanostenciling; functional nanostructures; ordered arrays; prototyping; device applications.

CONTENTS

1. Introduction 501
2. Nanostencil-based Lithography 503
   2.1. General background 503
   2.2. Nanostencil fabrication processes and deposition geometries 506
      2.2.1. Wafer flow process (WFP) 506
      2.2.2. Membrane flow process (MFP) 509
      2.2.3. Geometries and techniques for deposition 510
   2.3. Nanostenciling applications 514
      2.3.1. Ordered arrays of structures 514
      2.3.2. Nano-sensors and NEMS 517
      2.3.3. Biocompatible materials and molecular circuits 520
      2.3.4. Combinatorial materials 521
3. Nanoimprint Lithography 522
   3.1. General background 522
   3.2. Molds, polymers and tools for NIL 525
      3.2.1. Materials for molds and fabrication 525
      3.2.2. Polymers and tools 526

3.3. NIL applications 527
3.3.1. Patterning of organic thin films 528
3.3.2. NIL for optics 530
3.3.3. NIL for nanoelectronics and data storage media 531
3.3.4. NIL for bio-devices 533
4. Conclusions and Perspectives 535
Acknowledgments 536
References 536

1. Introduction

The ongoing quest for miniaturization has triggered tremendous interest in nanotechnology and nanoscience [1]. From a technological point of view, downsizing the critical features of microelectronic devices leads to more components per chip, faster operation, higher performance, lower power consumption and lower costs. Furthermore, the novel surface and quantum effects that arise when a material is confined to the nanoscale are of great interest in fundamental research. These properties are not present at larger scales (macro or micro) and therefore engineered nanoscale structures, either by way of a top-down approach (a "bulk" material is progressively thinned down to obtain ever smaller features) or a bottom-up approach (exploiting the natural tendency of atoms and molecules to assemble and form regular structures) go further than just another step towards miniaturization. Interesting properties (e.g. electronic, optical, catalytic, mechanical, magnetic, etc.) are revealed as the dimensions of a bulk crystal, practically an infinite and periodic system, are reduced to a system composed of a relatively small number of atoms [2]. Thus, exploring new routes to synthesize and process nanostructured materials and understanding the relationship between their size/structure and their properties is essential to provide the background knowledge needed to sustain the present pace of miniaturization and innovation.

For over a decade, the industrial and scientific communities have concentrated their efforts on the fabrication and characterization of nanostructured materials. The semiconductor industry continuously strives to downsize the features of integrated devices while preserving functionality [3], the optics community aims to build quantum dots (QDs) and wires with engineered energy levels, while the chemistry and biology communities endeavor to employ "self-assembly" to order molecular building blocks at the nanoscale [4]. In the near future, it is expected that applications of functional nanostructures will touch areas that have not been demonstrated yet, such as nanoscale electronics, bio-sensing and nano-biomedicine.

Currently, applications demanding the patterning of thin films of functional materials extend from the fabrication of integrated circuits, media for data storage and display units to the creation of micro/nano-electromechanical systems (MEMS/NEMS), miniaturized sensors and actuators, micro-fluidic devices, micro-optical components, photonic band gap crystals, bio-chips and biocompatible

nanostructured surfaces. For all these areas, advances in creating suitable nanoscale patterning techniques are the prerequisite for their successful development and commercialization [5]. As a result, tailoring nanoscale structures and patterning using a minimal number of processing steps, has become a central issue in nanotechnology.

The trend towards device miniaturization has been sustained thus far by the constant development of conventional CMOS technology for surface structuring and patterning and parallel large scale components production, mainly on Silicon. Optical projection lithography (OPL) has been the main form of lithography used in the semiconductor industry for several decades and most likely it will be used for no less than another decade [6]. The most remarkable example is the amazing miniaturization of transistors and data storage components by ever more sophisticated lithographic techniques. Nevertheless, the so far unbeaten fabrication techniques that have emerged from development efforts in microelectronics (e.g. deep-UV (DUV), extreme-UV (EUV) or electron-beam lithography (EBL)) are dedicated to patterning motifs in photo or electron-beam resists, spin-coated on planar, ultra-flat semiconductor surfaces. Adapting these lithographic methods to other areas of interest that may involve structuring and designing atypical materials or architectures [7] on non-conventional substrates represents a great challenge. Suitable patterning methods need to be explored to create and position nanostructures (<100 nm) on non-planar (e.g. previously processed, curved or rough) surfaces or other functionalized and often fragile surfaces (membranes, cantilevers, organic layers). Moreover, the well-established lithographic techniques are usually confined to a cleanroom environment that requires ever-increasing capital and operation costs. In this context, a variety of other forms of parallel lithography such as molding, stamping, imprinting or stenciling are revisited for their potential as (non-conventional) nanofabrication alternatives that alleviate conventional lithography limitations [8].

Major developments made in the quest for finding alternative nanostructuring procedures are comprised nowadays into the area known as "soft lithography". This is a set of methods that makes use of soft elastomeric stamps, molds and conformable photo-masks for patterning two and three-dimensional structures with feature sizes down to the nanometer regime. Micro-contact printing (μCP), originally developed by Whitesides' group at Harvard University, represents the front-runner of these methods, and recent work indicates the possibility of transferring the method out of the laboratory to manufacturing [9].

Significant advances in defining nano-patterns have been made by nanoimprint lithography (NIL), an alternative approach initially introduced by Chou in 1995 [10]. NIL is currently able to deliver features well below 100 nm, rapidly and with high accuracy and throughput, at least comparable to advanced optical lithography methods. Either by hot embossing technique (HET) [11] or by its related variant, step and flash imprint lithography (S-FIL) [12] introduced by Willson and Sreenivasan in 1999, nanoimprint has great potential for the semiconductor industry

and has been already placed on the International Technology Roadmap for Semiconductors (ITRS) for use in the coming years. HET and S-FIL are based on the mechanical transfer of a pattern from a hard mold to the substrate by direct contact, in a controlled pressure and alignment environment.

Controlled deposition through a miniature shadow-mask (nanostencil) has been further developed and is now considered as a suitable method to grow directly patterned nanostructures, in a single step, either in static [13] or dynamic [14] modes. The process is applicable to the deposition of arbitrary materials, directly on a wide range of substrates, with a reduced number of steps compared to resist–based lithography. Besides offering unlimited freedom in choosing the physical vapor deposition technique, pattern formation using nanostencils is a straightforward, low–cost and reliable method. Nowadays it represents a promising universal 'tool' for local deposition of high resolution and high purity nanostructures of functional materials under high and ultra high vacuum [15].

Other unconventional structuring approaches use maskless lithography to obtain ordered nanoscale features. Among them, scanning electron-beam (SEBL) and focused ion-beam (FIBL) lithography [16], laser-interference lithography (LIL) [17], zone-plate array lithography (ZPAL) [18], scanning probe lithography (SPL) [19] and dip-pen nanolithography (DPL) [20] represent further high–resolution and versatile patterning methods.

Very attractive approaches that allow building high aspect ratios structures with a wide range of shapes are electron-beam-induced deposition (EBID) and focused-ion-beam-induced deposition (FIBID) [21]. More exotic techniques, yet nevertheless exciting from a scientific point of view, are buffer–layer–assisted–growth (BLAG) [22] or laser–patterning (BLALP) [23] and controlled deposition on surfaces pre–patterned by laser interference [24].

In this chapter we will provide in-depth descriptions of stenciling and imprint processes and outline the main concepts behind the fabrication of both stencil-masks and molds. Then, through detailed examples, the importance of several particular parameters involved in these processes (e.g. methods and geometries of deposition for stenciling, molds, resists, and tools in the case of imprinting) will be explored. Subsequent examples will highlight nanostenciling and nanoimprint techniques that have been successfully employed for device applications. Finally we offer our perspective on future potential applications (prototyping) in areas where other forms of lithography are much less suitable.

2. Nanostencil-based Lithography

2.1. *General background*

The in-plane patterning of a thin film (functional layer), with accuracy on the nanometer scale, is an intricate and challenging task. This is partly due to the sequential processing nature of resist-based lithography (i.e. comprising resist

coating, exposure, thermal and chemical development) and often because of the selective etching incompatibility between the resist and the underlying functional material. Furthermore, nanostructure positioning on unusual substrates such as non-planar, fragile or functionalized surfaces cannot be achieved by means of ordinary lithographic processing or other alternative techniques such as soft-lithography or nanoimprint. A solution to these problems is a technique called nowadays as nanoscale shadow-masking or nanostenciling. The use of a miniature shadow mask with nano-apertures opened in a free-standing membrane (i.e. nanostencil) allows direct, selective and clean deposition of various materials on almost any type of surface, given that photoresist or other polymer processing is not involved and mechanical contact between mask and substrate is considerably avoided. It is a parallel process, does not interfere with the structures' growth dynamics, can be performed in high or ultra high vacuum and is highly suitable for parallel prototyping of fragile or functionalized surfaces. The patterning procedure becomes simple and rapid thus eliminating supplementary processing steps (Fig. 1).

The idea of using a shadow-mask for deposition on selected areas was demonstrated in 1986 by Dohler and co-workers [25] at HP Laboratories in Palo Alto, by forming selected contacts to doped GaAs superlattices (named n–i–p–i crystals). The authors used a silicon wafer drilled with rectangular windows on top of a GaAs substrate and were successful in achieving selective contacts to the n–i–p–i crystal structures that resulted in greatly improved electrical and optical characteristics. With the development of various technologies, new equipment became available (e.g. EBL, RIE, FIB) and stencil fabrication has been greatly improved in terms of minimum size and aspect ratios of the apertures. For instance, in 1989, Ralls and co-workers [26] presented a method for the fabrication of metal nanobridges by depositing metals through suspended SiN membranes (50 nm thick and 40 μm wide) that were previously processed by EBL and RIE. Later on, Gribov and

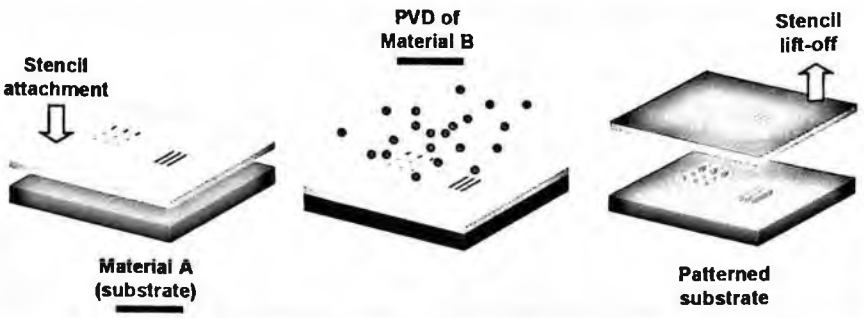

Figure 1. Schematic drawing of Nanostenciling approach: a miniature shadow-mask, with apertures opened in a thin membrane is brought into proximity with the substrate of choice (e.g. material A). Material B can be directly deposited through the apertures using various deposition techniques such as evaporation, sputtering or pulsed laser deposition. The shadow-mask is simply "lifted-off" at the end of the process. 3D arrays of structures are directly obtained on the substrate and accurately replicate the size and shape of the sieve apertures.

co-workers reported a new process for creating metallic point contacts making use of Si-membranes with tapered shape apertures that could be further fine-tuned in lateral size by thermal oxidation [27].

Yet, there were essential issues to be addressed for nanostenciling to be considered as a choice for top-down nanopatterning of surfaces. Among them: what materials should be used for nanostencil fabrication? What architectures should be designed and what deposition techniques should be employed? Will the traditional micron-scale screening work at the nanometer scale and if yes, with what throughput? A clogging effect (aperture closure after a number of uses of the masks) was anticipated, thus raising concerns about the stencil's life-time. However, the simplicity and the high flexibility of the technique to deliver ultra-pure and precisely positioned nanostructures were reasons to further develop it beyond the clogging concerns.

In 1996, stenciling via microfabricated solid-state membranes was applied on the micrometer scale to pattern materials in deep holes and non-planar surfaces by Burger *et al.* [28]. Along the way, other demonstrations of stenciling comprised the use of elastomeric stencils for micro-patterning cell cultures [29], self-aligning shadow-masks for patterning deeply recessed surfaces of MEMS devices [30], photoplastic microstencils with self-alignment for multi-layer surface patterning [31], microstencils for evaporated, sputtered and chemical vapor deposited metals, insulator and semiconductors [32], stencil-masks for ion implantation [33] or silicon-on-insulator (SOI)-based stencils for ion-beam patterning of magnetic films [34]. Design and fabrication ranged from stencils with mechanical alignment structures for depositions in isolated areas [35] to active nanostencils with integrated microshutters [36].

In terms of surface nanopatterning, the boom of selected area nanoscale shadow-masking deposition for highly ordered arrays of structures is represented by the period 1998–1999 when both static nanostenciling (S-NS) and dynamic nanostenciling (D-NS) were reported concurrently by several groups, as highly flexible approaches leading to high-resolution and high-purity patterned nanostructures. Kohler and co-workers [37] used Si_3N_4 membranes, with arrays of small holes drilled by FIB, to replicate shapes by depositing chromium structures directly onto germanium crystals. Brugger and co-workers [13] made use of microfabricated, thin free standing silicon nitride membranes, with 2-dimensional arrays of perforated apertures realized by laser interference lithography (LIL) and RIE, to pattern Cr/Au dots on free standing micromechanical beams and recessed surfaces. Luthi and co-workers [14] at IBM-Zurich presented D-NS as a novel resistless lithography technique that enables the rapid fabrication of complex, submicron-sized structures of various materials. Using a combination of scanning probe and shadow mask techniques, they fabricated structures such as rings and intersected lines, with widths below 0.1 μm, by local deposition through pinhole-like apertures situated in the proximity of a cantilever tip. The apertures with diameters ranging from 50

to 250 nm were fabricated in the proximity of the cantilever tip using FIB. The technique, compatible with metal, semiconductor, oxide and molecular deposition, was shown to allow direct and sequential patterning of complex heterostructures and their *in situ* inspection.

To promote nanostencil-based lithography as a reliable, ultra-high resolution patterning alternative, several issues remain to be improved. Among them, the control of the deposited material with the membrane apertures, the investigations of cleaning methods that will render stencils re-usable and alignment methods (down to 10 nm precision) that will enable the reliable fabrication of multilayer structures.

In the following we discuss the progress that nanostenciling has made along the way, from solutions found for stencils' fabrication to its application in various areas of nanotechnology.

2.2. *Nanostencil fabrication processes and deposition geometries*

The nanostenciling approach involves two basic issues: (i) the stencil itself (architecture and fabrication) and (ii) the type of physical vapor deposition (PVD).

For the fabrication of a stencil mask (consisting of a support-frame and a thin, free-standing perforated membrane), two main approaches can be applied: the Wafer Flow Process (WFP) and the Membrane Flow Process (MFP) [38] (Fig. 2). Following the WFP scheme, all cycles for pattern definition can be performed with typical processing tools for Si microfabrication (DUV, RIE), on the wafer, leaving as the final step the release of the perforated membrane. Choosing the MFP scheme, the free-standing membrane is first formed by lithography and etching processes, then the entire pattern definition process (e.g. EBL, FIB milling) takes place directly on the membrane.

2.2.1. *Wafer flow process (WFP)*

The WFP scheme for nanostencil fabrication has been extensively employed by several groups and details of the processes can be found in the literature [39–42]. We describe here only the key steps involved in the WFP processing (Fig. 2[a]).

As a general and initial step, low-stress silicon nitride (e.g. 500 nm thick Si_xN_y non-stoichiometric) is deposited by low-pressure chemical vapor deposition (LPCVD) on both sides of a (100) silicon wafer. The internal tensile stress of the Si_xN_y layer is kept in the range 100–200 MPa so that the membrane will not brake or collapse during further operations. Silicon nitride is generally chosen for its very good chemical, thermal and hardness properties, high etch selectivity with respect to Si (the etching rate is 100 μm/h for silicon and 0.02 μm/h for nitride resulting in a selectivity ratio of 5000 to 1) and due to its compatibility with well-established Si micromachining processes. In a second step, a photoresist is spun on the wafer's top-side and patterns are defined by means of conventional optical lithography (e.g. DUV). After development, the patterns made in the resist are transferred

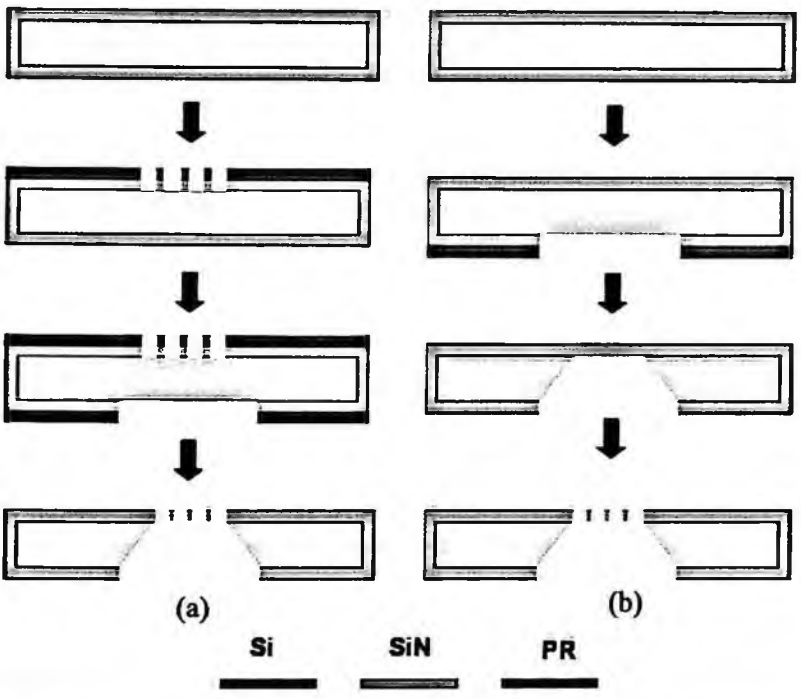

Figure 2. Schematic drawings of WFP (a) and MFP (b) sequences used for nanostencil fabrication. Colors chart: grey- silicon wafer; orange- low-stress LP-CVD SiN; brown- photoresist. Description of the processes involved in each approach is provided in sections (2.2.1.) and (2.2.2.) respectively.

into the Si_xN_y layer by anisotropic etching (e.g. RIE). The lithography and RIE processes are then repeated in the bottom-side silicon nitride to define large rectangular openings. Next the silicon between the patterned membrane layer and the back side of the stencil chip is removed with an anisotropic etch along the (111) planes with a KOH solution until the membrane layer is reached and the perforated membrane is released. Due to large differences in etching rates for the (100) and (111) direction (approximately 100 times faster in the <100> direction), windows are formed under an angle of 54.74 [39]. The nanostencils can be eventually diced into square pieces, e.g. stencil chips $5 \times 5\,mm^2$ in size, with membrane active areas covering $2 \times 2\,mm^2$, or used as full wafer-size shadow masks (Fig. 3).

To pattern efficiently the top-side membrane, while simultaneously providing high-resolution, several ways have been conceived. For instance, van Rijn reported in 1998 an original combination of laser interference lithography (LIL) and Si micromachining processes [43] to create nanosieves for filtration applications. A relatively inexpensive technique, LIL allows to pattern submicron periodic structures on large areas. Multiple-exposure interferometric lithography has been introduced in 1993 by Zaidi and Brueck [44] with the aim of creating periodic structures in

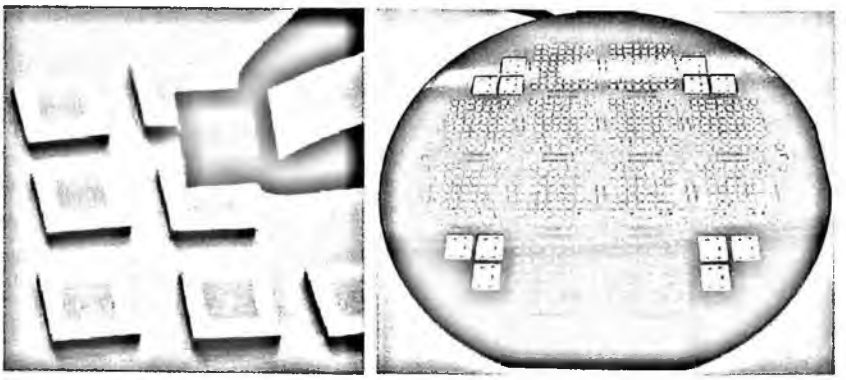

Figure 3. Left: Stencil chips (5×5 mm^2) produced at Aquamarijn Micro Filtration B.V., The Netherlands. (Courtesy of Dr. Cees van Rijn of Aquamarijn Micro Filtration, B.V., The Netherlands). Right: 4-inch, wafer-sized stencil designed and fabricated by Brugger's group at EPFL LMIS1, Lausanne, Switzerland. (Courtesy of Prof. Jurgen Brugger and Dr. M.A.F. van Boogaart of École Polytechnique Lausanne, LMIS1, Switzerland).

two dimensions. Van Rijn and co-workers made use of multiple exposure interference lithography for the fabrication of nanosieves with uniform pore size and pore spacing less than 500 nm (Fig. 4).

The steps of the process to create the nanosieve are very similar to those described above in the case of WFP[1]. Nevertheless, the main advantage is brought by the fact that using LIL there are no masks needed to pattern the top-side layer of the stencil[2]. The exposure set up used is known as 'Lloyd's mirror configuration' [45]. A part of an incoming plane wave is reflected by the mirror and forms an interference pattern on the substrate with the part that reaches the substrate undisturbed. The period of the generated interference pattern is defined by the relation $\Lambda = \lambda/2 \sin\theta$, where the angle 2θ between the interfering beams can be changed by rotating the mirror/substrate configuration. The minimum period reported by Rijn as being possibly fabricated with that configuration is $\Lambda = \lambda/2 = 175$ nm, for an Ar^+ ion laser with $\lambda = 351.1$ nm. The main drawback of LIL is that the technique is limited only to patterning of periodic structures without great flexibility in defining shapes.

[1] The backside of a single crystalline (100)-silicon wafer with a thickness of 380 µm, is pre-etched to a thickness of 15 µm using optical lithography and conventional KOH wet etching. On the front side of the pre-etched support a layer of amorphous silicon nitride with a thickness of about 100 nm is deposited by means of LPCVD by reaction of dichloresilane (SiH_2Cl) and ammonia (NH_3) at a temperature of 850°C. An etch mask layer of sputtered chromium with a thickness of 30 nm is deposited on the stencil's top-side, except on the area where the nanosieve pattern will later be formed. A layer of positive resist is spun on top of the latter and patterned using LIL.

[2] The interference pattern obtained on the resist is transferred into the silicon nitride membrane layer by means of reactive ion etching (CHF_3/O_2 at 10 mTorr and 75 W for 2 min) forming the required perforations. Subsequently, the silicon underneath the membrane layer is isotropically etched away (SF_6/O_2 at 100 mTorr and 100 W for 10 min) to form the macroscopic openings in the support.

In 2003, Heyderman *et al.* [46] presented a procedure for high volume fabrication of nano-pore membrane chips. They combined the techniques of hot embossing technique (HET) for replication of the nano-pore arrays and photolithography with silicon micromachining for production of alignment marks, break lines and free-standing membranes. Chips ($10 \times 10\,mm^2$) containing four nano-pore membranes were fabricated and some of the membranes were structured with arrays of pores with three different diameters. The use of electron beam writing (serial) rather than laser interference (parallel) for the formation of structures carry the flexibility to produce each membrane with a customized nanostructured design. This 'mix and match' technique opens the way for batch processing of nanostructured membranes, facilitating new avenues for research and technology.

2.2.2. *Membrane flow process (MFP)*

Other groups [47] preferred the MFP scheme for stencils fabrication (Fig. 2[b]). The process sequence starts like in the WFP with the LPCVD deposition of low-stress silicon nitride on both sides of a (100) silicon wafer. Further, photolithography and etching in aqueous KOH solution are used to remove selected regions of the Si to leave square suspended membranes. At this stage either electron-beam lithography or focused-ion-beam milling can be employed to "write" the desired pattern (e.g. array of holes, electrodes, etc) directly on the membrane. If EBL is used, after pattern development, an additional etching process (e.g. CFH_3/O_2 plasma RIE) is required to realize the perforations through the membrane. The choice of FIB milling could represent a more beneficial option with respect to EBL, since PMMA-coating, exposure and development steps are eliminated. Nevertheless, the ion milling processes carries its own challenges. To reduce charging effects and beam drifting caused by the Ga^+ ions implantation process into the nitride layer, a thin metallic layer (e.g. Au/Pd, 5–10 nm thick) has to be initially sputtered on both-sides of the membrane.

A very important aspect in the fabrication of the nanostencils is the aspect ratio ($A_r \sim$ width/height) of the apertures of the membrane. On one hand thin free-standing membranes are fragile, thus they should be made thick enough to survive processing, handling and usage. On the other hand, fairly thick membranes make difficult the opening of small apertures because of the intricacy of etching features with high aspect ratios. In this respect a 100-nm thick membrane, with an opening of 1–2 mm^2, has reliable values for processing and leads easily to apertures with a 1:1 aspect ratio (Fig. 5).

Drilling the membrane apertures directly by FIB has limitations imposed by the ion beam diameter, surface charging and in particular by the thickness of the SiN membrane layer (apertures usually realized are greater than 50 nm in diameter). Tong and co-workers [48] proposed a method to further reduce the size of the previously FIB-drilled apertures by micromachining an ultrathin nanosieve within a thin

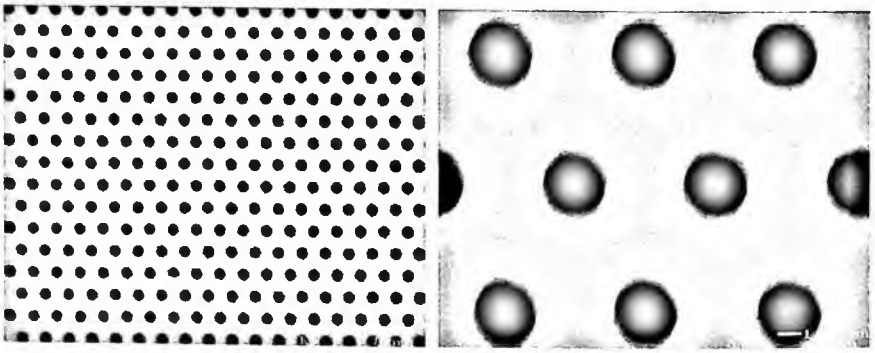

Figure 4. Scanning electron micrographs (SEM) of a low-stress silicon nitride (LS–SiN) nanosieve with 350 nm diameter pores and 700 nm pitch, fabricated via LIL and RIE. Stencils fabricated at Aquamarijn Micro Filtration, B.V. The Netherlands.

supporting microsieve[3]. These kinds of nanosieve membranes were meant mainly for use in bio-separation (size-exclusion-based cell separation) and additionally as shadow-masks for direct deposition of materials.

2.2.3. *Geometries and techniques for deposition*

Static nanostenciling (S-NS) offers unlimited freedom in choosing the deposition method, thus thermal or e-beam evaporation, sputtering or pulsed laser deposition can be equally employed. To replicate the designed features from the stencil onto a substrate of choice, the miniature shadow-masks are mechanically attached (clamped) and temporarily fixed onto the latter and the whole assembly is introduced in a deposition chamber. The most favorable geometry for deposition implies a "punctual" source (S), large distance source-substrate (D) and minimum gap between the mask and substrate (G). These are the basic conditions that will minimize "blurring" effects (enlargement of the deposits) always present during the direct growth through a shadow-mask. In a good approximation, and if lateral surface diffusion-like processes are excluded, the widths (w_B-bottom width and w_T-top width) of a structure realized in this way are given by the geometric equation depicted in Fig. 6:

$$w_{B,T} = w_A \pm S \cdot \frac{G}{D}, \tag{1}$$

where w_A is the initial aperture size opened in the membrane.

[3] The microsieves used consist in an array of 5-μm circular perforations etched by RIE that supports a 10-nm thin SiN nano-membrane. The nano-membrane has been drilled by low-current FIB forming the nanosieve with 25 nm pores in lateral size and a pore pitch of around 115 nm. By coating the 25-nm pores with another 10 nm LPCVD SiN layer, pores with lateral sizes below 10 nm have been finally obtained.

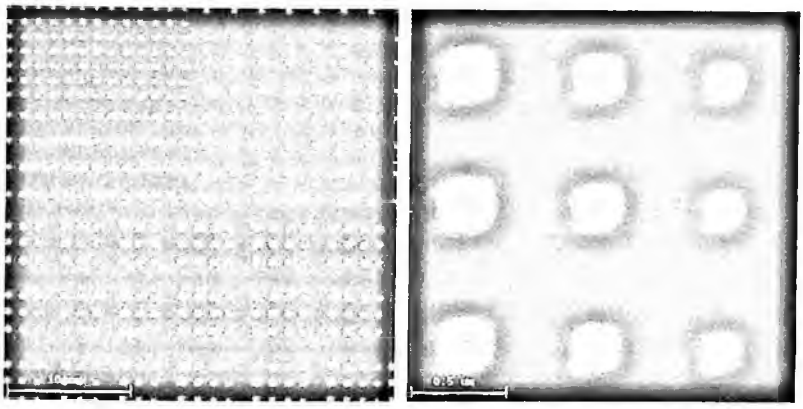

Figure 5. Focused Ion Beam (FIB) micrographs of 100–150 nm thick SiN membranes in which various aperture designs have been directly transferred by Ga^+ ion milling; aperture sizes range from 90 to 400 nm. Work has been performed by our group at the CM^2 facilities of École Polytechnique, Montréal, Canada.

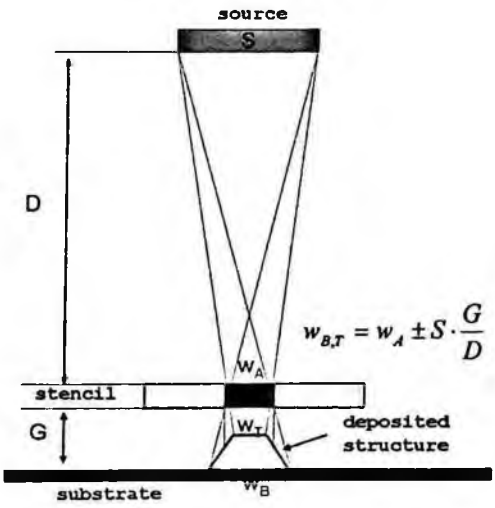

Figure 6. Schematic drawing of shadow-mask deposition (not to scale); the enlargement of the deposited structure w_B is highly dependent on the 3 main geometric parameters: the source dimension (S); distance source-stencil (D) and the gap (G) between the stencil and the substrate.

As a general rule, the gap between stencil and substrate should be as small as possible (ideally 100 nm or less) and must be kept uniform over the whole shadowed area. Nevertheless, the stencil-substrate spacing usually varies due to substrate surface irregularities, foreign particulates, roughness or bending of the membrane layer. To overcome this issue silica-spheres (1.6 μm in diameter) [47] or resist rings (2 μm thick) defined onto the mask have been introduced and used as spacers for nanostencils, so as to prevent them from touching the substrate in an uncontrolled

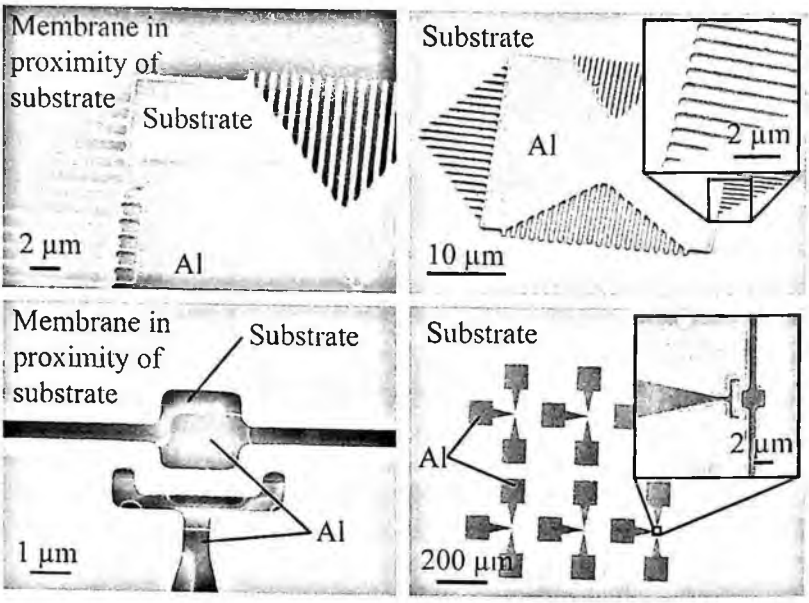

Figure 7. SEM-images showing stencil-masks with a gap (approximately 5 μm, (upper-left image) and approximately 1 μm (lower-left image) to a substrate after evaporation. SEM images showing the corresponding Al pattern replicated from the stencils. Reprinted with permission from [42] by AIP.

way, trading off a larger substrate-shadow mask distance against a much better uniformity.

When using the D-NS approach the gap stencil-substrate has been controlled by employing techniques adapted from scanning probe microscopy. Controlled engagement of a cantilever tip towards the surface [14] or an inchworm and piezo tube where used for coarse approach and distance fine tuning respectively [15]. In the latter case, to ensure that complex structures are designed in a controlled way, Egger and co-workers realized an automated control for both mask approach and positioning and control of the evaporation processes via dedicated software. The evaporator, having multiple crucibles, can be controlled by a step motor so that the active crucible is always brought in the same position avoiding thus undesired misalignments.

State-of-the art D-NS is achieved by the combination of SPM, multishadow-mask patterning and electronic probing (four-probe) realized by Zahl and co-workers [49] (IBM Zurich), a system that allows all *in situ* complex direct patterning, pattern inspection and testing. The "all-in-one" static and dynamic stenciling system provides indeed the recipe for easy prototyping of various nanostructures and offers the possibility of intermittent checking by STM or AFM procedures during growth. The optional capability of using multiple aligned masks allows for shadow evaporation processes both in a static and dynamic approach. The stencil architecture is based on a set of aligned and exchangeable mask carriers to allow maximal flexibility

for patterning. A precision carousel-like turntable with a snap-in lock mechanism provides a set of highly precise (<1 μm) repeated positions, and accepts the transferable mask carriers. Similar to the mask carrier, a four-point-probe and the SPM detector, i.e., the STM tip or AFM cantilever can be placed and turned to the reference position. This key feature of the nanostencil setup ensures that even a single nanostructure can easily be found within the SPM's scan range. Using this setup, tests were performed on SiO_2 surfaces using Cu and C_{60} fullerenes, resulting in structures down to 40 nm [FWHM] for Cu and 110 nm [FWHM] for C_{60}, the broadening for the latter being caused by diffusion of C_{60} at room temperature. Test structures of crossed C_{60} and Cu wires on native silicon oxide have also been realized with the aim of electronic characterization of thin and long nanowires and junctions of different metallic and organic materials.

Turning now our attention towards the options in choosing the vapor deposition method to be combined with stenciling it is important to mention that each technique has advantages and drawbacks. For instance, thermal evaporation even if attractive from the point of view of costs, allows only the deposition of elemental materials and the adjustment of few parameters (e.g. distance stencil-substrate, deposition time). In contrast, a PVD process like pulsed laser deposition (PLD) allows to vary more parameters such as target materials (e.g. complex compounds), laser fluence on the target, background pressure (vacuum or gas), kinetic energies of the ablated species, target-substrate distances. These are key parameters that can be varied and tuned during the process to control growth features (and therefore their properties), and to increase or decrease the aspect ratio of the structures [50]. In fact PLD, which emerged as a convenient deposition method because of its high versatility in growing stoichiometric thin films [51] on a wide range of substrates, can bring a convenient way for rapid prototyping of nanostructured materials when used in combination with stenciling. A drawback of PLD through nanostencils might be induced be the droplets (particulate conglomerates) present in the plume together with the ablated species, that can lead to premature closure of the aperture or pattern alteration. To overcome this issue it is essential to fine-tune and control the deposition parameters.

One major limitation of nanostenciling is the progressive clogging (decrease of the hole size) of the mask's apertures during deposition. Clogging occurs as the evaporated material, deposited on the membrane itself, is also accumulated inside the apertures. This phenomenon changes the geometrical shape of the aperture during the deposition process and leads to the deformation of the deposited pattern and eventually to the complete closure of the aperture. Kölbel *et al.* [41] demonstrated the use of self-assembled monolayers (SAM) as an anti-adhesion layer. The SAM coated SiN membranes showed a reduced aperture clogging, which improved their performance and lifetime.

A circular hole has been estimated to clog after evaporating a thickness equivalent up to 5 times its diameter. However, practice shows that this strongly depends

on the deposited material, mask material and beam collimation (ref [15] and references therein). Nevertheless the choice of the physical vapor deposition technique plays an important role and the optimal control of the interaction of the deposited material with the membrane apertures remains a matter of further research. Moreover, certain materials (e.g. gold, platinum) can be removed by selective aqueous chemical etching. Alternatively, dry plasma cleaning is also possible provided that a selective removal of the deposited film with respect to the stencil material is feasible.

A second limitation of the membrane stencil is the stress-induced bending. The mechanically fragile membranes deform under influence of the deposited material due to a different thermal expansion coefficient and a deposition related internal stress. Efforts have been made to stabilize the membrane locally by introducing some stabilization structures. Van den Boogaart *et al.* presented recently stabilized membranes with SiN corrugated support structures [52]. These corrugated support structures are used to reduce the membrane deformation due to the deposition-induced stress and thus to improve the dimensional control over the surface patterns created by stencil lithography. The numerical simulation performed and experimental results confirmed that introducing stabilization structures in the membrane could significantly reduce out-of-plane deformations (up to 94%) of the membrane. The results of this study can be applied as a guideline for the design and fabrication of mechanically stable, complex stencil membranes for direct deposition.

2.3. *Nanostenciling applications*

2.3.1. *Ordered arrays of structures*

Even though a large number of techniques are proposed as alternatives to conventional optical lithography, the reality shows that only a few are close to the CMOS industry's requirements. Combining high resolution, with high throughput at low-cost, is a real challenge in nanotechnology, given the huge interest for rapid and cost-effective fabrication of highly ordered arrays of nanosized structures, from a broad range of materials. Nevertheless, nano-stenciling approach, either in the static or the dynamic mode is a very attractive technique, demonstrated so far at the laboratory scale. As previously stated, NS emerged as a highly-flexible approach to control the parallel patterning of clean nanosized structures, providing thus convenient ways for their further investigations.

Most of the work has focused on metal patterning by evaporation [13,37,41,47] and later by pulsed laser deposition (PLD) [53,54]. Using e-beam evaporation, Boogaart and co-workers, patterned a variety of structures (e.g. Al, Au, Bi, Cr, Cu, Ni, and Ti), with dimensions ranging from 200 nm up to 300 μm, with high throughput and reproducibility at a wafer scale, on a large variety of surfaces [42]. The results showed that full-wafer mesoscopic stencils can be practically applied for direct and rapid patterning, on large surface areas, without lithography of multiple length scale patterns (Fig. 7).

Another important example is to be found in the work by Yan *et al.* [55] who reported fabrication of uniform sub-50-nm platinum Pt nanoparticles by e-beam evaporation through a 50-nm thick, low-stress SiN patterned stencil. Using the conformal deposition of LPCVD silicon dioxide, the authors reduced the size of the features in the silicon nitride stencil from an initial value of 56 to 36 nm. The particle pattern replicated well that of the stencil and the patterned metal nanoparticles can serve as model catalysts for the study of reaction rates and chemical selectivity [56]. A self-assembled monolayer (SAM) of tridecafluoro-1,1,2,2-tetrahydrooctyl-1-trichlorosilane was used to reduce clogging of the nanosized holes during deposition as well as to protect the stencil during the post-deposition Pt removal. The efficiency of SAM protection on the stencil, during the post-deposition Pt removal, was confirmed by X-ray photoelectron spectroscopy (XPS) measurements.

Probing different routes for deposition methods, Vroegindeweij and co-workers carried out experiments to investigate the ability of pulsed laser depositions (PLD) through microstencils, and performed experiments with the deposition of nickel (Ni), nickel oxide (NiO) and gold (Au) islands on TiO_2-terminated $SrTiO_3$ substrates [53]. The authors pointed out the advantages brought by PLD: a wide range of possible materials to be ablated, a wide working pressure range and above all, the highly energetic particle flux as the main attribute that enables a sharp replication on the substrate. However, even at room temperature, since the ablated species have high activation energy on arrival at the substrate, it has been found that the material tends to diffuse under the stencil due to the mobility of the particles. The gas pressure during deposition is found to be an important parameter, since a larger broadening effect becomes apparent when the gas pressure is higher. Another demonstration of the versatility PLD-nanostenciling is reported in 2004 by Speets and co-workers with the aim of avoiding metal diffusion effect when the latter is patterned on thiolate self-assembled monolayers (SAM) by evaporation[4]. The authors argue that in principle, this method easily allows variation of substrate, SAM composition, and deposited material, thus representing a practical approach for the exploration of molecular electronics, and in particular of the role of molecule-metal contacts. The choice for PLD is also motivated by the fact that it enables the control of the kinetic energy of the atoms in the gas phase by means of background gas and laser energy (in this case low kinetic energy gold deposition on SAMs has been used). In a follow-up of their previous work, Speets *et al.* reported on noble-metal cluster patterns, deposited through micro/nanostencils, being used as catalysts for selective electroless deposition (ELD) of Cu. Cu structures were grown on SAMs on both Au and SiO_2 substrates and were analyzed by X-ray photoelectron spectroscopy element mapping. The combination of PLD through stencils on SAMs followed by ELD is suggested as a new method for the creation of sub-micrometer-sized metal

[4] The method yielded arrays of Au-SAM-Au "sandwich" structures (nanoscale capacitors) 600 nm in diameter, approximately 10 nm high and spaced 1.6 μm apart.

structures on top of SAMs, thus minimizing the gas-phase deposition step, which is often responsible for damage to, or electrical shorts through, the latter.

More recently, nanostencil-based patterning of complex oxide materials by PLD was also reported. Our group [57] reported the direct patterning of barium titanate ($BaTiO_3$), a typical perovskite ferroelectric oxide, on silicon and strontium titanate $SrTiO_3(100)$ substrates, via PLD nanostenciling (Fig. 8[a],[b]). The replication process (structures down to 250 nm in width [FWHM]) was achieved at room temperature, and then a post-deposition annealing treatment was used to crystallize the structures. Their local ferroelectric properties were investigated using piezoresponse force microscopy (PFM) (Fig. 8[c]), a technique that tests the piezoelectric and switching properties of ferroelectric materials at the nanoscale, using a modified AFM [58]. Beyond demonstrating the direct growth of ordered complex oxide nanostructures (applicable in high-density data storage media), the authors also investigated possible size effects (i.e. suppression of ferroelectricity below a critical size at room temperature) in patterned ferroelectric ABO_3-type nanostructures.

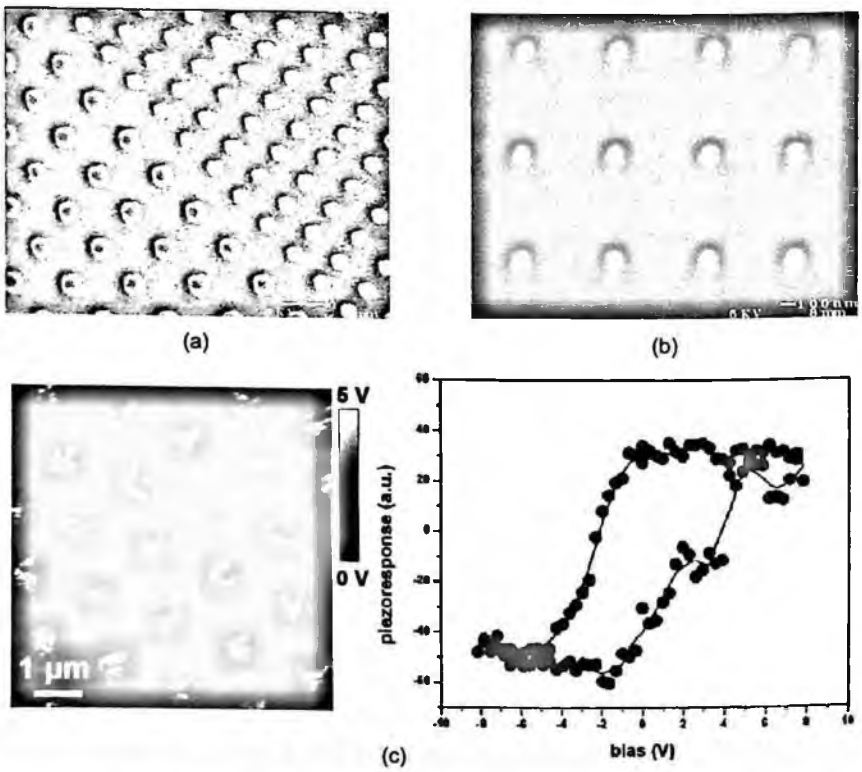

Figure 8. (a) and (b) SEM micrographs of ordered $BaTiO_3$ structures (125–250 nm in width) on Pt coated Si(100) oriented substrates deposited at room temperature; (c) Piezoresponse domain image (left) of patterned ferroelectric $BaTiO_3$ on 0.1% Nb doped $SrTiO_3$ and piezoresponse hysteresis loop obtained from an individual structure.

Later on, Shin *et al.* reported on the patterning of lead-zirconium titanate (PZT), another widely used functional oxide that exhibits piezoelectric and ferroelectric properties [59]. Nanodots with diameter of ~120 nm were realized by means of PLD nanostenciling on $SrRuO_3/SrTiO_3$ substrates. The dots could be polarized individually and the authors determined that a polarized state remained un-relaxed for ~20 minutes.

Our group has also investigated a multi-level-stenciling approach [50], further extending the versatility of the PLD-stenciling process, thus proposing a solution for rapid prototyping of stacks of functional materials (such as metal-oxide-metal and/or multiferroic structures) by sequential depositions through the same stencil, without removing it from the substrate in between target changing. Ultimately our aim is the epitaxial growth of ferroelectric and multiferroic nanostructures (e.g. $BaTiO_3$, PZT or $BiFeO_3$) thus leading to an enhancement of the piezoelectric/ferroelectric properties of the latter.

2.3.2. *Nano-sensors and NEMS*

One of the most challenging aspects in nanofabrication is the ability of fabricating devices on non-planar (e.g. curved) surfaces, for instance on the surface of an atomic-force-microscope (AFM) tip. The reason for such endeavors would be the development of advanced forms of scanning-probe microscopy (SPM) [60] that employ nanofabricated structures that serve as scanning sensors or "functional" probes. Aiming at this aspect, Champagne and co-workers [61] reported a lithographic procedure employing stencil-masks that enabled the fabrication of a variety of devices at the apex of AFM tips (Figs. 9 and 10), with a spatial resolution controllable down to 10 nm. The authors described the fabrication of high spatial resolution magnetic force microscopy (MFM) tips as a specific application of the technique. Commercial MFM tips are usually coated with a continuous ferromagnetic film. However, both the spatial resolution of MFM and the degree to which magnetic samples are perturbed by the tip can be improved by limiting the magnetic material to a small volume near the apex of the tip. Champagne and co-workers deposited single dots of 90% Co/10% Cr alloy, with diameter ranging from 140 to 25 nm, at the end of sharp commercially available AFM tips using the nanostencil-based technique. The authors point out that by using cantilevers with smaller spring constants, the force gradient sensitivity can be enhanced by as much as a factor of 1000 meaning that magnetic dots potentially as small as 10 nm, approaching the paramagnetic limit, may be used as MFM sensors. Furthermore, because the stencil allows for the patterning of metal shapes down to the 10 nm scale, the magnetic structure of the tip could be controlled to be a well-oriented dipole, making quantitative analysis of MFM images more straightforward. The stencil technique also has the potential to produce many other types of functional SPM tips. The possibility of making both gated-STM tips and scanning single-electron transistors with pattern definitions close to 10 nm has been anticipated. This would greatly increase

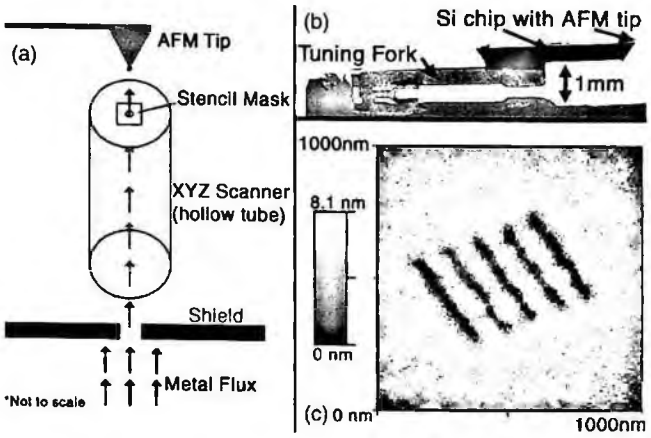

Figure 9. (a) Schematic diagram of the deposition geometry (not to scale). Metal is deposited from the source, through holes in the stencil membrane, onto the AFM tip. (b) Picture of a commercial AFM tip mounted on a tuning fork used for sensing the tip–surface interaction. (c) AFM image of a pattern of holes in a stencil membrane, acquired prior to deposition. Reprinted with permission from [61] by AIP.

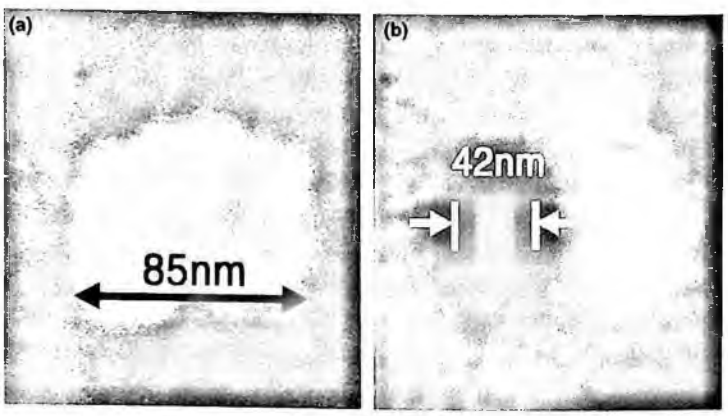

Figure 10. (a) SEM micrograph showing a cobalt (Co) nanopillar used to test the MFM resolution. (b) MFM image of a nanopillar recorded with an AFM tip having a CoCr dot (deposited through a stencil) at the apex of the tip. Reprinted with permission from [61] by AIP.

the sample-gate coupling in gated STM, and would allow operation of scanning single electron transistors at temperatures well above 1 K. Other applications might include improved near-field optical probes.

NEMS have attracted increased interest as miniaturized force-sensing and resonating devices because they combine simultaneously low force constants ($k < 1$ N/m) and ultra-fast resonance frequencies ($f > 1$ MHz) [62]. High-speed AFM and mass-sensitive resonating sensors are two potential applications. Since the cantilever can be approximated as a simple harmonic oscillator, the only way to increase the resonance frequency f, without raising the spring constant k, for a rectangular

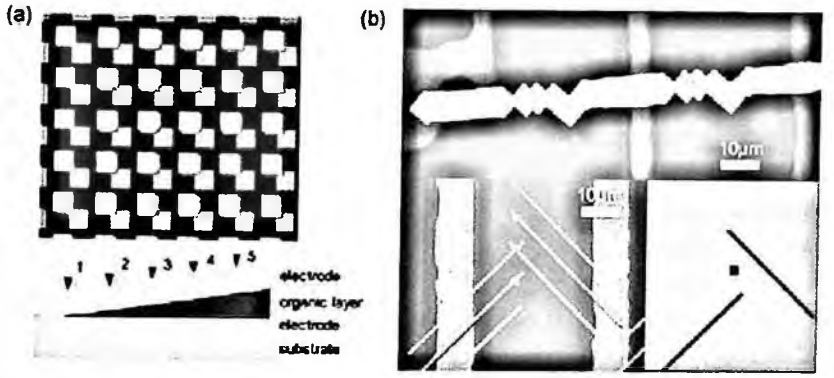

Figure 11. (a) Array of Ti/C_{60}/Ti structures on a quartz substrate, fabricated using an array of squares as a shadow mask. A global shadow mask was used to create a linear variation of the thickness of the C_{60} film, from 10 to 90 nm. The square electrodes are $60 \times 60\mu m^2$ and the overlapping regions $11 \times 11\mu m^2$. (b) Examples of electrically connected devices fabricated using FIB patterned silicon nitride membrane masks: (up) Two devices formed using 6-μm square apertures; (down) C_{60} island sandwiched between crossing metal lines. The structure was fabricated in three steps using a stencil with FIB cuts. Reprinted with permission from [68] by ACS.

cantilever with mass m is to lower its mass by further downscaling the device feature into the submicron regime. Presently, the typical fabrication process to create free-standing elements for MEMS involves a multitude of manufacturing steps similar to those used for integrated circuits (ICs), namely photolithography with "deposition-pattern-etching" cycles and associated sub-steps. Sacrificial layer etching is typically used to release the structure. In particular, special care is required during the final etching step to avoid surface-tension-related sticking of the nanostructures upon release. To alleviate some of these processing issues, Kim and co-workers [63] described the use of direct nanopatterning via nanostencils to fabricate suspended nanomechanical elements in two simple steps without the need for photolithography. The method is based on the local deposition through a nanostencil of a well-defined aluminum pattern onto a silicon/silicon-nitride (Si/SiN) substrate, followed by plasma etching to release the structures[5]. The resulting suspended (e.g. 100nm-wide, 2 mm-long, and 300-nm-thick) nanolevers and nanobridges showed natural resonance frequencies of 50 and 91 MHz, respectively (measured using a heterodyne laser Doppler interferometer). The authors are stressing out that the fabrication method is scalable to a full 4-inch wafer [40] and allows for a variety of materials to be structured on arbitrary surfaces, thus opening new types of nanoscale mechanical systems.

[5] A 100-nm-thick Al material layer was shadow-evaporated via the apertures opened in the nanostencil onto the SiN layer by means of e-beam evaporation. After removing the nanostencil, the Al nanostructures on the surface represent a copy of the aperture pattern in the membrane and form an effective etch mask for a subsequent pattern transfer etch step into the underlying SiN and sacrificial Si layer.

2.3.3. *Biocompatible materials and molecular circuits*

Planar microelectrode arrays (MEA) constitute powerful tools for a wide range of applications in neuro-technological research. The disadvantage of these systems is the low density of electrodes caused by the problem of wiring a great number of electrodes. In turn this results in a low number of good quality cells-electrode contacts, making impossible the measurement of cells that are lying within the electrodes. In addition, cells usually do not adhere exactly on the electrode area. As a consequence, the signal to noise ratio is not optimal and the signal cannot be detected properly.

Bucher and co–workers [64] proposed a solution to these problems by using an array of light-addressable sub-μm electrodes providing thus a freely selectable cell–electrode contact with a high signal-to-noise ratio and high spatial resolution. To realize this, a great number of laterally isolated sub-μm electrodes is placed on a photoconductor layer such as amorphous silicon (a-Si:H). By use of a laser beam, only those sub-μm electrodes lying under the cell can be selected to form an electrical contact to one of the underlying indium tin oxide (ITO) leads providing a high seal resistance at the cell-electrodes interface. Bucher and co-workers designed a biocompatible and biostable composite layer of electrodes (e.g. Au and TiN, 100–500 nm) and insulator by means of nanostencil technology facilitating thus the measurements of dark to bright ratio (D) of the a:SiH photoconductor layer. The work demonstrated an easy and economic fabrication approach (compared to e-beam lithography) of TiN and Au sub-μm electrodes embedded in a passivation layer.

Molecular devices are frequently based on nanowires or nanotubes that are grown or deposited on a substrate and subsequently contacted using electron-beam or optical lithography. Using these approaches, the polymer (resist) layer applied to the sample and its consequent processing, can alter the nanowires or tubes under investigation or even destroy delicate samples. Thus, the advantage of depositing nanoscale metal contacts, directly without the damage associated with the chemistry and thermal stresses of conventional lithography become immediate. To achieve this goal, Zhou and co-workers [65] followed this route based on metal evaporation through a nanoscale stencil created in a suspended silicon nitride membrane. Electrode fabrication has been accomplished by placing the nanoscale stencil in direct contact with a flat substrate (e.g. oxidized silicon or mica) with pre-deposited nanowires on the surface and evaporating metal through the stencil. CVD-grown single-walled carbon nanotubes contacted in this fashion behaved similarly to samples contacted using conventional lithography but showed more robustness to failure at high bias. Using the same approach, the authors contacted in a leads-on-top geometry λ-DNA networks, which were previously deposited on mica substrates, and investigated their conductivity. Either nanotubes or DNA fibers would be destroyed by the solvents used in conventional (electron-beam) lithography. Thus the nanostencil approach offers an excellent way to perform transport measurements on such samples with sub-micrometer contact separation.

2.3.4. *Combinatorial materials*

The use of MEMS tools for combinatorial materials investigation was proposed recently by Ludwig *et al.* [66] in order to improve both quality and quantity, in terms of resolution and throughput, for the synthesis and analysis of new materials and new material combinations at micron and sub-micron scales. In particular, fabrication of material libraries directly on micro-machined sensor/actuator arrays without the use of photolithography is very promising. Examples for such MEMS tools are micro-fabricated shadow masks such as micro/nanostencils. They allow for rapid, clean and direct patterning of laterally confined layers of a thin film on a large variety of surfaces. Using stencil masks, laterally structured films can be fabricated in a single processing step. The combination of micro/nanostructured shadow-masking technology with combinatorial material deposition methodologies, could lead the way to a new direct fabrication or optimization of novel sensors and actuators based on nanoscale materials without the use of photolithography. In particular, the combination of these two technologies allows the variation of composition (e.g. by opposing wedge type multilayer films) [67] and nanostructure (by the nanostencil) in one experiment. Thus, screening for nanoscale effects, or generally the study of materials properties depending on the length scale, in thin films can be facilitated.

More recently, Egger and co–workers [68] demonstrated that the working principle of the dynamic stenciling (D-NS) is compatible with the basic principles of the combinatorial approach: parallelization and variation. The target is to incorporate organic thin film materials, into devices with high potential in electronics and opto-electronics. Compared to a static mask, the ability to precisely control the motion of the shadow mask (embedded in an UHV-chamber-AFM-evaporator setup) gives a significant increase in the number of possible geometries. Using a simple patterned mask with square apertures allows creating an entire device. Once the bottom electrode is grown, the mask is moved sequentially at different positions to grow the active layer(s). Finally the top electrode is deposited and an additional insulating capping layer can be added, if necessary (Fig. 11).

To apply a combinatorial methodology, the authors used a large array of apertures of the type described above, together with a second "global" shadow mask that was moved over the whole array area. This global mask allows one to vary one or two parameters over the device array, thus generating structures for an entire device library. The variation can involve the active layer (its thickness, doping level, or composition), the electrodes (to change their chemical composition, work function or chemical reactivity), or the capping layer. Arrays of $Ti/C_{60}/Ti$ structures on a quartz substrate, were fabricated as outlined above (without capping layer) and using an array of squares as a shadow mask. A global shadow mask was used to create a linear variation of the thickness of the C_{60} layer, from 10 to 90 nm. To grow smaller structures, FIB cut stencil-masks, with very well-defined edges, were necessary. The same strategy with overlapping regions, as described above,

but on a smaller scale was used again to generate Ti/C_{60}/Ti/quartz structures at room temperature. Then a different principle, consisting in the combination of different shapes generated by different parts from the same stencil mask was applied. This strategy extends the possible device geometries and complex devices can be assembled from several components. In both cases, the structures were electrically connected with larger wires to bonding pads. These large patterns were fabricated *in situ* with separate, micrometer-scale patterned stencils. Various *in situ* characterizations (e.g. electrical transport measurements) followed once the structures were realized. Thus, a highly flexible UHV fabrication and *in situ* characterization method which allows one the use of efficient strategies as established in combinatorial discovery was demonstrated. Straightforward applications suggest the design of organic/metallic (or organic/semiconducting) multilayer devices.

3. Nanoimprint Lithography

3.1. *General background*

Presently there are several types of Nanoimprint Lithography (NIL) approaches. The mostly used ones are: Hot Embossing Technique (HET) or Thermoplastic Nanoimprint Lithography (T-NIL) and Step and Flash Nanoimprint Lithography (S-FIL), both depicted in Fig. 12. NIL presents several advantages over conventional nanofabrication methods: it is parallel and offers high-resolution and high-throughput at a lower cost. For this reasons it has attracted a lot of attention from a technological standpoint. Moreover, it has been recently placed on the

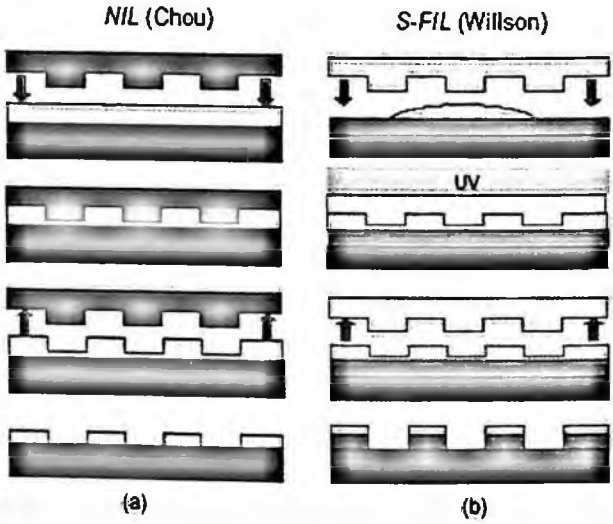

Figure 12. Schematics of (a) thermoplastic (T-NIL) and (b) step and flash imprint lithography (S-FIL) processes. Reprinted with permission from [90] by IOP.

International Technology Roadmap for Semiconductors (ITRS) at the 32 nm node, which is expected to be reached in a few years [69].

T-NIL was reported for the first time in 1995 by Chou's group [10] and shortly thereafter emerged as an attractive research topic for many other research groups. T-NIL is based on two distinct steps: imprint and pattern transfer as shown in Fig. 12(a). In the first step (imprint) a mold (made of metals, dielectrics, or semiconductors) with nanofabricated patterns on its surface is pressed into a thin polymer (often referred to as a resist) spun on a substrate. This step duplicates the nanopatterns from the mold into the polymer film creating a thickness contrast pattern in the latter. During the imprint step, the resist is heated to a temperature typically 50–100 °C above its glass transition temperature (T_g). At this temperature, the resist, which is thermoplastic, becomes a viscous liquid and can flow under pressure (about 50–100 bar) and therefore can easily conform to the shape of the mold. The mold is then removed from the imprinted substrate after cooling both the mold and substrate. The second step consists in transferring the pattern by an anisotropic etching process. For example, reactive ion etching (RIE) is used to remove the residual resist in the embossed area. This step transfers the thickness contrast pattern into the entire thickness of the polymer, which is in turn used as an etching mask for further pattern transfer into the functional layer (substrate). As a first demonstration of the feasibility of this technique, metal dot arrays with a minimum feature size of 25 nm and a period of 70–100 nm were fabricated [70–71]. It was then predicted that with further development NIL would lead to the fabrication of sub-10-nanometer structures with the potential to become a commercially viable approach for manufacturing integrated circuits and nanodevices.

The Step and Flash Imprint Lithography (S-FIL) variant is a step and repeat nano-replication technique developed by Willson's group at the University of Texas at Austin in 1999 [12]. In S-FIL, a low viscosity UV curable liquid resist is applied to the sample substrate in forms of drops and a mold, usually made of transparent material like fused silica, is pressed against it (Fig. 12[b]). After the mold and the substrate are pressed together, the resist is cured in UV light and becomes solid. Following mold separation, a similar pattern transfer described for the T-NIL process can be used to transfer the pattern formed into the resist onto the underlying material. The use of low viscosity monomers (viscosity of <5 cps) leads to a low imprint pressure process (<0.25 psi) resulting in significantly lower defect density. Several sensible challenges need to be addressed, if the promise of nanoimprint is to be extended to a larger set of applications. Among them, the ability to print with high throughput fields with non-uniform pattern density, the ability to etch nanostructures with appropriate critical dimension (CD) control, precise alignment and overlay, and minimization of process-induced defects thus S-FIL was at first introduced to address these challenges. In particular S-FIL uses a bi-layer approach in which the imprinted material is a silicon-containing material that is deposited on an underlying organic layer. This allows the patterning of relatively low aspect ratio features which can then be amplified in aspect ratio by using an O_2 RIE to

etch the underlying organic. This low aspect ratio patterning turns out to be the solution in minimizing defects, particularly during the separation of the template from the UV cured material [72,73].

Over the last decade, there have been several milestones attained in the development of NIL as an alternative nanofabrication technique and its applications [11]. Two years after the inception of NIL, Chou's group reported arrays of 10 nm diameter holes with a periodicity of 40 nm imprinted in PMMA covered silicon and gold substrates and achieved the smallest hole diameter of 6 nm imprinted in PMMA. They further used NIL together with optical lithography to fabricate silicon QDs, wires, ring transistors, and nanocompact disks with 10 nm features and 400 Gbits/in^2 data density [74]. In 1999, Wang and co-workers from the same group, demonstrated how NIL serves to directly pattern organic light-emitting structures with submicron resolution while preserving their optical properties [75].

Later on, in 2000, polymers developed specifically for NIL become commercially available [76] and NIL demonstrated single level patterning over a six-inch wafer scale [77]. Studer and co-workers [78] reported in 2001 the first microfluidic device made using NIL and in the same year, the feasibility of multi-level alignments on four-inch wafers by NIL was demonstrated by Zhang and Chou [79]. One year later, thin films of the organic semiconductors alfa-sexithiophene (T6) were imprinted and interdigitated nanoelectrodes to be used as the source and drain in thin film transistors (TFTs) were printed down to 100 nm [80]. An anti-adhesion treatment for stamps containing sub-100 nm features is reported by Beck [81] in the same year. Laser-assisted direct imprint (LADI) [82], a variant of NIL by which a single excimer laser pulse melts a thin surface layer of silicon and a mold is embossed into the resulting liquid layer, is introduced by Chou and co-workers. Application of NIL to fabricate two-dimensional photonic crystals has been reported by Seekamp *et al.* [83]. D.Y. Khang and co-workers reported in 2004 on the feasibility of low-pressure NIL [84] and E. Mele and co-workers [85] presented in 2005 room-temperature nanoimprint lithography (RT-NIL) applied to multilevel patterning of organic light-emitting polymers. Jung and co-workers [86] reported on the surface modification of the substrate, prior to NIL, as to enhance the resist adhesion to the substrate. As the pitch size was very much reduced (30 nm half-pitch), this solution lead to a better pattern transfer in the polymer layer, preventing the latter to adhere to the nanogaps between the protrusions of the mold. More recently H. Y. Low and co-workers discussed combinatorial-mold imprint lithography for fabrication of three-dimensional polymer structures [87] and Yang and co-workers [88] proposed UV nanoimprint lithography as a versatile way to pattern phase change materials as media for data storage.

An elegant method combining NIL and superlattices nanowire pattern transfer (SNAP) has been recently used by Jung and co-workers [89] to generate 17 nm half-pitch metal nanowire arrays and cross-bar circuits. High-density silicon nanowire arrays generated by the SNAP technique were utilized as a mold and a carefully engineered bilayer resist structure was used for the NIL, as to reliably reproduce the

mold's small features. Nanowire patterns at 17 nm half-pitch were transferred to the underlayer by selective RIE without collapsing the resist patterns. As an example, the authors produced an array of 150 separated platinum nanowires and a corresponding cross-bar structure was achieved by repeating the imprinting process with the same mold and a 90° rotation. It was then suggested that such combined techniques may lead to a manufacturing approach that can generate electrical circuits at near molecular scales.

3.2. *Molds, polymers and tools for NIL*

Nanoimprint lithographic techniques involve the following key elements: (i) a mold (often referred as stamp), (ii) a material to be embossed (i.e. a polymer or resist) and (iii) the tools for mold-substrate alignment and uniform pressure and temperature application. These three elements will be discussed in the following sections.

3.2.1. *Materials for molds and fabrication*

Since the inception of NIL, it was predicted that the ultimate resolution of the technique would be dictated by the minimum feature size achievable in the mold. Consequently, many groups have directed their efforts towards investigating and improving this intrinsic aspect of the process. Currently, features are fabricated onto a stamp by optical lithography, electron beam lithography or FIB. To obtain sub-micron features, optical lithography is often used followed by dry etching. If features smaller than 100 nm are desired, electron beam lithography or FIB are necessary. For instance, in the pioneering work of Chou a mold was patterned with dots and lines with a minimum lateral feature size of 25 nm using electron beam lithography and RIE. The protrusions of the mold were from 40 to 200 nm with an aspect ratio of 3:1 for the smallest mold feature.

The mold material selection comprises among others, the compatibility with conventional microfabrication processing, hardness and thermal expansion coefficients, as presented by Guo in a recent review on various aspects of NIL [90]. For instance, the molds for T-NIL have mostly been made of Si or SiO_2. Other materials like CVD-SiC/Si, SiC, Ta, SiN/Si, Ta/Si and quartz (for those used in S-FIL approach) have been envisioned later as the mold material (Fig. 13). Metal molds with features smaller than 10 nm have been fabricated by electron beam lithography and lift-off. However, the metal roughness was found to be a problem for sizes below 10 nm due to the granularity of the evaporated metal. Taniguchi *et al.* [91] have investigated diamond as a potential mold material for NIL.

The thermal expansion coefficient is a very important parameter in thermal NIL, where the usual temperature required in the imprinting step exceeds 100 °C. A thermal mismatch between the mold and the substrate could result in pattern distortions or a stress build-up during the cooling cycle, which would affect the pattern fidelity. For example, using Si for both mold and substrate is a very good

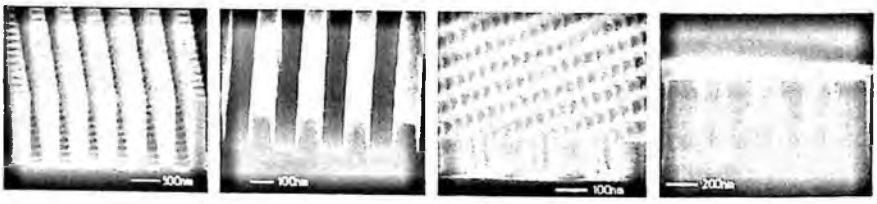

Figure 13. Molds for nanoimprint: from the left Si, SiO_2, SiC and quartz. Si molds have been designed with features as small as 20 nm; SiC molds offer high mechanical strength and chemical resistance; quartz molds are offering high transparency for UV nanoimprint lithography. (Courtesy of NTT-Advanced Technology Corporation (NTT-AT), Tokyo, Japan, www.ntt-at.com/products_e/mold/index.html)

choice and studies reported by several groups have demonstrated that Si and SiO_2 have sufficient hardness and durability for the nanoimprint application.

Mold durability is maintained by choosing the proper polymer (resist) layer thickness such that the mold protrusions do not come into direct contact with the hard substrate. Thus, a thin viscous polymer fluid always exists between the mold protrusions and the substrate surface and acts as a 'buffer', which effectively protects the nanofeatures patterned on the mold. The trade-off is a remaining resist layer that is present in recessed areas of the imprinted substrate, which has to be removed by an additional step (plasma etching) before pattern definition can be completed.

A mold used for NIL typically has a high density of nanoscale protrusion features on its surface. This increases the total surface area that contacts the imprinted polymer and therefore leads to a strong tendency of adhesion of the imprinted polymer to the mold. This effect can be seen from the sticking of the resist material onto a mold that has not undergone special treatment. The solution to this problem is to apply a low surface tension coating to the mold to reduce its surface energy. This can be done by plasma deposition of fluropolymers or by using a monolayer of perfluorosilane. Another very important issue in terms of mold durability is related to the wearing and stability of this surfactant coating layer and ref. [90] provides in-depth details regarding these aspects.

3.2.2. *Polymers and tools*

The stamp design is intrinsically correlated to the polymer to be printed which is typically spin coated (e.g. a few hundred nanometers thick) onto a substrate. Polymer flow in NIL has been studied for PMMA and other printable polymers [76]. It has been found to depend on the molecular weight of the polymer and, more importantly, on the rate of application of both pressure and temperature during embossing. This is expected since the viscosity of the polymer changes over several orders of magnitude around the glass transition temperature (Fig. 14). Thus, the viscoelastic properties of the printable polymer, the stamp design and the process parameters, determine the thickness of the polymer and the residual layer. For a

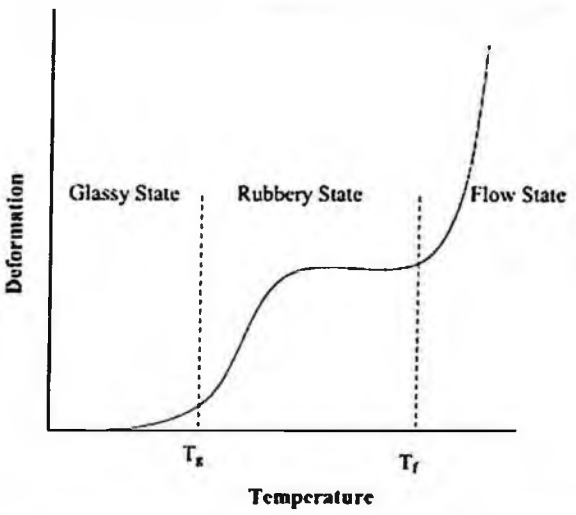

Figure 14. Typical deformation behavior of thermal plastic polymers as a function of temperature. Reprinted with permission from [90] by IOP.

comprehensive review of different polymers used in NIL, the reader can consult the references within ref. [11].

A notable development, with big potential impact in a range of applications, was the synthesis of a particular polymer, such as mr-L6000 developed by Micro-Resist Technology, a polymer that is suitable for NIL and concurrently is UV- and electron beam-sensitive [92]. mr-L6000 has high electron sensitivity ($\sim$5 μC/cm^2 compared to 80-200 μC/cm^2 for PMMA) which results in shorter electron beam writing times. The limits of its resolution are still under investigation and previously these were reported to be around 20 nm. Moreover, the appeal of this material is its suitability for mix-and-match lithography with applications in MEMS, NEMS and microfluidics [11]. More details, a comparison of thermally and photochemically cross-linked polymers for nanoimprinting and further examples can be found in ref. [76].

The need to keep the stamp parallel to the substrate during the process is an essential condition to obtain uniform thickness of the residual layer and the patterned features across the sample area. Thermal gradients must be avoided using suitable heating and cooling elements as well. These thermo-mechanical aspects are always included in the design of nanoimprint lithography equipment. Other relevant factors concerning stamp size, adhesion, curing, cleaning and lifetime, which determine throughput, have been discussed extensively by Zankovich *et al.* [93].

3.3. *NIL applications*

As described previously, NIL creates nanoscale 3D-features by mechanical deformation of a polymer using a hard mold. As a prime application, after embossing the polymer, the thickness contrast realized on the substrate can be primarily used

as an etch mask for dry etching and subsequent pattern transfer onto a substrate if the etching selectivity of the polymer with respect to the underlying material is good enough. NIL can serve as an intermediate step in a lift off process (e.g. deposition of a metal through the patterns realized in the polymer) or, if the embossed polymer has functionality (e.g. conductivity, optical linear or nonlinear response) it can be the active component of a device. Research efforts were not limited only to these straight-forward applications. In the last decade NIL has been proposed as an alternative and versatile technique for the fabrication of devices for electronics, optics, photonics and biology. The progress made in these fields is reviewed here.

3.3.1. *Patterning of organic thin films*

It has been shown that NIL can be employed to pattern organic semiconductors, with submicron resolution and no degradation of optical properties [75]. This is particularly relevant since the sensitivity of organic semiconductors to light or electrons and their solubility in organic solvents do not allow patterning by conventional lithographic methods (e.g. OPL). NIL offered thus a high-resolution patterning technique that paved the way for the fabrication of novel photonic devices. NIL has been used by Wang to fabricate electroluminescent devices based on DCMII (4-(dicyanomethylene)-2-methyl-6-(p-dimethylaminostyryl)-4H-pyran) doped AlQ3 (Fig. 15). AlQ3 (8-hydroxyquinoline aluminum) is a molecule widely used for in highly efficient Organic Light Emitting Diodes (OLEDs) and optically pumped lasers. AlQ3 was doped with 2 wt% DCMII dye molecules to achieve high luminescence efficiency. The organic films were prepared either by thermal evaporation or by spin coating. The same authors studied also a combination of materials consisting of a PMMA matrix into which various semiconducting small molecules, like AlQ3 and DCMII, were imbedded. This type of blend material had been previously used in OLEDs and organic lasers. The grating molds used by Wang were made in SiO_2,

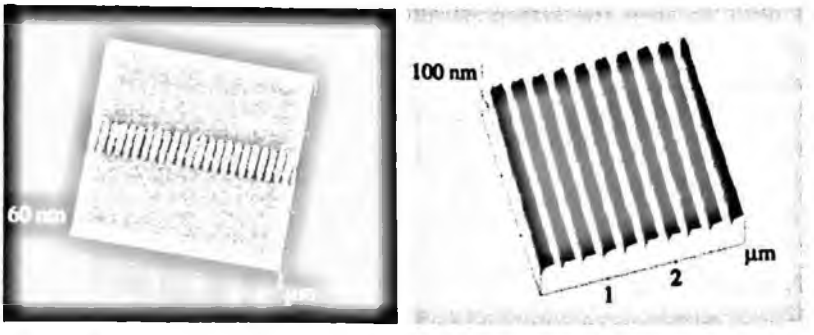

Figure 15. AFM 3D topography images of Alq3/DCMII gratings with a period of 200 nm (left) and 300 nm (right), directly patterned by nanoimprint. Reprinted with permission from [75] by AIP.

by interference lithography, with a period of 200-300 nm and a height of 180 nm[6]. The comparison of luminescence efficiency before and after patterning showed that nanoimprint did not cause degradation in the optical property of the materials.

Lithography based on stamps in intimate contact with the film emerged as the most promising nano-fabrication approach for organics. Nonetheless, many types of molecules are weakly soluble and therefore difficult to process as ink like in soft lithography (microcontact printing). Since transport phenomena in organics have characteristic length scales in the nanometer range, down-scaling to this range constitutes a promising route for enhancing device response [94,95]. These aspects motivated the investigation of NIL for organic electronics, especially in aiming at devices with lateral feature sizes below 100 nm and with tolerances below 10 nm.

Clavijo-Cedeno and co-workers [80] reported in 2002 on the capability of NIL to print and structure three different organic semiconductor materials, namely, alpha-sexithiophene (T6-a thiophene oligomer), poly(4-diphenyl-aminostyrene) (PDAS) and poly(phenyl bis-4-aminostyrene) (PBAS) for fabrication of organic thin-film transistors (TFTs) (Fig. 16). Interdigitated source and drain nanoelectrodes were printed down to 100 nm in T6 films. PDAS and PBAS could be printed at room temperature and they preserved their printed features provided they were cross-linked afterwards[7]. It was shown that printing on thin films of T6 resulted in a spatial modulation of the roughness of the as-deposited film, where the printed areas exhibit a smoother surface. By carefully choosing the thickness of the T6 film and the depth of the stamp features, one could control the thickness of the residual layer down to tens of nanometers. This may be relevant for applications where single domains are needed. Ideally, one would like to have FETs with nanoelectrodes separated by a distance comparable to a single domain in order to reach high mobility values without the influence of grain boundaries [96].

More recently Mele and co-workers [85] have demonstrated multilevel patterning of organic light-emitting polymers by room-temperature nanoimprint lithography (RT-NIL) (Fig. 17). This is impossible to obtain by conventional hot embossing because of typical high values of the temperature (up to 200C) reached during the embossing process. In particular, they realized one- and two-dimensional photonic crystals with 500 nm periodic features and investigated the changes in the optical properties (luminescence and quantum yield) of the organic active layer. The

[6] NIL was performed in a vacuum environment of ~1 Torr, at a pressure of about 800 psi and a temperature of 150°C

[7] The substrates coated with the polymers were printed either using a commercially available unit or using a home-built press. Silicon stamps ($2 \times 2\,cm^2$) with fields of $5 \times 5\,mm^2$, containing 200 nm lines spaced by 800 nm, were made by UV lithography and were dry etched to a depth in the range of 200–400 nm into silicon. Another type of stamp was designed having chromium structures on silicon dioxide/silicon substrates, by EBL onto PMMA films followed by a chromium layer lift-off. Silicon and mica substrates covered with T6 were imprinted using a simple hydraulic press at a temperature of 200°C and a pressure of 100 bar. PDAS and PBAS films were imprinted at ambient temperature with a pressure of 100 bar.

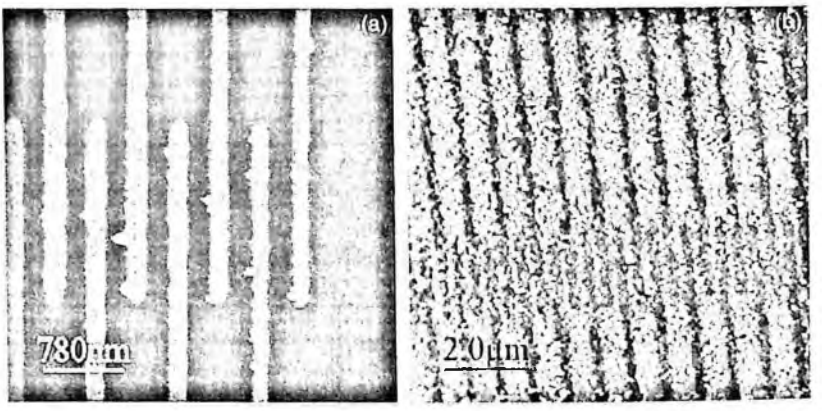

Figure 16. (a) AFM topography image of interdigitated Cr lines patterned on native SiO_2 covered silicon. (b) AFM topography image of a print from a 10-nm high Cr on Si stamp in a sexithiophene (T6) film of a nominal thickness of 10 nm. Reprinted with permission from [80] by Elsevier.

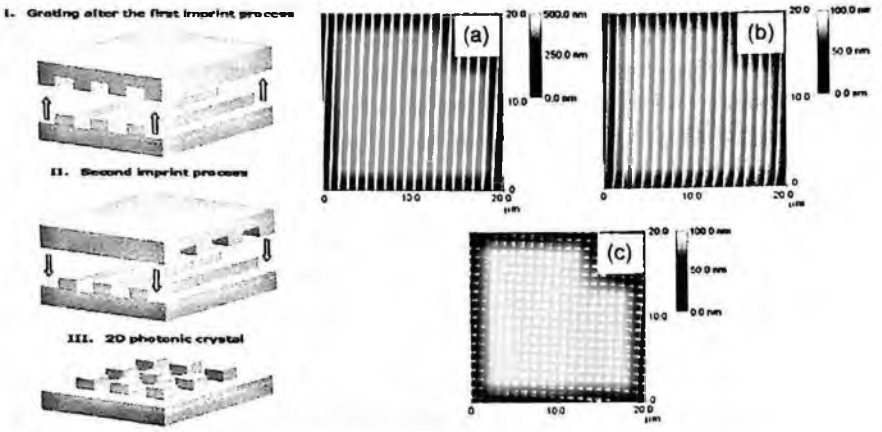

Figure 17. (left) Schematic diagram of the RT-NIL process for the realization of 1D and 2D photonic crystals-like patterns (features are not to scale); (right) AFM topography image ($20 \times 20\mu m^2$) of the 1 µm periodic quartz master (a) and of the polymer semiconductor 1D (b) and 2D (c) imprinted gratings. Reprinted with permission from [85] by ACS.

employment of RT-NIL to pattern polymer semiconductors without degradation of their optical properties is thus foreseen as a strategic route for the realization of novel nanopatterned optoelectronic devices.

3.3.2. *NIL for optics*

Another excellent niche for NIL has been found in optics and photonics. Parallel fabrication of planar optical systems, containing waveguides, mirrors, filters and complex optics, on a low refractive index contrast polymer platform is highly attractive for polymer based photonic circuits. This should be accompanied by accurate

control of feature sizes down to 10 nm, along with accuracy, repeatability, compatibility and low fabrication costs. With the introduction of low refractive index materials, e.g. polymers as suitable materials for photonic circuits (PC) applications, the option of directly printing a complete photonic integrated optical system in one step has emerged.

Seekamp and co-workers [83] reported on the fabrication by NIL of low refractive index passive optical devices such as diffraction gratings printed in PMMA, rib waveguides printed in polystyrene (PS), and one-dimensional photonic structures printed in PS. The authors used these structures to evaluate the imprint quality combining optical and morphological characterization on size scales from millimeter to nanometer. Stamps with areas up to $2 \times 2\text{cm}^2$ containing structures down to 100 nm were produced by a mix and match approach using UV lithography for the larger structures and adding smaller features in a subsequent EBL step. Stamps with silicon surfaces were treated with commercially available perfluorinated organosilanes to form an anti-sticking layer. Minimal adhesion was observed when Si molds were used, whereas no adhesion occurred when molds were coated with the anti-sticking layer and no wear was observed for these molds over 20 imprints. A hydraulic press with two brass printing blocks and commercially printing equipment optimized for high parallelism in large area NIL [77] were used as embossing tools. Prints were made into polystyrene (PS) and PMMA, with glass transition temperatures of $T_g = 90$ and 105C respectively, on silicon, silicon-on-insulator (SOI) and silicon oxide substrates[8].

Gratings with an area of $5 \times 5\,\text{mm}^2$ showed less than 3% variation in their periodicity and PS rib waveguides on silicon oxide have shown acceptable losses for such devices fabricated in a laboratory environment. The periodic structures on waveguides behave as 1D photonic structures showing higher order Bragg diffraction. The remaining layer thickness, typical for NIL processes, did not affect the quality of light confinement in a PC. The fabrication of devices fitting the calculated dimensions and material systems was anticipated. These experiments demonstrated that NIL is highly suitable for imprinting passive optical devices in organic materials such as PS on SiO_2 (Fig. 18).

3.3.3. *NIL for nanoelectronics and data storage media*

Up to date, NIL has demonstrated multi-level alignments on four-inch wafers, and also single level patterning over a six-inch wafer scale. Mingtao Li *et al.* [97] investigated the pattern transfer fidelity of NIL on a six inch wafer scale by patterning sub-micron MESFET gates on six inch wafers. The critical dimensions (CDs) of

[8] The mold was placed on the polymer-covered substrate; the ensemble was then placed between the printing plates and heated about 80 C above T_g. A pressure between 4–10 MPa was applied for about one minute, and temperature kept constant to allow the polymer to flow. Finally the set-up was cooled below T_g, the pressure released and the mold and substrate separated.

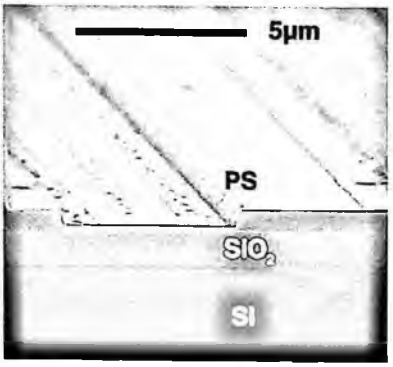

Figure 18. Cleaved-edge of a 4 μm waveguide printed in polystyrene (PS) on an oxidized Si substrate. The depth of the imprint is 400 nm and the thickness of the residual layer between the waveguides is about 100 nm. Reprinted with permission from [83] by IOP.

gate patterns in the resist were found to be, on average, 37 nm larger than those on the mold, with a standard deviation of 1.2%. The CDs after oxygen RIE and metal lift-off were 296 nm larger than those on the mold with a standard deviation of 8%. Compared with conventional photolithography, NIL has been found having higher resolution and better pattern transfer fidelity with CD control of about four times smaller.

A significant demonstration of the NIL progress and its versatility in the employment in manufacturing integrated nano-circuits are represented by the work reported in 2003 by Zhang and Chou concerning the fabrication of operational 60 nm metal–oxide–semiconductor field-effect transistors (MOSFETs) over a full 4 in. wafer, using nanoimprint at all lithography levels[9]. The nano-transistors were designed to have four lithographical layers to form the active area, gate, via, and metal contact. The first NIL step was used to define the active areas of nano-MOSFETs and the patterns were transferred into the underlying Si_3N_4 layer by CHF_3 reactive ion etching. In the second NIL step the gates of the nano-MOSFETs were defined[10]. The third NIL step defined the vias of nano-MOSFETs[11]. The fourth NIL step defined the metal contacts of the nano-MOSFETs. A metal contact layer of 140 nm of Al was fabricated by e-beam evaporation and lift-off. Finally, the completed devices were sintered in H_2/N_2 ambient. It is worthy to stress out that in the third and fourth lithographic layers, the imprints were carried out over a non-flat surface.

[9] The resist used by Zhang was an in-house prepared thermoplastic polymer and the multilevel NILs were carried out with an in-house developed tool. To avoid misalignment caused by thermal expansion during NIL, both the mold and the substrate used were Si.

[10] The polycrystalline silicon gates were made by Cr lift-off and Cl_2 RIE with Cr as an etching mask.

[11] The vias holes were etched through passivation SiO_2 layer by CHF_3 (RIE). Ti ~40 nm was filled into the holes by e-beam evaporation and lift-off.

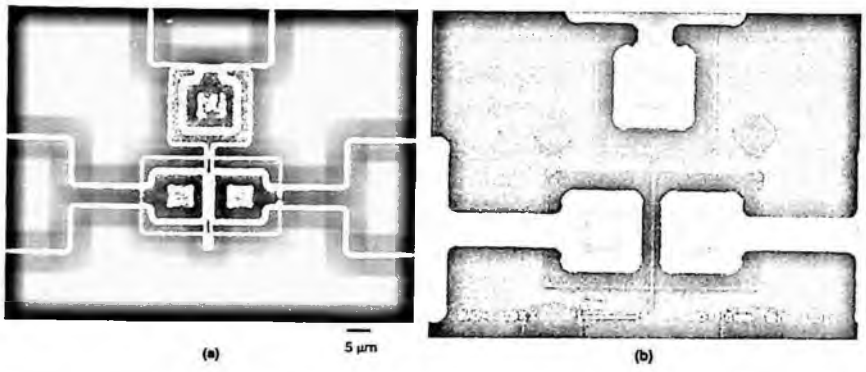

Figure 19. MOSFETs fabricated on 4-inch wafer, using NIL at all - four lithographic steps. (a) Dark-field optical image of a 1-μm-gate-length MOSFET. (b) SEM micrograph of a MOSFET having a channel length of 60-nm. Reprinted with permission from [APL83, (2003), 1632-1634] by AIP.

I–V measurements of the nano-MOSFETs over the entire 4 in. wafer demonstrated that the devices were operating properly and that their fabrication achieved submicron overlay accuracy (Fig. 19).

Nevertheless, to meet the stringent requirements imposed by the semiconductor industry in micro/nanoelectronics, NIL has yet to improve several aspects such as multilevel capability (alignment better than 10 nm for very large scale integration), throughput (seen as the time involved in printing and alignment) and standards (what counts as tolerances for a good print) [93].

Other applications for which NIL has been suggested for include high-density data storage media and an elegant approach to realize patterned arrays of functional structures, suitable as data storage media, is reported in 2003 by Harnagea and coworkers [98]. They fabricated, by a combination of sol-gel deposition and NIL, arrays of ferroelectric structures on conductive substrates such as Pt coated silicon and Nb-doped $SrTiO_3(100)$ single crystals. The lead zirconium titanate (PZT) precursor solution was spun onto the substrate, forming thin films of 100–150 nm thickness. These films were then imprinted and after imprint, the mesoscopic structures from the precursor film were crystallized into PZT by annealing at 650°C for 1h (Fig. 20). An optimum imprint pressure of 1 kbar was applied using a laboratory press at room temperature. The molds used were macroporous silicon, prepared by electrochemical methods [99]. The smallest size of the negative features (pores, holes) was ca. 250 nm. The individual probing of the structures was achieved using the unique technique for probing ferroelectric materials at the nanoscale, namely PFM [100].

3.3.4. *NIL for bio-devices*

The imprint lithography techniques discussed by Truskett and Watts in a recent review [101] indicate biotechnology as the most probable area for future imprint applications. Imprinting has already proven to be advantageous in terms of cost

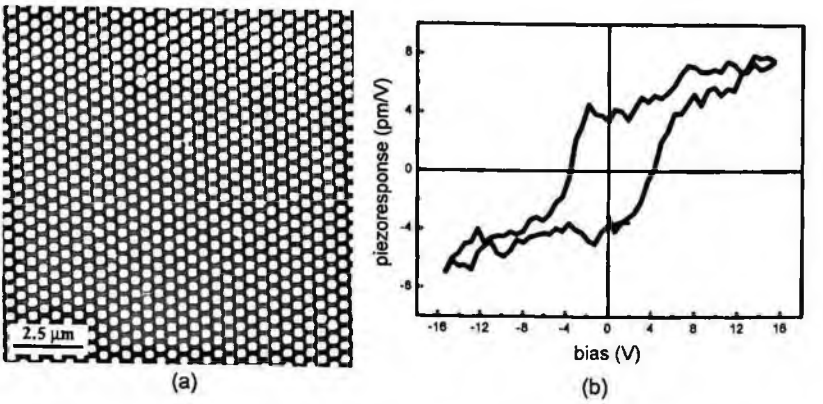

Figure 20. (a) AFM topography image of an array of ferroelectric PZT cells on Nb doped $SrTiO_3$ substrate prepared by imprint lithography. (b) Piezoelectric hysteresis loop of a single ferroelectric cell proving its functionality. Courtesy of Dr. C. Harnagea of INRS-EMT, Montréal, Québec, Canada.

and simplicity, for both academia and industrial research, by demonstrating the fabrication of structures less then 100 nm on non-planar surfaces, fabrication of 2D and 3D structures, and patterning and modification of functional materials other than photoresists. In their article Truskett and Watts identify several areas of high-potential interest for NIL, S-FIL and micromolding applications such as microarrays for genomics and proteomics or tissue engineering. We will address here only NIL and S-FIL for fabricating bio-devices; micromolding (with all derivatives) will not be discussed since it involves a different type of mold (stamp) namely elastomeric one and this falls under the category of soft lithography that can be consulted for a complete review in [8].

Truskett and Watts were pointing that DNA and protein microarrays are essential tools for handling miniaturized processes that require small sample volumes, parallel processes and high throughput. Improvements in microarray manufacturing are necessary in order to increase the sensitivity and accuracy of these devices. Moreover an anticipated worldwide sales growth for DNA sequencing and proteomics is driven by pharmaceutical and biotech companies searching for lower-cost and faster turn-around solutions in the discovery and development of new drugs and diagnostics.

The DNA microarrays (also known as genes or genome chips) are a collection of DNA samples attached to a solid surface, such as glass, plastic or silicon, at fixed locations (spots or sites) forming an array for the purpose of simultaneously investigation of thousands of genes. The sites where reactions occur will identify a specific characteristic of the sample. Currently, the DNA microarrays are fabricated by photo-lithography (similar to semiconductor-chip production) or by ink-jet printing. For instance the methods known as "*in situ* synthesis" (direct synthesis at the target site) uses lithographic masks to direct UV light on the substrate, which de-protects

localized regions for coupling with biological probes. However, photolithographic processes are realized with elevated costs thus several academic developments are prompting that molding (embossing) and contact printing techniques are viable for fabrication of these arrays. For instance, for DNA sequencing purposes, nanochannels (100 nm wide and 200 nm deep), created by imprinting, were used to stretch DNA that was subsequently assayed to identify protein binding sites [102]. In 2004, Ohtake and co-workers [103] reported on DNA nanopatterning using NIL. They used a glass substrate coated with poly-L-lysine, a material known for DNA immobilization by UV radiation[12]. Further on, a polyvinyl alcohol (PVA) solution was spin-coated on the substrate. The resulting sample was then imprinted (100°C and 6 MPa for 5 min) with a SiO_2/Si mold fabricated by electron-beam lithography and dry etching. The amount of residual polymer still present at the bottom of the trenches has been removed by means of a short oxygen plasma etch. Finally, the DNA nanopatterning was obtained by rinsing the PVA layer in water and DNA patterns were observed by fluorescence microscopy.

Another area of interest is that of the protein microarray biochips that enable many proteins to be studied simultaneously in order to understand their interactions with each other or with other molecules such as nucleic acids, lipids and organic compounds [101]. Currently there are two groups of protein microarrays: capture biochips and interaction biochips. Capture biochips detect the presence and quantity of proteins while interaction biochips measure real-time interactions among immobilized proteins and other proteins or bio-molecules. Most of the current protein microarrays are capture biochips, which are designed on a planar substrate. A convenient way to produce these surface structures is to emboss the pattern directly on the substrate using NIL or S-FIL, followed by microcontact printing to chemically functionalize the structures, thus eliminating the need to use photolithography-related processes.

For instance, Hoff *et al.* [104] showed that selective patterning of proteins with high throughput, using NIL, is possible for structures with a minimum size of 75 nm. In addition, increases in the sensitivity and detection levels of proteins were observed when using a combination of NIL and molecular assembly patterning by lift-off (MAPL) for fabricating large-area, high-density protein patterns with 25 nm feature sizes [105,106].

4. Conclusions and Perspectives

Semiconductors and insulators technology has always relied on the top-down approach. The most remarkable example is the seemingly never ending miniaturization of transistors and microelectronic devices by ever more sophisticated lithographic techniques. Without any doubt, as optical (advanced) lithography becomes

[12] The DNA solution was applied, dried at 60°C for an hour, and then irradiated by UV for 2 min.

more and more expensive and complex, non-conventional techniques for nanofabrication can alleviate the costs and limitations of the former. Given the enormous interest for fabrication of highly ordered arrays of nanostructured materials, to combine high resolution, with high throughput at low-cost, became the main target in nanotechnology. Nanostenciling approach, either in the static or the dynamic mode, shows attractive assets, proved so far at the laboratory scale. As previously stated, NS emerged as a highly-flexible approach to control the parallel patterning of clean nanosized structures, providing thus convenient ways for their further investigations. Further developments of this approach will lead to the realization of novel architectures and devices, also providing solutions for critical patterning issues not yet solved. More mature, NIL is already able to deliver features below 100 nm, rapidly and with high accuracy and throughput (4 and 6-inch wafer scale) comparable to advanced optical lithography methods. Thus, nanoimprint shows great potential for the semiconductor industry and has been already placed on the International Technology Roadmap for Semiconductors (ITRS), in the coming years (for 32-nm node). Offering the advantages of high throughput and reproducibility at low cost, and the capability of creating nanopatterns for a broad range of applications (spinning from optical devices to biosensors and molecular electronics) NIL is envisioned to play a major role in the coming years of nanotechnology.

Acknowledgments

We are grateful to Dr. Catalin Harnagea, Dr. Cees van Rijn, Prof. Juergen Brugger and Dr. M.A.F. van Boogaart for permission to use their original figures, reprinted in this work. The Nano-Femto laboratory of INRS-EMT, is supported by FQRNT (Quebec), NSERC (Canada) and the Canada Research Chairs program. We thank Dr. Catalin Harnagea and Prof. Alain Pignolet for helpful discussions and for their participation in the Nanostencil project.

References

1. H. Rohrer, The nanoworld: chances and challenges, *Microelectron. Eng.*, **32**, (1996), 5–14.
2. F. Rosei, Nanostructured surfaces: challenges and frontiers in nanotechnology, *J. Phys.: Condens Matter*, **16**, (2004), S1373–S1436.
3. T. Ito and S.Okazaki, Pushing the limits of lithography, *Nature* **406**, (2000), 1027–1031.
4. W. M. Tolles, Nanoscience and nanotechnology in Europe, *Nanotechnology* **7**, (1996), 59–105.
5. M. Geissler and Y. Xia, Patterning: Principles and some new developments, *Adv. Mater.* **16**, (2004), 1249–1269.
6. M. Rothschild, Projection optical lithography, *Mat. Today* **2**, (2005), 18–24.
7. F. Cacialli, P. Samori and C. Silva, Supramolecular architectures, *Mat. Today* **7**, (2004), 24–32.

8. Y. Xia and G. M. Whitesides, Soft lithography, *Angew. Chem. Int. Ed.* **37**, (1998), 550–575.
9. J. A. Rogers and R. G. Nuzzo, Recent progress in soft-lithography, *Mat. Today* **2**, (2005), 50–56.
10. S. Y. Chou, P. R. Krauss and P. J. Renstrom, Imprint of sub-25nm vias and trenches in polymers, *Appl. Phys. Lett.* **67**, (1995), 3114–3116.
11. C. M. Sotomayor Torres, S. Zankovych, J. Seekamp, A. P. Kam, C. C. Cedeno, T. Hoffmann, J. Ahopelto, F. Reuther, K. Pfeiffer, G. Bleidiessel, G. Gruetzner, M. V. Maximov and B. Heidari, Nanoimprint lithography: an alternative nanofabrication approach, *Mat. Sci. Eng.* **C 23**, (2003), 23–31.
12. D. J. Resnick, S. V. Sreenivasan and C. G. Wilson, Step & flash imprint lithography, *Mat. Today* **2**, (2005), 34–42.
13. J. Brugger, J. W. Berenschot, S. Kuiper, W. Nijdam, B. Otter and M. Elwenspoek, Resistless patterning of sub-micron structures by evaporation through nanostencils, *Microelectron. Eng* **53**, (2000), 403–405.
14. R. Luthi, R. R. Schlittler, J. Brugger, P. Vettiger, M. E. Welland and J. K. Gimzewski, Parallel nanodevice fabrication using a combination of shadow mask and scanning probe methods *Appl. Phys. Lett.*, **75**, (1999), 1314–1316.
15. S. Egger, A. Ilie, Y. Fu, J. Chongsathien, D.-J. Kang and M. Welland, Dynamic Shadow Mask Technique: A Universal Tool for Nanoscience, *Nano Lett.*, **5**, (2005), 15–20.
16. A. A. Tseng, Recent developments in micromilling using focused ion beam technology, *J. Micromech. Microeng.* **14**, (2004), R15–R34.
17. C. J. M.van Rijn, Laser interference as a lithographic nanopatterning tool, *J. Microlith., Microfab., Microsyst.* **5**, (2006), 011–012.
18. R. Menon, A. Patel, D. Gil and H. I. Smith, Maskless lithography, *Mat.Today* **2**, (2005), 26–33.
19. C. F. Quate, Scanning probes as the gateway to nanotechnology, *Jpn. J. Appl. Phys.* **1**, (2003), 4777–4779.
20. R. D. Piner, J. Zhou, F. Xu, S. Hong and Chad A. Mirkin, Dip-Pen Nanolithography, *Science* **283**, (1999), 661–663.
21. F. Cicoira, K. Leifer, P. Hoffmann, I. Utke, B. Dwir, D. Laub, P. A. Buffat, E. Kapon and P. Doppelt, Electron beam induced deposition of rhodium from the precursor [RhCl(PF3)(2)](2): morphology, structure and chemical composition, *J. of Cryst. Growth* **265**, (2004), 619–626.
22. C. Haley and J. H. Weaver, Buffer-layer-assisted nanostructure growth via two-dimensional cluster–cluster aggregation, *Surf. Sci.* **518**, (2002), 243–245.
23. G. Kerner and M. Asscher, Buffer Layer Assisted Laser Patterning of Metals on Surfaces, *Nano Lett.* **4**, (2004), 1433–1437.
24. M. Schildenberger, Y. Bonetti, J. Gobrecht and R. Prins, Nano-pits: supports for heterogeneous model catalysts prepared by interference lithography *Top. Catal.* **13**, (2000), 109–120.
25. G. H. Döhler, G. Hasnain and J. N. Miller, In situ grown-in selective contacts to n i-p-i doping superlattice crystals using molecular beam epitaxial growth through a shadow mask, *Appl. Phys. Lett.*, **49** (1986), 704.
26. K. S. Ralls, R. A. Buhram and R. C. Tiberio, Fabrication of thin-metal nanobridges, *Appl. Phys. Lett. 55*, (1989), 2459–2461.
27. N. N. Gribov, S. J. C. H. Theeuwer, J. Caro and S. Radelaar, A new fabrication process for metallic point contacts, *Microelectron. Eng.* **35**, (1997), 317–320.

28. G. J. Burger, E. J. T. Smulders, J. W. Berenschot, T. S. J. Lammerink, J. H. J. Fluitman and S. Imai, High-resolution shadow-mask patterning in deep holes and its application to an electrical wafer feed-through, *Sens. Actuators* A **54**, (1996) 669–673.
29. A. Folch, B.-H. Jo, O. Hurtado, D. J. Beebe and M. Toner, Microfabricated elastomeric stencils for micropatterning cell cultures, *J. Biomed. Mater. Res.*, **52**, (2000), 346–353.
30. J. Brugger, C. Andreoli, M. Despont, U. Drechsler, H. Rothuizen and P. Vettiger, Self-aligned 3D shadow mask technique for patterning deeply recessed surfaces of micro-electro-mechanical systems devices, *Sens. Actuator*, A **76**, (1999), 329–334.
31. G. Kim, B. Kim and J. Brugger, All-photoplastic microstencil with self-alignment for multiple layer shadow-mask patterning, *Sens. Actuator* A, **107**, (2003), 132–136.
32. M. Graff, S. K. Mohanty, E. Moss and A. B. Frazier, Microstenciling: A generic technology for microscale patterning of vapor deposited materials, *J. Microelectromech. S.*, **13**, (2004), 956–962.
33. T. Shibata, K. Suguro, K. Sugihara, H. Mizumo, A. Yagaishita, T. Saito and K. Okumura, Stencil mask ion implantation technology, *IEEE. T. Semiconduct. M.*, **15**, (2002), 183–188.
34. B. D. Terris, L. Folks, D. Weller, J. E. E. Baglin and A. J. Kellock, Ion beam patterning of magnetic films using stencil masks, *Appl. Phys. Lett.*, **75**, (1999), 403–405.
35. A. Tixier, Y. Mita, J. P. Gouy and H. Fujita, A silicon shadow mask for deposition on isolated areas, *J. Micromech. Microeng.*, **10**, (2000), 157–162.
36. R. W. Tjerkstra, P. Ekkels, G. Krijnen, S. Egger, E. Berenschot, K. C. Ma and J. Brugger, Fabrication of an active nanostencil with integrated microshutters, *IEEE Conf. Proc., Transducers* **2**, (2003), 1651–1654.
37. J. Kohler, M. Albrecht, C. R. Musil and E. Bucher, Direct growth of nanostructures by deposition through an Si3N4 shadow mask, *Phys. E*, **4**, (1999), 196–200.
38. J. Butschke, A. Ehrmann, B. Höfflinger, M. Irmscher, R. Ksmaier, F. Letzkus, et al. SOI wafer flow process for stencil mask fabrication *Microelectron. Eng.* **46**, (1999), 473–476.
39. C. J. M. van Rijn, Nano and micro engineered membrane technology, *Elsevier Amsterdam* 2004, ISBN 0444-51489 9.
40. G. M. Kim, M. A. F. van den Boogaart and J. Brugger, Fabrication and application of a full wafer size micro/nanostencil for multiple length-scale surface patterning, *Microelectron. Eng.*, 67–68, (2003), 609–614.
41. M. Kölbel, R. W. Tjerkstra, J. Brugger, C. J. M. van Rijn, W. Nijdam, J. Huskens and D.N. Reinhoudt, Shadow-Mask Evaporation through Monolayer-Modified Nanostencils, *Nano Lett.*, **2**, (2002), 1339–1343.
42. M. A. F. van den Boogaart, G. M. Kim, R. Pellens, J. P. van den Heuvel and J. Brugger, Deep-ultraviolet–microelectromechanical systems stencils for high-throughput resistless patterning of mesoscopic structures *J. Vac. Sci. Technol. B*, **22**, (2004), 3174–3177.
43. C. J. van Rijn, Nanosieve with microsystem technology for microfiltration applications, *Nanotechnology*, **9**, (1998), 343–345.
44. S. H. Zaidi and S. R. J. Brueck, Multiple-exposure interferometric lithography, *J. Vas. Sci. Technol. B*, **13**, (1993), 658–666.
45. X. Mai, R. Moshrefzadeh, U. J. Gibson, G. I. Stegemen and C. T. Seaton, Simple versatile method for fabricating guided-wave gratings, *Appl. Opt.*, **24**, (1983), 3155–3161.

46. L. J. Heyderman, B. Ketterer, D. Bachle, F. Glaus, B. Haos, H. Schift, K. Vogelsang, J. Gobrecht, L. Tiefanauer, O. Dubochet, P. Surbled and T. Hessler, High volume fabrication of customised nanopore membrane chips, *Microelectron. Eng.* 67–68, (2003), 208–213.
47. M. M. Deshmukh, D. C. Ralph, M. Thomas and J. Silcox, Nanofabrication using a stencil mask, *Appl. Phys Lett.*, (1999), **75**, 1631–1633.
48. H. D. Tong, H. V. Jansen, V. J. Gadgil, C. G. Bostan, E. Berenschot, C. van Rijn and M. Elwenspoek, Silicon Nitride Nanosieve Membrane, *Nano Lett.* **4**, (2004), 283.
49. P. Zahl, M. Bammerlin, G. Mayer and R. R. Schlittler, All in one static and dynamic nanostencil atomic force microscopy/scanning tunneling microscopy system, *Rev. Sci. Instr.* **76**, (2005), 023707.
50. C. V. Cojocaru, C. Harnagea, A. Pignolet and F. Rosei, Nanostenciling of Functional Materials by Room Temperature Pulsed Laser Deposition, *IEEE. T. Nanotechnol.*, **5**, (2006), 470–477.
51. Pulsed laser deposition of thin films, edited by D. B. Chrisey and G.K. Hubler, Naval Research Laboratories, Washington, DC, J. Wiley & Sons, 1994.
52. M. A. F. Boogaart, M. Lishchynska, L. M. Doeswijk, J. C. Greer and Jurgen Brugger Corrugated membranes for improved pattern definition with micro/nanostencil lithography *Sens. Actuator* A 130–131, (2006), 568–574.
53. F. Vroegindeweij, E. A. Speets, J. A. J. Steen J. Brugger and D. H. A. Blank, Exploring microstencils for sub-micron patterning using pulsed laser deposition *Appl. Phys.* A, **79**, (2004), 743–745.
54. E. A. Speets, B. J. Ravoo, F. J. G. Roesthuis, F. Vroegindeweij, D. H. A. Blank and D. N. Reinhoudt, Fabrication of Arrays of Gold Islands on Self-Assembled Monolayers Using Pulsed Laser Deposition through Nanosieves, *Nano Lett.* **4**, (2004), 841–844.
55. X. M. Yan, A. M. Contreras, M. M. Koebel, J. A. Liddle and G. A. Somorjai, Parallel Fabrication of Sub-50-nm Uniformly Sized Nanoparticles by Deposition through a Patterned Silicon Nitride Nanostencil *Nano.Lett.*, **5**, (2005), 1129–1134.
56. G. A. Somorjai and R. M. Rioux, High technology catalysts towards 100% selectivity: Fabrication, characterization and reaction studies, *Catal. Today*, **100**, (2005), 201–215.
57. C. V. Cojocaru, C. Harnagea, F. Rosei, A. Pignolet, M. A. F. van den Boogaart and J. Brugger, Complex oxide nanostructures by pulsed laser deposition through nanostencils, *Appl. Phys. Lett.* **86**, (2005), 183107.
58. C. Harnagea and A. Pignolet, in Nanoscale Characterization of Ferroelectric Materials-Scanning Probe Microscopy Approach, edited by M. Alexe and A. Gruverman, Springer, Berlin, 2004, pp. 47–64.
59. H. J. Shin, J. H. Choi, H. J. Yang, Y. D. Park, Y. Kuk and C. J. Kang, Patterning of ferroelectric nanodot arrays using a slicon nitride shadow mask, *Appl. Phys. Lett.* **87**, (2005), 113–114.
60. K. Wilder and C. F. Quate, Scanning probe lithography using a cantilever with integrated transistor for on-chip control of the exposing current, *J. Vac. Sci. Technol.* B **17**, (1999), 3256–3261.
61. A. R. Champagne, A. J. Couture, F. Kuemmeth and D. C. Ralph, Nanometer-scale scanning sensors fabricated using stencil lithography *Appl. Phys. Lett.* **82**, (2003), 1111–1113.
62. H. G. Craighead, Nanoelectromechanical Systems, *Science* 290, (2000), 1532–1535.
63. G. M. Kim, S. Kawai, M. Nagashio, H. Kawakatsu and J. Brugger, Nanomechanical structures with 91 MHz resonance frequency fabricated by local deposition and dry etching, *J. Vac. Sci. Technol.* B **22**, (2004), 1658–1661.

64. V. Bucher, J. Brugger, D. Kern, G. M. Kim, M. Schubert and W. Nisch, Electrical properties of light-addressed sub-μm electrodes fabricated by use of nanostencil-technology, *Microelectron. Eng.*, 61–62, (2002), 971–980.
65. Y. X. Zhou, A. T. Johnson, Jr., J. Hone and W. Smith, Simple Fabrication of Molecular Circuits by Shadow Mask Evaporation, *Nano Lett.* **3**, (2003), 1371–1374.
66. A. Ludwig, J. Cao, J. Brugger and I. Takeuchi, MEMS tools for combinatorial materials processing and high-throughput characterization, *Meas. Sci. Technol.* **16** (2005), 111–118.
67. A. Ludwig, Combinatorial fabrication of magnetic multilayer films, *Appl. Surf. Sci.* **223**, (2004), 78–83.
68. S. Egger, S. Higuchi and T. Nakayama, A Method for Combinatorial Fabrication and Characterization of Organic/Inorganic Thin Film Devices in UHV, *J. Comb. Chem.*, **8**, (2006), 275–279.
69. http://www.itrs.net/Links/2005ITRS/Home2005.htm.
70. S. Y. Chou, P. R. Krauss and P. J. Renstrom, Imprint Lithography with 25-Nanometer Resolution, *Science* 272, (1996), 85–87.
71. S. Y. Chou, P. R. Krauss and P. J. Renstrom, Nanoimprint lithography, *J. Vac. Sci. Technol. B* **14**, (1996), 4129–4133.
72. S. V. Sreenivasan, C. G. Willson, N. E. Schumaker and D. J. Resnick, Low-cost nanostructure patterning using step and flash imprint lithography, *Proc. of the International Society for Optical Engineering (SPIE)* 4608, (2002), 187–194.
73. M. Colburn, T. Bailey, B. J. Choi, G. Eckerdt, S. V. Sreenivasan and C.G. Willson, Development and Advantages of Step and Flash Imprint Lithography, *Solid State Technol.*, July 2001.
74. S. Y. Chou, P. R. Krauss, W. Zhang, L. Gou and L. Zhuang, Sub-10nm imprint lithography and its applications, *J. Vac. Sci. Technol.* **B 15**, (1997), 2897–2904.
75. Wang, X. Sun, L. Chin and S. Y. Chou, Direct nanoimprint of submicron organic light-emitting structures, *Appl. Phys. Lett.* **75** (1999), 2767–2769.
76. K. Pfeiffer, G. Bleidissiel, G. Gruetzner, H. Schulz, T. Hoffman, H. C. Scheer, Sotomayor-Torres and J. Ahopelto, Suitability of new polymer materials with adjustable glass temperature for nanoimprinting, *Microelectron. Eng.* **46**, (1999), 431–434.
77. B. Heidari, I. Maximov and L. Montelius, Nanoimprint lithography at the 6 in. wafer scale *J. Vac. Sci. Technol.* **B 18**, (2000), 3557.
78. V. Studer, A. Pepin and Y. Chen, Nanoembossing of thermoplastic polymers for microfluidic applications, *Appl. Phys. Lett. 80*, (2002), 3614–3616.
79. Wei Zhang and Stephen Y. Chou, Multilevel nanoimprint lithography with submicron alignment over 4 in. Si wafers, *Eppl. Phys. Lett. 79*, (2001) 845–847.
80. C. Clavijo Cedeno, J. Seekamp, A. P. Kam, T. Hoffmann, S. Zankovych, C. M. Sotomayor Torres, C. Menozzi, M. Cavallini, M. Murgia, G. Ruani, F. Biscarini, M. Behl, R. Zentel and J. Ahopelto, *Nanoimprint lithography for organic electronics, Microelectron. Eng* 61–62, (2002), 25–31.
81. M. Beck, M. Graczyk, I. Maximov, E.-L. Sarwe, T. G. I. Ling, M. Keil and L. Montelius, Improving stamps for 10 nm level wafer scale nanoimprint lithography, *Microelectron. Eng.* 61–62, (2002), 441–448.
82. S. Y. Chou, C. Keimel and J. Gu, Ultrafast and direct imprinting of silicon nanostructures, *Nature*, **417**, (2002), 835–837.
83. J. Seekamp, S. Zankovych, A. H. Helfer, P. Maury, C. M. Sotomayor Torres, G Bottger, C Liguda, M Eich, B Heidari, LMontelius and J Ahopelto, Nanoimprinted passive optical devices, *Nanotechnology* **13**, (2002), 581–586.

84. D. Y. Khang, H. Kang, T. Kim and Hong H. Lee, Low-Pressure Nanoimprint Lithography, *Nano Lett.* **4**, (2004), 633–637.
85. E. Mele, F. di Benedetto, L. Persano, R. Cingolani and D. Pisignano, Multi Level Room temperature nanoimprint lithography for conjugated polymer-based photonics, *Nano Lett.*, **5**, (2005), 1915–1919.
86. G. Jung, Z. Li, W. Wu, S. Ganapathiappan, X. Li, D. L. Olynick, S. Y. Wang, William M. Tong and R. Stanley Williams, Improved pattern transfer in nanoimprint lithography at 30 nm hlf-pitch by substrate-surface functionalization, *Langmuir* **21**, 92005), 6127–6130.
87. H. Y. Low, W. Zhao and J. Dummond, Combinatorial-mold imprint lithography: A versatile technique for fabrication of three-dimensional polymer structures, *Appl. Phys. Lett. 89*, (2006), 023109.
88. K.-Y. Yang, S.-H. Hong, D. Kim, B. Cheong and H. Lee, Patterning of Ge2Sb2Te5 phase change material using UV nano-imprint lithography, *Microelectron. Eng.* (2006), doi;10.1016/j.mee.2006.07.004.
89. G. Jung, E. Johnston-Halperin, Wei Wu, Z. Yu, S. Wang, W. M. Tong, Z. Li, J. E. Green, B. A. Sheriff, A. Boukai, Y. Bunimovich, J. R. Heath and R. Stanley Williams, Circuit fabrication at 17 nm half-pitch by nanoimprint lithography, *Nano Lett.*, **6**, (2006), 351–354.
90. L. J. Guo, Recent progress on nanoimprint technology and its applications, *J. Phys. D.; Appl. Phys.*, **37**, (2004), R123–R141.
91. J. Taniguchi, Y. Tokano, I. Miyamoto, M. Komuro, M. Komuro and H. Hiroshima, Diamond nanoimprint technology, *Nanotechnology* **13**, (2002), 592–596.
92. K. Pfeiffer, M. Fink, G. Aherens, G. Gruetzner, F. Reuther, J. Seekamp, S. Zankovych, C. M. Sotomayor Torres, I. Maximov, M. Beck, M. Grazcyk, L. Montelius, H. Schulz, H.-C. Scheer and F. Steingrueber, Polymer stamps for nanoimprinting, *Microelectron. Eng.* 61–62, (2002), 393.
93. S. Zankovych, T. Hoffman, J. Seekamp, J.-U. Bruch and C. M. Sotomayor-Torres, Nanoimprint lithographu: challenges and prospects, *Nanotechnology*, **12**, (2001), 91–95.
94. M. Austin and S. Y. Chou, Fabrication of 70 nm channel length polymer organic thin-film transistors using nanoimprint lithography, *Appl. Phys. Lett.* **81**, (2002), 4431–4433.
95. J. Jo, J. J. Heremans, F. Bradbury, Hong Chen and V. Soghomonian,Gate tunable electron injection in submicron pentacene transistors, *Nanotechnology* **15**, (2004), 1023–1026.
96. J. Collet, O. Tharaud, A. Chapoton and D. Vuillaume, Low-voltage, 30 nm channel length, organic transistors with a self-assembled monolayer as gate insulating films, *Appl. Phys. Lett.* **76**, (2000), 1941–1943.
97. Mingtao Li, Lei Chen, Wei Zhang and Stephen Y. Chou, Pattern transfer fidelity of nanoimprint lithography on six-inch wafers, *Nanotechnology* **14** (2003) 33–36.
98. C. Harnagea, M. Alexe, J. Schilling, J. Choi, R. B. Wehrspohn, D. Hesse and U. Gosele, *Appl. Phys. Lett* **83**, (2003), 1827–1829.
99. R. B. Wehrspohn and J. Schilling, *MRS Bull.* **26**, (2001), 623.
100. C. Harnagea, A. Pignolet, M. Alexe, D. Hesse and U. Gösele, *Appl. Phys.* **A 70**, (2000), 261.
101. V. N. Truskett and M. P. C. Watts, Trends in imprint lithography for biological applications, *Trends in Biotechnol.*, **24**, (2006), 312–317.
102. Morton, K. *et al.* Quantitative protein/DNA analysis in nanoimprinted channels, Third International Conference on Nanoimprint and Nanoprint Technology (2004).

103. T. Ohtake, K. Nakamatsu, S. Matsui, H. Tabata and T. Kawai, DNA nanopatterning with self-organization by using nanoimprin, *J. Vac. Sci. Technol.* **B 22**, (2004), 3275.
104. J. D. Hoff, L. Cheng, E. Meyhöfer, L. Jay Guo and Alan J. Hunt, Nanoscale protein patterning by imprint lithography, *Nano Lett.* **4**, (2004), 853–857.
105. D. Falconnet, D. Pasqui, S. Park, R. Eckert, H. Schift, J. Gobrecht, R. Barbucci and M. Textor, A novel approach to produce protein nanopatterns by combining nanoimprint lithography and molecular self-assembly, *Nano Lett.* **4**, (2004), 1909–1914.
106. Park, S. *et al.*, Chemical patterning of sub 50 nm half pitches via Nanoimprint lithography and its application to protein patterning, Third International Conference on Nanoimprint and Nanoprint Technology, (2004).

CHAPTER 16

NANOFABRICATION OF NANOELECTROMECHANICAL SYSTEMS (NEMS): EMERGING TECHNIQUES

K. L. EKINCI*

Aerospace and Mechanical Engineering Department,
Boston University, Boston, MA 02215, USA

J. BRUGGER

Microsystems Laboratory,
Institute of Microelectronic and Microsystems,
Ecole Polytechnique Federale de Lausanne (EPFL),
1015 Lausanne, Switzerland

Nanoelectromechanical systems (NEMS) are commonly realized in the form of simple movable suspended nanostructures, such as doubly-clamped beams, cantilevered beams or torsion pedals. NEMS come with extremely high fundamental resonance frequencies, diminished effective masses, low spring constants and high *in vacuo* quality (Q) factors. As such, these structures have received much recent attention for their potential technological applications as well as for realizing a mesoscopic quantum harmonic oscillator.

This chapter presents a review of the variety of approaches for fabricating NEMS devices. The mainstay approach for patterning freely suspended nanostructures is nanomachining based upon electron beam lithography (EBL). This approach has been applied to fabricate silicon, gallium arsenide, silicon carbide, aluminum nitride, diamond and silicon nitride NEMS; variations of EBL based nanomachining have also been used to fabricate nanotube and nanowire NEMS. Among other emerging approaches reviewed herein are approaches based upon nanoimprint lithography, focused ion beams and stencil masks. Important remaining research issues in the field, such as large scale integration of NEMS, are discussed along with concluding remarks.

Keywords: Nanoelectromechanical systems (NEMS); nanomechanics; suspended nanostructures.

*Corresponding author: ekinci@bu.edu

CONTENTS

1. Introduction to NEMS 544
2. Nanomachining of NEMS Based Upon Electron Beam Lithography 546
   2.1. Silicon 547
   2.2. Epitaxial GaAs/AlGaAs systems 549
   2.3. Aluminum nitride 549
   2.4. Silicon nitride 550
   2.5. Silicon carbide 551
   2.6. Nanocrystalline diamond 552
   2.7. Nanotube and nanowire NEMS 553
3. Fabrication of NEMS Using Nanoimprint Lithography 554
4. NEMS Fabricated Using Polymeric Nanofiber Templates 556
5. NEMS Fabricated by Focused Ion Beam Doping and Wet Chemical Etching 557
6. NEMS Fabrication by Stencil Lithography and Sacrificial Etching 558
7. Large Scale Integration of NEMS 561
8. Conclusions and Outlook 562
Acknowledgments 562
References 562

1. Introduction to NEMS

Micron scale mechanical devices have found important technological applications in the past few decades. These micromechanical elements along with their microelectronic control circuits are called Microelectromechanical Systems (MEMS). MEMS have found successful applications in a number of consumer products; in addition, certain MEMS devices, e.g., the microcantilever, have emerged as an important platform for fundamental measurements in experimental physics. Given the success of MEMS and the potential nanoscale has to offer, a rigorous effort has surfaced to develop sub-micron mechanical devices — simply referred to as nanoelectromechanical systems (NEMS) [1,2,3].

With few notable exceptions [4], most NEMS operated to date are resonant devices — much like simple tuning forks or quartz resonators. NEMS resonators are commonly realized in the form of freely suspended doubly-clamped or cantilevered beams as shown in Fig. 1. In resonant operation, one actuates the nanomechanical element *harmonically* at its fundamental resonance frequency; the subsequent mechanical response, namely the motion of the device, is detected in the electronic or optical domain. In this size regime, resonant NEMS come with extremely high fundamental resonance frequencies extending into the microwaves [5]. The effective spring constant of a NEMS resonator is typically much lower than a bulk acoustic wave (BAW) or a surface acoustic wave (SAW) resonator operating at the same frequency range. The effective mass, namely the mass involved in the motion of

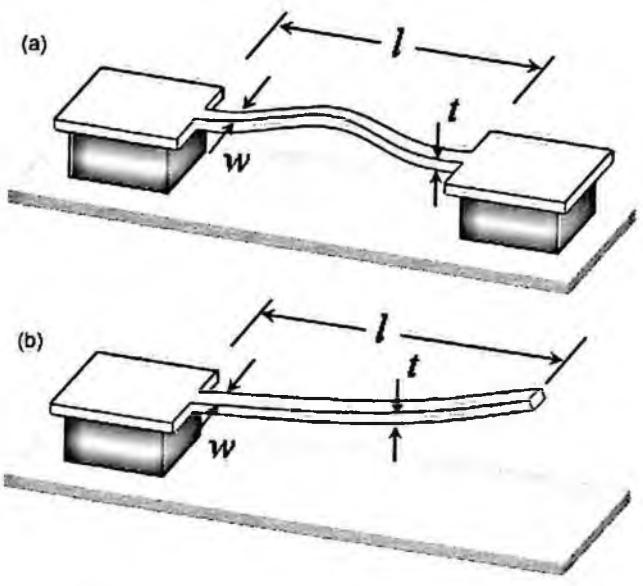

Figure 1. (a) A clamped-clamped (doubly-clamped) beam. (b) A cantilevered beam.

a NEMS device, is in the sub-picograms [6]. The *in vacuo* resonance quality (Q) factors attained in NEMS are in the $10^3 - 10^5$ range; Q factors go down to $\sim 10^2$ in ambient atmosphere [7]. Clearly, NEMS offer access to a parameter space that is unprecedented and intriguing [2].

Even at this early stage of their development, it seems clear that NEMS will find use in a broad range of applications. Recent demonstrations of nanomechanical electrometry [8], optomechanical and electromechanical signal processing [9,10], and mass sensing [6,11,12], have attracted much attention. Among the most promising of these applications is NEMS-based mass sensing. Their minuscule active masses render NEMS extremely sensitive to added mass. By driving a NEMS resonator at its fundamental resonance frequency and detecting small resonance frequency shifts while the device is mass loaded by analyte molecules, *real-time* attogram (10^{-18} g) and zeptogram (10^{-21} g) mass sensitivities have been demonstrated in 2004 [6], and 2006 [13], respectively. This sensitivity level spans the mass range for an *individual* molecule [14] and indicates the immense potential of effectively *weighing* a single molecule, a virus or a protein, simply by accreting them one-by-one onto a NEMS device. At the other end of the spectrum, NEMS are regarded as the ultimate platforms for investigations of the quantum behavior of mesoscopic mechanical systems [15,16].

To date, several approaches have been used to fabricate NEMS devices out of a number of different materials systems. This chapter presents a review of these available approaches. Emerging techniques as well as commonly used techniques are reviewed in detail.

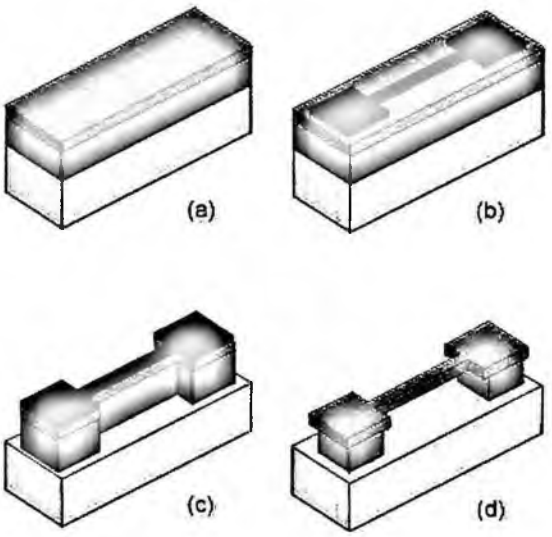

Figure 2. Surface nanomachining of NEMS. (a) Fabrication starts on a semiconductor heterostructure with structural (top) and sacrificial (middle) layers on top of a substrate (bottom). (b) First an etch mask is defined using optical lithography, electron beam lithography (EBL), film deposition and lift-off. (c) Then, the pattern is transferred into the sacrificial layer using an anisotropic etch such as a plasma etch. (d) Finally, the sacrificial layer under the structure is removed using a selective etch. The structures can be metallized after or during the process depending upon the specific measurement requirements.

2. Nanomachining of NEMS Based Upon Electron Beam Lithography

The most straightforward process for patterning semiconductor NEMS is referred to as surface nanomachining. Surface nanomachining can be regarded as an extension of the bulk micromachining of MEMS into the submicron length scales. Here, fabrication of NEMS is typically carried out on a semiconductor wafer with a heterostructure comprising structural and sacrificial layers on top of a substrate. One first defines large area contact pads using optical lithography. The extension into the nanometer scale is realized through electron beam lithography (EBL): the actual nanodevice, i.e., the nanomechanical element, is patterned via EBL. This mask pattern is transferred into the sacrificial layer using an anisotropic etch. Finally, the sacrificial layer under the structure is removed using a selective etch. The generic process is outlined in Fig. 2.

Surface nanomachining techniques have been used to fabricate suspended structures out of different materials such as silicon [17,18], gallium arsenide [19,20,21], silicon carbide [22], aluminum nitride [23], nanocrystalline diamond [24] and amorphous silicon nitride [25,26,27,15]. Most of these materials are available with high purity, grown with a precise control of the layer thicknesses. This latter aspect yields dimensional control in the vertical (out-of-plane) dimension at the monolayer level. This is compatible with the lateral dimensional precision of EBL, which is in

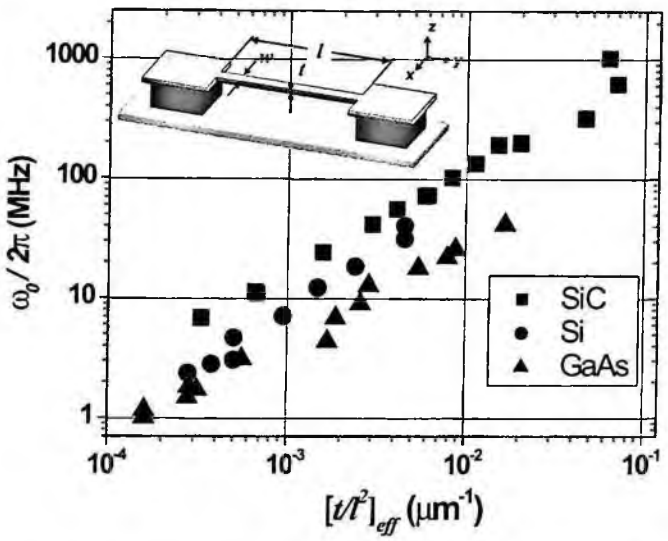

Figure 3. Frequency versus effective geometry for doubly-clamped beams made from single-crystal SiC, Si and GaAs. The inset shows the doubly-clamped beam geometry with length l, width w, and thickness t. The fundamental out-of-plane (in-plane) flexural resonance frequency of this structure is given by the expression, $\omega_0/2\pi = 1.05\sqrt{E/\rho}(t/l^2)$ ($\omega_0/2\pi = 1.05\sqrt{E/\rho}(w/l^2)$). In the plot, t/l^2 values have been normalized to remove the effect of additional stiffness and mass loading due to electrode metallization. Courtesy of K.L. Ekinci and M.L. Roukes.

the deep submicron. It is important to note that different material systems offer different capabilities in device applications. For example, piezoresistivity and piezoelectricity, which are important material properties for enabling transducers, exist only in certain material systems. In addition, Young's modulus E and the mass density ρ determine important mechanical parameters of the devices such as the resonance frequency. In the nanoscopic size regime of NEMS where surface-area-to-volume ratios are extremely large, materials with resilient surface constructions may enable superior devices. Figure 3 shows the resonance frequencies of NEMS in different materials, and is a good example of the effect of material properties on device parameters.

2.1. *Silicon*

Suspended submicron silicon (Si) structures were among the first to be fabricated — given the fact that the tools for silicon device fabrication have been commonly available for the past two decades [28]. Several different approaches for fabricating Si NEMS have been reported. Here, fabrication from bulk Si and silicon on insulator (SOI) wafers is reviewed.

In order to fabricate NEMS on Si wafers, A.N. Cleland and M.L. Roukes [17] reported an approach that used pyrogenic steam oxidation. An initial 1-μm-thick oxide layer was grown on a <100> n-type Si wafer. The contact pads and the device

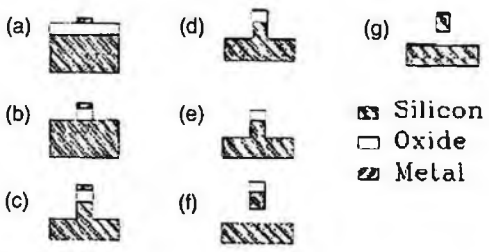

Figure 4. NEMS fabrication steps on bulk Si. Courtesy of A.N Cleland and M.L. Roukes.

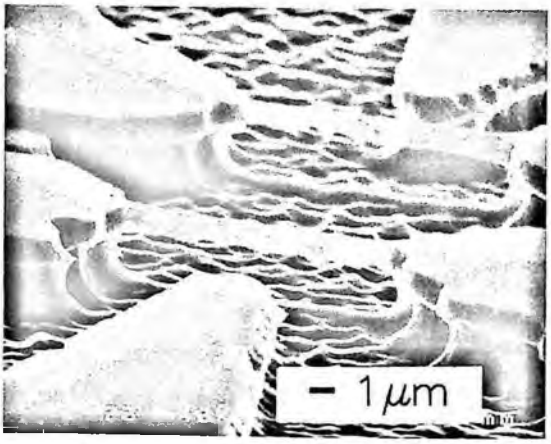

Figure 5. Scanning electron micrograph of nanomechanical Si beams fabricated from bulk Si. The beams shown have length of 7.7 μm, width of 0.33 μm, and height of 0.8 μm. They were fabricated on bulk Si using the process outlined in Fig. 4. Courtesy of A.N. Cleland and M.L. Roukes.

mask were patterned using optical lithography and EBL, respectively. The mask was an rf-sputtered 100-nm-thick layer of nickel (Ni). This pattern was transferred into the pyrogenically grown oxide layer, and subsequently, into the Si beneath it using two anisotropic reactive ion etch (RIE) steps. After the Ni mask was removed by wet chemical etching, a second shorter pyrogenic oxidation was performed to grow sidewall oxide layers — to be used as masks in the subsequent etches. At this point, the substrates had vertical ribs of single crystal Si, with a thick oxide layer on the upper surface and a thin sidewall oxide on the vertical sidewalls. In the final step, the vertical ribs were undercut and the remaining oxide layers were removed, again, using RIE steps. The process is illustrated in Fig. 4; Scanning Electron Microscope (SEM) images of fabricated structures are shown in Fig. 5.

Several groups [29,18] have used SOI substrates for the fabrication of Si NEMS. In this case, the standard optical lithography and EBL mask definition steps are followed by the deposition and lift-off of a metal mask. Aluminum (Al), Chromium (Cr) and Nickel (Ni) has been used as effective etch masks on SOI. The step following mask definition is usually a RIE that goes all the way into the oxide layer. After this etch, the underlying oxide is exposed and can be etched away in an isotropic

buffered hydrofluoric acid (BHF) etch. The timing in this etch step is usually critical; the etch needs to be stopped in order to avoid large undercutting in the anchors. The availability of SOI wafers in a variety of thicknesses and the straightforward fabrication steps has made this process the mainstay in NEMS fabrication.

2.2. *Epitaxial GaAs/AlGaAs systems*

The advances in III–V epitaxial growth processes have resulted in single-crystal lattice-matched heterostructures with superior electronic, optical and mechanical properties. Epitaxially grown III–V materials are commonly used for high-speed VLSI circuits, integrated microwave circuits, and optical communication systems. The combination of well-defined layer thicknesses, and tunable electronic and mechanical properties makes III-V compounds excellent candidates for NEMS technologies.

GaAs/AlGaAs heterostructures have been the III-V material system of choice for NEMS. In the simplest case of heterostructures with structural GaAs and sacrificial AlGaAs layers on top of a GaAs substrate, the chemistry difference between AlGaAs and GaAs has been exploited to selectively etch the sacrificial layers and to suspend the devices. But the real interest in GaAs/AlGaAs-based NEMS stems from the fact that a two-dimensional electron gas (2DEG) can be incorporated into the GaAs/AlGaAs interface; this opens up a number of interesting possibilities for coupling the 2DEG to the displacement/strain fields in the moving nanomechanical element.

A.N. Cleland and coworkers [21] recently fabricated a nanomechanical resonator in an epitaxially grown heterostructure made up of the following layers: 700 nm of $Al_{0.7}Ga_{0.3}As$ (sacrificial layer), 600 nm of GaAs, 40 nm of $Al_{0.3}Ga_{0.7}As$, a Si delta-doped layer, 70 nm of $Al_{0.3}Ga_{0.7}As$, and a 10 nm GaAs capping layer. The suspended mechanical device included all the layers above the sacrificial layer. The 2DEG, which was used to create a quantum point contact, was formed at the lower GaAs-$Al_{0.3}Ga_{0.7}As$ interface. This device, shown in Fig. 6, was fabricated using the standard lithography, isotropic and selective etching steps. Electrostatic voltages applied to the top gates on the device were used to form a quantum point contact in the 2DEG. J. Kirschbaum *et al.* [30] reported the fabrication of a NEMS device on a comparable GaAs/AlGaAs heterostructure. Here, a quantum dot realized by means of fabricated constrictions in the 2DEG was coupled to the NEMS resonator capacitively. H.X. Tang *et al.* [20] fabricated a NEMS device on a similar heterostructure to realize high-gain electromechanical displacement sensing through combined piezoelectric and piezoresistive mechanisms arising from the presence of the 2DEG.

2.3. *Aluminum nitride*

Aluminum nitride (AlN) is a light, stiff and piezoelectrically active material. It is proving to be a useful material in the semiconductor industry, as it can be grown epitaxially on Si substrates. The large piezoelectric constant $e_{33} = 1.5\,\mathrm{C/m^2}$

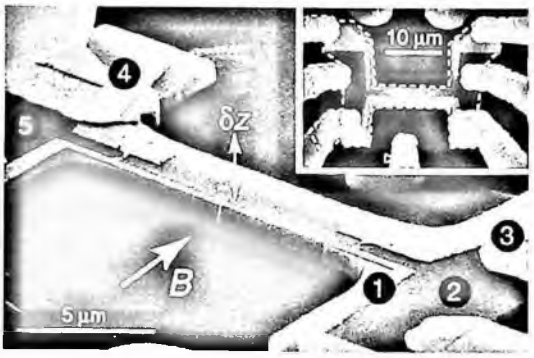

Figure 6. SEM micrograph of a nanomechanical device fabricated on GaAs/AlGaAs heterostructure. A quantum point contact (QPC) is formed in the buried 2DEG by using the electrodes defined on the surface of the suspended beam. The magnetic field B used for magnetomotive actuation is indicated, as is the direction of flexure δz. The numbers identify the electrodes: (1) is the drive electrode that also serves as a QPC gate, (2) and (5) define the source and drain ohmic contacts, (3) and (4) the other sides of the two QPC gates. Only one QPC was used at a time. Inset: Larger scale image of the structure, with the dotted line outlining the suspended area. Courtesy of A.N. Cleland.

corresponds to a significant electromechanical coupling thus making the material a clear platform for the integration of surface-acoustic wave devices on chip with silicon-based electronics. Moreover, the material is fracture resistant and chemically nonreactive — with negligible etching rates when exposed to most strong acids and bases. For NEMS devices, AlN provides both the possibility for very high resonance frequencies and piezoelectric actuation. First NEMS on AlN was fabricated by A.N. Cleland *et al.* [23]. In this study, the AlN films were deposited on Si using metalorganic chemical vapor deposition (MOCVD). NEMS were fabricated using the standard combination of optical lithography and EBL. Ni served as an etch mask during the anisotropic Cl_2-based RIE of AlN. The structures were released by etching the Si substrate with an isotropic wet etchant.

2.4. *Silicon nitride*

Silicon nitride is an amorphous material that is usually deposited on Si or silicon oxide by low pressure chemical vapor deposition (LPCVD). Silicon nitride offers several attractive possibilities as a material for NEMS. By playing with the deposition parameters, for instance, one can obtain a film in high residual tension. The doubly-clamped beam resonators fabricated in such systems behave as wires in tension rather than flexural beams; a recent study shows that such resonators exhibit ultrahigh Q values [31]. Membrane fabrication techniques developed for silicon nitride on Si allow the fabrication of devices, which do not have a substrate below in close proximity and which can be accessed from both the top and bottom surfaces for a variety of detection purposes.

Here, two approaches to fabricate silicon nitride NEMS are reviewed. The first approach applies to silicon nitride grown on silicon oxide, and follows identical steps as on SOI [25]. The second approach involves first the fabrication of a thin silicon nitride membrane, and then, patterning the NEMS on top of the membrane using EBL. NEMS fabrication steps on silicon nitride membranes and examples of such devices are shown in Fig. 7 and Fig. 8, respectively [15,26,27].

2.5. *Silicon carbide*

Silicon Carbide (SiC) is an excellent material for high frequency NEMS. There are two important reasons for this. First, given its larger $\sqrt{E/\rho}$, SiC yields devices that operate at significantly higher frequencies for a given geometry than otherwise possible using conventional materials. Second, SiC possesses excellent chemical stability. This makes surface treatments an option for higher quality (Q) factors of resonance.

Yang *et al.* [22] successfully developed a process for fabricating monocrystalline SiC NEMS. Here, the starting material was a 259 nm-thick single crystalline 3C-SiC film heteroepitaxially grown on a 100 mm-diameter <100> Si wafer. Fabrication of the devices began by defining a Cr device and contact pad mask by the usual optical lithography and EBL steps. The pattern in the Cr metal mask was then

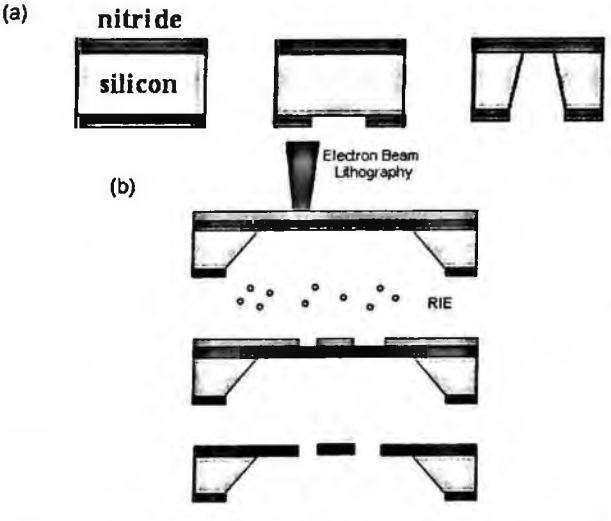

Figure 7. (a) Fabrication of silicon nitride membranes. One starts with a <100> Si wafer with thin coatings of silicon nitride on both sides. Photolithography and RIE steps result in a back etch window. A subsequent wet etch in potassium hydroxide (KOH) solution dissolves the Si preferentially along the <100> plane, at a 57° angle to the <111> plane with high selectivity. The wet etch terminates at the silicon nitride layer. (b) NEMS fabrication on silicon nitride membranes. The membrane is coated with PMMA and patterned using EBL. The unmasked regions are etched using RIE, resulting in suspended structures.

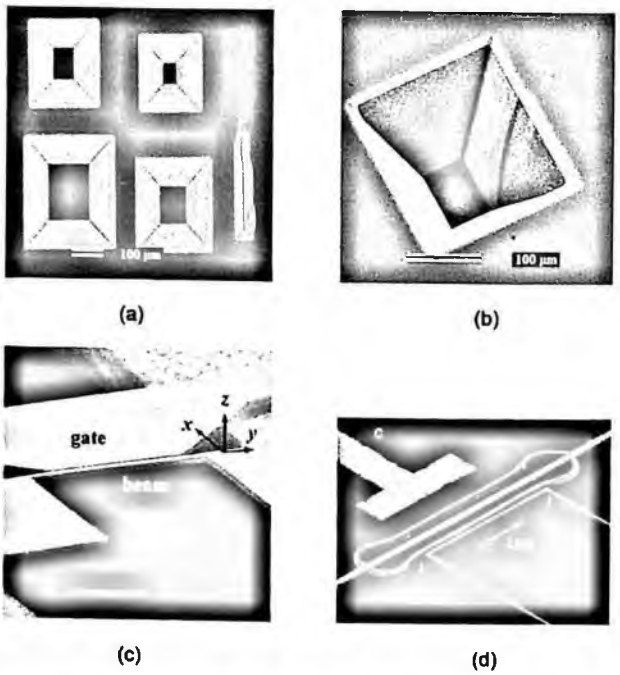

Figure 8. (a) SEM image of a group of four silicon nitride membranes taken from the back side. (b) Close up of a membrane. (c)–(d) Doubly-clamped beams fabricated on silicon nitride membranes. Courtesy of K.L. Ekinci and K.C. Schwab.

transferred to the 3C-SiC beneath by anisotropic plasma etching. The vertically-etched structures were then released by controlled local etching of the Si substrate using a selective isotropic Si etch. After the structures were suspended, the Cr etch mask was removed. The chemical stability and the mechanical robustness of the structures allowed subsequent lithographic fabrication steps for the requisite metallization step on the *released* structures.

2.6. *Nanocrystalline diamond*

Nanocrystalline diamond is a desirable material for many applications because it is chemically very resistant, has a high hardness and thermal conductivity. Doping during deposition allows for a wide range of electrical conductivities. In particular, the high Young's modulus, $E \approx 1000\,\mathrm{GPa}$, of diamond as well as the relatively low mass density, $\rho \approx 3500\,\mathrm{kg/m^3}$, result in a very high sound velocity — as in SiC described above.

Sekaric *et al.* [24] used nanocrystalline diamond films for fabricating NEMS structures. The nanocrystalline diamond was deposited on a 1-μm-thick oxide layer grown on a Si wafer. The film deposition was done by microwave plasma enhanced chemical vapor deposition (CVD). The films had a columnar growth structure with grains that ranged in size from 5–15 nm on the nucleation side to ~10% the thickness

Figure 9. Nanocrystalline diamond NEMS device. The close-ups in (a) and (b) show the thin beam region and the anchor regions. Courtesy of L. Sekaric and H.G. Craighead.

of the film on the growth surface. The structures shown in the SEM micrographs in Fig. 9 were fabricated using EBL. The pattern was transferred into the diamond films using a CF_4/O_2 reactive ion etch with the diamond film protected by a metal mask. After the removal of the mask, the structures were released in buffered hydrofluoric acid which removed the underlying oxide layer.

2.7. *Nanotube and nanowire NEMS*

Fabrication and operation of NEMS with progressively smaller size, ultimately down to the molecular scale, is critical for the advancement of nanotechnology. Nanomaterials such as nanowires and nanotubes offer immense potential in this regard. Nanotubes come as muti-walled and single-walled structures. Both nanotubes and nanowires possess near-perfect surfaces; they can be tailored to desired lengths and diameters.

Several groups have successfully fabricated suspended doubly-clamped and cantilevered nanowire structures [32,33]. The generic approach is to synthesize the nanowires, suspend them in a solution, and then disperse them on top of a substrate. Then, one determines the location of the deposited wires using optical microscopy or Atomic Force Microscopy (AFM). Metallic leads to individual nanowires are subsequently patterned by EBL, evaporation, and lift-off. Finally, the nanowires are suspended above the substrate by etching the substrate selectively. Fig. 10(a) shows the Pt nanowire NEMS fabricated by Husain *et al.* [32].

Similar lithographic approaches have been used to fabricate suspended nanotube structures. P.A. Williams *et al.* [34], for instance, fabricated torsional resonators with multi-walled carbon nanotubes as the torsional spring elements. The fabrication approach depended upon EBL to pattern metal pads over the ends of a nanotube to pin it down, and a strip of metal over the center of the nanotube to form the paddle. Another approach in creating suspended nanotube NEMS is to first lithographically pattern the catalyst sites, and then, grow the nanotubes between these sites. V. Sazanova *et al.* [35] used chemical vapor deposition (CVD) to grow nanotubes with diameters between 1 and 10 nm at lithographically defined catalyst sites on a Si substrate with a 500 nm oxide. Metal contacts were made using photolithography. A final HF etch followed by critical point drying resulted in the suspended nanotubes. Fig. 10(b) shows a SEM image of this device.

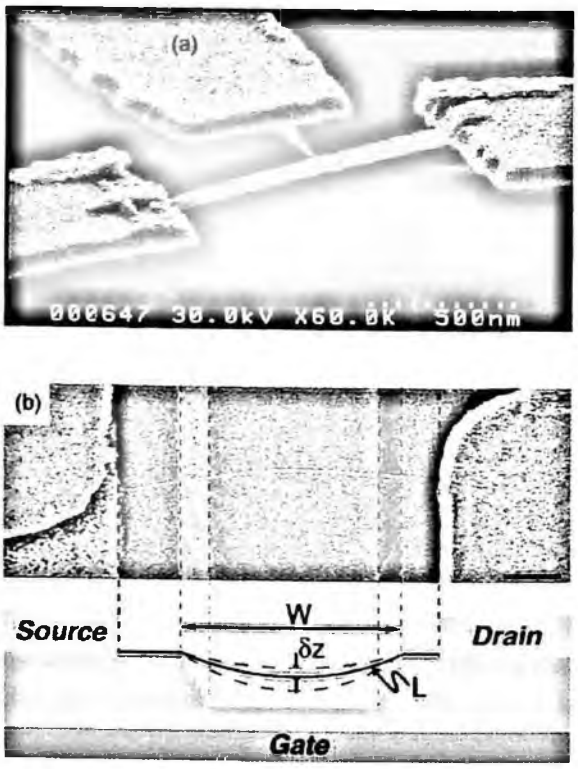

Figure 10. (a) Pt nanowire NEMS. (b) Nanotube NEMS. The nanotubes were CVD grown and usually single-walled or double-walled. Courtesy of M.L. Roukes and P. McEuen.

3. Fabrication of NEMS Using Nanoimprint Lithography

Nanoimprint lithography (NIL) is a high volume, low cost patterning technique with spatial resolution down to ~5 nm [36]. In basic NIL, a pattern is defined by physically deforming a polymer resist. One typically uses a solid template as the imprint mold, which is prepared by electron beam lithography (EBL) and reactive ion etching (RIE). The mold is pressed upon a polymer-coated substrate, deforms the polymer at elevated temperature, and is removed from the substrate after cool down. The pattern imprinted on the polymer can then be transferred into the substrate by a variety of techniques. NIL has already been used to fabricate electronic, photonic and microfluidic devices in the past decade.

Recently, C.C. Huang and K.L. Ekinci [37] extended the NIL technique to the fabrication of freely suspended nanostructures. This approach potentially possesses all the desirable aspects of NIL; it also lends itself to simple layer-by-layer fabrication. With this approach, one can generate suspended nanostructures upon an existing structure, such as anchors, without modifying the structure — given that the polymer patterning resist serves as the sacrificial layer.

The device fabricated in the preliminary work of Huang and Ekinci contained two layers: an anchor layer and a freely suspended layer. The anchors were rectangular structures with dimensions $l \times w \times t = 70\,\mu\text{m} \times 12\,\mu\text{m} \times 300\,\text{nm}$; they were made up of silicon oxide and Al, and fabricated by conventional nanoimprint and film deposition steps. After their fabrication, the anchors were spin coated by a thick PMMA for the second layer imprint. Subsequently, a flattening step was used. The Si mold for the upper structural layer was fabricated by EBL and RIE, and coated with an anti-adhesion layer. The imprint process was performed in a flip-chip bonder with careful alignment between the layers. After the removal of the residual PMMA through a carefully timed O_2 RIE, a 200-nm-thick Aluminum film was thermally deposited on the pattern. Simple lift-off step in a solvent such as acetone did not work reliably due to the fact that the imprint pattern did *not* have an *undercut*, and the deposited film was essentially connected over the entire sample area. In order to overcome this challenge, a relatively flat protective photoresist coating was generated over the whole sample chip; the photoresist was etched downwards until the elevated, excess metal area was reached. A wet aluminum etchant was used to remove the Al in the unprotected areas. As expected, the devices survived under the protective coatings. The final step in the fabrication was the release of the nanostructures in acetone. The complete process is illustrated in Fig. 11.

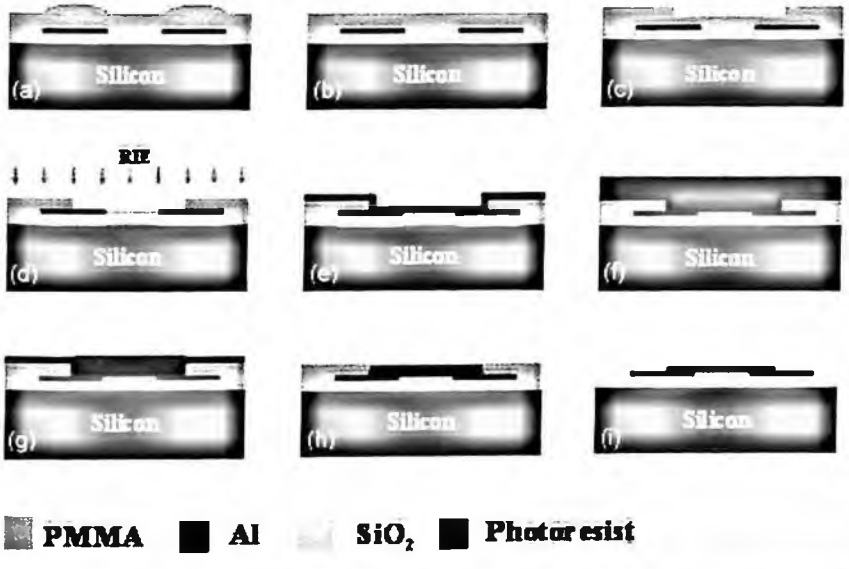

Figure 11. Use of nanoimprint lithography for the fabrication of suspended nanostructures. (a) The anchor structures were coated with the imprint polymer (PMMA). (b) The polymer was flattened. (c) The device layer was imprinted. (d) Residual polymer was removed using RIE. (e) Al was deposited as the device layer. (f) The chip was coated with a flat photoresist layer. (g) The photoresist was etched in RIE until the upper metal was exposed. (h) Al etchant was used to remove the exposed Al. (i) Acetone was used to release the structures. Courtesy of C.C. Huang and K.L. Ekinci.

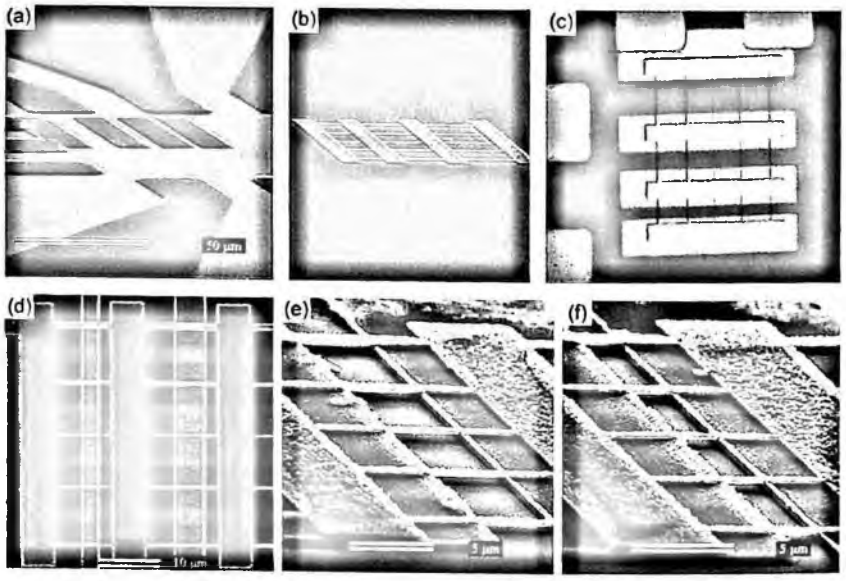

Figure 12. Different stages during suspended structure fabrication using nanoimprint lithography. (a) SEM image of the anchor structure. (b) The imprint mold for the suspended structures. (c) Optical micrograph of the chip coated with the resist right after the imprint step. (d)–(f) SEM images of the resulting suspended structures. Courtesy of C.C. Huang and K.L. Ekinci.

Optical and electron micrographs of the device at various points during the fabrication are displayed in Fig. 12. Figure 12(a) shows a Scanning Electron Microscope (SEM) image of the anchors on the sample chip. The imprint mold is shown in Fig. 12(b). The optical micrograph of the resist after the imprint step is shown in Fig. 12(c). Figure 12(d)–(f) shows the completed devices.

4. NEMS Fabricated Using Polymeric Nanofiber Templates

Electrospinning deposition is the electric field-assisted formation of fibers from a polymeric solution. Using this process, one can produce polymer fibers with diameters in the range of hundreds of nanometers, which cannot be fabricated by conventional extrusion technologies. H. Craighead and coworkers [38,39] have fabricated silicon nitride NEMS devices by electrospinning PMMA nanofibers on lithographically defined support structures, and using these nanofibers as etch masks. The technique eliminates the need for the high resolution lithography step.

The electrospinning process described by Czaplewski *et al.* [39] used a microfabricated tip loaded with the polymeric solution to be dispensed. The target substrates were attached to an aluminum counter electrode fixed to the front of a speed-controlled rotational motor. A voltage was applied between the tip and the counter electrode. Once a stable Taylor cone was established at the tip, the counter electrode was set into motion, producing nanofibers on the target substrate. The nanofibers

used to define the nanomechanical structures were deposited by electrospinning a PMMA solution. The target substrate consisted of two films, the device layer on top of a sacrificial oxide layer on a silicon substrate. After the fibers were deposited on the target substrate, the substrate was heated to 115°C to increase the adhesion of the PMMA fibers to the substrate surface. Then photoresist was spun over the fibers and conventional photolithography was used to define the support structures of the nanomechanical devices. Next, the unmasked areas of the device layer were etched in a CF_4 plasma, and then the remaining photoresist and nanofibers were removed in an oxygen plasma. The devices were released by etching the sacrificial oxide in hydrofluoric acid, rinsing in water, and drying with nitrogen.

5. NEMS Fabricated by Focused Ion Beam Doping and Wet Chemical Etching

A recently demonstrated technique based on local ion implantation and subsequent wet chemical etching presents interesting prospects for fabricating suspended nanomechanical devices. Briefly, one uses a focused ion beam (FIB) to locally implant impurity ions into a Si wafer. The FIB implantation of ions into Si at a sufficiently high dose (above $10^{15}/cm^2$) renders the implanted Si region much less susceptible to chemical etching; this effect has been observed for FIB implantation of Ga, Au and Si impurity ions. A subsequent wet etch, e.g., in potassium hydroxide (KOH) solution, affects only areas that are not doped by the FIB — given that a high impurity concentration in Si forms an efficient etch stop. Using this technique it has been possible to define arbitrary shapes by direct-write patterning down to the nanometer scale. The main advantage of the technique stems from the fact that no intermediate mask pattern transfer step is necessary. Similar to EBL, however, this is a serial approach.

Steckl *et al.* [40], Schmidt *et al.* [41] and Brugger *et al.* [42] have used this technique to successfully fabricate suspended Si nanostructures. Suspended structures were fabricated by generating appropriately oriented doping patterns with respect to the crystal planes of Si. The penetration depth of the ions determined the structural thickness of the suspended layer. In order to fabricate ultrahigh-frequency cantilever beams, Brugger *et al.* [42] used a 10 Ω-cm *n*-type background doped <100> Si wafer. The Si was ion-implanted using an FIB system, which was operated at a 30-kV ion beam acceleration voltage with currents in the range 12–150 pA; this voltage resulted in a structural layer that was to typically 30 nm for Ga+ ions. The FIB modified samples were then etched in aqueous KOH solution. Freestanding structures were realized by appropriately orienting the FIB pattern at 45° with respect to the <110> silicon crystal plane. Figure 13(a) illustrates the above-described process steps to fabricate cantilevers with a rectangular cross-section; Fig. 13(b) shows the orientation of the structures with respect to the crystal directions; Fig. 13(c) is a SEM image of cantilevers fabricated using this technique. The profile of the

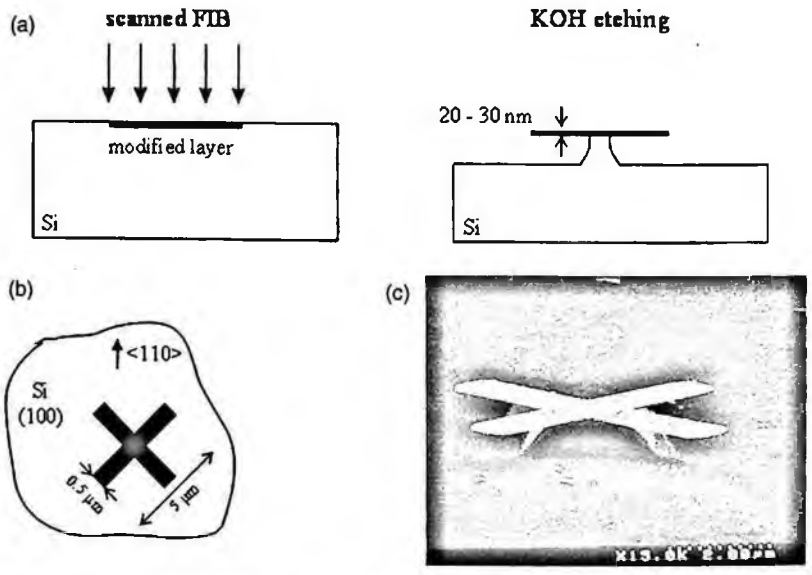

Figure 13. (a) Process sequence for fabricating cantilevers by a combination of local doping by a focused ion beam (FIB) and KOH etching (cross section). (b) Top view of the surface modification layout showing the crystal directions in the substrate. (c) SEM image of fabricated cantilevers. The cantilevers had the following dimensions: $l = 2\,\mu\text{m}$, $w = 500\,\text{nm}$, $t = 30\,\text{nm}$. Courtesy of J. Brugger.

Ga+ doping determined the cross sectional shape of the beams. The structures had nearly rectangular cross sections with a 30-nm thickness and varying widths ranging from $0.5\,\mu\text{m}$ to $10\,\mu\text{m}$; the lengths were in the 0.1–$1\,\mu\text{m}$ range.

In the case of a shallow, uniform implantation, the cross section of the resulting suspended structures were nearly rectangular. Interestingly, when a hole was milled into Si by continued FIB exposure, back scattering of Ga+ ions resulted in equally doped sidewalls, which subsequently became etch resistant. This made it possible to fabricate three-dimensional elements with vertical sidewalls. Using this approach, cantilevers with U-shaped cross sections were fabricated by Brugger *et al.* [42]. The U-shaped cross section resulted in an increase of the moment of inertia by two orders of magnitude as compared to the moment of inertia of cantilevers with similar size and mass but rectangular cross sections. Consequently, the U-shaped cantilevers had a mechanical stiffness that was increased by a factor of 100, which, in turn, increased the beam resonance frequency by a factor of 10. Figure 14(a) illustrates this fabrication process; Fig. 14(b) is a SEM image of the cantilevers.

6. NEMS Fabrication by Stencil Lithography and Sacrificial Etching

Another novel method for the fabrication of suspended nanomechanical devices is based on a combination of stencil lithography and etching. Stencil lithography is an emerging surface patterning technique that relies on the local deposition of

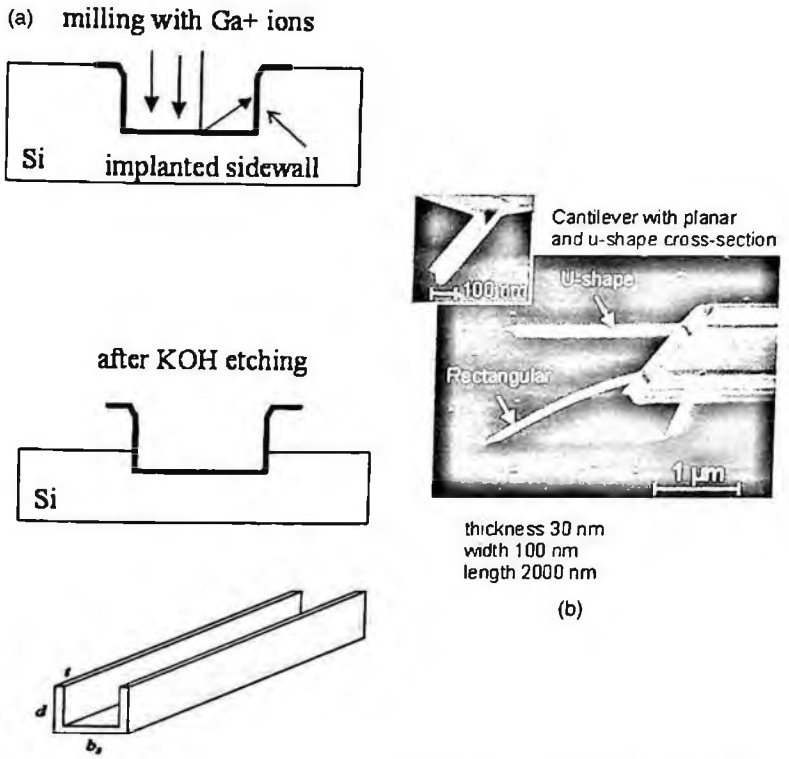

Figure 14. (a) Fabrication of free-standing nanomechanical elements with increased structural stiffness by 3D FIB milling and sidewall doping. The illustrations show the structures after various fabrication stages: after FIB exposure (top), in mid-process during KOH etching (middle) and when etching is completed (bottom). (b) SEM image of NEMS cantilevers with rectangular and U-shaped cross section. The cantilever with the U-shaped cross section (inset) had an increased mechanical stiffness such that it could withstand the capillary force exerted by the retracting liquid used for the final rinse step in the process. Courtesy of J. Brugger.

material through miniaturized shadow mask membranes [43,44,45,46]. This method has been particularly useful for the deposition of thin film patterns on surfaces in applications where the surfaces are fragile and don't allow the harsh process steps typically involved in the photolithography process. Stencil lithography is scaleable down to sub-100 nanometers; this property makes stencil lithography a very promising method for rapid *in vacuo* prototyping of nanostructures without the risk of contamination. Stencils are also useful for patterning surface structures that span multiple length-scales from mm to sub-100 nm.

The fabrication of stencils is based on a set of advanced micromachining steps including DUV exposure and a combination of reactive ion etching and wet etching [47]. The stencil mask membrane is typically 100 nm thick, and hence, is mechanically very fragile and compliant, often bending due to the stress of the added thin film. The mechanical stiffness of the ultra-thin low-stress silicon nitride membranes

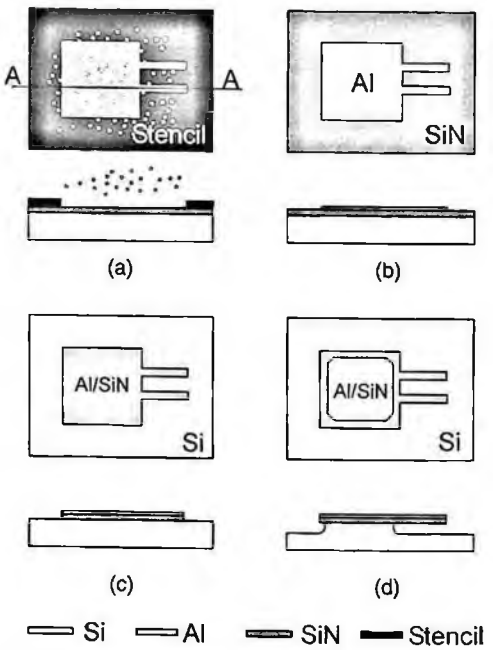

Figure 15. Process steps for the fabrication of NEMS devices based on stencil lithography and dry etching. (a) Deposition of a patterned thin metal film through the stencil mask. (b) Metal layer after the stencil is removed. (c) Pattern transfer into the structural SiN layer below by means of anisotropic dry plasma etching. (d) Dry releasing of suspended nanomechanical structures by isotropic dry etching of Si substrate. If necessary the metal etch mask can be selectively removed by further etching. Courtesy of J. Brugger.

can be considerably improved by topographic reinforcement rims [48,49]. As a result, the membranes deform less under the stress of the deposited film, and consequently, the surface patterns can be better defined down to the 10-nm scale.

The fabrication of NEMS using stencil lithography is based on the local deposition of a structural layer or a mask layer, and subsequent plasma etching as shown schematically in Fig. 15. Using a stencil mask, Kim *et al.* [50] defined an Al layer in the shape of a ~100-nm-wide beam connected to an anchor pad, which was in the μm range. A subsequent etch step released the narrow beam making it freely suspended. Using this technique, it was possible to use the Al layer as the structural layer for the NEMS device; alternatively, the Al could be used as a mask to transfer the pattern into the layer below. Figure 16 shows SEM images of cantilevers and doubly-clamped beams fabricated using the stencil lithography technique.

Using stencil lithography, free-standing nanomechanical elements can be fabricated in virtually any desired material as long as the material has a sufficiently high etch selectivity with respect to the substrate. The all-dry, two-step, stencil lithography method allows fabrication of nanomechanical elements without a photolithography step. Moreover, the fabrication method is scalable to a full wafer.

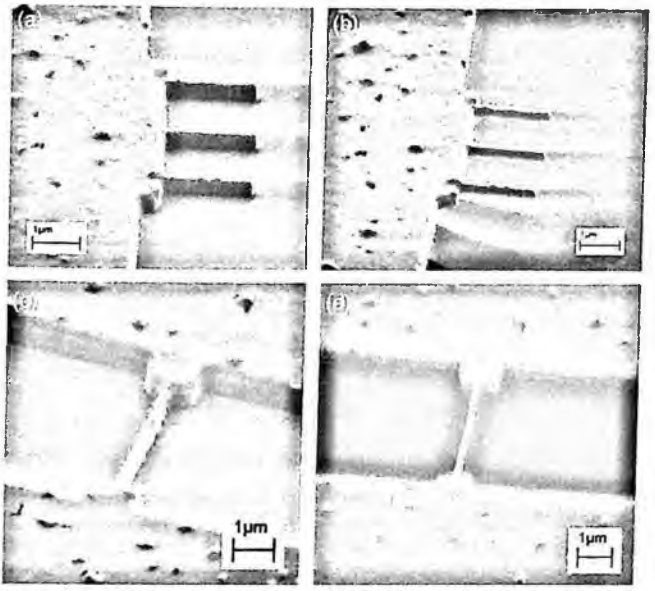

Figure 16. SEM images of NEMS cantilevers and doubly-clamped beams at various stages during stencil lithography based fabrication. (a) After Al film deposition through the stencil mask and pattern transfer by dry etching. (b) After isotropic Si etch to release the cantilever beams. (c) and (d) show similar SEM images taken during nanomechanical doubly-clamped beam fabrication. Courtesy of J. Brugger.

7. Large Scale Integration of NEMS

Up to date, most NEMS work has been done on single devices. A single NEMS sensor or a single NEMS signal processor, while exceptionally capable and sensitive, will probably not be of significant use in a macroscopic world application. The reason, of course, is that the efficiency obtained by employing a single NEMS device is extremely small. This impediment can be overcome by fabricating and operating many NEMS devices *in parallel.*

Kawakatsu *et al.* [51] have developed a fabrication method for the parallel manufacturing of millions of identical single-crystal silicon cantilevers for high resolution scanning probe microscopy (SPM). Their method is based on anisotropic etching of silicon by KOH. Arcamone *et al.* [49] have recently demonstrated full wafer scale NEMS fabrication and CMOS-integration by using stencil lithography. The fabrication strategy of Arcamone *et al.* [49] was based on using the polysilicon and silicon oxide CMOS layers as the respective structural and sacrificial layers for the suspended nanomechanical resonators. The stencil mask used was a 100-mm wafer that contained more than 2000 device masks for the single-step, parallel fabrication of nanoresonators. During CMOS circuit design and processing, an area was reserved for the integration of the nanodevices. After concluding the fabrication of the CMOS circuits using standard CMOS technology, the integration area was patterned using

stencil lithography by evaporation of 80 nm of Al. Subsequent process steps consisted of RIE of Si to transfer the pattern to the polysilicon structural layer and silicon oxide wet etching to release the mechanical structures. This strategy simplifies the processing and facilitates the electrical contact between the nanomechanical devices and the circuits [52].

8. Conclusions and Outlook

NEMS are anticipated to find a number of significant technological applications in the near future. There remain, however, several challenges in front of realizing the full potential of NEMS. The development of simple, reliable, parallel, reproducible and scaleable NEMS fabrication technologies, which are compatible with standard microelectronic processing, is of central importance for the success of NEMS-based applications. This chapter aimed to give an introduction to the fabrication of NEMS, highlighting both mainstay and emerging technologies. While some of these technologies offer promise for the future, much research is needed in this active field.

Acknowledgments

KLE gratefully acknowledges support from the ARL under grant DAAD19-00-2-0004 and the NSF under grants CMS0324416, BES-0216274, DMR-0315662 and ECS-0089061. JB gratefully acknowledges support from the Swiss Commission for Technology and Innovation (CTI) under the project CTI 6640.2 NMSNM, the Swiss Federal Office for Science and Education (OFES) in the framework of the EC-funded FP6 project NaPa (NMP4-CT-2003-500120), and the EPFL Center of Micro- and Nano-Technology (CMI).

References

1. M. L. Roukes, Nanoelectromechanical systems face the future, *Phys. World* **14**, 25 (2001).
2. K. L. Ekinci and M. L. Roukes, Nanoelectromechanical systems, *Rev. Sci. Instrum.* **76**, 061101 (2005).
3. H. G. Craighead, Nanoelectromechanical Systems, *Science* **24**, 1532 (2000).
4. T. Rueckes, K. Kim, E. Joselevich, G. Tseng, C.-L. Cheung and C. M. Lieber, Carbon nanotube-based nonvolatile random access memory for molecular computing, *Science* **289**, 94 (2000).
5. X. M. H. Huang, C. Zorman, M. Mehregany and M. L. Roukes, Nanodevice Motion at Microwave Frequencies, *Nature* **421**, 496 (2003).
6. K. L. Ekinci, X. M. H. Huang and M. L. Roukes, Ultrasensitive Nanoelectromechanical Mass Detection, *Appl. Phys. Lett.* **84**, 4469 (2004).
7. Rustom B. Bhiladvala and Z. Jane Wang, Effect of fluids on the Q factor and resonance frequency of oscillating micrometer and nanometer scale beams, *Phys. Rev.* **E 69**, 036307 (2004).
8. A. N. Cleland and M. L. Roukes, A Nanometer-Scale Mechanical Electrometer, *Nature* **392**, 160 (1998).

9. A. Erbe, H. Krömmer, A. Kraus, R. H. Blick, G. Corso and K. Richter, Mechanical mixing in nonlinear nanomechanical resonators, *Appl. Phys. Lett.* **77**, 3102 (2000).
10. L. Sekaric, M. Zalalutdinov, S. W. Turner, A. T. Zehnder, J. M. Parpia and H. G. Craighead, Nanomechanical resonant structures as tunable passive modulators of light, *Appl. Phys. Lett.* **80**, 3617 (2002).
11. B. Ilic, H. G. Craighead, S. Krylov, W. Senaratne, C. Ober and P. Neuzil, Attogram detection using nanoelectromechanical oscillators, *J. Appl. Phys.* **95**, 3694 (2004).
12. N. V. Lavrik and P. G. Datskos, Femtogram mass detection using photothermally actuated nanomechanical resonators, *Appl. Phys. Lett.* **82**, 2697 (2003).
13. Y. T. Yang, C. Callegari, X. L. Feng, K. L. Ekinci and M. L. Roukes, Zeptogram-Scale Nanomechanical Mass Sensing, *Nano Lett.* **6**, 583 (2006).
14. K. L. Ekinci, Y. T. Yang and M. L. Roukes, Ultimate Limits to Inertial Mass Sensing Based upon Nanoelectromechanical Systems, *J. Appl. Phys.* **95**, 2682 (2004).
15. M. D. LaHaye, O. Buu, B. Camarota and K. C. Schwab, Approaching the quantum limit of a nanomechanical resonator, *Science* **304**, 74 (2004).
16. R. Knobel and A. N. Cleland, Nanometre-scale displacement sensing using a single electron transistor, *Nature* **424**, 291 (2003).
17. A. N. Cleland and M. L. Roukes, Fabrication of high frequency nanometer scale mechanical resonators from bulk Si crystals, *App. Phys. Lett.* **69**, 2653 (1996).
18. D. W. Carr, S. Evoy, L. Sekaric, H. G. Craighead and J. M. Parpia, Measurement of mechanical resonance and losses in nanometer scale silicon wires, *Appl. Phys. Lett.* **75**, 920 (1999).
19. R. H. Blick, M. L. Roukes, W. Wegscheider and M. Bichler, Freely suspended two-dimensional electron gases, *Physica* B **249–251**, 784 (1998).
20. H. X. Tang, X. M. H. Huang and M. L. Roukes, M. Bichler and W. Wegscheider, Two-dimensional electron-gas actuation and transduction for GaAs nanoelectromechanical systems, *Appl. Phys. Lett.* **81**, 3879 (2002).
21. A. N. Cleland, J. S. Aldridge, D. C. Driscoll and A. C. Gossard, Nanomechanical displacement sensing using a quantum point contact, *Appl. Phys. Lett.* **81**, 1699 (2002).
22. Y. T. Yang, K. L. Ekinci, X. M. H. Huang, L. M. Schiavone, C. Zorman, M. Mehregany and M. L. Roukes, Monocrystalline silicon carbide nanoelectromechanical systems, *Appl. Phys. Lett.* **78**, 162 (2001).
23. A. N. Cleland, M. Pophristic and I. Ferguson, Single-crystal aluminum nitride nanomechanical resonators, *Appl. Phys. Lett.* **79**, 2070 (2001).
24. L. Sekaric, J. M. Parpia, H. G. Craighead, T. Feygelson, B. H. Houston and J. E. Butler, Nanomechanical resonant structures in nanocrystalline diamond, *Appl. Phys. Lett.* **81**, 4455 (2002).
25. L. Sekaric, D. W. Carr, S. Evoy, J. M. Parpia and H. G. Craighead, Nanomechanical resonant structures in silicon nitride: fabrication, operation and dissipation issues, *Sensors and Actuators* A **101**, 215 (2002).
26. D. Karabacak, T. Kouh, C. C. Huang and K. L. Ekinci, Optical knife-edge technique for nanomechanical displacement detection, *Appl. Phys. Lett.* **88**, 193122 (2006).
27. T. Kouh, O. Basarir and K. L. Ekinci, Room-temperature operation of a nanoelectromechanical resonator embedded in a phase-locked loop, *Appl. Phys. Lett.* **87**, 113112 (2005).
28. R. C. Jaeger, Introduction to microelectronic fabrication, Prentice Hall (2002).
29. T. Kouh, D. Karabacak , D. H. Kim and K. L. Ekinci, Diffraction Effects in Optical Interferometric Displacement Detection in Nanoelectromechanical Systems, *Appl. Phys. Lett.* **86**, 013106 (2005).

30. J. Kirschbaum, E. M. Hoehberger, R. H. Blick, M. Bichlerb and W. Wegscheider, Integrating suspended quantum dot circuits for applications in nanomechanics, *Appl. Phys. Lett.* **81**, 280 (2002).
31. Scott S. Verbridge, Jeevak M. Parpia, Robert B. Reichenbach, Leon M. Bellan and H. G. Craighead, High quality factor resonance at room temperature with nanostrings under high tensile stress, *J. Appl. Phys.* **99**, 124304 (2006).
32. A. Husain, J. Hone, H. W. Ch. Postma, X. M. H. Huang, T. Drake, M. Barbic, A. Scherer and M. L. Roukes, A nanowire-based very-high-frequency electromechanical resonator, *Appl. Phys. Lett.* **83**, 1240 (2003).
33. M. F. Yu, G. J. Wagner, R. S. Ruoff and M. J. Dyer, Realization of parametric resonances in a nanowire mechanical system with nanomanipulation inside scanning electron microscope, *Phys. Rev.* **B 66**, 073406 (2002).
34. P. A. Williams, S. J. Papadakis, A. M. Patel, M. R. Falvo, S. Washburn and R. Superfine, Torsional Response and Stiffening of Individual Multiwalled Carbon Nanotubes, *Phys. Rev. Lett.* **89**, 255502 (2002).
35. Vera Sazonova, Yuval Yaish, Hande Üstünel, David Roundy, Tomás A. Arias and Paul L. McEuen, A tunable carbon nanotube electromechanical oscillator, *Nature* **431**, 284 (2004).
36. M. D. Austin, H. Ge, W. Wu, M. Li, Z. Yu, D. Wasserman, S. A. Lyon and S. Y. Chou, Fabrication of 5 nm linewidth and 14 nm pitch features by nanoimprint lithography, *Appl. Phys. Lett.* **84**, 5299 (2004).
37. C. C. Huang and K. L. Ekinci, Fabrication of freely suspended nanostructures by nanoimprint lithography, *Appl. Phys. Lett.* **88**, 093110 (2006).
38. David Czaplewski, Jun Kameoka and H. G. Craighead, Nonlithographic approach to nanostructure fabrication using a scanned electrospinning source, *J. Vac. Sci. Technol.* **B 21**, 2994 (2003).
39. David A. Czaplewski, Scott S. Verbridge, Jun Kameoka and H. G. Craighead, Nanomechanical Oscillators Fabricated Using Polymeric Nanofiber Templates, *Nano Lett.* **4**, 437 (2004).
40. A. J. Steckl, H. C. Mogul and S. Mogren, Localized Fabrication of Si Nanostructures by Focused Ion-Beam Implantation. *Appl. Phys. Lett.*, **60**, 1833–1835 (1992).
41. B. Schmidt, L. Bischoff and J. Teichert, Writing FIB implantation and subsequent anisotropic wet chemical etching for fabrication of 3D structures in silicon. *Sensor Actuator* **A 61**, 369–373 (1997).
42. J. Brugger, G. Beljakovic, M. Despont, N. F. deRooij and P. Vettiger, Silicon micro/nanomechanical device fabrication based on focused ion beam surface modification and KOH etching, *Microelectron. Eng.* **35**, 401–404 (1997).
43. R. Lüthi, R. R. Schlitter, J. Brugger, P. Vettiger, M. E. Welland and J. K. Gimzewski, Parallel nanodevice fabrication using a combination of shadow mask and scanning probe methods. *App. Phys. Lett.* **75**, 1314–1316 (1999).
44. J. Koehler, M. Albrecht, C. R. Musil and E. Bucher, Direct growth of nanostructures by deposition through an Si_3N_4 shadow mask. *Physica E* **4**, 196–200 (1999).
45. M. M. Deshmukh, D. C. Ralph, M. Thomas and J. Silcox, Nanofabrication using a stencil mask, *App. Phys. Lett.* **75**, 1631–1633 (1999).
46. J. Brugger, J. Berenschot, S. Kuiper, W. Nijdam, B. Otter and M. Elwenspoek, Resistless patterning of sub-micron structures by evaporation through nanostencils, *Microelectron. Eng.* **53**, 403–405 (2000).
47. M. A. F. van den Boogaart, G. M. Kim, R. Pellens, J. P. van den Heuvel and J. Brugger, Deep-ultraviolet-microelectromechanical systems stencils for high-throughput

resistless patterning of mesoscopic structures, *J. Vac. Sci. Technol.* **B 22**, 3174–3177 (2004).

48. R. Hammer, Solving the "stencil" problem in vacuum deposition masks using rib-supported structures, *J. Vac. Sci. Technol.* **14**, 1208–1210 (1977).
49. J. Arcamone, M. v. d. Boogaart, F. Serra-Graells, S. Hansen, J. Brugger, F. Pérez-Murano, *Full wafer integration of NEMS on CMOS by nanostencil lithography*, IEEE International Electron Device Meeting, San Francisco, Dec, 2006; San Francisco, 2006.
50. G. M. Kim, S. Kawai, M. Nagashio, H. Kawakatsu and J. Brugger, Nanomechanical structures with 91 MHz resonance frequency fabricated by local deposition and dry etching, *J. Vac. Sci. Technol.* **B 22**, 1658–1661 (2004).
51. Hideki Kawakatsu, Daisuke Saya, Atsushi Kato, Kimitake Fukushima, Hiroshi Toshiyoshi and Hiroyuki Fujita, Millions of cantilevers for atomic force microscopy, *Rev. Sci. Instrum.* **73**, 1188 (2002).
52. J. Verd, G. Abadal, J. Teva, M. V. Gaudo, A. Uranga, X. Borrise, F. Campabadal, J. Esteve, E. F. Costa, F. Perez-Murano, Z. J. Davis, E. Forsen, A. Boisen and N. Barniol, Design, fabrication, and characterization of a submicroelectromechanical resonator with monolithically integrated CMOS readout circuit, *J. Microelectromech. S.* **14**, 508–519 (2005).

INDEX

D_2GaN_3, 417
Ge_2H_6, 420
μ Walker, 107, 108
(Fast) secondary electrons, 355, 356
(Maximum) beam current, 350
3D lithography, 425

α-helix, 138, 139
Aberration coefficient, 352, 408, 409
Aberrations in the objective lens, 409
Accelerating voltage, 404, 405, 409, 414
Actuation, 74, 75, 97, 99, 100, 113
Adenine (A), 130
Adsorbed, 400–402, 410, 411, 415, 416, 425
Adsorbed precursor molecules, 402, 415
Adsorption, 407
Aggregates, 360
Aluminum nitride, 543, 546, 549
Amino acids, 135–137
Angle limiting aperture, 405
Angular distribution, 411
Anisotropy, 187, 188
Anodization of aluminum, 161, 162
Antibody, 111
Apertures, 407–409, 504–506, 509, 513, 514, 519, 521
Aperture function, 353
Arbitrary shape, 399, 401, 402, 405
Arizona State University logo, 402, 403
Artificial synthesis, 143
Aspect ratio, 503, 504, 509, 513, 523–525
Aspherical mirror, 235, 244–246, 249, 272, 273, 277
Atomic Force Imaging, 96, 97
Atomic Force Microscopy (AFM), 68, 70, 71, 75, 78, 79, 81, 82, 84, 85, 87, 89, 94, 95, 424
Atomic resolution, 68, 79, 85, 87
Auger electrons, 411

β-sheet, 138, 139
Background energy, 358, 359
Backscattered, 405, 406, 415
Backscattering/backscattered (electrons), 357
Bakeable system, 421
Beam damage, 431, 434, 455, 465
Beam semi-angle, 352, 354, 371
Bethe, 409, 410
Bethe-Bloch formula, 344
Bio-devices, 533, 534
Biocompatible materials, 520
Block copolymer, 110, 485–487
Boersch effect, 352
Bottom-up, 187, 189, 197, 204, 501
Bragg grating, 80, 81, 89, 91

Calixarene, 365
Cantilevered, 543–545, 553
Cantilevers, 557–561
Capillary, 196
Carbon, 404, 406, 420–423
Carbon compounds, 421
Carbon contamination dots, 404

Carbon Nano Tubes (CTN), 71, 72, 83, 90–92, 113
Carbonaceous precursors, 421
Carbonyl groups, 420, 421
CdS, 199, 201
Cell surface display (CSD), 151
Central maximum, 408, 409
Ceramic films, 477, 480, 482, 489, 490
Ceramic nanostructures, 474, 485
Channeling, 457, 458, 461–463
Chemical vapor deposition, 401, 417
Chemically amplified resist, 359, 363
Chromatic aberration, 352, 353
Chromosome, 129
Clamped-clamped (doubly-clamped) beam, 545
Clogging, 505, 513, 515
$Co_2(CO)_8$, 418, 424
Coarsening, 423
Codon, 132, 133, 135
Combinatorial materials, 521
Complex nanostructures, 485
Complex oxides, 516
Complex protein structure, 140
Composition control, 421, 423
Composition of deposit, 417, 422, 423
Compound semiconductors, 417
Concentration gradient, 416
Conduction band electron, 344
Confocal laser microscope, 370
Contact Mode, 85, 87, 96
Contamination, 400, 401, 404, 417, 421, 422, 424, 426
Contrast (of resist), 363
Convergent wave, 408
Coulomb blockade, 367
Coulomb effect, 352
Coulomb interaction, 352
Cross-link (of resist polymer), 344
Cross-sectioning, 431, 432, 444, 445, 448, 450–452, 463
CTAB, 190
Cu film, 414
Cu surface, 414
Current distribution, 407, 408
Cutting (of resist polymer), 344
Cytosine (C), 130

De-localized process, 413
Defect tolerance, 187, 202, 204
Defects, 201, 202
Deflection frequency, 350
Deflection noise, 348, 352, 362
Delocalization, 413
Deoxyribose, 130
Deposit, 399, 401–407, 409, 410, 412–417, 420–424, 426
Deposit composition, 399, 417
Deposited material, 401, 410
Deposition chamber, 407, 417
Deposition parameters, 399, 401, 415
Deposition process, 401, 411
Deposition rate, 401, 406, 407, 409, 413, 415, 416, 422
Depth of focus, 353, 371
Desorption, 407
Detection semi-angle, 350, 351
Diamond, 70–72, 543, 546, 552, 553
Diblock copolymer thin films, 486
Dielectric, 69, 70, 73, 74
Dielectrophoresis, 192, 194
Differential (scattering) cross-section, 345, 346
Differential pumping systems, 406
Diffraction, 352
Diffusion, 407
Digermane, 420
Direct write technique, 399–401
Dissociate, 399–402, 409–411, 414–417, 421
Dissociated hydrocarbon vapors, 401
Dissociation, 401, 402, 409–413, 415–417, 420
Dissociation cross sections, 410, 412, 413, 415
Dissociative electron attachment, 411
DNA, 129, 194, 200
DNA arrays, 147
DNA junction, 147
DNA metallization, 149
DNA microarrays, 534
DNA nanofabrication, 145–149
DNA origami, 149
DNA self-assembly, 145
DNA structure, 129
Doping, 74, 84, 93
Dose, 425
Dots, 402–404, 415, 417, 420, 424
Double helix, 130

Dry etch, 72
Dynamic stenciling, 512, 521

EBID, 399–418, 421–426
EBID applications, 413, 424
EBID depositions, 417
EBL, 399, 424–426
EDX, 405, 406
EELS, 406, 417, 421, 422
EID (Exposure Intensity Distribution), 354–356
Elastic collisions, 436, 440, 460
Elastic scattering, 344, 345, 411
Electrical contacts, 424
Electrochemical deposition, 169
Electrochemical sensing, 93
Electrodeposition, 187, 191, 198
Electron beam, 399–402, 404–406, 409–411, 414–416, 421, 424
Electron beam lithography, 399, 424, 473, 543, 546, 554
Electron current distribution, 408
Electron detection, 405
Electron Detector, 405
Electron diffraction, 411
Electron energy, 408–410, 413, 415, 421
Electron energy-loss spectroscopy, 406
Electron irradiation, 402, 417, 420–422
Electron precursor interactions, 407
Electron probe, 401, 406–409, 411, 424
Electron probe formation, 401, 407, 408
Electron substrate interactions, 407
Electron transistor, 424
Electron wavefunction, 408
Electron wavevector, 408
Electron-beam specimen interaction, 399
Electron-beam-induced deposition, 400, 401
Electron-beam-induced deposition, 399
Electron-gas scattering, 410
Electron-solid-gas interactions, 407
Electronic excitations, 411
Electronic noise, 77
Electronic structure, 417
Electrospinning, 191, 192
Electrostatic deflector, 348
Electrostatic forces, 141
Electrostatic lens, 347
Emission, 401
Energy landscape, 202, 203
Energy-dispersive x-ray spectroscopy, 405
Enthalpy, 142
Entropy, 142
Environmental cell, 406
Environmental scanning transmission electron microscope, 402
Escape depth, 417
Etching, 424, 426
Etching gases, 426
Evanescent wave, 228–230
Excited molecule, 402
Exposure dose, 425
Exposure time, 404
External sensing, 76, 83, 114
Extreme ultraviolet, 237, 238

Fabrication, 399–401, 403, 405, 407, 409, 413, 417, 424
FEI F20 Tecnai, 406
Ferroelectric, 87, 106, 108, 516, 517, 533, 534
Ferromagnetic ceramics, 473
FIB, 431–436, 444–454, 456–458, 461–465
Field effect transistors, 199, 204
Field emission electron source, 402
Field emission tips, 424
Field emitter arrays, 424
Field emitters, 424
Field-emission gun, 405, 407
Flicker noise, 85
Flux of electrons with energy E, 415
Focus, 408
Focused Electron Beam (FEB), 72, 73, 399–401, 411, 421
Focused Ion Beam (FIB), 72, 73, 101, 109, 400, 406, 425, 431, 432, 434, 511, 543, 557, 558
Focusing lens, 405, 407
Force Distance Curves (FDC), 103, 105
Formation of subnanometer electron probes, 407
Forward scattering (electrons), 355
Fragment, 400, 409, 411

GaAs/AlGaAs, 549, 550
Gallium ions implanted, 400
GaN, 417, 419, 420
Gas Injector, 405
Gas layer, 407
Gas source, 405

Gas systems, 406
Gas-solid reactions, 399
Gaseous precursor, 400, 401, 405, 409
Gasify the carbon, 422
Gaussian beam, 342, 343, 347–350
Ge, 420
Genetic code, 132
Geometrical optics, 352, 353
Germane, 409, 410
GHOST, 357, 358
Gibbs free energy, 142
Glass nanowires, 213–215, 220–222, 227–230
Glycerol, 110
Gold, 190, 197
Gold binding polypeptide (GBP), 151
Gold-palladium, 424
Graphene component, 421
Growth rate, 407
Gryzinski formula, 345
Guanine (G), 130

Heated substrates, 417
Heterodyne, 82, 83, 98
High and ultra-high vacuum, 503
High resolution, 400, 401, 404, 415
High Resolution EBID, 406, 407, 415, 416
High-brightness, 405, 407, 424, 426
High-energy electron beams, 400, 415
High-energy primary electrons, 410, 411, 415
High-energy subnanometer focused electron beams, 399
High-resolution EBID, 401, 405–408, 421, 424
High-resolution objective lens, 405
Holliday junction, 145
Homodyne, 82
HSQ (hydrogen silsesquioxane), 365–367
Hydrocarbon, 401
Hydrocarbon species, 421
Hydrogen, 422
Hydrogen bond, 130, 140
Hydrophobic, 196
Hydrophobic forces, 141

Imaging systems, 405
Implantation of gallium ions, 424
Imprint, 500, 502, 503, 522–524, 526, 529–535
In situ, 406, 425
Inelastic collision, 436, 440, 461
Inelastic scattering, 344, 345, 411
Injection needle, 406
Injection systems, 406
Inner shell electron, 344
Inorganic resist, 344, 363
Insulators, 535
Interaction of electron probe with substrate, 411
Interaction of electrons with molecular precursors on surfaces, 409
Interferometry, 75, 82, 83
Into subnanometer, 409
Ion beam induced deposition, 399, 400
Ion probe sizes, 425
Ionization, 409–411, 417
Ionization cross section, 409–411
Ionization of the precursor, 409, 410
Ionization potential, 409, 411
Irradiated area, 416
Irradiation by the primary electron, 410

Knife-edge, 350–352

LaB_6, 347
Langmuir-Blodgett, 196
Large Scale Integration, 543, 561
Laser ablation, 192
Laser interference lithography, 505, 507
Laser plasma source, 249
Laser processing, 475, 476
Laser-induced plasma – assisted ablation, 476
Latent image, 343, 357, 360
Laterally, 417
LER (line-edge roughness), 359
Lindhard dielectric function, 346
Lithography, 399, 400, 424–426
Lithography masks, 424
Localized, 402
Low-energy electrons, 410–412
Low-energy secondary electrons, 410, 411

Magnetic, 194, 195
Magnetic deflector, 347, 348
Magnetic force microscopy, 424, 517
Magnetic lens, 347
Magnetic stress sensor, 92
Magnetic tips, 424

Magnetostriction, 92
Magnetostrictive, 83, 93
Mask repair, 400, 424
Mass deposition, 400, 417
Mean free path, 345–348, 412, 415
Mechanism for dissociation, 410
Membranes, 499, 502, 504, 505, 509–511, 513, 514
MEMS/NEMS, 499, 501
Microcontact printing, 477, 480
Microelectromechanical Systems (MEMS), 544
Microfluidic channel, 112
Micromanipulation, 222–224
Micromolding, 471, 480, 481, 484, 488–492
Micromolding in capillaries, 480, 481
Microtransfer molding, 480
Milling, 425
Millipede, 106, 107, 114
Miniaturization, 499, 501, 502, 535
Mo/Si multilayer, 249, 256, 259, 260, 262, 263, 269
Modeling, 409
Molds, 500, 502, 503, 525, 526, 528, 531, 533
Molecular devices, 520
Molecular fragmentation, 411
Molecular precursor, 480, 481
Monolayer–Directed Patterned Deposition, 476
Monte Carlo simulation (of electron scattering), 344, 346, 350, 351, 355, 365, 366, 372
Monte Carlo simulations, 413, 414, 416
Morphology, 405
MOSFET, 85, 86
Mould, 69, 71–74
Multi-Wall Carbon Nano Tubes (MWCNT), 71, 87, 91, 92
Multifunctional oxides, 474
Multilevel patterning, 524, 529
Multiple electron beams in parallel, 400
Multiple scattering processes, 413
Multipole lens, 347
Mutation, 134

Nano-Patterning, 171, 179
Nano-sensors, 517
Nano-transistors, 153
Nanoarchitectures, 485
Nanoelectronics, 531, 533
Nanofabrication, 400, 401, 409
Nanofiber, 556, 557
Nanoimprint Lithography, 543, 554–556
Nanoimprinting, 483
Nanomachining, 472
Nanometer resolution, 402
Nanopatterning, 472, 474, 486
Nanoscale resolution, 473, 492, 493
Nanosecond laser ablation, 476
Nanostructured alumina, 488
Nanostructures, 399, 401, 402, 406, 407, 422–425
Nanotube, 543, 553, 554
Nanowire, 543, 553, 554
Nanoworld, 402, 403
NEB, 363
Needle, 406
Noise, 69, 79–83, 85, 86, 92, 93, 98
Non-cylindrical symmetry, 406
Non-planar substrates, 403
Non-volatile, 402, 409, 415, 417, 420
Non-volatile components, 400, 402, 409, 415, 417, 420
Nonvolatile, 400, 417, 420
Nucleotide, 130, 134

Objective lens, 405, 407–409
Oligonucleotide synthesis, 143
Optical loss, 214, 226–230
Optical path difference (OPD), 82, 83
Optical traps, 195
Optimum aperture, 409
Ordered array, 417
Organic films, 411
Organic thin films, 528
Overlay, 354, 361, 362, 366, 367, 369, 370
Oxidation sharpening, 74
Oxidization environments, 422

Partial wave expansion, 345
Pattern-edge roughness, 359, 363–365
Peptide immobilization, 152
Phage display (PD), 151
Phase shifts into, 408
Phosphodiester bond, 130
Photo-enhanced CVD, 411
Photonic circuits, 530, 531
Physical deposition methods, 491, 492

Physical vapor deposition, 488, 500, 503, 506, 514
Piezoelectric effect, 84, 86
Piezoresistive coefficient, 84, 86
Piezoresistive effect, 74, 84
Piezoresponse force microscopy, 516
Pillar, 416, 417
Plane wave, 407
Plasma etching, 519, 526
PMMA (polymethylmethacrylate), 346
Poisson statistics, 404
Polymer, 69, 71, 73, 85, 110, 114, 524–527, 529, 531
Polymer films, 401
Polymerase chain reaction (PCR), 144
Polyvinylpyrrolidone, 190
Post deposition processing, 422
Potassium Hydroxide (KOH), 71
Precursor, 399–407, 409–413, 415–418, 420–426
Precursor molecules, 402, 415
Precursor pressure, 404, 415, 416
Primary protein structure, 136
Probe formation, 401, 407, 408
Probe forming aperture, 407
Protein, 129, 135
Protein and DNA microarrays, 534
Protein folding, 142
Protein nanofabrication, 149–152
Protein structure, 136
Proximity effect, 343, 344, 348, 354, 355, 357–359
Proximity effect correction, 348, 355–358
$Pt(CH_3)_3CH_3C_5H_4$, 402, 421, 422
Pulsed laser deposition, 490, 504, 510, 513–515
PVP, 190

Quantum dots (QDs), 152
Quaternary protein structure, 140

Rate, 401, 406, 407, 409, 413, 415–417, 422
Rectification, 182
Reflection optics, 267
Reflow, 198
Relaxation processes, 411
Repair, 400, 424
Replication, 71, 73, 129, 134, 488, 489
Residence time, 422
Resist, 399, 400, 425
Resist-based lithography, 400
Resistors, 424
Resolution, 401
Resonance frequency, 69, 75, 78, 87, 99, 544, 545, 547, 558
Resonant, 544
RNA, 129, 134
Roughness, 196

Sacrificial layer, 70, 73
Scanning Coils, 405
Scanning Electrochemical Microscopy (SECM), 68, 93, 94, 100, 101, 112
Scanning electron microscope, 401, 405
Scanning Probe Methods (SPM), 68, 69, 72, 74, 75, 78, 103, 108, 113, 114
Scanning probe microscopy tips, 424
Scanning system, 405
Scanning Thermal Microscopy (SThM), 68, 95, 96, 102
Scanning transmission electron microscope (ESTEM), 402
Scanning transmission electron microscope (STEMs), 406
Scanning Tunnelling Microscopy (STM), 68, 93, 106
Scattered transmitted electrons, 406
Scattering probabilities, 413
Scattering processes, 411, 413
Schottky emitter, 347
Screened Rutherford, 345
Secondary electron generation, 401
Secondary electrons, 401, 405, 409–416
Secondary protein structure, 138
Self sensing, 76, 83, 88, 91, 93, 100, 114
Self supporting structures, 403
Self-assembled monolayers, 73, 111, 476, 477, 480, 489
Self-assembly, 471, 484–487, 492
Self-organization, 485, 487, 492
SEM, 401, 404–406, 409, 413
Semiconductor, 188, 195, 197, 199, 200, 500, 503, 505, 523, 524, 528, 530, 535, 536
Semiconductor quantum dots, 424
Sensitivity, 69, 76–80, 85–87, 89, 91, 93, 97, 99, 114
Sensitivity (of resist), 349, 350
Sensitivity curve, 364

Shadow-mask, 500, 503–505, 510–512, 521
Shot noise, 425
Shot noise (effect), 359
Shot noise limit, 425
Si substrate, 417
Si_3N_4, 402, 421, 424
Si_3N_4 substrate, 402
Signal-to-noise ratio, 425
Silicon, 543, 546, 547, 550, 551, 555–557, 559, 561, 562
Silicon carbide, 543, 546, 551
silicon microfabrication, 506
Silicon nitrate (Si_xN_y), 71, 74, 86, 93
Silicon nitride, 543, 546, 550, 551, 556, 559
Silicon oxide (SiO_2), 71–73, 88, 89, 99
Silver particles, 424
Simulating, 410
Simulation, 409, 413, 414, 416
Single electron circuits, 363
Single electron devices, 363, 366, 367, 369
Single electron devices/circuits, 362
Single electron transistor, 366, 367
Single-Wall Carbon Nano Tubes (SWCNT), 71, 90–92
Sol gel techniques, 480
Sol–gel films, 484
Sol-gel synthesis, 169
Solar cells, 201
Solid phase peptide synthesis (SPPS), 144
Space charge effect, 352
Spatial distribution, 401, 409, 412–415
Spatial distribution of emitted secondary electrons, 414
Spatial resolution, 401, 409, 412, 417, 420, 422
Spectral density, 78
Spherical aberration, 347, 352, 408, 409
Sputtering, 432, 436, 437, 440, 442–444, 446, 448–450, 455, 456, 461, 465
Stamps, 502, 524, 529, 531
Stannous chloride precursor, 401
Static stenciling, 505
Statistical variation, 425
STEM, 403, 404, 406, 408
Stencil Lithography, 558–562
Sticking coefficient, 416, 417
Stitching, 354, 362
Stochastic interaction, 352
Stop codon, 135
Stress, 75, 76, 83–86, 88–92, 97, 100
Subnanometer electron probes, 407
Substrate surface, 400, 402, 406, 415, 422
Substrate thickness, 414, 415
Subwavelength, 214, 215, 217, 227, 230, 231
Super-secondary protein structure, 139
Superconducting tin films, 401
Supercritical, 189
Surface, 399–402, 406, 409–416, 420–422, 424, 426
Surface functional groups, 477, 478
Surface nanomachining, 546
Surface tension, 192, 196
Surfactants, 190, 191, 196
Syringe-type gas supply, 406

Tail, 408, 409, 415
Taper-drawing method, 214, 215, 223
Tapping mode, 96, 113
Tecnai, 406
Templates, 424
TEMs, 409
Tertiary protein structure, 140
Thermal decomposition, 417, 420
Thermal dissociation, 417, 420
Thermal emitter, 347
Thermal field emitter, 347
Thermal noise, 77, 78
Thermal sensing, 95, 107
Thickness dependence, 415
Thymine (T), 130
Tip-surface interaction, 76, 93
Tomographic imaging, 94
Top-down, 499, 501, 505, 535
Topographical imaging, 94–96
Transcription, 129, 134
Translation, 129, 135
Transmission electron, 347, 350, 370
Transmission electron microscope, 402, 406, 409
Transmission function, 353
Transmittance, 351
Tungsten-based precursor, 402

UHV, 421
Ultra-high-resolution EBID, 408
Ultrahigh vacuum, 421
Universal curves, 412
Universal genetic code, 133
UV light, 400, 411

Vacuum-assisted microfluidic lithography, 483
Valence band electrons, 344, 346
Van der Waals forces, 142
Vapor pressures, 417
Vapor-liquid-solid, 187, 189, 190
Variable shaped beam, 342, 343, 347, 348
Virus, 192, 194, 200
VLS, 187, 189, 190
Volatile, 400, 402, 417, 422
Volatile component, 400, 402, 417
Voltammetry, 101

$W(CO)_6$, 404, 416, 419, 420
Water, 422
Wave function, 408
Wave guide, 88–91
Wave mechanical, 407, 408
Wave optics, 353, 354
Wet etch, 71, 72
Windowed cells, 406
World, 402, 403, 407

Y-junction carbon nanotube arrays, 181
Yield, 201, 202, 204

Z-contrast images, 403, 404, 406, 417, 420
Z-contrast STEM, 403, 404
ZEP, 360, 363
Zr/O/W, 347

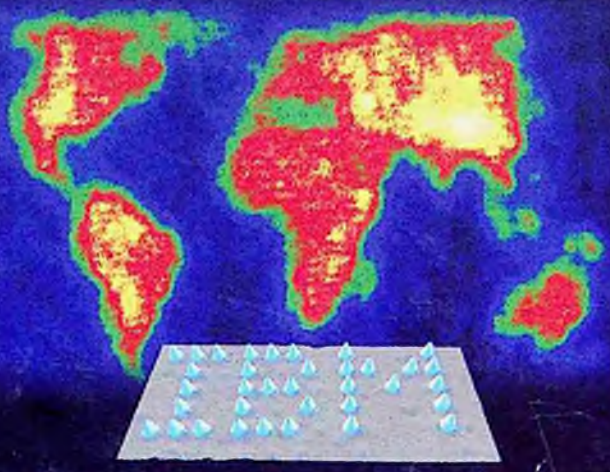

Nanofabrication

Fundamentals and Applications

Many of the devices and systems used in modern industry are becoming progressively smaller and have reached the nanoscale domain. Nanofabrication aims at building nanoscale structures, which can act as components, devices, or systems, in large quantities at potentially low cost. Nanofabrication is vital to all nanotechnology fields, especially for the realization of nanotechnology that involves the traditional areas across engineering and science. This is the first book solely dedicated to the manufacturing technology in nanoscale structures, devices, and systems and is designed to satisfy the growing demands of researchers, professionals, and graduate students.

Both conventional and non-conventional fabrication technologies are introduced with emphasis on multidisciplinary principles, methodologies, and practical applications. While conventional technologies consider the emerging techniques developed for next generation lithography, non-conventional techniques include scanning probe microscopy lithography, self-assembly, and imprint lithography, as well as techniques specifically developed for making carbon tubes and molecular circuits and devices.

Top: "World map"
Front page picture is a nanoscale map of the world drawn using electron beam induced deposition (EBID) with W based precursor on silicon nitride substrate (courtesy of P. A. Crozier and W. van Dorp, see Chapter 12).

Bottom: "IBM"
STM image of lateral manipulation of xenon atoms on nickel(110) surface by STM in writing company logo of "IBM" by D. M. Eigler and E. K. Schweizer (courtesy of IBM Research, Almaden Research Center, see Chapter 1).

World Scientific
www.worldscientific.com
6276 hc

ISBN-13 978-981-270-076-6
ISBN-10 981-270-076-5
9 789812 700766